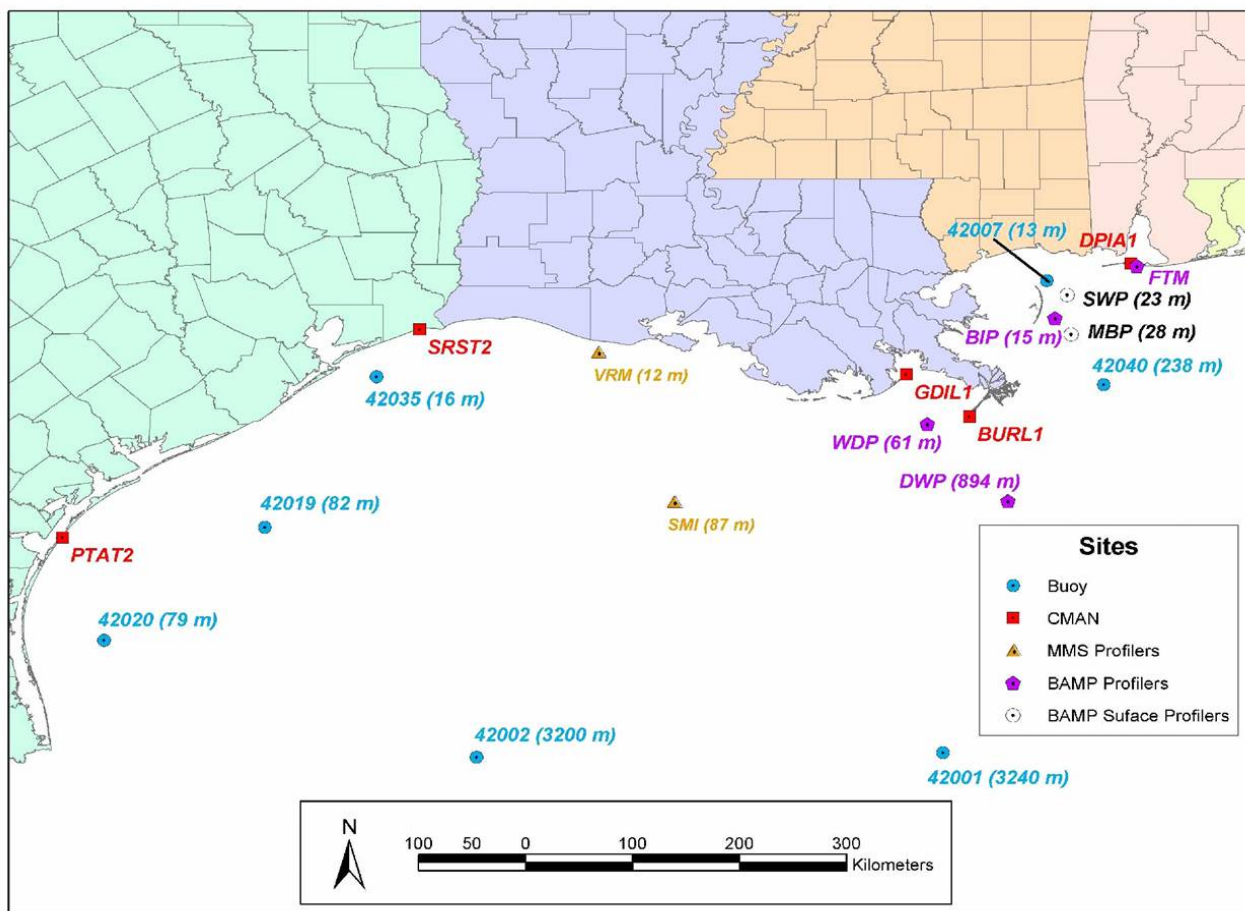




# Boundary Layer Study in the Western and Central Gulf of Mexico

## Final Report



# Boundary Layer Study in the Western and Central Gulf of Mexico

## Final Report

### Authors

Clinton P. MacDonald  
Paul T. Roberts  
Mark R. Lilly  
Charley A. Knoderer  
Dianne S. Miller  
Sonoma Technology, Inc.  
Petaluma, California

Steven R. Hanna  
Hanna Consultants  
Kennebunkport, Maine

Prepared under MMS Contract  
1435-01-99-CT-30919  
by  
Sonoma Technology, Inc.  
1360 Redwood Way, Suite C  
Petaluma, California 94954-1169

Published by

**U.S. Department of the Interior  
Minerals Management Service  
Gulf of Mexico OCS Region**

**New Orleans  
October 2004**

## **DISCLAIMER**

This final report was prepared under contract between the Minerals Management Service (MMS) and Sonoma Technology, Inc. This Final Report has been technically reviewed by the MMS, and it has been approved for publication. Approval does not signify that the contents necessarily reflect the views and policies of the MMS, nor does mention of trade names or commercial products constitute endorsement or recommendation for use. It is, however, exempt from review and compliance with the MMS editorial standards.

## **REPORT AVAILABILITY**

Extra copies of this report may be obtained from the Public Information Office (Mail Stop 5034) at the following address:

U.S. Department of the Interior  
Minerals Management Service  
Gulf of Mexico OCS Region  
Public Information Office (MS 5034)  
1201 Elmwood Park Boulevard  
New Orleans, Louisiana 70123-2394

Telephone: (504) 736-2519 or  
1-800-200-GULF

## **CITATION**

Suggested citation:

MacDonald C.P., P.T. Roberts, M.R. Lilly, C.A. Knoderer, D.S. Miller, and S.R. Hanna. 2004.  
Boundary layer study in the western and central Gulf of Mexico: final report.  
U.S. Dept. of the Interior, Minerals Management Service, Gulf of Mexico OCS Region,  
New Orleans, LA. OCS Study MMS 2004-060. 606 pp.

## ACKNOWLEDGMENTS

This research was sponsored by the Minerals Management Service of the U.S. Department of Interior. We thank the current Contracting Officer's Technical Representative (COTR), Dr. C.H. Huang, and Dr. Alexis Lugo-Fernandez the COTR early in the study, for their support and technical advice. We appreciate the technical advice from the Scientific Review Board, Dr. Stephen Burk, Dr. S.A. Hsu, and Dr. Richard McNider, and one of the developers of the COARE model, Dr. Christopher Fairall. We acknowledge the hard work and assistance given by numerous persons responsible for meteorological data collection, validation, and processing. We thank Lisa DiStefano, Jana Schwartz, and Sandy Smethurst of STI for editing and producing this report, and Jeffrey Prouty, Timothy Dye, and Eric Gray of STI for their invaluable role in designing the database and the data visualization tool.

# TABLE OF CONTENTS

<u>Section</u>	<u>Page</u>
ACKNOWLEDGMENTS .....	v
LIST OF FIGURES .....	xi
LIST OF TABLES .....	xxvii
LIST OF VARIABLES.....	xxix
EXTENDED ABSTRACT .....	EA-1
EA.1 Deliverables and Conclusions.....	EA-1
EA.2 Recommendations.....	EA-3
1. INTRODUCTION .....	1-1
2. DATA AVAILABILITY AND VISUALIZATION TOOL.....	2-1
2.1 Available Data .....	2-1
2.1.1 Aloft Meteorological Measurements .....	2-1
2.1.2 Surface Meteorological Measurements.....	2-2
2.1.3 Model Simulations .....	2-2
2.1.4 Derived Data .....	2-2
2.1.5 Data Classifications .....	2-3
2.1.6 Averaged Aloft Data.....	2-3
2.2 Data Validation Objectives and Results .....	2-3
2.3 Environmental Data Analysis Tool (EDAT) .....	2-4
3. GENERAL METEOROLOGY .....	3-1
3.1 Introduction.....	3-1
3.2 Upper-air patterns .....	3-1
3.2.1 Methods of Obtaining and Classifying Data.....	3-1
3.2.2 Data Classification Results .....	3-3
3.3 Surface Flow Characteristics .....	3-5
3.3.1 Methods of Determining Surface Flow Characteristics.....	3-5
3.3.2 Results of Determining Surface Flow Characteristics .....	3-6
4. UPPER-AIR WINDS AND VIRTUAL TEMPERATURES .....	4-1
4.1 RWP and RASS Data.....	4-1
4.2 Profiler Results and Interpretations .....	4-1
4.2.1 Overall Average Wind Profiles.....	4-2
4.2.2 Yearly Wind Profiles .....	4-2
4.2.3 Seasonal Wind Profiles .....	4-3
4.2.4 Monthly Wind Profiles .....	4-3
4.2.5 Wind Profiles by Upper-air Classification.....	4-4

## TABLE OF CONTENTS (Continued)

<u>Section</u>	<u>Page</u>
4.3	RASS Results and Interpretations..... 4-5
4.3.1	Overall Average Temperature Profiles ..... 4-5
4.3.2	Yearly Average Virtual Temperature Profiles ..... 4-6
4.3.3	Seasonal Virtual Temperature Profiles ..... 4-7
4.3.4	Virtual Temperature Profiles by Upper-air Classification..... 4-7
4.3.5	Caveats..... 4-8
5.	CHARACTERIZATION OF THE SURFACE FLUXES AND OTHER PARAMETERS IN THE ATMOSPHERIC BOUNDARY LAYER USING THE COARE ALGORITHM ..... 5-1
5.1	Summary of COARE Program Versions and Modifications ..... 5-1
5.2	Background on the COARE Model ..... 5-2
5.3	Implementation of the COARE Program..... 5-6
5.4	Comparison of COARE Measurements with TOGA-COARE Measurements ..... 5-6
5.5	Application of the COARE Program to Data Collected in the Gulf of Mexico ..... 5-7
5.6	Climatological Results ..... 5-9
5.6.1	COARE Results Grouped by Monthly Averages ..... 5-9
5.6.2	COARE Results Grouped by Synoptic Class and General Flow Direction ..... 5-12
5.6.3	Diurnal Variations by Month ..... 5-16
5.7	Case Study Analyses..... 5-18
5.7.1	Analysis of January 20-25, 2000 ..... 5-19
5.7.2	Analysis of January 4-6, 2001 ..... 5-21
5.7.3	Analysis of July 30-August 1, 1999..... 5-23
5.7.4	Analysis of September 18-20, 2001 ..... 5-25
5.7.5	Summary of Results of Four Case Studies ..... 5-27
6.	METEOROLOGICAL AND AIR QUALITY MODELING ..... 6-1
6.1	Radar Wind Profiler – EDAS Comparison..... 6-1
6.1.1	Method ..... 6-1
6.1.2	Results..... 6-3
6.1.3	Conclusions..... 6-4
6.2	CALMET Meteorological Modeling ..... 6-4
6.2.1	High Frequency RWP and RASS Measurements and Data Manipulation for Input to CALMET ..... 6-6
6.3	CALPUFF Dispersion Modeling ..... 6-8
6.4	Transport Analysis ..... 6-9

## TABLE OF CONTENTS (Concluded)

<u>Section</u>	<u>Page</u>
6.5 Case Studies.....	6-9
6.5.1 July 30–August 1, 1999: Summer Period with Strong Upper-Level Ridge and Surface High Causing Weak Winds.....	6-10
6.5.2 January 20-25, 2000: Winter Case Study with Shift in Wind Direction.....	6-11
6.5.3 January 4-6, 2001: Winter Period Post Upper-level Trough Transitioning into Weak Upper-level Ridge.....	6-13
6.5.4 January 29, 2001: Winter Case with Strong Southerly Winds .....	6-14
6.5.5 April 14-15, 2001: Onshore Wind Case Study .....	6-15
6.5.6 May 14-15, 2001: Spring Case Study with Light Winds and Regional High Ozone.....	6-16
6.5.7 September 18-20, 2001: Nearly Stationary Front Along the Gulf Coast.....	6-17
6.6 Conclusions.....	6-19
7. SUMMARY OF MAJOR FINDINGS AND RECOMMENDATIONS .....	7-1
7.1 Summary of Findings.....	7-1
7.1.1 Data and Data Viewer (Section 2) .....	7-1
7.1.2 Atmospheric Boundary Layer Characteristics (Sections 3-5) .....	7-2
7.1.3 Wind Fields, Transport, and Dispersion (Section 6).....	7-9
7.2 Recommendations.....	7-11
8. REFERENCES .....	8-1
APPENDIX A: EDAT DATABASE FORMAT .....	A-1
APPENDIX B: COARE DOCUMENTATION FROM NOAA’S FTP SITE .....	B-1
APPENDIX C: COARE FORTRAN CODE.....	C-1
APPENDIX D: BOUNDARY LAYER STUDY IN THE WESTERN AND CENTRAL GULF OF MEXICO FINAL MEETING, OCTOBER 15-16, 2003 .....	D-1

## LIST OF FIGURES

<b><u>Figure</u></b>	<b><u>Page</u></b>
2-1. Map of the MMS study region depicting locations of C-MAN, buoy, and RWP platform monitors .....	2-6
2-2. SMI offshore oil platform showing the RWP and RASS upper-air measurement systems .....	2-7
2-3. EDAT screen shot showing a spatial plot, time series plots, the time-height cross-section, and the vertical profile .....	2-8
2-4. Sequence of events for creating a time series plot in EDAT: open a new time series graph, select data to be displayed, and create the plot .....	2-9
3-1. An upper-level high pressure system with ridge axis .....	3-8
3-2. Example of an upper-air ridge pattern for the Gulf of Mexico region for March 22, 2000, at 1200 UTC (0600 CST) .....	3-9
3-3. Example of an upper-air weak ridge pattern for the Gulf of Mexico region for July 30, 1998, at 1200 UTC (0600) CST).....	3-10
3-4. Example of an upper-air trough pattern for the Gulf of Mexico region for January 5, 1999, at 0000 UTC (January 4, 1999, at 1800 CST).....	3-11
3-5. Example of an upper-air weak trough pattern for the Gulf of Mexico region for May 31, 1999, at 0000 UTC (May 30, 1999, at 1800 CST).....	3-12
3-6. Example of an upper-air cut-off low pattern for the Gulf of Mexico region for March 30, 1999, at 0000 UTC (March 29, 1999, at 1800 CST).....	3-13
3-7. Example of an upper-air post-trough pattern for the Gulf of Mexico region for December 18, 1998, at 0000 UTC (December 17, 1998, at 1800 CST).....	3-14
3-8. Example of an upper-air flat pattern for the Gulf of Mexico region for October 1, 2000, at 1200 UTC (0600 CST).....	3-15
3-9. Example of an upper-air zonal pattern for the Gulf of Mexico region for November 15, 2000, at 0000 UTC (November 14, 2000, at 1800 CST).....	3-16
3-10. Example of an upper-air hurricane pattern for the Gulf of Mexico region for August 23, 1999, at 0000 UTC (August 22, 1999, at 1800 CST).....	3-17
3-11. Overall frequency distribution of grouped upper-air patterns observed for the study period.....	3-18
3-12. Frequency distribution of upper-air patterns observed for the study period.....	3-18
3-13. Frequency distribution of grouped upper-air patterns observed for each MMS year, June through May, during the study period .....	3-19
3-14. Frequency distribution of nine upper-air patterns observed for each MMS year during the study period .....	3-20

## LIST OF FIGURES (Continued)

<b><u>Figure</u></b>	<b><u>Page</u></b>
3-15. Frequency distribution of grouped upper-air patterns observed for each season for all years during the MMS study period.....	3-21
3-16. Frequency distribution of nine upper-air patterns observed for each season for all years during the MMS study period.....	3-22
3-17. Frequency distribution of grouped upper-air patterns observed for each month for all years during the MMS study period.....	3-22
3-18. Wind rose plot for the SMI platform for the study period.....	3-23
3-19. Monitoring sites in the Gulf of Mexico region .....	3-24
3-20. Yearly frequency distributions of surface wind direction and surface wind speed and for the near-shore site, buoy 42035, and the offshore site, SMI .....	3-24
3-21. Frequency distribution of seasonal surface flow directions for near-shore and offshore sites .....	3-25
3-22. Frequency distribution of surface flow typing for upper-air ridge, upper-air trough, and other upper-air patterns at the four selected sites during the MMS study period.....	3-26
3-23a. Wind rose for VRM .....	3-27
3-23b. Wind rose for buoy 42040 .....	3-28
3-24. Spatial plot depicting wind roses for Group A and Group B for the fall season .....	3-29
3-25. Spatial plot depicting wind roses for Group A and Group B for the winter season .....	3-30
3-26. Spatial plot depicting wind roses for Group A and Group B for the spring season .....	3-31
3-27. Spatial plot depicting wind roses for Group A and Group B for the summer season....	3-32
4-1. Overall average winds at SMI from 0000 to 2300 CST, June 1, 1998, to May 31, 2001 .....	4-9
4-2. Overall average winds at VRM from 0000 to 2300 CST, June 1, 1998, to May 31, 2001 .....	4-9
4-3. 1998 year average winds at SMI from 0000 to 2300 CST, June 1, 1998, to May 31, 1999 .....	4-10
4-4. 1998 year average winds at VRM from 0000 to 2300 CST, June 1, 1998, to May 31, 1999 .....	4-10
4-5. 1999 year average winds at SMI from 0000 to 2300 CST, June 1, 1999, to May 31, 2000 .....	4-11
4-6. 1999 year average winds at VRM from 0000 to 2300 CST, June 1, 1999, to May 31, 2000 .....	4-11

## LIST OF FIGURES (Continued)

<b><u>Figure</u></b>	<b><u>Page</u></b>
4-7. 2000 year average winds at SMI from 0000 to 2300 CST, June 1, 2000, to May 31, 2001 .....	4-12
4-8. 2000 year average winds at VRM from 0000 to 2300 CST, June 1, 2000, to May 31, 2001 .....	4-12
4-9. Fall average winds at SMI from 0000 to 2300 CST, September 24 to December 22, for all study years.....	4-13
4-10. Fall average winds at VRM from 0000 to 2300 CST, September 24 to December 22, for all study years.....	4-13
4-11. Winter average winds at SMI from 0000 to 2300 CST, December 23 to March 21, for all study years.....	4-14
4-12. Winter average winds at VRM from 0000 to 2300 CST, December 23 to March 21, for all study years.....	4-14
4-13. Spring average winds at SMI from 0000 to 2300 CST, March 22 to June 22, for all study years .....	4-15
4-14. Spring average winds at VRM from 0000 to 2300 CST, March 22 to June 22, for all study years.....	4-15
4-15. Summer average winds at SMI from 0000 to 2300 CST, June 23 to September 23, for all study years.....	4-16
4-16. Summer average winds at VRM from 0000 to 2300 CST, June 23 to September 23, for all study years.....	4-16
4-17. Ridge pattern average winds at SMI from 0000 to 2300 CST, for all study years.....	4-17
4-18. Ridge pattern average winds at VRM from 0000 to 2300 CST, for all study years.....	4-17
4-19. Weak ridge average winds at SMI, 0000 to 2300 CST, for all study years.....	4-18
4-20. Weak ridge average winds at VRM, 0000 to 2300 CST, for all study years.....	4-18
4-21. Weak trough average winds at SMI, 0000 to 2300 CST, for all study years.....	4-19
4-22. Weak trough average winds at VRM, 0000 to 2300 CST, for all study years.....	4-19
4-23. Trough average winds at SMI, 0000 to 2300 CST, for all study years.....	4-20
4-24. Cut-off low average winds at SMI, 0000 to 2300 CST, for all study years.....	4-20
4-25. Trough average winds at VRM, 0000 to 2300 CST, for all study years.....	4-21
4-26. Cut-off low average winds at VRM, 0000 to 2300 CST, for all study years .....	4-21
4-27. Flat average winds at SMI, 0000 to 2300 CST, for all study years .....	4-22
4-28. Flat average winds at VRM, 0000 to 2300 CST, for all study years .....	4-22
4-29. Zonal average winds at SMI, 0000 to 2300 CST for all study years .....	4-23

## LIST OF FIGURES (Continued)

<b><u>Figure</u></b>	<b><u>Page</u></b>
4-30. Zonal average winds at VRM, 0000 to 2300 CST, for all study years.....	4-23
4-31. Post-trough average winds at SMI, 0000 to 2300 CST, for all study years.....	4-24
4-32. Post-trough average winds at VRM, 0000 to 2300 CST, for all study years.....	4-24
4-33. Tropical storm average winds at SMI, 0000 to 2300 CST, for all study years.....	4-25
4-34. Tropical storm average winds at VRM, 0000 to 2300 CST, for all study years.....	4-25
4-35. Average overall daytime and nighttime $T_v$ profiles at SMI, June 1, 1998, to May 31, 2001 .....	4-26
4-36. Average overall daytime and nighttime $T_v$ profiles at VRM, June 1, 1998, to May 31, 2001 .....	4-26
4-37. 1998 year average daytime and nighttime $T_v$ profiles at SMI, June 1, 1998, to May 31, 1999 .....	4-27
4-38. 1998 year average daytime and nighttime $T_v$ profiles at VRM, June 1, 1998, to May 31, 1999 .....	4-27
4-39. 1999 year average daytime and nighttime $T_v$ profiles at SMI, June 1, 1999, to May 31, 2000 .....	4-28
4-40. 1999 year average daytime and nighttime $T_v$ profiles at VRM, June 1, 1999, to May 31, 2000 .....	4-28
4-41. 2000 year average daytime and nighttime $T_v$ profiles at SMI, June 1, 2000, to May 31, 2001 .....	4-29
4-42. 2000 year average daytime and nighttime $T_v$ profiles at VRM, June 1, 2000, to May 31, 2001 .....	4-29
4-43. Fall average daytime and nighttime $T_v$ profiles at SMI, September 24 to December 22 .....	4-30
4-44. Fall average daytime and nighttime $T_v$ profiles at VRM, September 24 to December 22 .....	4-30
4-45. Winter average daytime and nighttime $T_v$ profiles at SMI, December 23 to March 21 .....	4-31
4-46. Winter average daytime and nighttime $T_v$ profiles at VRM, December 23 to March 21 .....	4-31
4-47. Spring average daytime and nighttime $T_v$ profiles at SMI, March 22 to June 22.....	4-32
4-48. Spring average daytime and nighttime $T_v$ profiles at VRM, March 22 to June 22.....	4-32
4-49. Summer average daytime and nighttime $T_v$ profiles at SMI, June 23 to September 23 .....	4-33

**LIST OF FIGURES (Continued)**

<b><u>Figure</u></b>	<b><u>Page</u></b>
4-50. Summer average daytime and nighttime $T_v$ profiles at VRM, June 23 to September 23 .....	4-33
4-51. Ridge average daytime and nighttime $T_v$ profiles at SMI.....	4-34
4-52. Ridge average daytime and nighttime $T_v$ profiles at VRM.....	4-34
4-53. Weak ridge average daytime and nighttime $T_v$ profiles at SMI.....	4-35
4-54. Weak ridge average daytime and nighttime $T_v$ profiles at VRM.....	4-35
4-55. Weak trough average daytime and nighttime $T_v$ profiles at SMI .....	4-36
4-56. Weak trough average daytime and nighttime $T_v$ profiles at VRM .....	4-36
4-57. Trough average daytime and nighttime $T_v$ profiles at SMI .....	4-37
4-58. Trough average daytime and nighttime $T_v$ profiles at VRM .....	4-37
4-59. Cut-off low average daytime and nighttime $T_v$ profiles at VRM .....	4-38
4-60. Flat average daytime and nighttime $T_v$ profiles at SMI.....	4-38
4-61. Flat average daytime and nighttime $T_v$ profiles at VRM.....	4-39
4-62. Zonal average daytime and nighttime $T_v$ profiles at SMI.....	4-39
4-63. Zonal average daytime and nighttime $T_v$ profiles at VRM.....	4-40
4-64. Post-trough average daytime and nighttime $T_v$ profiles at SMI .....	4-40
4-65. Post-trough average daytime and nighttime $T_v$ profiles at VRM .....	4-41
4-66. Tropical storm average daytime and nighttime $T_v$ profiles at VRM .....	4-41
5-1a. COARE monthly average sensible heat fluxes by site for May 1998 through October 2001.....	5-31
5-1b. COARE monthly average sensible heat fluxes by BAMP site for September 2000 through September 2001 .....	5-32
5-2a. COARE monthly average latent heat fluxes by site for May 1998 through October 2001.....	5-33
5-2b. COARE monthly average latent heat fluxes by BAMP site for September 2000 through September 2001 .....	5-34
5-3a. Observed monthly average wind speed by site for May 1998 through October 2001.....	5-35
5-3b. Observed monthly average wind speed by BAMP site for September 2000 through September 2001 .....	5-36
5-4a. Monthly average skin temperature minus air temperature by site for May 1998 through October 2001 .....	5-37

**LIST OF FIGURES (Continued)**

<b><u>Figure</u></b>	<b><u>Page</u></b>
5-4b. COARE monthly average skin temperature minus air temperature by BAMP site for September 2000 through September 2001 .....	5-38
5-5a. COARE monthly average of total heat fluxes by site for May 1998 through October 2001.....	5-39
5-5b. COARE monthly average total heat fluxes by BAMP site for September 2000 through September 2001 .....	5-40
5-6. Eta monthly average latent heat fluxes by site for May 1998 through October 2001, for the 6- to 12-hr forecast .....	5-41
5-7. Eta monthly average sensible heat fluxes by site for May 1998 through October 2001, for the 6- to 12-hr forecast .....	5-42
5-8a. COARE monthly average friction velocity by site for May 1998 through October 2001.....	5-43
5-8b. COARE monthly average friction velocity by BAMP site for September 2000 through September 2001 .....	5-44
5-9. Eta monthly average friction velocity by site for May 1998 through October 2001, for the 6- to 12-hr forecast .....	5-45
5-10a. COARE calculated monthly average temperature scaling parameter by site for May 1998 through October 2001 .....	5-46
5-10b. COARE calculated monthly average temperature scaling parameter by BAMP site for September 2000 through September 2001 .....	5-47
5-11a. COARE calculated monthly average humidity scaling parameter by site for May 1998 through October 2001 .....	5-48
5-11b. COARE calculated monthly average humidity scaling parameter by BAMP site for September 2000 through September 2001 .....	5-49
5-12a. Observed monthly average air temperature by site for May 1998 through October 2001.....	5-50
5-12b. Observed monthly average air temperature by BAMP site for September 2000 through September 2001 .....	5-51
5-13a. Observed monthly average skin temperature by site for May 1998 through October 2001.....	5-52
5-13b. Observed monthly average skin temperature by BAMP site for September 2000 through September 2001 .....	5-53
5-14. Eta average downwelling longwave radiation by synoptic class by site for May 1998 through October 2001, for the 6- to 12-hr forecast.....	5-54
5-15. Eta average shortwave radiation by synoptic class by site for May 1998 through October 2001, for the 6-to 12-hr forecast .....	5-55

**LIST OF FIGURES (Continued)**

<b><u>Figure</u></b>	<b><u>Page</u></b>
5-16a. COARE average humidity scaling parameter by synoptic class by site for May 1998 through October 2001 .....	5-56
5-16b. COARE average humidity scaling parameter by synoptic class by BAMP site for September 2000 through September 2001 .....	5-57
5-17a. COARE average temperature scaling parameter by synoptic class by site for May 1998 through October 2001 .....	5-58
5-17b. COARE average temperature scaling parameter by synoptic class by BAMP site for September 2000 through September 2001 .....	5-59
5-18a. COARE surface roughness by synoptic class by site for May 1998 through October 2001 .....	5-60
5-18b. COARE surface roughness by synoptic class by BAMP site for September 2000 through September 2001 .....	5-61
5-19a. COARE average sensible heat fluxes by synoptic class by site for May 1998 through October 2001 .....	5-62
5-19b. COARE average sensible heat fluxes by synoptic class by BAMP site for September 2000 through September 2001 .....	5-63
5-20a. COARE average latent heat fluxes by synoptic class by site for May 1998 through October 2001 .....	5-64
5-20b. COARE average latent heat fluxes by synoptic class by BAMP site for September 2000 through September 2001 .....	5-65
5-21a. COARE average friction velocity by synoptic class by site for May 1998 through October 2001 .....	5-66
5-21b. COARE average friction velocity by synoptic class by BAMP site for September 2000 through September 2001 .....	5-67
5-22. Observed average wind speed by synoptic class by site for May 1998 through October 2001 .....	5-68
5-23. Eta average downwelling longwave radiation by general flow direction by site for May 1998 through October 2001, for the 6-to 12-hr forecast .....	5-69
5-24. Eta average shortwave radiation by general flow direction by site for May 1998 through October 2001, for the 6-to 12-hr forecast .....	5-70
5-25a. COARE average humidity scaling parameter by general flow direction by site for May 1998 through October 2001 .....	5-71
5-25b. COARE average humidity scaling parameter by general flow direction by BAMP site for September 2000 through September 2001 .....	5-72
5-26a. COARE average temperature scaling parameter by general flow direction by site for May 1998 through October 2001 .....	5-73

**LIST OF FIGURES (Continued)**

<b><u>Figure</u></b>	<b><u>Page</u></b>
5-26b. COARE average temperature scaling parameter by general flow direction by BAMP site for September 2000 through September 2001 .....	5-74
5-27a. COARE average surface roughness by general flow direction by site for May 1998 through October 2001 .....	5-75
5-27b. COARE average surface roughness by general flow direction by BAMP site for September 2000 through September 2001 .....	5-76
5-28a. COARE average sensible heat fluxes by general flow direction by site for May 1998 through October 2001 .....	5-77
5-28b. COARE average sensible heat fluxes by general flow direction by BAMP site for September 2000 through September 2001 .....	5-78
5-29a. COARE average latent heat fluxes by general flow direction by site for May 1998 through October 2001 .....	5-79
5-29b. COARE average latent heat fluxes by general flow direction by BAMP site for September 2000 through September 2001 .....	5-80
5-30a. COARE average friction velocity by general flow direction by site for May 1998 through October 2001 .....	5-81
5-30b. COARE average friction velocity by general flow direction by BAMP site for September 2000 through September 2001 .....	5-82
5-31. Observed average wind speed by general flow direction by site for May 1998 through October 2001 .....	5-83
5-32. COARE hourly average sensible heat fluxes over buoy 42001 for May 1998 through October 2001 .....	5-84
5-33. COARE hourly average sensible heat fluxes over SMI for May 1998 through October 2001 .....	5-85
5-34. COARE hourly average friction velocity over SMI for May 1998 through October 2001 .....	5-86
5-35. COARE hourly average latent heat fluxes over VRM for May 1998 through October 2001 .....	5-87
5-36. COARE hourly average sensible heat fluxes over VRM for May 1998 through October 2001 .....	5-88
5-37. Hourly average skin temperature minus air temperature over VRM for May 1998 through October 2001 .....	5-89
5-38. COARE hourly average sensible heat fluxes over buoy 42040 for May 1998 through October 2001 .....	5-90
5-39. COARE hourly average latent heat fluxes over buoy 42040 for May 1998 through October 2001 .....	5-91

**LIST OF FIGURES (Continued)**

<b><u>Figure</u></b>	<b><u>Page</u></b>
5-40. COARE hourly average sensible heat fluxes over GDIL1 for May 1998 through October 2001.....	5-92
5-41. Hourly skin temperature minus air temperature over GDIL1 for May 1998 through October 2001 .....	5-93
5-42. COARE hourly friction velocity over GDIL1 for May 1998 through October 2001.....	5-94
5-43. COARE hourly average latent heat fluxes over GDIL1 for May 1998 through October 2001.....	5-95
5-44. COARE hourly average sensible heat fluxes over BIP for September 2000 through September 2001 .....	5-96
5-45. COARE hourly average latent heat fluxes over BIP for September 2000 through September 2001 .....	5-97
5-46. COARE hourly average friction velocity over BIP for September 2000 through September 2001 .....	5-98
5-47. Hourly skin temperature minus air temperature over BIP for September 2000 through September 2001 .....	5-99
5-48. Observed hourly average wind speed over BIP for September 2000 through September 2001 .....	5-100
5-49. Observed hourly average wind speed over DWP for September 2000 through September 2001 .....	5-101
5-50. COARE hourly average sensible heat fluxes over DWP for September 2000 through September 2001 .....	5-102
5-51. COARE hourly average latent heat fluxes over DWP for September 2000 through September 2001 .....	5-103
5-52. COARE hourly average friction velocity over DWP for September 2000 through September 2001 .....	5-104
5-53. Hourly skin temperature minus air temperature over DWP for September 2000 through September 2001 .....	5-105
5-54. Air and skin temperatures and wind speed at buoy 42040 for January 20 through 25, 2000 .....	5-106
5-55. COARE and Eta hourly sensible heat fluxes at buoy 42040 for January 20 through 25, 2000 .....	5-107
5-56. COARE and Eta hourly latent heat fluxes at buoy 42040 for January 20 through 25, 2000 .....	5-108
5-57. Hourly air and skin temperatures, wind speed, and relative humidity at VRM for January 4 through 6, 2001.....	5-109

**LIST OF FIGURES (Continued)**

<b><u>Figure</u></b>	<b><u>Page</u></b>
5-58. COARE hourly average latent and sensible heat fluxes and friction velocity at VRM for January 4 through 6, 2001 .....	5-110
5-59. Estimated wave height and period, wind speed, and surface roughness length at VRM for January 4 through 6, 2001 .....	5-111
5-60. COARE and Eta latent and sensible heat fluxes at VRM for January 4 through 6, 2001 .....	5-112
5-61. COARE and Eta friction velocity and z/L at VRM for January 4 through January 6, 2001 .....	5-113
5-62a. Hourly air and skin temperatures, wind speed, and relative humidity at VRM for July 30 through August 1, 1999 .....	5-114
5-62b. Hourly air and skin temperatures, wind speed, and relative humidity at SMI for July 30 through August 1, 1999 .....	5-115
5-63a. COARE latent and sensible heat fluxes and friction velocity at VRM for July 30 through August 1, 1999.....	5-116
5-63b. COARE latent and sensible heat fluxes and friction velocity at SMI for July 30 through August 1, 1999.....	5-117
5-64a. Estimated wave height and period, and surface roughness length and wind speed at VRM for July 30 through August 1, 1999 .....	5-118
5-64b. Estimated wave height and period, and surface roughness length and wind speed at SMI for July 30 through August 1, 1999 .....	5-119
5-65a. COARE and Eta latent and sensible heat fluxes at VRM for July 30 through August 1, 1999 .....	5-120
5-65b. COARE and Eta latent and sensible heat fluxes at SMI for July 30 through August 1, 1999 .....	5-121
5-66a. COARE and Eta friction velocity and z/L at VRM for July 30 through August 1, 1999 .....	5-122
5-66b. COARE and Eta friction velocity and z/L at SMI for July 30 through August 1, 1999 .....	5-123
5-67a. Hourly air and skin temperatures, wind speed, and relative humidity at VRM for September 18 through 20, 2001 .....	5-124
5-67b. Hourly air and skin temperatures, wind speed, and relative humidity at SMI for September 18 through 20, 2001 .....	5-125
5-68a. COARE latent and sensible heat fluxes and friction velocity at VRM for September 18 through 20, 2001 .....	5-126
5-68b. COARE latent and sensible heat fluxes and friction velocity at SMI for September 18 through 20, 2001 .....	5-127

**LIST OF FIGURES (Continued)**

<b><u>Figure</u></b>	<b><u>Page</u></b>
5-69a. Estimated wave height and period, wind speed, and surface roughness length at VRM for September 18 through 20, 2001 .....	5-128
5-69b. Estimated wave height and period, wind speed, and surface roughness length at SMI for September 18 through 20, 2001 .....	5-129
5-70a. COARE and Eta latent and sensible heat fluxes at VRM for September 18 through 20, 2001 .....	5-130
5-70b. COARE and Eta latent and sensible heat fluxes at SMI for September 18 through 20, 2001 .....	5-131
5-71a. COARE and Eta friction velocity and z/L at VRM for September 18 through 20, 2001 .....	5-132
5-71b. COARE and Eta friction velocity and z/L at SMI for September 18 through 20, 2001 .....	5-133
6-1. Gulf of Mexico study region with site locations for the six RWPs .....	6-21
6-2. Comparison of RWP wind speeds and directions with EDAS simulations: wind speed and direction mean bias, mean standard deviation, and mean absolute error for all RWP sites shown in Figure 6.1 .....	6-22
6-3. Locations of meteorological stations used to provide inputs to the CALMET diagnostic meteorological model to derive three-dimensional wind fields and other ABL parameters.....	6-23
6-4. CALMET modeling domain for the Gulf of Mexico coastal region from mid-Texas to western Florida; 860 X 560 km; 5-km horizontal grid resolution .....	6-24
6-5. EDAS modeling domain using a horizontal resolution of 40 km.....	6-24
6-6. Standard options for incorporating gridded model output into a CALMET analysis....	6-25
6-7. Locations oil platform where the arbitrary hypothetical tracers were assumed to be emitted for the air quality modeling exercise .....	6-26
6-8. CALMET 24-hr forward trajectory at 10 m based on CALMET diagnostic wind fields for July 29 at 0000 CST through August 1, 1999, at 0800 CST.....	6-27
6-9. HYSPLIT 24-hr forward trajectory at 10 m based on EDAS wind fields for July 29 at 0000 CST through August 1, 1999, at 0800 CST .....	6-27
6-10. CALMET 24-hr forward trajectory at 75 m based on CALMET diagnostic wind fields for July 29 at 0000 CST through August 1, 1999, at 0800 CST .....	6-28
6-11. HYSPLIT 24-hr forward trajectory at 75 m based on EDAS wind fields for July 29 at 0000 CST through August 1, 1999, at 0800 CST .....	6-28
6-12. CALMET 24-hr forward trajectory at 350 m based on CALMET diagnostic wind fields for July 29 at 0000 CST through August 1, 1999, at 0800 CST.....	6-29

## LIST OF FIGURES (Continued)

<u>Figure</u>	<u>Page</u>
6-13. HYSPLIT 24-hr forward trajectory at 350 m based on EDAS wind fields for July 29 at 0000 CST through August 1, 1999, at 0800 CST .....	6-29
6-14. CALPUFF dispersion simulations for hypothetical tracers originating from SMI, DWP, and BIP ending on July 30, 1999, at 2200 CST .....	6-30
6-15. CALPUFF dispersion simulations for hypothetical tracers originating from SMI, DWP, and BIP ending on July 31, 1999, at 1600 CST .....	6-30
6-16. CALPUFF dispersion simulations for hypothetical tracers originating from SMI, DWP, and BIP ending on August 1 at 1700 CST .....	6-31
6-17. CALMET 24-hr forward trajectory at 10 m based on CALMET diagnostic wind fields for January 19 at 0000 CST through January 22, 2000, at 1600 CST .....	6-31
6-18. HYSPLIT 24-hr forward trajectory at 10 m based on EDAS wind fields for January 19 at 0000 CST through January 22, 2000, at 1600 CST .....	6-32
6-19. CALMET 24-hr forward trajectory at 75 m based on CALMET diagnostic wind fields for January 19 at 0000 CST through January 22, 2000 at 1600 CST .....	6-32
6-20. HYSPLIT 24-hr forward trajectory at 75 m based on EDAS wind fields for January 19 at 0000 CST through January 22, 2000 at 1600 CST .....	6-33
6-21. CALMET 24-hr forward trajectory at 350 m based on CALMET diagnostic wind fields for January 19 at 0000 CST through January 22, 2000, at 1600 CST .....	6-33
6-22. HYSPLIT 24-hr forward trajectory at 350 m based on EDAS wind fields for January 19 at 0000 CST through January 22, 2000, at 1600 CST .....	6-34
6-23. CALMET 24-hr forward trajectory at 10 m based on CALMET diagnostic wind fields for January 22 at 0000 CST through January 25, 2000, at 0800 CST .....	6-34
6-24. HYSPLIT 24-hr forward trajectory at 10 m based on EDAS wind fields for January 22 at 0000 CST through January 25, 2000, at 0800 CST .....	6-35
6-25. CALMET 24-hr forward trajectory at 75 m based on CALMET diagnostic wind fields for January 22 at 0000 CST through January 25, 2000, at 0800 CST .....	6-35
6-26. HYSPLIT 24-hr forward trajectory at 75 m based on EDAS wind fields for January 22 at 0000 CST through January 25, 2000, at 0800 CST .....	6-36
6-27. CALMET 24-hr forward trajectory at 350 m based on CALMET diagnostic wind fields for January 22 at 0000 CST through January 25, 2000, at 0800 CST .....	6-36
6-28. HYSPLIT 24-hr forward trajectory at 350 m based on EDAS wind fields for January 22 at 0000 CST through January 25, 2000, at 0800 CST .....	6-37
6-29. CALPUFF dispersion simulations for hypothetical tracers originating from SMI, DWP, and BIP ending on January 20, 2000, at 1600 CST .....	6-37
6-30. CALMET-derived mixing heights for January 20, 2000, at 1400 CST .....	6-38

**LIST OF FIGURES (Continued)**

<b><u>Figure</u></b>	<b><u>Page</u></b>
6-31. CALPUFF dispersion simulations for hypothetical tracers originating from SMI, DWP, and BIP ending on January 21, 2000, at 1600 CST .....	6-38
6-32. CALMET-derived mixing heights for January 21, 2000, at 1400 CST .....	6-39
6-33. CALPUFF dispersion simulations for hypothetical tracers originating from SMI, DWP, and BIP ending on January 22, 2000, at 1900 CST .....	6-39
6-34. CALMET-derived mixing heights for January 22, 2000, at 1400 CST .....	6-40
6-35. CALPUFF dispersion simulations for hypothetical tracers originating from SMI, DWP, and BIP ending on January 23, 2000, at 1200 CST .....	6-40
6-36. CALMET-derived mixing heights for January 23, 2000, at 1400 CST .....	6-41
6-37. CALPUFF dispersion simulations for hypothetical tracers originating from SMI, DWP, and BIP ending on January 24, 2000, at 1200 CST .....	6-41
6-38. CALPUFF dispersion simulations for hypothetical tracers originating from SMI, DWP, and BIP ending on January 25, 2000, at 1400 CST .....	6-42
6-39. CALMET-derived mixing heights for January 24, 2000, at 1400 CST .....	6-42
6-40. CALMET-derived mixing heights for January 25, 2000, at 1400 CST .....	6-43
6-41. CALMET 24-hr forward trajectory at 10 m based on CALMET diagnostic wind fields for January 3, at 0000 CST through January 6, 2001, at 0000 CST .....	6-43
6-42. HYSPLIT 24-hr forward trajectory at 10 m based on EDAS wind fields for January 3 at 0000 CST through January 6, 2001, at 0000 CST .....	6-44
6-43. CALMET 24-hr forward trajectory at 75 m based on CALMET diagnostic wind fields for January 3 at 0000 CST through January 6, 2001, at 0000 CST .....	6-44
6-44. HYSPLIT 24-hr forward trajectory at 75 m based on EDAS wind fields for January 3 at 0000 CST through January 6, 2001, at 0000 at 0800 CST .....	6-45
6-45. CALMET 24-hr forward trajectory at 350 m based on CALMET diagnostic wind fields for January 3 at 0000 CST through January 6, 2001, at 0000 CST .....	6-45
6-46. HYSPLIT 24-hr forward trajectory at 350 m based on EDAS wind fields for January 3 at 0000 CST through January 6, 2001, at 0000 CST .....	6-46
6-47. CALPUFF dispersion simulations for hypothetical tracers originating from SMI, DWP, and BIP ending on January 4, 2001, at 0800 CST .....	6-46
6-48. CALPUFF dispersion simulations for hypothetical tracers originating from SMI, DWP, and BIP ending on January 5, 2001, at 0300 CST .....	6-47
6-49. CALPUFF dispersion simulations for hypothetical tracers originating from SMI, DWP, and BIP ending on January 5, 2001, at 1700 CST .....	6-47
6-50. CALPUFF dispersion simulations for hypothetical tracers originating from SMI, DWP, and BIP ending on January 6, 2001, at 1000 CST .....	6-48

## LIST OF FIGURES (Continued)

<b><u>Figure</u></b>	<b><u>Page</u></b>
6-51. CALMET 24-hr forward trajectory at 10 m based on CALMET diagnostic wind fields for January 27 at 0000 CST through January 30, 2001, at 0000 CST .....	6-48
6-52. HYSPLIT 24-hr forward trajectory at 10 m based on EDAS wind fields for January 27 at 0000 CST through January 30, 2001, at 0000 CST .....	6-49
6-53. CALMET 24-hr forward trajectory at 75 m based on CALMET diagnostic wind fields for January 27 at 0000 CST through January 30, 2001, at 0000 CST .....	6-49
6-54. HYSPLIT 24-hr forward trajectory at 75 m based on EDAS wind fields for January 27 at 0000 CST through January 30, 2001, at 0000 CST .....	6-50
6-55. CALMET 24-hr forward trajectory at 350 m based on CALMET diagnostic wind fields for January 27 at 0000 CST through January 30, 2001, at 0000 CST .....	6-50
6-56. HYSPLIT 24-hr forward trajectory at 350 m based on EDAS wind fields for January 27 at 0000 CST through January 30, 2001, at 0000 CST .....	6-51
6-57. CALPUFF dispersion simulations for hypothetical tracers originating from SMI, DWP, and BIP ending on January 29, 2001, at 1200 CST .....	6-51
6-58. CALMET 24-hr forward trajectory at 10 m based on CALMET diagnostic wind fields for April 13 at 0000 CST through April 16, 2001, at 0000 CST .....	6-52
6-59. HYSPLIT 24-hr forward trajectory at 10 m based on EDAS wind fields for April 13 at 0000 CST through April 16, 2001, at 0000 CST .....	6-52
6-60. CALMET 24-hr forward trajectory at 75 m based on CALMET diagnostic wind fields for April 13 at 0000 CST through April 16, 2001, at 0000 CST .....	6-53
6-61. HYSPLIT 24-hr forward trajectory at 75 m based on EDAS wind fields for April 13 at 0000 CST through April 16, 2001, at 0000 CST .....	6-53
6-62. CALMET 24-hr forward trajectory at 350 m based on CALMET diagnostic wind fields for April 13 at 0000 CST through April 16, 2001, at 0000 CST .....	6-54
6-63. HYSPLIT 24-hr forward trajectory at 350 m based on EDAS wind fields for April 13 at 0000 CST through April 16, 2001, at 0000 CST .....	6-54
6-64. CALPUFF dispersion simulations for hypothetical tracers originating from SMI, DWP, and BIP ending on April 14, 2001, at 1900 CST .....	6-55
6-65. CALMET-derived mixing heights for April 14, 2001, at 1400 CST .....	6-55
6-66. CALPUFF dispersion simulations for hypothetical tracers originating from SMI, DWP, and BIP ending on April 15, 2001, at 1100 CST .....	6-56
6-67. CALMET-derived mixing heights for April 15, 2001, at 1400 CST .....	6-56
6-68. CALMET 24-hr forward trajectory at 10 m based on CALMET diagnostic wind fields for May 13 at 0000 CST through May 16, 2001, at 0000 CST .....	6-57

**LIST OF FIGURES (Continued)**

<b><u>Figure</u></b>	<b><u>Page</u></b>
6-69. HYSPLIT 24-hr forward trajectory at 10 m based on EDAS wind fields for May 13 at 0000 CST through May 16, 2001, at 0000 CST .....	6-57
6-70. CALMET 24-hr forward trajectory at 75 m based on CALMET diagnostic wind fields for May 13 at 0000 CST through May 16, 2001, at 0000 CST .....	6-58
6-71. HYSPLIT 24-hr forward trajectory at 75 m based on EDAS wind fields for May 13 at 0000 CST through May 16, 2001, at 0000 CST .....	6-58
6-72. CALMET 24-hr forward trajectory at 350 m based on CALMET diagnostic wind fields for May 13 at 0000 CST through May 16, 2001, at 0000 CST .....	6-59
6-73. HYSPLIT 24-hr forward trajectory at 350 m based on EDAS wind fields for May 13 at 0000 CST through May 16, 2001, at 0000 CST .....	6-59
6-74. CALPUFF dispersion simulations for hypothetical tracers originating from SMI, DWP, and BIP ending on May 14, 2001, at 0600 CST .....	6-60
6-75. CALMET-derived mixing heights for May 14, 2001, at 1400 CST.....	6-60
6-76. CALPUFF dispersion simulations for hypothetical tracers originating from SMI, DWP, and BIP ending on May 15, 2001, at 2200 CST .....	6-61
6-77. CALMET-derived mixing heights for May 15, 2001, at 1400 CST.....	6-61
6-78. CALMET 24-hr forward trajectory at 10 m based on CALMET diagnostic wind fields for September 17 at 0000 CST through September 21, 2001, at 0000 CST.....	6-62
6-79. HYSPLIT 24-hr forward trajectory at 10 m based on EDAS wind fields for September 17 at 0000 CST through September 21, 2001, at 0000 CST .....	6-62
6-80. CALMET 24-hr forward trajectory at 75 m based on CALMET diagnostic wind fields for September 17 at 0000 CST through September 21, 2001, at 0000 CST.....	6-63
6-81. HYSPLIT 24-hr forward trajectory at 75 m based on EDAS wind fields for September 17 at 0000 CST through September 21, 2001, at 0000 CST .....	6-63
6-82. CALMET 24-hr forward trajectory at 350 m based on CALMET diagnostic wind fields for September 17 at 0000 CST through September 21, 2001, at 0000 CST.....	6-64
6-83. HYSPLIT 24-hr forward trajectory at 350 m based on EDAS wind fields for September 17 at 0000 CST through September 21, 2001, at 0000 CST .....	6-64
6-84. CALPUFF dispersion simulations for hypothetical tracers originating from SMI, DWP, and BIP ending on September 18, 2001, at 2200 CST .....	6-65
6-85. CALPUFF dispersion simulations for hypothetical tracers originating from SMI, DWP, and BIP ending on September 19, 2001, at 1900 CST .....	6-65
6-86. CALPUFF dispersion simulations for hypothetical tracers originating from SMI, DWP, and BIP ending on September 20, 2001, at 1300 CST .....	6-66

## LIST OF TABLES

<b><u>Table</u></b>	<b><u>Page</u></b>
2-1. C-MAN, buoy, and RWP platform sites.....	2-10
2-2. C-MAN, buoy, and RWP platform sites and their available surface meteorological data.....	2-11
2-3. Derived COARE parameters.....	2-12
2-4. Aloft synoptic classifications used in the 1998-2001 MMS Boundary Layer Study ....	2-12
2-5. Surface wind flow speed and direction classification used in the 1998-2001 MMS Boundary Layer Study .....	2-12
3-1. Speed classifications .....	3-6
5-1. Number of occurrences of each synoptic classification by year for the MMS Boundary Layer Study.....	5-12

## LIST OF VARIABLES

$\theta$	Potential temperature
$h$ or $Z_i$	Mixing depth
$H_s$	Sensible heat flux
$L$	Monin-Obukhov length
$L_e$ or $H_e$ or $H_l$	Latent heat flux
$q^*$	Humidity scaling parameter
$q^r$	Water vapor mixing ratio
RH	Relative humidity
$T$	Air temperature
$T^*$	Temperature scaling parameter
$T_s$	Sea Skin temperature or sea surface temperature
$T_v$	Virtual temperature
$u$	Wind speed
$u^*$	Friction velocity
$u_s$	Water current speed
$x_r$	Any variable measured at the reference height
$z_o$	Surface roughness length
$z_r$	Standard reference height or observing height

## EXTENDED ABSTRACT

This report presents the results from the U.S. Department of the Interior, Minerals Management Service (MMS) atmospheric boundary layer (ABL) study. Observations and model predictions from the Gulf of Mexico were analyzed with a focus on better parameterizing the over-water ABL. In addition, the ABL results were used to calculate the transport and dispersion of pollutants in the western and central Gulf of Mexico.

The analysis incorporated new observations of vertical profiles in the ABL from six meteorological stations in the Gulf of Mexico. These stations include 915-MHz radar wind profilers (RWP), 2-KHz Radio Acoustic Sounding Systems (RASS), and surface meteorological stations. Two stations collected ABL data for three years from May 1998 through October 2001, and four stations collected data from September 2000 through October 2001. The RWPs and RASS measure winds and virtual temperatures ( $T_v$ ), respectively, from near the surface to heights of a few kilometers, and the surface stations measure skin temperature as well as wind speed, wind direction, air temperature, and water vapor mixing ratio at an elevation of about 25 m on an oil platform. In addition to the new data from the vertical profilers, routine meteorological observations from buoys and from shoreline stations were included in the analysis.

The new and routine data collected were analyzed to investigate the over-water surface energy balance, the climatology of latent heat versus sensible heat fluxes, mixing depths, the frequency of occurrence of very stable conditions, and the horizontal spatial variability of wind speed and direction. Estimates of the scaling velocity ( $u^*$ ) and scaling temperature ( $T^*$ ) were studied. Three-dimensional prediction fields of surface winds, heat and momentum fluxes, and wind profiles from the National Center for Environmental Protection's (NCEP) Eta model were compared with the observations from the RWPs and buoys. The annual, seasonal, and diurnal variations of the ABL characteristics were determined. Using the new data as inputs, test runs with CALMET and CALPUFF were made for several case study periods to determine typical plume trajectories and relative dispersion rates. The various data sets described above were collected and quality assurance/quality control (QA/QC) procedures were applied to produce a single, user-friendly database.

### EA.1 DELIVERABLES AND CONCLUSIONS

- Data collected as part of this study, as well as other relevant data, were placed in a common Microsoft SQL Server database and are also contained in quarterly Microsoft Access databases. These data sets, which were delivered to MMS, are generally available from May 1998 through September 2001; RWP, RASS, and rawinsonde data, over-water and land-surface data, over-water boundary layer parameters using the Coupled Ocean-Atmosphere Response Experiment (COARE) model, Eta forecast model data, and daily synoptic weather classifications and surface flow classifications are included in the data sets. In addition, external to the database, CALMET gridded wind fields were generated for selected case studies. To effectively display this diverse set of data for use in data analysis, the Environmental Data Analysis Tool (EDAT) was developed and delivered to

MMS. EDAT can produce four types of plots—time series, time-height cross-sections, vertical profiles, and spatial plots—and can display images.

- To assist in characterizing ABL surface fluxes and scaling parameters, the COARE algorithm was modified and used to estimate hourly surface fluxes of momentum, sensible heat, and latent heat, based on observations of wind speed, air temperature, and water vapor mixing ratio at a standard reference height near the water surface and the skin temperature at the water surface. The COARE algorithm was originally derived from the Tropical Ocean-Global Atmosphere (TOGA)-COARE research project. The COARE algorithm has proved to be a useful tool to parameterize boundary layer characteristics in the western and central Gulf of Mexico and is recommended for use in future studies.
- The Eta Data Assimilation System (EDAS)-simulated wind fields and the observed RWP winds from six sites were compared. EDAS is based on a combination of Eta model forecast winds and diagnostic interpolations of observed winds but does not include RWP data. The mean wind speed (WS) bias was near zero close to the shore but increased with offshore distance, so that the EDAS mean WS exceeded the RWP mean WS by 1 to 2 m/s at 50 km offshore and by 2 to 6 m/s at 100 to 200 km offshore. Mean wind direction (WD) bias was small, a difference of about 10° to 20° (e.g., if the RWP WD was 180°, then the EDAS WD would be 160°). Standard deviations of the differences (with mean bias removed) were 1 to 2 m/s for WS and 20° to 40° for WD, in agreement with findings for other domains and models. This analysis indicates that the EDAS wind field can be improved if it ingests offshore measurements of aloft wind data; such data can be obtained from offshore RWPs.
- The fluxes and scaling parameters calculated by the COARE algorithm in the Gulf of Mexico are physically consistent with expectations and are similar in magnitude to the observations and COARE calculations for TOGA, which took place in the warm western Pacific Ocean near the equator. Calculated monthly average sensible heat fluxes in the Gulf of Mexico ranged from 5 to 30 W/m<sup>2</sup>, typical of other over-water areas. Similarly, calculated monthly average latent heat fluxes ranged from 50 to 150 W/m<sup>2</sup>, also typical of other over-water areas. Both the latent and sensible heat fluxes were highest in the late fall and early winter and lowest in the late spring and summer. Sensible heat flux is maximized for post-trough synoptic conditions, which are likely to be marked by above average wind speeds and by low air temperature. The latent heat flux is consistently large during the post-trough synoptic condition, due to higher wind speeds and low dew points that follow a cold front. The calculated fluxes are generally in good agreement with the monthly average Eta model latent and sensible heat fluxes.
- The COARE-calculated monthly average friction velocity ( $u^*$ ) using data from the buoys, the C-MAN sites at the shoreline, and the South Marsh Island (SMI) platform near shore shows agreement among these sites well within a factor of two and often within 20%. This agreement is important because the monthly average friction velocity is the key scaling velocity for estimating transport speeds and dispersion rates. However the COARE-calculated monthly average friction velocities using data from the platform sites further from shore are 30% to 40% less than at the other sites. These platforms (the Vermillion offshore oil platform [VRM], the Breton Island Platform [BIP], the Deep

Water Platform [DWP], the Mid Buoy Platform [MBP], the Shallow Water Platform [SWP], and the West Delta Platform [WDP] are typically in deeper water. A possible explanation is that the wave height and frequency are estimated from empirical relations given observations of wind speed at the platforms, whereas they are directly measured at the buoys. The monthly average Eta model friction velocity was usually within about 10% to 20% of the COARE-calculated friction velocity.

- The differences between the observed water “skin” and air temperatures were, on average, +1 to +3°C at most sites all year. The differences were lower in late spring and greater in late fall and early winter. This persistent positive temperature difference suggests that the ABL is usually well-mixed and unstable.
- For seven multi-day case studies, the CALPUFF transport and dispersion model was applied using arbitrary assumptions for hypothetical tracer releases from three oil platforms, BIP, SMI, and SWP. Twenty-four-hour trajectories were calculated for releases at heights of 10 m, 75 m, and 350 m using (1) CALMET wind fields and an in-house STI trajectory model (TRAJMOD) and (2) EDAS wind fields and the NOAA HYSPLIT trajectory model. The seven case study periods covered a range of representative synoptic conditions and seasons, such as strong-wind January days and light-wind July days. The CALMET and EDAS-HYSPLIT trajectories agree within 20° to 30° most of the time, although the speeds of the EDAS trajectories are larger by as much as a factor of two (due to the mean bias discussed above). The CALPUFF-simulated plumes from the three oil platforms sometimes impact the shoreline or offshore islands, depending on wind direction. The concentrations are higher during light winds, when dilution is less. It is fortunate that the most persistent winds, associated with onshore impact near the same location for several hours, are nearly always marked by high winds and consequently lower concentrations. When winds are light and variable, the local centerline concentration may be higher, but the plume does not remain for long over a specific point.
- The CALMET-CALPUFF estimates of over-water mixing depth were low, about 100 to 200 m, in contrast to observed mixing depths of about 600 m. This factor of three to six difference causes model overpredictions in concentrations, since the plume is constricted to the mixing layer. The underpredictions of mixing depth appear to be due to the neglect of convective mixing processes offshore, where CALMET currently assumes that the mixing depth is due solely to mechanical mixing and is therefore proportional to wind speed.

## **EA.2 RECOMMENDATIONS**

Based on our analysis and modeling results, and our interactions with other researchers, we have prepared a number of recommendations that, if implemented, will further advance the current scientific understanding of the ABL in the central and western Gulf of Mexico and further develop and improve the tools available to understand the ABL in the central and western Gulf of Mexico. Thus, these activities will improve future estimates of the transport and dispersion of pollutants in the central and western Gulf of Mexico. The recommendations are arranged into groups with other similar recommendations. Some recommendations involve

interaction among various researchers and the publication of research results, others involve additional analysis and modeling efforts using existing data, while others involve the collection of new data.

## **Collaborations**

- Work with NCEP to better understand over-water wind differences between the Eta model and observed RWP winds. Analysis has shown that Eta model winds are biased high compared to RWP winds away from shore.
- Work with National Oceanic and Atmospheric Administration's (NOAA) Environmental Technology Laboratory (ETL) to design a scheme to remove sea-clutter from profiler data so that mixing heights can be automatically estimated for data from the ABL study and future studies using existing mixing-height algorithms.
- Work with NOAA to improve COARE predictions of large surface roughness. Roughness increases under very low wind speeds, which influences estimations of the ABL parameters. Conduct a joint meeting on COARE to further improve the model for use in the Gulf of Mexico.
- Make better use of ABL measurements and analyses in other MMS-sponsored projects by reviewing plans and progress and recommending ways to incorporate ABL data and analysis and modeling results.

## **Publication**

- Plan a special journal issue (e.g., *Journal of Applied Meteorology*, *Journal of Geophysical Research*, *Boundary Layer Meteorology*) on ABL issues in the Gulf of Mexico and prepare specific papers on, for example, the following topics: Eta/RWP wind comparisons, climatology of surface ABL parameters calculated using COARE in a shallow-water ocean and modifications made to COARE, modeled and estimated mixing heights in the Gulf of Mexico, and results from related MMS-sponsored projects.

## **Analysis**

- Compare satellite-derived sea-surface temperatures to radiometer temperatures and buoy temperatures measured during this study. Compare estimates of sea-surface temperatures to the radiometer temperatures when clouds obscure the satellite's view of the Gulf (currently estimated using hole-filling techniques). Comparison results and the subsequent improvements in predictions of spatial sea-surface temperatures will improve model results.
- Identify several additional periods of super-stable conditions in the existing data set (i.e., a period of southerly flow occurring immediately after a cold outbreak has cooled the water in the shallow portion of the Gulf) and perform an ABL case study similar to other case studies.

- Determine the best method for estimating wave height and frequency as a function of water depth from wind speed alone. When wave data are not available at the platforms, inaccurate knowledge of wave characteristics can result in inaccurate estimates of surface roughness, which influence ABL parameterizations.
- Determine the relationship between wind speed and RWP sea-clutter.
- Use buoyancy flux to estimate mixing heights when winds are less than 6 m/sec and compare to RWP-derived mixing heights.

## **Modeling**

- Update the CALMET model to correct the large underestimates of over-water mixing heights due to the neglect of the buoyant heat flux; perform additional comparisons of observation-based estimations of mixing heights to model mixing heights.
- Update the CALPUFF dispersion runs using new CALMET output created with an improved mixing-height scheme. Compare results from the new runs to those created as part of the current project.
- Compare CALMET diagnostic model runs to MM5 prognostic model runs (from a separate MMS project) and observational data and create best estimates of gridded mixing heights and winds.
- Modify the way diagnostic and prognostic models treat the diffuse shoreline of the Gulf of Mexico; operate the models and compare results with observations.
- Quantify the differences between the CALMET and HYSPLIT trajectories. For example, two trajectories can be compared by calculating the difference in the two positions after certain travel times. The differences can then be expressed as function of time for that trajectory and a root mean square error (rmse) calculated for a group of trajectories. The difference can be categorized by its components (e.g., radial distance and angular distance).
- Compare CALPUFF concentration predictions quantitatively because the same amount of tracer was released in each case. For example the following outputs could be compared:
  - Maximum concentration at the point the shoreline is hit.
  - Maximum (centerline) concentration at specific downwind times (e.g., 3 hrs, 6 hrs, etc.) and distances (50 km, 100 km, etc.)
  - Penetration distance (downwind distance) for a given concentration.
  - Width of plume for a given concentration contour at a given travel time or distance.
- Develop an alternative procedure within CALMET to handle missing upper-air measurements.

## Measurements

- Conduct continuous meteorological (aloft and surface) and air quality measurements in offshore and coastal areas to (1) support routine source-based modeling for lessees and special-research MMS objectives; (2) provide long-term information on spatial and temporal ABL characteristics; and (3) support routine comparisons with Eta model predictions for routine estimates of ABL characteristics, for real-time modeling, and for special research studies.
- Collocate a radiometer and underwater temperature sensor to better determine the relationship and accuracy of the COARE-estimated warm-layer and cool-skin effects.
- Routinely operate a measurement system on an offshore platform that measures a range of meteorological parameters at several depths of the surface layer and boundary layer. Such a system could include a mini-Sodar, an RWP/RASS system, and a surface meteorological monitoring system on a platform to obtain wind and temperature measurements. The addition of the mini-Sodar would fill the measurement void that exists from 30 m to 200 m; this hole is often the location of plumes.
- Improve the RWP and RASS sounders so that they are not so susceptible to interferences due to objects on the platform and to sea-surface (wave) characteristics.

## 1. INTRODUCTION

This report presents the results from the U.S. Department of the Interior, Minerals Management Service (MMS) atmospheric boundary layer (ABL) study. Sonoma Technology, Inc. (STI) and Hanna Consultants analyzed ABL observations and investigated how the ABL structure influences the transport and dispersion of pollutants in the western and central Gulf of Mexico. The results of this study will be used by the MMS to support techniques for evaluating the effects of oil and gas exploration, development, and production activities in the Outer Continental Shelf (OCS) on air quality over coastal areas.

The vertical and horizontal variability of the ABL in the Gulf of Mexico has been an uncertainty. For example, the depth of the ABL and its vertical stability and wind and turbulence structure can vary greatly in OCS zones due to horizontal variations in water skin temperature and the overlying air mass. The MMS now has available new observations of vertical profiles in the ABL for the OCS in the Gulf of Mexico from six meteorological stations. These meteorological stations include 915-MHz radar wind profilers (RWP), 2-KHz Radio Acoustic Sounding Systems (RASS), and surface meteorological stations. Two stations collected ABL observations for three years from May 1998 through October 2001, and four stations collected observations from September 2000 through October 2001. The RWPs and RASS measure winds and virtual temperatures ( $T_v$ ), respectively, from near the surface to heights of a few kilometers, and the surface stations measure skin temperature as well as wind speed, wind direction, air temperature, and water vapor mixing ratio at an elevation of about 25 m on an oil platform. In addition to the vertical profilers, routine meteorological observations from buoys and from shoreline stations are available. For the first time in the Gulf of Mexico region, we are able to input the full vertical profiles of meteorological variables that are required by transport and dispersion models.

There are several similarities between over-land and over-water boundary layers. The basic boundary layer theories and equations apply over any surface, as long as care is taken to correctly apply definitions (i.e., the heat flux used in calculating  $L$ , the Monin-Obukhov length, must include the effects of the latent heat flux). Mesoscale eddies, with time scales from one minute to one hour, are present over both land and water and are not observed to diminish even over the open ocean. Over both surfaces, it is possible to parameterize the entire ABL based on simple observations of wind speed near the surface, air-skin temperature differences, and relative humidity. However, there is no substitute for observations through the entire depth of the ABL because elevated inversion layers and shear layers are unpredictable.

Some fundamental differences between over-land and over-water boundary layers need to be accounted for. For example, roughness length,  $z_0$ , is a strong function of wind speed over water. In addition, because water has high thermal conductivity and there is mixing in the ABL, the surface temperature of water slowly reacts to changes in air temperature. Consequently, the atmospheric stability over water does not follow the typical diurnal cycle characteristic of the atmospheric stability over land. In fact, the atmosphere can be stable during the day and unstable at night, or it can be stable or unstable for weeks at a time. Strong stability (positive or negative) occurs over water only when there is advection of a warm air mass over cold water or a cold air mass over warm water. Most of the time, the latent heat flux over water is larger than the

sensible heat flux. It is essential that the calculation of any stability parameter, such as the Monin-Obukhov length, includes the vertical gradient of water vapor along with the vertical gradient of temperature. It is possible to have a temperature inversion and still have unstable conditions, due to a decrease of specific humidity with height.

The new and routine data collected have been analyzed to investigate the following technical issues:

1. The over-water surface energy balance was studied using near-surface observations for both steady-state, horizontally homogeneous conditions and for conditions variable in time and space. A climatology of latent heat versus sensible heat fluxes has been developed for both situations.
2. The extensive virtual temperature profiles from RASS were studied in order to estimate the mixing depths.
3. The frequency of occurrence of very stable conditions near the surface and in layers aloft was investigated because these layers are important for defining worst-case conditions for air pollutants.
4. The horizontal spatial variability of wind speed and direction was studied to identify the fraction of time that wind directions and speeds persist over several hours in the Gulf of Mexico, thus causing straight-line transport of pollutants towards receptors on the shoreline.
5. Estimates of the scaling velocity ( $u^*$ ) and scaling temperature ( $T^*$ ) were created and studied. These scaling parameters are directly related to surface momentum and heat fluxes. Because turbulent velocities (important to dispersion) are directly proportional to  $u^*$ , it should be possible to derive improved parameterizations for the dispersion coefficients  $\sigma_y$  and  $\sigma_z$ .
6. Three-dimensional prediction fields of surface winds, heat and momentum fluxes, and wind profiles—from the National Center for Environmental Protection's (NCEP's) Eta Model—are available for the Gulf of Mexico and were compared with the observations from the RFPs and buoys.
7. The annual, seasonal, and diurnal variations of the ABL characteristics (item 5) were determined.
8. Synoptic (regional) classification schemes were developed so that meteorological characteristics of the ABL and pollutant transport and dispersion can be estimated by synoptic class.
9. Using the new data as inputs, test runs with CALMET and CALPUFF were made for several case study periods to determine typical plume trajectories and relative dispersion rates.
10. The various data sets described above were collected and quality assurance/quality control (QA/QC) procedures were applied to produce a single, user-friendly database. The database includes statistical summaries of the data and derived ABL parameters, as well as all of the observed data.

This report describes the results of the study and demonstrates that the technical issues listed above have been addressed. Section 2 describes the data and how they were collected into a comprehensive database. It also describes specialized software that allows the data to be extracted and visualized. The database and software were delivered to MMS at the final project meeting on October 15, 2003, in New Orleans. Section 3 describes the general meteorology and the synoptic classification results. Section 4 summarizes the characteristics of the ABL as determined by the RWP and RASS data. Section 5 describes additional characteristics of the ABL, including application of the Coupled Ocean-Atmosphere Response Experiment (COARE) algorithm to estimate the terms of the surface energy balance and comparisons of these terms with Eta model simulations. Section 6 discusses the CALMET wind field modeling and transport and dispersion analyses. Section 7 presents a summary of the important findings and recommendations. Appendix A contains information on the format and structure of the MMS EDAT database, which is discussed in Section 2. Appendix B contains additional information about the COARE program, which is discussed in Section 5. Appendix C contains FORTRAN code of the COARE program that was modified for use in this project. Appendix D contains the final presentation delivered to MMS on October 15, 2003, in which there are many additional data plots.

## 2. DATA AVAILABILITY AND VISUALIZATION TOOL

This section presents the data availability, sources, quality control (QC), and display tool used for this study.

### 2.1 AVAILABLE DATA

The measurements collected during the June 1998-October 2001 MMS Boundary Layer Study include data from continuous surface and aloft monitoring of meteorological conditions on two oil platforms; standard surface data collected at buoy and Coastal Marine Automated Network (C-MAN) stations; rawinsonde data; and data from surface land sites. For September 2000 through October 2001, continuous surface and aloft monitoring of meteorological conditions were collected from three additional oil platforms and a land-base site as part of the Breton Island Aerometric Program (BAMP). Model simulations include three-dimensional Eta model simulations and the Eta's four-dimensional data assimilation system, EDAS (Eta Data Assimilation System). The three-dimensional Eta model simulations and surface observations were used to create derived data of boundary layer parameters using the Coupled Ocean-Atmosphere Response Experiment (COARE) computer program. The COARE program is described in Section 5.

All observational and derived data and selected Eta model simulations were reviewed for accuracy, completeness, and internal consistency and were imported into a Microsoft SQL Server database. **Figure 2-1** shows the locations of the buoy, C-MAN, and platform monitoring sites.

In addition to the data contained in the database, CALMET wind fields for seven selected case studies are available in their native binary format.

#### 2.1.1 Aloft Meteorological Measurements

Aloft (non-surface) meteorological measurements were collected as part of the 1998-2001 MMS Boundary Layer Study. In addition, aloft data collected from the September 2000 through October 2001 BAMP study were also integrated into this project. For the MMS study, the RWP and RASS  $T_v$  data were collected at the Vermillion offshore oil platform (VRM) and the South Marsh Island offshore oil platform (SMI) (**Figure 2-2**). For the BAMP study, the RWP and RASS  $T_v$  data were collected at the West Delta Platform (WDP), the Deep Water Platform (DWP), the Breton Island Platform (BIP), and Fort Morgan (FTM). All RWP and RASS data were quality-controlled and are considered Level 1 validated as discussed in Section 2.2. See Lindsey et al. (1997b) for more details about the RWP and RASS data.

Rawinsonde data were collected from Lake Charles and Slidell, Louisiana, at 0000 UTC and 1200 UTC for each day during the study. These data were not quality controlled; however, they are available in the Microsoft SQL Server database and will be utilized for case study analyses and modeling.

### 2.1.2 Surface Meteorological Measurements

Surface meteorological data were collected at the VRM and SMI sites for the 1998-2001 MMS study period and at six sites as part of the BAMP study (See Figure 2-2). In addition, surface data were obtained from buoy and C-MAN sites located in the MMS study region through the National Buoy Data Center. **Table 2-1** lists buoy, C-MAN, and platform sites and their locations. **Table 2-2** lists the parameters available for the C-MAN, buoy, and platform sites. The routine data collected at most sites include wind speed and direction, temperature, relative humidity, station pressure, and skin temperature. The buoy sites also collect wave height and wave period data.

Surface data collected at the platform sites were quality-controlled and are considered Level 1 validated (discussed in Section 2.2). In addition, all other surface data listed in Table 2-1 were reviewed for reasonableness.

Additional hourly surface data were obtained through The National Climatic Data Center (NCDC) for land-based surface sites throughout the Gulf of Mexico region. These data were input into a Microsoft SQL Server database; however, they were not quality-controlled.

### 2.1.3 Model Simulations

Three-dimensional Eta model simulations and the EDAS were obtained from the University Corporation for Atmospheric Research (UCAR) for the entire study period. The Eta forecast model contains forecast fields out to 48 hours from initial states at 0000 UTC and 1200 UTC. The EDAS generates eight 3-hourly initial states or analyses during each 24-hr period, utilizing a vast set of observed data. From the Eta forecast model, geopotential height, friction velocity, latent heat flux, sensible heat flux, low cloud cover, middle cloud cover, and high cloud cover were extracted for each over-water site and placed in the database. Wind speed and wind direction were extracted from the EDAS model simulations. The Eta model simulations, along with the surface observations, were placed in the database.

Both Eta and EDAS utilize the AWIPS Grid 212 as their standard output grid. This grid is defined on a Lambert Conformal projection with a spatial resolution of 40 km by 40 km. Both Eta and EDAS contain 38 vertical levels and cover most of North America and the surrounding oceans.

In addition to the Eta and EDAS predictions, CALMET wind fields for seven selected case studies are available in their native binary format. Section 7 discusses the CALMET modeling.

### 2.1.4 Derived Data

Three-dimensional model simulations and surface observations at the sites listed in Table 2-2 were used to create the derived COARE data set. The derived data were created for the entire 1998-2001 MMS study period. **Table 2-3** shows the derived variables. These derived variables were placed in the database for analysis.

### 2.1.5 Data Classifications

Aloft synoptic weather maps were reviewed and nine classifications were created based on the review. The classifications are discussed in Section 3. The classification of each hourly period was imported into the database as a derived data set. These data are different from other data sources because they refer to the Gulf of Mexico region as a whole and not to a single point location. **Table 2-4** shows the aloft classifications that were used for this study.

Surface flow classifications were created using a simple set of queries to determine the wind direction and observed wind speeds. These surface flow classifications are contained in the database. Details of how the classifications were created are provided in Section 3. **Table 2-5** lists the classifications.

### 2.1.6 Averaged Aloft Data

In addition to the data discussed above, the database also contains averages of RWP wind and RASS  $T_v$  data. Averages were created for the entire 1998-2001 study period by year, season, month, and aloft classification.

## 2.2 DATA VALIDATION OBJECTIVES AND RESULTS

Data validation is the process of evaluating the data quality through objective and subjective comparisons with other data sets, such as those from rawinsondes or model simulations. The data validation process was a necessary component of this project because it allowed us to identify data with errors, biases, and physically unrealistic values before they were used for analysis and modeling. The objectives of the data validation process were to

- produce a working database with values that are validated and of a known quality;
- evaluate the internal, spatial, temporal, and physical consistency of the data; and
- determine the suitability of the data for analysis and modeling.

To indicate the validity of a data point, we used QC flags that are stored with the data in the database. The following QC flags were used:

- Valid data (QC flag = 0). Observations that were judged accurate within the performance limits of the instruments.
- Invalid data (QC flag = 8). Observations that were judged inaccurate or in error.
- Missing data (QC flag = 9). Observations that were not collected. In addition to a QC flag signifying missing data, the data values were assigned a missing value indicator (-999.0).

All platform data were previously validated by STI as part of the data collection process. Details of the data collection and validation process can be found in Vaisala Meteorological Systems, Inc. and Sonoma Technology, Inc. (2002). Visual comparisons of the spatial and temporal variability of all buoy and C-MAN surface meteorological data were performed. This was accomplished by reviewing time series and spatial plots for consistency in time and space.

Outliers were removed and flagged as invalid. Very few changes to the data validity were necessary.

In addition to these QC flags, QC “out flags” were created for the derived COARE data set. The following out flags were used:

- Out flag = 0 indicates that radiation from Eta model cloud data and all observations needed by COARE exist.
- Out flag = 3 indicates that the observations were interpolated in time, and radiation data exist from Eta model cloud data.
- Out flag = 6 indicates that the observations were interpolated in time. The radiation was estimated by time of year, day, and latitude.
- Out flag = 7 indicates that the observations exist. The radiation was estimated by time of year, day, and latitude.
- Out flag = 9 indicates no observations were available.

Most derived data for this study have out flags of 0 or 3.

### 2.3 ENVIRONMENTAL DATA ANALYSIS TOOL (EDAT)

To effectively display the diverse set of MMS data for use in data analysis, the Environmental Data Analysis Tool (EDAT) was developed. EDAT is designed to work with environmental data sets such as RWP, RASS, rawindsonde, air quality, surface meteorological, and modeling data sets. EDAT reads from a Microsoft Access or Microsoft SQL Server database. Details about the structure of the database can be found in Appendix A. This section discusses the EDAT features.

EDAT can produce four types of plots—time series, time-height cross-sections, vertical profiles, and spatial plots—and can display images. In addition, these plots can be displayed all at once, simplifying visual comparison of several different data types (see **Figure 2-3**).

EDAT can plot two time series plots on a single graph and the variables do not have to be the same. For example, one can plot wind speed versus time as one time series and temperature as a separate time series on the same graph. In addition, these two variables may be from different sites. It is also possible to plot wind barbs as a time series. Figure 2-3 shows three examples of time series plots. Time series plots provide a means for the data analyst to look at trends within the data and evaluate how they might relate to other variables.

Time-height cross-sections are designed to plot either wind barbs or wind vectors. An example of a wind barb time-height cross-section is shown in Figure 2-3(c). Time-height cross-sections are important for looking at how winds vary with height and time. For example, winds that change direction rapidly with height may indicate a shear layer, which may be important for determining the source of air pollutants.

Vertical profile plots are plots of a particular variable versus height. Vertical profiles are useful for examining the vertical structure of the atmosphere. For example,  $T_v$  profiles are useful for determining the mixing height. EDAT can display one or more profiles on the same graph; however, it is limited to one variable at one site.

Spatial plots are plots of a variable at a site displayed in map view. Multiple sites are normally displayed, and up to two types of data may be displayed on one spatial plot. An example plot of wind barbs and ozone bars is shown in Figure 2-3(a). EDAT allows a base map of the user's choice to be displayed in the background and referenced using latitude and longitude coordinates. Data can be displayed in the spatial plot with barbs, vectors, scalar values, and/or bars. EDAT also allows the user to change altitude by using the up/down cursor keys or the height toolbar.

EDAT has an interactive screen that allows the user to create the graph displays discussed above. Once a graph type is selected, a new screen pops up requesting additional information to be used for creating the graph. **Figure 2-4** illustrates how the user creates a time series plot. The first step is to select "New Time Series Graph" under the "Window" menu option. A selection screen pops up that requests the site name, data class, parameter, and height. A feature called Auto Scale then searches the database for maximum and minimum values. Once the search is completed, it is possible to change the scales by unchecking the "Auto Scale" boxes and typing the desired scales into the minimum and maximum value boxes. The "Time Window" feature allows the user to choose to plot one day, one week, one month, or all available data.

EDAT can also link all of the resulting graphs in time and height (when applicable). This allows an analyst to scroll through a large set of data values as all the graphs scroll at the same time. This facilitates spatial and temporal analyses. In addition, the user can click on any point on any plot to see the data value, QC code, and height at any time.

EDAT can save graph layouts to a configuration file. Layouts are a type of template that allows the user to make the same plots at a later time. These layouts are not to be confused with saving a file. In EDAT, graphs can be saved as bitmap (.bmp) images and/or printed.

EDAT can also save data in formats used by other programs. In particular, EDAT allows users to save data for plotting by the U.S. Environmental Protection Agency's (EPA) WRLPlot wind rose program. In addition, wind fields can be created for use in the CALMET diagnostic meteorological model. This is useful since any set of data in the database can be converted to either of these two formats for plotting in other programs.

EDAT users can create a subset of data. This feature is useful for large databases that may take too long to create displays.

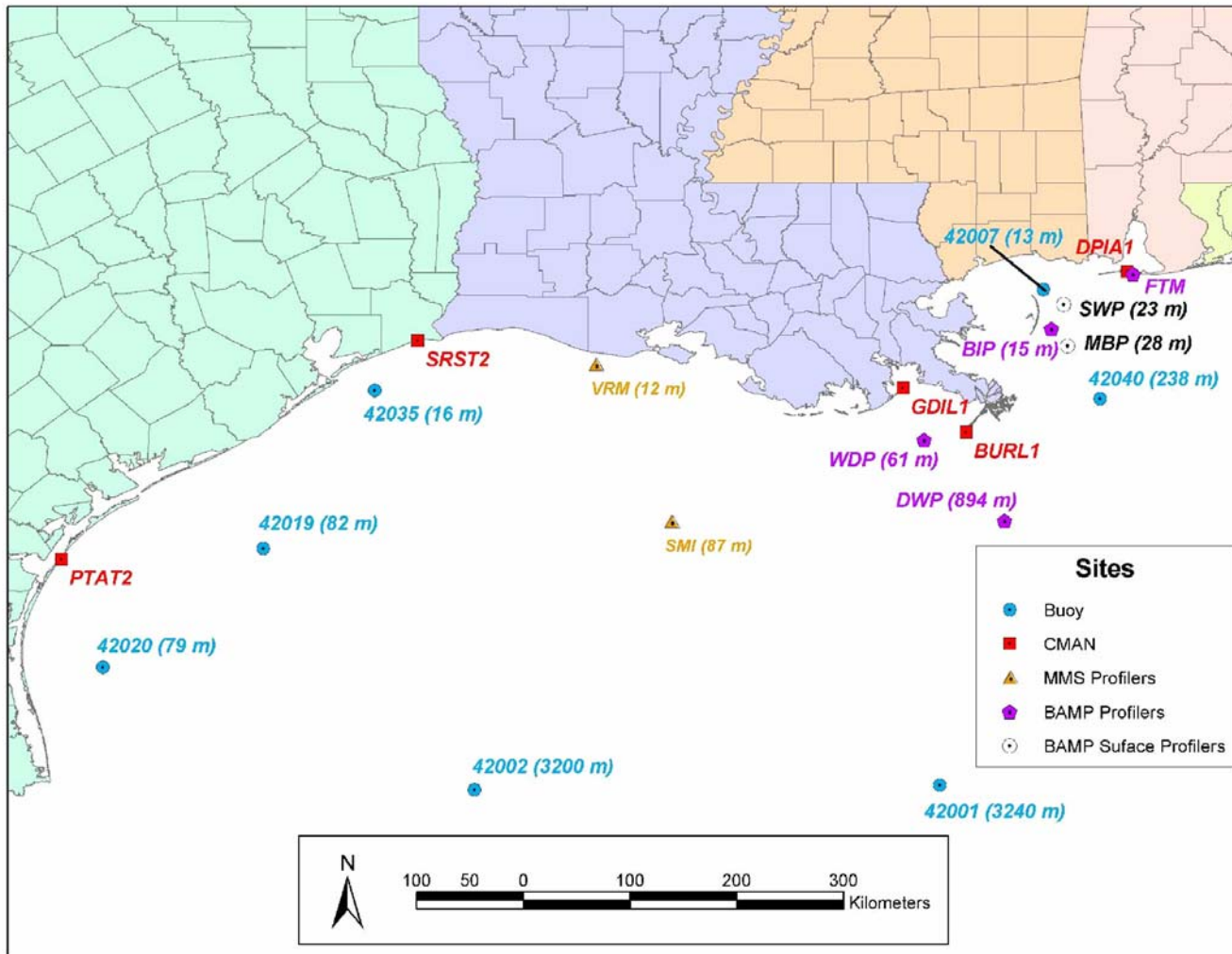


Figure 2-1. Map of the MMS study region depicting locations of C-MAN, buoy, and RWP platform monitors. The water depths are provided in parenthesis.



Figure 2-2. SMI offshore oil platform showing the RWP and RASS upper-air measurement systems.

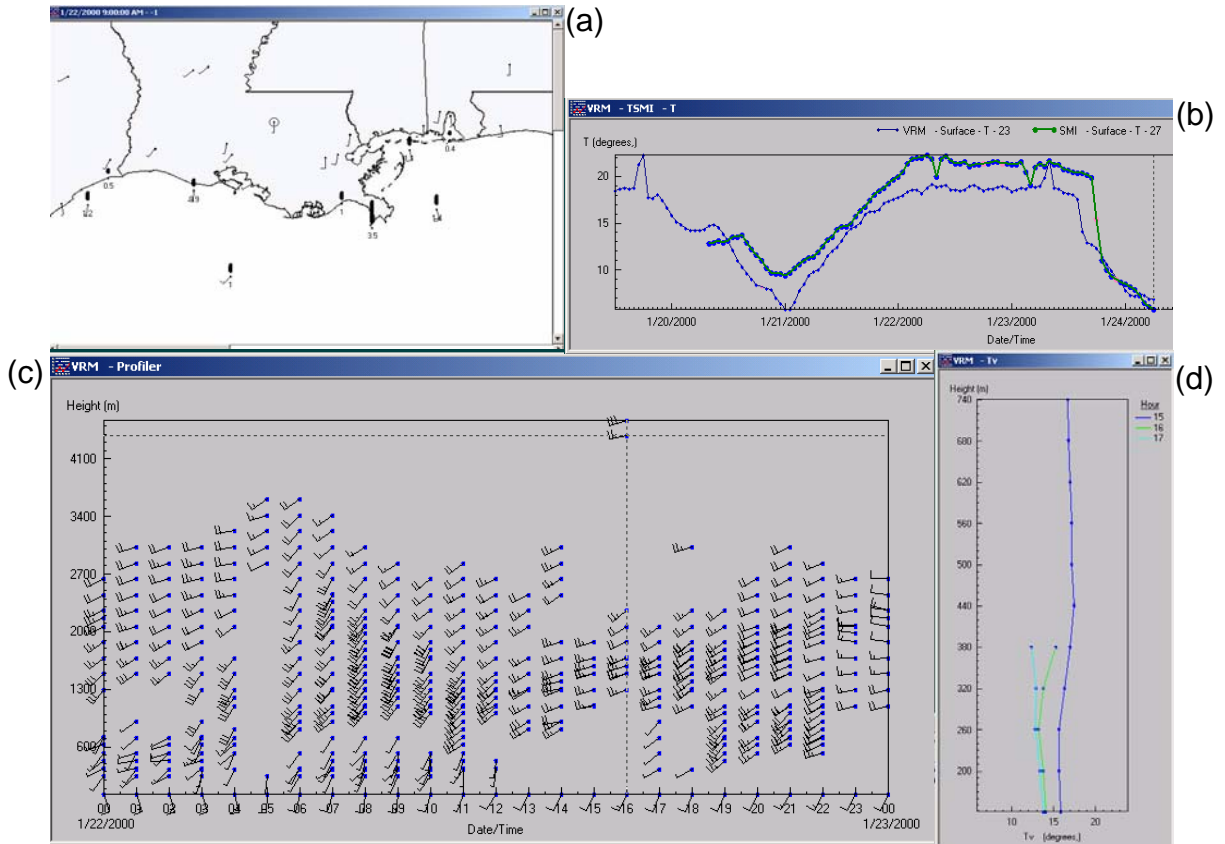


Figure 2-3. EDAT screen shot showing (a) a spatial plot, (b) time series plots, (c) the time-height cross-section, and (d) the vertical profile.

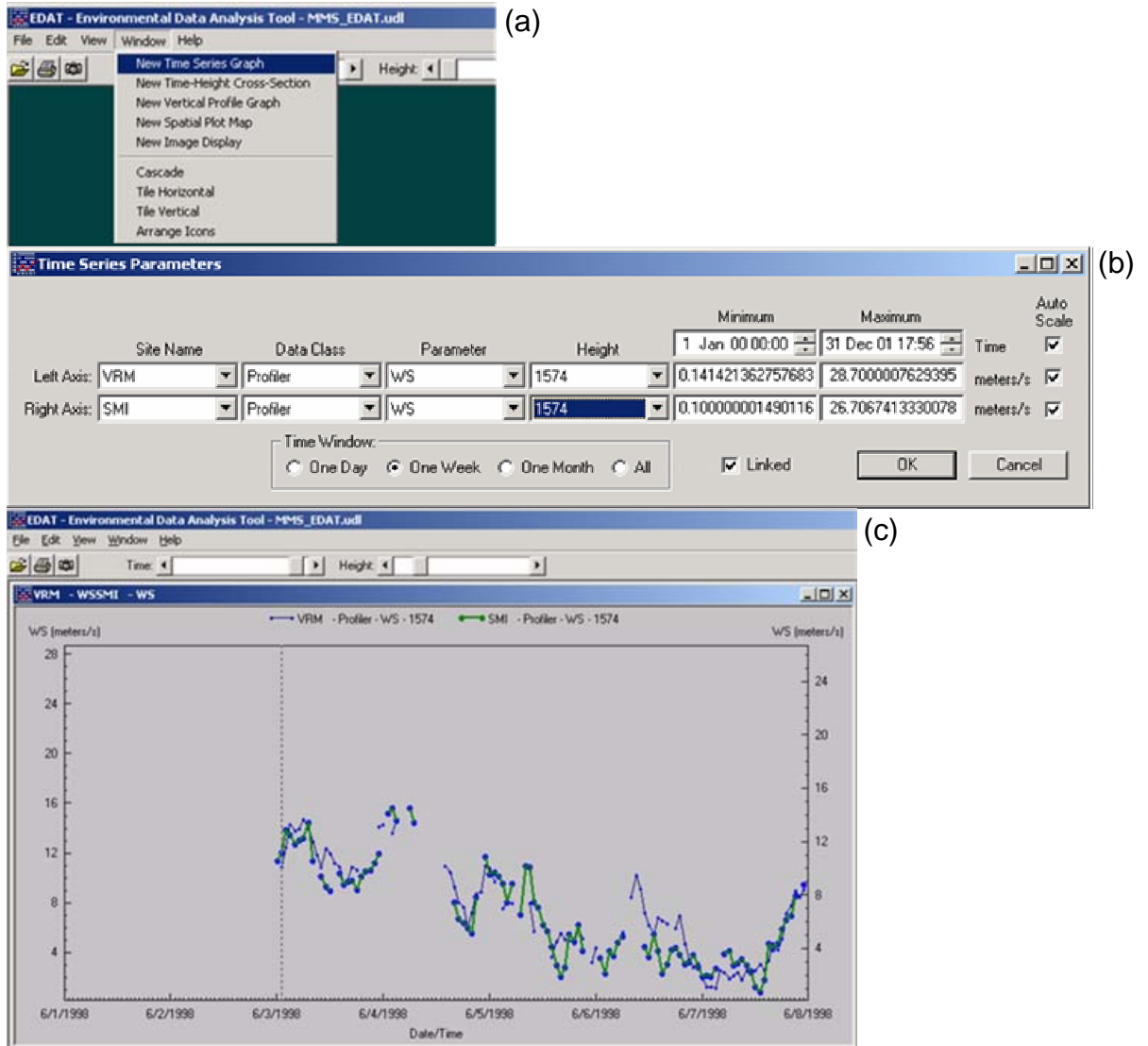


Figure 2-4. Sequence of events for creating a time series plot in EDAT: (a) open a new time series graph, (b) select data to be displayed, and (c) create the plot.

Table 2-1. C-MAN (five-character alphabetic), buoy (five-character numeric), and RWP platform sites. Included are the air temperature, anemometer, and sea temperature sensor heights. Sensor heights are in m above the site's elevation.

Site Name	Site	Latitude (degrees N)	Longitude (degrees W)	Elevation (m msl)	Air Temperature Height Above Site (m)	Anemometer Height Above Site (m)	Sea Temperature Height (m)
Mid Gulf 180 nm South of Southwest Pass LA	42001	25.93	89.65	0.0	10.0	10.0	-1.0
West Gulf 240 nm South-Southeast of Sabine TX	42002	25.89	93.57	0.0	10.0	10.0	-1.0
Biloxi 22 nm South-Southeast of Biloxi MS	42007	30.10	88.78	0.0	4.0	5.0	-0.6
Freeport TX. 60 nm South of Freeport TX	42019	27.92	95.35	0.0	4.0	5.0	-0.6
Corpus Christi TX 50 nm Southeast of Corpus Christi	42020	26.92	96.70	0.0	4.0	5.0	-0.6
Galveston 22 nm East of Galveston TX	42035	29.25	94.41	0.0	4.0	5.0	-0.6
Mobile South 64 nm South of Dauphin Island AL	42040	29.18	88.30	0.0	4.0	5.0	-0.6
Southwest Pass LA	BURL1	28.90	89.43	0.0	11.9	30.5	-0.5
Dauphin Island AL	DPIA1	30.25	88.07	0.0	9.1	17.4	-0.5
Grand Isle LA	GDIL1	29.27	89.96	1.8	15.2	15.8	-0.5
Port Arkansas TX	PTAT2	27.83	97.05	0.0	9.1	14.9	-0.5
Sabine TX	SRST2	29.67	94.05	0.9	11.9	12.5	-0.5
Breton Island Platform	BIP	29.77	88.71	20.0	2.0	3.0	0.0
Deep Water Platform	DWP	28.15	89.10	41.0	2.0	3.0	0.0
Shallow Water Platform	SWP	29.98	88.60	20.0	2.0	2.0	0.0
Mid Buoy Platform	MBP	29.62	88.57	20.0	2.0	3.0	0.0
West Delta Platform	WDP	28.83	89.78	20.0	2.0	3.0	0.0
Vermillion Gulf of Mexico	VRM	29.47	92.55	21.0	2.0	3.0	0.0
South Marsh Gulf of Mexico	SMI	28.15	91.91	25.0	2.0	3.0	0.0

Table 2-2. C-MAN (alphabetic), buoy (numeric), and RWP platform sites and their available surface meteorological data. Checkmarks indicate data were available.

Site	Site ID	Air Temperature	Near-Sea Surface Temperature	Skin Temperature	Relative Humidity	Wind	Pressure	Wave Height and Period
Mid Gulf 180 nm South of Southwest Pass LA	42001	✓	✓		✓	✓	✓	✓
West Gulf 240 nm South-Southeast of Sabine TX	42002	✓	✓		✓	✓	✓	✓
Biloxi 22 nm South-Southeast of Biloxi MS	42007	✓	✓		✓	✓	✓	✓
Freeport TX. 60 nm South of Freeport TX	42019	✓	✓			✓	✓	✓
Corpus Christi TX 50 nm Southeast of Corpus Christi	42020	✓	✓		✓	✓	✓	✓
Galveston 22 nm East of Galveston TX	42035	✓	✓		✓	✓	✓	✓
Mobile South 64 nm South of Dauphin Island AL	42040	✓	✓		✓	✓	✓	✓
Southwest Pass LA	BURL11	✓			✓	✓	✓	
Dauphin Island AL	DPIA11	✓	✓		✓	✓	✓	
Grand Isle LA	GDIL11	✓	✓		✓	✓	✓	
Port Aransas TX	PTAT21	✓	✓		✓	✓	✓	
South Marsh Gulf of Mexico	SMI	✓		✓	✓	✓	✓	
Sabine TX	SRST21	✓			✓	✓	✓	
Vermillion Gulf of Mexico	VRM	✓		✓	✓	✓	✓	
Breton Island Platform	BIP	✓		✓	✓	✓	✓	
Deep Water Platform	DWP	✓		✓	✓	✓	✓	
Shallow Water Platform	SWP	✓		✓	✓	✓	✓	
Mid Buoy Platform	MBP	✓		✓	✓	✓	✓	
West Delta Platform	WDP	✓		✓	✓	✓	✓	

Table 2-3. Derived COARE parameters.

Description
Sensible heat flux
Latent heat flux
Wind stress
Velocity scaling parameter (friction velocity)
Humidity scaling parameter
Temperature scaling parameter
Roughness Reynolds number
Height/Monin-Obukhov length
Roughness length
Total warm layer temperature difference
Thickness of warm layer
Cool skin temperature difference
Skin temperature

Table 2-4. Aloft synoptic classifications used in the 1998-2001 MMS Boundary Layer Study.

Classifications
Ridge
Weak Ridge
Flat
Zonal
Post-trough
Weak Trough
Trough
Cut-off Low
Tropical Storm

Table 2-5. Surface wind flow speed and direction classification used in the 1998-2001 MMS Boundary Layer Study.

Flow Direction	Flow Speed
Onshore	Light
Offshore	Moderate
Parallel east	Strong
Parallel west	

### **3. GENERAL METEOROLOGY**

#### **3.1 INTRODUCTION**

This section defines the upper-air and surface patterns observed in the Gulf of Mexico for the study period from June 1, 1998, to October 2, 2001, and describes the climatology of the upper-air and surface wind flow patterns. The results from this work were used to understand how the upper-air and surface wind flow patterns influence ABL characteristics, transport, and dispersion.

#### **3.2 UPPER-AIR PATTERNS**

Upper-level synoptic-scale weather features are large-scale (1000 km or more) weather circulations that produce regional meteorological conditions. It is necessary to analyze these patterns because they have a direct influence on the production, accumulation, and transport of pollutants. For example, an upper-level trough is an area of generally lower pressure in the upper levels of the troposphere. These troughs are typically associated with lifting of air, cloudy skies, and cooler temperatures. These weather conditions result in more vertical mixing of air, which tends to cause the ABL to grow quite large, increasing the vertical dispersion of pollutants. Upper-level troughs are often associated with surface weather systems that result in stronger winds and hence more horizontal dispersion. Another example of a general pattern is an upper-level ridge. The upper-level ridge is a region of generally higher pressure in the upper levels of the troposphere. These ridges are typically associated with sinking air, clear skies, and warm temperatures. These weather conditions result in decreased vertical mixing of air, which tends to suppress the growth of the ABL, which leads to less vertical dispersion of pollutants. Upper-level ridges also tend to result in surface-based highs downstream of the upper-level ridge axis. These surface highs can either lead to transport by influencing the wind directions or they can lead to light winds (and hence less horizontal dispersion). They may also allow mesoscale circulations to dominate the local flows, such as the sea breeze.

##### **3.2.1 Methods of Obtaining and Classifying Data**

To determine the upper-air meteorological patterns for the Gulf of Mexico region, we obtained EDAS meteorological plots of the 500-mb geopotential height pattern for the United States twice per day, once at 0000 UTC and once at 1200 UTC. We also obtained National Oceanic and Atmospheric Administration (NOAA)/National Weather Service (NWS)/National Center for Environmental Prediction (NCEP) Daily Weather Maps, which provide 500-mb geopotential height patterns and winds for the entire United States once per day at 0600 CST. The 500-mb geopotential height patterns depict the large-scale weather patterns across a region.

The upper-level patterns were classified based on observations of the 500-mb geopotential height pattern, locations of ridge and trough axes, and circulations apparent in the 500-mb winds. Anti-cyclonic circulations (clockwise in the northern hemisphere) indicate high pressure while cyclonic circulations (counterclockwise in the northern hemisphere) represent low

pressure. All classifications were compiled based on the positions of weather systems with respect to the study region over the Gulf of Mexico.

**Figure 3-1** shows an example of an upper-level ridge over the Gulf of Mexico region. The ridge axis is defined by connecting the peak amplitude of each line into a single line, or axis. The weather patterns associated with the upper-level ridge are likely to be strongest near the axis.

Transitions between upper-level patterns were observed in this study; therefore, it was necessary to determine the average daily pattern based on the pattern that was observed for a majority of that day.

We looked at the upper-level synoptic pattern at 500 mb for every day, twice per day, during the study period and determined a dominant set of upper-air patterns. We then assigned a pattern to each day. These patterns were put into the database. **Figure 3-2** shows the 500-mb heights on March 22, 2000, at 1200 UTC generated by the EDAS model output. This particular day was classified as a ridge pattern (see below) for the study area.

In our statistical review of the upper-level synoptic patterns, the frequency of occurrence of each upper-air pattern was determined using queries of the daily data available in the database. Queries were used to group each upper-air pattern by the entire study period, by year, by month, and by season.

The following upper-level synoptic classifications were used:

- **Ridge:** An example of a ridge is shown in Figure 3-2. A ridge pattern usually leads to high pollution levels as a result of conditions such as subsidence of air, clear skies, and warming of surface and aloft temperatures. These weather conditions decrease the height of the ABL and often allow mesoscale circulations, such as the sea breeze/land breeze circulation, to dominate the boundary layer winds.
- **Weak Ridge:** An example of a weak ridge is shown in **Figure 3-3**. A weak ridge pattern can lead to high pollution levels as a result of subsidence of air, clear skies, and warming of surface and aloft temperatures. However, weak ridges tend to result in weaker subsidence, which may allow the ABL to grow vertically more than it can under a ridge pattern.
- **Trough:** An example of a trough is shown in **Figure 3-4**. A trough pattern is associated with rising air, cloudy skies, strong winds, and cool aloft temperatures. All of these weather conditions tend to result in more vertical mixing and horizontal dispersion. In addition, the mixing height of the ABL may be very high under these conditions.
- **Weak Trough:** An example of a weak trough is shown in **Figure 3-5**. A weak trough may be associated with rising air, cloudy skies, stronger winds, and cooler temperatures; however, not all conditions may occur. Weak troughs are typically associated with the same dispersion characteristics as troughs; however, these characteristics may not be as strong so the mixing height of the ABL may not be as large.

- **Cut-off Low:** An example of a cut-off low is shown in **Figure 3-6**. A cut-off low is similar to a trough; however, cut-off lows tend to move more slowly than troughs. Sometimes, cut-off lows may be too weak to produce much vertical mixing; therefore, it may be possible to see higher pollution levels and less dispersion than expected under a trough pattern.
- **Post Trough:** A post trough is typically found after a trough has passed through a region, but prior to a ridge building in. **Figure 3-7** shows an example of this pattern over southern Louisiana. A post trough typically indicates clearing skies and northerly surface winds. Since a post trough immediately follows a trough, background pollution levels are typically low.
- **Flat:** A flat upper-air pattern is typically found when neither a ridge nor a trough is near the region. **Figure 3-8** shows an example of this pattern over the Gulf of Mexico. In this case, winds were driven by mesoscale meteorological conditions, such as a sea breeze. For this pattern, ABL characteristics are strongly dependent on the mesoscale meteorological conditions.
- **Zonal:** A zonal weather pattern is depicted in **Figure 3-9** over the Gulf Coast states. Zonal weather patterns typically do not last long and are often replaced by ridges and troughs. The ABL characteristics are once again dependent on mesoscale meteorological conditions, such as the sea breeze.
- **Tropical Storm:** Tropical storms occur on only a few days of a year, at most, in the Gulf region. **Figure 3-10** depicts hurricane Bret over southeast Texas, extending into the eastern Gulf of Mexico. A tropical storm is typically associated with cloudy skies, strong winds, and low air pollution levels; however, it is possible for these patterns to introduce subsidence in nearby regions as a result of outflow at the upper levels. This increased subsidence away from the storm center may decrease winds, warm temperatures, and enhance pollutant levels.

To simplify some of the analyses, it was necessary to group similar patterns into broader categories. Therefore, we combined the ridge and weak ridge into the “grouped ridge” category. We grouped the trough, weak trough, and cut-off low into the “grouped trough” category, and the remaining patterns, post-trough, flat, zonal, and tropical storm, were grouped into the “grouped others” category.

### 3.2.2 Data Classification Results

**Figure 3-11** shows the grouped upper-air synoptic pattern for the three general groups for the study period and shows an almost equal representation of both ridges and troughs. Other patterns (the post trough, flat, zonal, and tropical storm patterns) were observed less than 20% of the time.

**Figure 3-12** shows the frequency of occurrence of each of the nine upper-air patterns during the study period. Note that the ridge pattern was the dominant upper-air pattern,

occurring approximately one-third of the time. This is important because the ridge pattern is often associated with ABL characteristics that lead to high pollutant concentrations. The trough was the second-most predominant upper-air feature, which was observed about a quarter of the time. This is important because the ABL characteristics under trough scenarios typically lead to low pollution episodes. Weak troughs occurred less frequently and were observed on about one out of every six days. The other patterns were found to occur far less frequently, with tropical storms being rare.

**Figure 3-13** shows the frequency distribution of the grouped upper-air patterns observed during the study period by “MMS year”. Since the study began in June 1998 and ended in October 2001, an MMS year is defined as June 1 through May 31. Thus, the year 1998 refers to the period from June 1, 1998, through May 31, 1999. MMS year 2001 contains June 1, 2001, through October 1, 2001, data. Therefore, the results for 2001 are biased because they contain only four months of data. As shown in Figure 3-13, the frequency of occurrence of each pattern did not vary significantly from year to year with the exception of 1998. During 1998, the trough pattern was observed approximately 10% more often than the ridge pattern. This is important because the ABL characteristics may have been significantly affected by the presence of more troughs during that year. Fewer troughs occurred in 2001 than in other years; however, since most of the 2001 data came from the summer months, this observation is biased.

**Figure 3-14** shows the frequency distribution of the individual upper-air patterns observed during the study period by MMS year. Although the frequency of occurrence of grouped trough and ridge patterns were generally similar, further examination of the upper-air patterns show that the ridge pattern dominated followed by the trough pattern, but the weak ridges occurred less frequently than the weak troughs.

In 2000, a ridge pattern occurred almost 10% more often than during the other years. The other five patterns occurred far less frequently, and tropical storms were a rare occurrence. An anomalously high percentage of flat pattern days occurred in 2001, probably due to bias in the data for that shortened year.

**Figure 3-15** shows the frequency distribution of the grouped upper-air patterns by season for all years during the study period. Although there was a relatively even distribution in the annual upper-air characteristics between the trough and ridge patterns, seasonal breakdowns show that both the fall and winter seasons are dominated by a trough pattern, while spring is equally distributed between troughs and ridges, and summer is dominated by a ridge pattern. These seasonal variations imply that the ABL characteristics will also be different as the seasons change. For example, in the winter, with more troughs, we would expect vertical mixing and horizontal dispersion to be high, leading to lower pollutant concentrations than during the summer.

**Figure 3-16** shows the frequency distribution of the individual upper-air patterns for all years by season. Recall that the summer season was dominated by the grouped ridge pattern while fall and winter were predominantly characterized by the grouped trough pattern. The refined classifications show that the ridges that are not weak account for about 45% of the summer days; whereas, the weak ridges account for less than 10% of summer days. In the fall and winter months, the troughs account for approximately one-third of the days; whereas, the

weak troughs account for about 15% of the days. These facts are important because strong patterns will have a stronger impact on the ABL characteristics and, therefore, a stronger impact on air pollution.

Analysis shows that during the spring, a majority of the troughs were actually weak troughs. Weak troughs have a different impact on the ABL characteristics than strong troughs. While the impact on the ABL is significant when tropical storms are present, they occur only during the summer months.

**Figure 3-17** shows the monthly frequency distribution of the grouped upper-air patterns. June, July, August, and September produced more days of data because the study period ran from June 1, 1998, through October 2, 2001. The ridge pattern dominated from June through October, as expected for this region. However, September had significantly more troughs compared to the other months. This implies that the ABL characteristics may differ during September in contrast to other summer months. November through March was dominated by a trough pattern.

### **3.3 SURFACE FLOW CHARACTERISTICS**

Surface wind speed and direction data collected at the C-MAN, buoy, and platform surface monitors were analyzed to characterize the surface flow patterns in the Gulf of Mexico. The analysis involved creating wind rose plots for all sites to characterize surface flows and classifying the flow at selected sites on each day of the study period as onshore, offshore, parallel west, or parallel east. The daily surface speed and direction flow classifications are included in the database. The buoy and platform sites are separated by large distances, stretching from buoy 42019 a few hundred km southwest of Houston, to buoy 42040 near southern Alabama, to as far as 100 km offshore. These distances alone provide expected variability in the nature of the onshore and offshore flow characteristics.

#### **3.3.1 Methods of Determining Surface Flow Characteristics**

To determine the onshore/offshore surface flow patterns and the wind roses, we obtained hourly surface wind speed and wind direction data from the MMS platform sites at VRM and SMI. We also obtained surface wind speed and wind direction data for several C-MAN and buoy sites located in the Gulf of Mexico, as shown in Figure 2-1.

#### **Daily Flow Characteristic Analysis**

Two buoy sites and two platform sites were chosen to characterize the surface flows on each day. Buoy 42035 (15 km offshore from Galveston, Texas) and the VRM platform site (10 km offshore from central Louisiana) were selected to represent the near-shore characteristics. Buoy 42019 (100 km offshore from Freeport, Texas) and the SMI platform site (about 100 km south of South Marsh Island) were selected to represent the offshore characteristics. Onshore flows were classified by wind directions between 100° and 260°. Offshore flows were classified by wind directions between 280° and 80°. Wind directions between 80° and 100° were designated “parallel east” and wind directions between 260° and 280° were designated “parallel

west”. Note, since the parallel directions exist within a 40° range, an even distribution of winds would be eight times more likely to occur than wind directions parallel to the shore. Yearly, seasonal, and upper-air averages of the daily surface flow directions and speeds were created and analyzed. Flow types were classified by speed. **Table 3-1** depicts the categories used for speed classifications. Three classifications were developed based on the Beaufort Wind Scale: light, moderate, and strong.

Table 3-1. Speed classifications.

Wind Speed > 10 m/s	Strong
Wind Speed > 5 m/s and ≤ 10 m/s	Moderate
Wind Speed ≤ 5 m/s	Light

### Wind Rose Analysis

Wind roses were created using the WRPLOT View wind rose program based on data collected from all of the buoy and platform monitors within the MMS study region. Wind roses are useful for determining surface flow speed and direction characteristics for the entire study period and by season. Wind roses provide a quick indication of the flow characteristics for individual sites. An example of a wind rose plot is given in **Figure 3-18**. The dashed circles indicate the percentage of time the winds are from a particular direction. The different colors within the bars indicate the percentage of time each range of wind speeds was observed.

The wind rose data results were grouped based on initial comparisons of all of the sites. **Figure 3-19** shows the site groupings. Group A sites represent the western Gulf of Mexico. Group B sites represent the eastern portion of the study region.

### 3.3.2 Results of Determining Surface Flow Characteristics

#### Daily Flow Characteristic Analyses

A predominant onshore flow that was light to moderate in speed was observed for the entire study period at the four sites used for analyzing the daily flow characteristics. **Figure 3-20** shows the frequency distribution of surface flow types by year for the near-shore buoy site (42035) and the offshore site (SMI). All four sites show onshore flow about twice as often as offshore flow. The flow is rarely parallel to the coastline, and when it is, it is predominantly from the east. In 1999, less onshore flow was observed at buoy 42019 and VRM compared to 1998 and 2000. This pattern was not observed at buoy 42035 or SMI. This is important because these differences may impact the characteristics of the ABL.

**Figure 3-21** shows the seasonal frequency distribution of surface flow directions. Once again the onshore flow direction clearly dominates during all seasons, except for one notable exception. For the buoy 42035, VRM, and SMI sites, surface flow during the fall is predominantly offshore (occurring approximately half of the time). Summer and spring at all

sites are characterized by onshore flow between 70% and 80% of the time. Winter and fall tend to have a more even distribution of offshore and onshore days, with each occurring 40% to 50% of the time. These observations are important to the transport and dispersion characteristics as well as the ABL structure. For example, the onshore flow suggests that offshore sources may impact onshore areas more often in the spring and summer. The winds during all seasons were seldom strong. During fall, winter, and spring, moderate winds dominated, while during the summer, light winds dominated.

**Figure 3-22** shows the frequency distribution of flow speeds and directions based on upper-air synoptic pattern. For all of the upper-air patterns, light-to-moderate winds and offshore or onshore flow dominated. Annual and seasonal results were similar. Stronger winds were observed under the trough pattern as opposed to the ridge pattern, which is consistent with the fact that more horizontal dispersion is expected with a trough. In general, stronger winds were observed more often at the offshore sites.

Onshore flow occurs 70% to 80% of the time a ridge is present; whereas, it occurs 50% to 60% of the time for the other upper-air patterns. This shows that under a ridge pattern, the offshore flow occurrences are extremely low, especially when compared with the trough and other upper-air patterns. Consistent with the yearly and seasonal breakdowns, parallel flows were a rare occurrence no matter what upper-air pattern was present.

### Wind Rose Analysis

The wind roses show that the dominant flow within the region was southeasterly, with a secondary, less predominant flow from the northeast. Westerly flow within the region was less predominant.

For the wind rose analysis, the sites were divided into two groups: Group A and Group B. Group A sites were characterized by a strong southeasterly flow (as shown in **Figure 3-23a** at VRM) and very little southwest through northeast flow. The southeasterly flow is likely a reflection of the predominant weather feature, the Bermuda high, as well as the sea breeze. The northeasterly flow is likely a result of continental high pressure systems. The Group B sites, although dominated by a southeasterly flow, did not have a strong southeasterly flow (**Figure 3-23b** shows this for buoy 42040). In addition, winds were more evenly distributed in other directions. The strongest winds for the Group B sites occurred predominantly from the northeast. The Group A sites had an even distribution of strong winds. These differences are important as they suggest that different areas of the Gulf of Mexico region may experience different ABL characteristics.

The seasonal wind rose patterns revealed general agreement with the overall patterns and have the following characteristics.

- The fall wind rose plots (**Figure 3-24**) show that Group B sites had predominantly north-northeast flows and very little southwesterly flow. Group A sites had a predominantly southeasterly flow with secondary flows from the north-northeast, with the exception of buoy 42001, which was dominated by an easterly flow.

- The winter wind rose plots (**Figure 3-25**) were similar to fall wind rose plots except for a stronger southeast flow at the Group B sites. Buoy 42007 had a more even peak distribution than the other Group B sites.
- The flow in the spring (**Figure 3-26**) in both groups was very different than in the fall and winter. Spring is characterized by a predominant southeasterly flow with very little northerly flow at the Group A sites. Group B sites were dominated by a broad peak from the east-southeast to the southwest.
- The summer wind rose plots with a dominant southeast peak show that the summer flow was similar to the spring flow for Group A sites (**Figure 3-27**). The near-shore sites show a more frequent southerly peak, likely due to the land/sea breeze circulation. Group B sites had an evenly distributed peak from east through south to west, with the exception of SMI, which only had a southwest peak.

These seasonal differences indicate that seasonal variability in surface wind speeds and directions exist and that attention needs to be paid to these differences with respect to the ABL characteristics, case study analyses, and modeling.

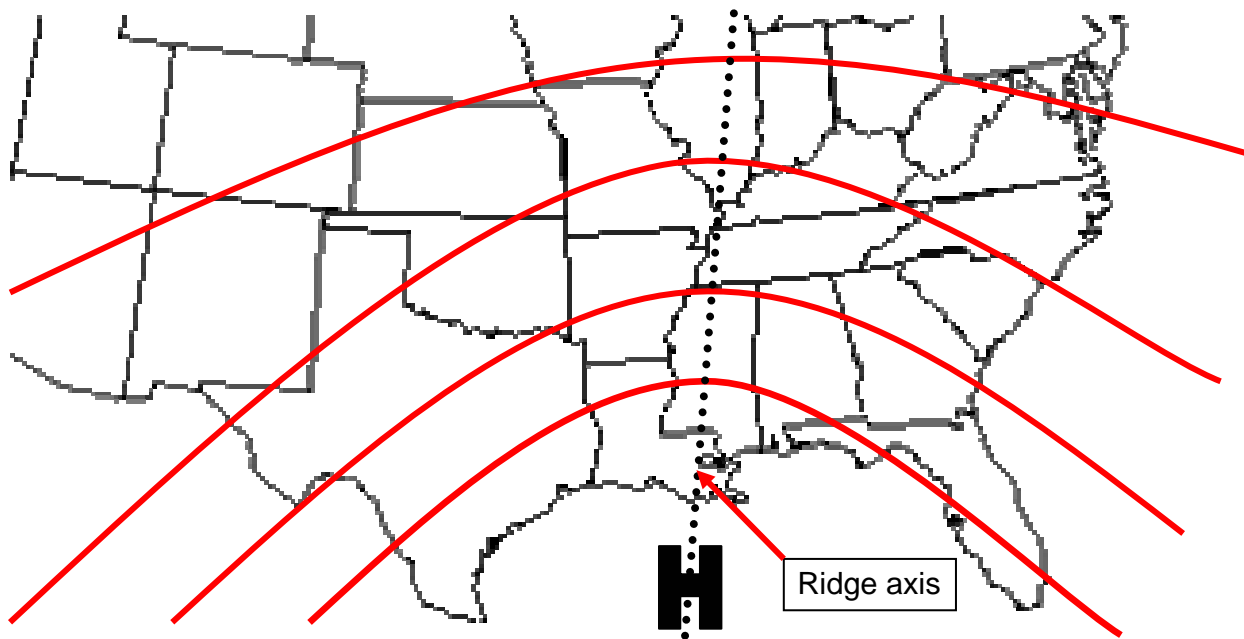
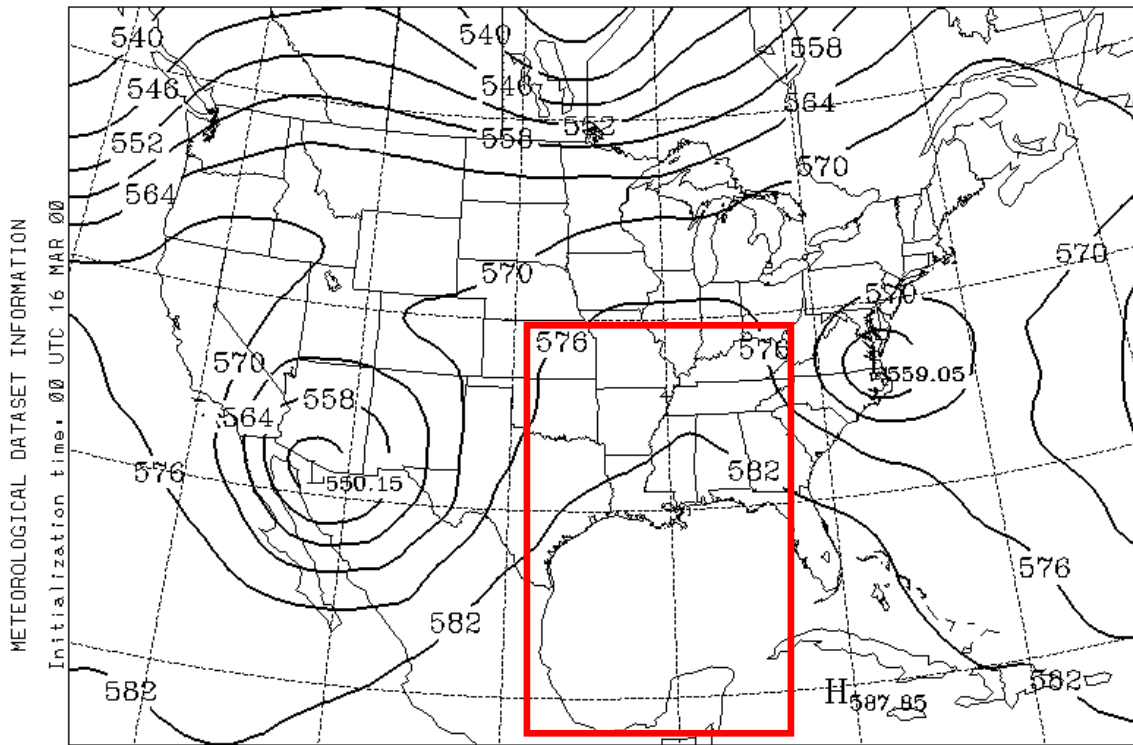


Figure 3-1. An upper-level high pressure system with ridge axis (dotted line). The contours represent geopotential heights, with the highest heights located near the “H” over the Gulf of Mexico.



EDAS Archive



NATIONAL OCEANIC AND ATMOSPHERIC ADMINISTRATION - AIR RESOURCES LABORATORY

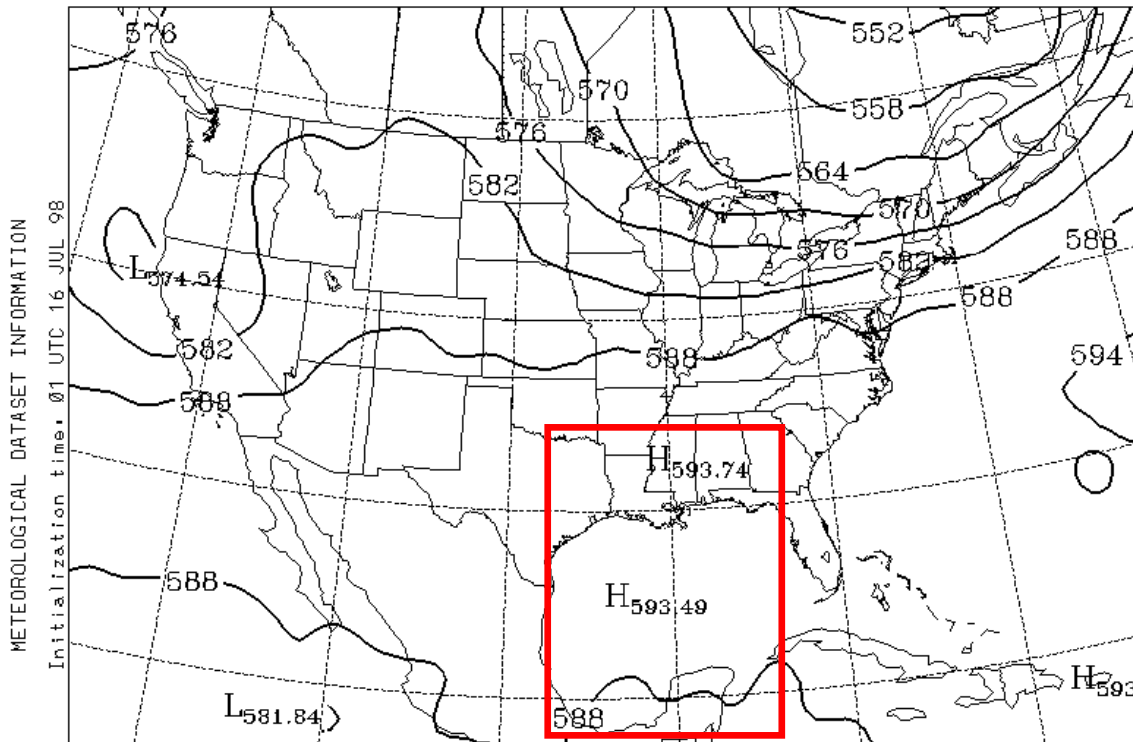
HEIGHT

HGTS ( DM ), LVL= 500., 12 UTC 22 MAR 00 (+ 00 H )

Figure 3-2. Example of an upper-air ridge pattern (box) for the Gulf of Mexico region for March 22, 2000, at 1200 UTC (0600 CST). Solid lines indicate height contours (decameters).



EDAS Archive



NATIONAL OCEANIC AND ATMOSPHERIC ADMINISTRATION - AIR RESOURCES LABORATORY

HEIGHT

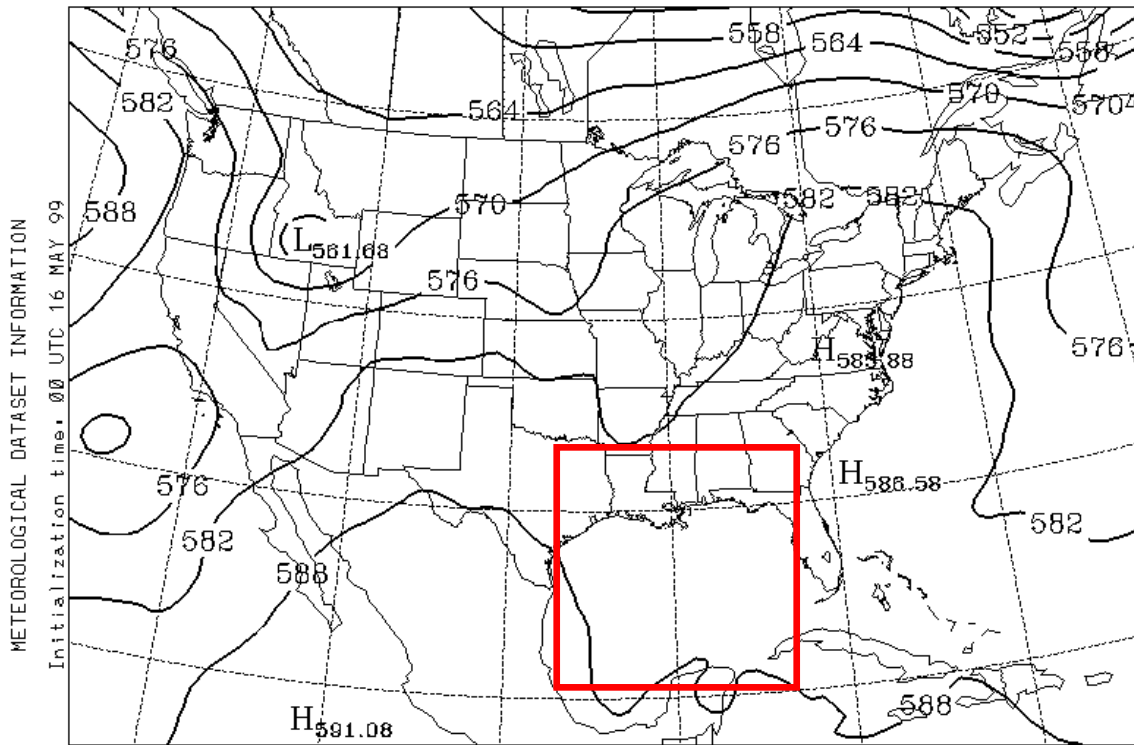
HGTS ( DM ), LVL= 500., 12 UTC 30 JUL 98 (+ 00 H )

Figure 3-3. Example of an upper-air weak ridge pattern (box) for the Gulf of Mexico region for July 30, 1998, at 1200 UTC (0600 CST). Solid lines indicate height contours (decameters).





EDAS Archive



NATIONAL OCEANIC AND ATMOSPHERIC ADMINISTRATION - AIR RESOURCES LABORATORY

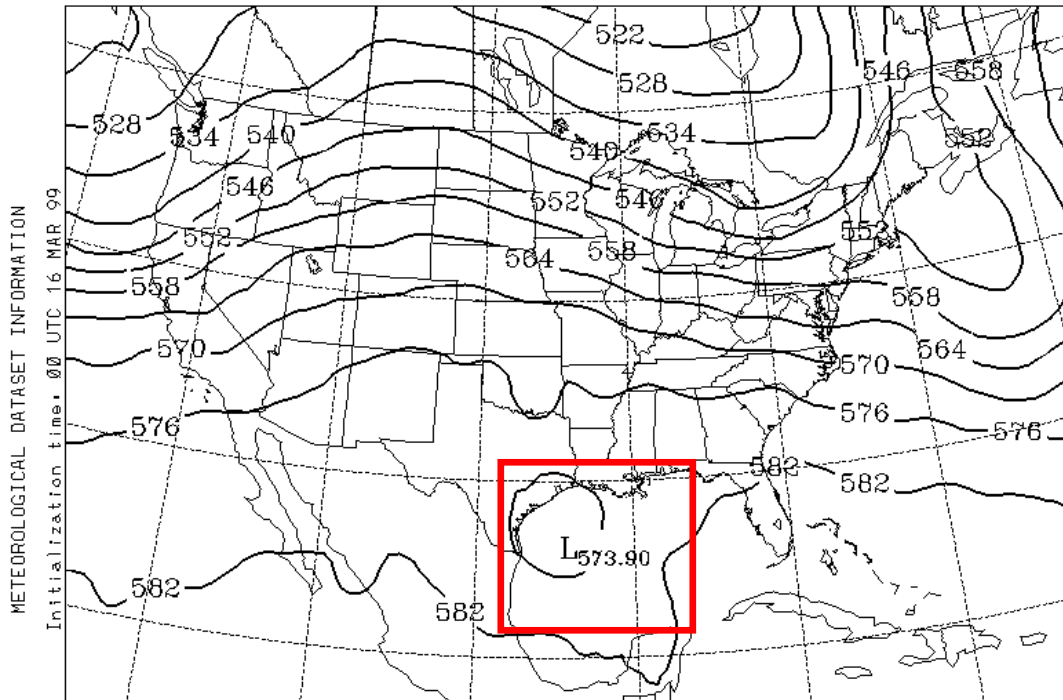
HEIGHT

HGTS ( DM ), LVL= 500., 00 UTC 31 MAY 99 (+ 00 H )

Figure 3-5. Example of an upper-air weak trough pattern (box) for the Gulf of Mexico region for May 31, 1999, at 0000 UTC (May 30, 1999, at 1800 CST). Solid lines indicate height contours (decameters).



EDAS Archive



NATIONAL OCEANIC AND ATMOSPHERIC ADMINISTRATION - AIR RESOURCES LABORATORY

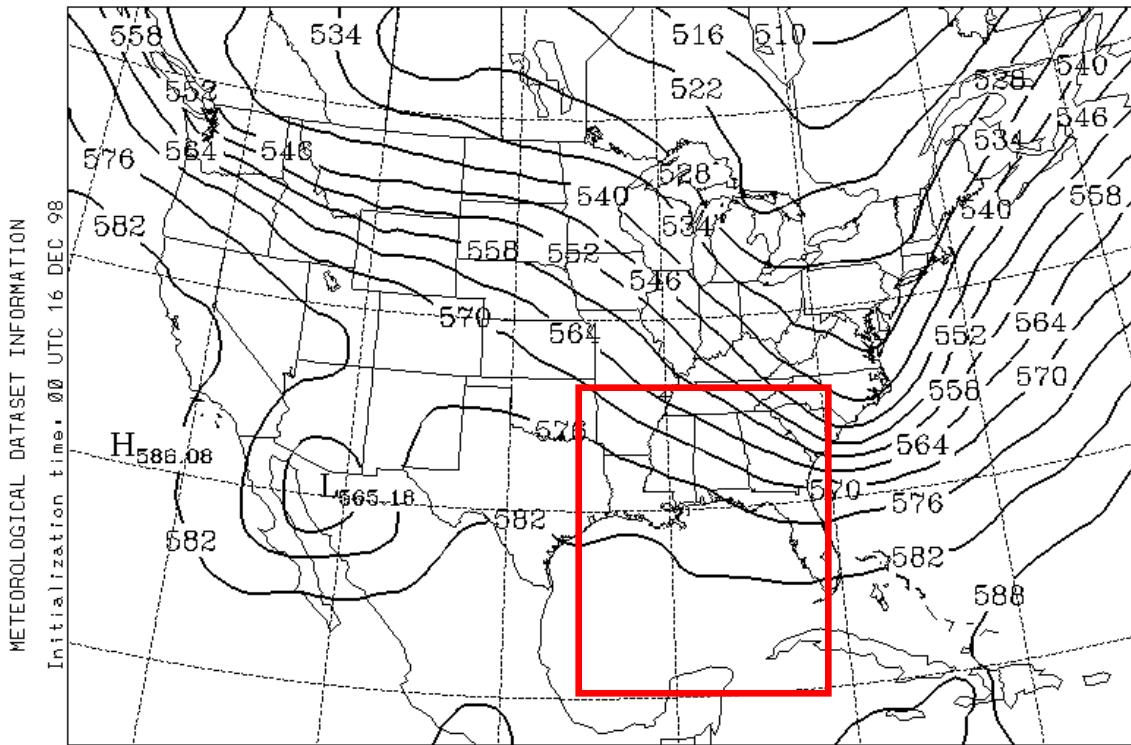
HEIGHT

HGTS ( DM ), LVL= 500., 00 UTC 30 MAR 99 (+ 00 H )

Figure 3-6. Example of an upper-air cut-off low pattern (box) for the Gulf of Mexico region for March 30, 1999, at 0000 UTC (March 29, 1999, at 1800 CST). Solid lines indicate height contours (decameters).



EDAS Archive



NATIONAL OCEANIC AND ATMOSPHERIC ADMINISTRATION - AIR RESOURCES LABORATORY

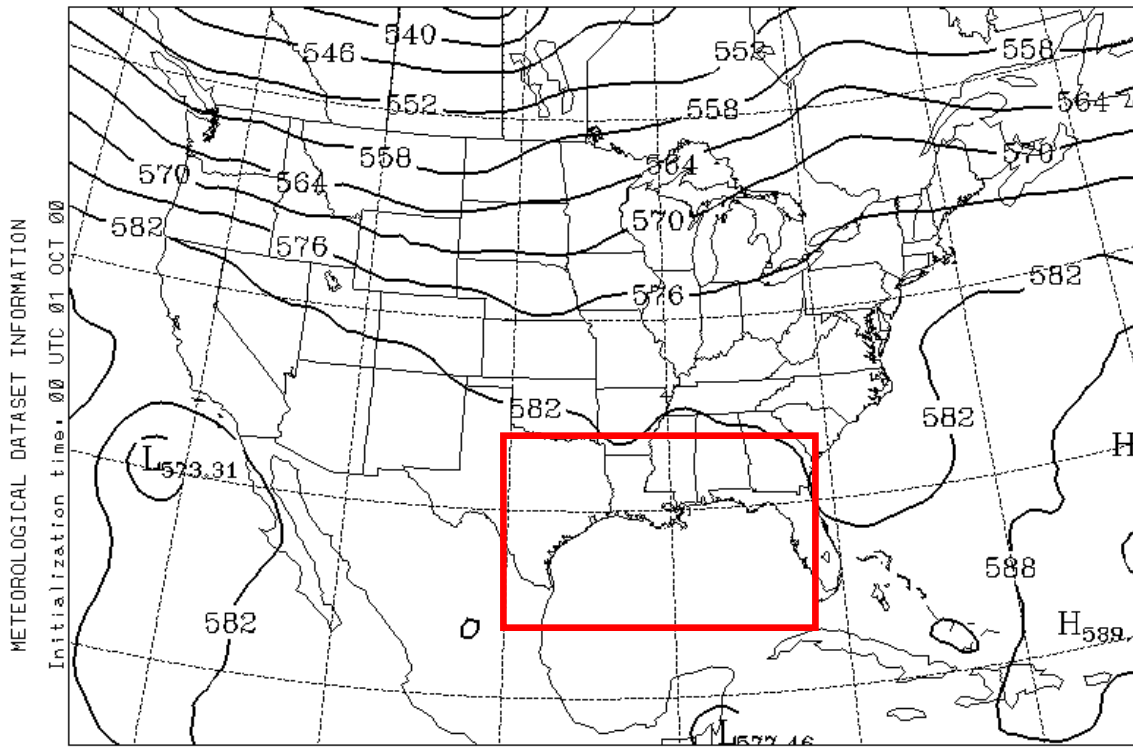
HEIGHT

HGTS ( DM ), LVL= 500., 00 UTC 18 DEC 98 (+ 00 H )

Figure 3-7. Example of an upper-air post-trough pattern (box) for the Gulf of Mexico region for December 18, 1998, at 0000 UTC (December 17, 1998, at 1800 CST). Solid lines indicate height contours (decameters).



EDAS Archive



NATIONAL OCEANIC AND ATMOSPHERIC ADMINISTRATION - AIR RESOURCES LABORATORY

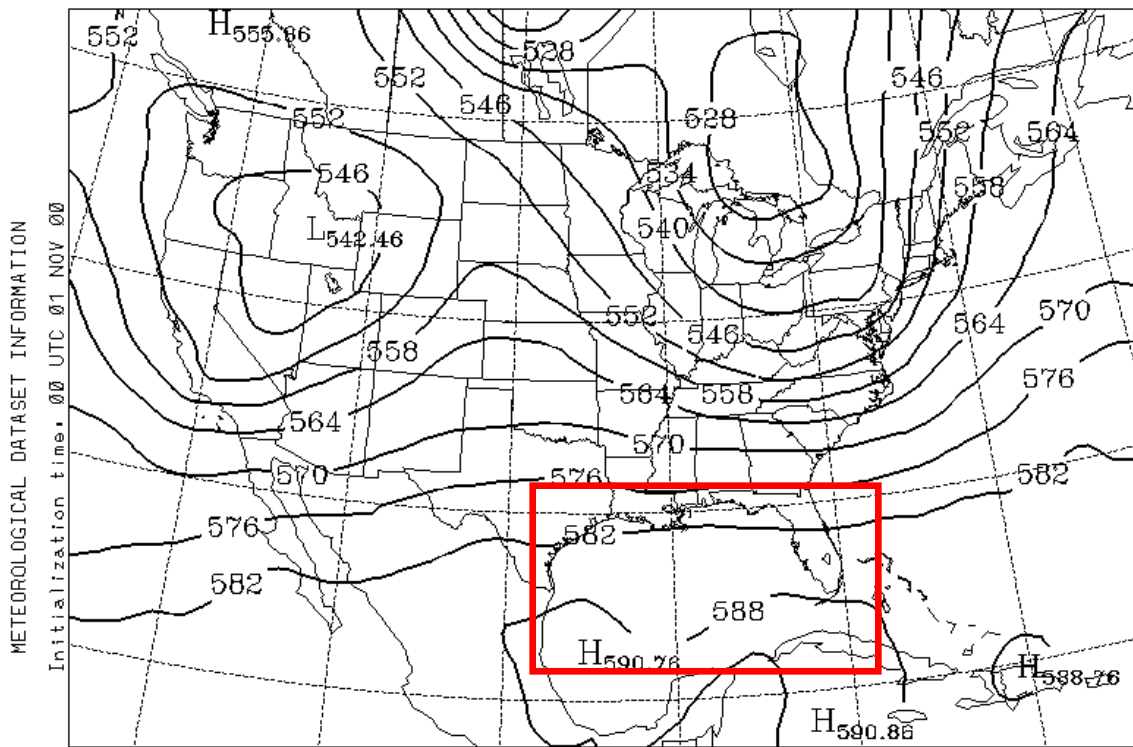
HEIGHT

HGTS ( DM ), LVL= 500., 12 UTC 01 OCT 00 (+ 00 H )

Figure 3-8. Example of an upper-air flat pattern (box) for the Gulf of Mexico region for October 1, 2000, at 1200 UTC (0600 CST). Solid lines indicate height contours (decameters).



EDAS Archive



NATIONAL OCEANIC AND ATMOSPHERIC ADMINISTRATION - AIR RESOURCES LABORATORY

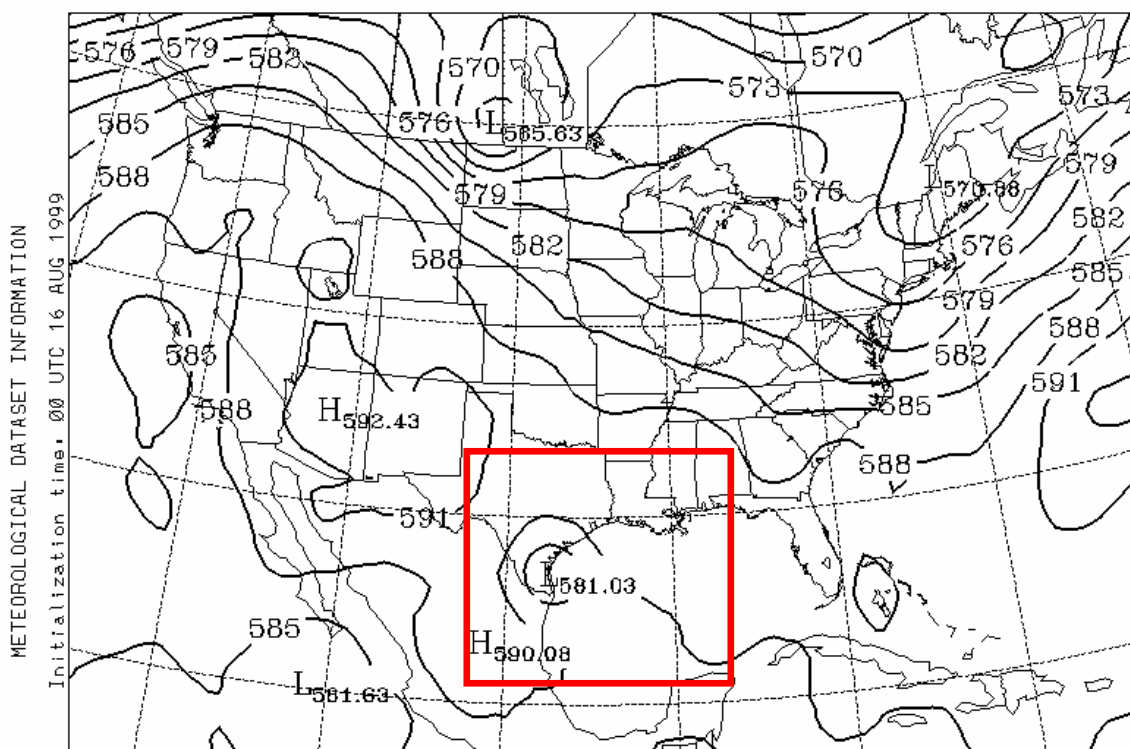
HEIGHT

HGTS ( DM ), LVL= 500., 00 UTC 15 NOV 00 (+ 00 H )

Figure 3-9. Example of an upper-air zonal pattern (box) for the Gulf of Mexico region for November 15, 2000, at 0000 UTC (November 14, 2000, at 1800 CST). Solid lines indicate height contours (decameters).



EDAS Archive



NATIONAL OCEANIC AND ATMOSPHERIC ADMINISTRATION - AIR RESOURCES LABORATORY

HEIGHT

HGTS ( DM ), LVL= 500., 00 UTC 23 AUG 1999 (+ 00 H )

Figure 3-10. Example of an upper-air hurricane pattern (box) for the Gulf of Mexico region for August 23, 1999, at 0000 UTC (August 22, 1999, at 1800 CST). Solid lines indicate height contours (decameters). This upper-air pattern depicts hurricane Bret over southeast Texas, extending east into the western Gulf of Mexico.

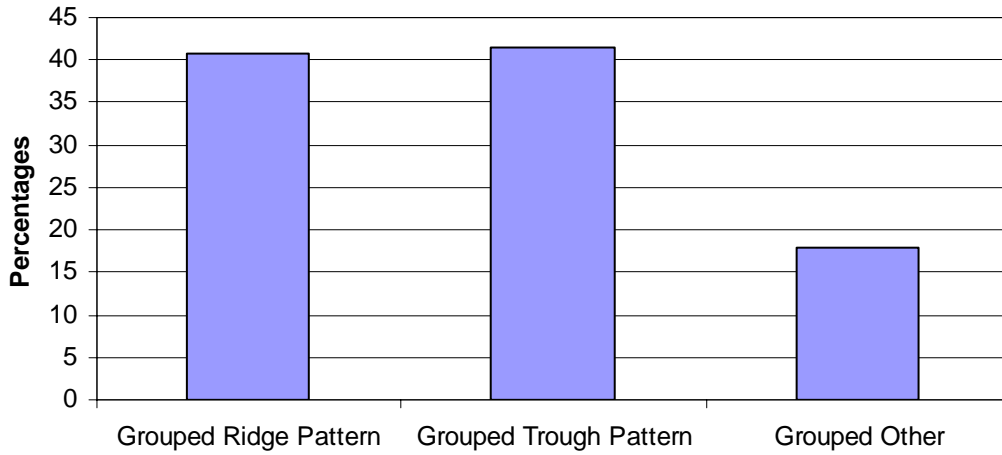


Figure 3-11. Overall frequency distribution of grouped upper-air patterns observed for the study period.

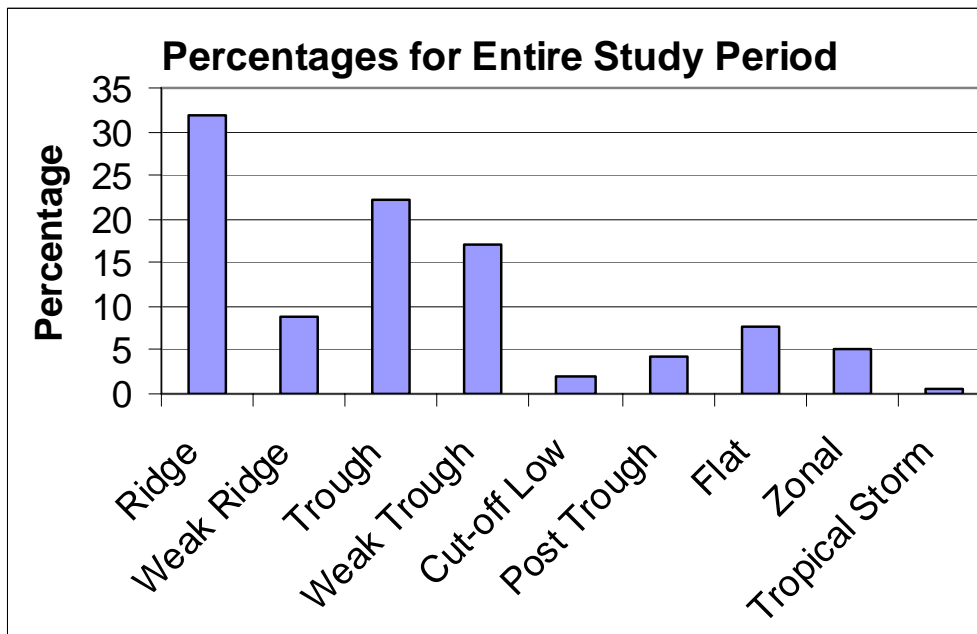


Figure 3-12. Frequency distribution of upper-air patterns observed for the study period.

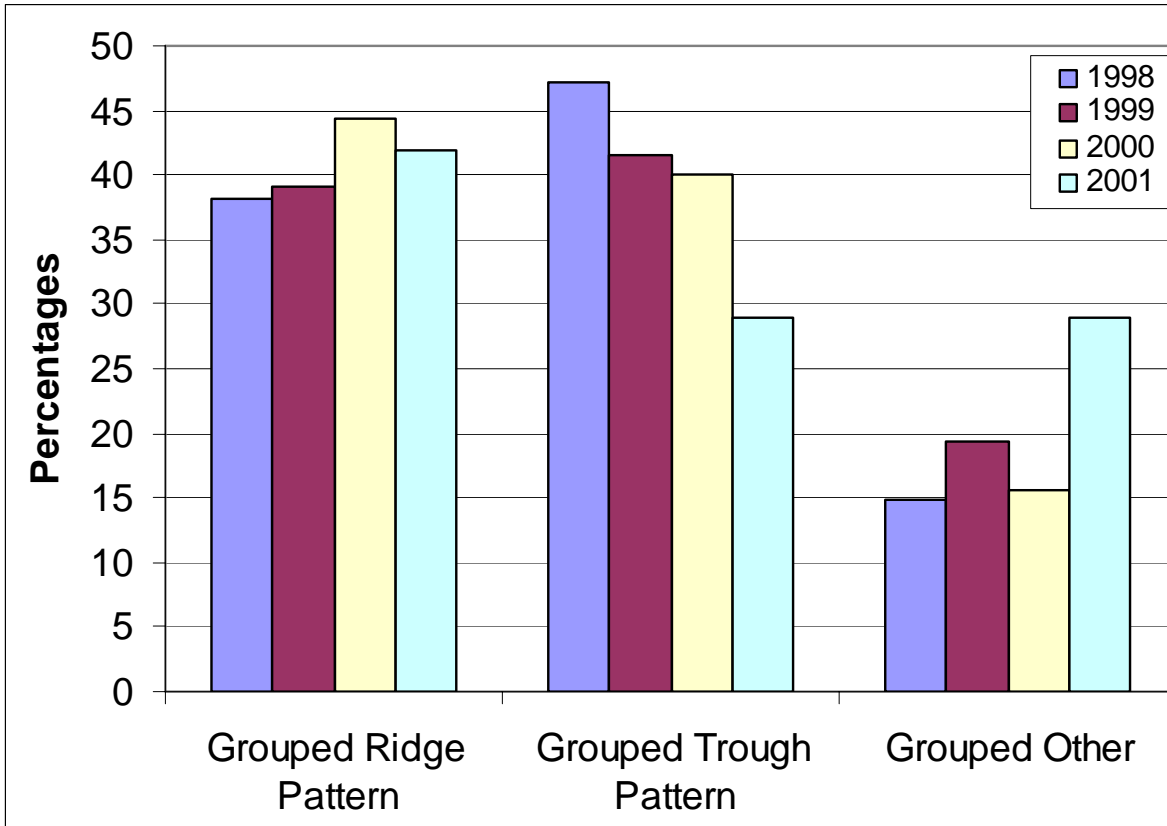


Figure 3-13. Frequency distribution of grouped upper-air patterns observed for each MMS year, June through May, during the study period.

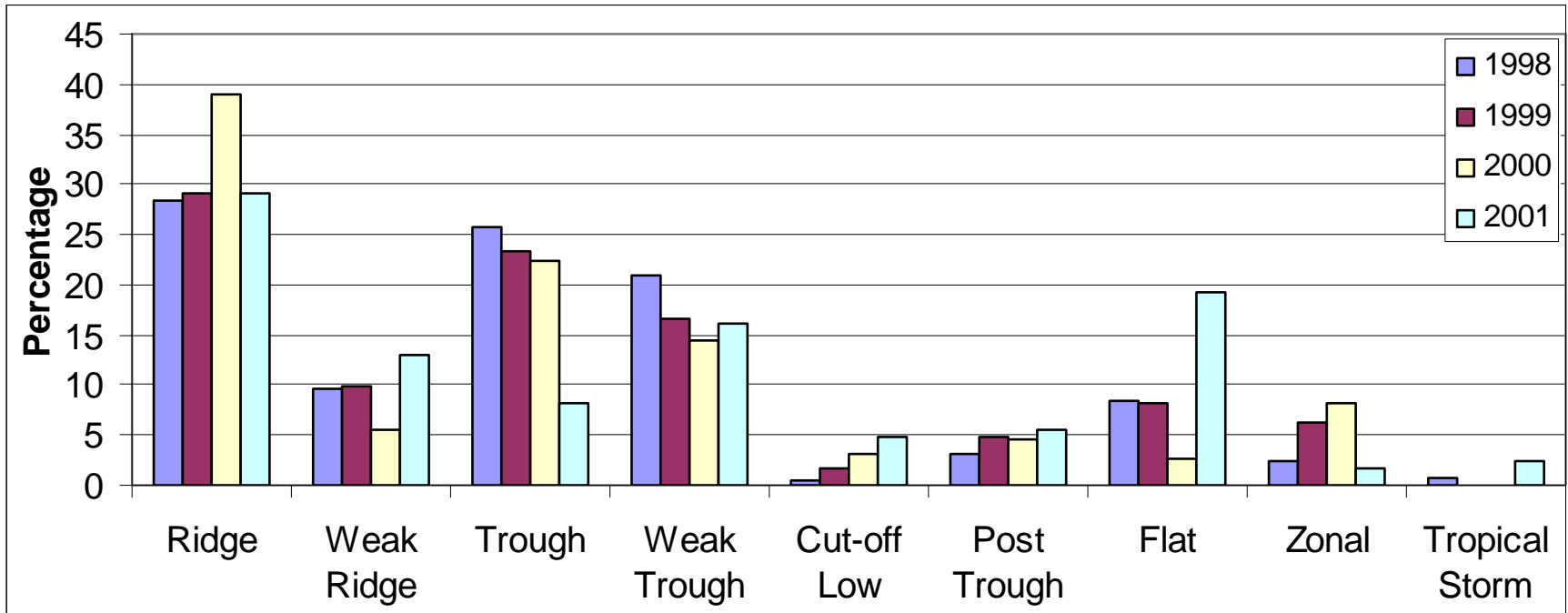


Figure 3-14. Frequency distribution of nine upper-air patterns observed for each MMS year during the study period.

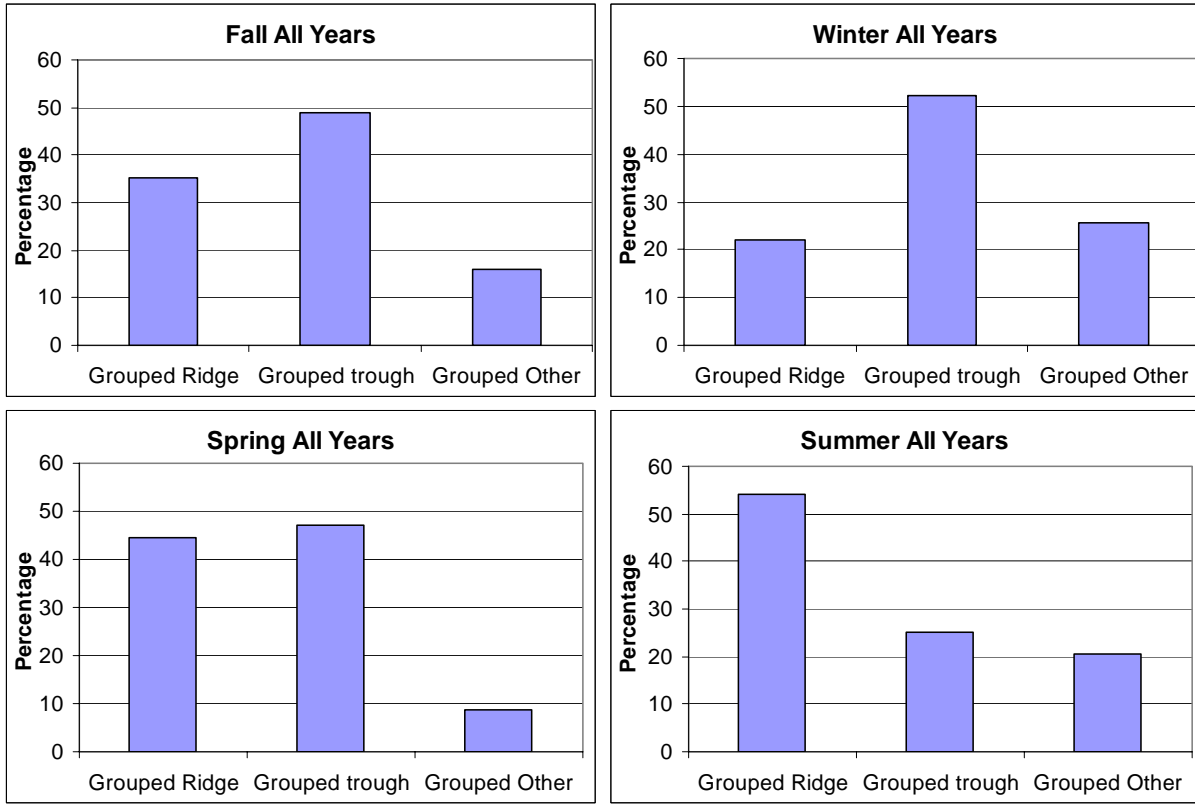


Figure 3-15. Frequency distribution of grouped upper-air patterns observed for each season for all years during the MMS study period.

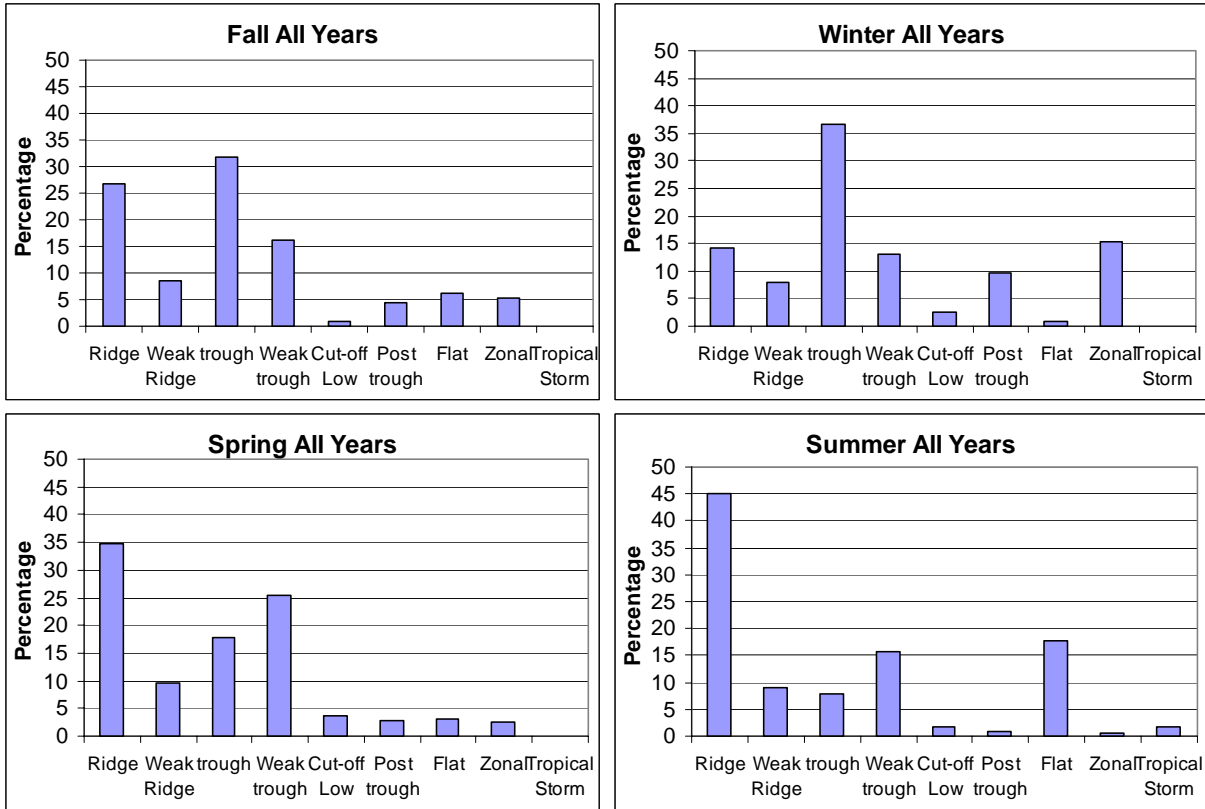


Figure 3-16. Frequency distribution of nine upper-air patterns observed for each season for all years during the MMS study period.

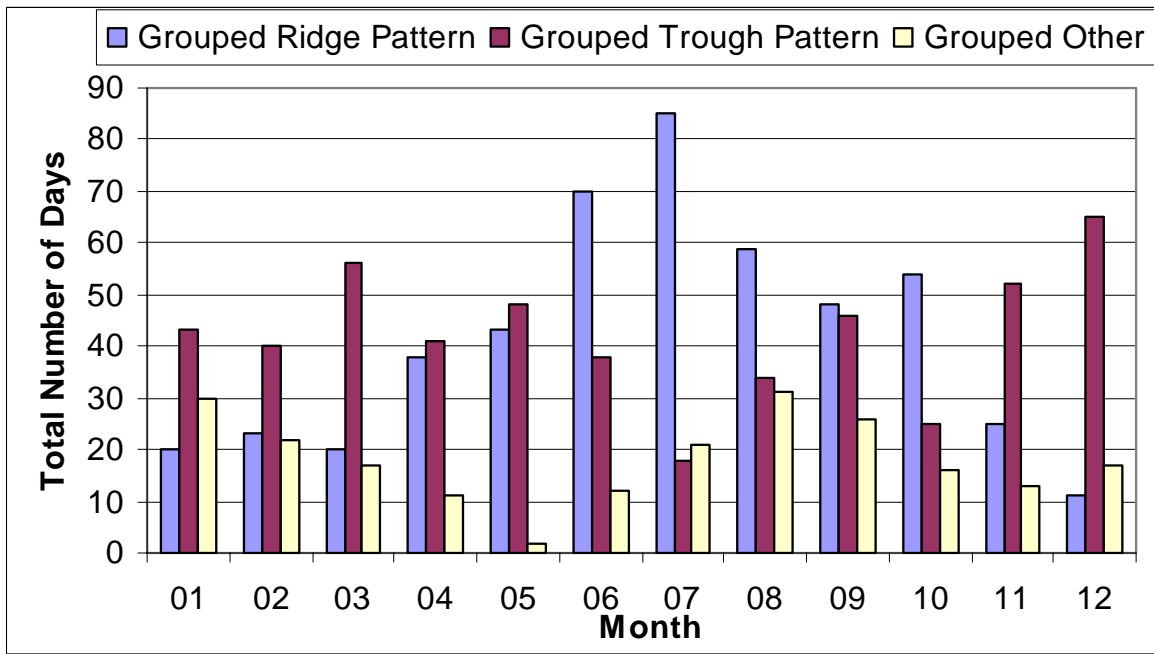
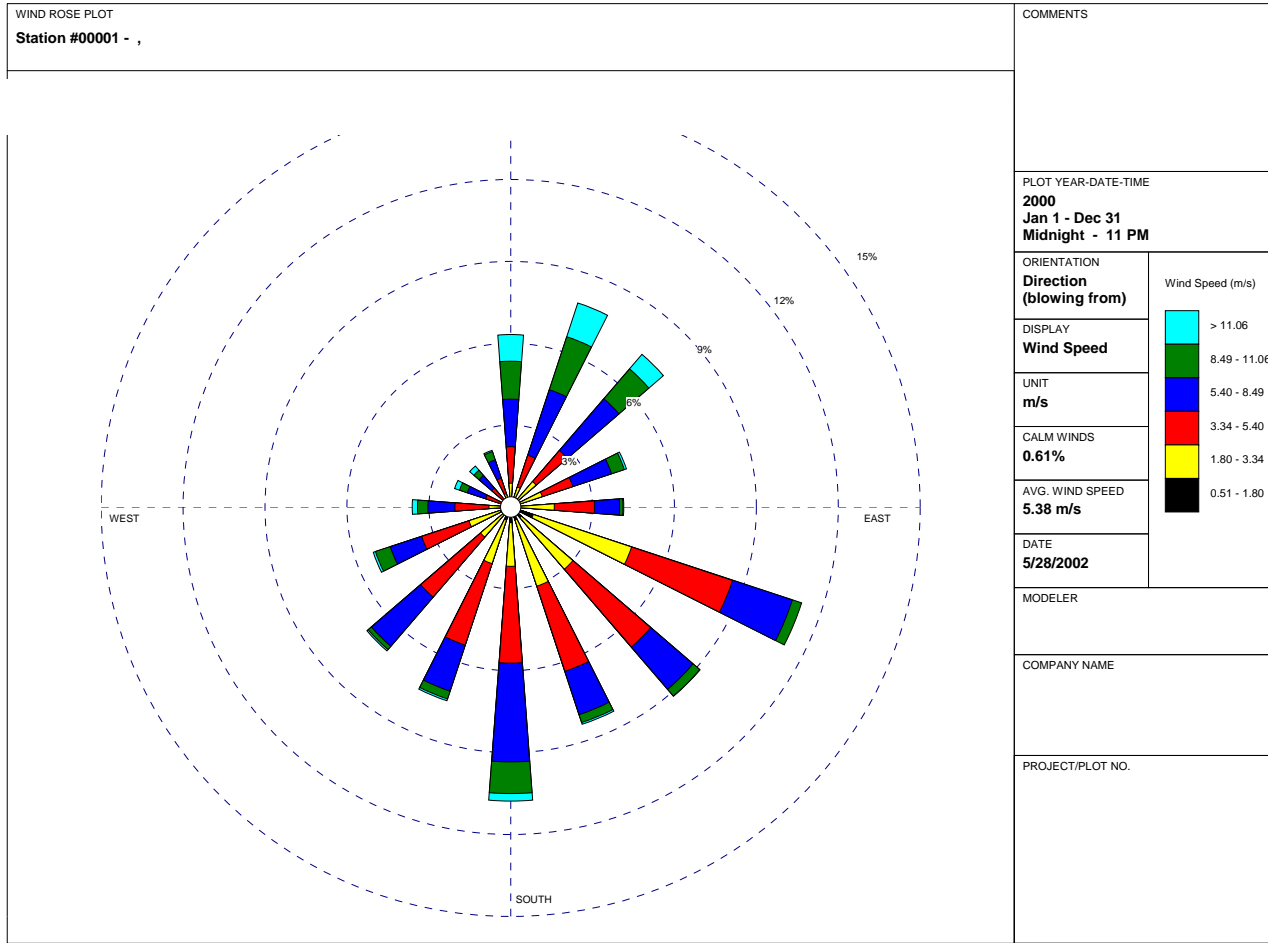


Figure 3-17. Frequency distribution of grouped upper-air patterns observed for each month for all years during the MMS study period.



WRPLOT View 3.5 by Lakes Environmental Software - www.lakes-environmental.com

Figure 3-18. Wind rose plot for the SMI platform for the study period.

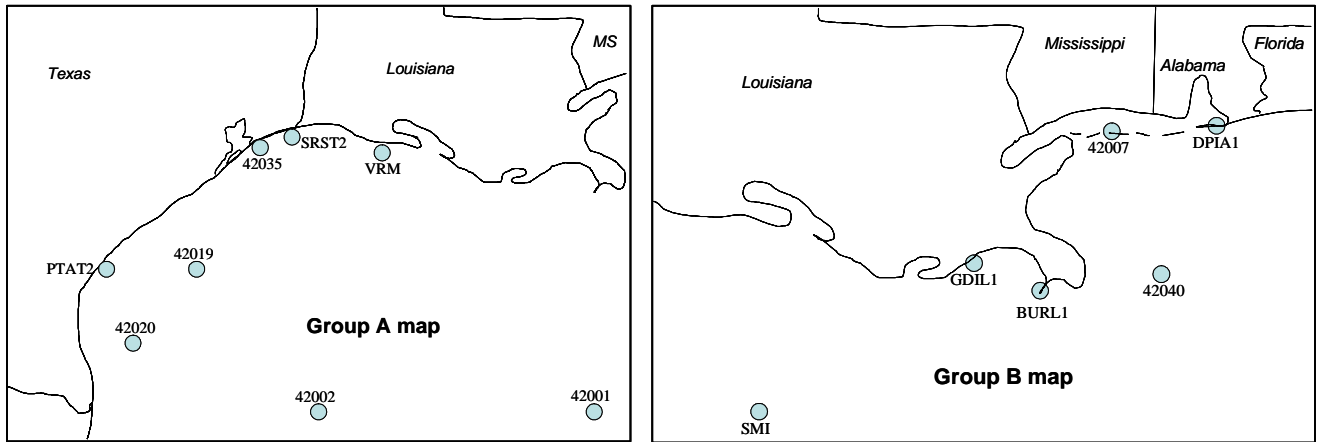


Figure 3-19. Monitoring sites in the Gulf of Mexico region. Group A sites are shown on the left, Group B sites on the right.

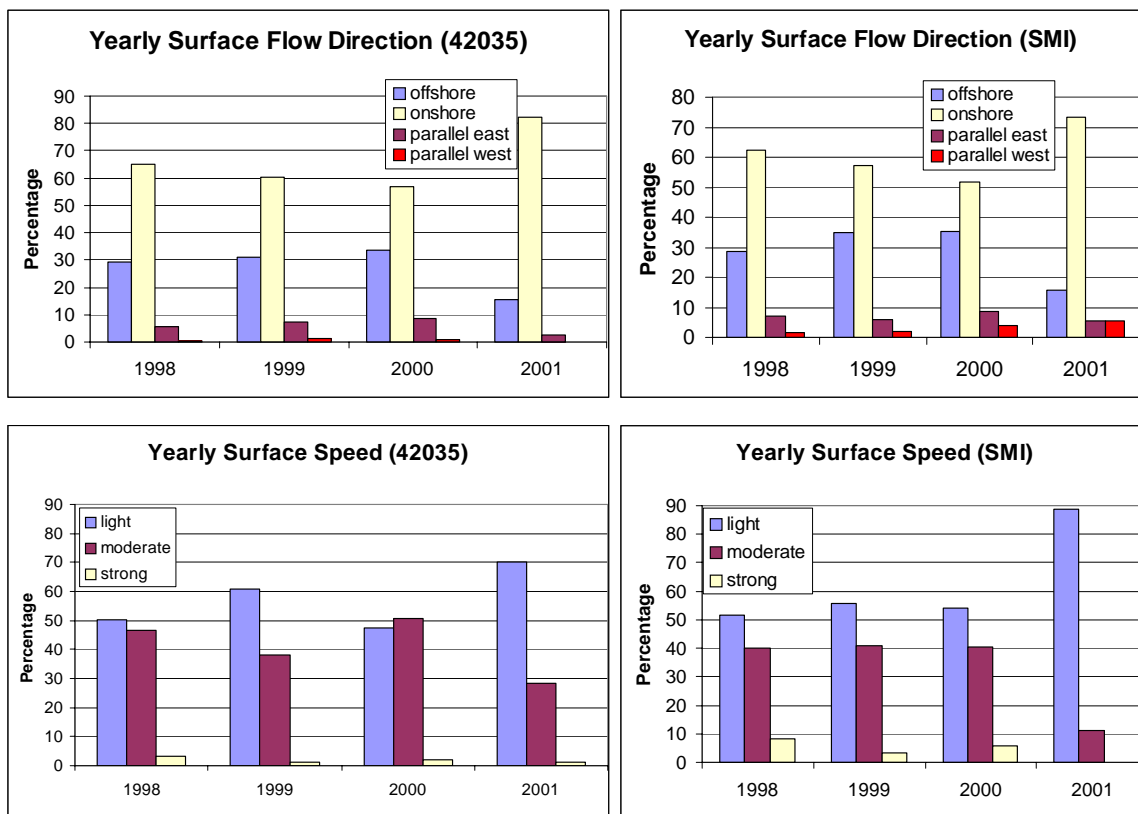


Figure 3-20. Yearly frequency distributions of surface wind direction (top graphs) and surface wind speed (bottom graphs) and for the near-shore site, buoy 42035, and the offshore site, SMI. Recall that these two sites are separated by about 200 km.

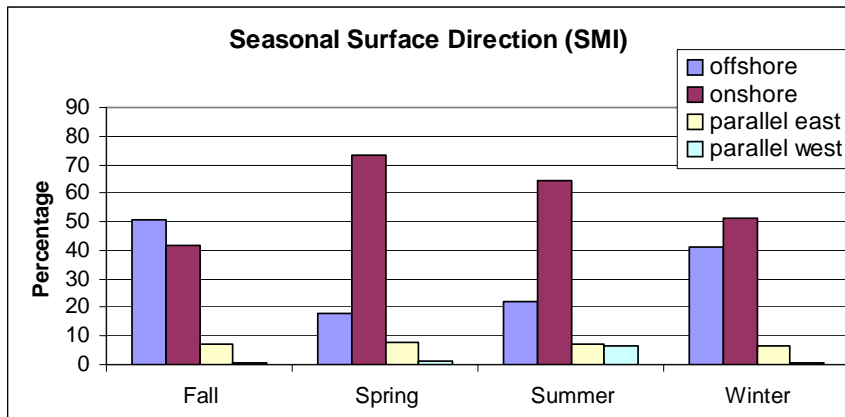
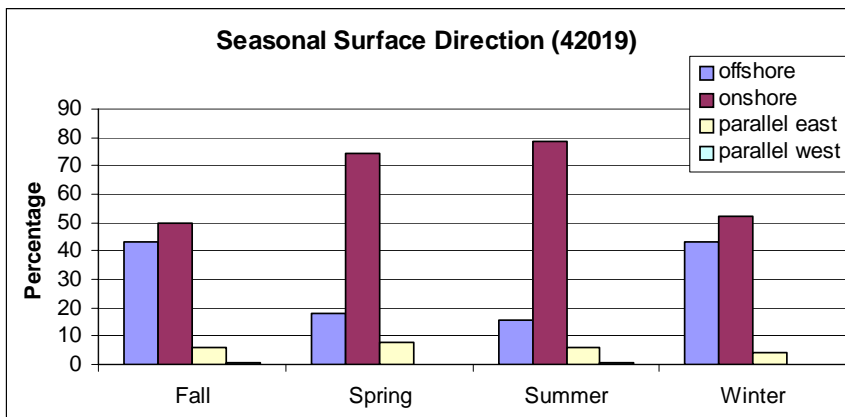
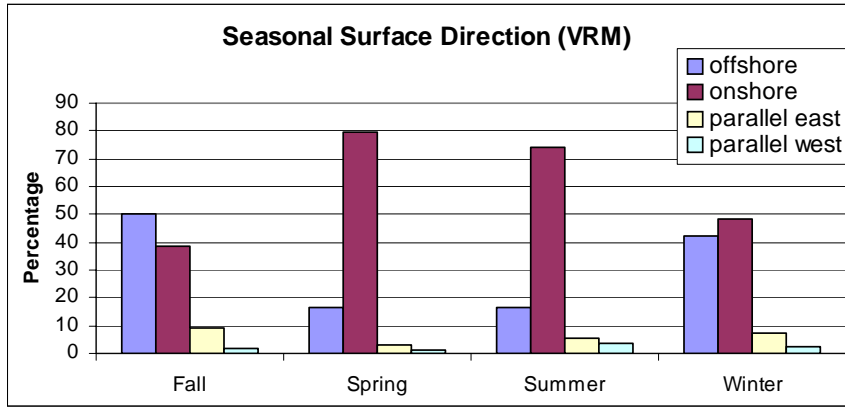
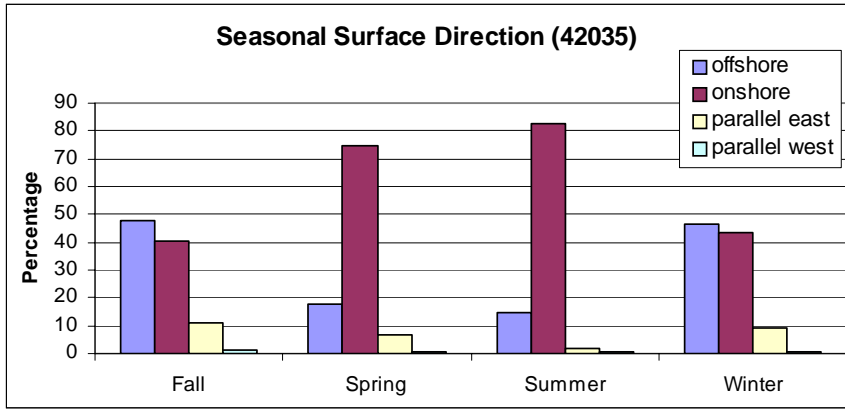


Figure 3-21. Frequency distribution of seasonal surface flow directions for near-shore and offshore sites.

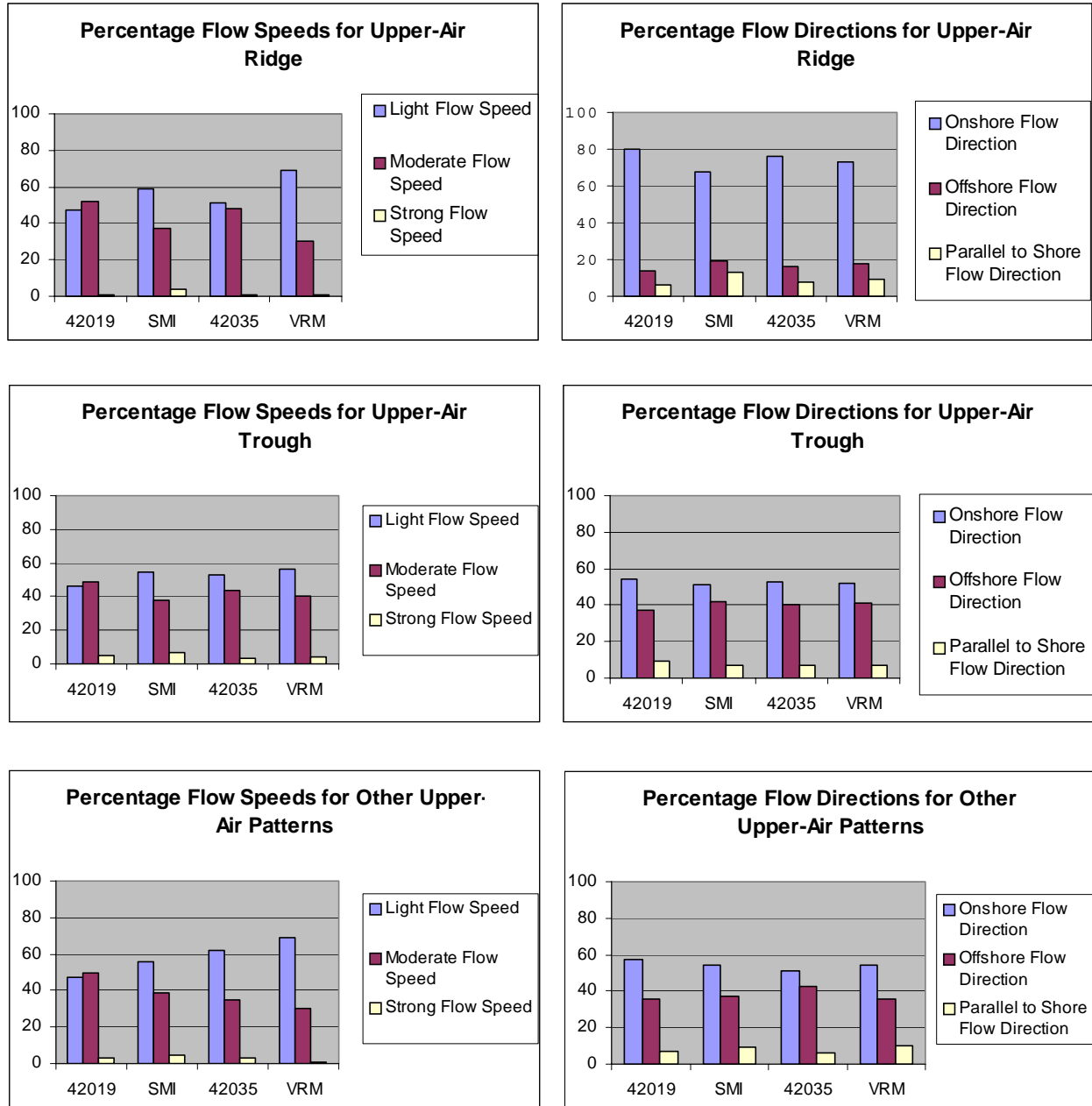


Figure 3-22. Frequency distribution of surface flow typing for upper-air ridge, upper-air trough, and other upper-air patterns at the four selected sites during the MMS study period.

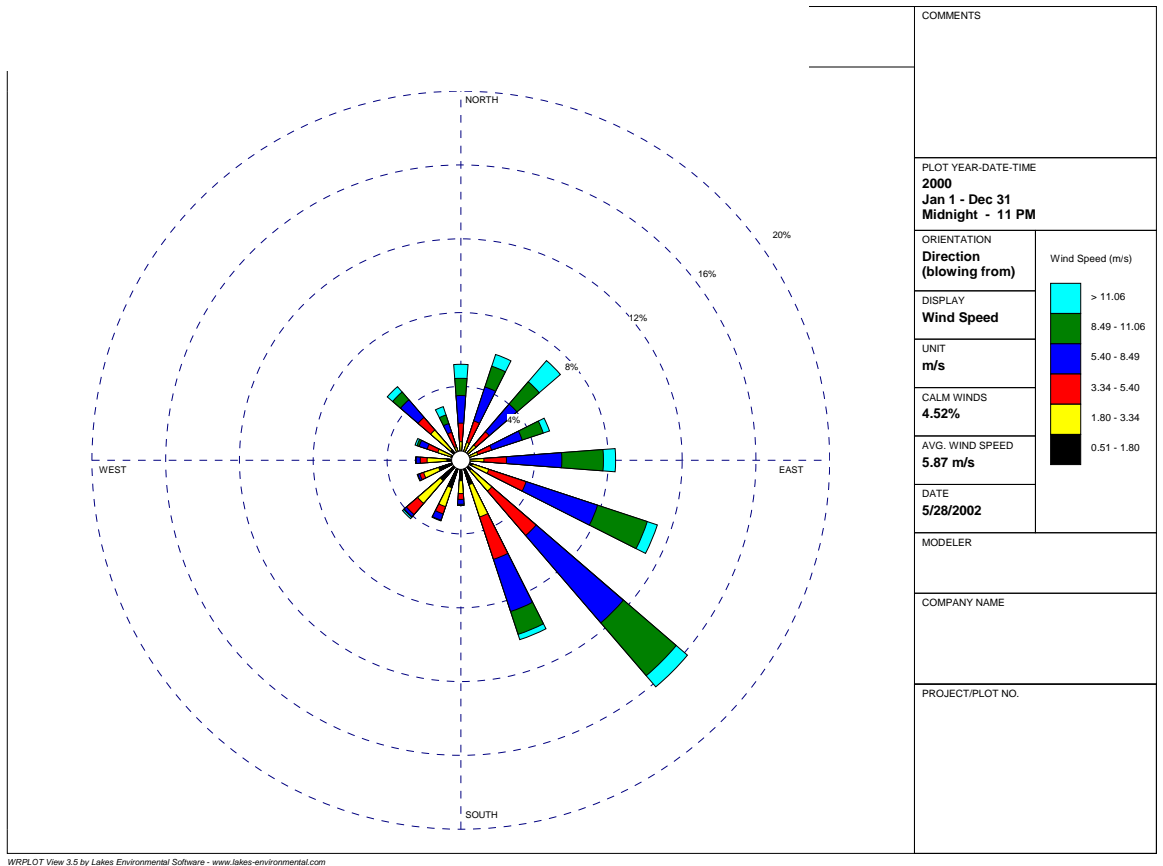


Figure 3-23a. Wind rose for VRM. This plot is representative of the wind rose plots for Group A sites.

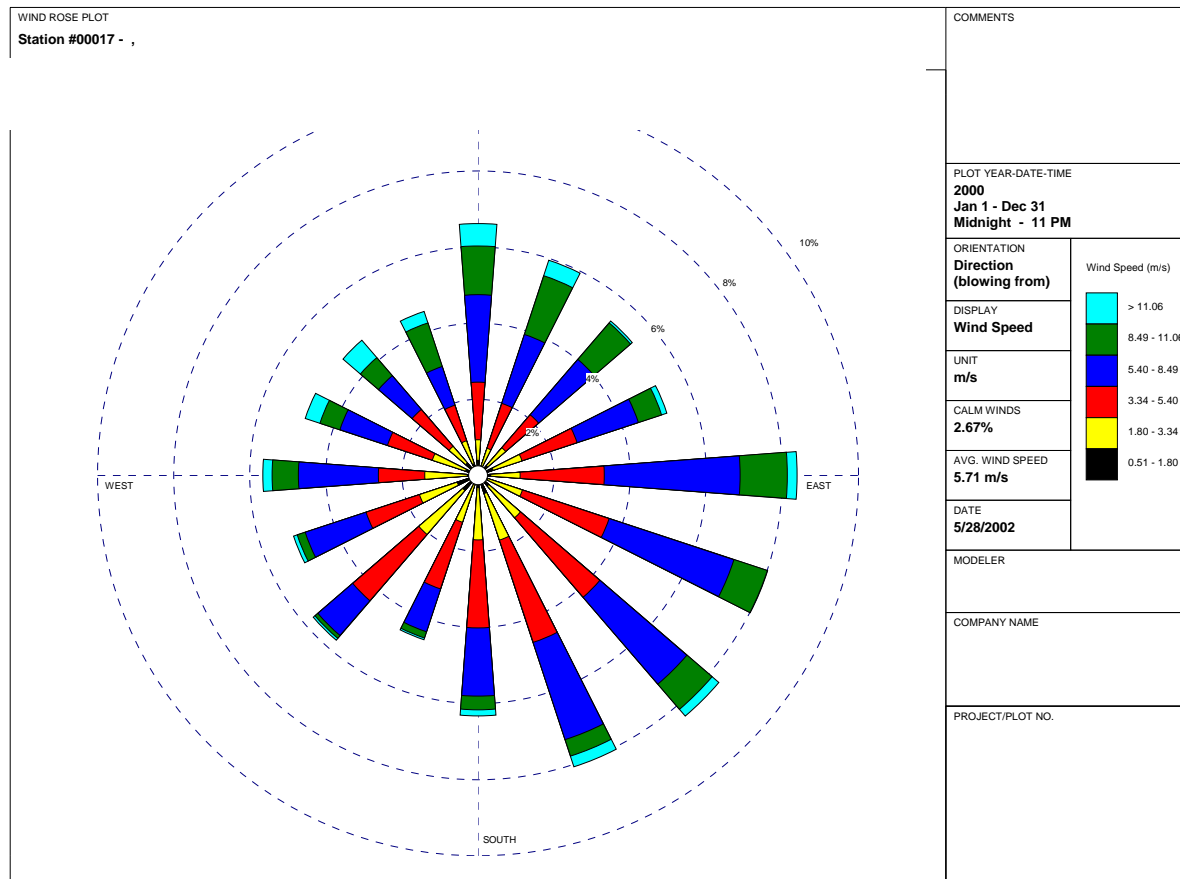


Figure 3-23b. Wind rose for buoy 42040. This plot is representative of the wind rose plots for Group B sites.

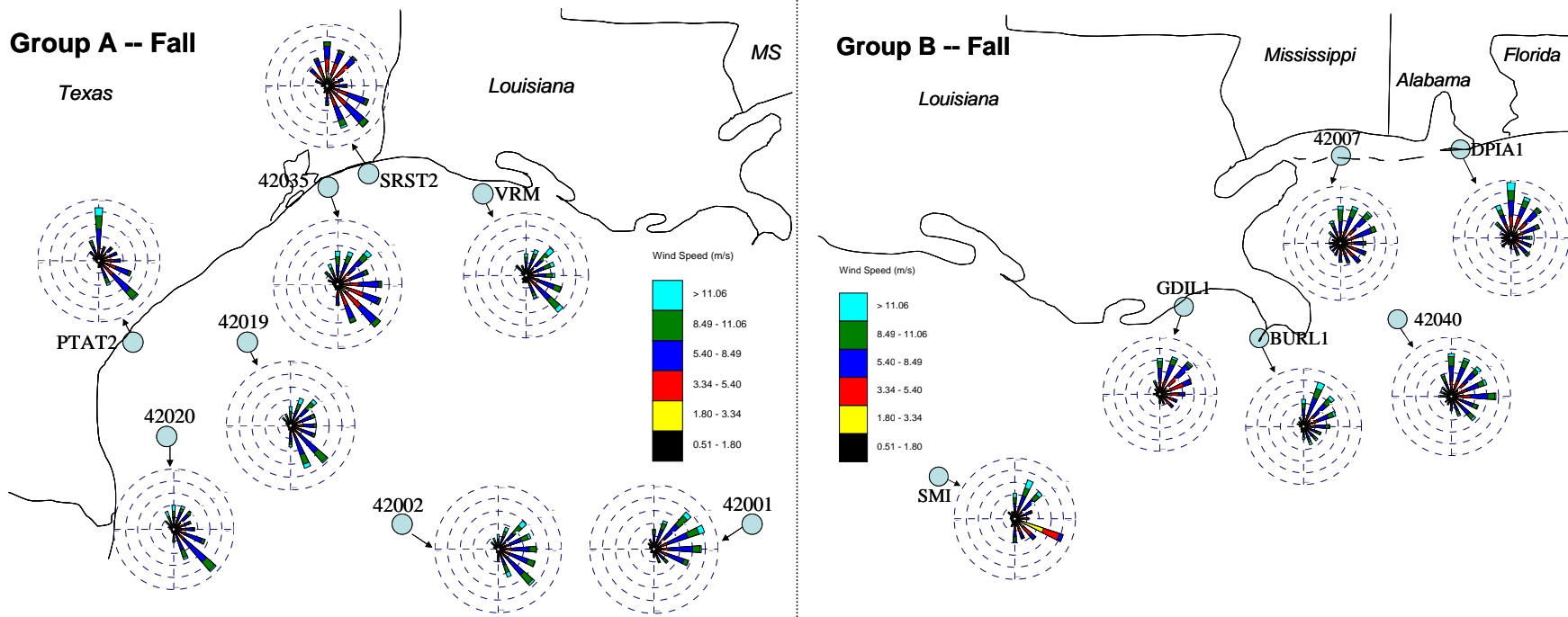


Figure 3-24. Spatial plot depicting wind roses for Group A (left) and Group B (right) for the fall season.

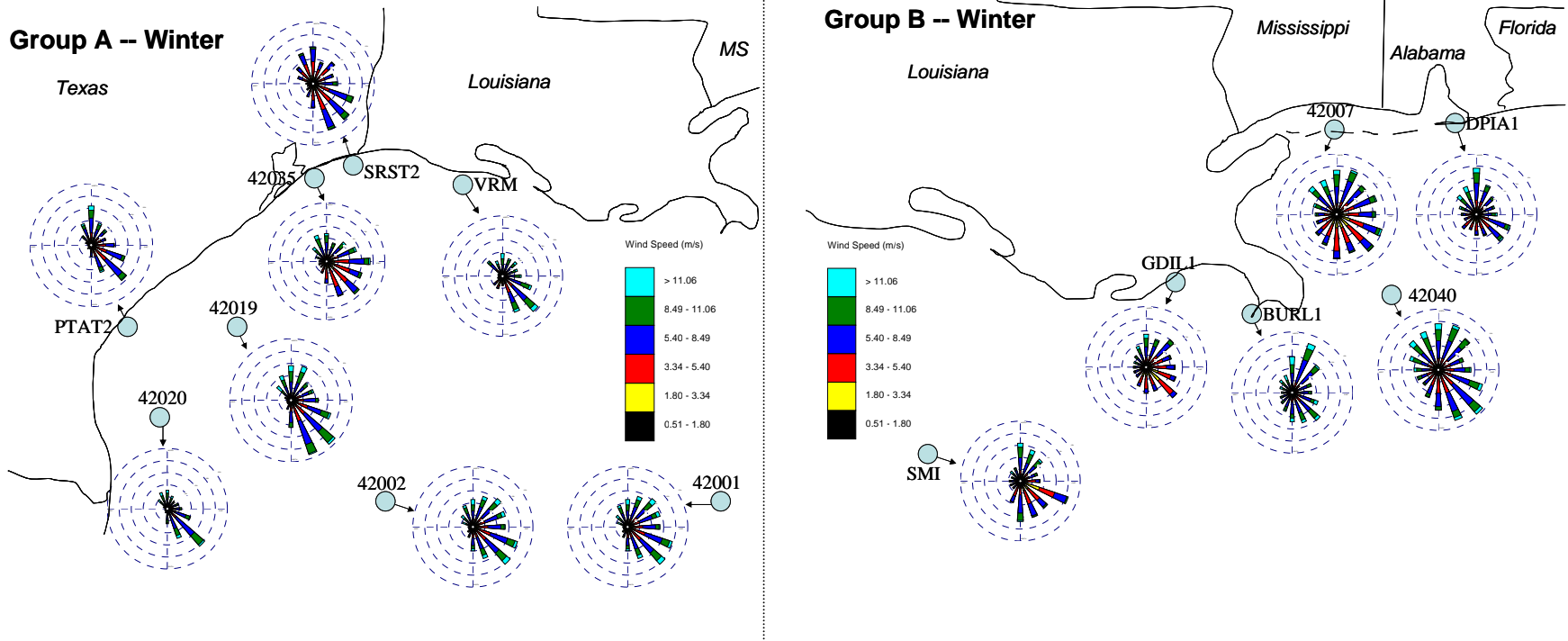


Figure 3-25. Spatial plot depicting wind roses for Group A (left) and Group B (right) for the winter season.

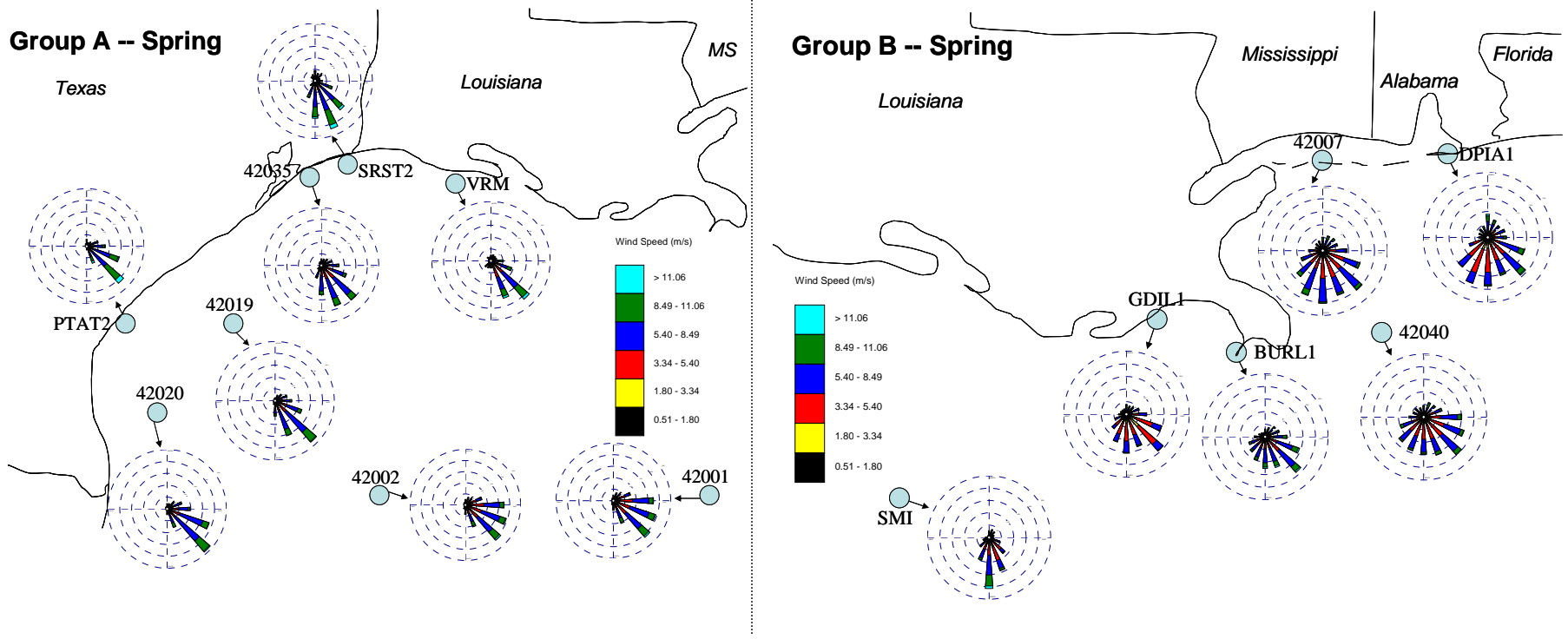


Figure 3-26. Spatial plot depicting wind roses for Group A (left) and Group B (right) for the spring season.

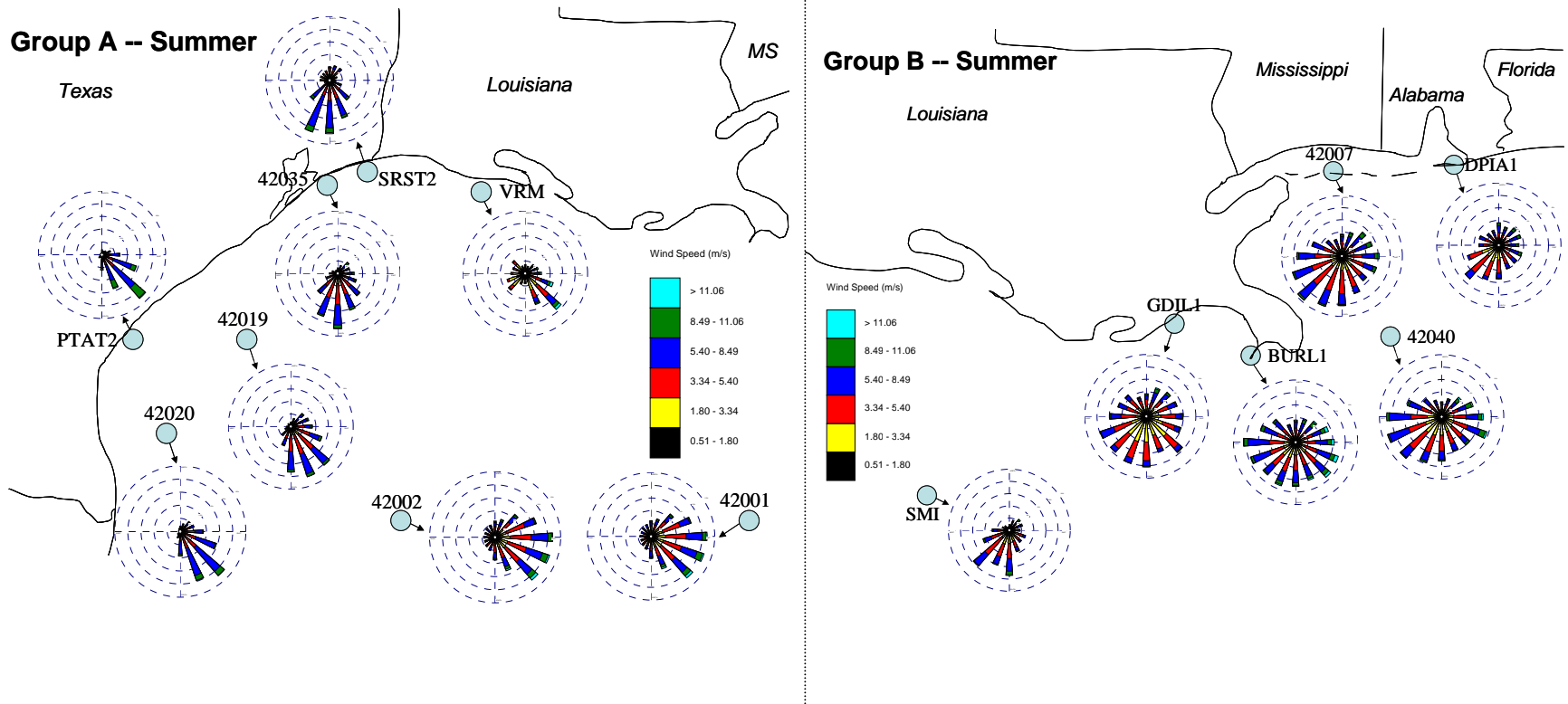


Figure 3-27. Spatial plot depicting wind roses for Group A (left) and Group B (right) for the summer season.

## **4. UPPER-AIR WINDS AND VIRTUAL TEMPERATURES**

The MMS now has available new boundary layer observations for the OCS in the Gulf of Mexico from six meteorological stations. These meteorological stations contain 915-MHz RWP, 2-KHz RASS, and surface meteorological stations. Two stations collected observations of the ABL for three years from May 1998 through October 2001 and four stations collected observations from September 2000 through October 2001 (as described in Section 1).

This section presents an evaluation of the characteristics of the boundary layer winds and  $T_v$  profiles and how these characteristics change by year, by season, by month, by upper-air classification, and among sites. The analysis of the characteristics yields insight into the spatial and temporal processes that occur vertically in the atmosphere. This information was used to support modeling efforts discussed in Section 6.

### **4.1 RWP AND RASS DATA**

Quality-controlled RWP and RASS data from the six profiler sites were averaged over several intervals to determine the characteristics and patterns in these data. Averaging was done by month, season, year, upper-air classification, and the 1998-2001 period (for VRM and SMI). Surface wind and  $T_v$  data were averaged and analyzed along with the aloft data to give a more complete picture of the atmospheric boundary layer. The winds were vector averaged, which inherently produces lighter wind speeds than are typically observed. Data from each of the six profiler and RASS sites were characterized both individually and comparatively for each averaging period.

Wind data were grouped by hour and height prior to averaging, creating an average diurnal profile for the given interval.  $T_v$  data were grouped by height and also into day (0600 to 1800 CST) and night (1800 to 0600 CST) categories prior to averaging, yielding a daytime and nighttime  $T_v$  profile for each averaging period. Averages were only calculated if at least 50% of the possible measurements contributing to that average were valid.

Figures showing the results for the wind and temperature analyses for selected sites are contained in this section and figures for all sites can be found in the final project presentation (MacDonald et. al. 2003) delivered to MMS on October 15, 2003, and are included in Appendix D.

### **4.2 PROFILER RESULTS AND INTERPRETATIONS**

RWP data showed several distinct patterns at various averaging intervals. The following is a description of those patterns, along with a basic interpretation of their causes. Note that averages above 3500 m are not available because the return signal was lost above that height on more than 50% of the days. Averages are also often not available from 131-500 m due to sea clutter. This analysis focuses on VRM and SMI but also includes information from the four BAMP sites. Data plots for the BAMP sites are included in Appendix D.

In summary, the average wind profiles from the platform height of 25 m to the top of the RWP range (about 3500 m) show

- Southwest through easterly flow throughout all seasons, years, and sites; southeasterly was the most frequent flow direction.
- At WDP, more easterly winds in the lowest 500 m compared to southerly at the other sites. In the fall, easterly flow at lower levels and southwesterly flow aloft with the transition height near 1000 m.
- In the winter, easterly surface flow very decoupled from south to southwesterly flow aloft.
- In the spring, coupled surface and aloft flow with southerly winds up to 1000 m and southwesterly winds above 1000 m.
- In the summer, winds ranging from easterly to southwesterly below 2000 m and the most diurnal variability at VRM.
- With a ridge pattern, winds south to southeasterly below 1100 m, and southwest to easterly aloft.
- With a trough pattern, mostly southwesterly flow aloft, with southeasterly to northeasterly flow in the low levels. Stronger troughs have a more defined shear layer.

#### **4.2.1 Overall Average Wind Profiles**

The wind profiles at each site showed a general pattern of light winds (1-3 m/s), transitioning from southeasterly to easterly winds at the surface, through southerly winds at the mid-levels, to southwesterly winds above 1500-1700 m. Below 1400 m, pre-dawn winds had a prominent southeasterly component, especially at SMI (**Figure 4-1**). The surface winds generally matched the aloft winds at both sites, except from 1100 to 1500 CST at VRM (**Figure 4-2**), when the surface winds were easterly. With the exception of these slight discrepancies, the overall wind averages at the two sites correlate well with each other.

#### **4.2.2 Yearly Wind Profiles**

The yearly patterns in the wind profiles generally followed the overall patterns, with light winds transitioning from southeasterly at the surface, through southerly, to southwesterly above approximately 1400-1700 m. In general, the 1998-1999 year appeared very similar to the overall average for both sites (**Figures 4-3 and 4-4**). The 1999-2000 year showed a more easterly component to the lower-level winds than the previous year and produced poorer data quality, but was otherwise similar to the previous year (**Figures 4-5 and 4-6**). The 2000-2001 year provided less data with no points above 1600 m meeting the 50% averaging criteria. Within the lower levels at SMI, this year showed light winds transitioning from easterly in the pre-dawn hours, through southerly in the early morning, to southwesterly in the afternoon and evening (**Figure 4-7**). In addition, the surface winds remained the same as the overall pattern, east-southeasterly all day. As a result, the surface winds were discontinuous from the winds at 500 m and differed by as much as 180°. This suggests that the mixing height is, on average, below

500 m. The VRM profile matched well with the overall pattern, except for the lack of data aloft and the surface wind pattern, which showed northeasterly winds from 1100 to 1500 CST, leading to discontinuity with the aloft winds at 500 m (**Figure 4-8**).

### 4.2.3 Seasonal Wind Profiles

Fall profiles at both sites matched the overall pattern above 1700 m with light southwesterly winds. However, easterly winds dominated the lower levels. The height of the transition from east to south was the lowest in the middle of the day (500-800 m at VRM, 900-1200 m at SMI) and the highest at night (1200-1500 m at VRM, 1700-2000 m at SMI). The surface winds at both sites were constant throughout the day, but at VRM, they were northeasterly while at SMI the winds were east to east-northeasterly. With the exception of the transition-height differences and the surface wind directions, the fall profiles at the two sites correlate well (**Figures 4-9 and 4-10**).

Winter profiles had considerably fewer points meeting the 50% criteria, especially at VRM; this should be further investigated. The SMI winter profile appeared very similar to its overall average profile, with light winds from the south at 500 m transitioning into southwesterly winds above approximately 1500 m. There was no easterly component from 500 to 1000 m like the overall pattern had in the early morning hours. The few points available from VRM for the winter appear to correlate with the SMI profile. The surface winds at both sites were similar, with easterly flow all day, which was discontinuous from the aloft winds (**Figures 4-11 and 4-12**).

Spring profiles were nearly identical to the overall averages for both sites, but with a less easterly component in the morning hours. Surface winds at SMI were stronger than at VRM in the pre-dawn hours, with speeds averaging 5 m/s. However, aloft winds were stronger at VRM, with wind speeds averaging 5 m/s from 0500 to 1800 CST, while the average speed of aloft winds at SMI never exceeded 3 m/s (**Figures 4-13 and 4-14**).

The summer profile at SMI above 1500 m showed light, easterly winds through the early morning, becoming southeasterly from 0700 to 1600 CST before returning to easterly at night. Below 1500 m, the pattern was similar to the overall pattern below 1000 m (**Figure 4-15**). The summer pattern at VRM showed the most diurnal changes in any season at either site. There was little in common with the overall profile except for the southerly winds below 500 m from 1800 to 0700 CST. The winds aloft became easterly to northeasterly with the transition height at about 800 m at night to 1800 m during the afternoon (**Figure 4-16**).

### 4.2.4 Monthly Wind Profiles

RWP wind data were inconsistent in the winter months, and a January profile could not be generated that met the 50% averaging criteria. February had a limited number of data points, but profiles could be generated that matched well with the winter profile at each site. The only notable difference between the February profiles and the overall winter profiles was that the SMI low-level winds in February were slightly more southwesterly than the winds of its winter profile.

For March through May, monthly averages resembled seasonal averages at both sites aloft, with the same persistent pattern of light winds transitioning from southerly or southeasterly near the surface to southwesterly aloft. However, the surface winds at VRM in March were very different than those in February and April. During the day, winds were northeasterly, as opposed to east-southeasterly in February and south-southeasterly in April. The northerly flow did not show up at all in the aloft wind pattern. This may be due to the shallow nature of post-cold front northerly winds. At VRM in May, winds above 3000 m were westerly, but data at this height were not available from SMI for comparison.

In June at SMI, the winds above 1500 m resembled the summer pattern more than the spring pattern. Winds were southeasterly in the early morning before shifting to southerly for the remainder of the day. The winds below 1500 m, however, more closely matched the spring pattern. At VRM, the June profile was similar to the spring profile. In July at SMI, the profile matched the summer profile fairly well except for southwesterly flow that developed during the daytime hours up to 1500 m, and light and variable winds aloft after sunset. At VRM, the July profile was similar to the summer pattern. The August profiles at both sites correlate well with the summer pattern.

In September and October, at both sites, the profiles above 1000 m resembled the fall patterns, with southwesterly flow. Below 1000 m, the profiles at both sites resembled the summer patterns, with a southerly component to the winds. These months showed the transition from summer to fall. The November profiles at both sites correlate well with the fall profiles.

In December at SMI, data were sparse, but December appeared to be a transition month from fall to winter. There was a mixture of easterly and southerly winds at low levels. At VRM, data were again sparse, but the pattern was similar to the winter profiles as the southwesterly flow aloft started at 600 m, while the fall profile had all southwesterly flow above 1200 m.

#### **4.2.5 Wind Profiles by Upper-air Classification**

Both the ridge and weak ridge patterns were similar to the overall patterns at both sites. Winds were east to southeasterly below 1100 m (1500 m at VRM) and south to southwesterly above 1100 m (**Figures 4-17 to 4-20**). The ridge pattern had more of an easterly component than the overall pattern. At VRM, the surface winds did not shift to easterly from 1100 to 1500 CST like the overall pattern.

The weak trough patterns up to 1000 m at both sites were similar to the overall patterns at SMI (**Figure 4-21**), and throughout the profile at VRM (**Figure 4-22**). At SMI, winds were southwesterly aloft for weak trough, trough (**Figure 4-23**), and cut-off low patterns (**Figure 4-24**). At VRM, winds were southwest to westerly aloft for trough (**Figure 4-25**) and cut-off low patterns (**Figure 4-26**). At both sites, the trough pattern contained a shear layer between northerly flow at the surface and southwesterly flow aloft, with the transition height ranging from 300-700 m. Data were limited at SMI during cut-off low patterns, so little analysis could be done.

The flat patterns below 1100 m at both sites were similar to the overall patterns. Above 1100 m, winds were mostly easterly, except from 0700 to 1200 CST when they were southerly

(**Figures 4-27 and 4-28**). Both sites had limited data for zonal patterns and showed mostly southwesterly winds (**Figures 4-29 and 4-30**). Winds were southerly below 700 m at SMI and surface winds at both sites were easterly (**Figures 4-31**). The post-trough patterns had northerly winds at all levels at both sites except from 300-900 m at VRM, where the winds were easterly in the afternoon and evening (**Figure 4-32**). Winds for the tropical storm pattern were more variable at both sites, but only three to six days of data went into the averages. Winds were constant out of the southeast at the surface, with mostly southerly to southeasterly winds aloft at both sites (**Figures 4-33 and 4-34**). The winds at VRM were stronger than those in any other pattern.

### **4.3 RASS RESULTS AND INTERPRETATIONS**

This subsection presents observations of  $T_v$  observed by RASS at elevations ranging from 131 m (above the level of the instrument on the oil platform) to about 700 m. The RASS data in the figures in this subsection are combined with  $T_v$  observations collected by thermometers on short towers on the oil platforms at heights of about 25 msl.

It should be noted that errors or biases of about 1°C in RASS observations are expected. As a result, small discontinuities, shallow inversion, or superadiabatic layers in the plots may not be real.

In summary, the average temperature profiles from the platform height of 25 m to the top of the profile (about 1500 m) show the following characteristics:

- There is often a discontinuity in temperature gradient at the lower two or three RASS levels (e.g., 131 m), due to a known cold bias.
- The surface temperature and the 131-m temperature are measured by two types of instruments, which may influence the diagnosis of stable or unstable temperature gradients.
- The average profiles, which extend to about 700 m, do not show an elevated inversion or mixing height, despite the fact that a mixing depth of 500 to 700 m is expected and often observed in the RWP reflectivity data
- VRM is more stable than other sites.
- BIP has a strong stable inversion in the lowest layer; other sites do not.
- In fall, FTM has surface inversion at night; others do not.
- In winter, all sites have an inversion during the day and night except VRM and BIP. Inversion may be a result of platform radiational cooling.
- In spring and summer, all sites are about adiabatic.

#### **4.3.1 Overall Average Temperature Profiles**

The  $T_v$  data in this subsection are averaged over three years. Subsequent subsections describe single-year averages.

At SMI, which is about 100 km offshore, the daytime and nighttime  $T_v$  profiles were very similar. The overall average daytime profile for SMI indicates an average lapse rate of about  $-6^\circ\text{C}/\text{km}$  (**Figure 4-35**), which is close to the standard environmental lapse rate ( $-6.5^\circ\text{C}/\text{km}$ ). The average surface temperature was  $26^\circ\text{C}$ . The figure shows some cold bias in the RASS data at the lowest two range gates. The cold bias is an erroneous cold shift in the  $T_v$  profile due to non-coherent sound waves from the sound sources. The nighttime profile in Figure 4-35 also shows a lapse rate of about  $-6^\circ\text{C}/\text{km}$ . The average surface temperature was nearly the same as the daytime temperature, but the nighttime profile was about  $0.25^\circ\text{C}$  warmer than the daytime profile. This  $0.25^\circ\text{C}$  difference is less than the accuracy in the RASS  $T_v$  measurement ( $\pm 1^\circ\text{C}$ ). Again, there was some cold bias evident in the lowest two range gates at night.

At VRM, which is much closer to shore than SMI (18 km versus 100 km), the daytime and nighttime profiles were very similar to each other and showed more stability than did the SMI profiles. The overall daytime profile at VRM shows a lapse rate of  $-2.3^\circ\text{C}/\text{km}$  (**Figure 4-36**). The average surface temperature was  $23.9^\circ\text{C}$ . The nighttime profile shows a lapse rate of  $-0.7^\circ\text{C}/\text{km}$  and an average surface temperature of  $23.6^\circ\text{C}$ . It is suggested that the VRM profile is more stable than the SMI profile because of its nearness to land, which tends to have a higher frequency of stable conditions.

Note that there is no upper-level inversion marking the top of the mixing depth at either SMI or VRM. This suggests that the average mixing depth is at a level exceeding the 700 m upper range of the RASS profiles.

#### 4.3.2 Yearly Average Virtual Temperature Profiles

This subsection presents the averaged  $T_v$  profiles for individual years at the SMI and VRM sites.

For the 1998 MMS year (June 1, 1998, to May 31, 1999) at SMI, the  $T_v$  profiles were generally the same as the overall (three-year average)  $T_v$  profiles (**Figure 4-37**). However, the surface temperature was  $0.5$  to  $1^\circ\text{C}$  warmer in 1998 than the overall surface temperature. At VRM, the profiles were slightly warmer than the overall profiles up to 400 m and cooler above 400 m. In addition, at VRM the day and night surface temperature was about  $1.5^\circ\text{C}$  warmer than the overall temperature. Cold bias was evident at the lowest range gate (131 m) aloft (**Figure 4-38**), and the observations at that level should be given less credibility.

For the 1999 MMS year (June 1, 1999, to May 31, 2000) at SMI, both night and day  $T_v$  profiles were about  $0.5^\circ\text{C}$  cooler than the overall (three-year average) aloft  $T_v$  profiles, and the surface temperature was slightly cooler (**Figure 4-39**). The lapse rate is slightly closer to adiabatic. At VRM, the  $T_v$  profile was  $0.25$  to  $0.5^\circ\text{C}$  cooler aloft, and  $1$  to  $1.5^\circ\text{C}$  cooler at the surface (**Figure 4-40**) than the overall profiles. However, the lapse rates were nearly identical to the overall (three-year average) lapse rates.

For the 2000 MMS year (June 1, 2000, to May 31, 2001) at SMI, there were limited data. The existing data showed a slightly cooler  $T_v$  profile during the day and a slightly warmer  $T_v$  profile at night compared to the overall (three-year average) profile. Surface temperatures were about  $1^\circ\text{C}$  cooler both day and night (**Figure 4-41**). At VRM, the daytime profile was  $0.5$  to  $1^\circ\text{C}$

warmer aloft during the day compared to the overall (three-year average) profile. The nighttime profile was up to 1°C warmer above 300 m compared to the overall profile and had an inversion layer. Surface temperatures were 1 to 2°C cooler (**Figure 4-42**).

### 4.3.3 Seasonal Virtual Temperature Profiles

In the fall, the  $T_v$  profiles at SMI were 1.5 to 2°C cooler than the overall (three-year average) profiles, but the lapse rates remained the same (**Figure 4-43**). At VRM, the  $T_v$  profiles were 2.5 to 3°C cooler than the overall profiles, with a slightly more unstable lapse rate (**Figure 4-44**).

In the winter, the  $T_v$  profiles at SMI were 5° to 6°C cooler, with a more unstable lapse rate than the overall (three-year average) profiles (**Figure 4-45**). At VRM, there were very limited data for the winter season, but these data showed a  $T_v$  profile nearly 7°C cooler aloft and 8°C cooler at the surface (**Figure 4-46**).

In the spring, the  $T_v$  profiles at SMI were 0.5° to 1°C warmer than the overall (three-year average) profile and the lapse rate was the same (**Figure 4-47**). The surface temperatures were 1 to 1.5°C warmer. At VRM, the  $T_v$  profiles were warmer up to 500 m and cooler above 500 m compared to the overall profiles (**Figure 4-48**). This resulted in a lapse rate of about -6°C/km.

In the summer, at SMI, the  $T_v$  profiles were 4° to 6°C warmer than the overall  $T_v$  profiles, with less stable lapse rates (**Figure 4-49**). At VRM, the  $T_v$  profiles were 3° to 6°C warmer than the overall  $T_v$  profiles, and 9°C warmer at the surface, which resulted in an apparent superadiabatic layer. The lapse rate was more unstable than the overall three-year average, at nearly -6°C/km (**Figure 4-50**).

### 4.3.4 Virtual Temperature Profiles by Upper-air Classification

As expected, the  $T_v$  profiles at both sites for the ridge pattern were warmer than the overall profiles by 2° to 4°C (**Figures 4-51 to 4-54**). The lapse rates at SMI were the same as for the overall three-year average.

The  $T_v$  profiles for the weak trough pattern were warmer than the overall three-year average profiles by 0.5° to 1°C (**Figures 4-55 and 4-56**). The  $T_v$  profiles for the trough pattern at both sites were 3° to 4°C cooler than the overall profiles (**Figures 4-57 and 4-58**). The  $T_v$  profiles for the cut-off low pattern at VRM were cooler at the surface but were the same  $T_v$  aloft as the overall profile (**Figure 4-59**). There was no  $T_v$  profile for the cut-off low profile at SMI due to limited data.

The profiles for flat synoptic conditions were 3° to 6°C warmer at both sites than the overall  $T_v$  profiles (**Figures 4-60 and 4-61**). At SMI, the lapse rate was the same but at VRM the lapse rate was less stable than the overall profile. The profiles for the zonal patterns were 5°C cooler than the overall profiles at both sites, although data were limited at VRM (**Figures 4-62 and 4-63**). The profiles for the post-trough pattern at both sites were 6° to 7°C cooler than the overall average profiles (**Figures 4-64 and 4-65**). The profile for the tropical

storm pattern at VRM was about 6°C warmer than the overall profile, due to the warm and moist characteristics of tropical storms (**Figure 4-66**).

#### 4.3.5 Caveats

As mentioned earlier, more work is required to fully understand the observed  $T_v$  profiles. In particular, the following issues need to be resolved:

1. There is often a discontinuity in  $T_v$  at the lower two or three RASS levels (e.g., 131 m) due to a cold bias.
2. The surface temperature and the 131-m temperature are measured by two different instruments and an unexpected stable or unstable lapse rate often results. A nearly adiabatic gradient would be expected from theoretical arguments because water temperature is nearly always a few degrees warmer than air temperature, causing an upward heat flux and a well-mixed boundary layer that should extend to heights of several hundred meters.
3. The average  $T_v$  profiles, which extend to about 700 m, never show an elevated inversion or mixing height, despite the fact that we expect a mixing depth of 500 to 700 m.

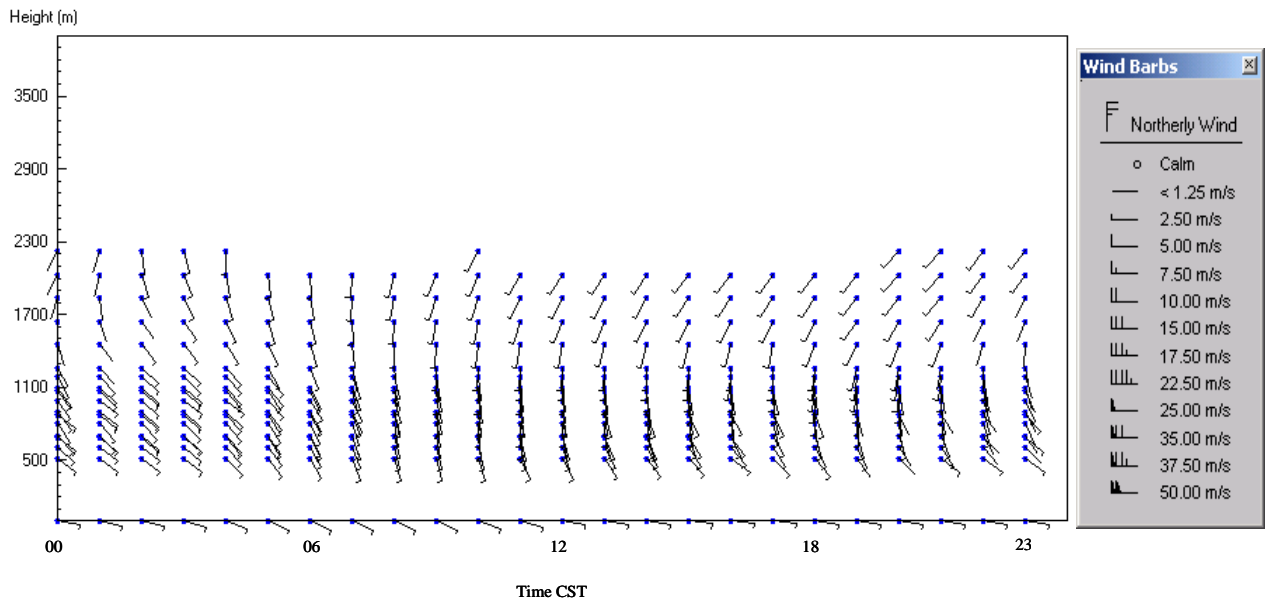


Figure 4-1. Overall average winds at SMI from 0000 to 2300 CST, June 1, 1998, to May 31, 2001.

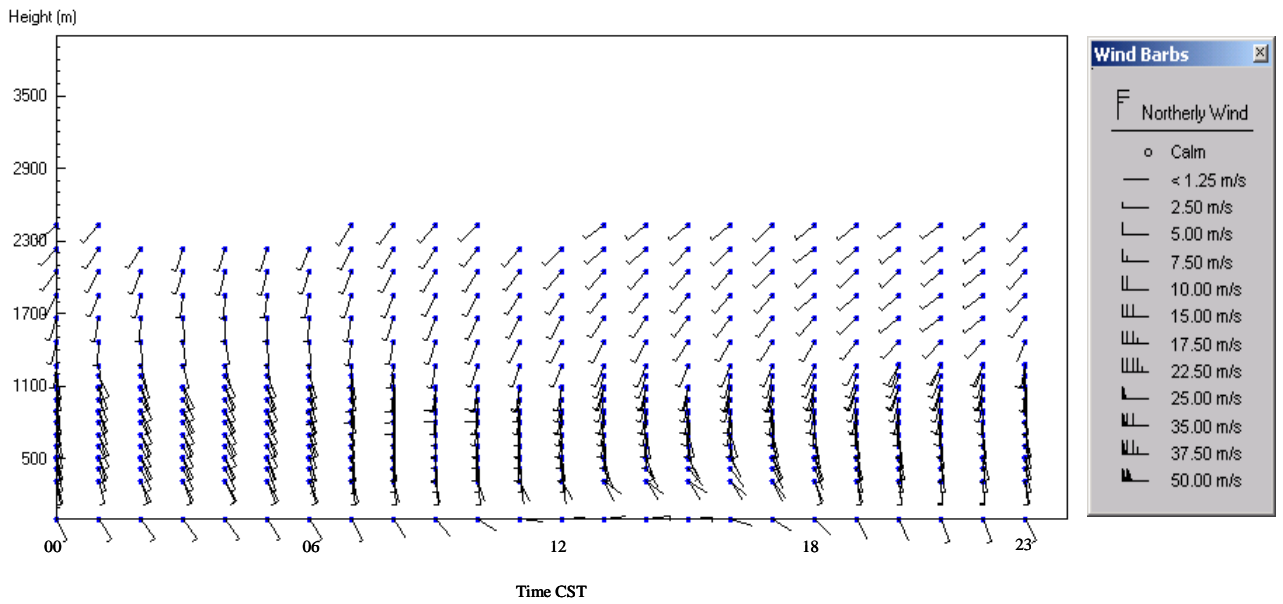


Figure 4-2. Overall average winds at VRM from 0000 to 2300 CST, June 1, 1998, to May 31, 2001.

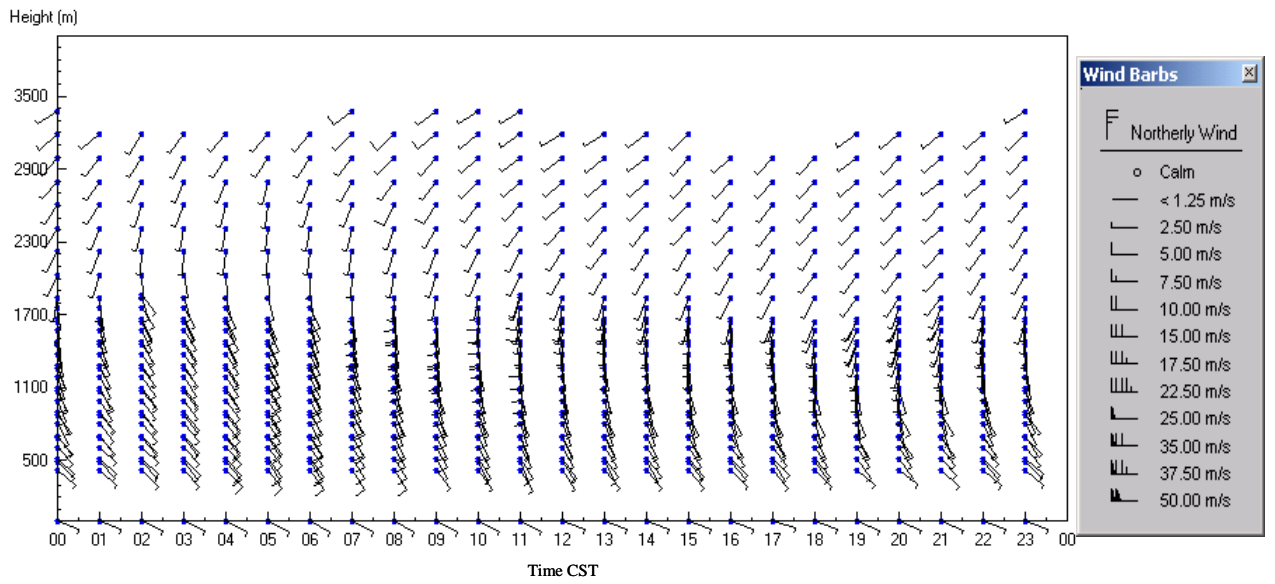


Figure 4-3. 1998 year average winds at SMI from 0000 to 2300 CST, June 1, 1998, to May 31, 1999.

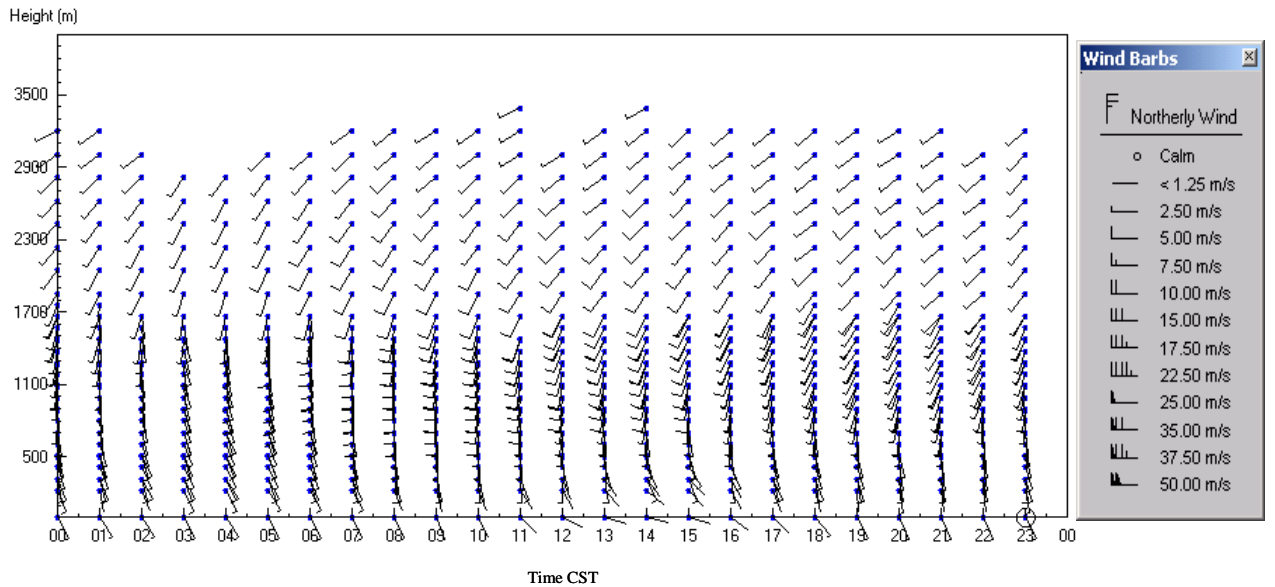


Figure 4-4. 1998 year average winds at VRM from 0000 to 2300 CST, June 1, 1998, to May 31, 1999.

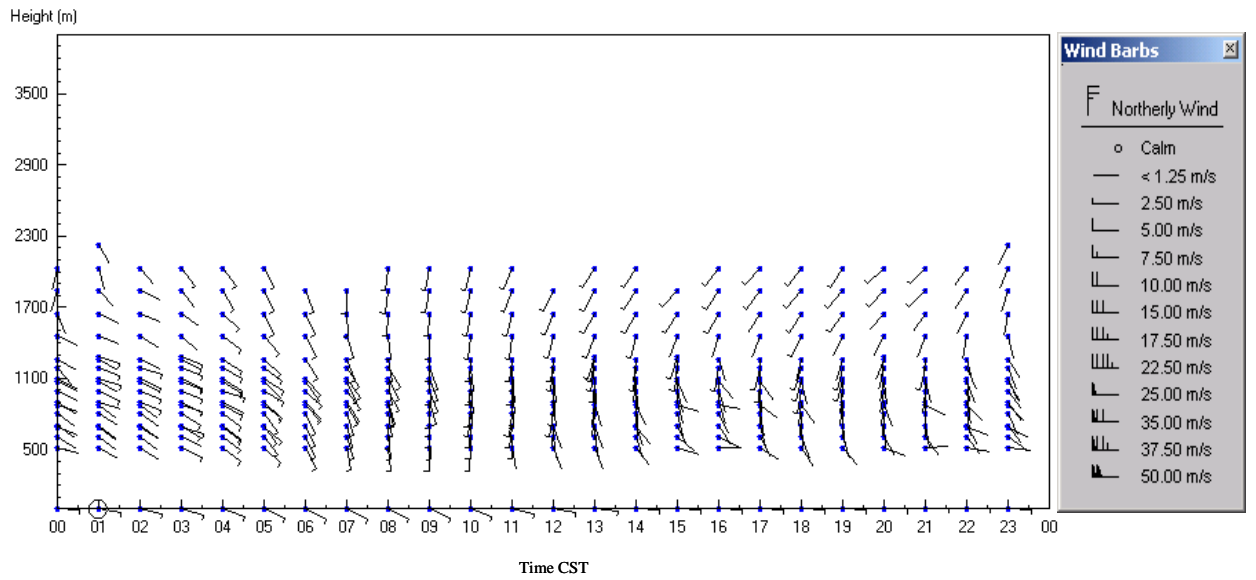


Figure 4-5. 1999 year average winds at SMI from 0000 to 2300 CST, June 1, 1999, to May 31, 2000.

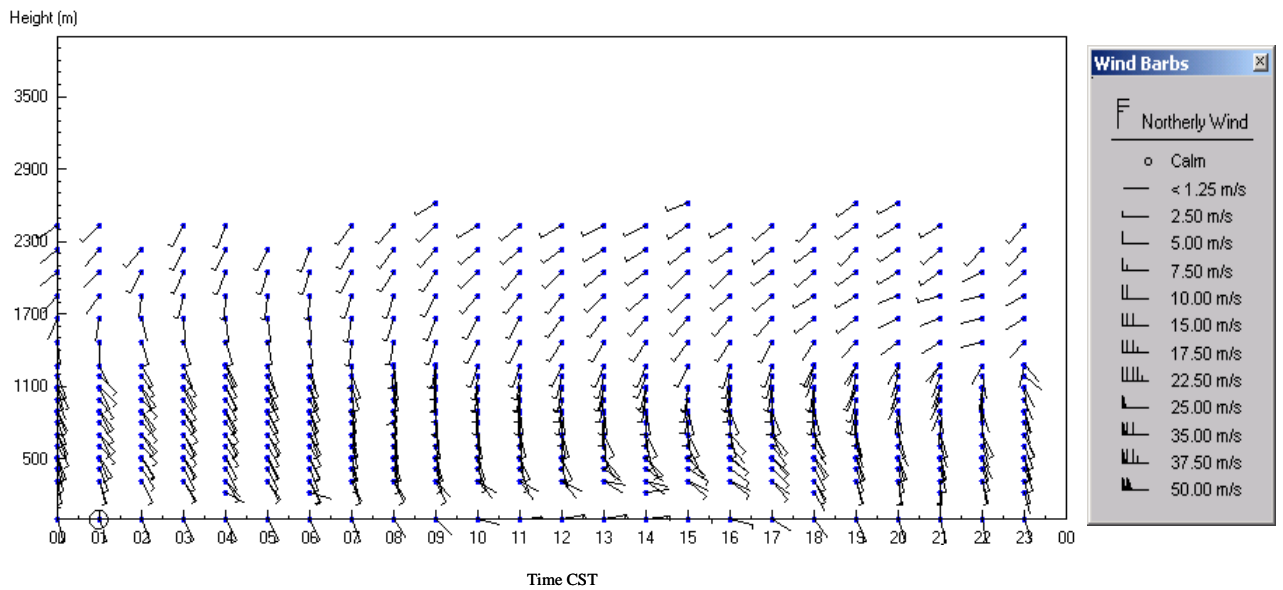


Figure 4-6. 1999 year average winds at VRM from 0000 to 2300 CST, June 1, 1999, to May 31, 2000.

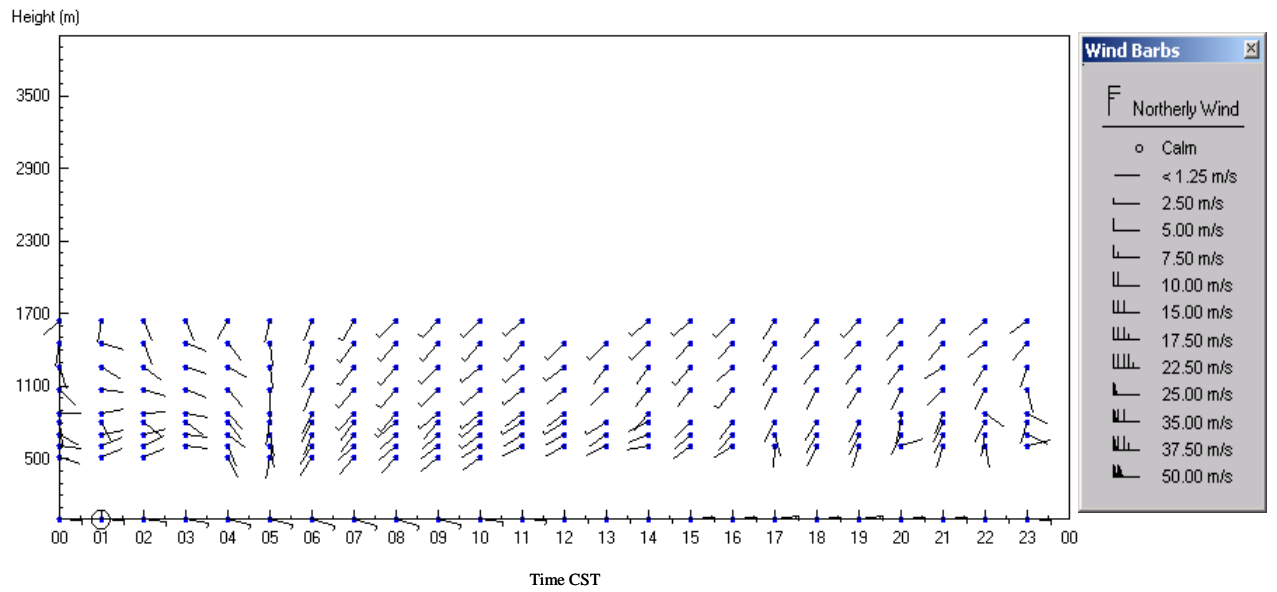


Figure 4-7. 2000 year average winds at SMI from 0000 to 2300 CST, June 1, 2000, to May 31, 2001.

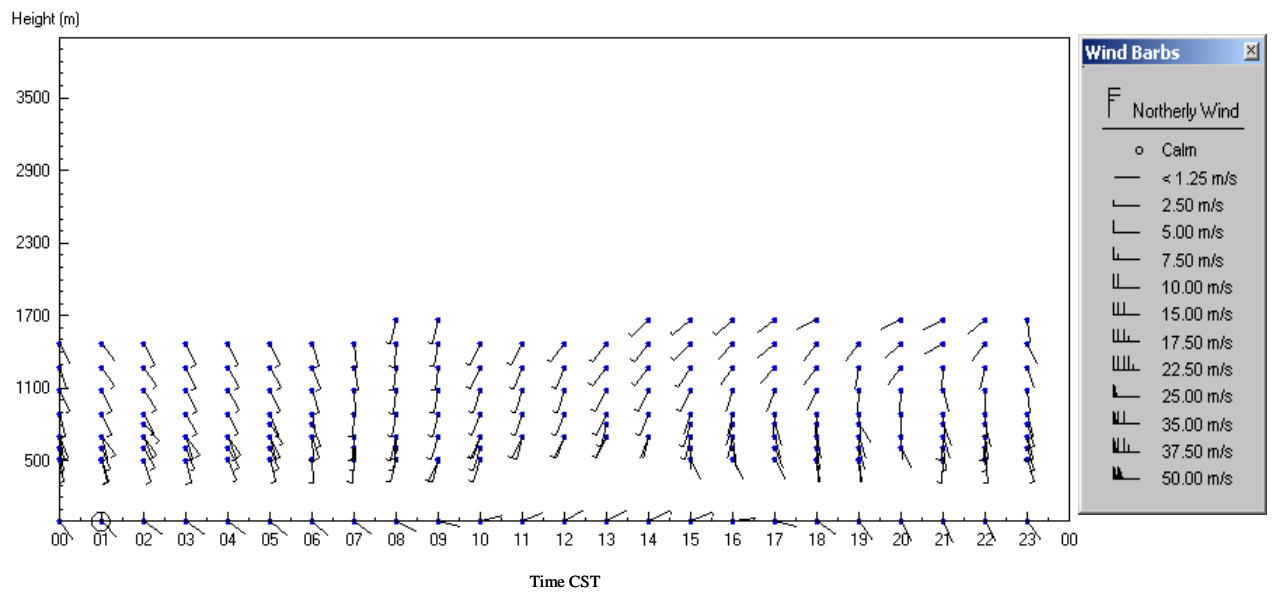


Figure 4-8. 2000 year average winds at VRM from 0000 to 2300 CST, June 1, 2000, to May 31, 2001.

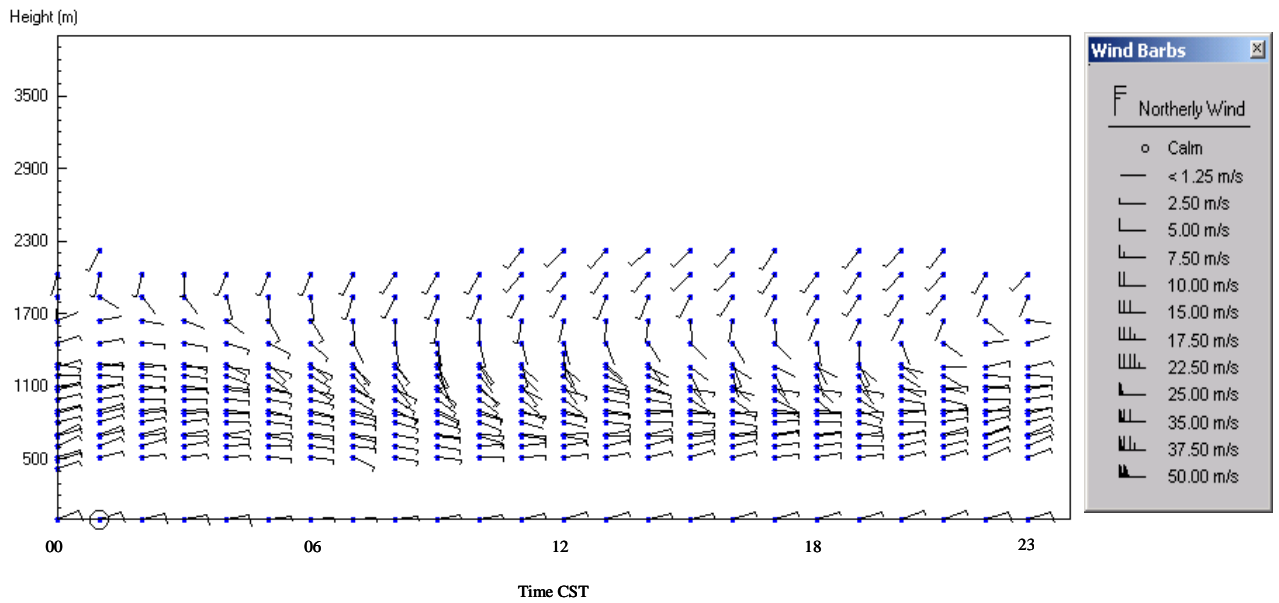


Figure 4-9. Fall average winds at SMI from 0000 to 2300 CST, September 24 to December 22, for all study years.

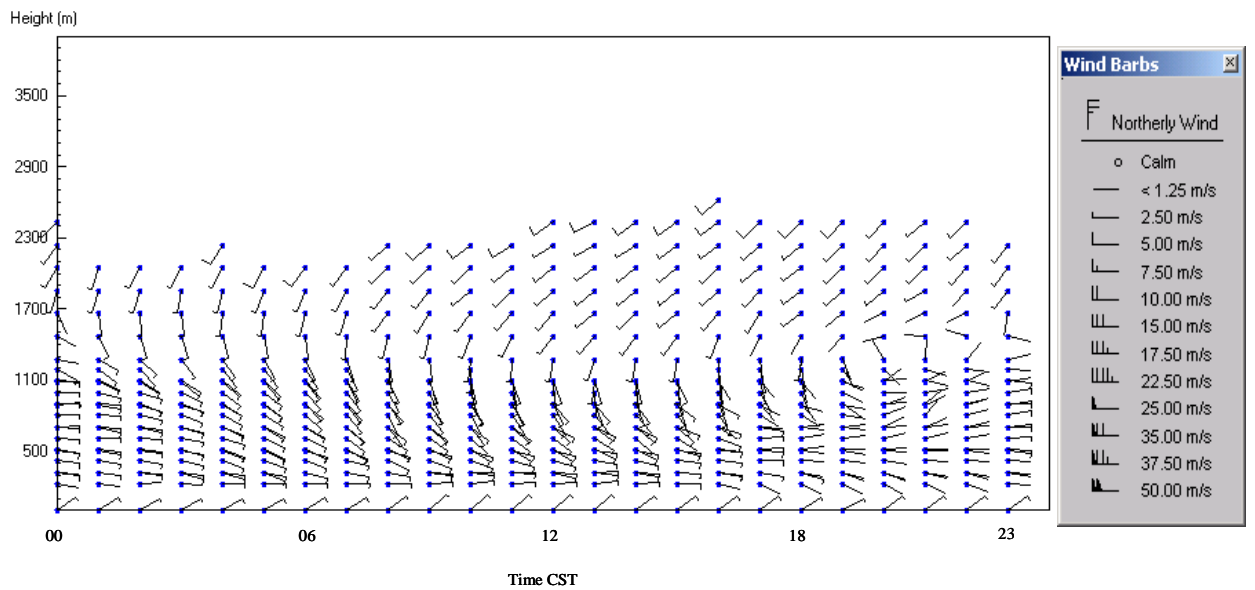


Figure 4-10. Fall average winds at VRM from 0000 to 2300 CST, September 24 to December 22, for all study years.

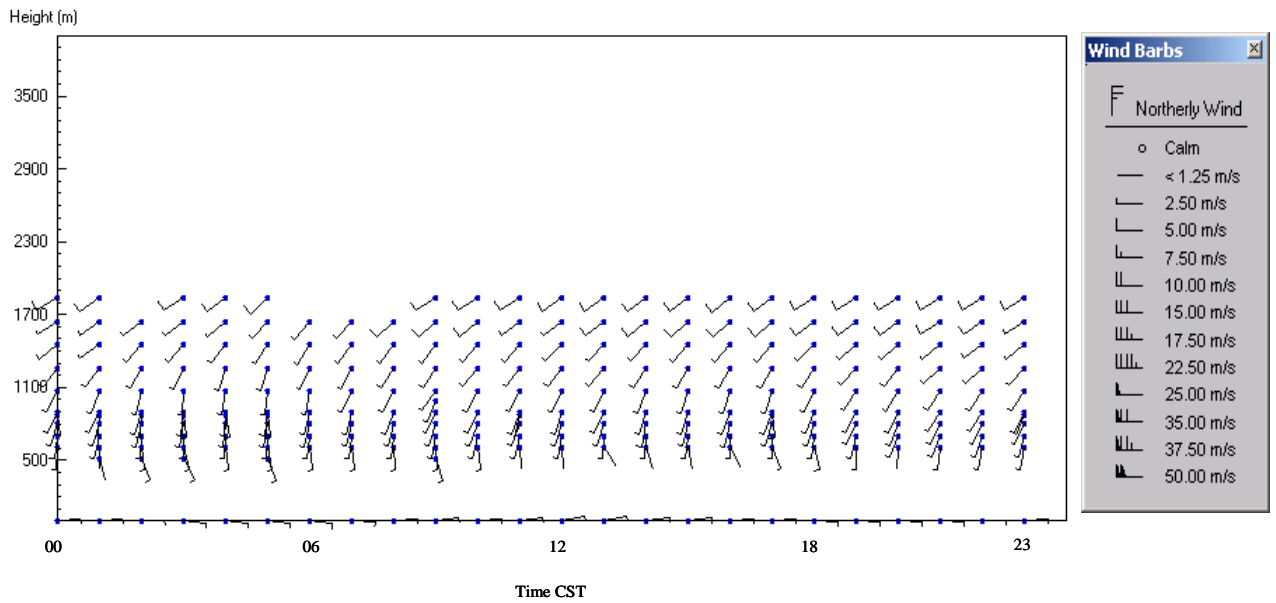


Figure 4-11. Winter average winds at SMI from 0000 to 2300 CST, December 23 to March 21, for all study years.

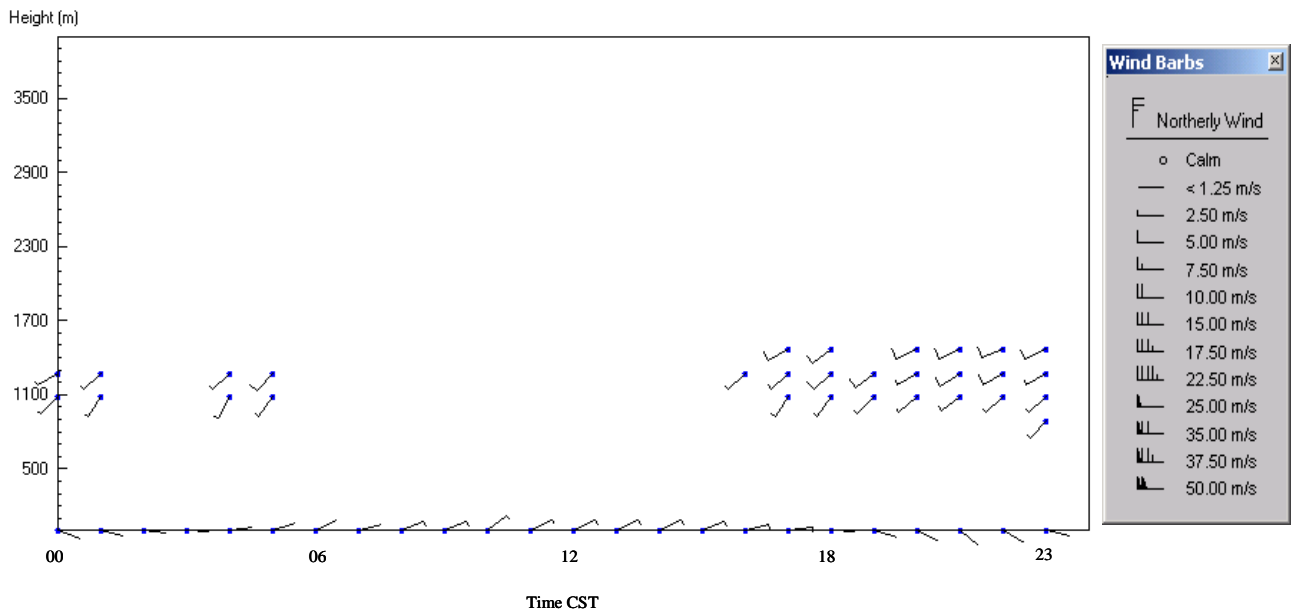


Figure 4-12. Winter average winds at VRM from 0000 to 2300 CST, December 23 to March 21, for all study years.

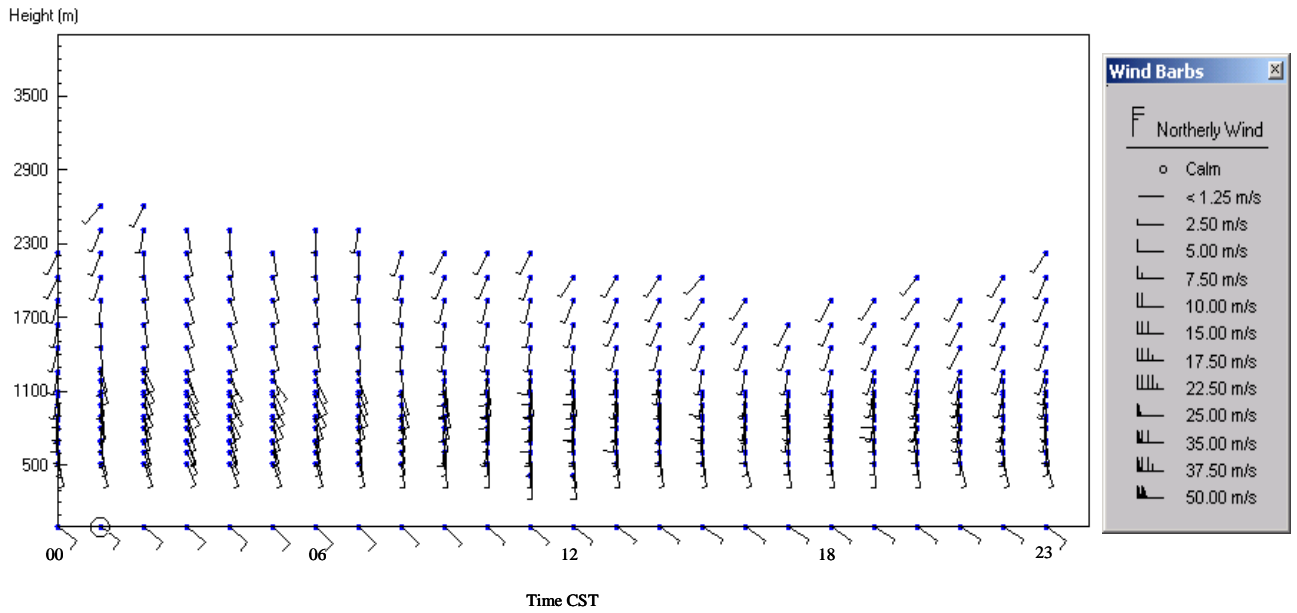


Figure 4-13. Spring average winds at SMI from 0000 to 2300 CST, March 22 to June 22, for all study years.

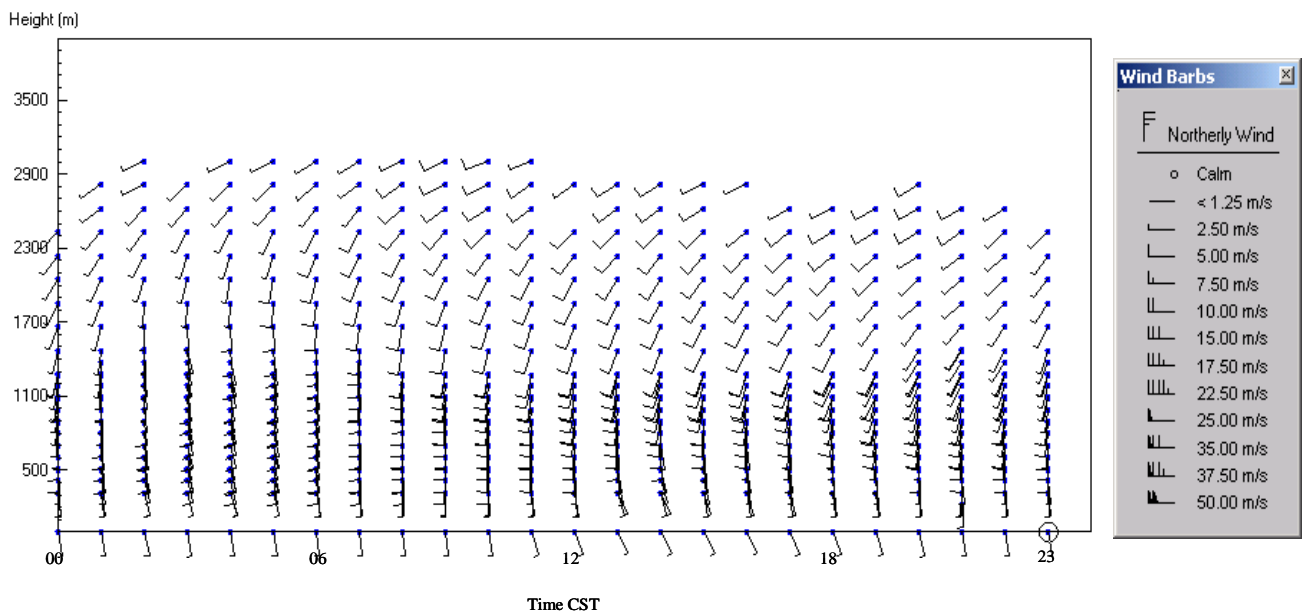


Figure 4-14. Spring average winds at VRM from 0000 to 2300 CST, March 22 to June 22, for all study years.

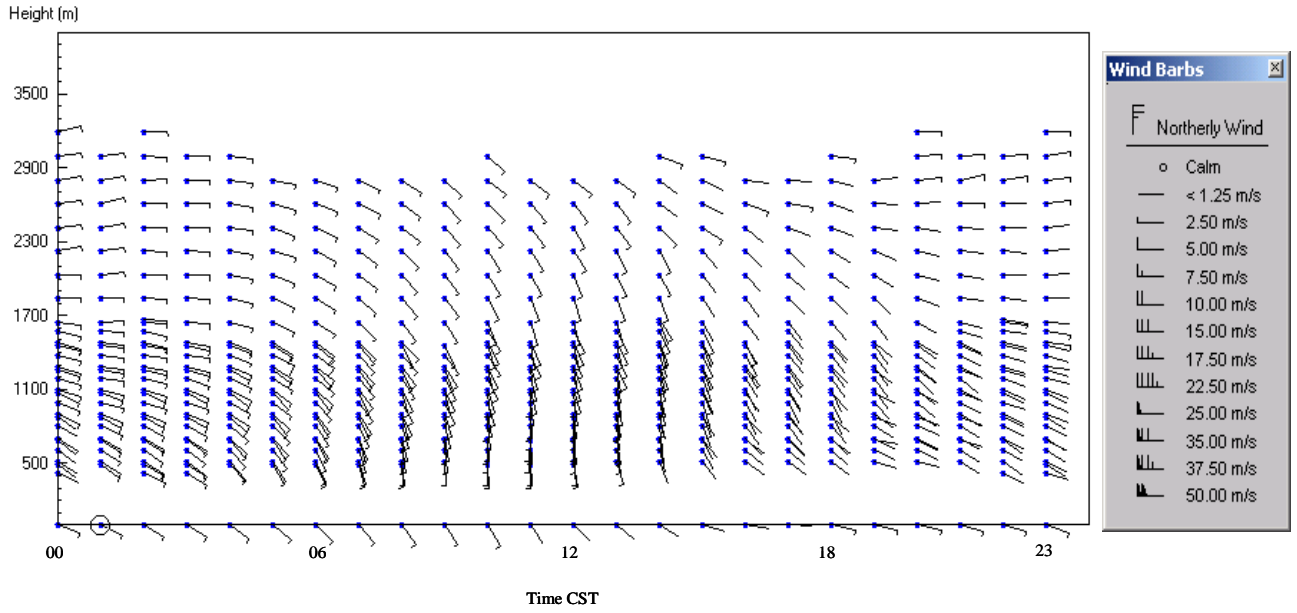


Figure 4-15. Summer average winds at SMI from 0000 to 2300 CST, June 23 to September 23, for all study years.

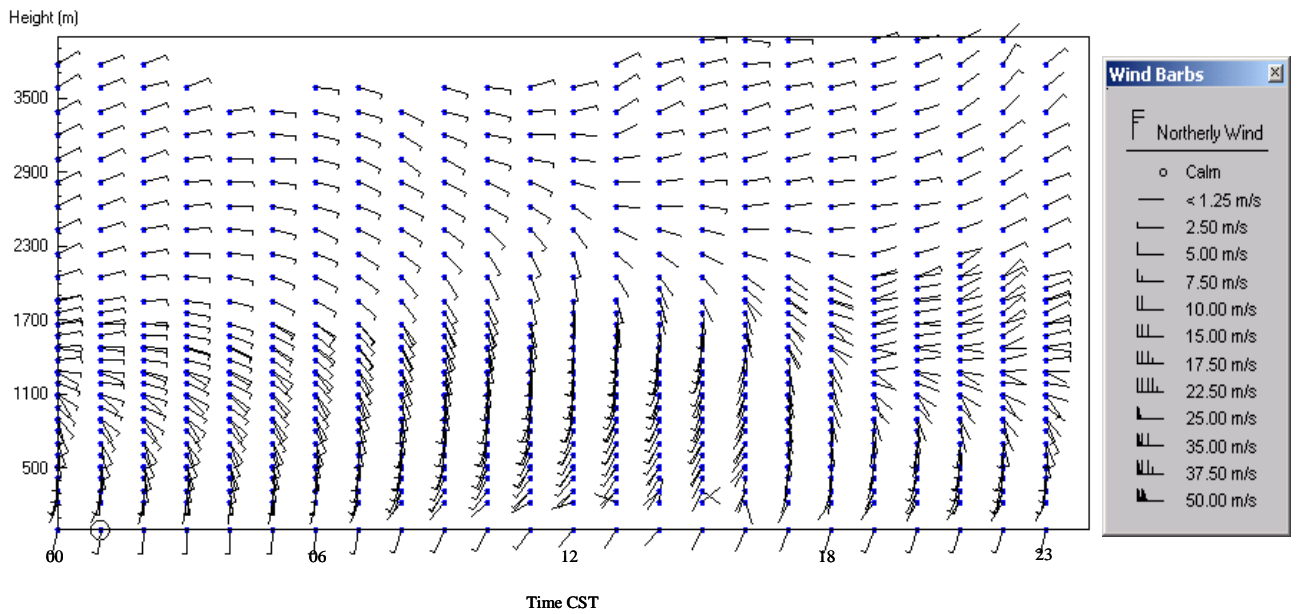


Figure 4-16. Summer average winds at VRM from 0000 to 2300 CST, June 23 to September 23, for all study years.

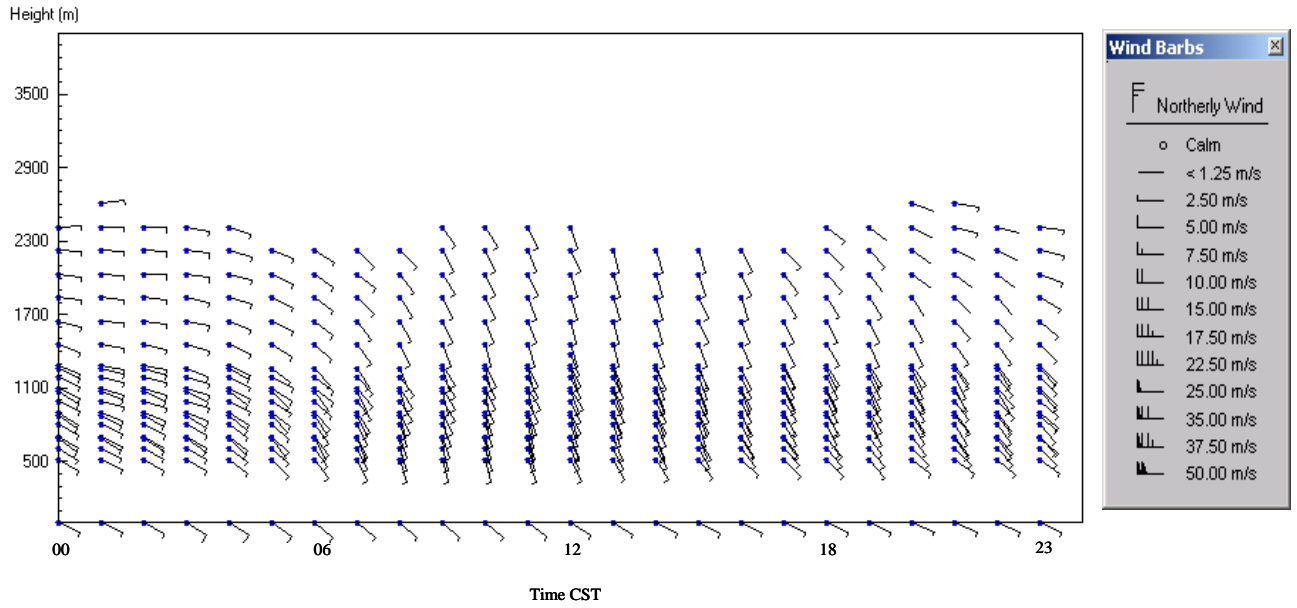


Figure 4-17. Ridge pattern average winds at SMI from 0000 to 2300 CST, for all study years.

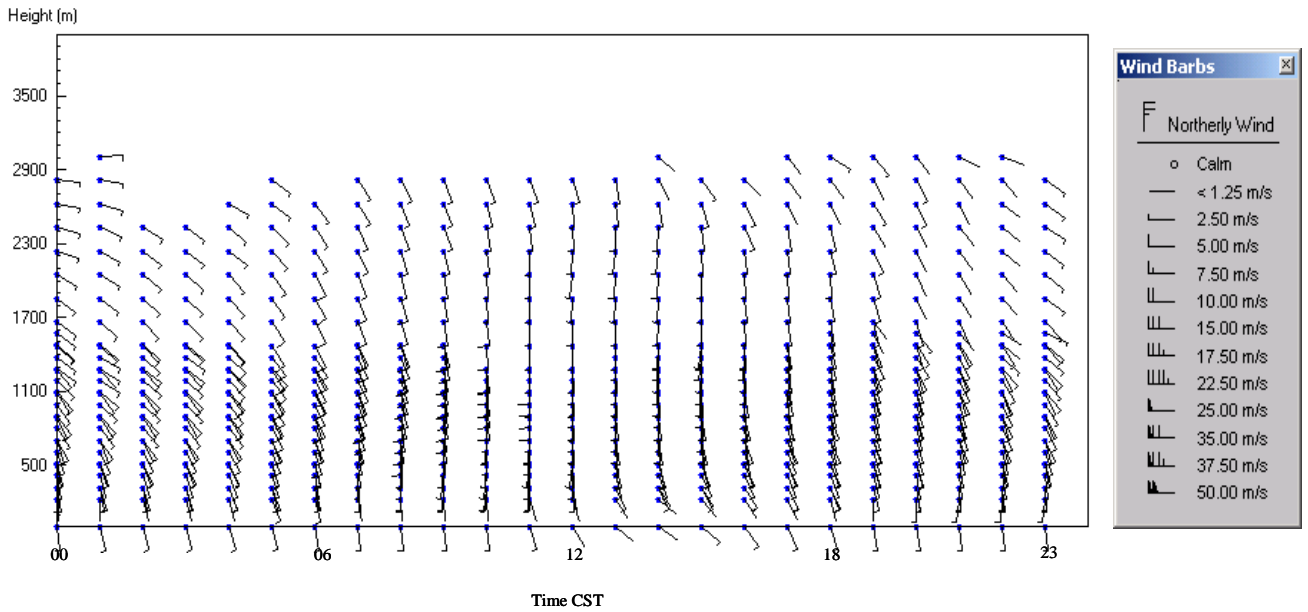


Figure 4-18. Ridge pattern average winds at VRM from 0000 to 2300 CST, for all study years.

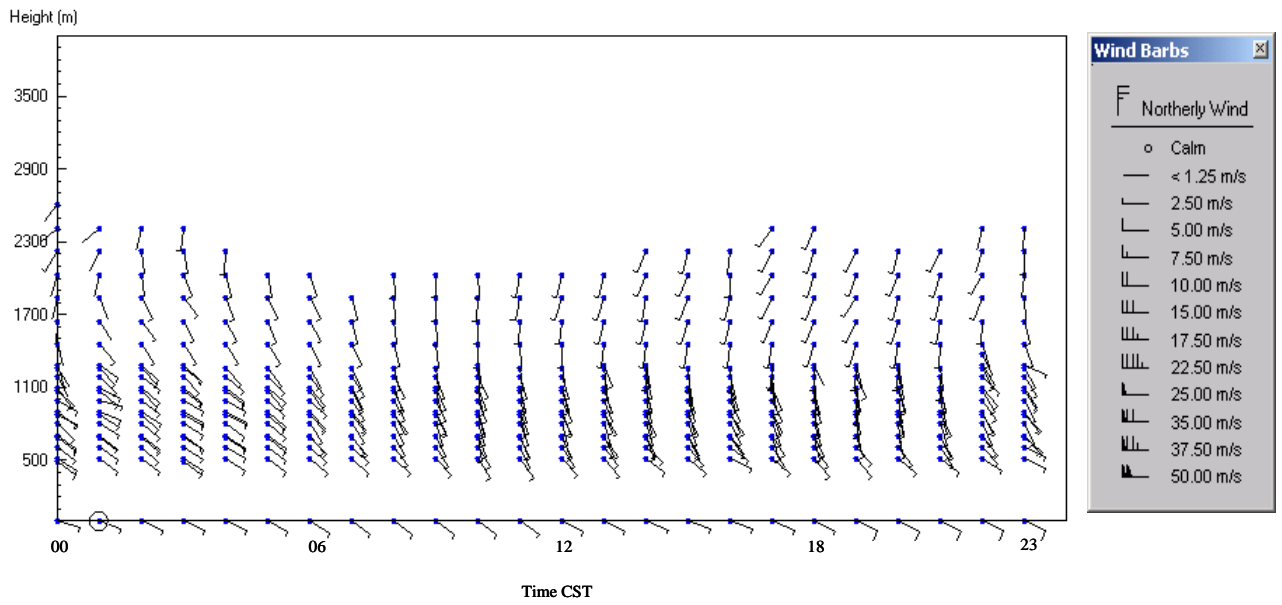


Figure 4-19. Weak ridge average winds at SMI, 0000 to 2300 CST, for all study years.

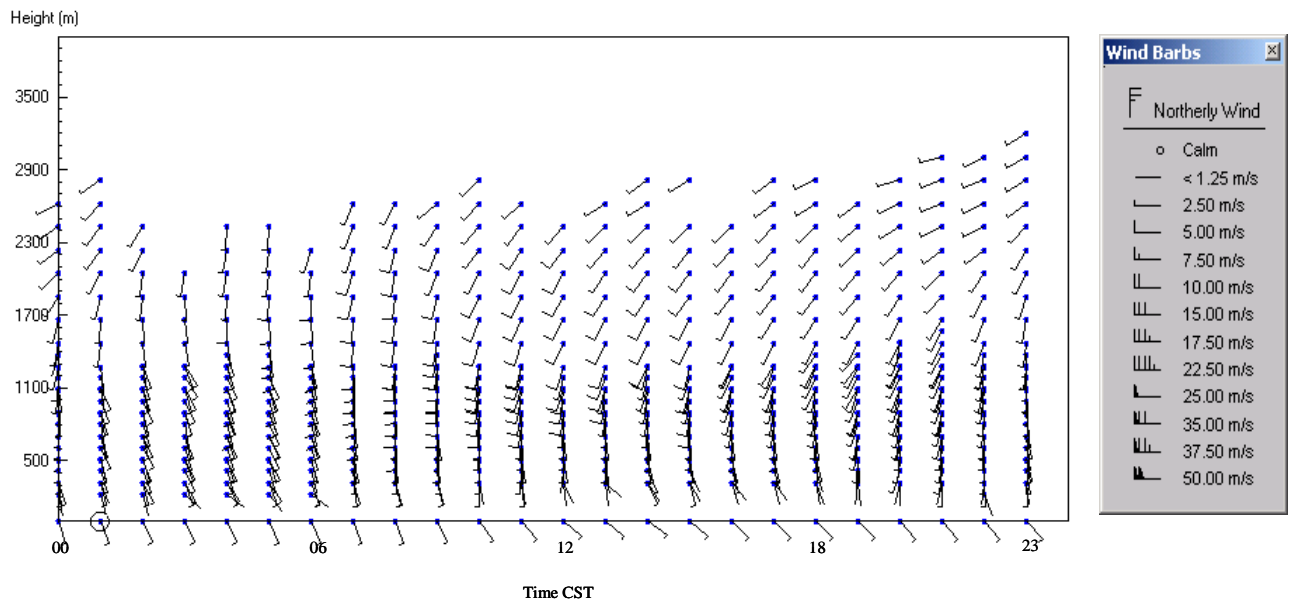


Figure 4-20. Weak ridge average winds at VRM, 0000 to 2300 CST, for all study years.

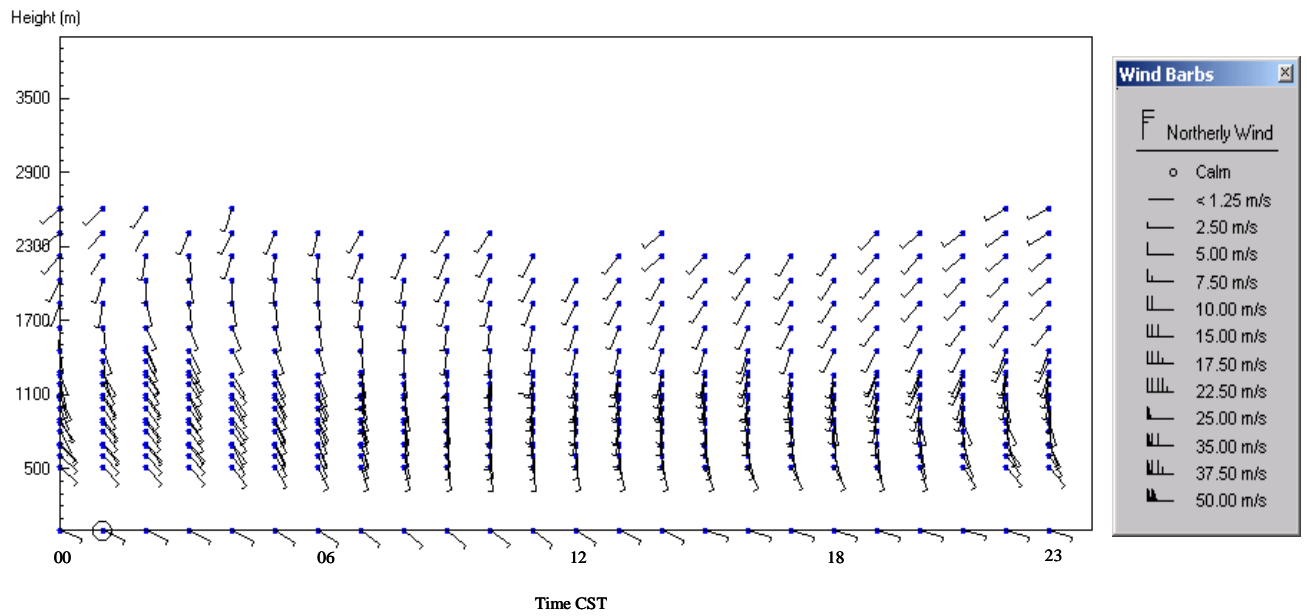


Figure 4-21. Weak trough average winds at SMI, 0000 to 2300 CST, for all study years.

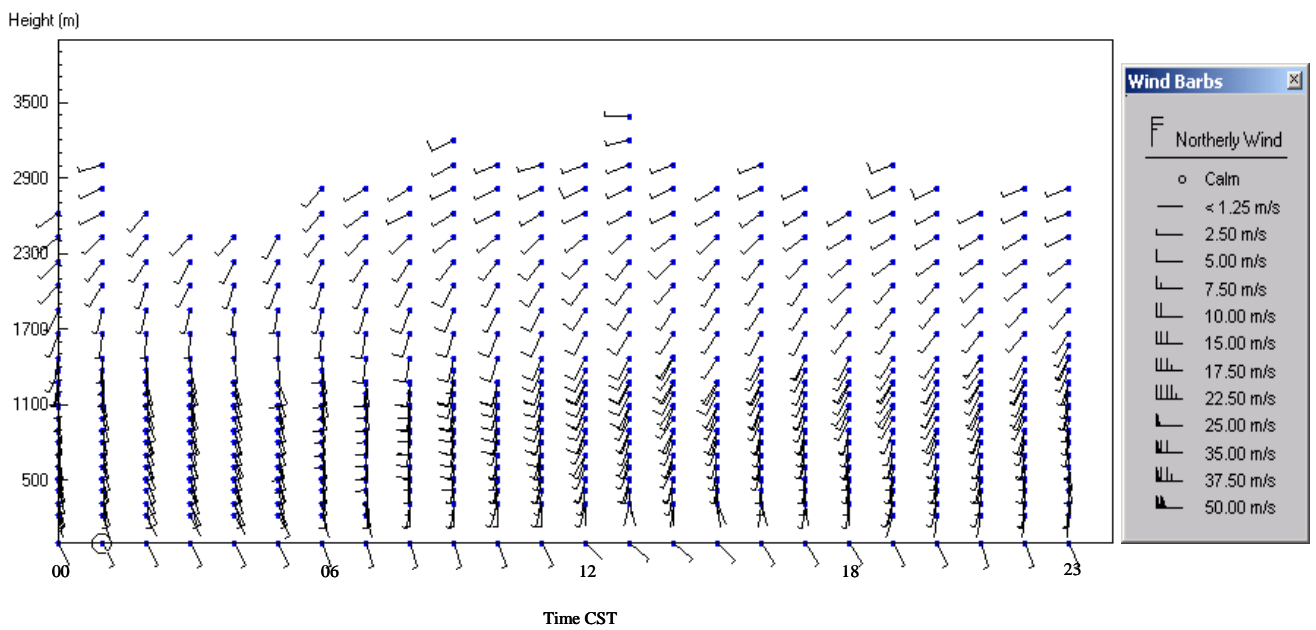


Figure 4-22. Weak trough average winds at VRM, 0000 to 2300 CST, for all study years.

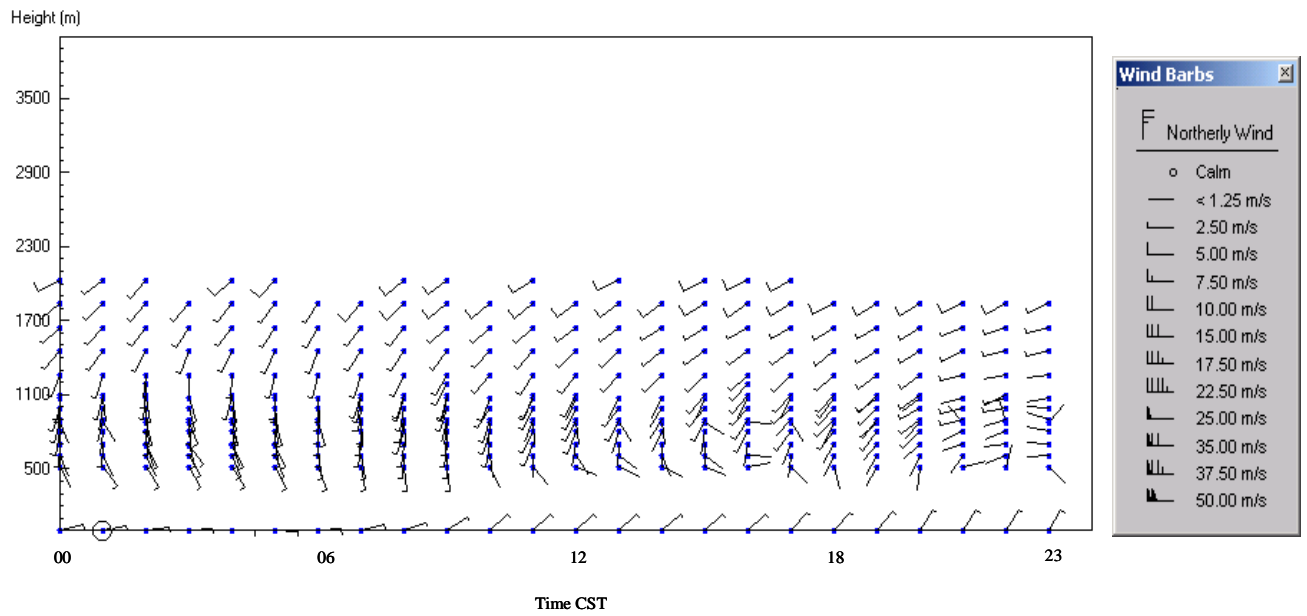


Figure 4-23. Trough average winds at SMI, 0000 to 2300 CST, for all study years.

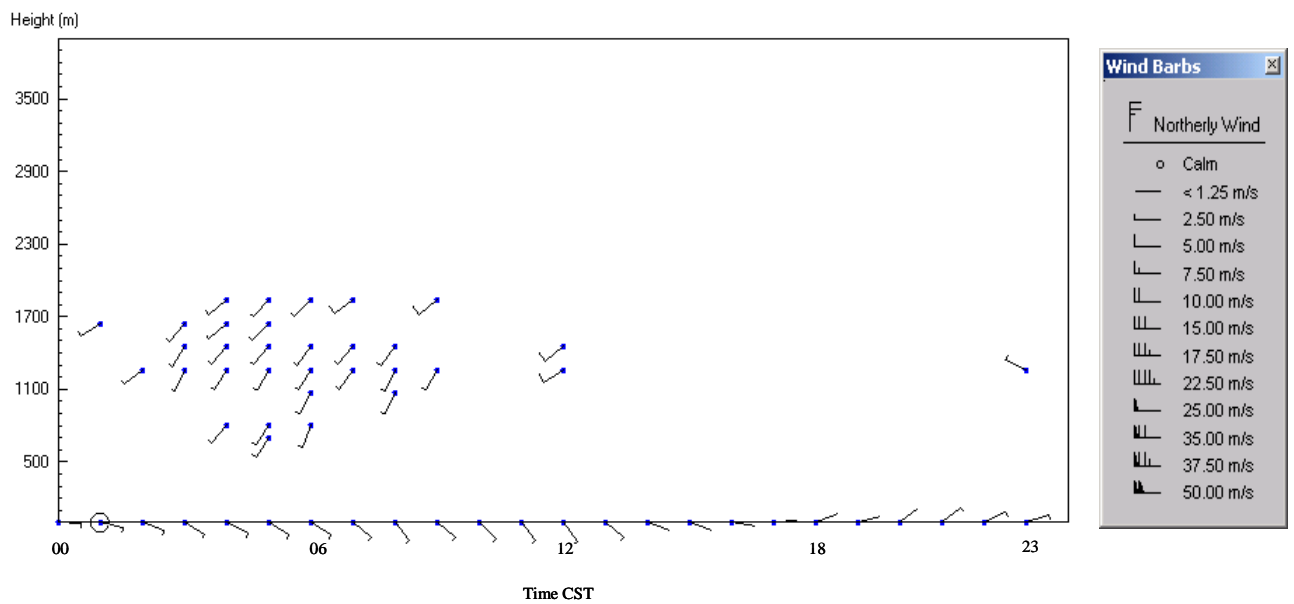


Figure 4-24. Cut-off low average winds at SMI, 0000 to 2300 CST, for all study years.

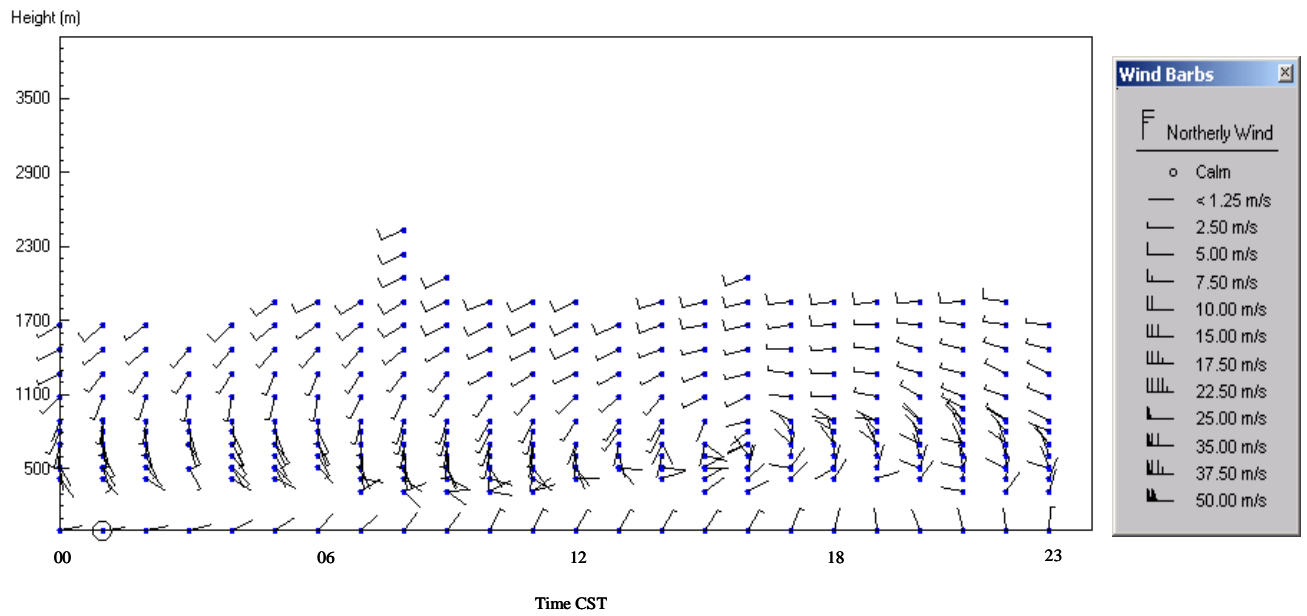


Figure 4-25. Trough average winds at VRM, 0000 to 2300 CST, for all study years.

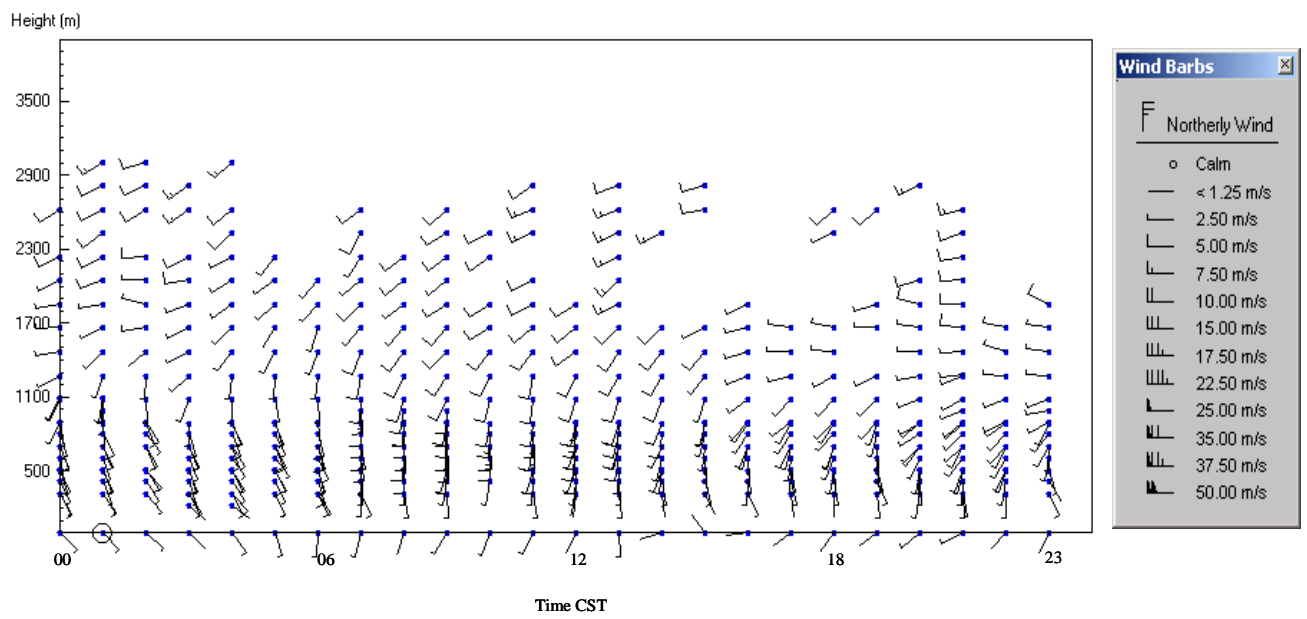


Figure 4-26. Cut-off low average winds at VRM, 0000 to 2300 CST, for all study years.

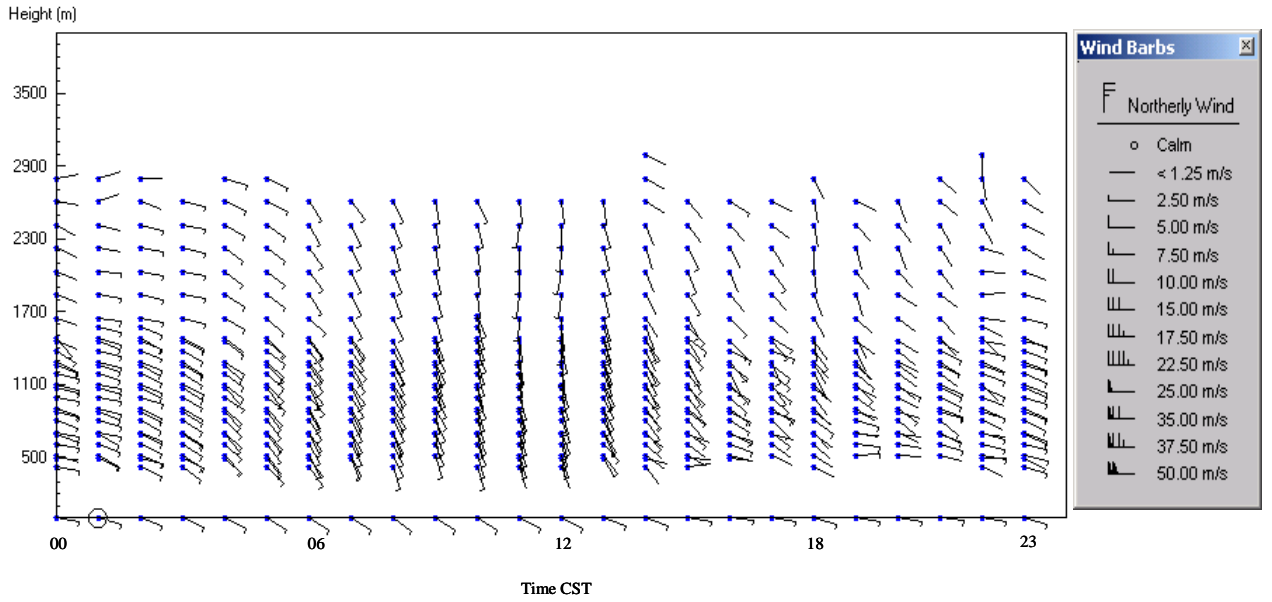


Figure 4-27. Flat average winds at SMI, 0000 to 2300 CST, for all study years.

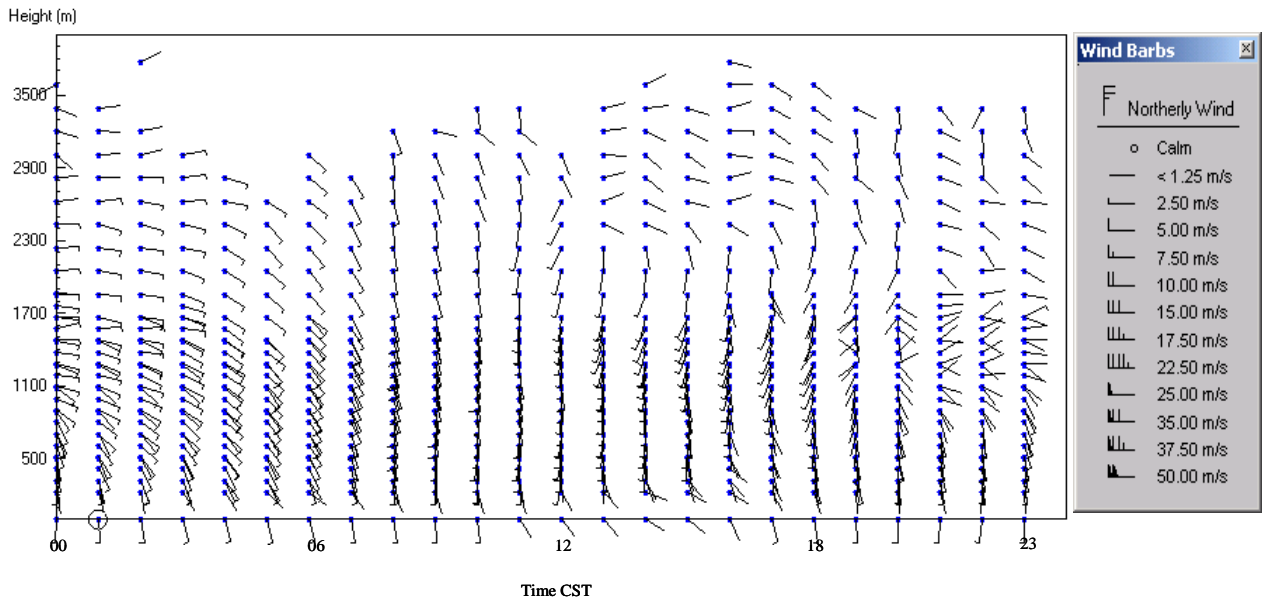


Figure 4-28. Flat average winds at VRM, 0000 to 2300 CST, for all study years.

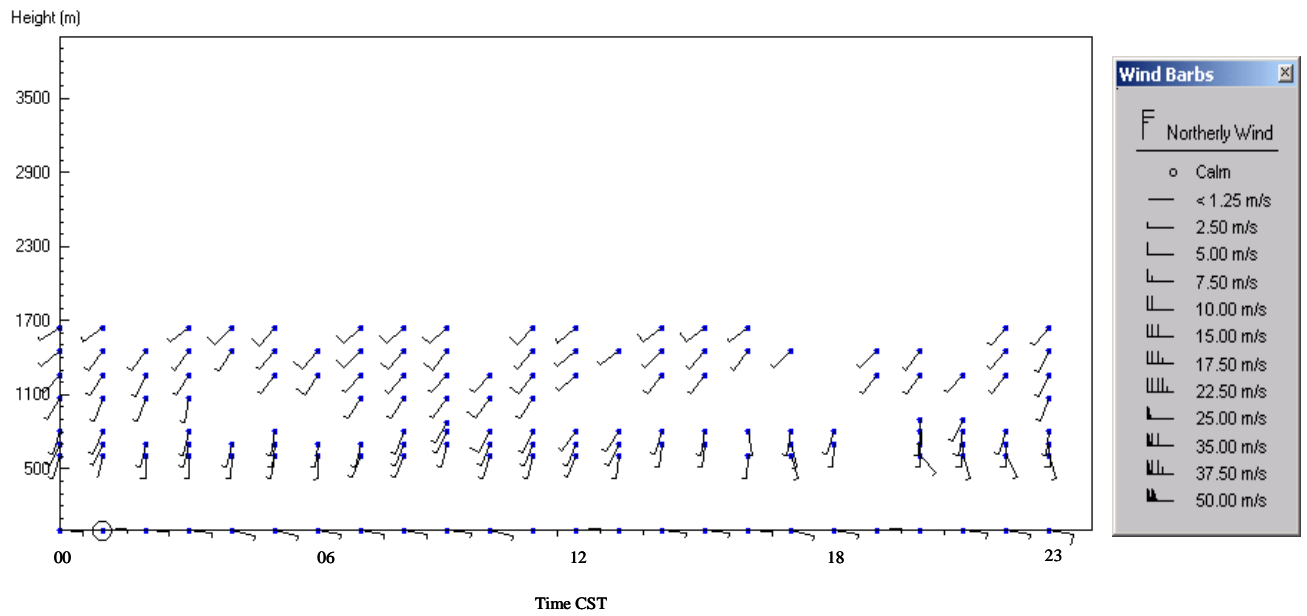


Figure 4-29. Zonal average winds at SMI, 0000 to 2300 CST for all study years.

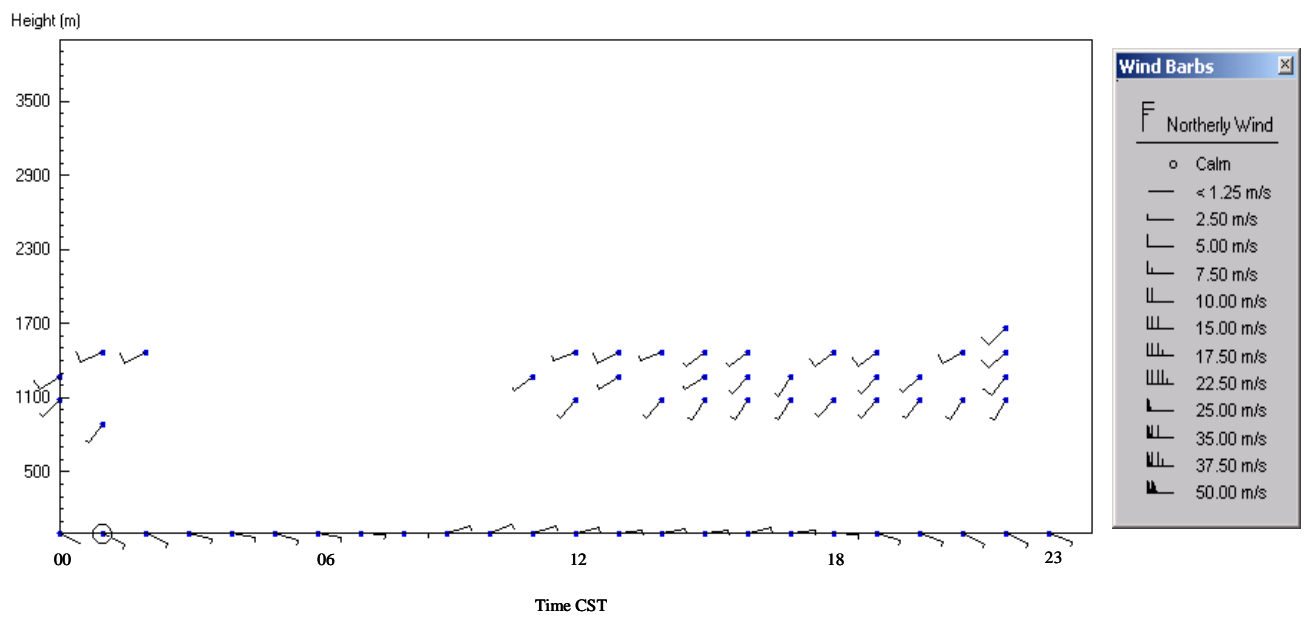


Figure 4-30. Zonal average winds at VRM, 0000 to 2300 CST, for all study years.

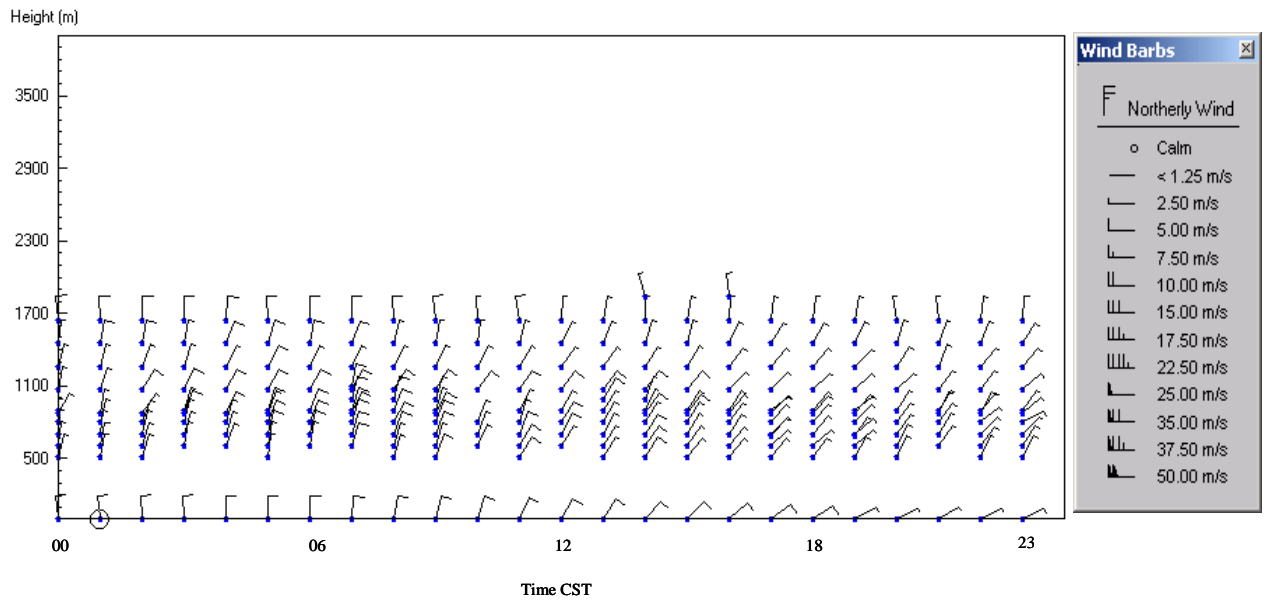


Figure 4-31. Post-trough average winds at SMI, 0000 to 2300 CST, for all study years.

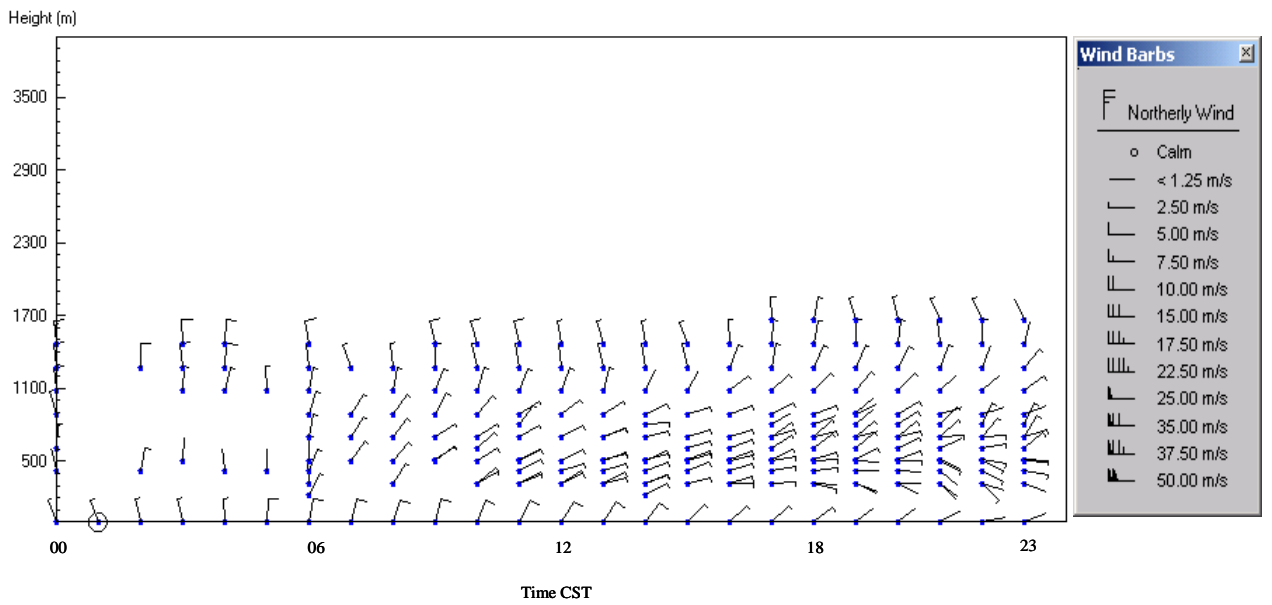


Figure 4-32. Post-trough average winds at VRM, 0000 to 2300 CST, for all study years.

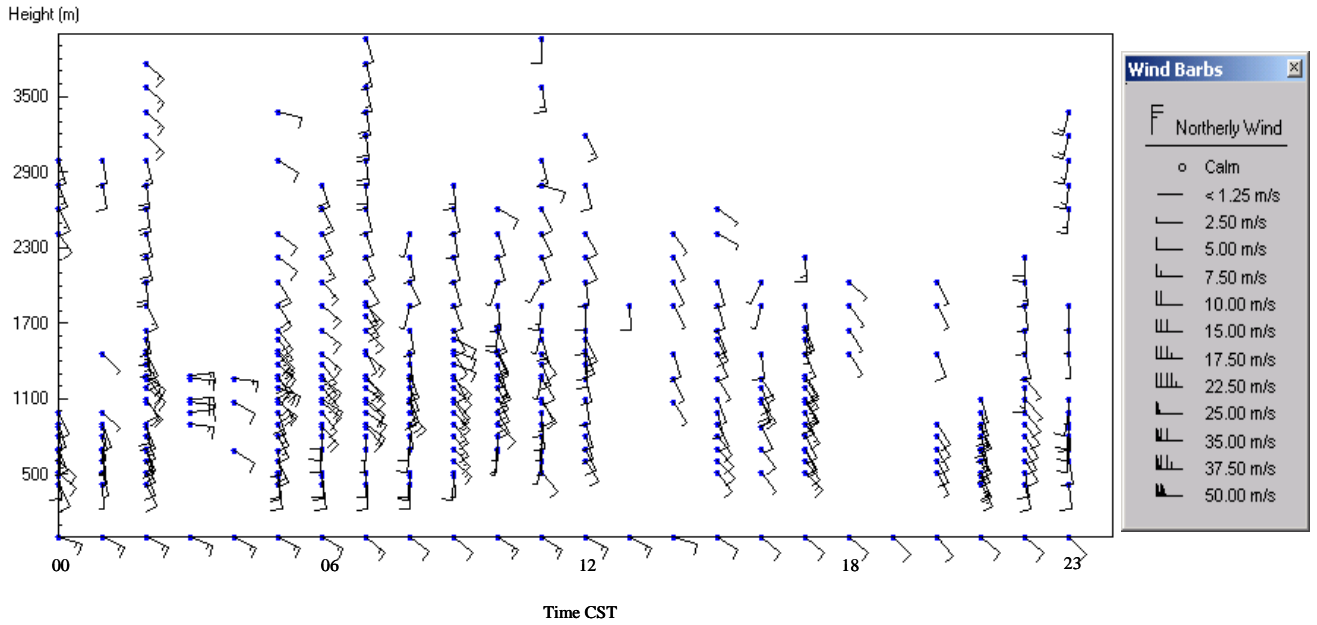


Figure 4-33. Tropical storm average winds at SMI, 0000 to 2300 CST, for all study years.

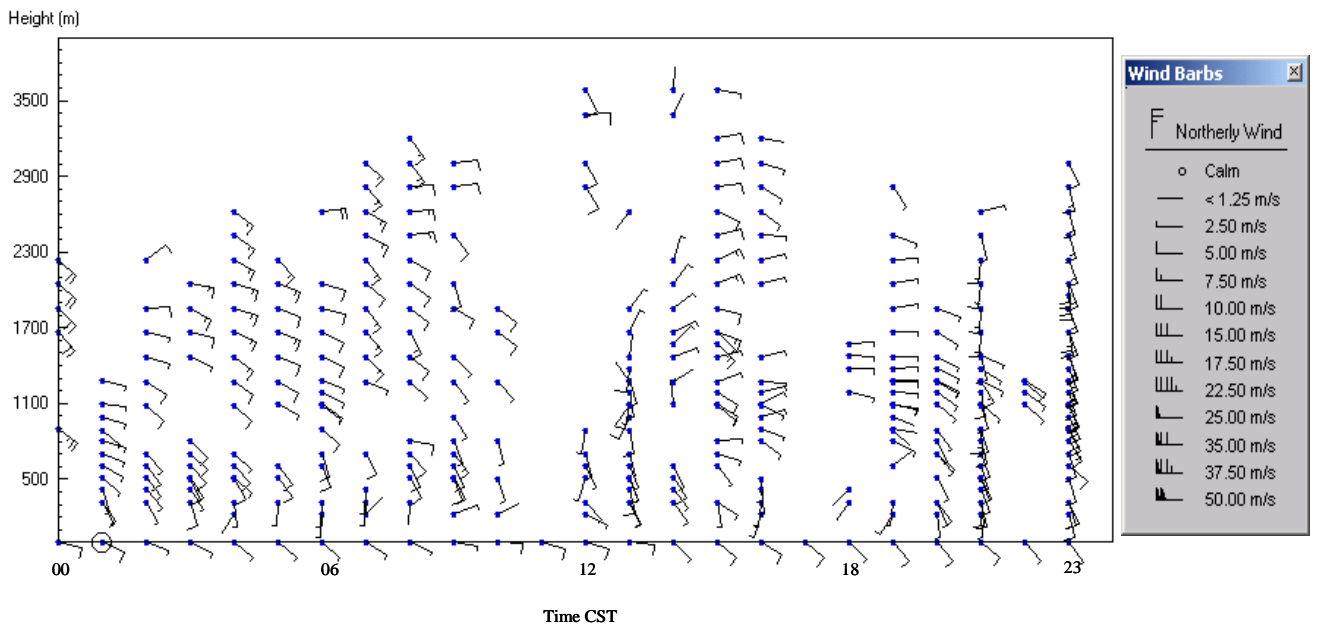


Figure 4-34. Tropical storm average winds at VRM, 0000 to 2300 CST, for all study years.

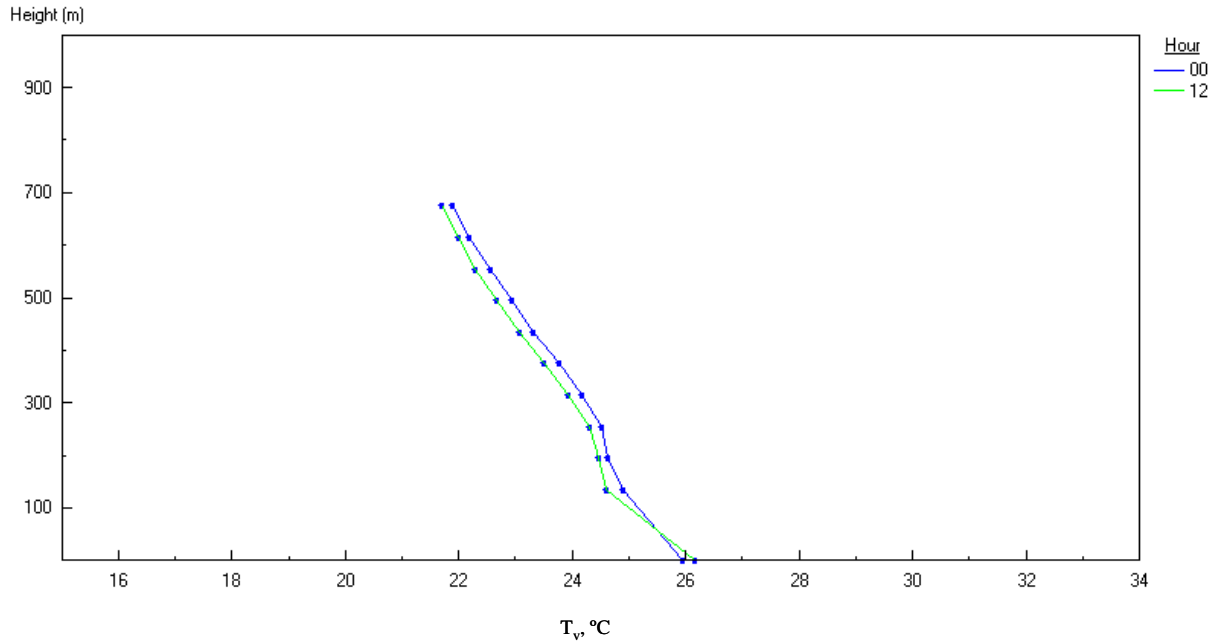


Figure 4-35. Average overall daytime and nighttime  $T_v$  profiles at SMI, June 1, 1998, to May 31, 2001. Hour 12 is the daytime profile and Hour 00 is the nighttime profile.

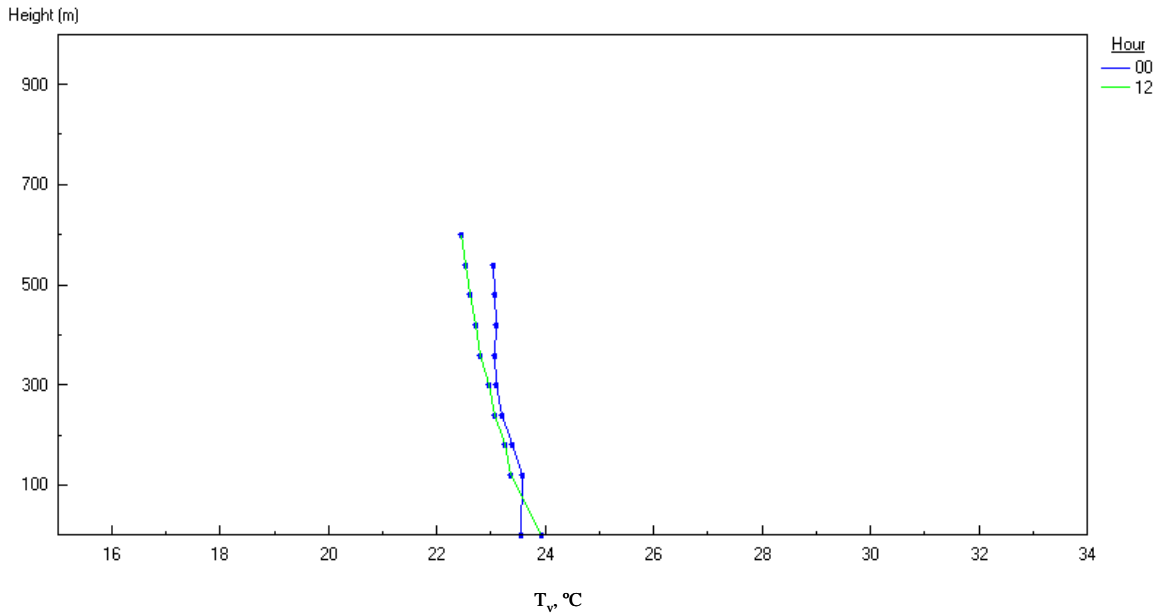


Figure 4-36. Average overall daytime and nighttime  $T_v$  profiles at VRM, June 1, 1998, to May 31, 2001. Hour 12 is the daytime profile and the Hour 00 is the nighttime profile.

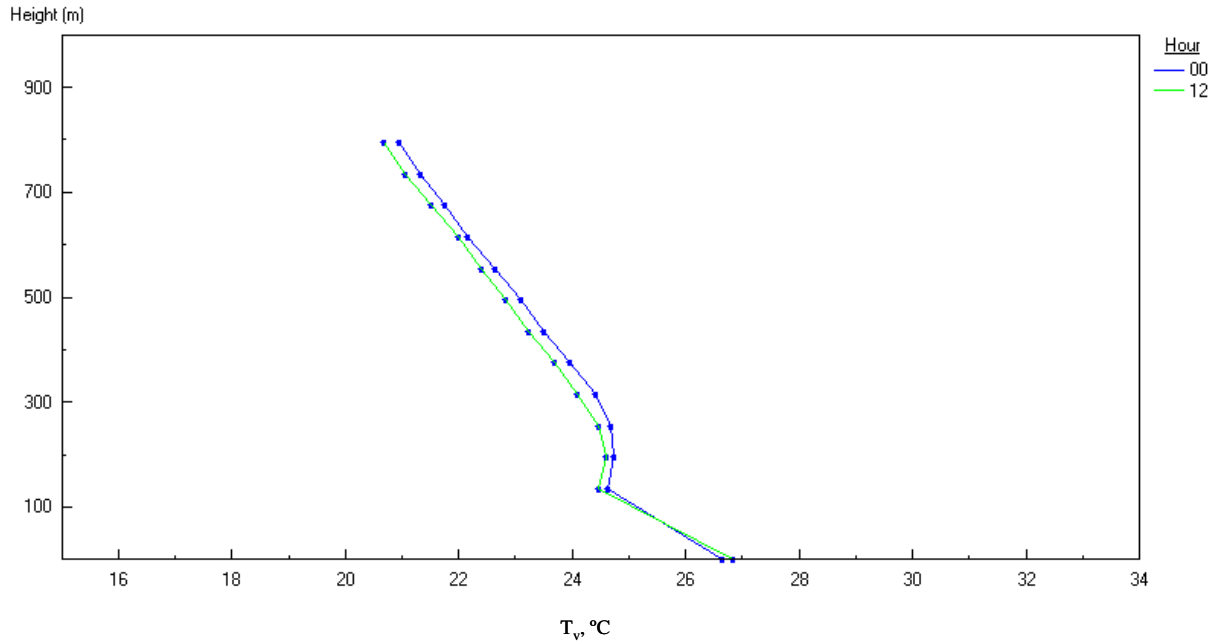


Figure 4-37. 1998 year average daytime and nighttime  $T_v$  profiles at SMI, June 1, 1998, to May 31, 1999. Hour 12 is the daytime profile and the Hour 00 is the nighttime profile.

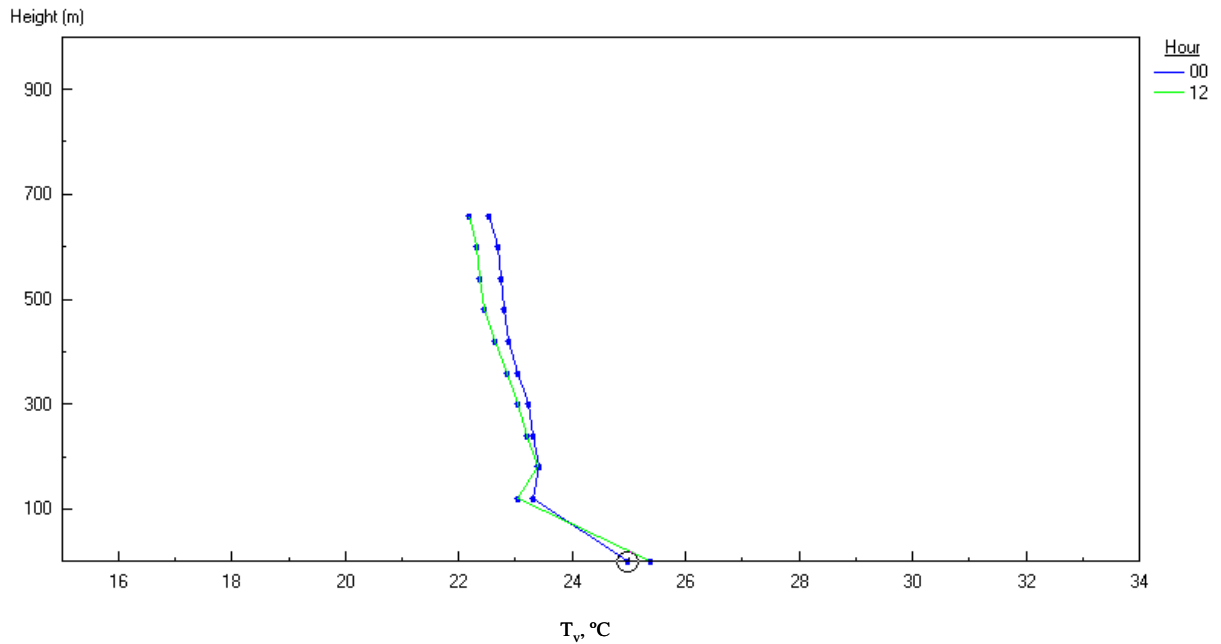


Figure 4-38. 1998 year average daytime and nighttime  $T_v$  profiles at VRM, June 1, 1998, to May 31, 1999. Hour 12 is the daytime profile and the Hour 00 is the nighttime profile.

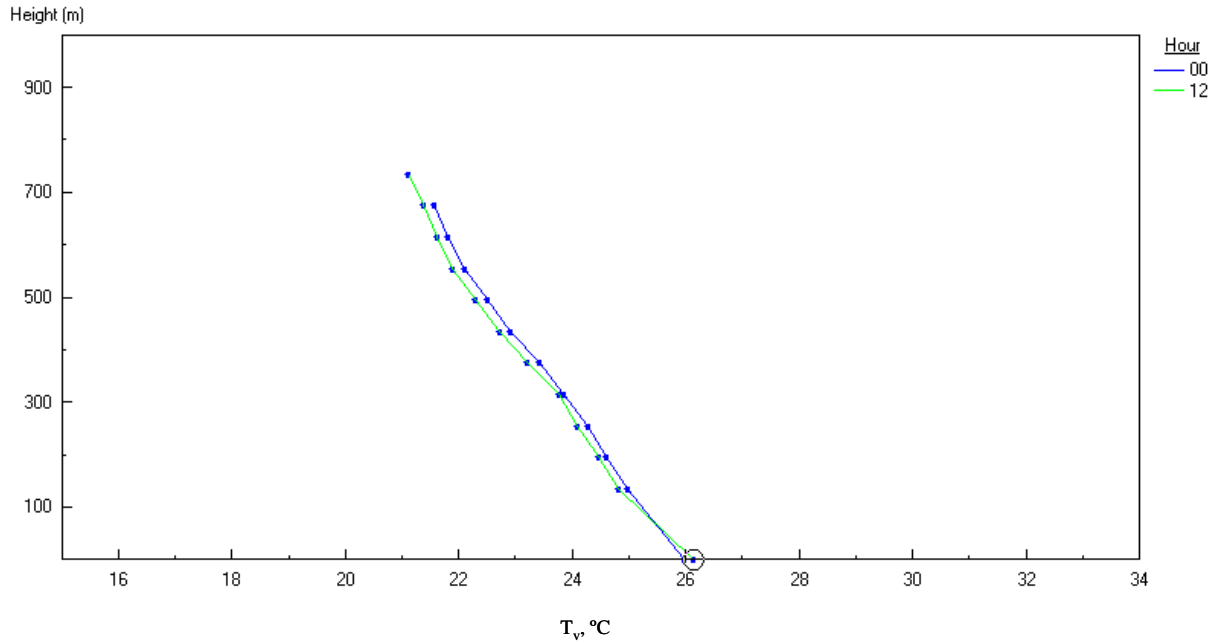


Figure 4-39. 1999 year average daytime and nighttime  $T_v$  profiles at SMI, June 1, 1999, to May 31, 2000. Hour 12 is the daytime profile and the Hour 00 is the nighttime profile.

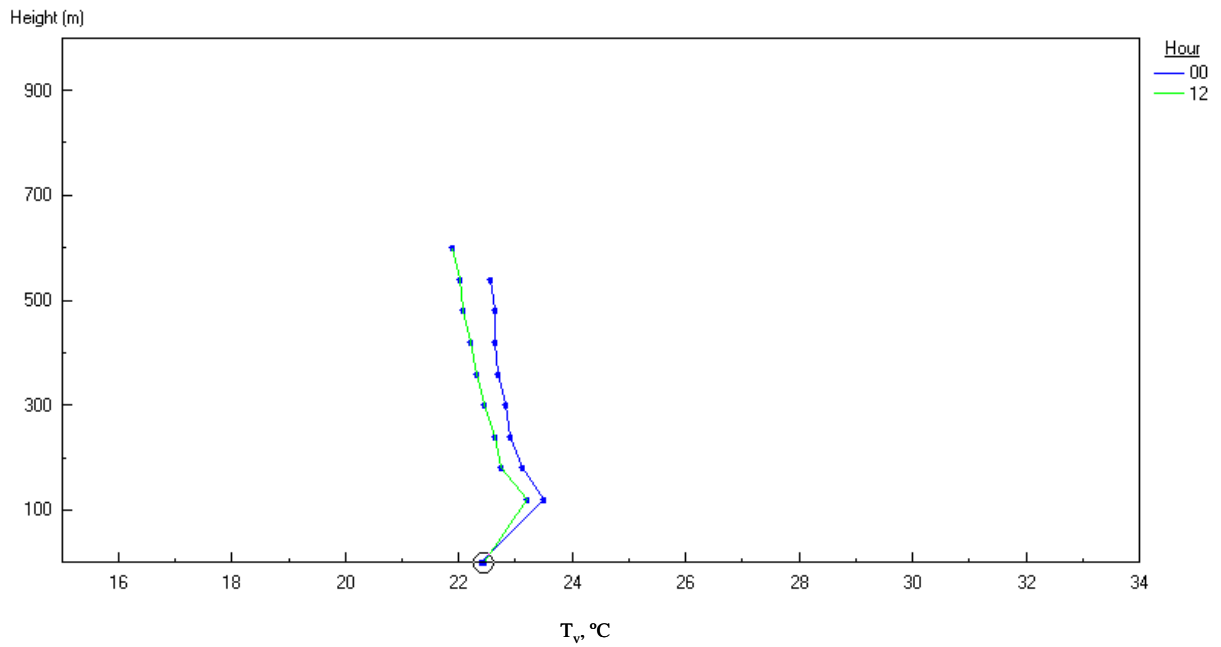


Figure 4-40. 1999 year average daytime and nighttime  $T_v$  profiles at VRM, June 1, 1999, to May 31, 2000. Hour 12 is the daytime profile and the Hour 00 is the nighttime profile.

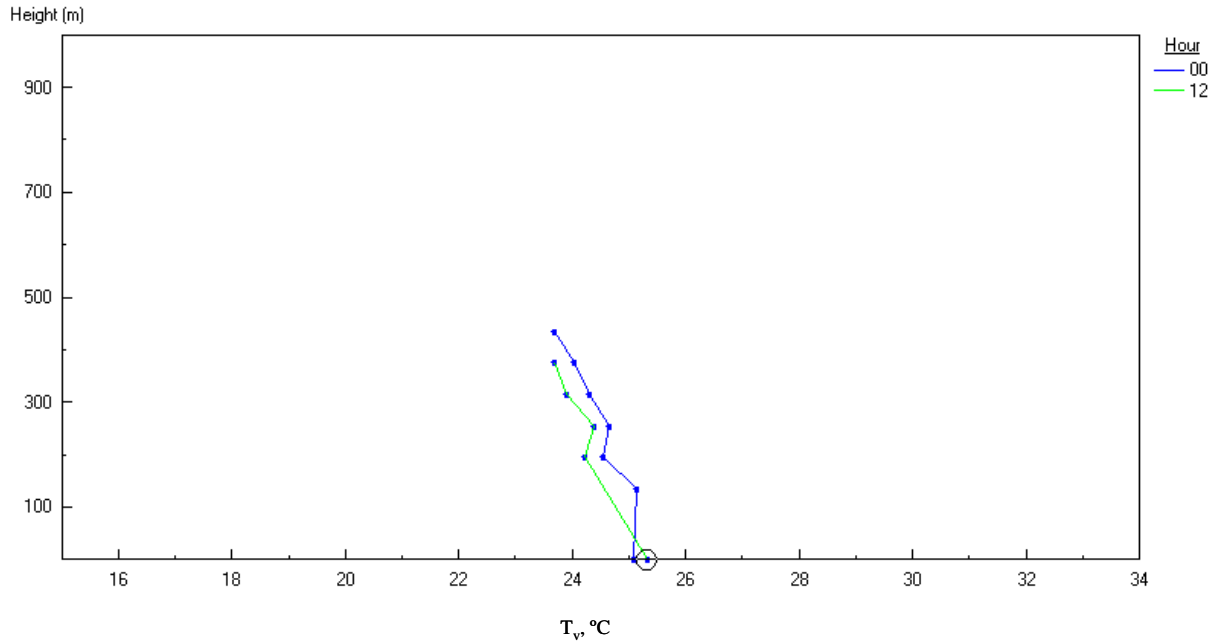


Figure 4-41. 2000 year average daytime and nighttime  $T_v$  profiles at SMI, June 1, 2000, to May 31, 2001. Hour 12 is the daytime profile and the Hour 00 is the nighttime profile.

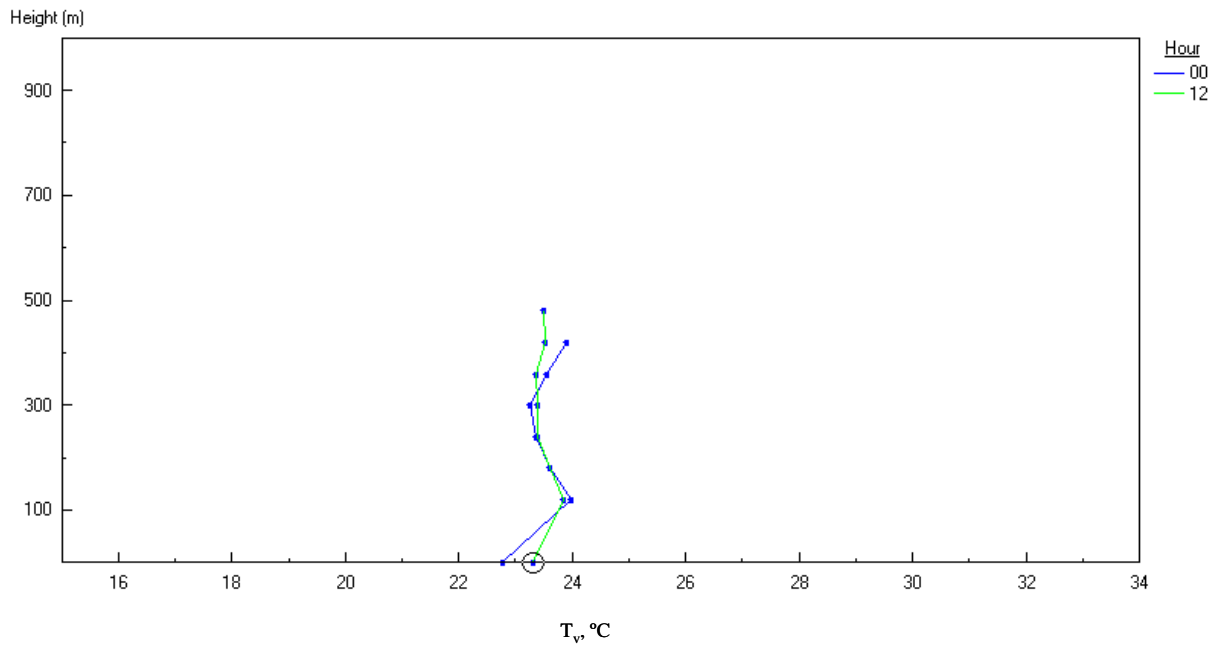


Figure 4-42. 2000 year average daytime and nighttime  $T_v$  profiles at VRM, June 1, 2000, to May 31, 2001. Hour 12 is the daytime profile and the Hour 00 is the nighttime profile.

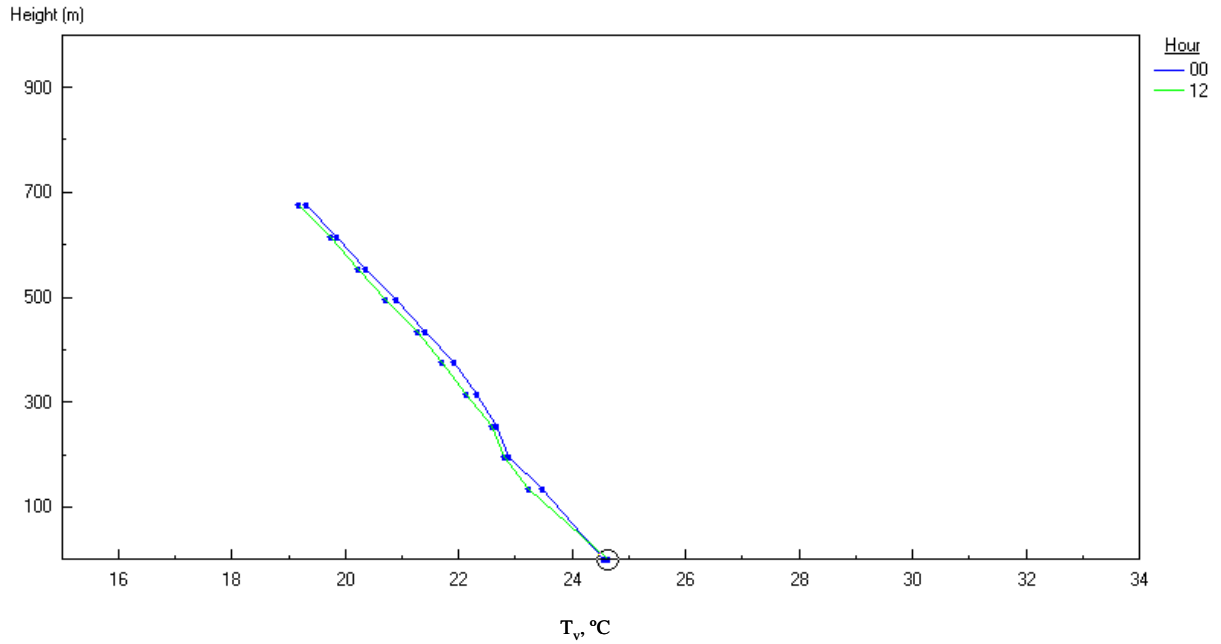


Figure 4-43. Fall average daytime and nighttime  $T_v$  profiles at SMI, September 24 to December 22. Hour 12 is the daytime profile and the Hour 00 is the nighttime profile.

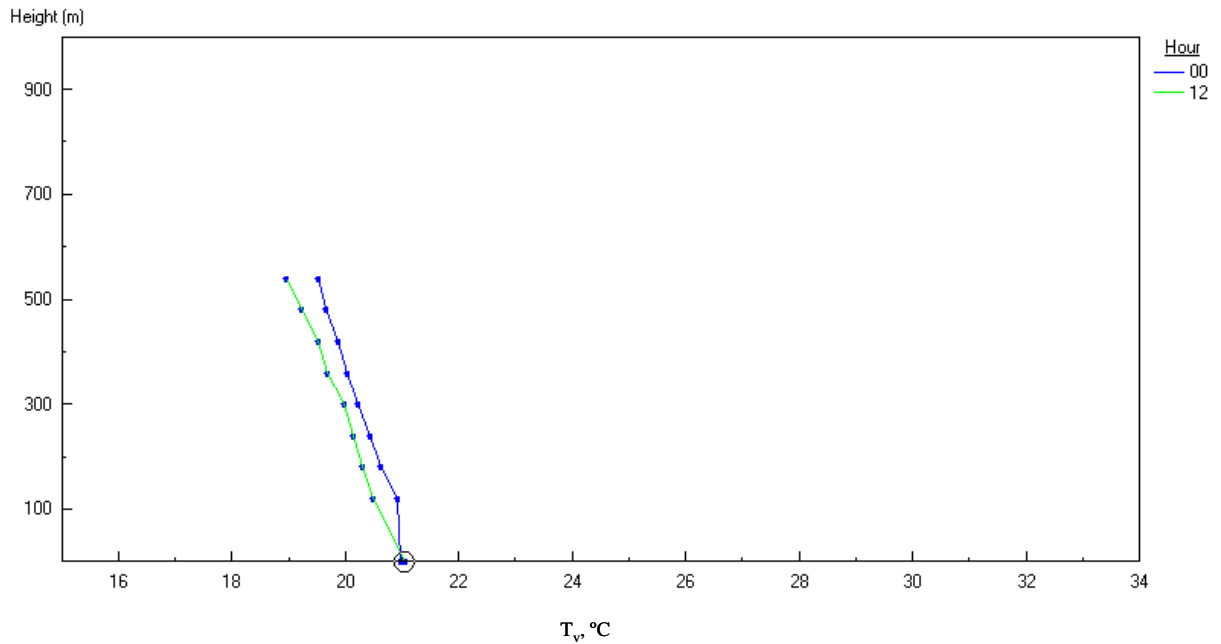


Figure 4-44. Fall average daytime and nighttime  $T_v$  profiles at VRM, September 24 to December 22. Hour 12 is the daytime profile and the Hour 00 is the nighttime profile.

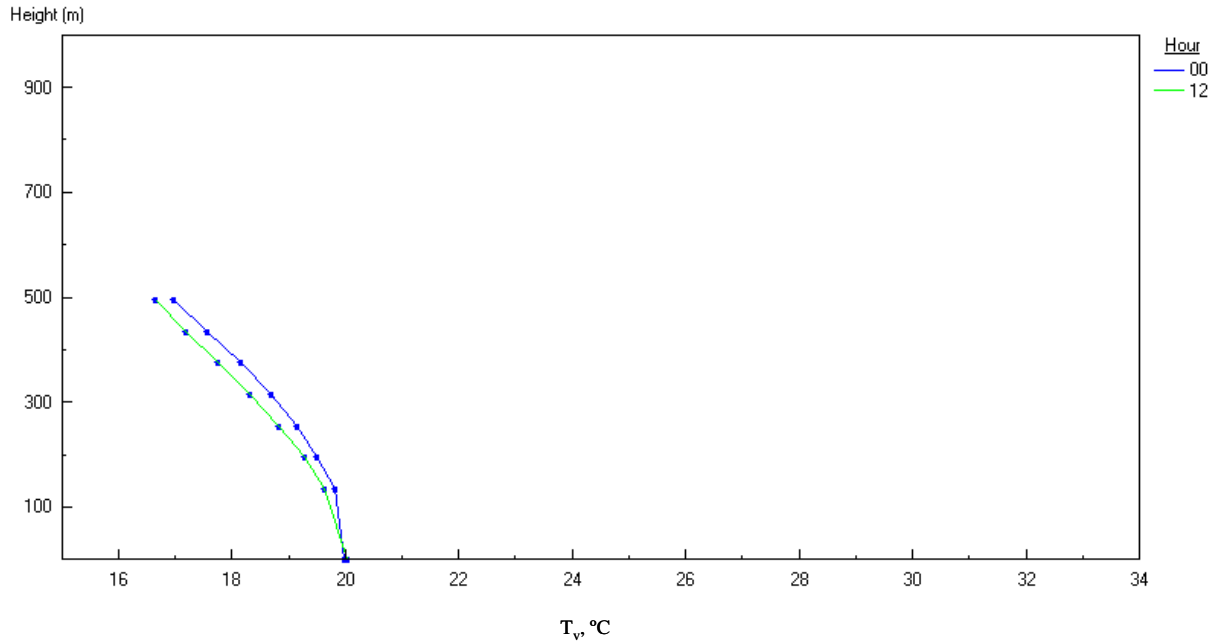


Figure 4-45. Winter average daytime and nighttime  $T_v$  profiles at SMI, December 23 to March 21. Hour 12 is the daytime profile and the Hour 00 is the nighttime profile.

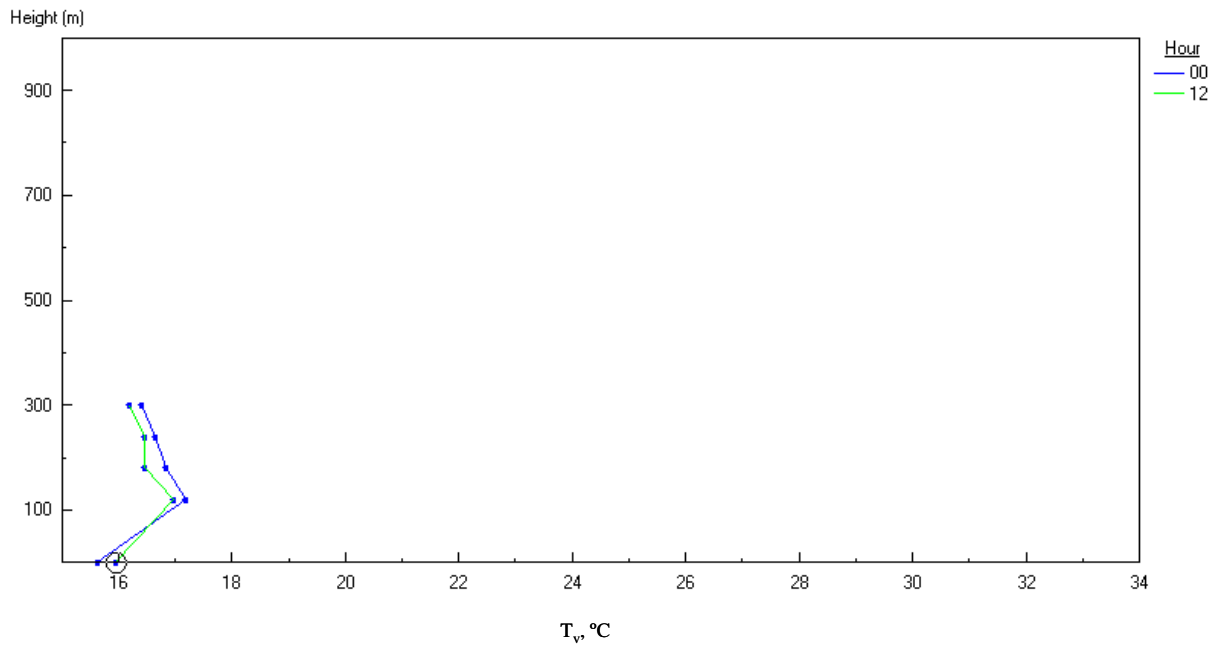


Figure 4-46. Winter average daytime and nighttime  $T_v$  profiles at VRM, December 23 to March 21. Hour 12 is the daytime profile and the Hour 00 is the nighttime profile.

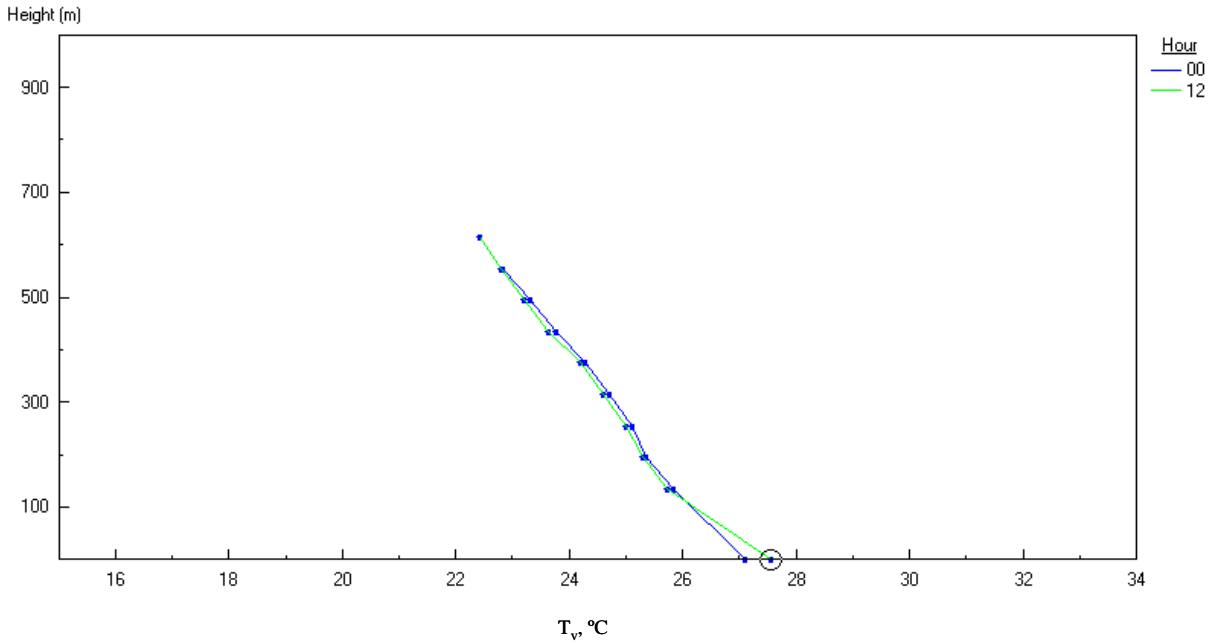


Figure 4-47. Spring average daytime and nighttime  $T_v$  profiles at SMI, March 22 to June 22. Hour 12 is the daytime profile and the Hour 00 is the nighttime profile.

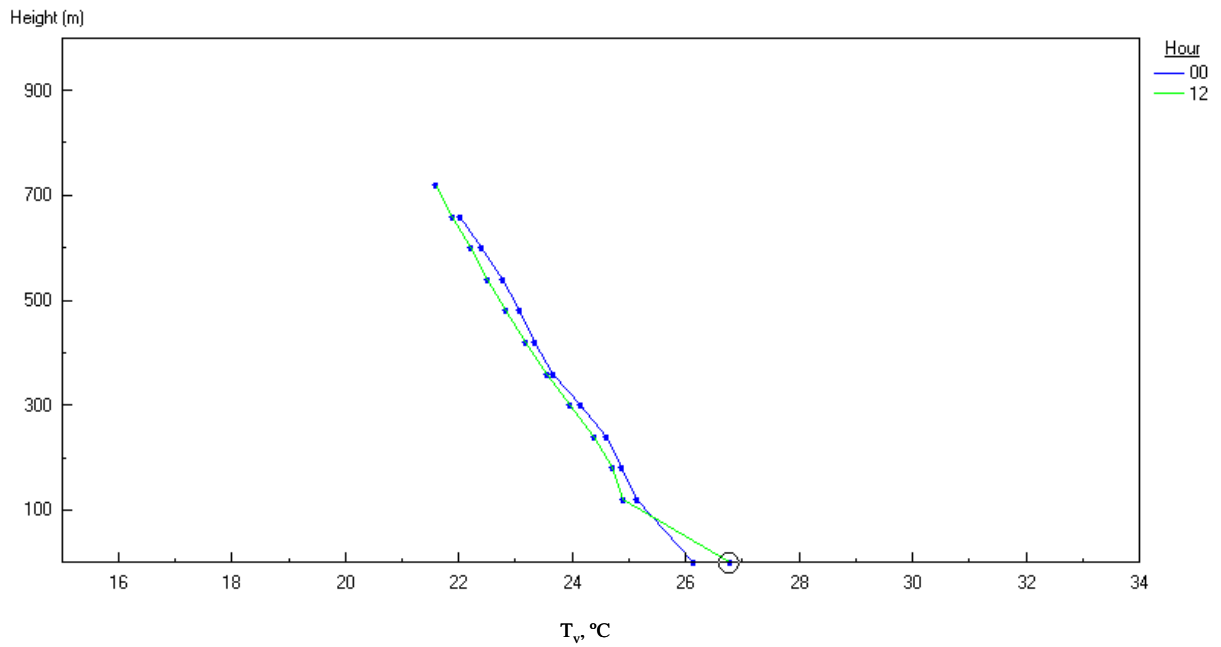


Figure 4-48. Spring average daytime and nighttime  $T_v$  profiles at VRM, March 22 to June 22. Hour 12 is the daytime profile and the Hour 00 is the nighttime profile.

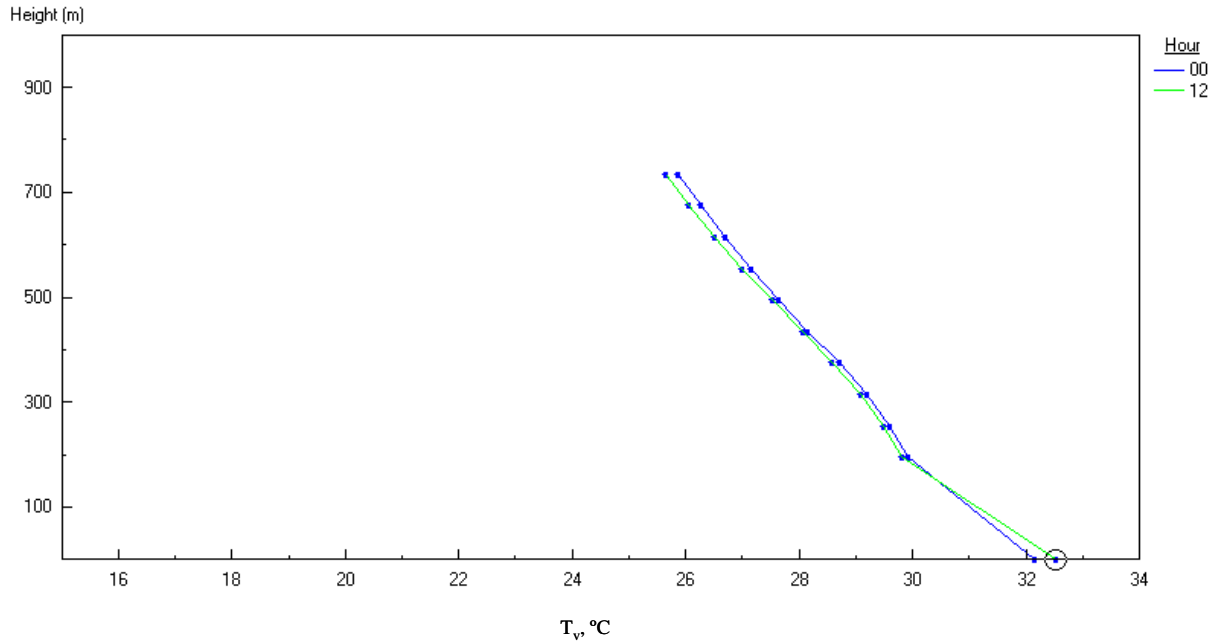


Figure 4-49. Summer average daytime and nighttime  $T_v$  profiles at SMI, June 23 to September 23. Hour 12 is the daytime profile and the Hour 00 is the nighttime profile.

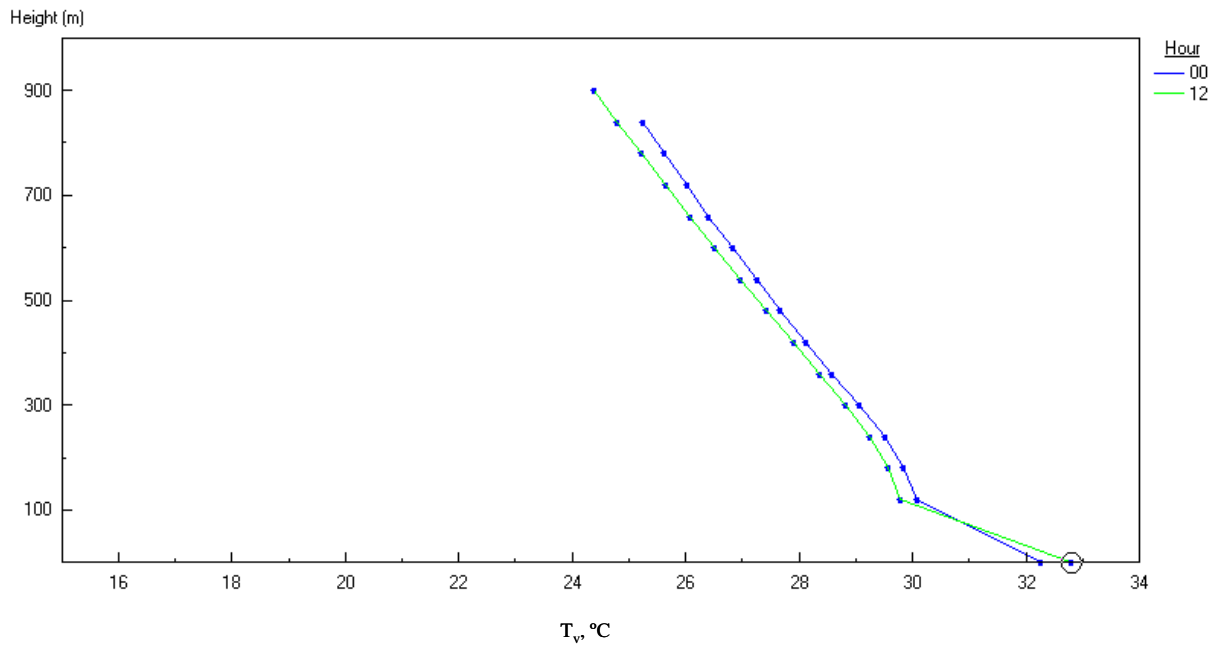


Figure 4-50. Summer average daytime and nighttime  $T_v$  profiles at VRM, June 23 to September 23. Hour 12 is the daytime profile and the Hour 00 is the nighttime profile.

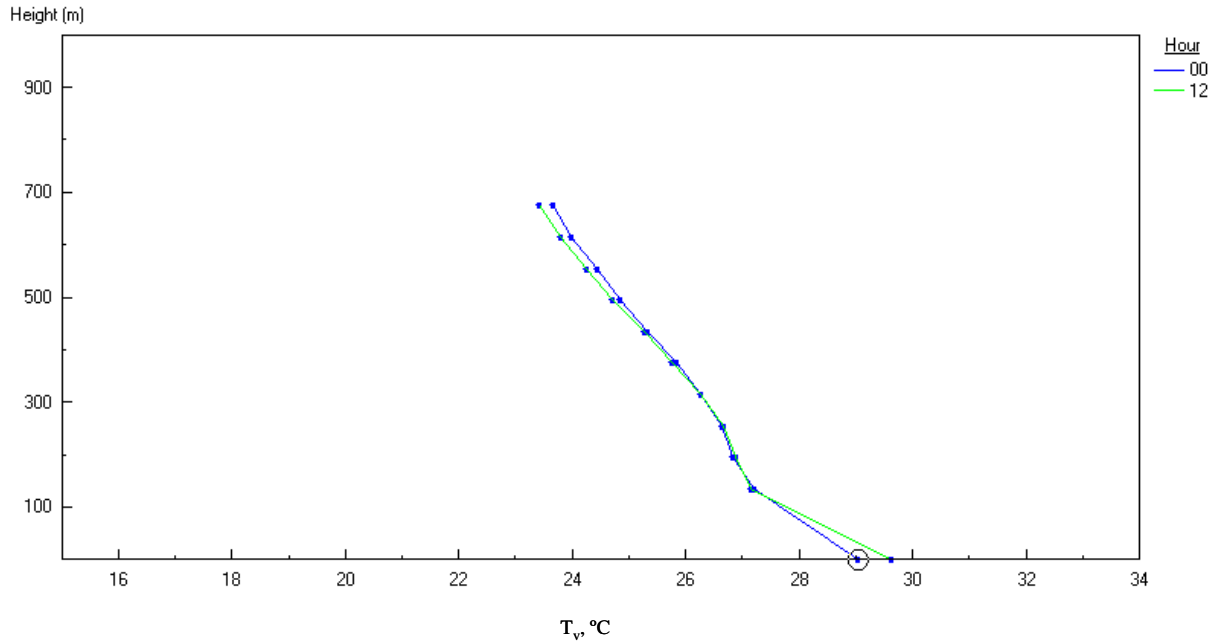


Figure 4-51. Ridge average daytime and nighttime  $T_v$  profiles at SMI. Hour 12 is the daytime profile and the Hour 00 is the nighttime profile.

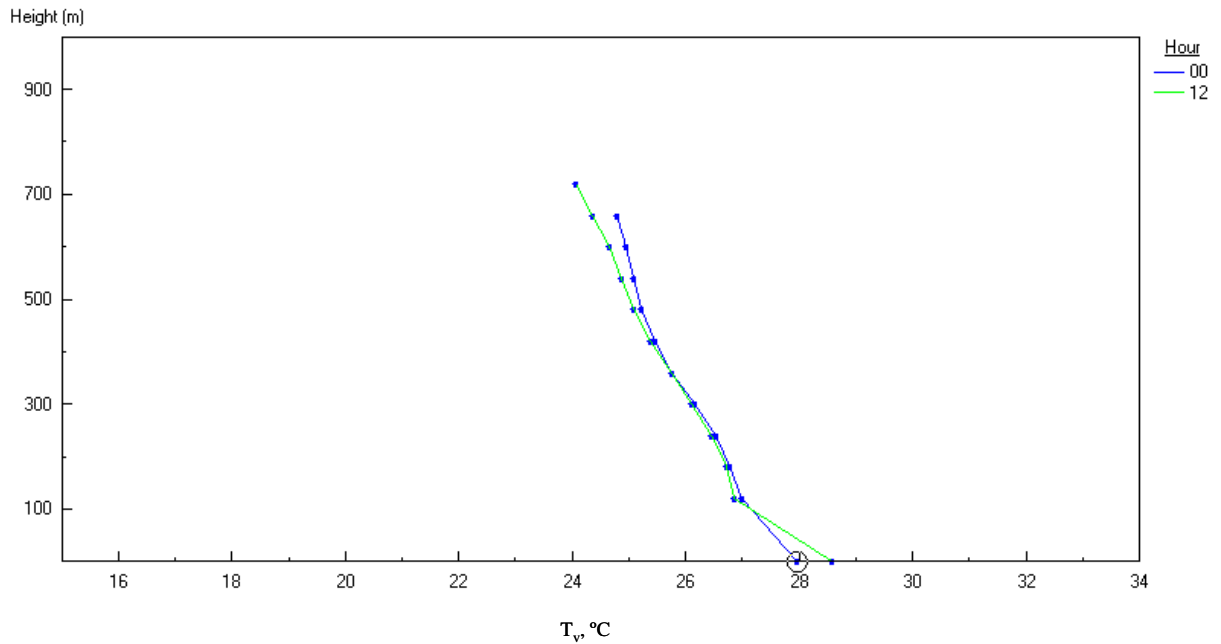


Figure 4-52. Ridge average daytime and nighttime  $T_v$  profiles at VRM. Hour 12 is the daytime profile and the Hour 00 is the nighttime profile.

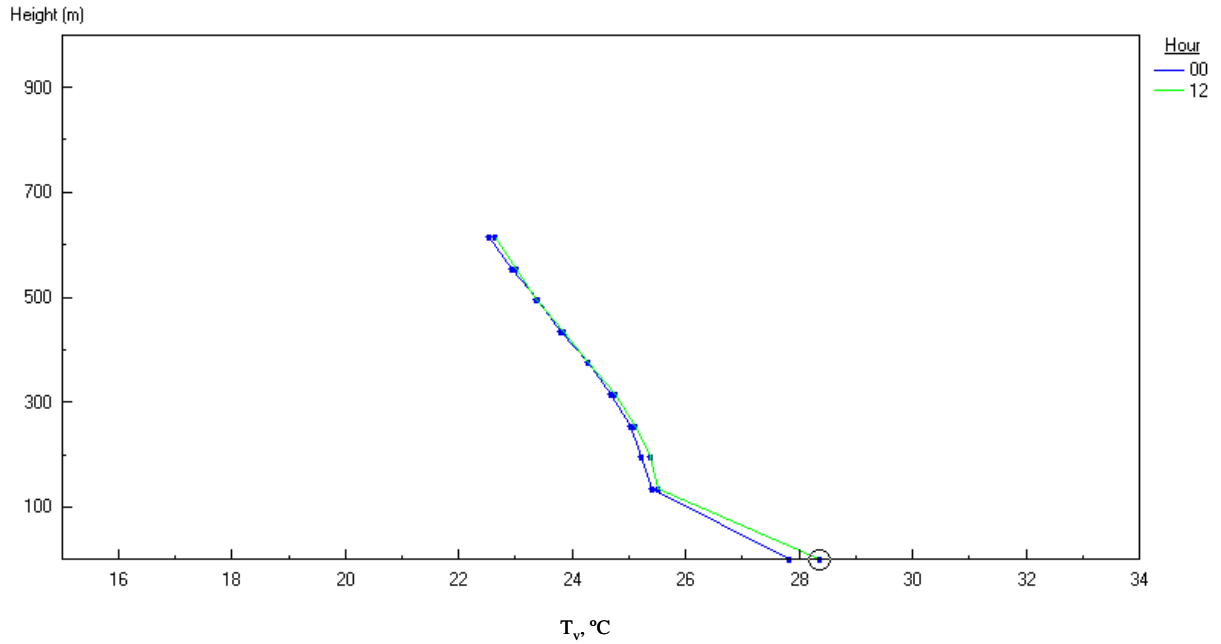


Figure 4-53. Weak ridge average daytime and nighttime  $T_v$  profiles at SMI. Hour 12 is the daytime profile and the Hour 00 is the nighttime profile.

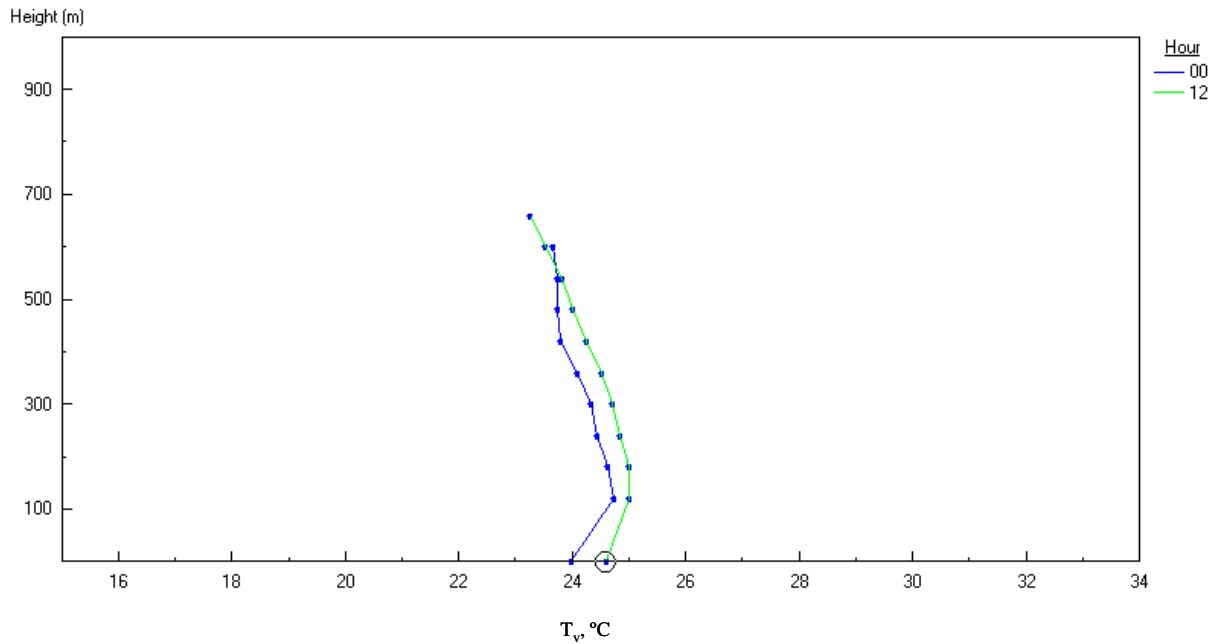


Figure 4-54. Weak ridge average daytime and nighttime  $T_v$  profiles at VRM. Hour 12 is the daytime profile and the Hour 00 is the nighttime profile.

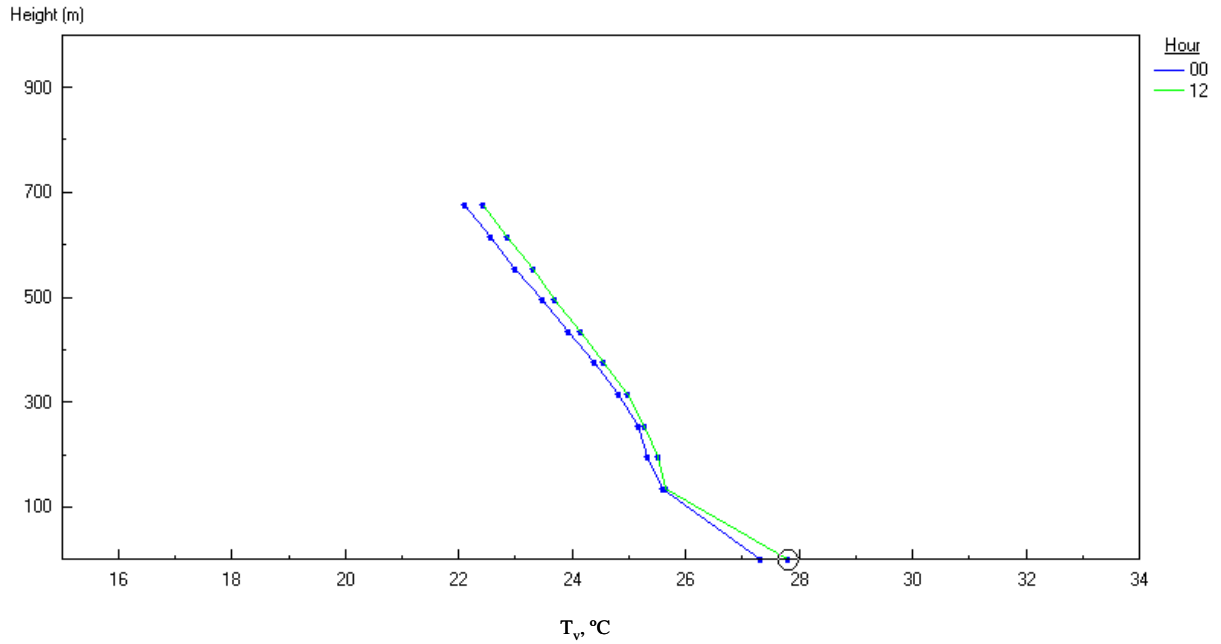


Figure 4-55. Weak trough average daytime and nighttime  $T_v$  profiles at SMI. Hour 12 is the daytime profile and the Hour 00 is the nighttime profile.

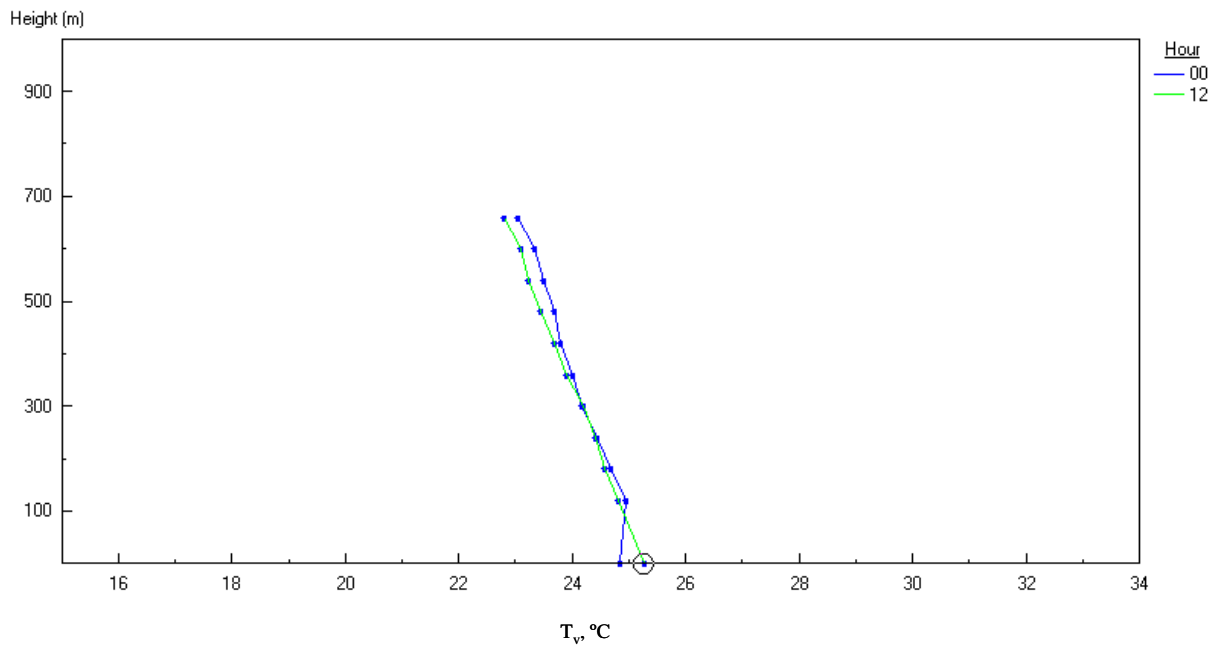


Figure 4-56. Weak trough average daytime and nighttime  $T_v$  profiles at VRM. Hour 12 is the daytime profile and the Hour 00 is the nighttime profile.

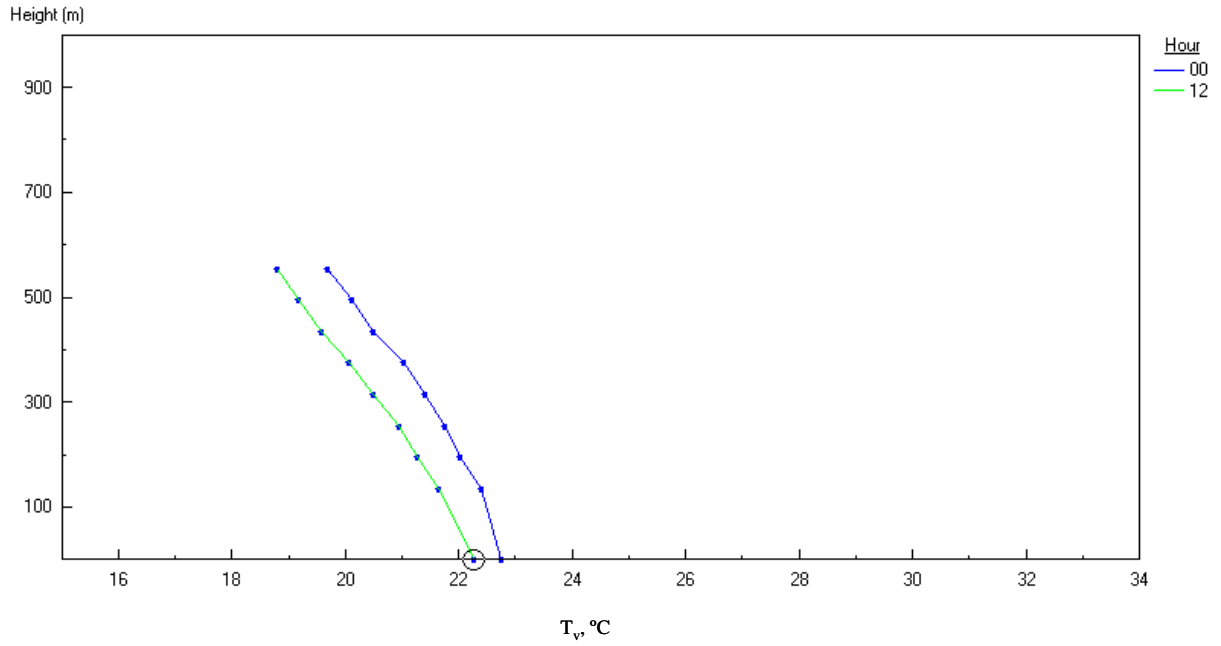


Figure 4-57. Trough average daytime and nighttime  $T_v$  profiles at SMI. Hour 12 is the daytime profile and the Hour 00 is the nighttime profile.

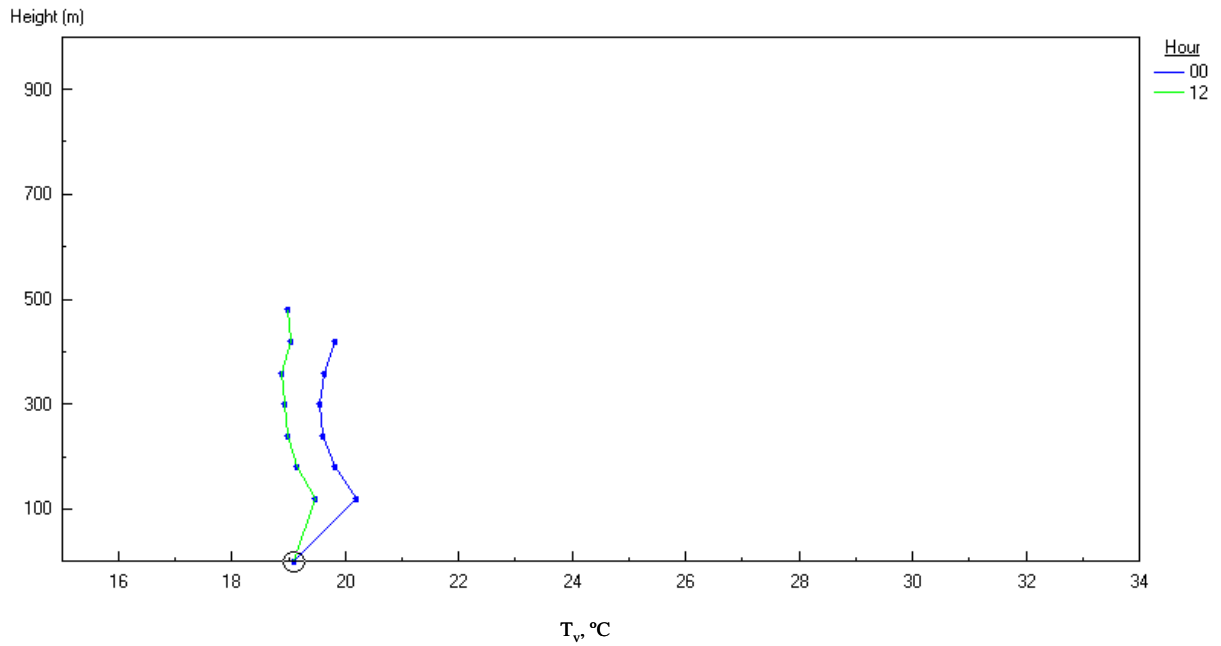


Figure 4-58. Trough average daytime and nighttime  $T_v$  profiles at VRM. Hour 12 is the daytime profile and the Hour 00 is the nighttime profile.

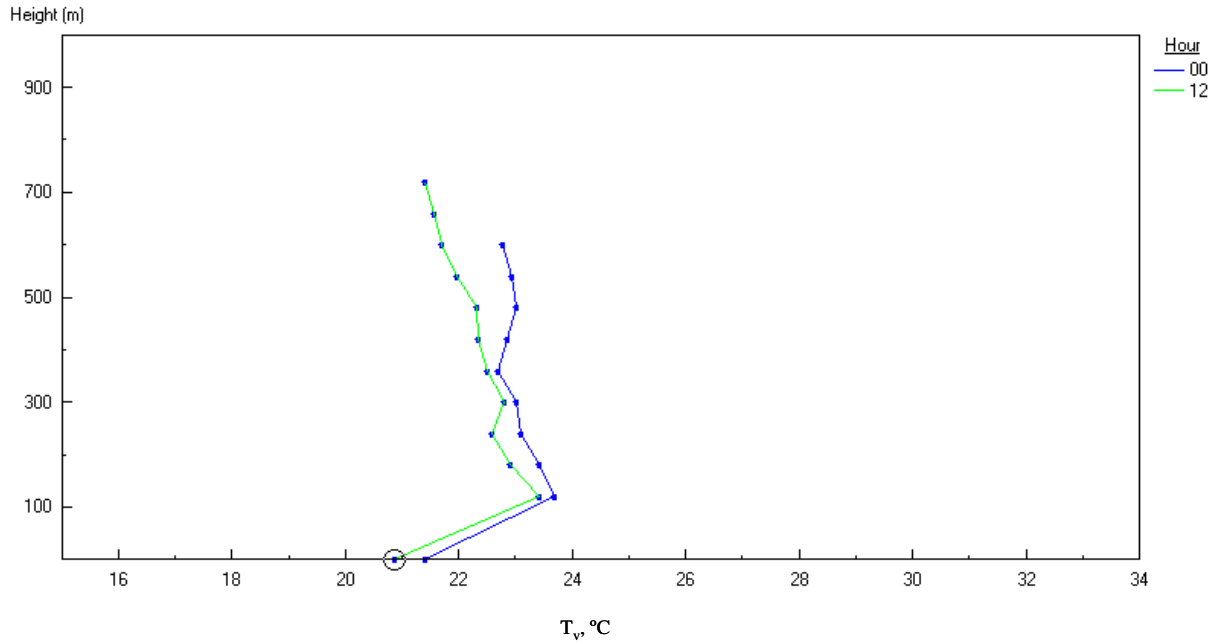


Figure 4-59. Cut-off low average daytime and nighttime  $T_v$  profiles at VRM. Hour 12 is the daytime profile and the Hour 00 is the nighttime profile.

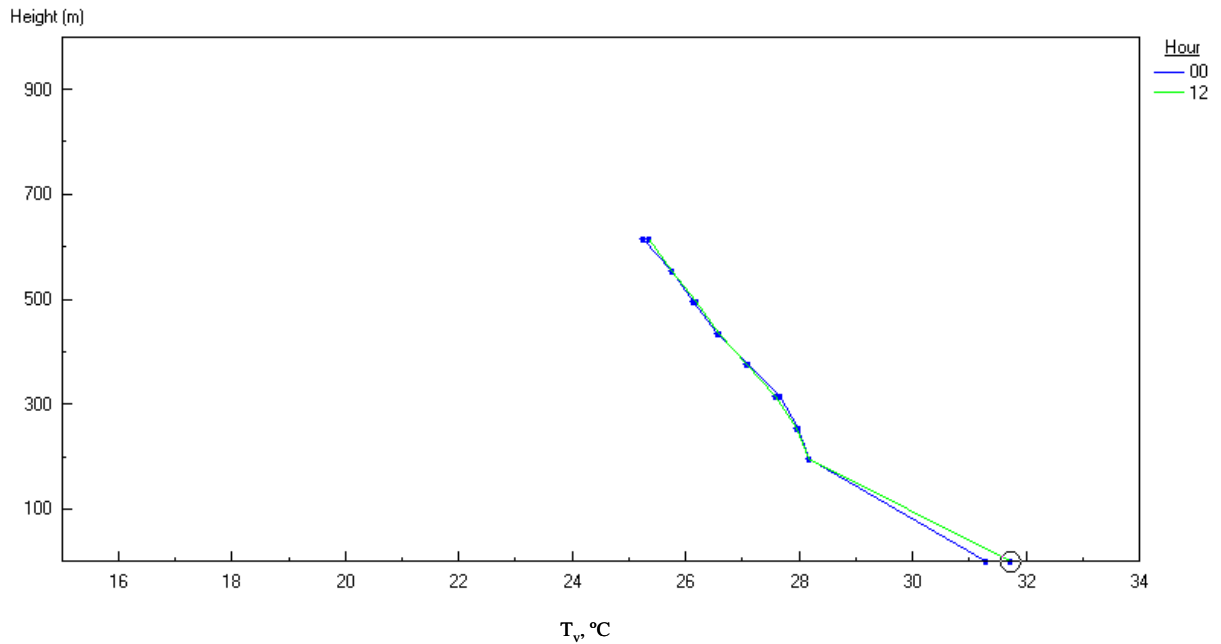


Figure 4-60. Flat average daytime and nighttime  $T_v$  profiles at SMI. Hour 12 is the daytime profile and the Hour 00 is the nighttime profile.

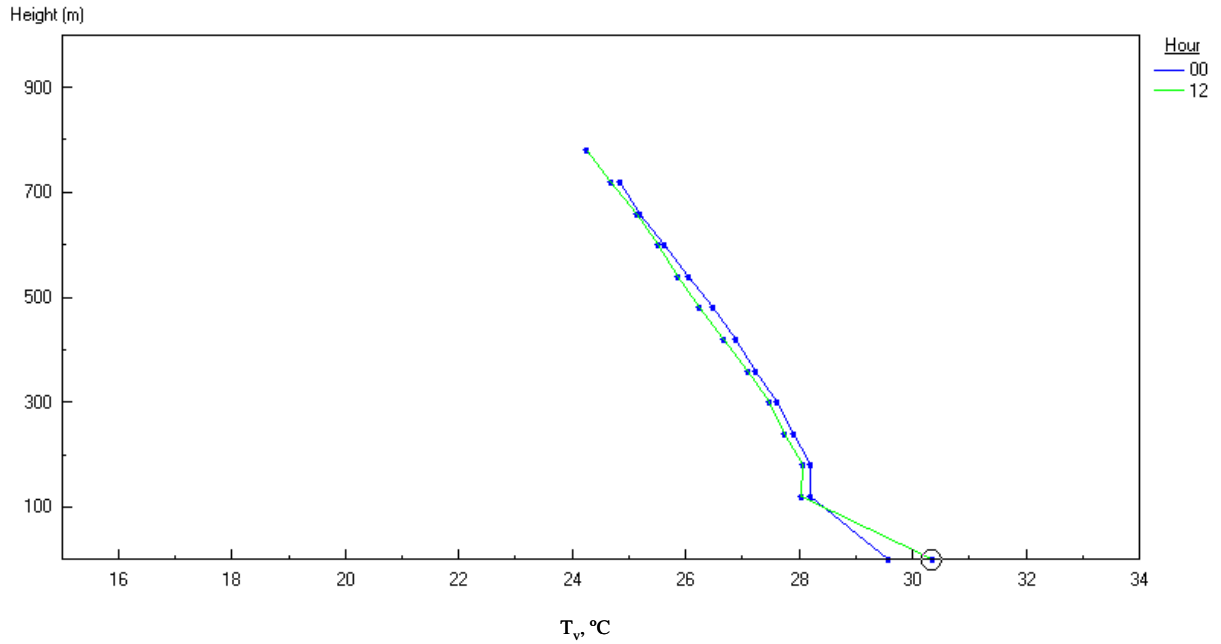


Figure 4-61. Flat average daytime and nighttime  $T_v$  profiles at VRM. Hour 12 is the daytime profile and the Hour 00 is the nighttime profile.

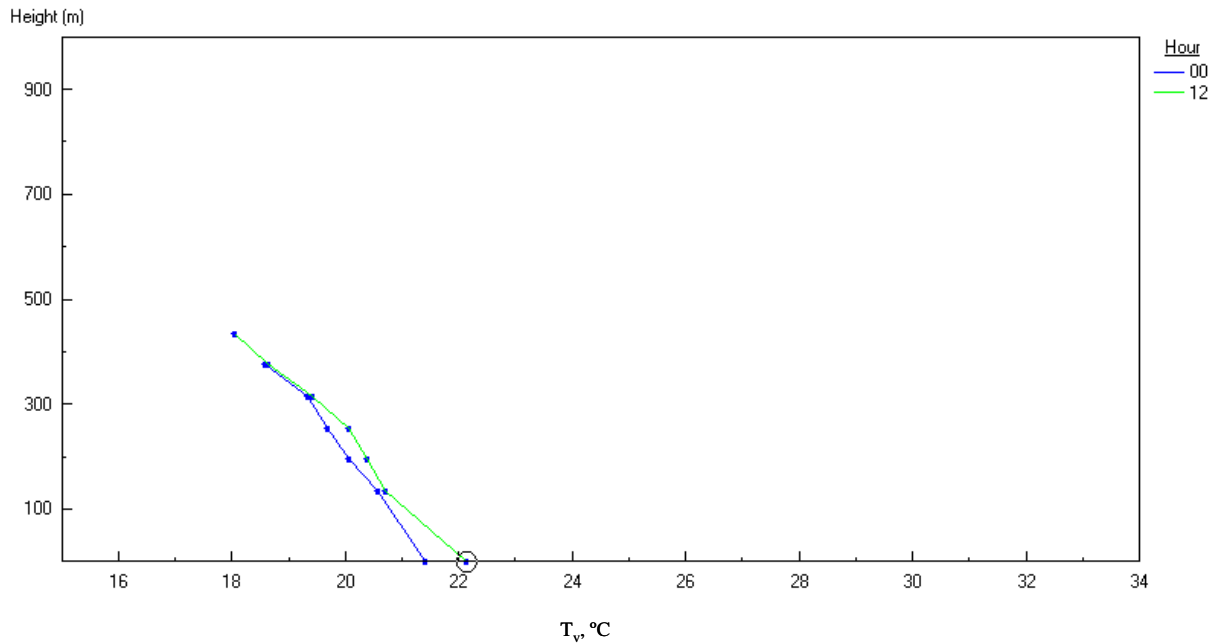


Figure 4-62. Zonal average daytime and nighttime  $T_v$  profiles at SMI. Hour 12 is the daytime profile and the Hour 00 is the nighttime profile.

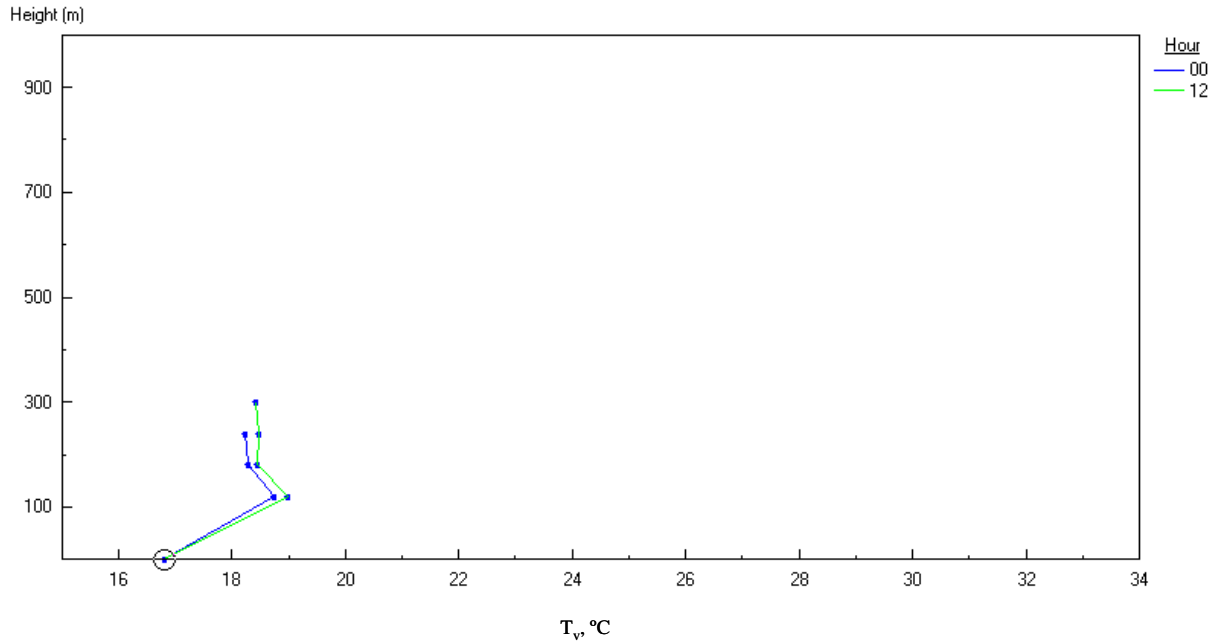


Figure 4-63. Zonal average daytime and nighttime  $T_v$  profiles at VRM. Hour 12 is the daytime profile and the Hour 00 is the nighttime profile.

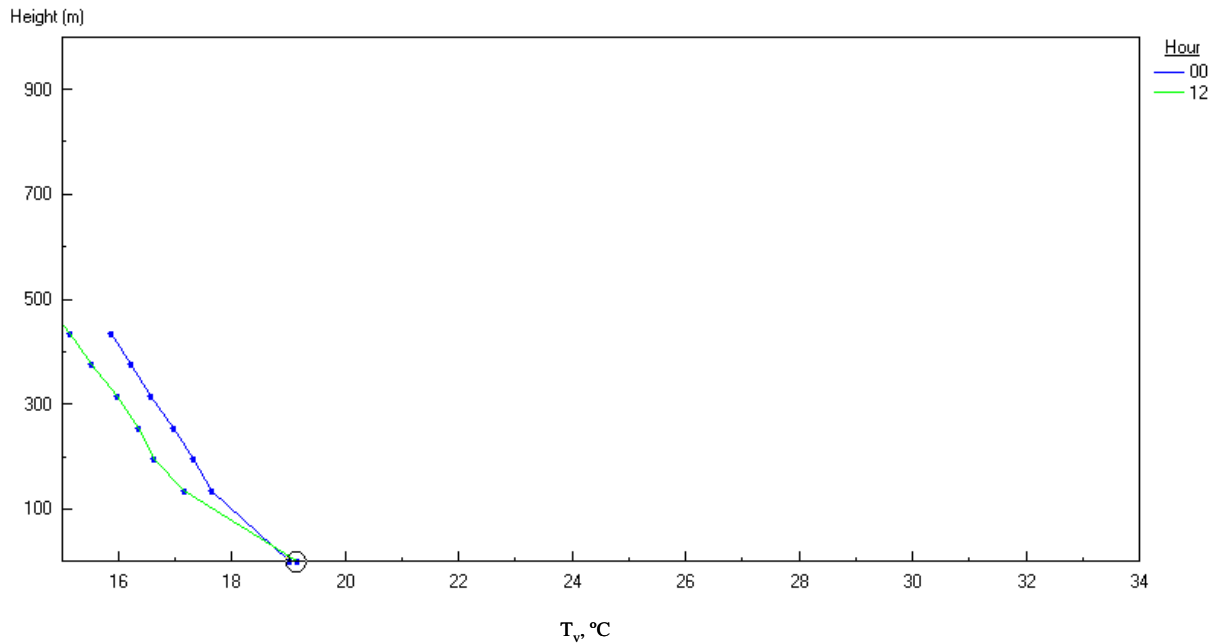


Figure 4-64. Post-trough average daytime and nighttime  $T_v$  profiles at SMI. Hour 12 is the daytime profile and the Hour 00 is the nighttime profile.

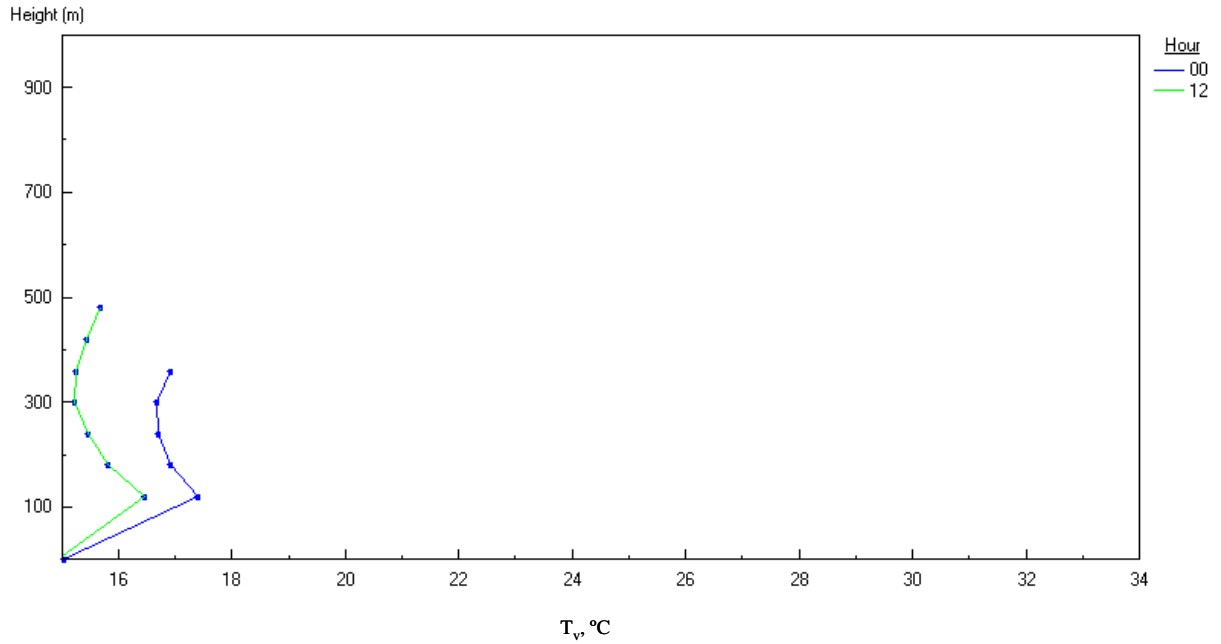


Figure 4-65. Post-trough average daytime and nighttime  $T_v$  profiles at VRM. Hour 12 is the daytime profile and the Hour 00 is the nighttime profile.

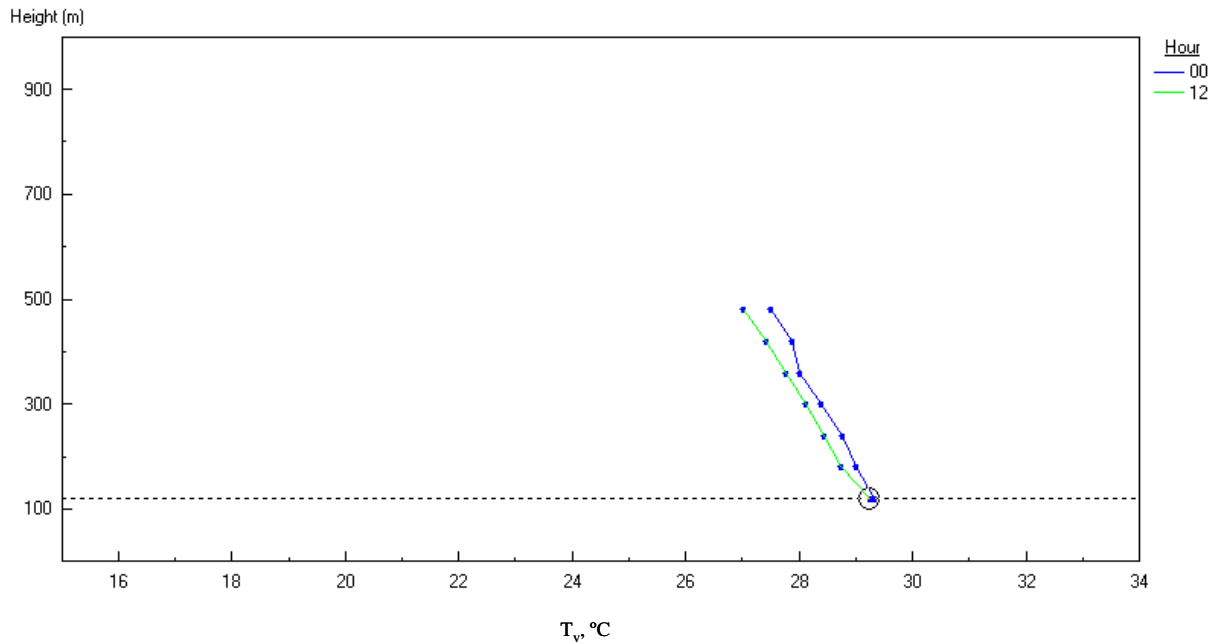


Figure 4-66. Tropical storm average daytime and nighttime  $T_v$  profiles at VRM. Hour 12 is the daytime profile and the Hour 00 is the nighttime profile.

## **5. CHARACTERIZATION OF THE SURFACE FLUXES AND OTHER PARAMETERS IN THE ATMOSPHERIC BOUNDARY LAYER USING THE COARE ALGORITHM**

This section describes atmospheric boundary layer analyses performed for the western and central Gulf of Mexico. The results presented here are largely based on output from the COARE algorithm. COARE has been demonstrated to accurately parameterize surface fluxes of momentum, heat, and moisture, and various boundary layer scaling parameters over the ocean using routine observations (Fairall et al., 1996a). COARE was originally derived from the Tropical Ocean-Global Atmosphere Coupled-Ocean Atmosphere Response Experiment (TOGA-COARE) research project. The TOGA program was intended to study the role of the tropical oceans in climate and annual climate variability (Webster and Lucas, 1992). The TOGA-COARE experiment made use of an extensive array of meteorological instruments and platforms. Most of the fast-response turbulence data were taken from a research vessel, the R/V Moana Wave, over several weeks. The data were then analyzed and the COARE program was developed by an international team of boundary layer researchers.

The basic structure of COARE is an outgrowth of the Liu-Katsaros-Businger (Liu et al., 1979) method, sometimes referred to as the LKB method. The COARE program was designed to improve estimates of surface fluxes and scaling parameters in the surface boundary layer of the atmosphere over the deep ocean in tropical regions (Fairall et al., 1996a). This program estimates fundamental boundary layer scaling parameters such as the surface roughness length, the friction velocity, the scaling temperature, the scaling water vapor mixing ratio, and the Monin-Obukhov length ( $L$ ). Standard boundary layer formulas can be used to estimate the mixing depth and the vertical profiles of wind speed,  $T_v$ , and water vapor mixing ratio (Stull, 1988; Garratt, 1992).

### **5.1 SUMMARY OF COARE PROGRAM VERSIONS AND MODIFICATIONS**

The COARE program was originally released in 1993, and three new versions have been used in the MMS Boundary Layer Study since it began in May 1998. Version 2.5b, released in May 1997, included updated transfer coefficients and was used for this study until January 2000, when version 2.6b was released. There were six minor differences between versions 2.5b and 2.6b, including a change in the Charnock “constant” to a parameter based on wind speed data from Hare et al. (1999) and Yelland and Taylor (1996). Version 2.6b was used for this study until June 2000. An improved version of COARE (version 2.6bw) was released in June 2000 and all COARE outputs presented in this report are from this latest version. An important difference between version 2.6bw and the prior versions is that version 2.6bw incorporates surface gravity wave information, based on wave height and period data. This change should increase the accuracy of the estimates of surface fluxes and scaling parameters over shallow areas, since the characteristics of waves differ from the deep ocean to the shallow coastal waters. Our comparisons between the outputs from the two versions show few differences, except in the derived roughness lengths,  $z_o$ , for low-wind conditions. A consequence of the differences in roughness lengths is a difference in the derived friction velocities,  $u^*$ . The two are directly related through the log wind profile relationship:  $u = (u^*/0.4)\ln(z/z_o)$ .

In addition to the changes made to the COARE program by its authors, STI made some minor changes to the program, with guidance and approval from one of its authors, Dr. Christopher Fairall. For example, we found that there was an occasional problem with the evaporative cooling calculation due to unrealistically high amounts of solar energy estimated to reach the ocean surface. The representation in COARE follows from laboratory measurements with artificial light sources and ignores the fact that the solar flux reaching the surface of the ocean has been partially absorbed by the atmosphere. In the equation for the net absorption by the ocean (Equation 5-1), the leading coefficient was changed from 0.137 to 0.060, based on tests performed by Dr. Christopher Fairall. This change provided a more realistic representation of the actual absorption, which caused the evaporative cooling calculations to better agree with observations. The original formula, still using the 0.137 coefficient, is given below:

$$\text{Net} = \text{SW} * (0.137 + 11 * \text{CST} - 6.6e-5 / \text{CST} * (1 - \exp(-\text{CST}/8.0e-4))) \quad (5-1)$$

where:

Net = Net absorption by the ocean (Watts/m<sup>2</sup>)

SW = Incoming short wave radiation (Watts/m<sup>2</sup>)

CST = Cool skin thickness (m)

We discovered another problem in the COARE program: during early daylight hours, under light-wind conditions with the air temperature warmer than skin temperatures (i.e., a stable lapse rate), COARE calculated unrealistic skin temperature increases (up to 500°C). This was caused by a lack of heat removal due to very small accumulated stress (surface momentum flux) and a very thin (almost zero) warm layer thickness. To correct this problem, a minimum stress of .002 N/m<sup>2</sup> was imposed for this calculation. This value was chosen after analysis of measured stresses during TOGA-COARE (personal communication with Dr. Christopher Fairall, July 2002).

In addition to the changes to the basic calculations described above, the COARE program was modified so that it could incorporate Eta model analyzed fields and/or predictions. The capability to flag the COARE output based upon the validity of the incoming data was also incorporated. (See Section 2 for a discussion of the QC flags.)

## 5.2 BACKGROUND ON THE COARE MODEL

To characterize the ABL characteristics in the Gulf of Mexico, we use the COARE model to estimate the surface fluxes of momentum (also called the surface stress,  $\tau$ ), sensible heat ( $H_s$ ), and latent heat ( $H_l$ ) from observations of wind speed ( $u$ ), air temperature ( $T$ ), and water vapor mixing ratio ( $q_r$ ) at some standard reference height ( $z = z_r$ ) near the water surface, and the skin temperature ( $T_s$ ) at the water surface. The standard height ( $z_r$ ) could be, for example, the height of the instruments on a buoy, a fixed tower (mounted on the sea floor), an oil platform, or a ship. However,  $z_r$  must be within the surface boundary layer, which usually has a depth of about 50 m. The wind speed at the water surface is assumed to equal the water current speed ( $u_s$ ) in the direction of the wind. The potential temperature ( $\theta$ ) at the height,  $z_r$ , is assumed to equal  $T(z_r) + (0.0098^\circ\text{C}/\text{m})z_r$ . The skin temperature is defined as the temperature of the water that is in contact with the air. The water vapor mixing ratio ( $q$ ) is calculated from measurements of

temperature and relative humidity (RH) through the relation  $q = RH q_{\text{sat}}(T)$ . The water vapor mixing ratio at the surface ( $q_{\text{sat}}$ ) is an interfacial value that is computed from the saturation mixing ratio for pure water at the skin temperature:

$$q_s = 0.98 q_{\text{sat}}(T_s) \quad (5-2)$$

where the dimensionless constant, 0.98, accounts for the reduction in water vapor pressure caused by a typical salinity of 34 parts per thousand.

With the above definitions, which are explained in more detail in boundary layer texts such as Garratt (1992) or Stull (1988), the standard bulk expressions for the surface fluxes (positive when directed upwards) are

$$\tau = -\rho_a C_d (u_s - u_r)^2 = \rho_a u^{*2} \quad (5-3)$$

$$H_s = \rho_a c_{pa} C_h u_r (T_s - \theta_r) = \rho_a c_{pa} u^* T^* \quad (5-4)$$

$$H_l = \rho_a L_e C_e u_r (q_s - q_r) = \rho_a L_e u^* q^* \quad (5-5)$$

where:

$\rho_a$  = air density

$c_{pa}$  = specific heat of air at constant pressure

$L_e$  = latent heat of water vapor

In Equations 5-3 through 5-8,  $C_d$ ,  $C_h$ , and  $C_e$  are known as the bulk transfer coefficients for stress or momentum, sensible heat, and latent heat, respectively. They are dimensionless quantities that have magnitudes of about 0.0011 when the reference height,  $z_r$ , equals about 10 m. These bulk transfer coefficients can be partitioned into coefficients  $c_d$ ,  $c_T$ , and  $c_q$  for individual variables  $u$ ,  $\theta$ , and  $q$ , respectively:

$$C_d = c_d^{1/2} c_d^{1/2} \quad (5-6)$$

$$C_h = c_d^{1/2} c_T^{1/2} \quad (5-7)$$

$$C_e = c_d^{1/2} c_q^{1/2} \quad (5-8)$$

The coefficients  $c_d$ ,  $c_T$ , and  $c_q$  can be written (see equations 5-10 through 5-12) in terms of Monin-Obukhov similarity theory as functions of reference height,  $z_r$ , surface roughness length ( $z_o$  for momentum,  $z_{oT}$  for heat, and  $z_{oq}$  for water vapor), and Monin-Obukhov length,  $L$ , which is defined as

$$L = (u^{*2}/0.4)/((g/T)(T^* + 0.61 Tq^*)) \quad (5-9)$$

The parameter, 0.4, in this equation is the von Karman constant. Note that  $L$  is defined so as to include the effects of the latent heat flux, which contributes to the flux of total buoyancy. The effects of water vapor (i.e., the second term in Equation 5-9) are usually ignored in calculations of  $L$  over land, but should be accounted for over warm ocean waters. Because water vapor is

lighter than dry air (molecular weight of 18 for water vapor and 29 for dry air), it is possible to have an upward flux of buoyancy (and hence an unstable boundary layer) when there is an upward latent heat flux even though the flux of sensible heat (as determined by the dry bulb temperature) is downward. Such a situation might occur when a hot dry air mass occurs over a cool water surface.

For nearly neutral conditions ( $n$ ), when  $z_r/L$  approaches 0.0, the coefficients  $c_d$ ,  $c_T$ , and  $c_q$  in Equations 5-6 through 5-8 are given by the neutral profile equations:

$$u^*/(u_r - u_s) = c_{dn}^{1/2} = 0.4/\ln(z_r/z_o) \quad (5-10)$$

$$T^*/(\theta_r - u_s) = c_{Tn}^{1/2} = 0.4a/\ln(z_r/z_{oT}) \quad (5-11)$$

$$q^*/(q_r - q_s) = c_{qn}^{1/2} = 0.4a/\ln(z_r/z_{oq}) \quad (5-12)$$

where the constant “a” equals about 0.74, and the surface roughness lengths for heat and water vapor are not necessarily the same as the surface roughness length for momentum (Garratt, 1992). These relationships lead to the following formulas for the scaling parameters:

$$u^* = (C_d (u_r - u_s)^2)^{1/2} \quad (5-13)$$

$$T^* = c_T^{1/2} (T_s - \theta_r) \quad (5-14)$$

$$Q^* = c_q^{1/2} (q_s - q_r) \quad (5-15)$$

For non-neutral conditions, when  $z/L$  is not zero, an additional term involving  $z/L$  has to be added to the  $\ln(z/z_o)$  term in Equations 5-10 through 5-12. In practice, an iterative procedure is followed where  $u^*$ ,  $T^*$ , and  $q^*$  are first estimated using the neutral Equations 5-10 through 5-12, then  $L$  (proportional to  $u^*$  and inversely proportional to  $T^*$  and  $q^*$ ) is calculated and used to recalculate  $u^*$  etc. This procedure continues until the solution converges according to a preset criterion.

The TOGA-COARE experiments verified the result from previous studies that, with moderate to high wind speeds, the surface roughness length,  $z_o$ , over the sea is proportional to the momentum flux or stress, and is given by the Charnock relation:

$$z_o = \alpha u^{*2} / g \quad (5-16)$$

with a constant,  $\alpha$ , equal to 0.011. For light wind speeds, the term  $0.11 \nu/u^*$  should be added to the right side of Equation 5-16, where  $\nu = 0.15 \text{ cm}^2/\text{s}$  is the molecular viscosity of air. Of course, over the land,  $z_o$  is independent of wind speed. For the latest version of COARE, there are options to replace the Charnock relation by

$$z_o = 1200 \cdot \text{hw}(\text{hw}/l)^{4.5} + 0.11 \nu/u^* \quad (\text{Taylor and Yelland, 2001}) \quad (5-17)$$

or

$$z_o = 50/2\pi l (u^*/c)^{4.5} + 0.11 \nu/u^* \quad (\text{Oost et al., 2001}) \quad (5-18)$$

These equations use wave height ( $hw$ ), wave length ( $l$ ), phase speed ( $c$ ), friction velocity ( $u^*$ ), and kinematic viscosity of dry air ( $\nu$ ) to calculate  $z_o$ .

The TOGA-COARE program also accounts for special situations such as periods with light winds, periods with rainfall, and periods with significant cooling of the surface by evaporation or warming of the near-surface layer by solar energy.

During light wind conditions, the effective average wind speed in the boundary layer never truly drops to zero because of the presence of convective eddies and other turbulent phenomena with time scales ranging from about 10 to 1000 seconds. Even though the measured average wind speed may be near 0.0, that average is made up of several non-zero wind speeds blowing from one direction and then another. The TOGA-COARE program, like other meteorological boundary layer preprocessors (e.g., Hanna and Chang, 1992a) assumes that the effective reference wind speed,  $u_r$ , during unstable conditions is given by two components:

$$u_r^2 = u_r^2 (\text{observed}) + (\beta w^*)^2 \quad (5-19)$$

where  $w^*$  is the convective scaling velocity, given by:

$$w^{*3} = (g/T) ((H_s/\rho_a c_{pa}) + 0.61 T (H_l/\rho_a L_c)) h \quad (5-20)$$

and  $h$  is the mixing height. Usually  $w^*$  is about 1 m/s. The COARE data from TOGA suggest that the constant,  $\beta$ , equals 1.25.

A “Webb effect” correction is made by the COARE algorithm. This correction of about  $4 \text{ w/m}^2$  to the latent heat flux term assures mass continuity when the density differences between updrafts and downdrafts are considered.

If the skin temperature is not observed at the surface (e.g., from a radiometer observation) but is observed by a sensor at some depth (say, 0.5 m to 1.0 m below the surface), the COARE program calculates the skin temperature from the observed near-skin temperature at that depth. The near-skin temperature is defined as the temperature of the water measured by the buoys at a depth of approximately .5 m. The COARE program contains an algorithm to account for the “cool skin” effect caused by evaporation of water from the surface, and also contains an algorithm to account for the “warm layer” effect caused by warming of the surface layer due to solar energy. The degree of surface warming is a function of the amount of vertical mixing in the water boundary layer, which is, in turn, a function of the wind speed. During light winds, the solar energy input can cause the water surface to warm by several degrees.

Corrections are also made to the momentum flux term and the heat flux term to account for the effects of rain. For example, if the rain has a different temperature than the water surface, the rain will contribute heat to the surface if the rain is warmer and will remove heat from the surface if the rain is cooler. Also, the momentum carried by the rain as it strikes the surface will affect the surface momentum flux. The surface stress due to heavy rain can be twice the surface stress due to wind (Fairall et al., 1996a).

### 5.3 IMPLEMENTATION OF THE COARE PROGRAM

The COARE program is being distributed by Fairall and his coauthors. The written material from the (NOAA's FTP site is reproduced in Appendix B and our modified version of the FORTRAN code, cor2\_6bfwMMS.for, is in Appendix C.

The COARE program requires input of the atmospheric measurement heights (wind speed, air temperature, relative humidity) and the near-skin temperature sensor depth. The mixing depth,  $h$ , is required, and Fairall et al. set a default value of  $h = 600$  m for their TOGA-COARE study area. Hanna et al. (1985) note that the  $h = 600$  m assumption is fairly good for most over-water boundary layers. The surface pressure and the approximate latitude and longitude are required as inputs to the program. All predetermined constants (e.g., von Karman constant) are automatically set to default values unless the user overrides them.

Next, a line of data in the form of a time series is input to COARE. Each line should contain local time,  $u_r$ ,  $T_s$ ,  $T_r$ ,  $q_r$ ,  $R$  (precipitation in mm/hr),  $R_l$  (downwelling longwave radiation flux in  $W/m^2$ ), and  $R_s$  (downwelling solar flux in  $W/m^2$ ).

For each line of input data, representing an averaging time of, say, one hour, the code assigns a minimum wind speed of 0.5 m/s and neutral stability as a first guess and then calculates a first estimate of  $u^*$ ,  $T^*$ , and  $q^*$ . It computes all temperature-dependent constants such as  $L_e$  and  $v$ . Then the program iterates or loops through successive calculations of  $u^*$ ,  $T^*$ , and  $q^*$  until the solutions converge within stated limits.

The COARE program is sufficiently general that it can be applied to a wide variety of platforms used for meteorological observations at sea. It has been tested with high-quality research ship observations, with routine ocean buoy observations, and with data from non-standard sources such as oil platforms. However, the COARE program has not been thoroughly tested with data from shallow water, marsh, beach, or other coastal scenarios.

### 5.4 COMPARISON OF COARE MEASUREMENTS WITH TOGA-COARE MEASUREMENTS

Fairall et al. (1996a) describe the detailed observations taken during TOGA-COARE, the observations used to calibrate constants in the COARE algorithm, and the various modules of the program. Because of the requirement (for climate change studies) to resolve the surface energy balance with an accuracy of  $10 W/m^2$  or less, it was important to measure the many atmospheric variables with an unprecedented degree of accuracy. The goals for the instrument accuracies were 0.2 m/s for wind speed, 0.2 K for skin temperature and air temperature, and 0.2 g/kg for water vapor mixing ratio. These goals were met during TOGA-COARE. Several figures containing examples of observations and COARE model predictions of fluxes are given by Fairall et al. (1996), showing agreement usually within about plus or minus 10% for stress, and within roughly  $5 W/m^2$  for sensible heat flux and  $25 W/m^2$  for latent heat flux. The covariance observations of fluxes have considerably more uncertainty than the inertial-dissipation observations, due to the difficulties in observing the turbulent fluctuations from moving platforms such as ships. In general, the relative uncertainties are largest for periods with light

wind speeds. The results of sensitivity studies are also presented in the figures in Fairall et al. (1996a), illustrating how the choice of “constants” such as  $\beta$  can have a large effect on the flux calculations, especially at low wind speeds.

Fairall et al. (1996a) also included comparisons of flux predictions by the COARE program with fluxes observed by the NCAR Electra Aircraft during flights at heights of 30 to 60 m. This comparison represents a good test of the method with independent data. A comparison of the predictions and observations of latent heat flux, sensible heat flux, and stress show that there is typically a range of about a factor of two, although the overall means are predicted within plus or minus 5%.

## **5.5 APPLICATION OF THE COARE PROGRAM TO DATA COLLECTED IN THE GULF OF MEXICO**

As stated in Section 5.3, the COARE program requires the following input data: time and site location; wind speed, air temperature, and relative humidity within the surface layer at reference height  $z_r$ ; skin temperature or near-skin temperature plus radiation estimates; and mixing height. If the near-skin temperature (i.e., observed at a depth of 0.5 to 1.0 m) is used (such as the data collected at buoys and C-MAN stations), then solar and downwelling longwave radiation fluxes need to be estimated from some alternate source in order to correct this observed temperature to a skin temperature. Precipitation data is not required but, if available, can be used by COARE to estimate the precipitation contribution to the energy balance equation. Wave height and period data are not required, but, if available, can be used with COARE version 2.6bw to account for the different wave structures and theoretically improve the accuracy of the estimates of surface fluxes and scaling parameters over shallow ocean areas, such as the Gulf of Mexico. For this application, the Taylor and Yelland (2001) method for calculating  $z_o$  was used (see Equation 5-17). If wave data were not measured, they were calculated from wind speed ( $u$ ) where wave height =  $0.018 * u^2 * (1 + 0.15 * u)$  and wave period =  $0.729 * u$ .

- Data collected at offshore buoys and at the VRM, SMI, BIP, DWP, MBP, SWP, and WDP platforms meet the COARE input data requirements.
- C-MAN stations collected all the required data except shortwave and longwave radiation. These sites are not located in deep water and sometimes are located in marshes or on beaches. The COARE program was “tuned” using deep-water data and may not adequately handle the sea-state at shallow-water sites such as C-MAN stations. However, based on discussions with Scientific Review Board members and Dr. Christopher Fairall, it was concluded that the error produced by inaccurate representation of the sea-state may be acceptable for the current study, where the emphasis is on flow patterns and dispersion of pollutant plume released over the Gulf of Mexico, and the accuracy requirements for surface fluxes are not as stringent as those for climate change studies. Therefore, data from C-MAN stations were included in the analysis, but we treat these COARE results with caution.
- The offshore buoy sites did not measure skin temperature or solar and downwelling longwave radiation; thus, radiation fluxes were estimated using 6-hourly Eta model cloud simulations and sun elevation data to estimate the required radiation fluxes needed to

calculate the skin temperatures from temperatures at depths of about 0.5 to 1.0 m. The 6-hourly radiation flux estimates from the Eta outputs were interpolated to hourly data for each buoy location.

The following data were acquired and processed for input to COARE for the period from May 1998 through October 2001:

- Offshore buoy data from seven sites,
- Shoreline C-MAN station data from three sites,
- Data collected as part of this project on the VRM, SMI, BIP, DWP, MBP, SWP, and WDP oil platforms, and
- Eta model predictions.

Figure 2-1 is a map of the Gulf of Mexico region, showing the locations of the meteorological sites discussed above and in the following analyses. The analyses are intended to identify similarities and differences among the boundary layer parameters at the sites. It is anticipated that the boundary layer parameters at the farther offshore sites such as DWP and SMI are more characteristic of the open ocean, with fewer variations by season and by time of day, whereas the parameters at the sites closer to shore, such as VRM and BIP, show some influence of the nearby land surfaces.

The latest version of COARE (cor2\_6bfwMMS.for) was used to calculate hourly sensible heat flux, latent heat flux, friction velocity, temperature and relative humidity scaling parameters ( $z_r/L$ ), and roughness length using the three-plus years of hourly meteorological data from 14 sites and one year of hourly data from the BIP, DWP, MBP, SWP, and WDP platform sites. Underwater temperature was corrected to skin temperature when no skin temperature was measured. An additional COARE sensitivity run for the buoy data was performed where underwater temperatures were used without correction to skin temperature. This was done to test the influence of this correction on the boundary layer parameters.

Both statistical and case study analyses of the COARE input and output data were performed. For the statistical analyses the following averages were computed:

- Monthly averages were calculated for the ABL observations and derived parameters at each site. Averages were not computed if more than 25% of the data in a given month were missing.
- Hourly averages were calculated by month for the ABL observations and derived parameters at each site to investigate the diurnal cycles. The averages were not computed if more than 25% of the data in a given month and hour were missing.
- Overall averages of the parameters were calculated for nine synoptic classes and for each site to investigate the relationship between the large-scale weather patterns that are characterized in Section 3 and the ABL parameters. No data availability criteria were applied.

- Averages were calculated for four surface flow direction classes (onshore, offshore, parallel east, and parallel west) and for each site to investigate the relationship between the flow direction and the ABL parameters. No data availability criteria were applied.

Four periods were selected for case study analysis. The periods selected capture a variety of meteorological conditions, especially conditions for which transport of materials from offshore areas is likely to impact onshore areas. The case study periods are

- July 30 through August 1, 1999,
- January 20 through 25, 2000,
- January 4 through 6, 2001, and
- September 18 through 20, 2001.

## 5.6 CLIMATOLOGICAL RESULTS

This section presents the results of the climatological analyses. Averages were reviewed by month, by synoptic class, by flow direction, and diurnally by month. The 14 stations that were analyzed are shown in Figure 2-1 and are denoted by the codes:

Buoys – 42001, 42002, 42007, 42019, 42020, 42035, and 42040

Oil Platforms – VRM, SMI, BIP, DWP, MBP, SWP, and WDP

C-MAN (coastal) – DPIA1, GDIL1, PTAT2, BURL1, and SRST2

Note that BURL1 and DPIA1 are missing data necessary for COARE but the available monthly average observations are described here.

The following discussions and figures are grouped separately: (a) the buoys, the VRM and SMI platforms, and the C-MAN stations and (b) the BIP, DWP, MBP, SWP and WDP platforms. The latter sites are part of the BAMP study which took place over a one-year period near the end of the three-year study of the other sites. The figures described in the discussions reflect the two groups and are designated (a) and (b).

### 5.6.1 COARE Results Grouped by Monthly Averages

Fluxes. The fluxes and scalar parameters calculated by the COARE algorithm in the Gulf of Mexico are physically consistent with expectations and are similar to observations and COARE calculations for TOGA, which took place in the warm western Pacific Ocean near the equator. Calculated monthly average sensible heat fluxes (**Figures 5-1a and 5-1b**) in the Gulf of Mexico ranged from about 5 to 30 W/m<sup>2</sup>, typical of other over-water areas. Similarly, calculated monthly average latent heat fluxes (**Figures 5-2a and 5-2b**) ranged from about 50 to 150 W/m<sup>2</sup>, also typical of other over-water areas. Both the latent and sensible heat fluxes were highest in the late fall and early winter and lowest in the late spring and summer, although the yearly cycle in latent heat values is less pronounced than the seasonal cycle. The largest fluxes shown in Figures 5-1(a) and 5-2(a) occur at near-shore and/or the buoy sites, whereas the fluxes at the VRM and SMI platforms shown in Figures 5-1(a) and 5-2(a) are more moderate and are similar to the fluxes from the five platforms shown in Figures 5-1(b) and 5-2(b).

These estimates of annual variations of latent and sensible heat fluxes are consistent with lighter winds (**Figures 5-3a and 5-3b**) and smaller skin-air temperature differences (**Figures 5-4a and 5-4b**) in the summer compared to other times of year. Calculated monthly average sensible heat fluxes were about one-fifth the calculated monthly average latent heat fluxes, and the differences between the two were generally greatest in the summer and smaller in the late fall and winter.

The monthly average calculated total heat flux (sensible plus latent) is in fair agreement (generally within a factor of two) among the sites in the Gulf of Mexico (**Figures 5-5a and 5-5b**). The largest relative variations (ranging from 20 to 170 W/m<sup>2</sup>) occurred in February when the total heat flux was small due to the cool water temperatures and the small difference between the skin and air temperatures. The smallest relative variations (ranging from 110 to 235 W/m<sup>2</sup>) occurred in September when the total heat flux was large due to the warm water temperatures and large difference between the skin and air temperature.

Eta Fluxes. The monthly average Eta model latent and sensible heat fluxes (**Figures 5-6 and 5-7**) were generally in good agreement with the calculated fluxes. However, the model fluxes did not show as great a variation between sites as the calculated fluxes. In addition, the model fluxes were about 20% greater than the calculated fluxes in the fall and early winter, but were very similar during the spring and summer.

Friction Velocity. The COARE-calculated monthly average friction velocity,  $u^*$ , shown in **Figures 5-8a and 5-8b**. Figure 5-8a (the buoys, the C-MAN sites, and the SMI platform) demonstrates agreement among the sites well within a factor of two and often within 20%. This agreement is important because the monthly average friction velocity is the key scaling velocity for estimating transport speeds and dispersion rates. However, Figure 5-8b (BIP, DWP, MBP, SWP, and WDP platforms) and Figure 5-8a (VRM only) show mean friction velocities that are about 30% to 40% less than those in Figure 5-8a (for all other sites). Possible explanations are that the wave height and frequency are estimated from wind speed at the platforms, whereas they are measured at the buoys. Also, the platform wind observations are corrected from 20+ m to 10 m and the wind speed is, on average, less than at the other non-platform sites. All data show that the calculated monthly average friction velocity was slightly lower from May through August and peaked in late fall and early winter. The monthly average Eta model friction velocity (Figure 5-9) showed the same yearly pattern as the calculated friction velocity. However, the Eta model friction velocity was about 10% to 20% higher than the calculated friction velocity in the fall and early winter. The difference in velocity likely explains why the Eta model fluxes were slightly high during the same period.

Temperature and Humidity Scaling Parameter. The calculated monthly average temperature scaling parameter and humidity scaling parameter generally showed a factor of two or better agreement among sites (**Figures 5-10a and 5-10b, and 5-11a and 5-11b**, respectively). The monthly average temperature scaling parameter tended to be smaller in April and May, when the difference between the skin and air temperatures was at its minimum, and tended to be larger in November through January, when the difference between the skin and air temperatures was at its maximum. Conversely, the monthly average humidity scaling parameter tends to be largest during the warmest period of the year (July through September) because moisture content of the atmosphere is a strong function of temperature.

Air Temperature. Monthly average air temperatures are plotted in **Figures 5-12a and 5-12b**. Very close agreement is evidenced among the sites from May through September when it is hot (over 25°C) and the air temperature differences are minimal between near-shore and far-offshore sites. At all sites, the temperatures were warmest in July and August (ranging from 24.5°C to 29°C) and coolest in winter (ranging from 11°C to 21°C). The difference in air temperature was much greater between near-shore and offshore sites in winter compared to summer (about 10°C in winter versus about 2°C in summer). This difference was probably due to wintertime cold fronts influencing near-shore sites more than offshore sites. For example, the average monthly air temperature at offshore buoys 42001 and 42002 was 21°C in January and 28°C in August (a 7°C range). On the other hand, the average monthly temperatures at the near-shore sites, VRM, BIP, SWP, and SRST, were 12.5°C in January and 28.5°C in August (a 16°C range).

Skin Temperature. Like the monthly average air temperatures, skin temperatures were warmest in July and August and coolest in January and showed a similar site grouping (**Figures 5-13a and 5-13b**). The far offshore near-skin temperatures at buoys 42001 and 42002 and at platform DWP showed the least amount of seasonal variation (about 6° to 8°C) compared to the near-shore sites (about 17.5°C maximum at VRM and BWP between September and January). The magnitudes of the sum of the latent and sensible heat fluxes generally follow the annual variation of the skin temperature, with maxima in the late fall and minima in the late spring.

Skin and Air Temperature Differences. The differences between the skin and air temperatures were, on average, about +1° to +3°C at most sites all year (Figures 5-4a and 5-4b). The differences were less in late spring and more in late fall and early winter. This persistent positive temperature difference has been noted by Dr. Christopher Fairall at most other sites located on warm water oceans.

Surface Wind Speed. Scalar monthly average wind speed showed good agreement among sites (Figures 5-3a and 5-3b). The lowest speeds occurred in July and August and the highest in December and January. For some years, there was a transition from lower wind speeds in August to higher winds speeds in September and October. Weather maps indicate that the high wind speeds in September and October on some years were probably a result of tropical storms.

Relative Humidity. Average relative humidity was similar among sites and was about 75% in all months.

## **5.6.2 COARE Results Grouped by Synoptic Class and General Flow Direction**

This section uses histograms to present information about the magnitudes of nine COARE parameters for 14 monitoring sites for nine classes of synoptic conditions and for the four general air flow directions (onshore, offshore, parallel east, and parallel west).

The nine COARE parameters are downwelling longwave radiation, shortwave radiation, humidity scaling parameter, temperature scaling parameter, roughness, sensible heat flux, latent heat flux, friction velocity, and wind speed.

The nine synoptic classes are discussed in Section 3 and are denoted by the terms ridge, weak ridge, flat, zonal, post-trough, trough, weak trough, cut-off low, and tropical storm. The occurrences of the nine synoptic classes are listed in the table below. The counts in some classes (**Table 5-1**), such as tropical storm and cut-off low, are quite low and, therefore, the numbers for the average COARE parameters in **Figures 5-14, 5-15, 5-16 through 5-21(a and b), 5-22 through 5-24, 5-25 through 5-30(a and b) and 5-31** have a broader confidence bound than the numbers for the more heavily populated classes such as ridge and trough.

Table 5-1. Number of occurrences of each synoptic classification by year for the MMS Boundary Layer Study.

MMS Year	Cut-off Low	Flat	Post-trough	Ridge	Trough	Tropical Storm	Weak Ridge	Weak Trough	Zonal	Total
1998	2	31	11	104	94	3	35	76	9	365
1999	6	30	18	107	85	0	36	61	23	366
2000	11	10	17	142	82	0	20	53	30	365
2001	6	24	7	36	10	3	16	20	2	124

The discussions in this section focus on the typical magnitudes and on the reasons for differences that are observed.

### Synoptic Class

Figures 5-14, 5-15, 5-16 through 5-21(a and b), and 5-22 contain histograms showing the results of the average COARE calculations, divided into nine synoptic classes, for nine COARE parameters and outputs. The wind speed data are observed rather than parameterized by COARE. The highlights of the results are discussed by COARE parameter.

Downwelling Longwave Radiation – Longwave radiation is emitted in all directions by gases and aerosols in the atmosphere; however, the component being analyzed is longwave radiation directed down towards the water’s surface. Its magnitude is a function of temperature and humidity and of the amount of cloud and fog. Longwave radiation was not observed by on-site radiometers so it was parameterized based on cloudiness and temperature. Note that this parameter is a COARE input rather than an output, and, when observations are not available, it is based on estimates made by the Eta prognostic meteorological model. Figure 5-14 shows that the Eta-predicted longwave radiation, averaged over a year or more, had little variation by synoptic class or by site, ranging from about 290 to 420 W/m<sup>2</sup>. The magnitude may be less for post-trough synoptic conditions since such periods are generally cool and clear. The magnitude of longwave radiation was largest for tropical storms, which are marked by warm temperatures, high humidity, and a maximum amount of aerosols (i.e., fog, clouds, and rain). Its magnitude may be less for the most northerly sites: the C-MAN sites on the coast or the buoys near the coast.

Shortwave Radiation – The incoming solar radiation flux is mostly in the shortwave range, which is a strong function of cloud cover. Sometimes the shortwave radiation was

observed by a solar radiometer, but usually it was parameterized based on time of day and year, latitude, and Eta model predictions of cloudiness and humidity. The range in Figure 5-15 is from 80 to 280 W/m<sup>2</sup>, which is a much larger range than for the longwave component. The distribution with synoptic class makes physical sense, with maximum amounts during ridge conditions which are known to be clear and sunny, and minimum amounts during weak troughs or tropical storms which are known to be cloudy. The figure suggests that there was little variation by monitoring site.

Humidity Scaling Parameter – The humidity scaling parameter is defined by Monin-Obukhov similarity theory and is proportional to the latent heat flux divided by the friction velocity. This parameter is not observed but must be calculated by COARE and has a factor of seven variability, as shown in Figures 5-16a and b. Because the latent heat flux tends to be maximized during periods with a low dew point in the air and/or periods when the skin temperature is much higher than the air temperature, such as in the middle of a large high pressure system, we expect the humidity scaling parameter to be largest as well during low humidity periods or hot high pressure periods. This expectation is borne out in Figures 5-16a and b, since the humidity scaling factor is larger during flat and ridge periods.

Temperature Scaling Parameter – The temperature scaling parameter is defined by Monin-Obukhov similarity theory and is proportional to the sensible heat flux divided by the friction velocity. It is calculated by COARE. This parameter has a large variability, from near zero to about  $-0.22^{\circ}\text{C}$ . Because the sensible heat flux tends to be maximized during periods when the air is cooler than the water, such as after a cold front passes, we expect the temperature scaling parameter to be largest during low temperature periods as well. This result is shown in Figure 5-17, since the temperature scaling factor is much larger during post-trough periods. It is smallest during tropical storms, when the air is likely to be at the same temperature as the water. This parameter is expected to be largest at sites near land, for example, the C-MAN sites; the sensible heat flux is larger over land than over water because land surface can heat up much more under the sun's effect at midday. Figure 5-17 suggests that the SRST2 C-MAN site has a larger temperature scaling parameter; however, the PTAT2 and GDIL C-MAN sites did not support this trend.

Roughness – The surface roughness over water is a function of wind speed. It is calculated by COARE based on the observed wind speed and the sea state. The Charnock relation used in COARE states that roughness is proportional to the square of friction velocity. Therefore, we would expect the roughness to be larger during synoptic periods with stronger winds. This is exemplified by the buoy 42002 and SMI sites in Figures 5-18a and 5-18b, since the largest roughness measurements occur during tropical storms; however, the opposite effect is shown at other sites. Part of the reason for this inconsistency may be the problem identified earlier, where a large roughness is calculated at small wind speeds (wind speed less than 2 m/s). This is due to a COARE algorithm that adjusts the wave period to be very short during low winds, but causes a large increase in roughness.

The variation in roughness is less at the BAMP platform sites (Figure 5-18b) and at the VRM platform (Figure 5-18a), and the average magnitude of roughness is about 40% to 50% less than the site data shown Figure 5-18a (excluding VRM). Possible explanations are that the wave height and frequency are estimated from wind speed at the platforms, whereas, they are

measured at the buoys. Also, the platform wind observations are corrected from 20+ m to 10 m and wind speeds are, on average, less than the other non-platform sites

Sensible Heat Flux – The sensible heat flux is calculated by COARE using observations of wind speed and the skin-air temperature difference. It increases as the wind speed and the skin-air temperature difference increase. Figures 5-19a and 5-19b show that sensible heat flux is maximized for post-trough synoptic conditions, which are likely to be marked by above-average wind speeds and low air temperature. There is a factor of 10 variability across the nine synoptic classes. There are some differences among the sites, but they are not consistent and need further investigation.

Latent Heat Flux – The average latent heat flux shown in Figures 5-20a and 5-20b is about an order of magnitude greater than the sensible heat flux shown in Figures 5-19a and 5-19b. In addition, less variability exists in the latent heat flux, perhaps because the latent heat flux (calculated by COARE based on observations of wind speed, skin-air temperature difference, and relative humidity) is generally positive, while the sensible heat flux can be negative (when air temperature is greater than skin temperature). As noted, the latent heat flux is consistently large during the post-trough synoptic condition due to higher wind speeds and lower dew points that follow a cold front. It can also be large during tropical storms due to high temperatures and strong winds.

Friction Velocity – The friction velocity is calculated by COARE using the log wind profile relation. Since that relation has friction velocity proportional to wind speed, the friction velocity values in Figures 5-21a and 5-21b are expected to be largest during high-wind periods. In fact, the figures show the highest friction velocity values at most sites during tropical storms. Aside from the anomaly during tropical storms, there is little variability in friction velocity from site to site or with synoptic class. The friction velocity averages 0.2 m/s in Figure 5-21a and 0.12 in Figure 5-21b; the difference is due to the difference in estimated roughness,  $z_o$  (see discussion of roughness and Figures 5-18a and 5-18b).

Wind Speed – Wind speed is the only COARE parameter that is observed at all sites. It is not calculated by COARE. Wind speed averages 6 m/s at non-platform sites and 4 m/s at platform sites and varies in a manner similar to that of friction velocity. Figure 5-22 shows a wind speed range of 4 m/s for ridge and flat classes at GDIL to 11.5 m/s for the tropical storm class at buoys 42002 and 42035. Wind speeds shown are not corrected to a standard height.

## **General Flow Direction**

Figures 5-23, 5-24, 5-25 through 5-30 (a and b), and 5-31 contain histograms showing the results of the average COARE calculations, grouped by the four general flow directions, for the nine COARE parameters. The highlights of the results are discussed by COARE parameter.

Downwelling Longwave Radiation –Downwelling longwave radiation shows little variation by flow direction or by station, ranging from 340 to 390 W/m<sup>2</sup> (Figure 5-23) Note that this parameter is a COARE input rather than an output and, when observations are not available, it is based on estimates made by the Eta prognostic meteorological model. The magnitude may be less for offshore flow directions since such periods are generally associated with post-frontal

northerly wind directions that would be cool and clear. The magnitude of longwave radiation is largest for tropical storms, which are marked by warm temperatures, high humidity and much cloud and rain. Its magnitude may be less for the most northerly sites, either the C-MAN sites on the coast or the buoys near the coast.

Shortwave Radiation – The incoming solar radiation flux is mostly in the shortwave range. This component is a strong function of cloud cover. If observations were not available, Eta prognostic meteorological model predictions were used. Figure 5-24 suggests that there little variation with site and with flow direction since the minimum and maximum values in the figure are 170 and 290 W/m<sup>2</sup>, respectively. The shortwave radiation behavior is consistent at the 14 monitoring sites; the higher values averaged 240 W/m<sup>2</sup> for onshore and parallel west flow directions, and lower values averaged 190 W/m<sup>2</sup> for offshore and parallel east flow directions. There probably was slightly more cloud cover for offshore and parallel east flow directions.

Humidity Scaling Parameter – This parameter has a small (factor of two) variability across the 14 sites and the four flow directions plotted in Figures 5-25a and 5-25b. Few obvious trends are apparent. The values appear to be slightly larger for offshore than for onshore flow directions, possibly reflecting drier air associated with offshore flows.

Temperature Scaling Parameter – The sensible heat flux tends to be maximized during periods when the air is cooler than the water, such as for northerly offshore wind flow patterns. Therefore, we expect the temperature scaling parameter to be largest during offshore flow periods as well. This is shown in Figures 5-26a and 5-26b, since the temperature scaling factor is much larger (usually more than a factor of two) at all 14 sites for offshore flow directions. It is smallest during onshore flow periods at the buoy sites, when the air is likely to be at the same temperature as the water. At the oil platform and C-MAN sites, the temperature scaling parameter is smallest during either onshore or parallel west flow directions.

Roughness – The surface roughness over water is a function of wind speed, wave height, and time period. Therefore, roughness is expected to be larger during flow directions with stronger winds. This effect is shown in Figure 5-27a for the seven buoy sites; the largest wind speeds and, therefore the largest roughness values, are found for offshore flow directions; however, there are no clear variations at the oil platform and C-MAN sites. Figure 5-27a illustrates more variability in roughness, and larger mean values (by almost a factor of two) than does Figure 5-27b (the BAMP platform sites).

Sensible Heat Flux – The sensible heat flux increases as the wind speed and the skin-air temperature difference increase. Figures 5-28a and 5-28b show that sensible heat flux is maximized for northerly offshore flow directions, which are more likely to be marked by above-average wind speeds and by low air temperatures. The sensible heat flux is lowest for onshore flow directions, when the boundary layer is in balance with the water surface. The average difference in sensible heat flux for offshore and onshore flow directions across the nine stations is about a factor of 10. Differences exist among the sites but they are not consistent and the reasons for the differences are not obvious.

Latent Heat Flux – The average latent heat flux shows some differences between offshore and onshore wind directions at most sites. The latent heat flux is usually largest during offshore (northerly) flows, which tend to be associated with post-trough synoptic conditions—higher wind speeds and lower dew points that follow a cold front. With any offshore flow the dew point in the air is likely to be less than that usually found over the water. The minimum latent heat fluxes in Figures 5-29a and 5-29b occur with onshore flows, which would tend to be boundary layer flows in balance with the water surface.

Friction Velocity – Friction velocity is calculated by COARE using the log wind profile relation. Figures 5-30a and 5-30b show the results. Because the friction velocity of the log wind relation is proportional to wind speed, the largest friction velocity values were associated with high-wind periods, which tended to occur with offshore winds. Minimum friction velocity occurred during parallel west wind directions. There is little variability in friction velocity from site to site. The average friction velocity at non-platform sites (Figure 5-30a) is larger, by about 50%, than the average friction velocity at the platforms (Figure 5-30b). As noted, the difference is probably due to differences in estimated roughness length,  $z_o$ .

Wind Speed – Wind speed, shown in Figure 5-31, ranges from 4 m/s for onshore flows at GDIL1 to 7.5 m/s for offshore flows at BURL1. At most sites, the maximum occurs during offshore flows, which may be associated with post-cold front conditions from the north quadrant.

### 5.6.3 Diurnal Variations by Month

Seven sites were selected to analyze the diurnal variations by month of latent and sensible heat fluxes, friction velocity, wind speed, and skin-air temperature differences. The sites include buoy 42001 (a deep-water buoy); the VRM (near shore) and SMI (far offshore) platforms; buoy 42040 (a near-shore buoy site); a C-MAN site, GDIL; the BIP platform (in a shallows near Breton Island); and the DWP platform (the deepest water platform site). The highlights of the results are discussed below.

Buoy 42001 – The sensible heat fluxes show almost no diurnal variation, which makes physical sense for an over-water site far from land (**Figure 5-32**). Maximum sensible heat fluxes occur in December and January, when the water-air temperature difference is the greatest.

SMI – The sensible heat flux shows very little diurnal variation, but slightly more than at buoy 42001 (**Figure 5-33**). At SMI in December, the greatest diurnal variation in sensible heat flux is observed and is only about 20% (about  $50 \text{ W/m}^2$  in the morning and  $40 \text{ W/m}^2$  in the afternoon). The variation is associated with a smaller friction velocity in the afternoon (see **Figure 5-34**) and not due to variations in the  $T_v$  profiles, which show almost no diurnal cycle in December. During May, sensible heat fluxes are near zero during most of the daylight hours because the water temperature is approximately equal to the air temperature. Figure 5-34 shows that the mean friction velocity is 2.5 times larger in December than in July, due to a combination of larger wind speeds and larger instabilities in December.

VRM – In June, July, August, and September, the latent heat flux shows minor peaks in both the morning and afternoon (**Figure 5-35**). During the other months, the latent heat flux shows very little diurnal variation. The latent heat flux is smaller in December and January than

in July through September ( $50 \text{ W/m}^2$  versus  $180 \text{ W/m}^2$ ) because there is more water vapor present in the atmosphere in the summer. In December, **Figure 5-36** shows that the sensible heat flux has a factor of two diurnal cycle, peaking at sunrise. The morning peaks in the sensible heat flux are due to peaks in the difference between the skin and air temperatures (**Figure 5-37**). The sensible heat flux in December is much higher ( $50 \text{ W/m}^2$  versus  $20 \text{ W/m}^2$ ) than during other months. The high sensible heat flux in December is a result of a higher than average difference between the skin and air temperatures and higher than average friction velocity. The slight diurnal trend seen at VRM may be caused by its nearness to shore.

Buoy 42040 – The diurnal monthly profiles of sensible heat flux, shown in **Figure 5-38**, are similar to those at SMI. They show a maximum diurnal variation of about 20% in December and January. The maximum sensible heat flux ( $65$  to  $70 \text{ W/m}^2$ ) occurs in December due to a combination of higher than average friction velocity and differences between the skin and air temperatures. Sensible heat fluxes in May and June drop to nearly zero due to the small water-air temperature differences. The latent heat flux at Buoy 42040 shows less diurnal variation and is also greatest in December (**Figure 5-39**). The December latent heat flux is about  $230 \text{ W/m}^2$  while the May latent heat flux is about  $80 \text{ W/m}^2$ .

GDIL1 – The sensible heat flux curve indicates that GDIL1 is not strongly influenced by land—the sensible heat flux is lowest in mid-afternoon (the opposite of a land station) and highest in the early morning (**Figure 5-40**). Average sensible heat flux is also never negative at night (land stations have negative sensible heat flux at night). However, the sensible heat flux curve shows a diurnal cycle, ranging from  $10$  to  $35 \text{ W/m}^2$  in the predawn hours to  $4$  to  $12 \text{ W/m}^2$  in the afternoon. The diurnal cycle closely follows the diurnal cycle of the difference between the skin and air temperatures (**Figure 5-41**). The friction velocity is nearly constant throughout the day (**Figure 5-42**). The latent heat flux curves are somewhat flatter than the sensible heat flux curves but show slight peaks in the afternoon during the summer months (**Figure 5-43**). The latent heat flux is not as sensitive as the sensible heat flux to water-air temperature difference.

BIP – **Figures 5-44 through 5-48** show diurnal curves, by month, for sensible heat flux, latent heat flux, friction velocity, skin minus air temperature, and wind speed for the Breton Island platform. Note that these data represent a shorter period (one year from September 2000 through September 2001) than data in previous figures (May 1998 through October 2001). **Figure 5-44** shows that the sensible heat flux has minimal diurnal variation and is largest ( $20$  to  $30 \text{ W/m}^2$ ) in late fall and early winter when the water temperature is warmer than air temperature. During other months, the sensible heat flux is small (less than  $10 \text{ W/m}^2$ ). **Figure 5-45** shows that the latent heat flux also has minimal diurnal variation and is largest ( $150$  to  $200 \text{ W/m}^2$ ) in July through October when the water temperature is highest. In February, when water temperatures are cool, the latent heat flux drops to about  $30 \text{ W/m}^2$ . The COARE-calculated friction velocity, seen in **Figure 5-46**, shows minimal diurnal variation and varies by as much as a factor of two from month to month. However, the month-to-month variation appears random and no physical causes can be identified. The difference between skin and air temperature shows a  $1^\circ$  to  $2^\circ\text{C}$  diurnal variation in **Figure 5-47**, with maximum values occurring between 0800 and 0900 CST and minimum values between 2000 and 2400 CST. As noted for other sites, the temperature difference is greater ( $2^\circ\text{C}$  or more) in the fall and is smaller (between  $-1^\circ$  and  $1^\circ\text{C}$  in the late winter). The wind speeds, plotted in **Figure 5-48**, show little diurnal

variation, and are about 30% less from July through September, when they are about 4 m/s versus 5 to 6 m/s for most other months.

**DWP – Figures 5-49 through 5-53** show diurnal curves, by month, for sensible heat flux, latent heat flux, friction velocity, skin minus air temperature, and wind speed for the Deep Water Platform. This site should be most representative of the “open ocean” for which the COARE algorithm was developed. As noted in the BIP discussion, these data represent a shorter period (one year from September 2000 through September 2001) than the data represented in Figures 5-32 through 5-43 (May 1998 through October 2001). The DWP wind speeds, plotted in Figure 5-49, show little diurnal variation and are about 30% less from July through October (behavior similar to the BIP wind speeds plotted in Figure 5-48), when they are about 3 m/s versus 4 to 5 m/s for most other months. Figure 5-50 shows that the sensible heat flux has very little diurnal variation and is largest (15 to 25 W/m<sup>2</sup>) in late fall and early winter, when the water temperature is warm relative to the air temperature (this is behavior similar to that shown in the BIP data in Figure 5-44). During the other months, the sensible heat flux is small (less than 10 W/m<sup>2</sup>, with the minimal average of 4 W/m<sup>2</sup> in May). Diurnal variation of the latent heat flux, plotted in Figure 5-51, is also insignificant, and the latent heat flux is largest (about 120 W/m<sup>2</sup>) in the fall, when the water temperature is greatest. In February, when water temperatures are cool, the latent heat flux drops to about 70 W/m<sup>2</sup>. The COARE-calculated friction velocity, seen in Figure 5-52, shows some diurnal variations but the variations are not consistent from month to month. The average friction velocity varies by as much as a factor of two from month to month. However, the month-to-month variation appears random and no physical causes can be identified. The difference between skin and air temperature shows a 1° to 2°C diurnal variation in Figure 5-53, with maximum values occurring between 0400 and 0500 CST and minimum values at about noon. The plots of the same variable for BIP in Figure 5-47 show the same diurnal shape but offset by 5 to 8 hours later in the day. As noted for other sites, the temperature difference is greater (4°C or more) in the late fall and is smaller (between –1° and 1°C) in the spring (e.g., negative or stable temperature differences occur in May in the afternoon). A negative temperature difference will lead to a negative sensible heat flux.

## 5.7 CASE STUDY ANALYSES

This section presents case study analyses of COARE model output for selected days and comparisons to Eta model simulations. Case studies were performed for the following periods:

- January 20 through 25, 2000 – a period characterized by post frontal offshore flow on January 20 and 21, followed by onshore flow on January 22 and 23, and strong offshore flow on January 24 and 25.
- January 4 through 6, 2001 – a period of post upper-level trough (January 4 and 5) fading into weak ridge, and a period with air temperature much warmer than skin temperature.
- July 30 through August 1, 1999 – a period with a strong upper-level ridge, surface high pressure, and light winds.

- September 18 through 20, 2001 – a period of weak onshore flow with a weak cold front orientated west to east along the Gulf Coast from Houston, Texas, to Mobile, Alabama, on September 20.

Time series of hourly-averaged observations, COARE-model outputs, and Eta-model simulations of surface boundary layer fluxes at the sites in the Gulf of Mexico were analyzed for several short (multi-day) time periods during different seasons and for different synoptic scenarios. Analyses were performed to explain the physical relationships between the observed variables and the calculated fluxes, and compare simulations of friction velocity, sensible heat flux, and latent heat flux.

The COARE-calculated variables are based on observations at a specific monitoring location. In contrast, the Eta model predictions represent averages over a grid square with dimensions of 40 km x 40 km. Also, since the Eta model is a three-dimensional, time-dependent, numerical weather prediction model, its predictions represent a solution to the equations of motion, using some assimilation of observations such as from buoys but based primarily on mass-conservation and other physical constraints.

The Eta model has no horizontal resolution at scales less than the grid size (40 km). Consequently, if a monitoring site is being investigated near the Gulf of Mexico coastline, the Eta model constructs an average of the land-use conditions within that grid square. If the grid square consists of 75% land and 25% sea, the model will simulate that square as if it were mostly land, with resulting diurnal patterns of heat fluxes more typical of land than sea.

### **5.7.1 Analysis of January 20-25, 2000**

Data from January 20-25, 2000, from buoy 42040 are discussed here to illustrate the analysis methods and the typical results. Buoy 42040 is located several tens of kilometers east of the Mississippi River Delta.

This case study analysis was carried out in summer 2001 as a preliminary exercise, and results were reported in a conference paper by Hanna et al. (2001). Subsequent subsections discuss more recent case study analyses.

The time series of observed hourly-averaged air and skin temperatures and wind speed are plotted in **Figure 5-54**. This was an active synoptic period, with large swings in wind speed and air temperature. Air temperatures were 5-20°C cooler than skin temperatures for the first two days and for the last day and a half. Wind speeds were moderate to strong (about 5 to 15 m/s) during these periods. However, from about 1800 CST on January 22 to about 1200 CST on January 25, the air warmed slowly to approach and even exceed the skin temperature for over 12 hours. The winds dropped to near zero just before a frontal passage occurred at about 0300 CST on January 24, after which time the air temperature dropped 5°C in an hour and wind speed rapidly increased to 16 m/s.

## Sensible Heat Fluxes

Eta model simulations were compared with COARE-estimated sensible and latent heat fluxes. Eta model simulations produce forecasts up to 48 hours in the future in 6-hr increments. In addition, the model is run every 12 hours, once at 0000 UTC (00 Z) and once at 1200 UTC (12 Z), everyday. The 6- and 12-hr forecasts from the 00 Z and the 12 Z model runs were combined to yield a continuous record of every sixth hour simulated sensible and latent heat fluxes. A second continuous record was prepared using the 30- and 36 hr forecasts from the 00 Z and 12 Z model runs. In addition, the Eta-simulated sensible and latent heat fluxes every six hours were interpolated to yield hourly values. The continuous records of simulated sensible and latent heat fluxes were then compared to the COARE-estimated sensible and latent heat fluxes.

**Figure 5-55** shows the COARE-calculated and Eta-simulated sensible heat fluxes during this time period. The COARE model used the buoy-observed meteorological variables and produced very large (for the ocean) sensible heat fluxes with magnitudes of about  $150 \text{ W/m}^2$  between 2200 CST on January 20 and 0600 CST on January 21, when the skin-air temperature differences were very large ( $5^\circ$  to  $10^\circ\text{C}$ ) and the wind speeds were also large (about 10 to 15 m/s). However, during the 12- to 15-hr period in the middle of the time series, when the air temperature exceeded the skin temperature (i.e., stable conditions), the COARE-calculated sensible heat fluxes were negative (i.e., towards the water surface) with magnitudes of about  $10 \text{ W/m}^2$ . COARE will always calculate a negative sensible heat flux when the air temperature exceeds the skin temperature. Figure 5-54 shows that the Eta model simulations of sensible heat flux are only about 30% larger than the COARE-calculated values during the periods with large unstable air-skin temperature differences. However, during the middle period, the Eta model simulated positive (upward) sensible heat fluxes, in contrast to the negative (downward) COARE sensible heat fluxes, although they are small (about 0 to  $20 \text{ W/m}^2$ ). This tendency is apparent for all sites and periods. Occasionally, sites show periods with observed air temperatures warmer than skin temperatures leading to COARE-calculated negative heat fluxes, while the Eta model usually simulates positive (but small) heat fluxes. During the late spring, the air temperature observed to be greater than the skin temperature about 20% to 40% of the time can lead to long periods of mismatches in the signs of the COARE-calculated and Eta simulated sensible heat fluxes.

## Latent Heat Fluxes

**Figure 5-56** shows the COARE-calculated and Eta-simulated latent heat fluxes from January 20-25 at buoy 42040. Large latent heat fluxes of about  $500 \text{ W/m}^2$  were calculated by both COARE and Eta for the unstable periods with moderate winds near the beginning and end of the five days. This is the same magnitude as the incoming solar heat flux at the water surface on a summer day. These large sensible heat fluxes are due to the large difference between the skin and air temperatures and the moderate wind speeds. Note from Figure 5-54 that, even in January, the Gulf of Mexico skin temperature is still fairly warm (about  $21^\circ\text{C}$ ) implying that the saturation-specific humidity is large and, therefore, allows large latent heat fluxes to occur.

During the 12- to 18-hr period on January 23 when the air temperature slightly exceeded the skin temperature and winds decreased, COARE-calculated latent heat fluxes decreased to values as low as  $20 \text{ W/m}^2$ .

The Eta-model simulations of latent heat flux plotted in Figure 5-56 approximately track the COARE calculations, with differences of about 30% during the two periods with high fluxes. During the period with small fluxes, the Eta simulations are similar to the COARE calculations. There appears to be no relation between the age of the Eta simulation and the agreement with the COARE curve in the figure.

### 5.7.2 Analysis of January 4-6, 2001

This case study is based on data collected at the VRM platform from January 4-6, 2001. The VRM site is only a few km off the Louisiana coast. Just prior to January 4, a trough had passed through the Gulf of Mexico region and a weak ridge was building into the area.

**Figure 5-57** contains time series plots of hourly averaged wind speed, air temperature, skin temperature, and relative humidity for the three-day period. All but the skin temperature were observed at an elevation of about 25 m msl, or about 3 m above the surface of the oil platform.

This case study was characterized by steadier conditions than those during the January 2000 case study. Air temperature varied between  $9^\circ$  and  $17^\circ\text{C}$  and skin temperature varied between  $7^\circ$  and  $13^\circ\text{C}$ , with a steady increase through the three days. Air temperature was warmer than skin temperature (i.e., a stable  $T_v$  profile) by  $1^\circ$  to  $5^\circ\text{C}$  during most of the period, except between 1300 and 1800 CST on January 6, when the air temperature was about  $1^\circ\text{C}$  less than the skin temperature (i.e., an unstable  $T_v$  profile). Wind speed was light (between 0 and 7 m/s) with periods of very light winds (wind speeds less than 2 m/s) on January 4 and 6. Relative humidity ranged from 55% to 95%, with the higher values associated with decreases in air temperature, probably due to cloudy conditions.

#### COARE Outputs of Friction Velocity and Sensible and Latent Heat Fluxes

**Figure 5-58** illustrates the COARE outputs of hourly-averaged friction velocity and sensible and latent heat fluxes. Friction velocity closely follows the shape of the wind speed time series observations, ranging from near zero during nearly calm periods to 0.18 m/s during periods with wind speeds of 6 to 7 m/s. In general, wind speed divided by friction velocity equals 30 to 40, which was a slightly larger value than at the buoys because the observing height was high (25 m) on the oil platforms. The sensible and latent heat fluxes were small (magnitudes of less than  $20 \text{ W/m}^2$ ) because of the stable  $T_v$  profile, cool temperatures, and weak winds.

The sensible heat flux was negative (i.e., downward towards the sea surface) or near zero most of the time because the air temperature was usually warmer than the skin temperature. An exception was midday on January 6, when skin temperature was greater than air temperature for a few hours and the sensible heat flux switched to positive values, still less than  $5 \text{ W/m}^2$ .

The latent heat flux reached maximum values of about  $20 \text{ W/m}^2$  from 0300 to 0400 CST on January 4 (with low relative humidity and high wind speeds) and from about 1500 to 1800 CST on January 6 (with high relative humidity and an unstable  $T_v$  profile). Note that the sensible heat flux does not necessarily have the same sign as the latent heat flux.

### **COARE Outputs of Wave Height and Period and Surface Roughness**

The wave characteristics and the surface roughness length estimated by COARE are plotted in **Figure 5-59**. The observed wind speed is also plotted. The estimated surface roughness length is bimodal, with a value of  $0.00005 \text{ m}$  (i.e.,  $0.05 \text{ mm}$ ) with wind speeds greater than  $2 \text{ m/s}$ . When wind speeds were greater than  $2 \text{ m/s}$ , the wave height ranged from  $0.5$  to  $1 \text{ m}$  and the wave period ranged from  $2$  to  $5$  seconds. However, when wind speeds were less than  $2 \text{ m/s}$  and wave height was small, the wave period was parameterized to drop to  $1$  second, and the surface roughness length was estimated to increase by an order of magnitude from  $0.0005$  to  $0.001 \text{ m}$  ( $0.5$  to  $1 \text{ mm}$ ). Estimates of surface roughness length when wind speeds were less than  $2 \text{ m/s}$  appeared to be too large and did not agree with the Charnock relation for surface roughness length over water that states that surface roughness length is proportional to friction velocity squared (or wind speed squared).

### **Comparison of COARE and Eta Outputs of Sensible and Latent Heat Fluxes**

The COARE estimates of sensible and latent heat fluxes were made using observations from the VRM oil platform. Eta forecasts of sensible and latent heat fluxes were based on fundamental solutions to the equations of motion, using some observations at buoys and on-shore rawinsonde sites to generate analyzed fields for inputs. **Figure 5-60** compares these estimates for the January 4-6, 2001, period.

Recall that over most of the period, sensible and latent heat fluxes were small and often negative because the air temperature was greater than the skin temperature during most of the three-day period. The COARE estimates were quite different from the Eta simulations, which had a marked diurnal variability that was not present in the COARE outputs. The Eta-predicted fluxes peaked at noon, with values of about  $150 \text{ W/m}^2$  for latent heat flux and about  $100 \text{ W/m}^2$  for sensible heat flux. These magnitudes were an order of magnitude larger than the magnitudes from COARE. Even at midnight, the Eta-predicted latent heat flux was still  $20$  to  $30 \text{ W/m}^2$ . In general, the Eta-predicted latent heat flux never dropped below zero. However, the Eta-predicted sensible heat flux predictions dropped below zero during the nights of January 5 and 6, somewhat in agreement with the COARE estimates.

### **Comparison of COARE and Eta Outputs of Hourly-averaged Friction Velocity**

The COARE and Eta estimates of hourly-averaged friction velocity are plotted in **Figure 5-61**. On average, the Eta-predicted hourly-averaged friction velocity values were about  $0.2 \text{ m/s}$  whereas the COARE hourly-averaged friction velocity values were about  $0.05 \text{ m/s}$ , a difference of a factor of four. This difference was probably caused by differences in the parameterized stability. COARE accounts for the observation that air temperature greater than skin temperature assumes stable conditions most of the time, while Eta assumes unstable conditions most of the time and much larger sensible and latent heat fluxes.

The COARE estimates of observing height divided by  $L$  are also shown in Figure 5-61. Positive (stable) values occurred most of the time. Observing height divided by  $L$  became slightly negative for a few hours on January 6 when both sensible and latent heat fluxes were negative (upward). Since the observing height was about 25 m, it can be inferred that  $L$  was as low as 0.2 m during the few periods (e.g., near noon on January 4 and near 0900 CST on January 6) with very light winds and air temperature greater than skin temperature. Because  $L$  is proportional to friction velocity cubed,  $L$  is a very strong function of wind speed.

### 5.7.3 Analysis of July 30-August 1, 1999

This case study is based on data collected at the VRM and SMI platforms from July 30 to August 1, 1999. The VRM site is only a few kilometers off the Louisiana coast, while the SMI site is about 100 km offshore. A strong upper-level synoptic ridge was present during this period with a surface high pressure system centered over the Gulf of Mexico and associated light winds. This is a typical mid-summer scenario.

**Figures 5-62a and 5-62b** are time series plots of hourly-averaged wind speed, air temperature, skin temperature, and relative humidity for the three-day period at VRM and SMI, respectively. All but the skin temperature were observed at an elevation of about 25 m msl, or about 3 m above the surface of the oil platform.

This case study was characterized by much warmer conditions than the January case studies. A major difference was the skin temperature—in January it was consistently lower than the skin temperature during the summer. For the July 30-August 1 period, air temperature was nearly constant at VRM and SMI, varying between 28° and 31°C. Skin temperature was also nearly constant at VRM and SMI, varying between 30° and 33°C. Skin temperature was warmer than air temperature (i.e., an unstable  $T_v$  profile) by an average of about 1° to 2°C during most of the period. An exception occurred during the few hours around noon each day, when the skin and air temperatures were nearly equal (i.e., neutral  $T_v$  profile). Wind speed averages were slightly higher at VRM than at SMI (4 m/s versus 2.5 m/s, respectively). The wind speed dropped below 2 m/s about half the time at SMI. Relative humidity was fairly constant at about 70% at both sites.

### COARE Outputs of Friction Velocity and Sensible and Latent Heat Fluxes

**Figures 5-63a and 5-63b** illustrate the COARE parameterizations of hourly-averaged friction velocity and sensible and latent heat flux. Friction velocity averaged about a factor of two lower at SMI than at VRM (0.07 m/s versus 0.14 m/s, respectively). In general, wind speed divided by friction velocity equaled about 30, in rough agreement with what was found for the January 5-6, 2001, case study. The COARE-estimated latent heat fluxes were always larger than 50 W/m<sup>2</sup> but reached larger maxima (220 W/m<sup>2</sup> versus 160 W/m<sup>2</sup>) at VRM than at SMI because of the larger wind speeds at VRM.

The sensible heat flux is also about twice as large at VRM as at SMI and is nearly always positive (i.e., upward from the sea surface) because the air temperature is usually a few degrees cooler than the sea temperature. An exception occurred at noon on all three days at SMI, when the skin temperature was approximately equal to or less than the air temperature for a few hours

and sensible heat flux values became negative (downward), but these values were small (less than  $5 \text{ W/m}^2$ ). The maximum upward sensible heat flux at VRM was about  $30 \text{ W/m}^2$  and at SMI about  $20 \text{ W/m}^2$ ; both maximums occurred during the night, from 0000 to 0600 CST on July 31.

The maximum latent heat fluxes are about seven times the maximum sensible heat fluxes, as is found at most over-water sites in mid-summer.

### **COARE Outputs of Wave Height and Period and Surface Roughness**

The hourly-averaged wave characteristics and the surface roughness length estimated by COARE for VRM and SMI for this case study are plotted in **Figures 5-64a and 5-64b**. The observed wind speed is also plotted. Because of the high frequency of wind speeds less than 2 m/s at SMI, there was a strong bimodal distribution of COARE-calculated surface roughness length at that site, with a value of about 0.00002 m (i.e., 0.02 mm) and wind speeds greater than 2 m/s. When the wind speed was greater than 2 m/s, the wave height ranged up to 0.5 m and the wave period ranged from 2 to 4 seconds. However, when the wind speed was less than 2 m/s and the wave height was small, the wave period was parameterized to drop to 1 second and the surface roughness length was estimated to increase by an order of magnitude to about 0.0005 m (i.e., 0.5 mm). These surface roughness length estimates when wind speed was less than 2 m/s appear to be too large and do not agree with the Charnock relation for surface roughness length over water that states that surface roughness length is proportional to friction velocity squared (or wind speed squared).

At VRM, where the wind speeds are generally higher than at SMI, the wind speed dropped below 2 m/s during the morning of August 1, and surface roughness length increased by an order of magnitude.

### **Comparison of COARE and Eta Outputs of Sensible and Latent Heat Flux**

The COARE estimates of sensible and latent heat flux were made using observations from the VRM and SMI oil platforms. The Eta forecasts of sensible and latent heat flux were based on fundamental solutions to the equations of motion, using some observations at buoys and on-shore radiosonde sites to generate analyzed fields for inputs. **Figures 5-65a and 5-65b** compare these estimates for the July 30 to August 1, 1999, period.

The COARE parameterizations of sensible and latent heat flux agree fairly well, on average, with the Eta forecasts of these fluxes. This is the type of scenario (warm summer periods) for which COARE was derived and calibrated, and Eta does well with these periods of persistent summertime conditions. Eta appears to match the average COARE latent heat flux values at VRM and SMI fairly well, although the time variations are not well-simulated. For example, at VRM, Eta predicts a strong diurnal variation of latent heat flux, while the diurnal variation is not found at all in the COARE parameterizations. The diurnal behavior simulated by Eta may be partly explained by the fact that the Eta grid square containing the VRM site includes a fraction of land surfaces.

The Eta sensible heat fluxes at SMI are in good agreement with the COARE values of 0 to  $20 \text{ W/m}^2$ . At VRM, the Eta forecasts of sensible heat flux tend to have a strong diurnal

variation, with a peak value of about  $50 \text{ W/m}^2$  at noon each day, dropping to zero or below at night. The COARE parameterizations of sensible heat flux do not show this diurnal variability and the values are lowest values at midday when the Eta forecast values have are highest.

### **Comparison of COARE and Eta outputs of hourly-averaged friction velocity**

The COARE and Eta estimates of hourly-averaged friction velocity are plotted in **Figures 5-66a and 5-66b** for VRM and SMI, respectively. On average, the Eta-predicted hourly-averaged friction velocity values are about a factor of two larger than the COARE values.

The COARE estimates of the observing height divided by  $L$  are also shown in the figures. Negative (unstable) values occurred all the time, with the observing height divided by  $L$  equal to about  $-3$  at VRM and  $-10$  at SMI. Since the observing height was about  $25 \text{ m}$ , it can be inferred that  $L$  was about  $-7 \text{ m}$  at VRM and about  $-2.5 \text{ m}$  at SMI. The smaller magnitudes of  $L$  at SMI were caused by the smaller wind speeds.

### **5.7.4 Analysis of September 18-20, 2001**

This case study was based on data collected at the VRM and SMI platforms from September 18-20, 2001. This period was marked by weak onshore flow. On September 20, a weak cold front was oriented west-to-east along the Gulf Coast from Houston, Texas, to Mobile, Alabama.

**Figures 5-67a and 5-67b** are time series plots of hourly-averaged wind speed, air temperature, skin temperature, and relative humidity for the three-day period for VRM and SMI, respectively. All but the skin temperature were observed at an elevation of about  $25 \text{ m}$  msl, or about  $3 \text{ m}$  above the surface of the oil platform.

This case study was characterized by conditions similar to, but slightly cooler than, those in the July-August case study. The air temperatures in September were only a few degrees lower than those in July, and the skin temperature was usually less than the skin temperature in July. Air temperature varied from  $24^\circ$  to  $33^\circ\text{C}$  at VRM and from  $26^\circ$  to  $30^\circ\text{C}$  at SMI. Skin temperature was more constant over the three days at VRM and SMI, varying between  $27^\circ$  and  $32^\circ\text{C}$ . Skin temperature was warmer than air temperature (i.e., an unstable  $T_v$  profile) by an average of about  $1$  to  $2^\circ\text{C}$  during the entire three-day period at SMI and about half the time at VRM. An exception occurred at VRM from 0500 to 1300 CST on September 19 and from 2100 CST on September 19 to 1200 CST on September 20, when air temperature exceeded skin temperature by as much as  $5^\circ\text{C}$  (i.e., a stable  $T_v$  profile). This phenomenon may have been related to the presence of a cold front along the coast, since VRM is much nearer the coast than SMI. Wind speed ranged from near zero to about  $8 \text{ m/s}$  at both VRM and SMI, with speeds of about  $5 \text{ m/s}$  for the first half of the period, dropping to  $1$  or  $2 \text{ m/s}$  for the last half of the period. The wind speed dropped below  $2 \text{ m/s}$  for a small fraction of the time at both sites. Relative humidity was fairly constant at about  $80\%$  at both sites.

## COARE Outputs of Hourly-averaged Friction Velocity and Sensible and Latent Heat Flux

**Figures 5-68a and 5-68b** (for VRM and SMI, respectively) illustrate the COARE parameterizations of hourly-averaged friction velocity and sensible and latent heat flux. Hourly-averaged friction velocity averaged about 0.15 m/s at SMI during the first half of the period, then averaged about 0.005 m/s during the last half of the period, due primarily to the reduction in wind speed in the last half of the period. In general, wind speed divided by friction velocity was about 30 to 40, in rough agreement with similar conditions in the January and July case studies.

The COARE-estimated latent heat fluxes were always larger than  $30 \text{ W/m}^2$  with a maximum of  $230 \text{ W/m}^2$  at SMI, where air temperature was always less than the skin temperature. At VRM, the maximum latent heat flux was the same as at SMI, but the minimum was near zero or slightly less than zero for the several hours when the air temperature was greater than the skin temperature.

The maximum sensible heat flux was about  $40 \text{ W/m}^2$  at both VRM and SMI. The maximum occurred at a time when the wind speed and the difference between the skin and air temperatures were large (8 m/s and  $5^\circ\text{C}$ , respectively). The minimum sensible heat flux at SMI was nearly zero when winds were low and the air and skin temperatures were nearly equal. However, at VRM, the minimum sensible heat flux was negative (about  $-10 \text{ W/m}^2$ ) because skin temperatures were lower than air temperatures at that site.

The maximum latent heat fluxes were about six times the maximum sensible heat fluxes, in agreement with results for the July case study and those found at most over-water sites in the summer.

## COARE Outputs of Wave Height and Period and surface Roughness

The hourly-averaged wave characteristics and the surface roughness length estimated by COARE for VRM and SMI in September are plotted in **Figures 5-69a and 5-69b**. The observed wind speed is also plotted. The results are similar to those found for the other case studies in that there was a strong bimodal distribution of COARE-calculated surface roughness length at both sites. A surface roughness length value of about 0.00003 m (0.03 mm) was calculated when wind speeds exceeded 2 m/s. However, when wind speeds were less than 2 m/s, surface roughness length was estimated to increase by more than an order of magnitude from 0.0005 to 0.001 m (0.5 to 1 mm).

## Comparison of COARE and Eta Outputs of Sensible and latent Heat Flux

The COARE estimates of sensible and latent heat flux were made using observations collected from the VRM and SMI oil platforms. The Eta meteorological forecast model bases its forecasts of sensible and latent heat flux on fundamental solutions to the equations of motion, using some observations at buoys and on-shore radiosonde sites to generate analyzed fields for inputs. **Figures 5-70a and 5-70b** show a comparison of these estimates for the September 18-20, 2001, case study period.

As with the July case study, the COARE parameterizations of sensible and latent heat flux agreed fairly well, on average, with the Eta forecasts of these fluxes. This was the type of scenario (warm summer periods) for which COARE was derived and calibrated. Eta appeared to match the average and the maximum COARE latent heat flux values at VRM and SMI, although the time variations were not well-simulated. For example, at VRM, Eta predicted a strong diurnal variation of latent heat flux, with peaks near noon and minima near midnight, while the diurnal variation was minimal in the COARE parameterizations. Part of the reason for the diurnal fluctuations forecasted by Eta may be that the grid cell in which VRM is located includes mostly land surfaces. Both COARE and Eta agree on the low latent heat flux values from 0000 to 0600 CST on September 20, when the cold front, which was oriented along the Gulf Coast, was near the VRM site.

At the SMI site, located 100 km south of the VRM site and the cold front, the COARE- and Eta-simulated latent heat flux did not drop as low as at VRM.

The Eta-simulated sensible heat fluxes at the far-offshore site, SMI, were in good agreement with the COARE values of 0 to 40 W/m<sup>2</sup>. At the VRM site nearer the shore, the Eta forecasts of sensible heat flux tended to have a strong diurnal variation, with a peak value of 40 to 110 W/m<sup>2</sup> at noon each day, dropping to below zero (about -10 W/m<sup>2</sup>) at night. The COARE parameterizations of sensible heat flux did not show this diurnal variability and were determined by the difference between the skin and air temperatures. For the few hours when the difference between the skin and air temperatures was greater than zero (i.e., stable), the COARE simulations of sensible heat flux ranged from -10 W/m<sup>2</sup> to zero.

### **Comparison of COARE and Eta Outputs of Hourly-averaged Friction Velocity**

The COARE and Eta estimates of hourly-averaged friction velocity for the September case study are plotted in **Figures 5-71a and 5-71b**, for VRM and SMI, respectively. As for the July case study, on average, the Eta-predicted hourly-averaged friction velocity values were a factor of two larger than the COARE values.

The COARE estimates of the observing height divided by L are also shown in the figures. Negative (unstable) values occurred all the time at SMI, with the observing height divided by L equal to -5 to -2 at the beginning of the period and -3 to -35 for the last half of the period. At VRM, where there were several stable periods (i.e., when the difference between the skin and air temperatures was greater than zero), observing height divided by L was both positive (stable) and negative (unstable), ranging from -10 to +65.

### **5.7.5 Summary of Results of Four Case Studies**

The case study analyses of COARE and Eta outputs focused on three monitoring sites: buoy 42040, the VRM platform, and the SMI platform. Buoy 42040 is a few tens of kilometers east of the Mississippi Delta, the VRM site is only a few kilometers off the Louisiana coast, and the SMI site is about 100 km offshore.

Four representative multi-day case study periods were chosen for analysis: January 20-24, 2000; January 5-6, 2001; July 30-August 1, 1999; and September 18-20, 2001.

The previous four subsections discussed the results of the analyses of the individual case studies, and this subsection provides summary conclusions.

For each case study period, time series of observed hourly-averaged wind speed, air temperature, skin temperature, and relative humidity were plotted for the multi-day period for each monitoring site. These observations were used as inputs to the COARE program, which provided estimates of friction velocity, sensible heat flux, and latent heat flux. The COARE estimates were compared with predictions made by the Eta numerical weather prediction model.

The four case studies cover a range of meteorological conditions. For example, the January 20-24, 2000, period was an active synoptic period, with frequent moderate winds, large fluctuations in air temperature, and large swings in sensible and latent heat flux. The January 5-6, 2001, period was cool but with the air temperature warmer than the skin temperature most of the time, leading to frequent stable conditions. The July 1999 and September 2001 periods were typical summertime periods when the skin temperature was usually greater than the air temperature (i.e., unstable conditions) and winds were light to moderate.

### **COARE Outputs of Friction Velocity and Sensible and Latent Heat Flux**

A few general conclusions can be reached about the COARE outputs. In general, wind speed divided by friction velocity equals 30 to 40 for the COARE estimates for all the case studies, in rough agreement with the logarithmic wind profile formula  $u/u^* = 2.5 \ln(z/z_0)$  where  $u$  is wind speed,  $u^*$  is friction velocity,  $z$  is observing height, and  $z_0$  is surface roughness length. This is valid for nearly neutral conditions and observing height divided by surface roughness length equal to about 1000 to 100,000. These ratios of surface roughness length are valid for the ranges of observing height (2 to 25 m) and surface roughness length (0.00002 to 0.001 m) encountered in the case studies.

On average, during most periods with skin temperatures greater than air temperatures (i.e., an unstable  $T_v$  profile), the COARE-estimated latent heat fluxes were 5 to 10 times larger than the sensible heat fluxes, in agreement with the results found at most over-water sites. At these times, both the sensible and latent heat fluxes were roughly proportional to friction velocity. The “skin temperature greater than air temperature” scenario occurred a majority of the time in the three and a half years of Gulf of Mexico data, at most ocean sites at low to mid latitudes.

Latent heat fluxes were estimated by COARE to equal about 100 to 200  $W/m^2$  when air temperatures were greater than skin temperatures during typical summertime periods. During the January 20-25, 2000, case study, there was a period of 20 or 30 hours, after a cold front passage, when a large difference between skin and air temperatures occurred with a large wind speed, which led to exceptionally large latent heat flux values of about 500  $W/m^2$ . Latent heat flux rarely becomes negative during periods with skin temperatures less than air temperatures and high relative humidity.

Sensible heat fluxes were usually positive upward with magnitudes of 50  $W/m^2$  or less when skin temperatures were less than air temperatures (i.e., most of the time). When skin

temperature was less than air temperature, the sensible heat flux became negative, but had a magnitude of less than  $10 \text{ W/m}^2$ .

The sensible heat flux was negative more often than the latent heat flux because the sensible heat flux is negative whenever the skin temperature is less than the air temperature. However, the latent heat flux becomes negative only when the skin temperature is less than the air temperature and the relative humidity of the air near the surface is very high.

### **COARE Outputs of Wave Height and Period and Surface Roughness Length**

The hourly-averaged wave characteristics and the surface roughness length estimated by COARE were plotted and analyzed. In general, the Charnock relation,  $z_o = au^{*2}$  (where  $z_o$  is surface roughness length,  $a$  is a constant, and  $u^*$  is friction velocity), was valid for moderate to high wind speeds (greater than 2 m/s), when an average surface roughness length value of 0.00002 m to 0.00005 m (0.02 to 0.05 mm) was estimated by COARE for these case studies. However, when wind speed was less than 2 m/s, surface roughness length was estimated by COARE to increase by more than an order of magnitude to 0.0005 to 0.001 m (0.5 to 1 mm). This strong bimodal distribution of COARE-calculated surface roughness length was found for all four case studies and is thought to be caused by the revised surface roughness length formulation, which allows surface roughness length to be prescribed as a function of wave height and period. For wind speeds less than 2 m/s, COARE parameterized a large decrease in wave period (from 4 to 5 seconds to 1 second), which translated into an increase in surface roughness length.

### **Comparison of COARE and Eta Outputs of Sensible and Latent Heat Flux**

The COARE estimates of  $H_s$  and  $H_l$  were made using observations at buoy 42040 or the VRM and SMI oil platforms. The Eta model forecasts of sensible and latent heat flux were based on fundamental solutions to the equations of motion, using some observations at buoys and on-shore radiosonde sites to generate analyzed fields for inputs.

As previously mentioned, for observing sites close to shore such as VRM, the encompassing Eta horizontal grid square may include a portion of the coast and the inland area. Consequently, Eta may model that grid square as if it is not 100% over water, affecting friction velocity and sensible and latent heat flux predictions.

The COARE parameterizations of sensible and latent heat flux agreed fairly well, on average, with the Eta simulations of these fluxes. Agreement was best for warm summer periods for which COARE was derived and calibrated. Despite the fact that Eta appears to match the average and the maximum COARE sensible and latent heat flux values, the time variations were not well-simulated. For example, at VRM in September, Eta predicted a strong diurnal variation of the latent heat flux, with peaks near noon and minima near midnight, while the diurnal variation was minimal in the COARE parameterizations. Part of the reason for the diurnal fluctuations forecasted by Eta may be that the grid cell in which VRM is located includes a large fraction of land surfaces.

The COARE-estimated sensible heat flux was determined primarily by the difference between the air temperature and the skin temperature. For the few hours when this temperature difference was greater than zero (i.e., stable), the COARE simulations of sensible heat flux ranged from  $-10 \text{ W/m}^2$  to zero. The Eta model sometimes matched these negative or near-zero values, but more often, the Eta model predicted a slight positive (upward) sensible heat flux during these periods when COARE sensible heat flux was negative.

### **Comparison of COARE and Eta Outputs of Hourly-averaged Friction Velocity**

The COARE and Eta estimates of hourly-averaged friction velocity were compared for the four case studies. Eta forecasts for two starting times were evaluated but there was little difference between the two Eta forecasts and the COARE results. On average, the Eta-predicted hourly-averaged friction velocity values were about a factor of two larger than the COARE hourly-averaged friction velocity values. Since the momentum flux or surface stress is proportional to friction velocity squared, the Eta momentum fluxes were a factor of two to four larger than the COARE estimates.

This difference is difficult to understand from a boundary layer perspective, since it has already been noted that the overall average and maximum sensible and latent heat flux values estimated by COARE and Eta agreed fairly well. Because both sensible and latent heat fluxes are proportional to hourly-averaged friction velocity, we would also expect the Eta-predicted sensible and latent heat flux values to be a factor of two larger than the COARE estimates.

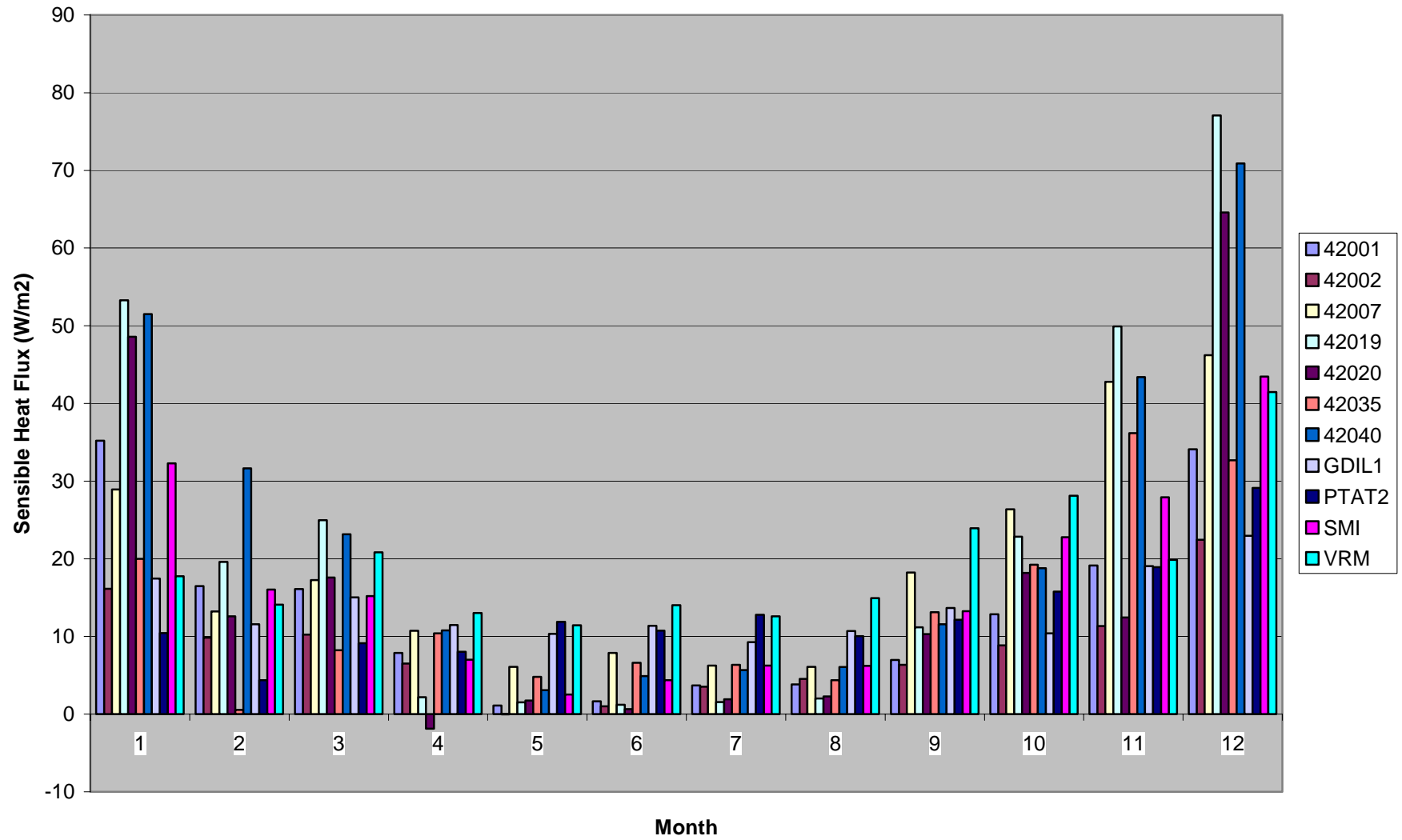


Figure 5-1a. COARE monthly average sensible heat fluxes by site for May 1998 through October 2001.

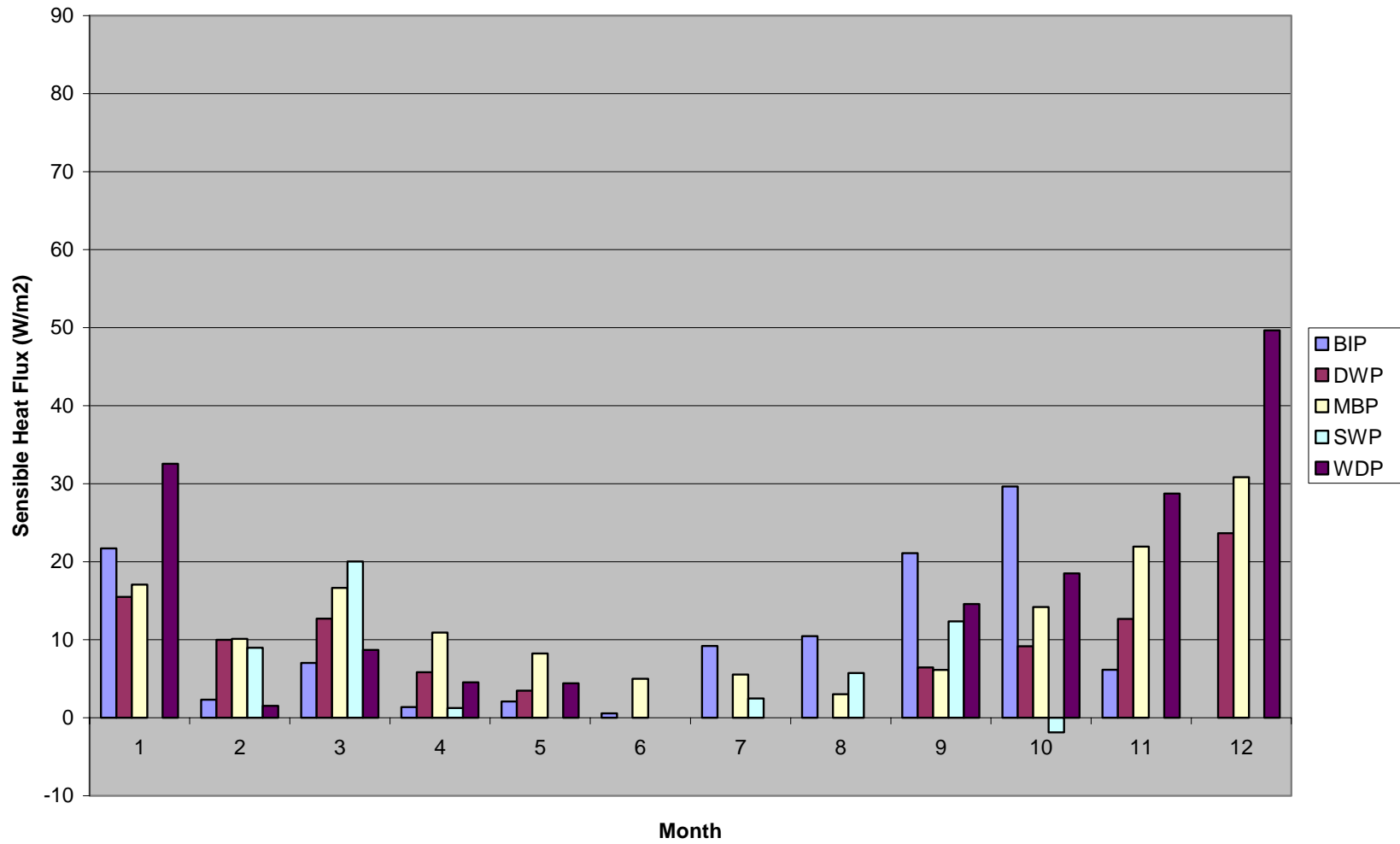


Figure 5-1b. COARE monthly average sensible heat fluxes by BAMP site for September 2000 through September 2001.

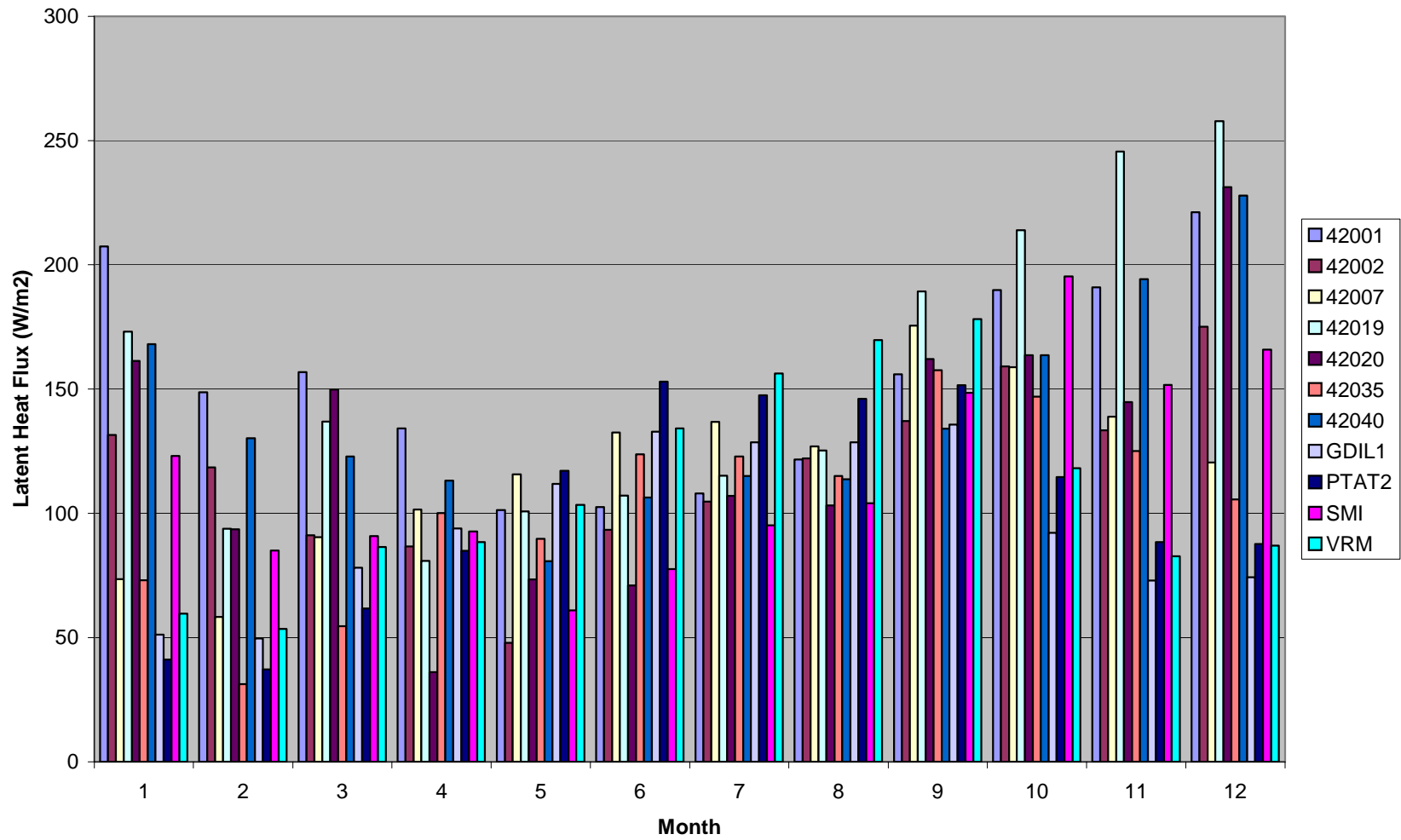


Figure 5-2a. COARE monthly average latent heat fluxes by site for May 1998 through October 2001.

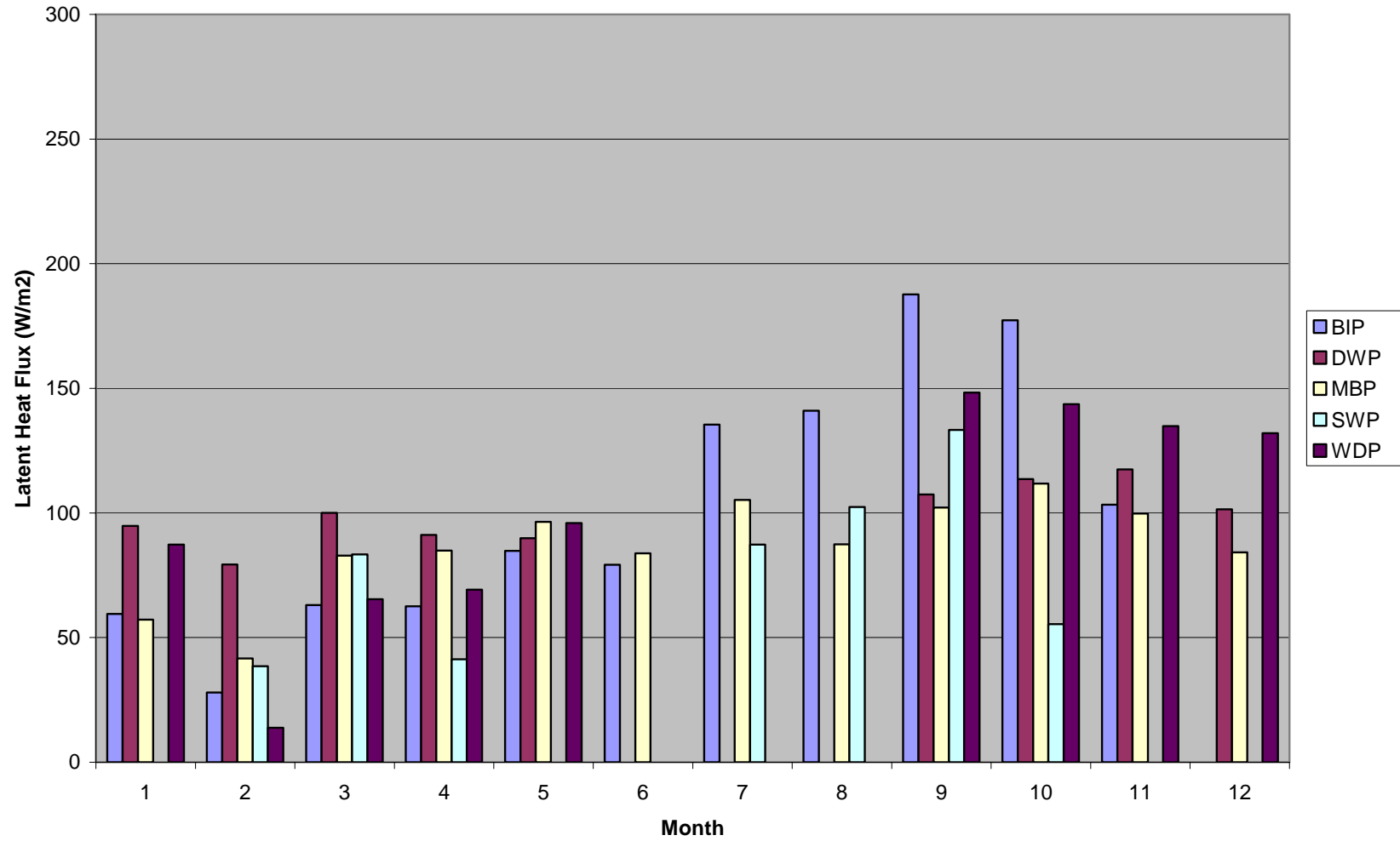


Figure 5-2b. COARE monthly average latent heat fluxes by BAMP site for September 2000 through September 2001

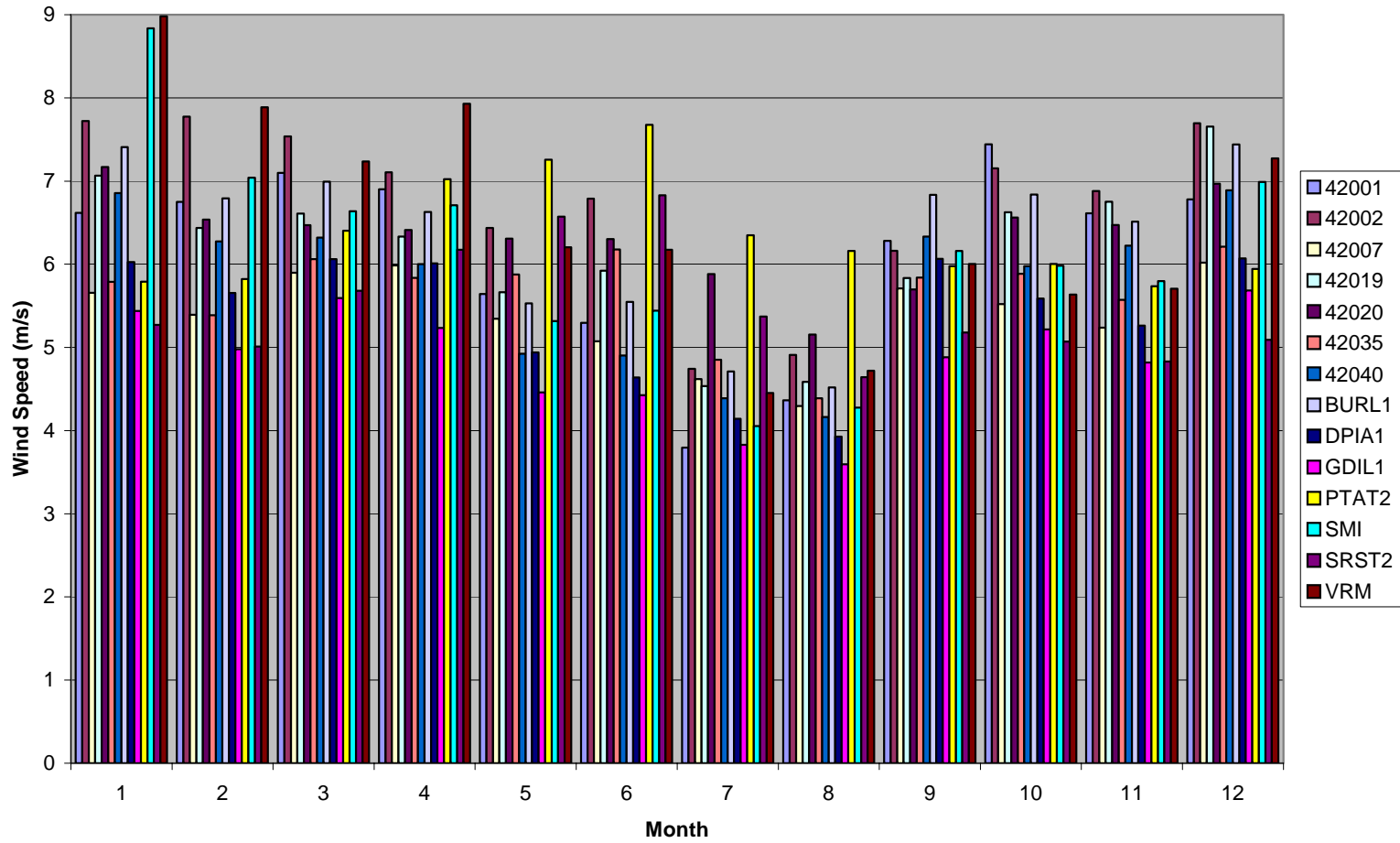


Figure 5-3a. Observed monthly average wind speed by site for May 1998 through October 2001.

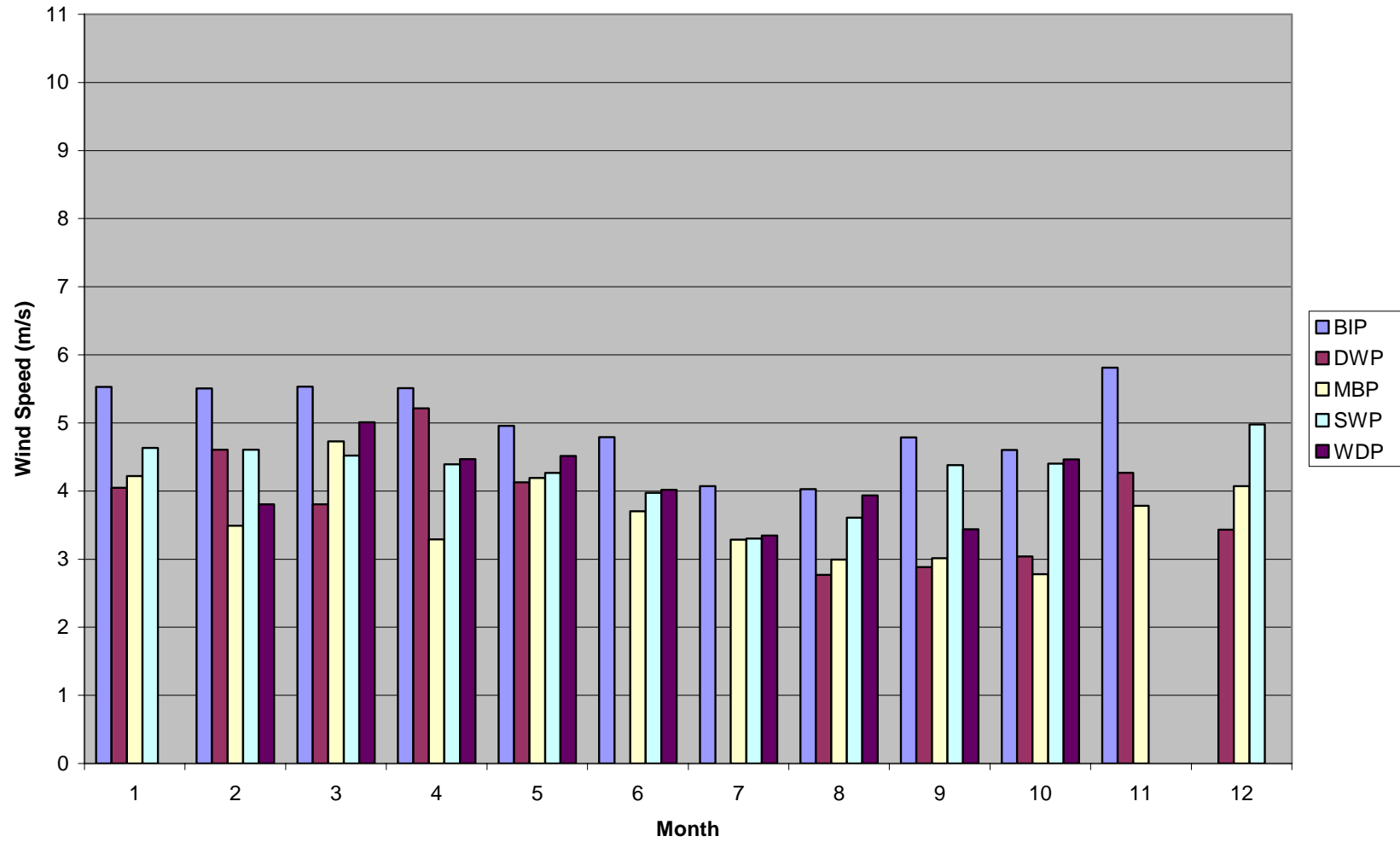


Figure 5-3b. Observed monthly average wind speed by BAMP site for September 2000 through September 2001.

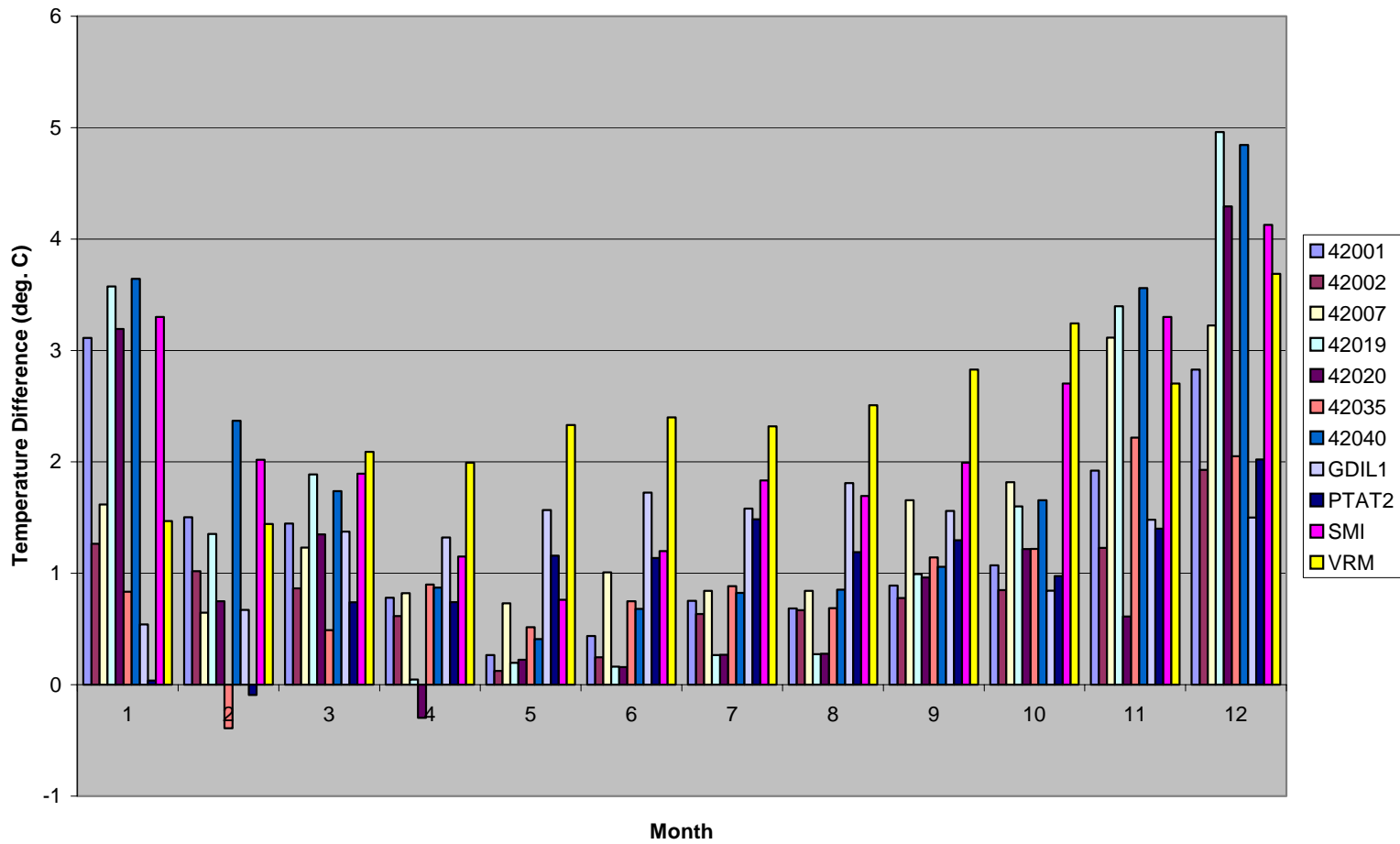


Figure 5-4a. Monthly average skin temperature minus air temperature by site for May 1998 through October 2001.

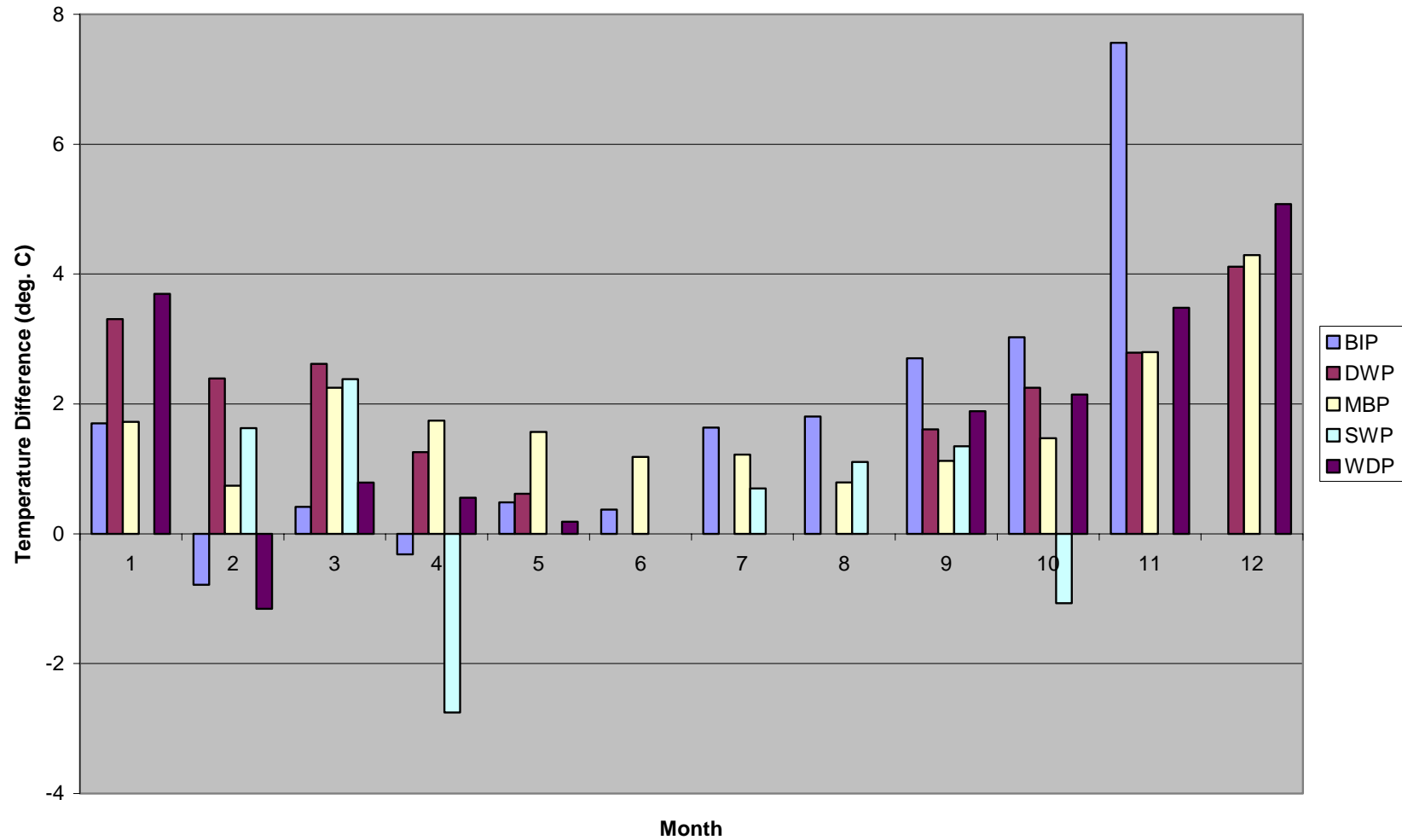


Figure 5-4b. COARE monthly average skin temperature minus air temperature by BAMP site for September 2000 through September 2001.

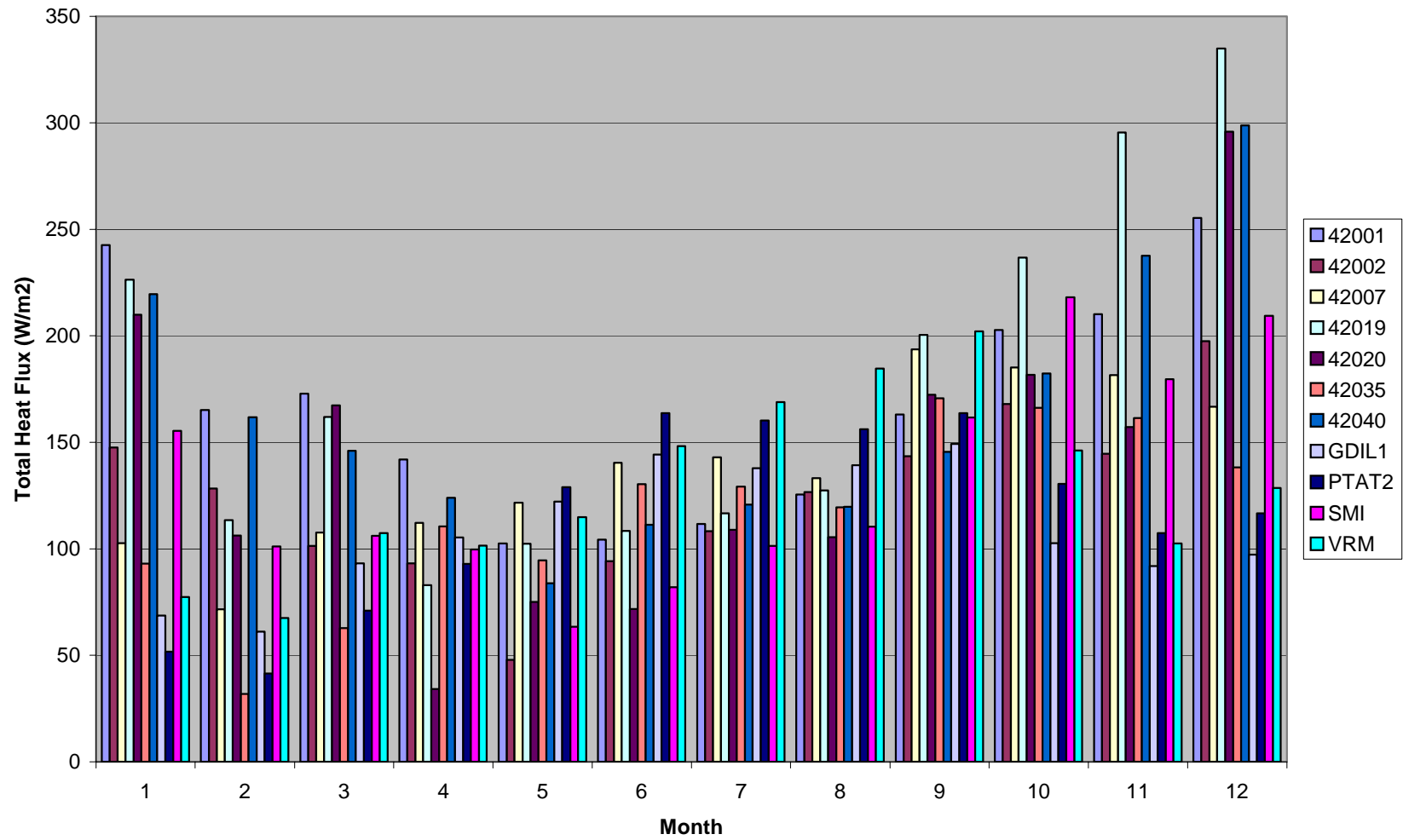


Figure 5-5a. COARE monthly average of total heat fluxes (sensible plus latent) by site for May 1998 through October 2001.

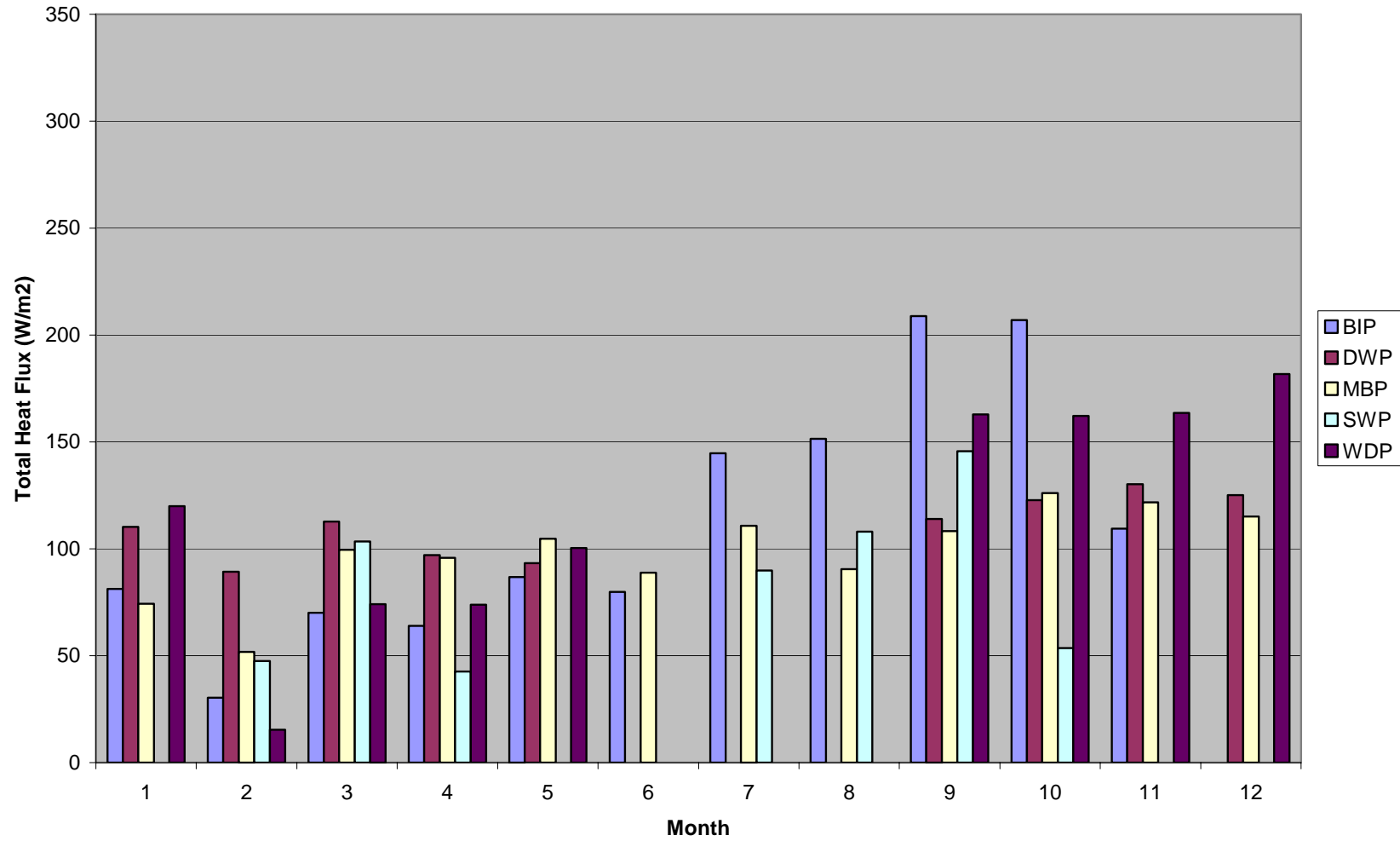


Figure 5-5b. COARE monthly average total heat fluxes (sensible plus latent) by BAMP site for September 2000 through September 2001.

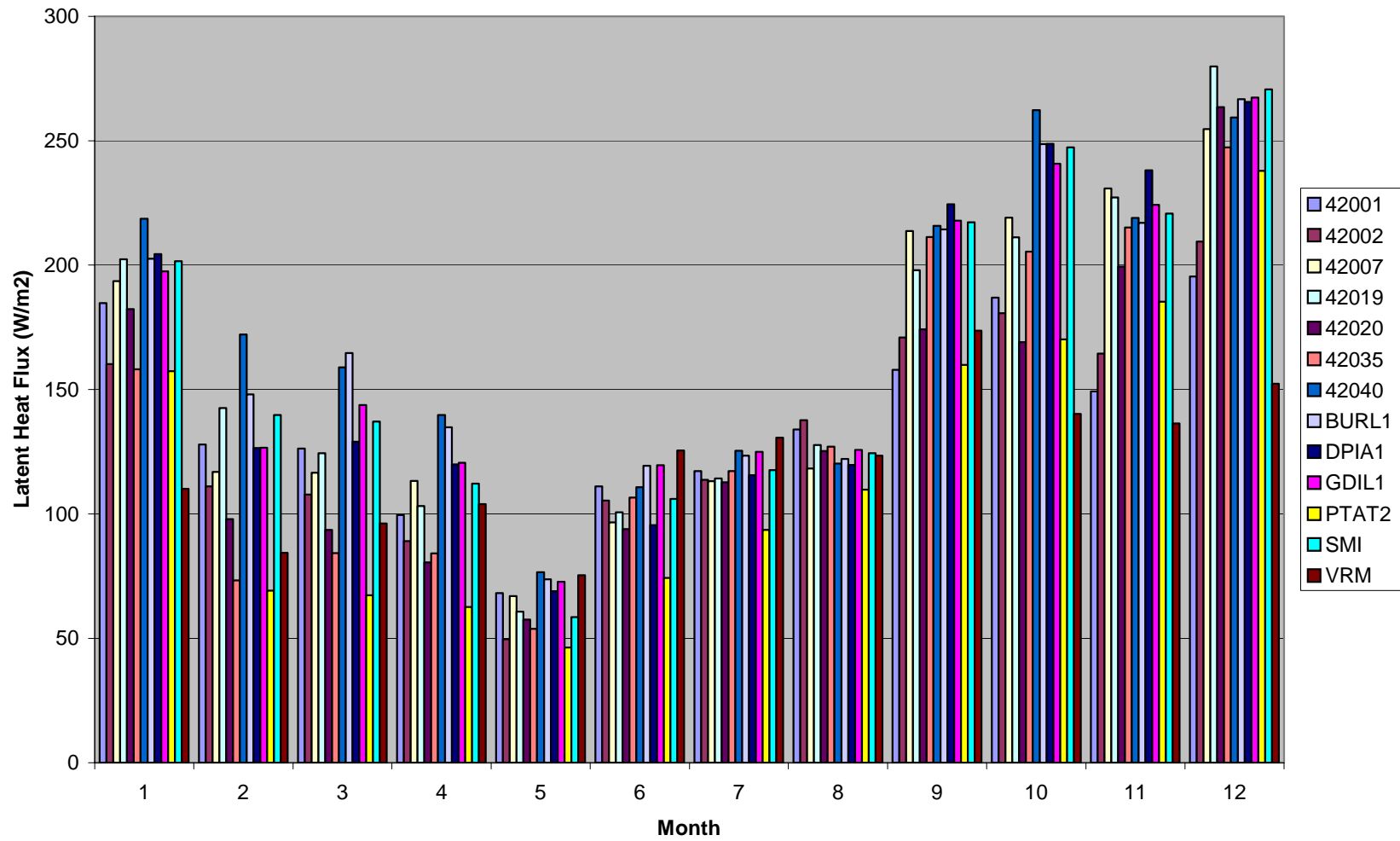


Figure 5-6. Eta monthly average latent heat fluxes by site for May 1998 through October 2001, for the 6- to 12-hr forecast.

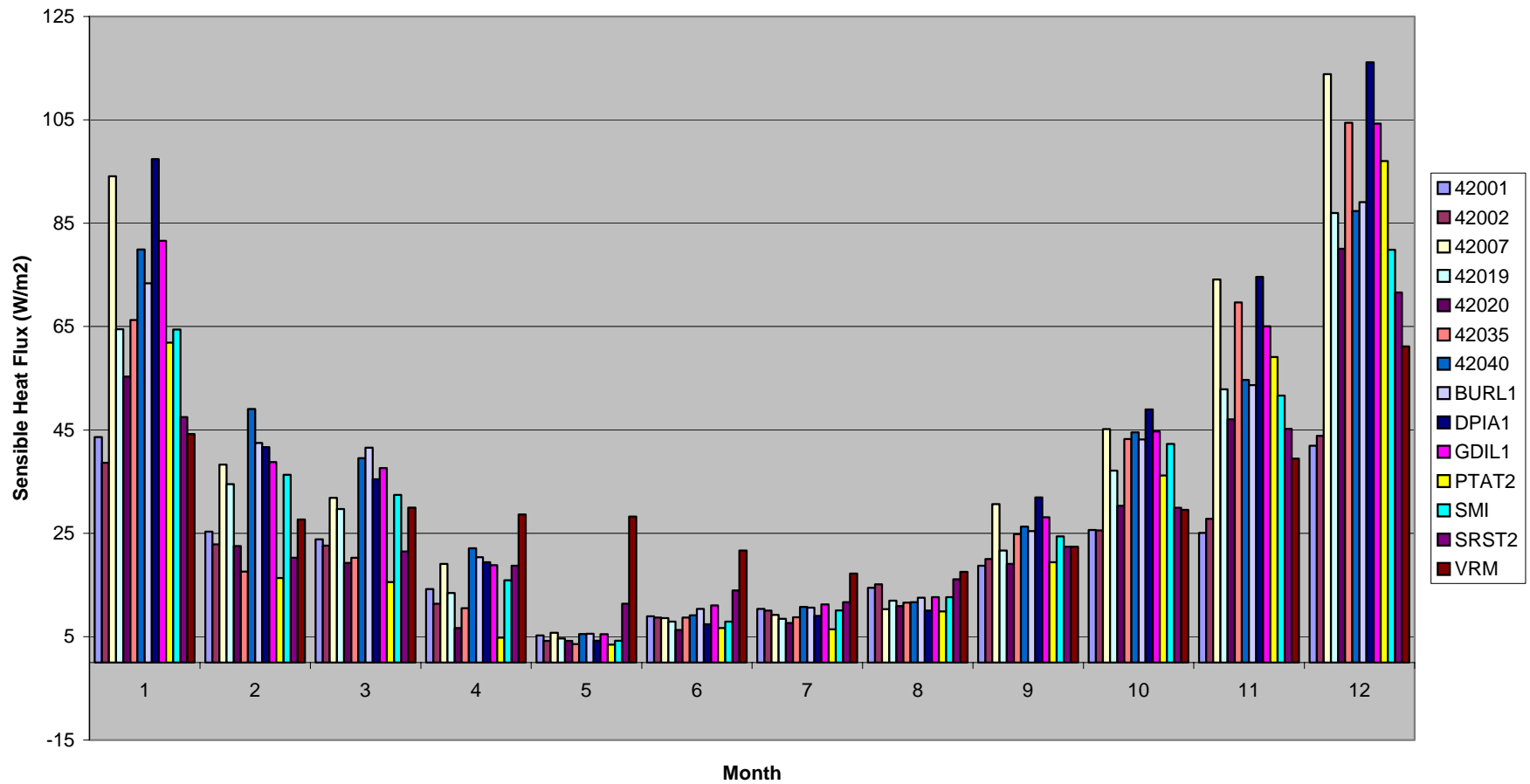


Figure 5-7. Eta monthly average sensible heat fluxes by site for May 1998 through October 2001, for the 6- to 12-hr forecast.

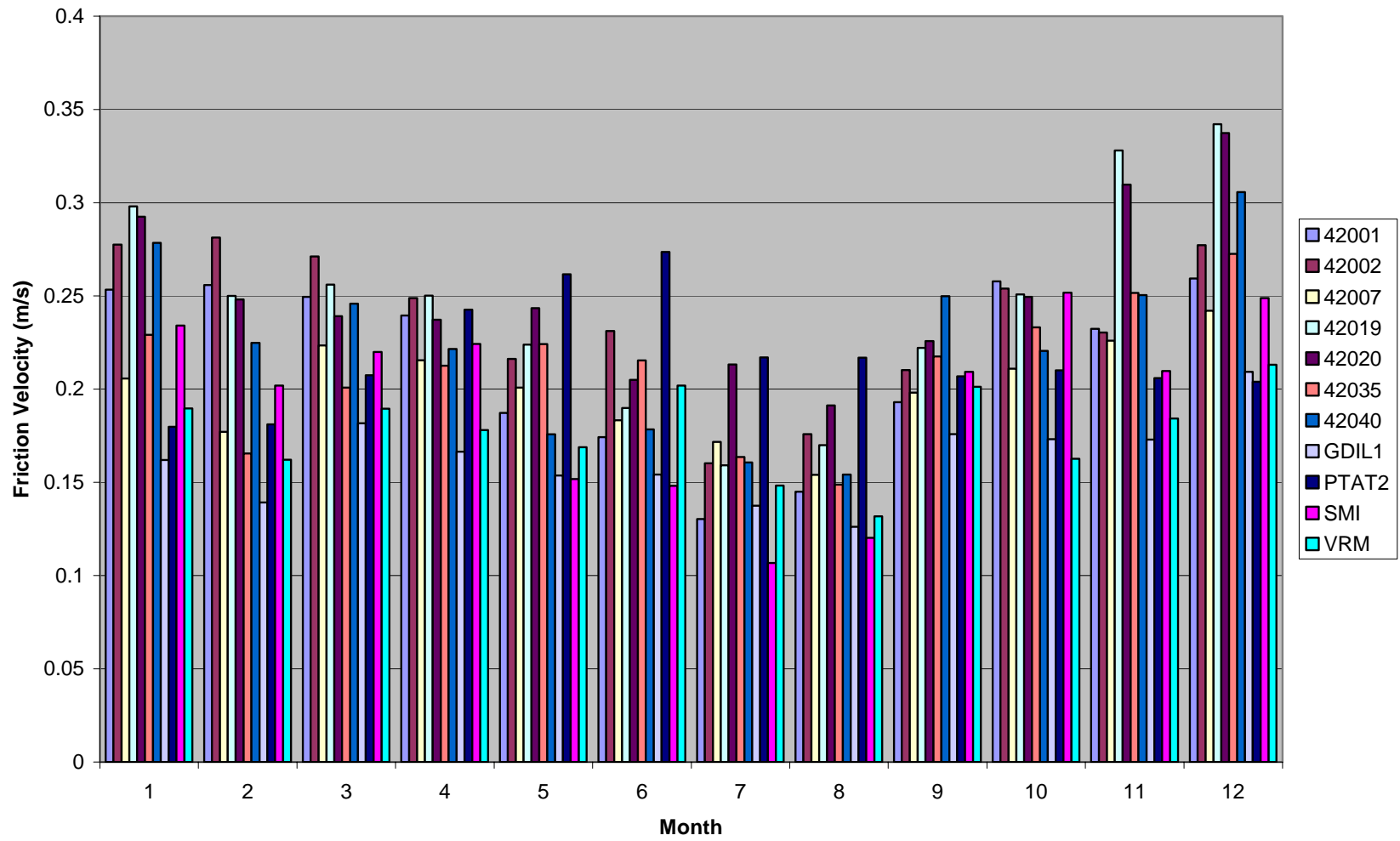


Figure 5-8a. COARE monthly average friction velocity by site for May 1998 through October 2001.

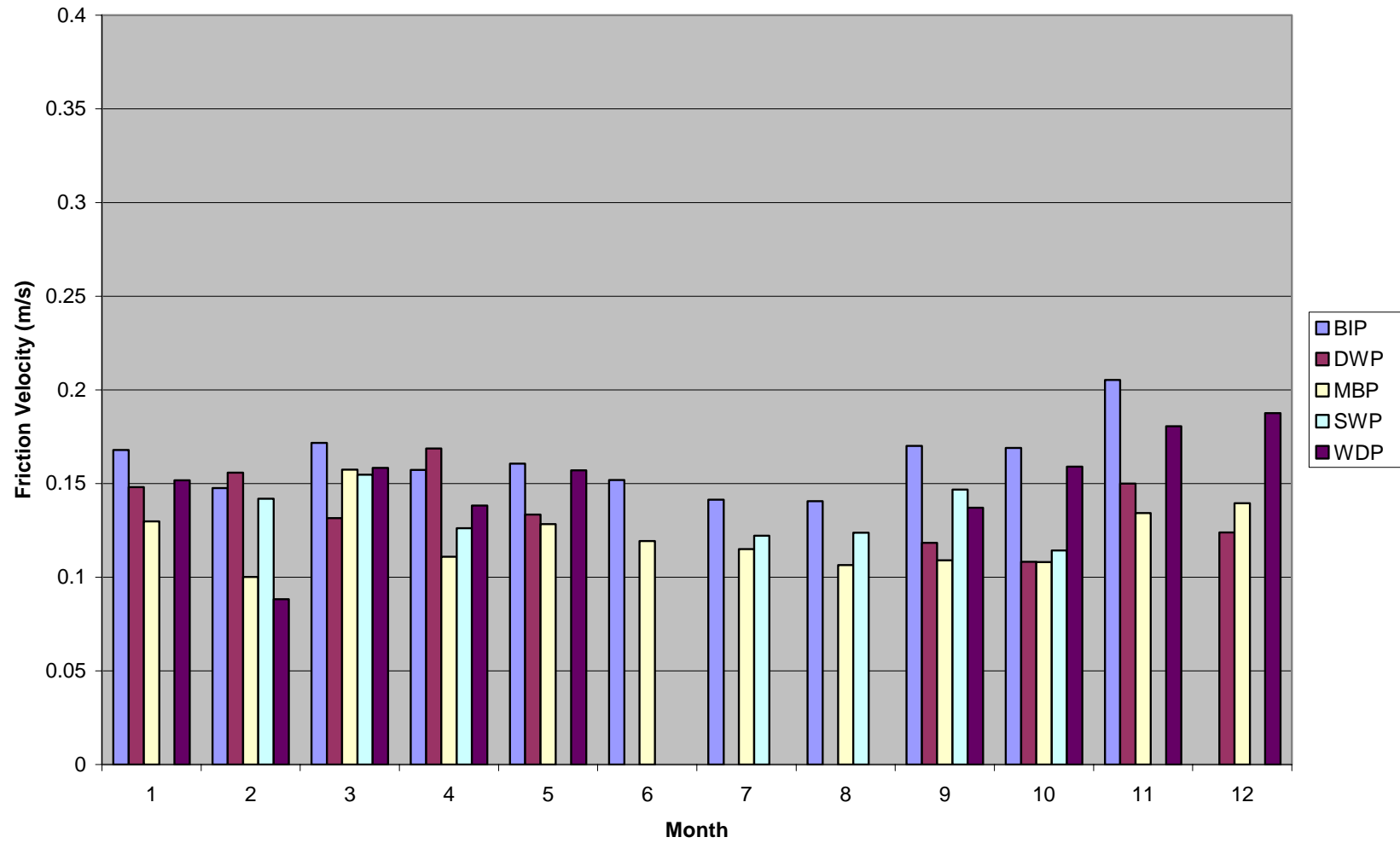


Figure 5-8b. COARE monthly average friction velocity by BAMP site for September 2000 through September 2001.

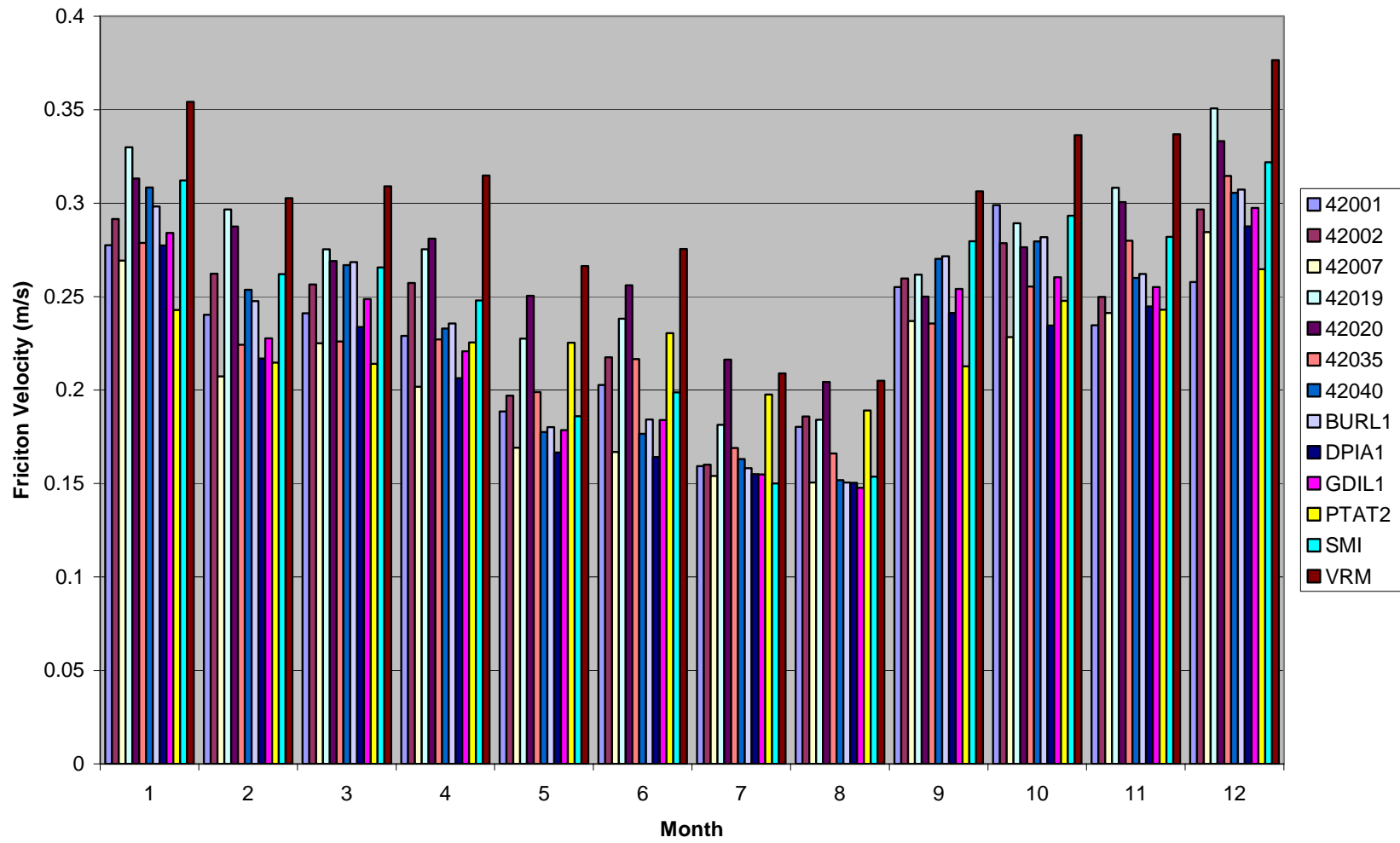


Figure 5-9. Eta monthly average friction velocity by site for May 1998 through October 2001, for the 6- to 12-hr forecast.

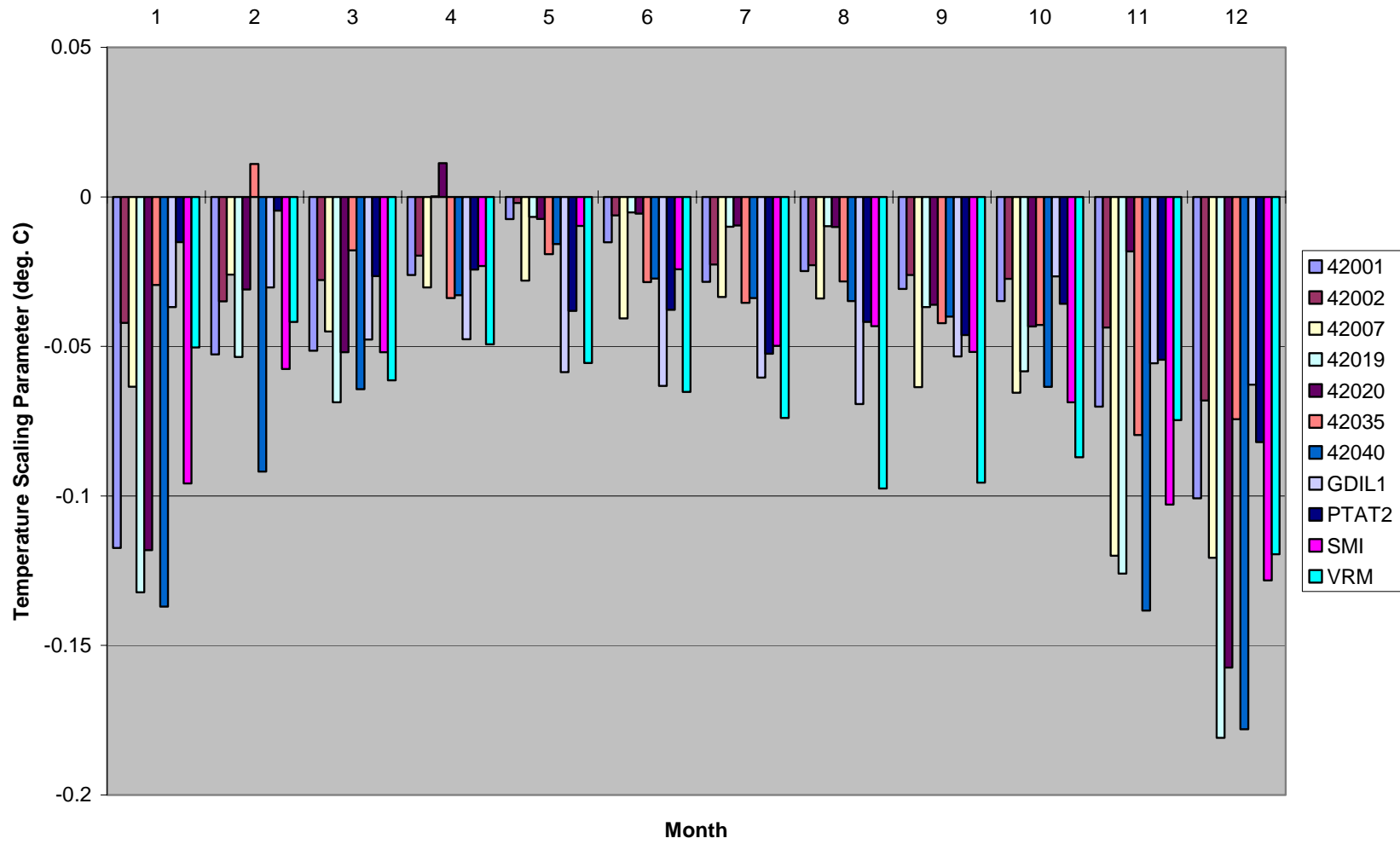


Figure 5-10a. COARE calculated monthly average temperature scaling parameter by site for May 1998 through October 2001.

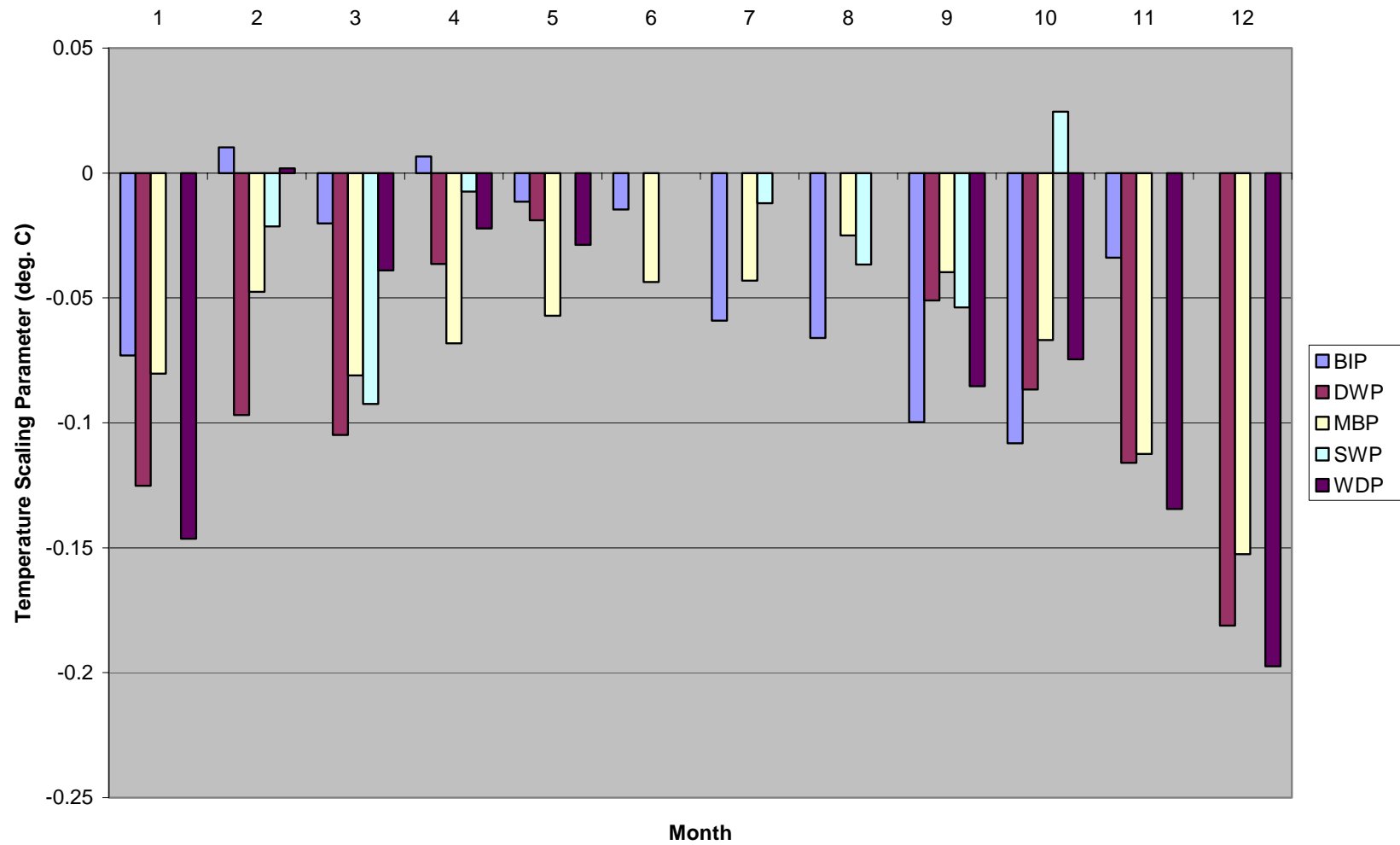


Figure 5-10b. COARE calculated monthly average temperature scaling parameter by BAMP site for September 2000 through September 2001.

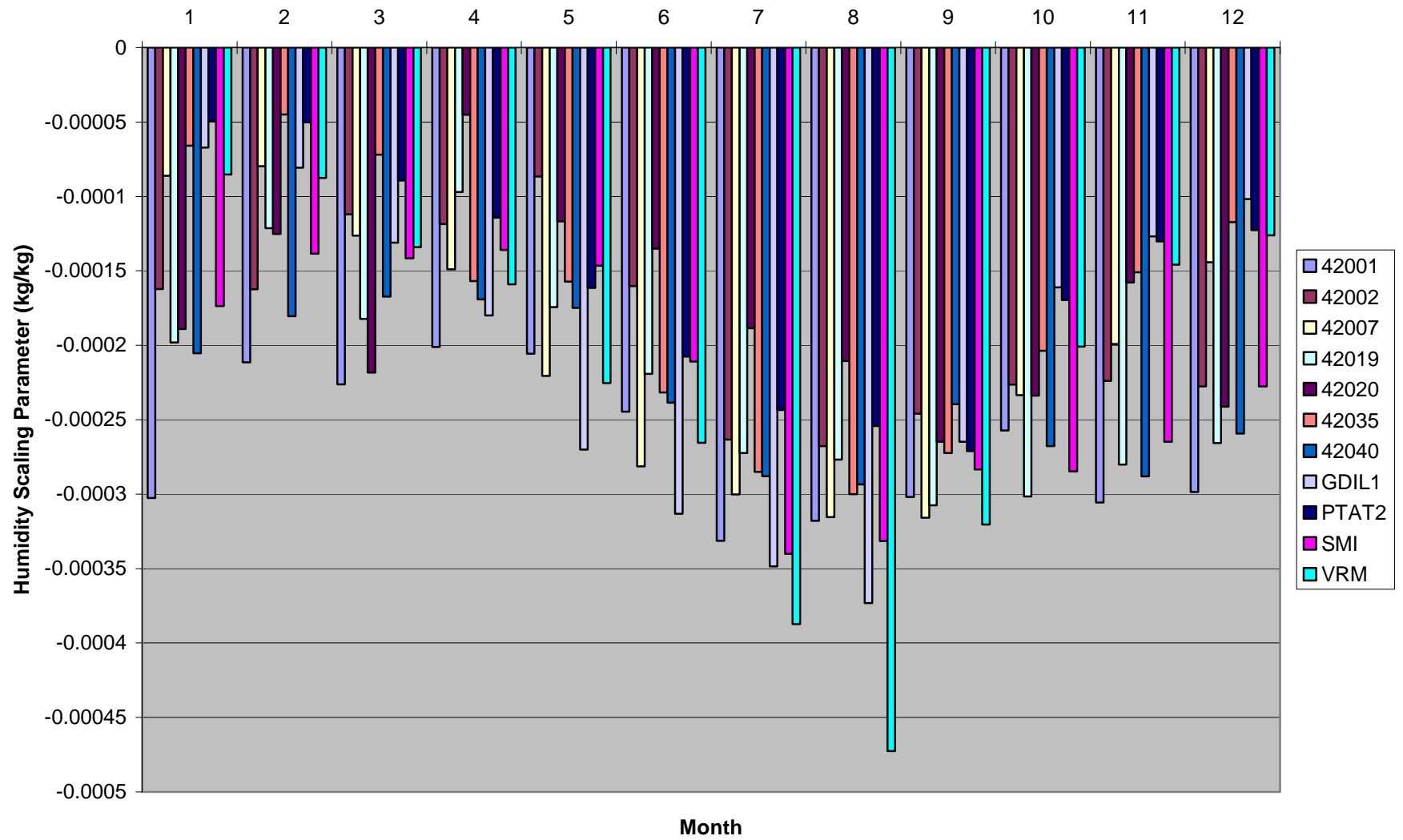


Figure 5-11a. COARE calculated monthly average humidity scaling parameter by site for May 1998 through October 2001.

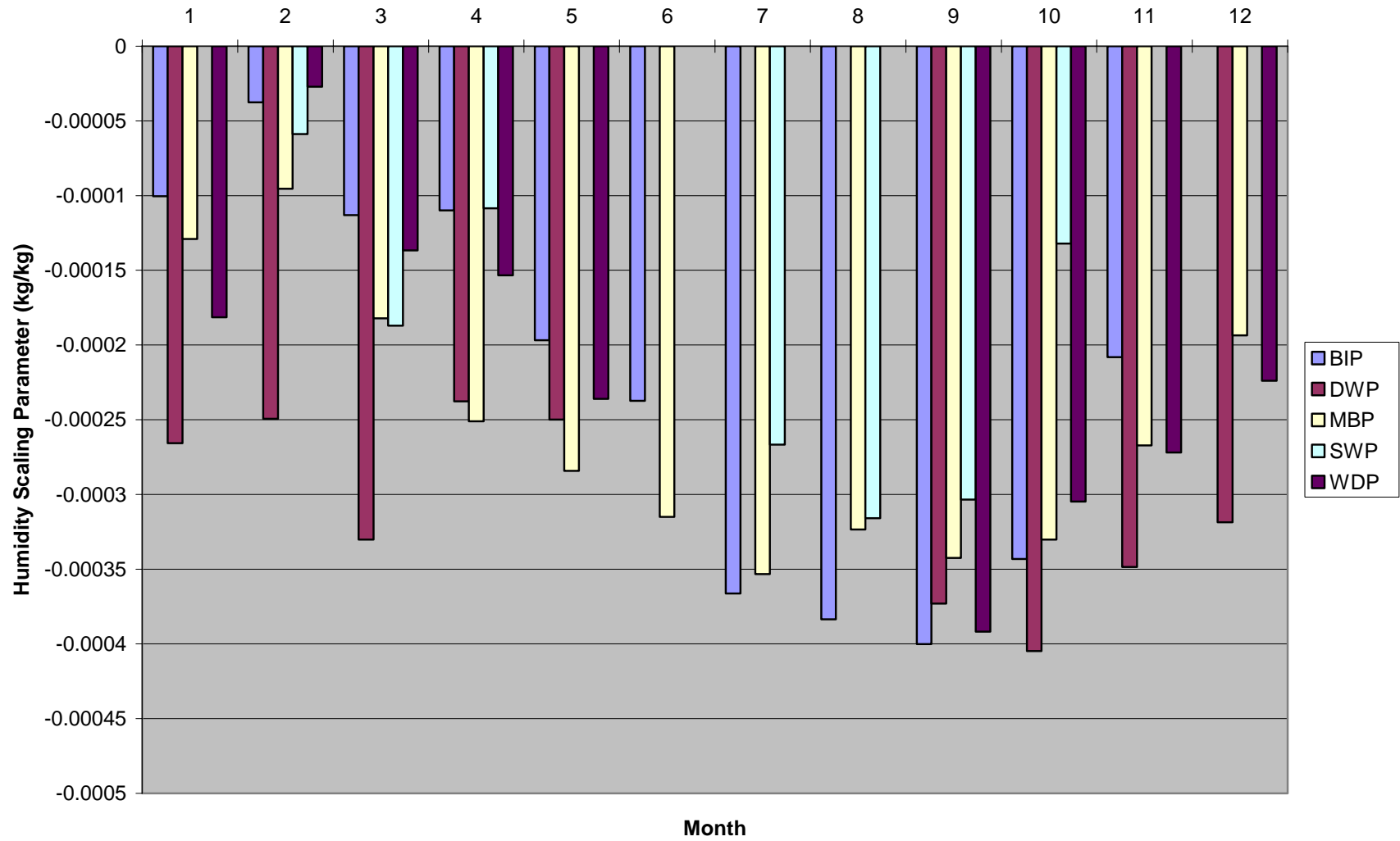


Figure 5-11b. COARE calculated monthly average humidity scaling parameter by BAMP site for September 2000 through September 2001.

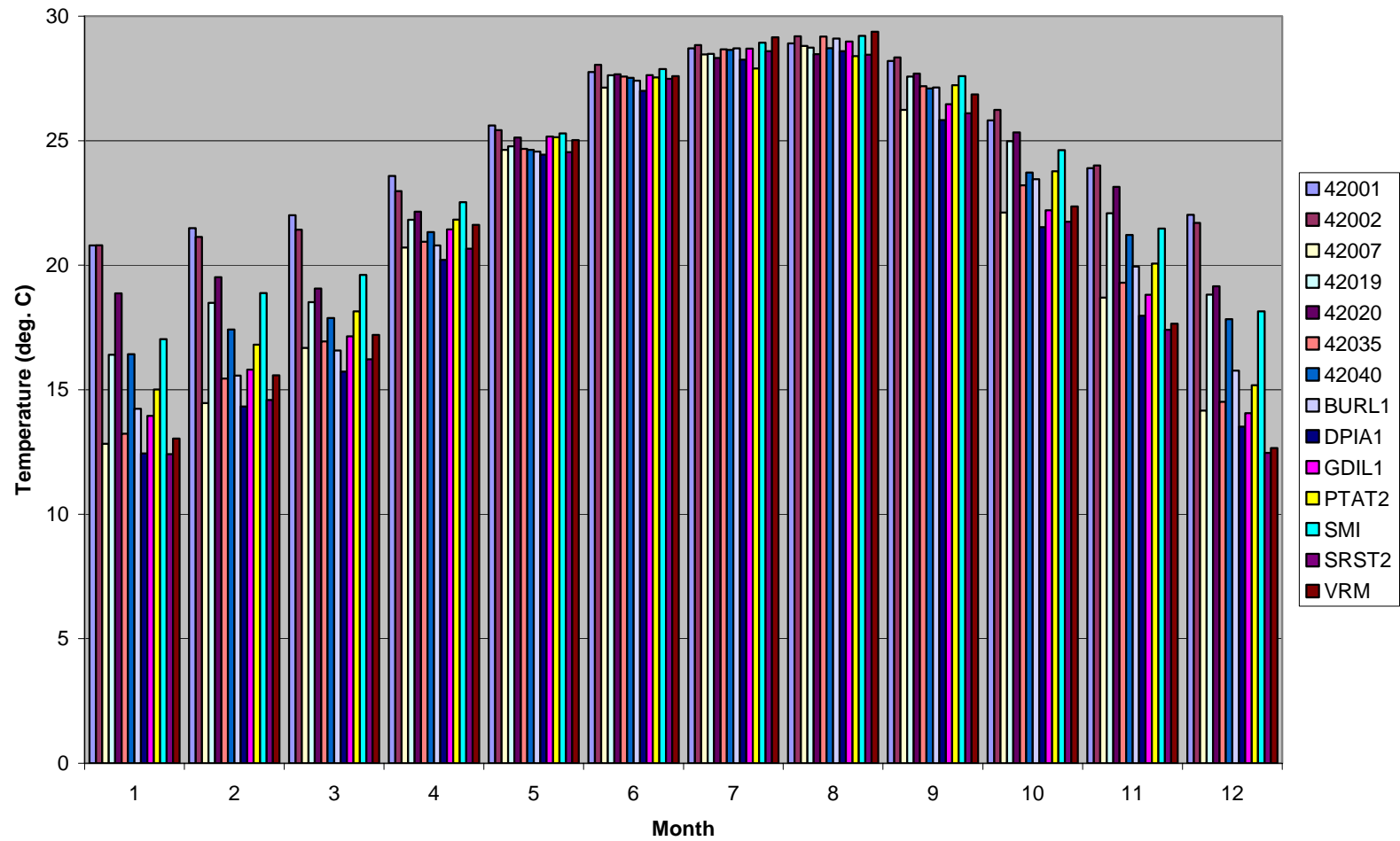


Figure 5-12a. Observed monthly average air temperature by site for May 1998 through October 2001.

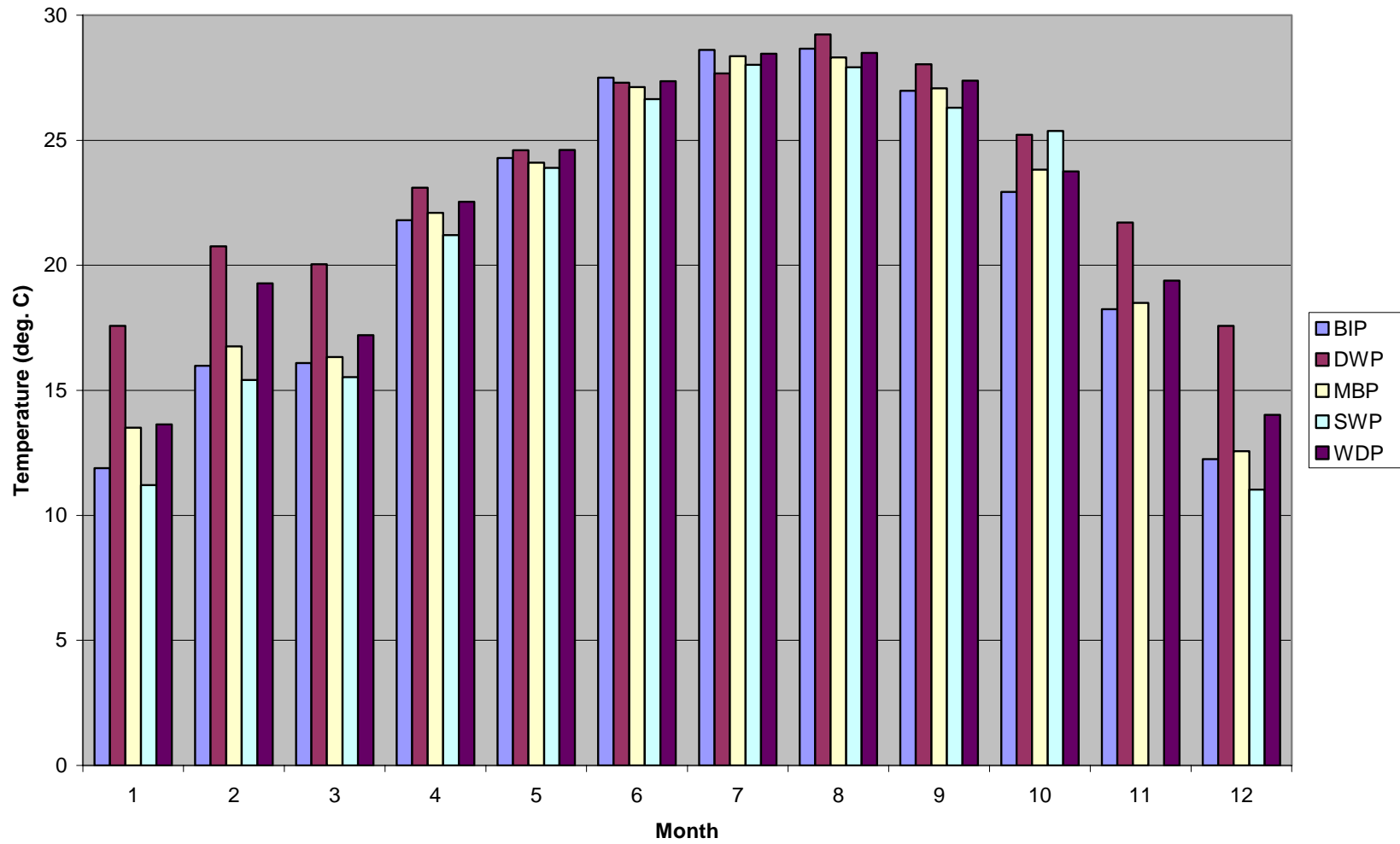


Figure 5-12b. Observed monthly average air temperature by BAMP site for September 2000 through September 2001.

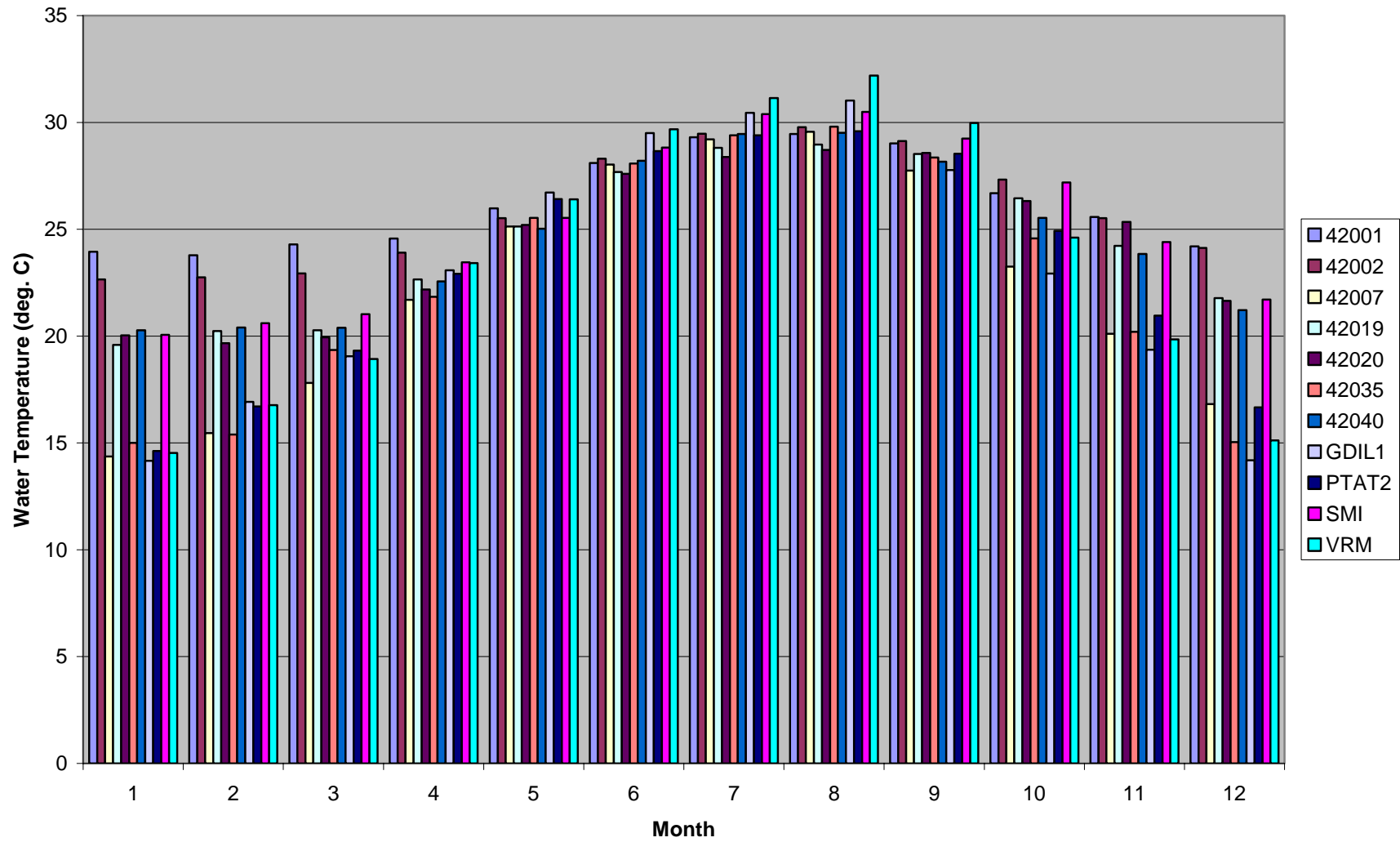


Figure 5-13a. Observed monthly average skin temperature by site for May 1998 through October 2001.

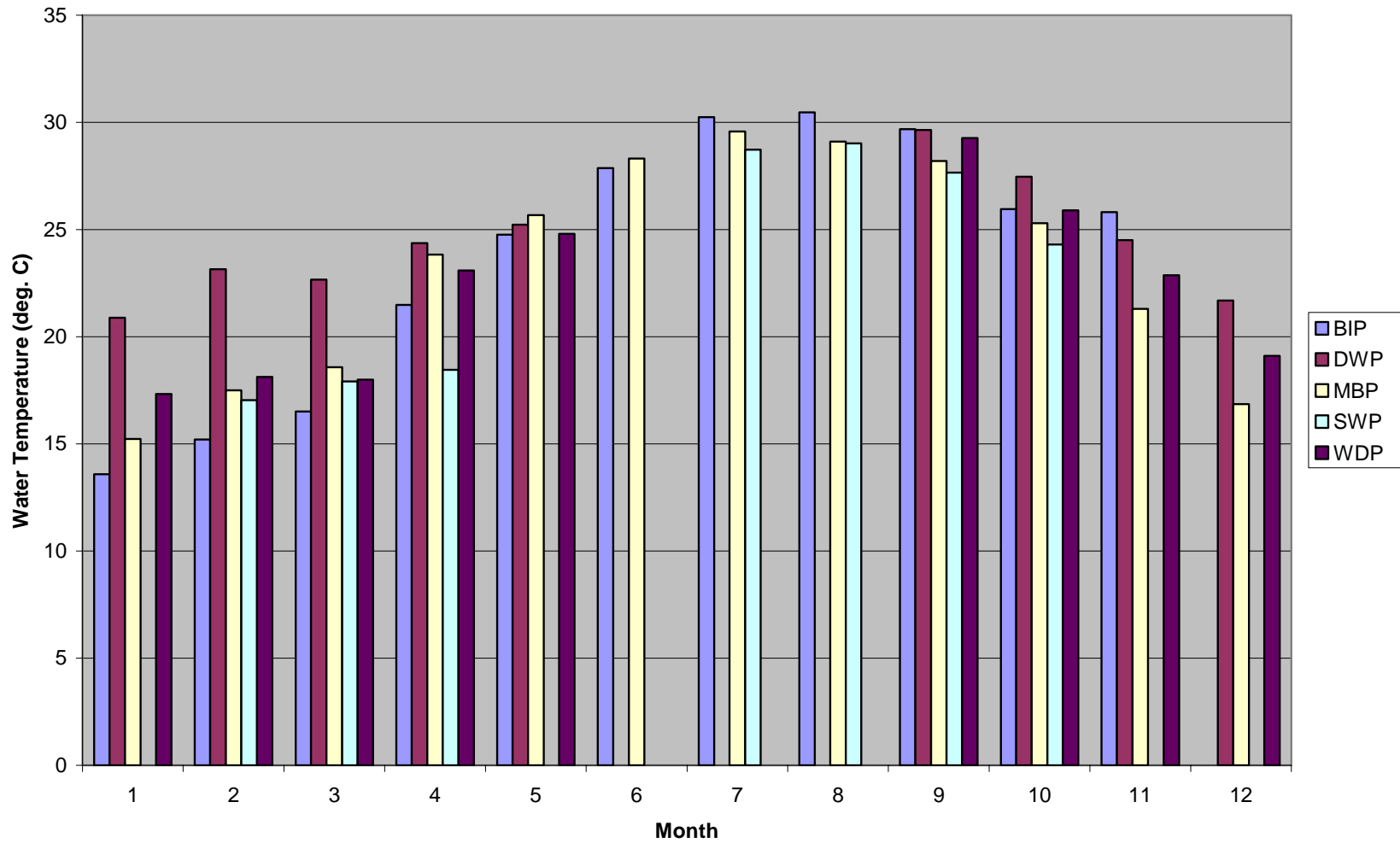


Figure 5-13b. Observed monthly average skin temperature by BAMP site for September 2000 through September 2001.

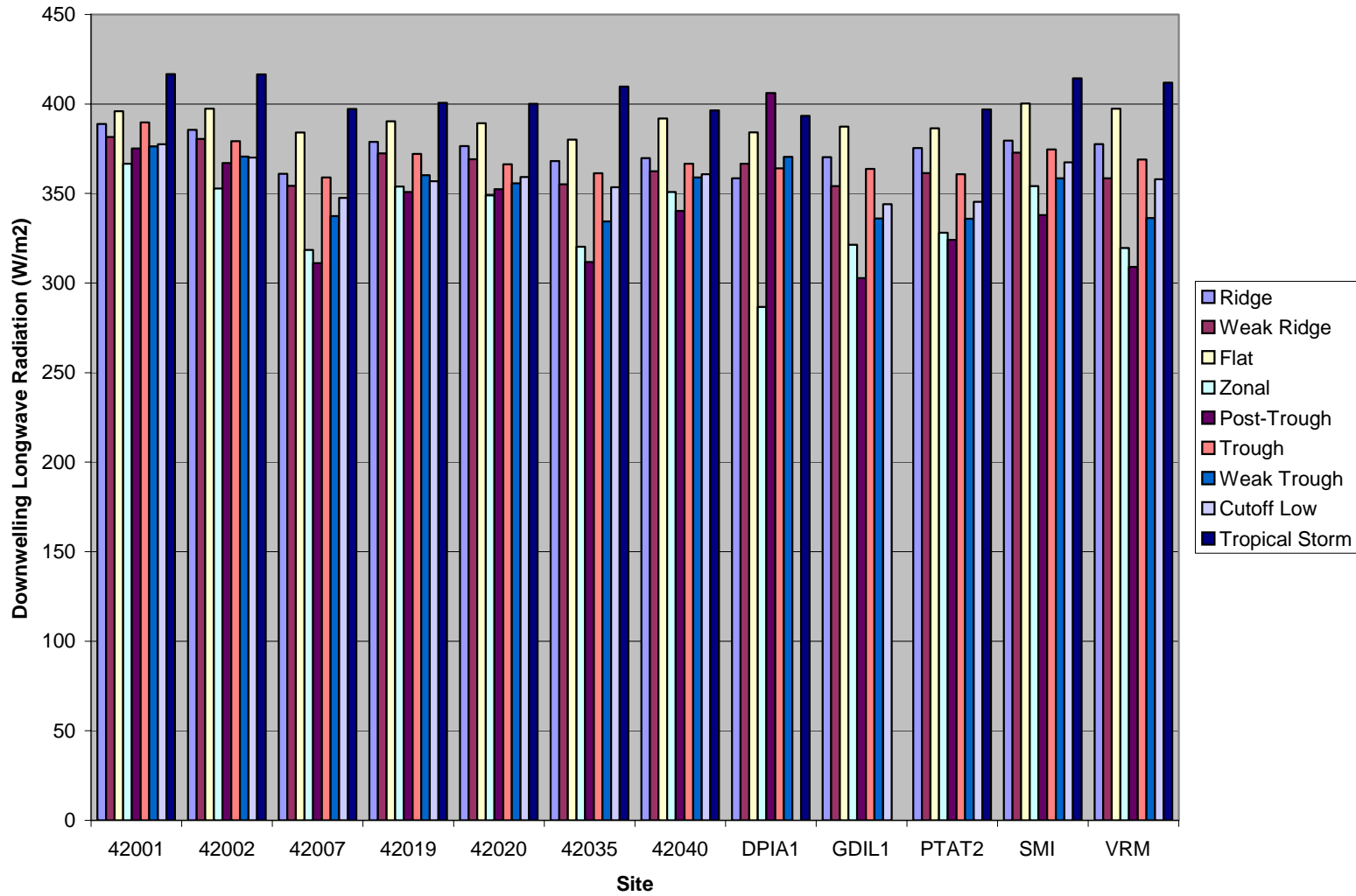


Figure 5-14. Eta average downwelling longwave radiation by synoptic class by site for May 1998 through October 2001, for the 6- to 12-hr forecast.

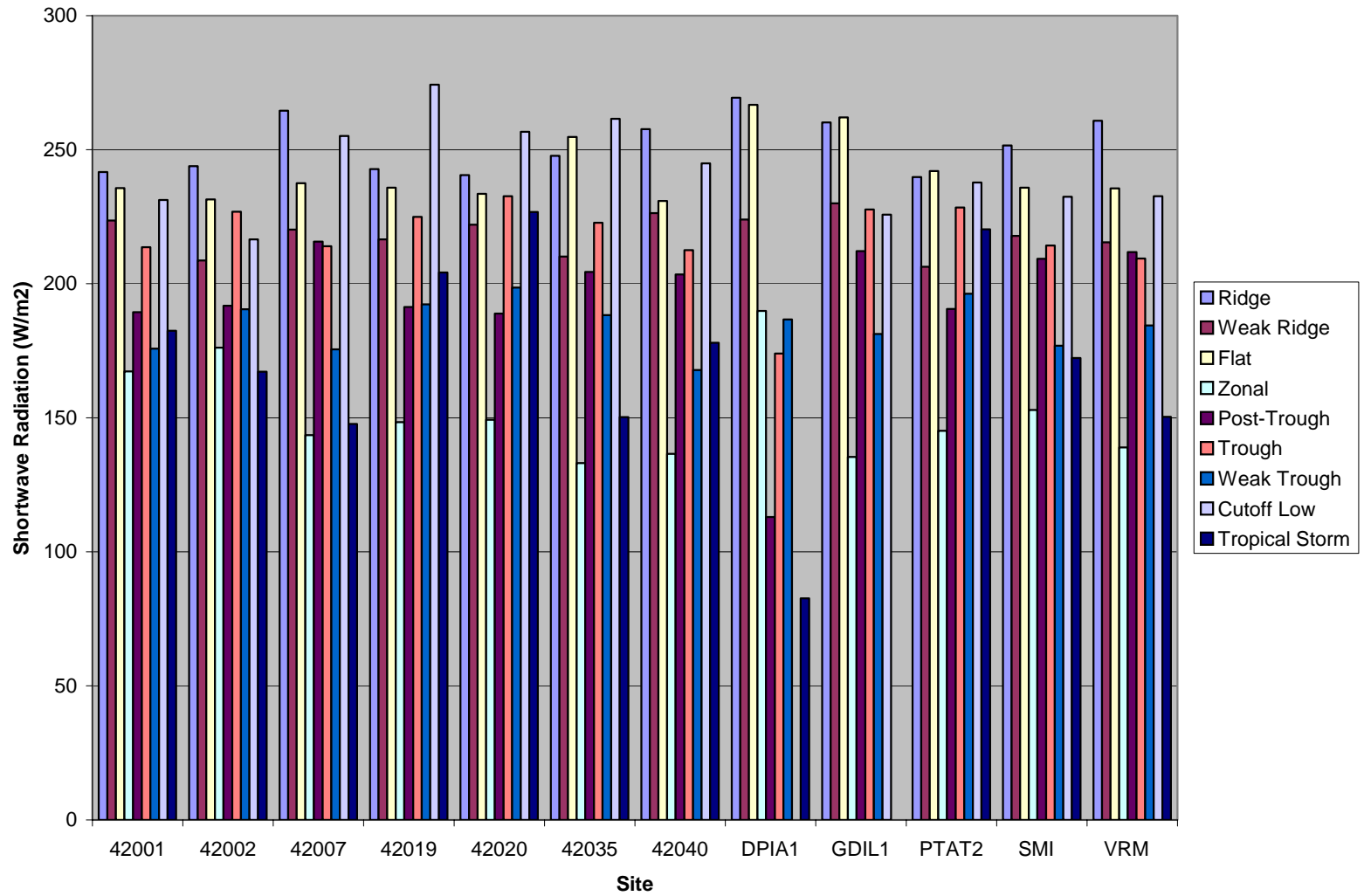


Figure 5-15. Eta average shortwave radiation by synoptic class by site for May 1998 through October 2001, for the 6-to 12-hr forecast.

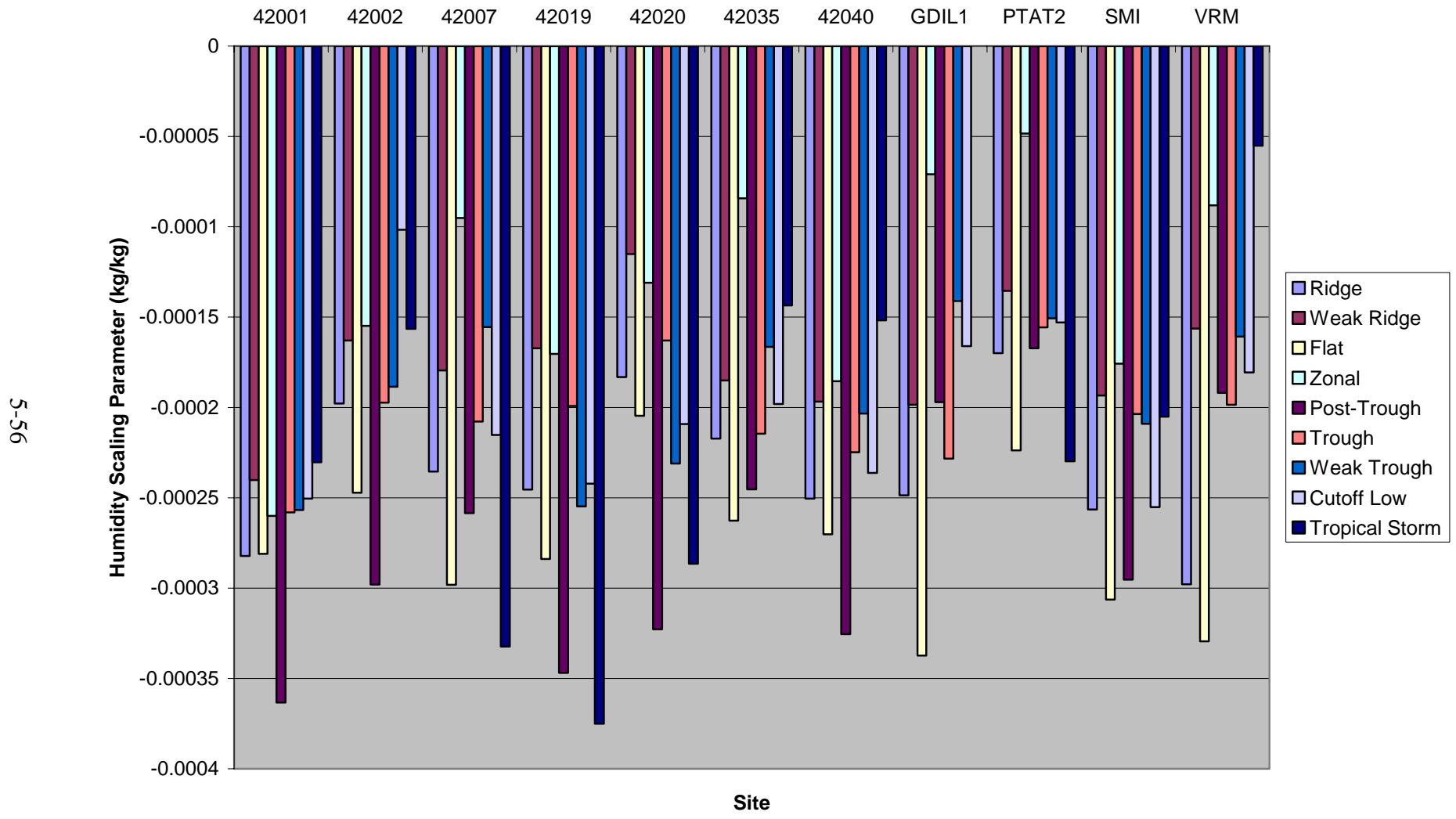


Figure 5-16a. COARE average humidity scaling parameter by synoptic class by site for May 1998 through October 2001.

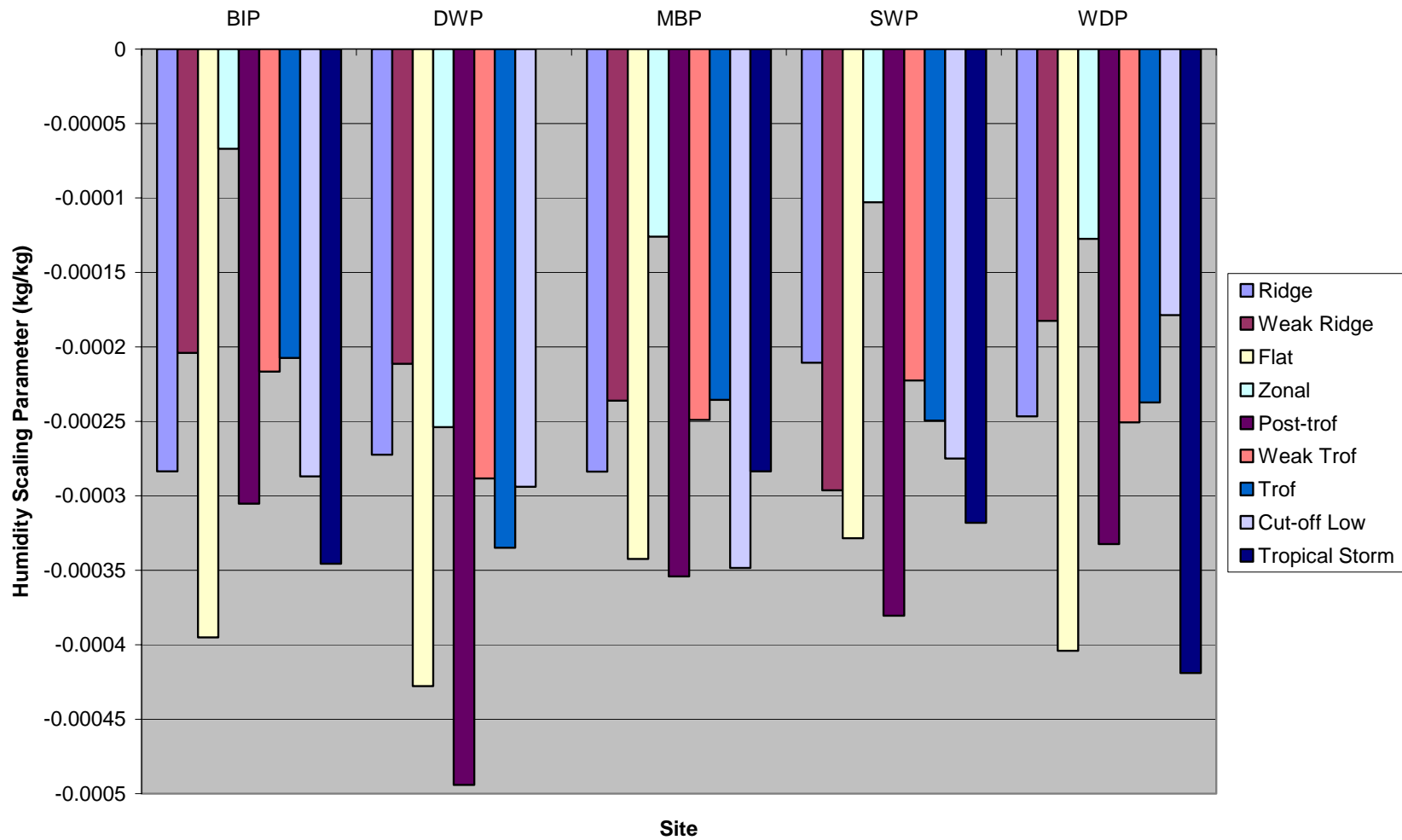


Figure 5-16b. COARE average humidity scaling parameter by synoptic class by BAMP site for September 2000 through September 2001.

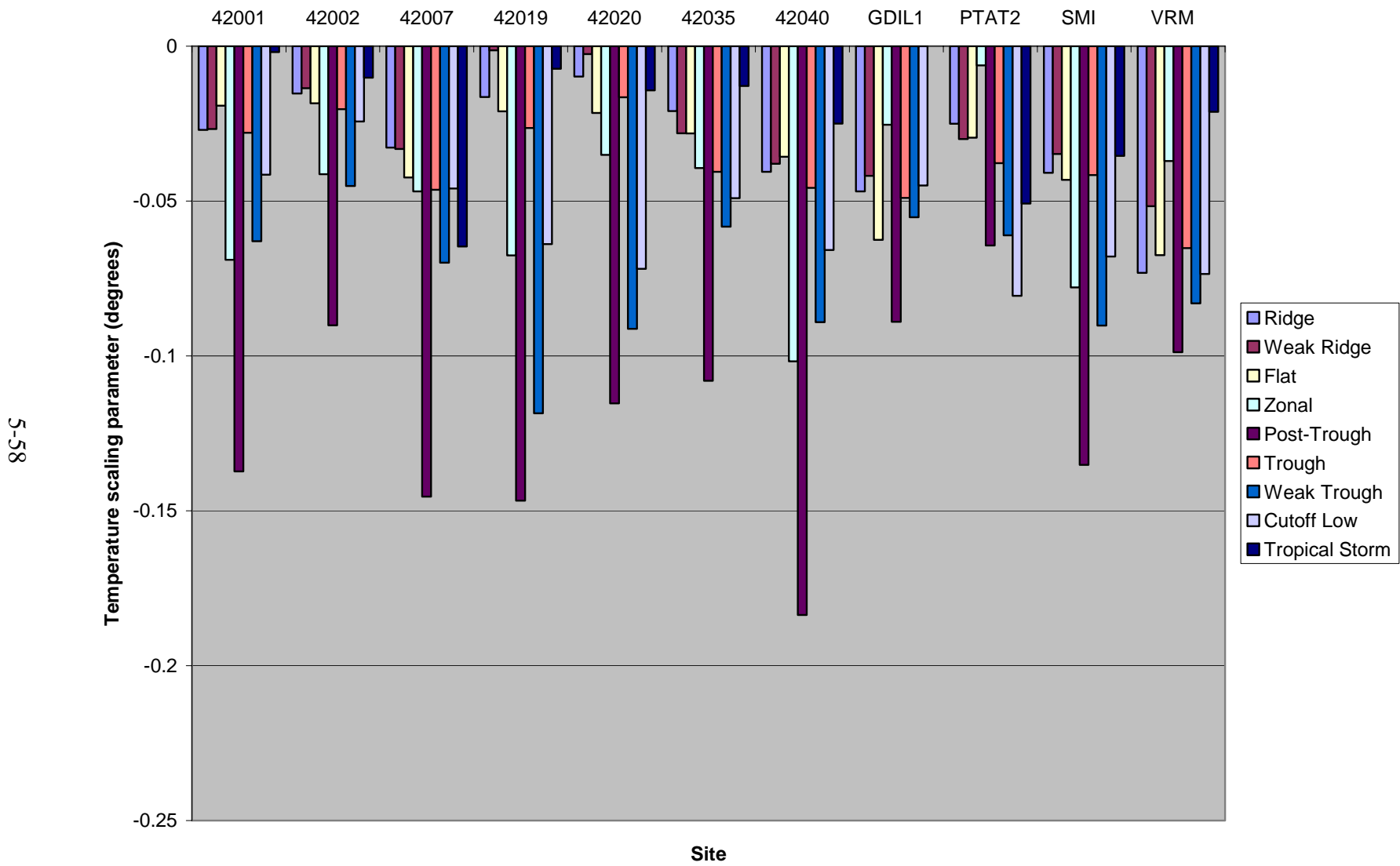


Figure 5-17a. COARE average temperature scaling parameter by synoptic class by site for May 1998 through October 2001.

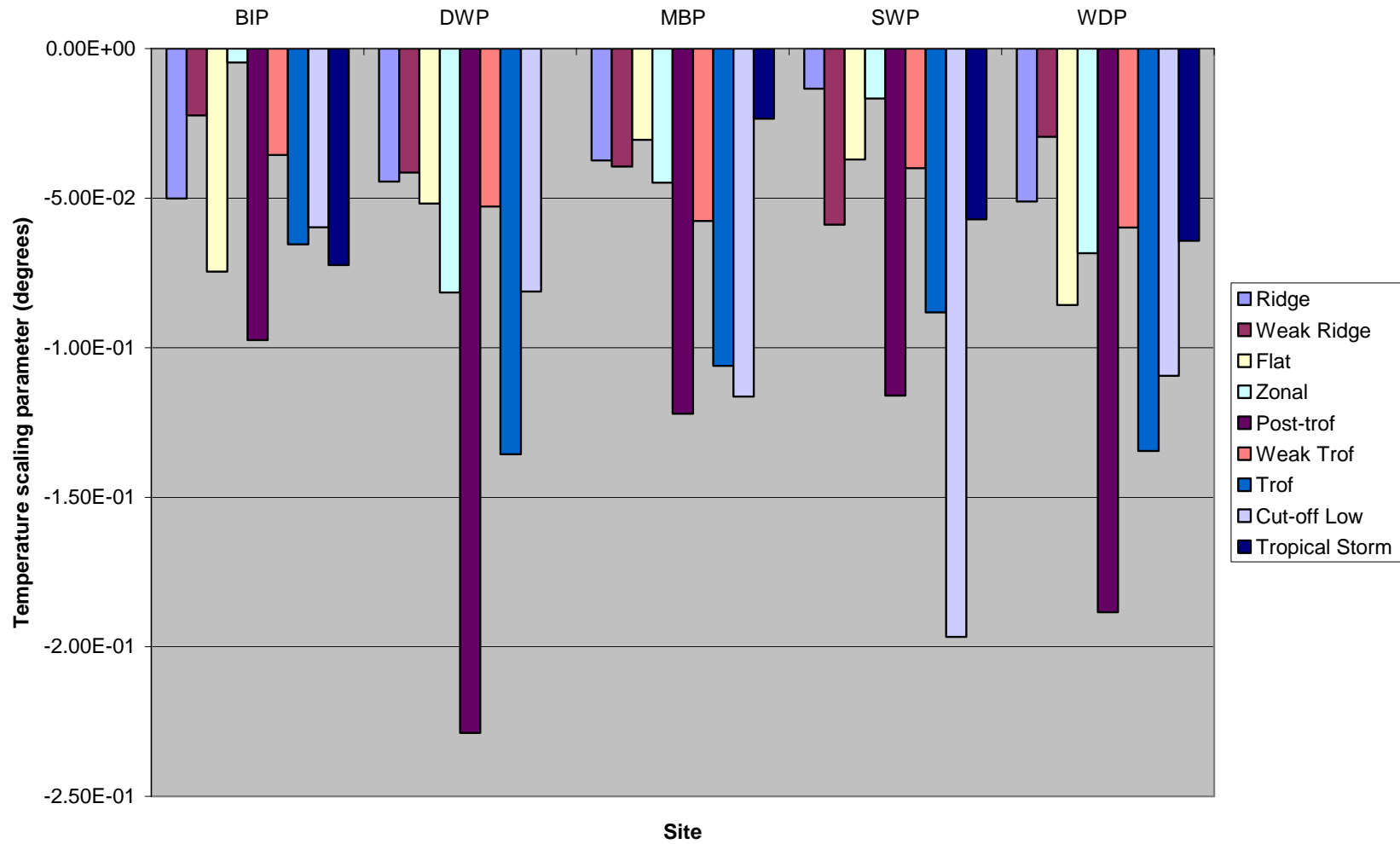


Figure 5-17b. COARE average temperature scaling parameter by synoptic class by BAMP site for September 2000 through September 2001.

09-5

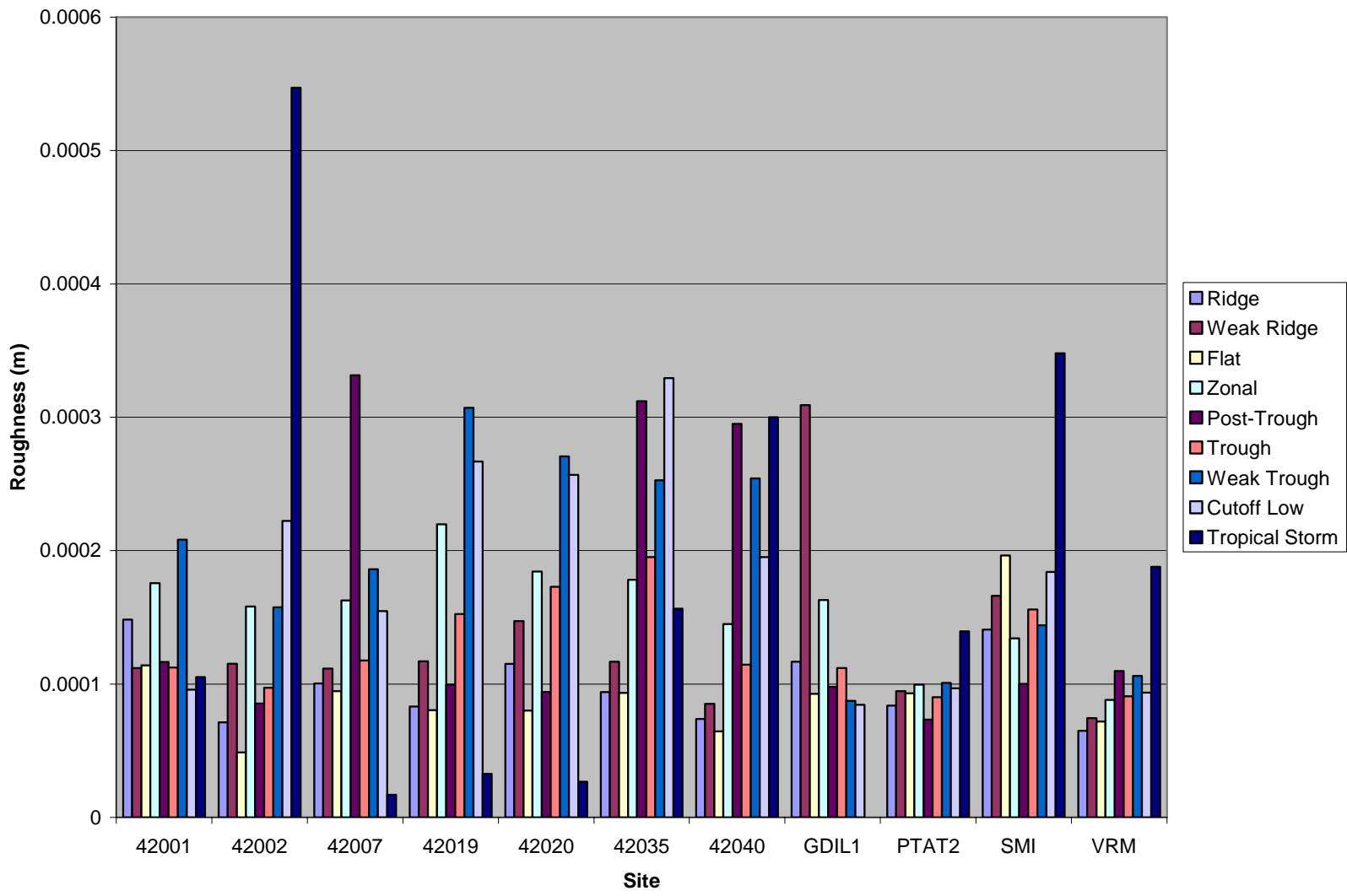


Figure 5-18a. COARE surface roughness by synoptic class by site for May 1998 through October 2001.

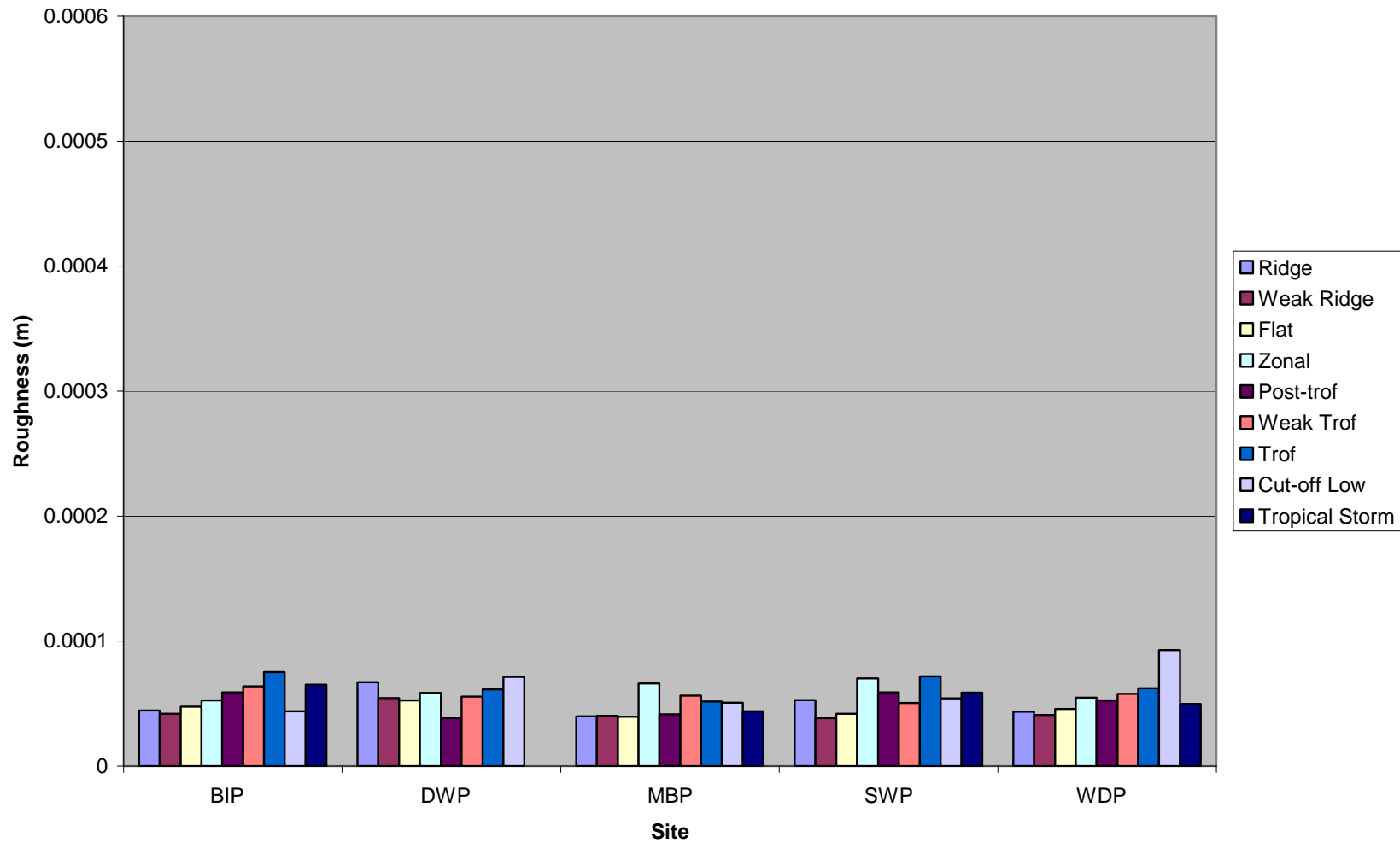


Figure 5-18b. COARE surface roughness by synoptic class by BAMP site for September 2000 through September 2001.

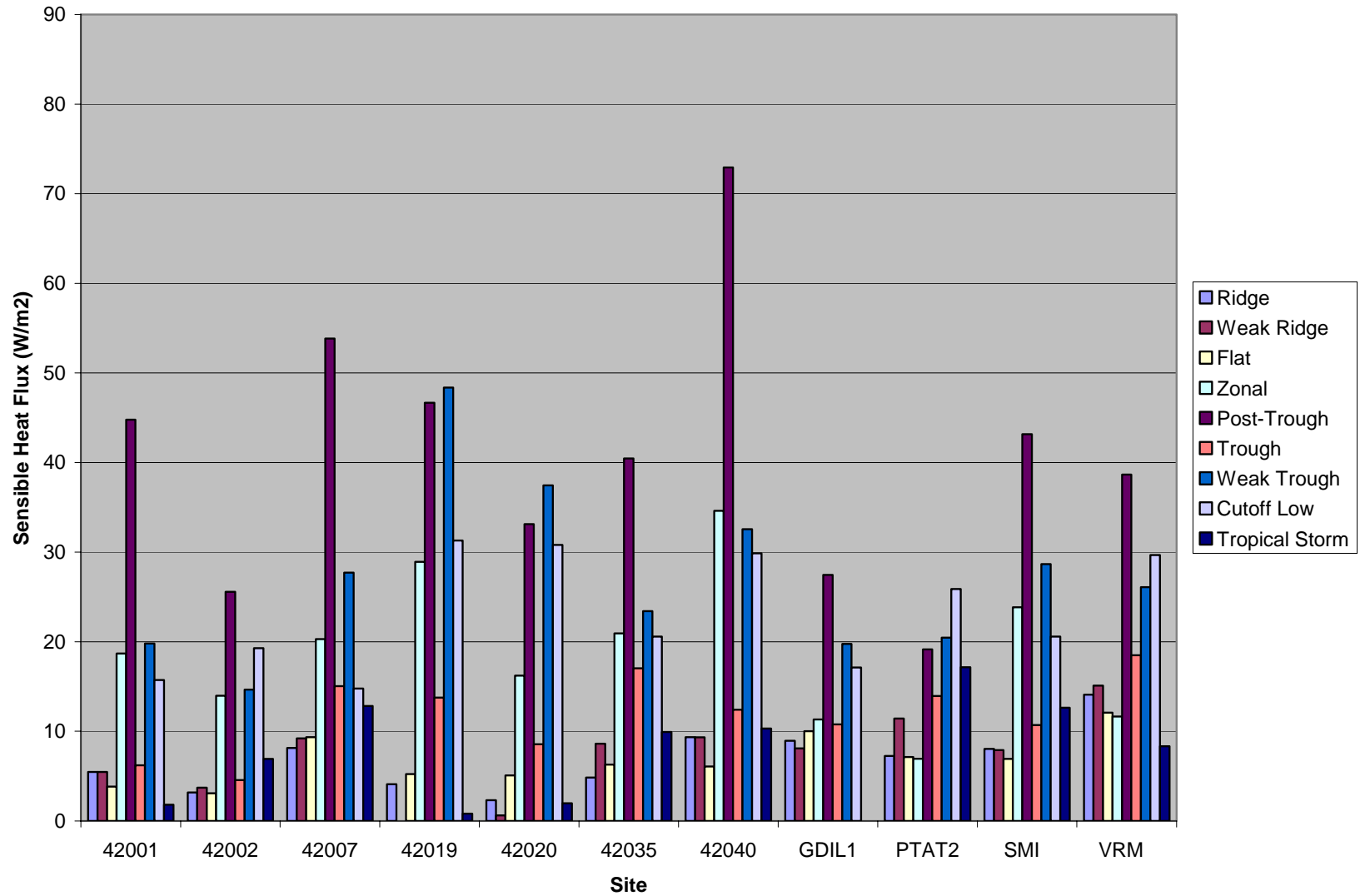


Figure 5-19a. COARE average sensible heat fluxes by synoptic class by site for May 1998 through October 2001.

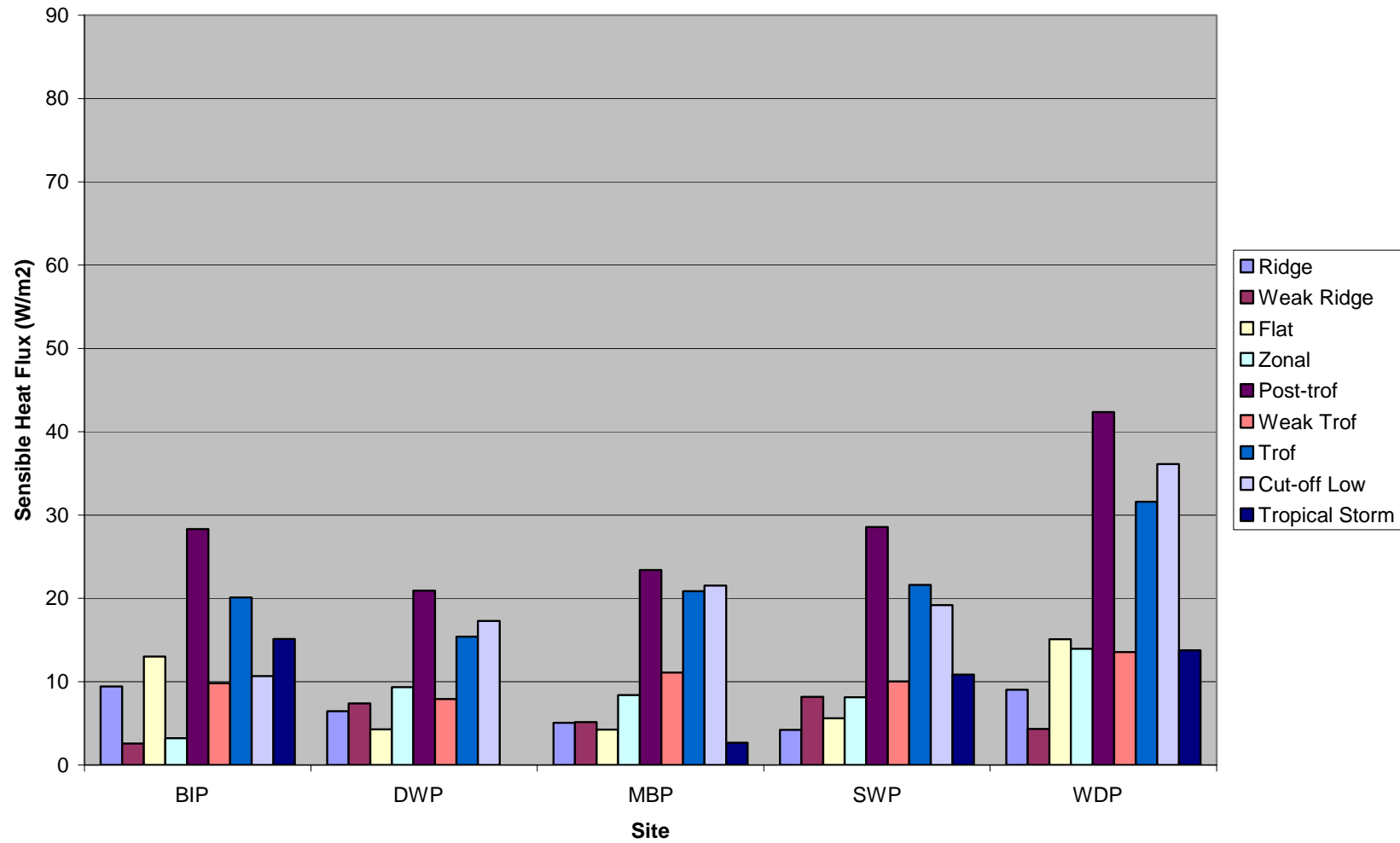


Figure 5-19b. COARE average sensible heat fluxes by synoptic class by BAMP site for September 2000 through September 2001.

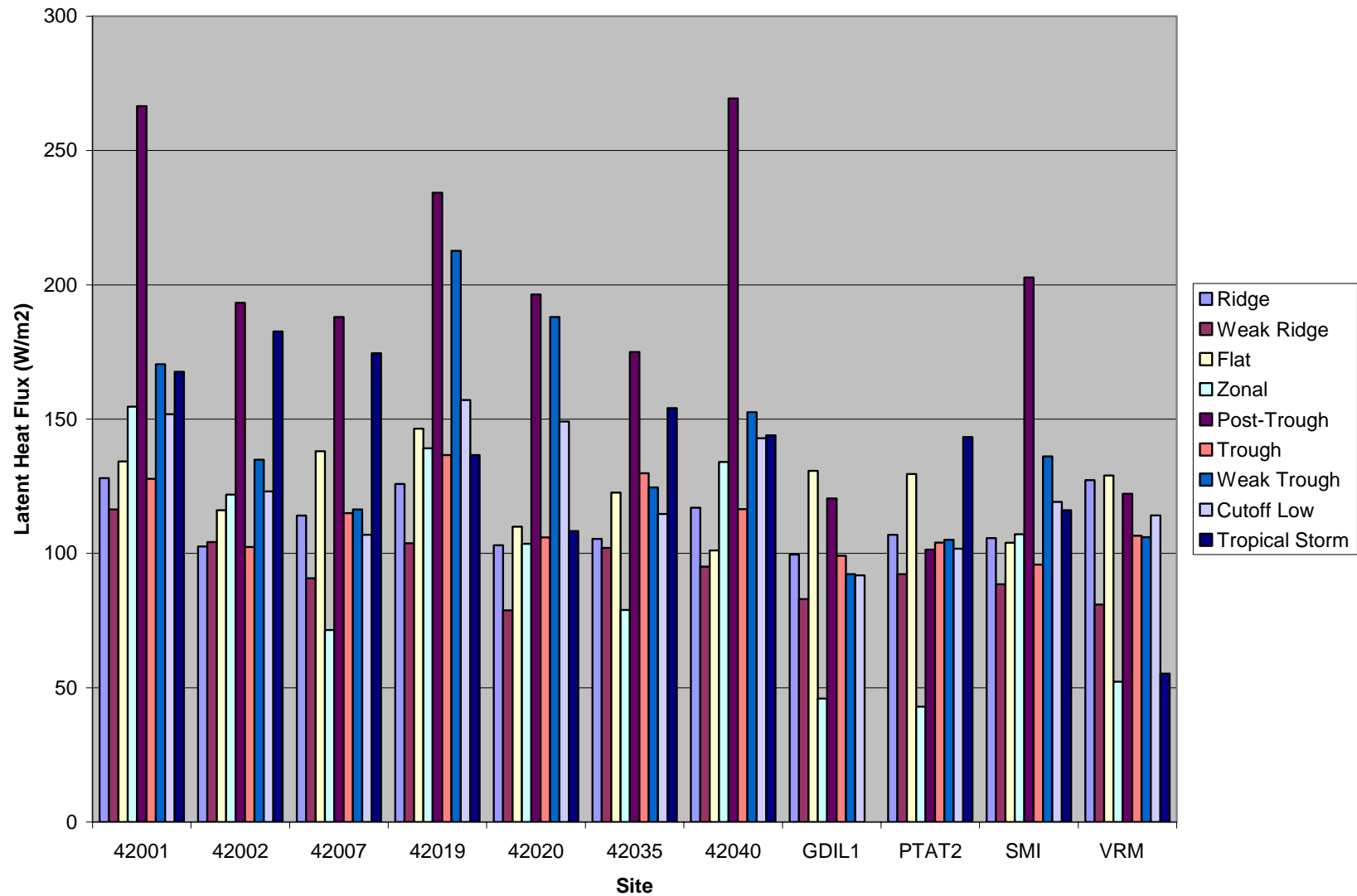


Figure 5-20a. COARE average latent heat fluxes by synoptic class by site for May 1998 through October 2001.

5-65

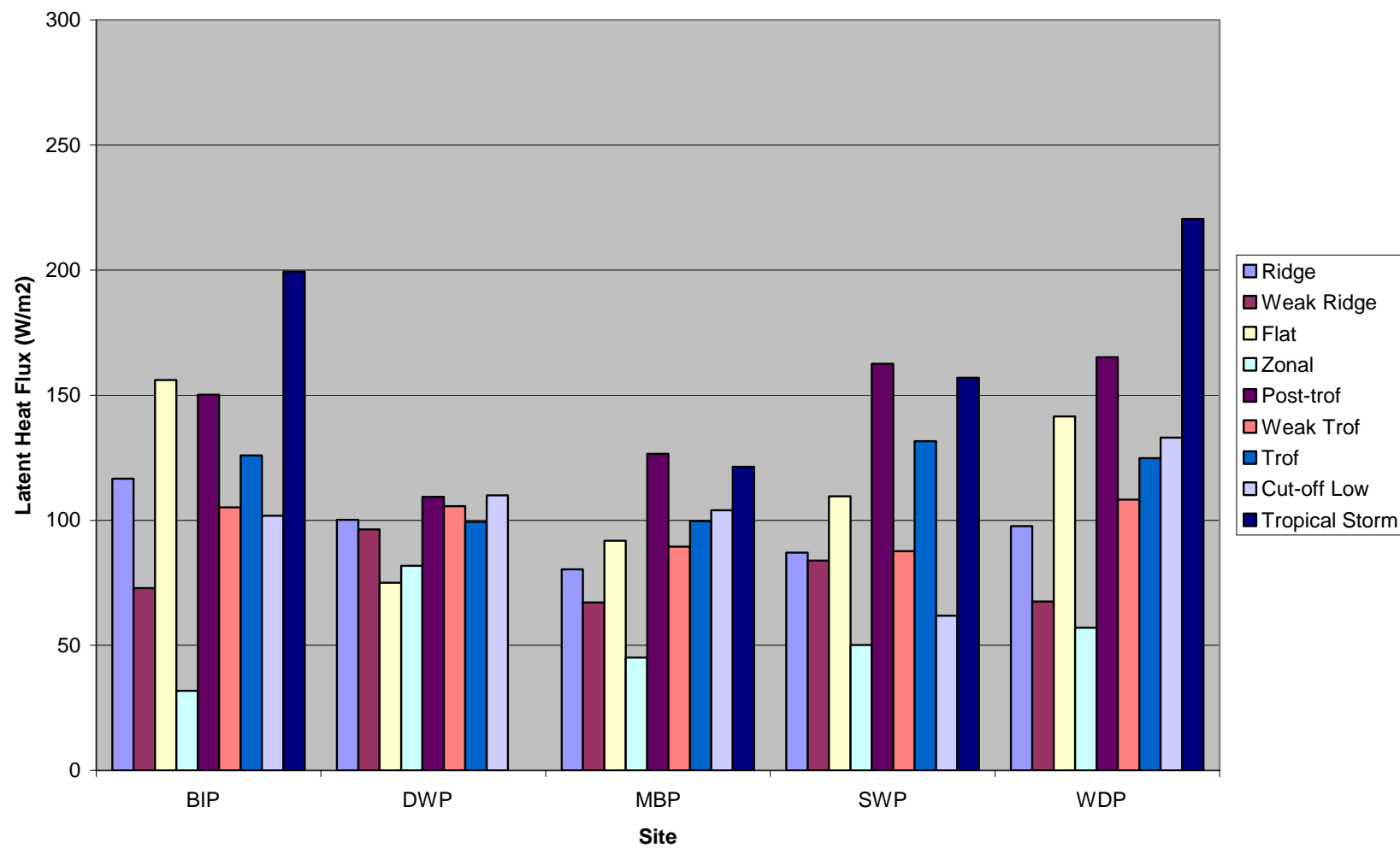


Figure 5-20b. COARE average latent heat fluxes by synoptic class by BAMP site for September 2000 through September 2001.

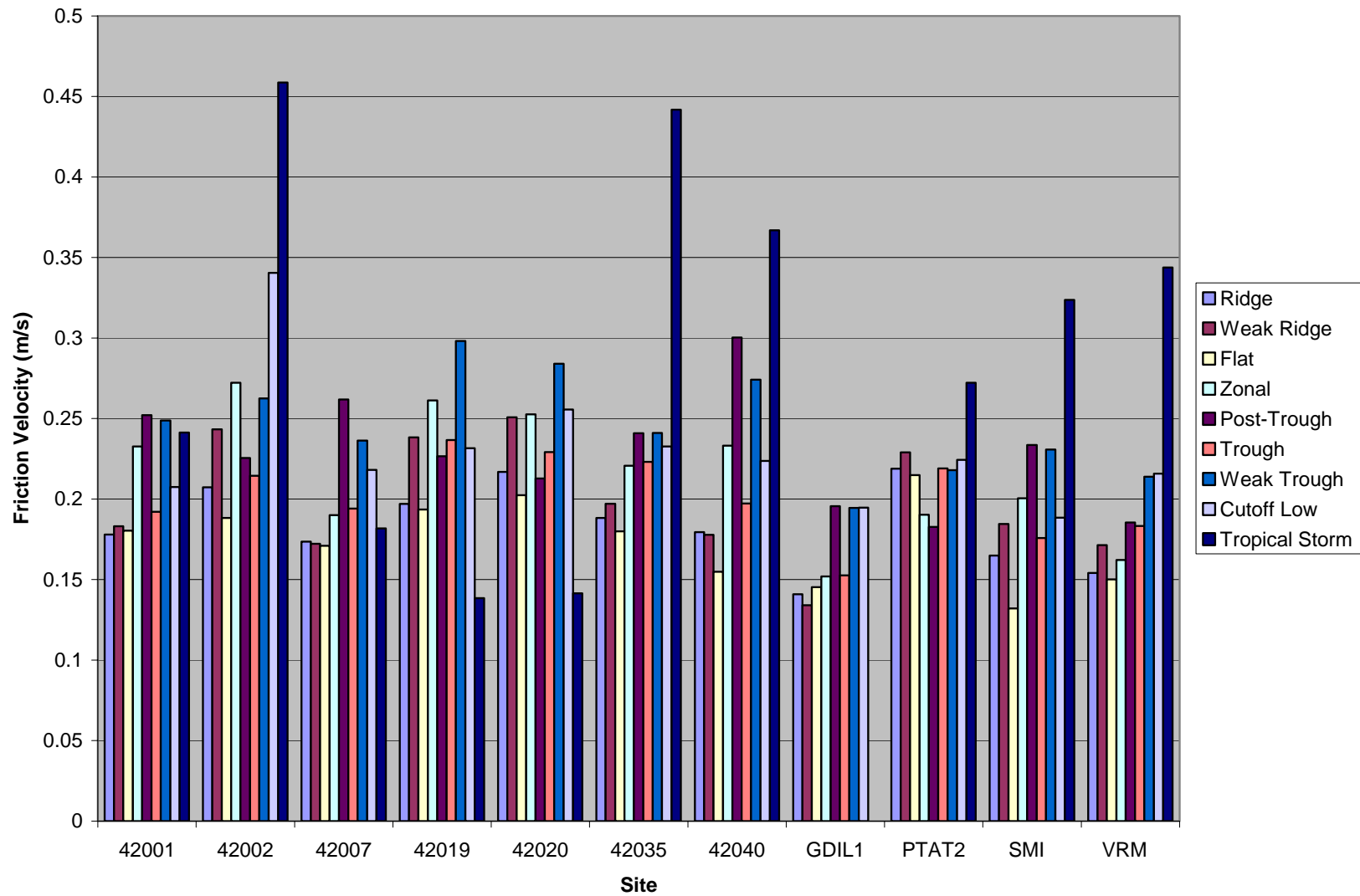


Figure 5-21a. COARE average friction velocity by synoptic class by site for May 1998 through October 2001.

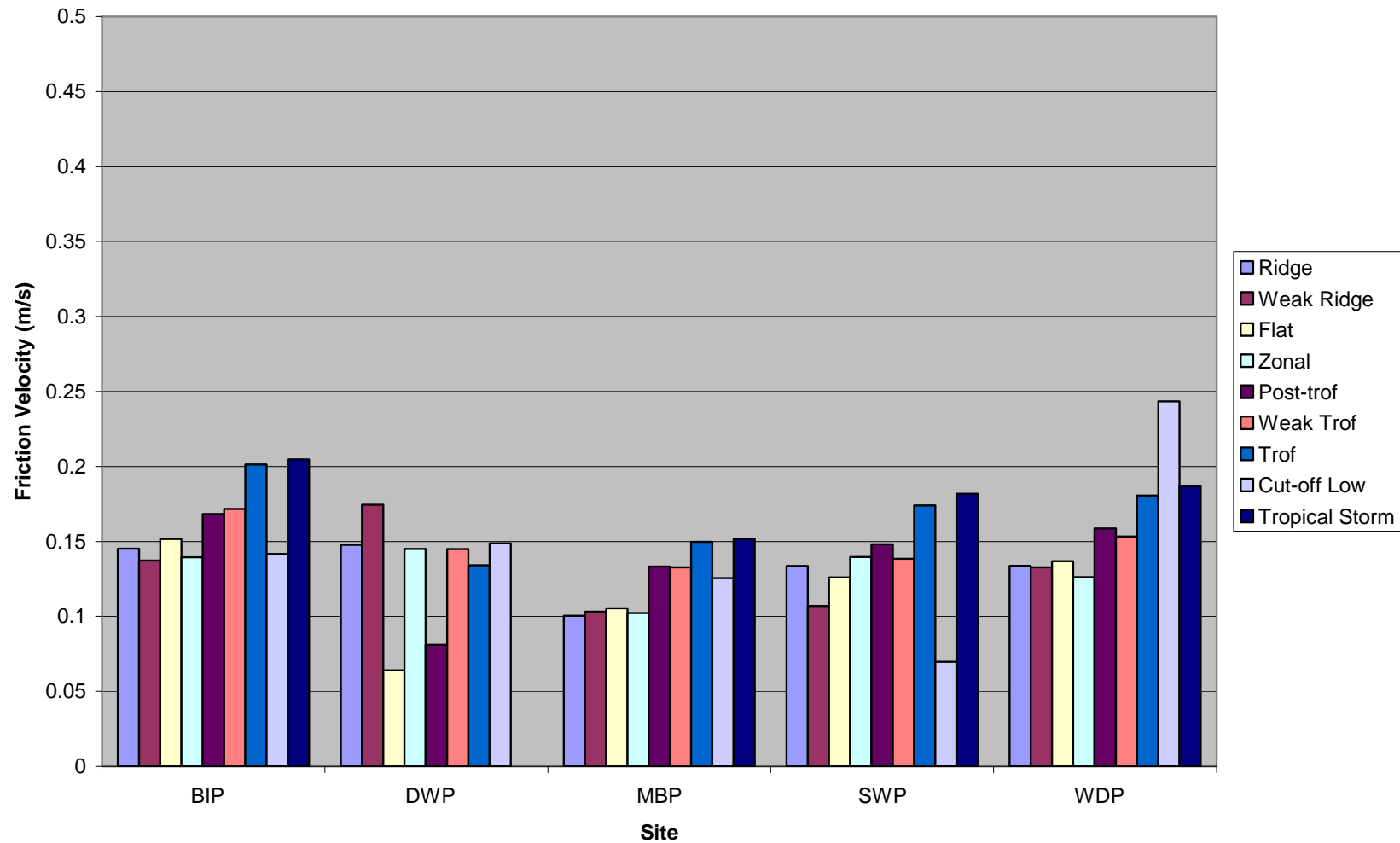


Figure 5-21b. COARE average friction velocity by synoptic class by BAMP site for September 2000 through September 2001.

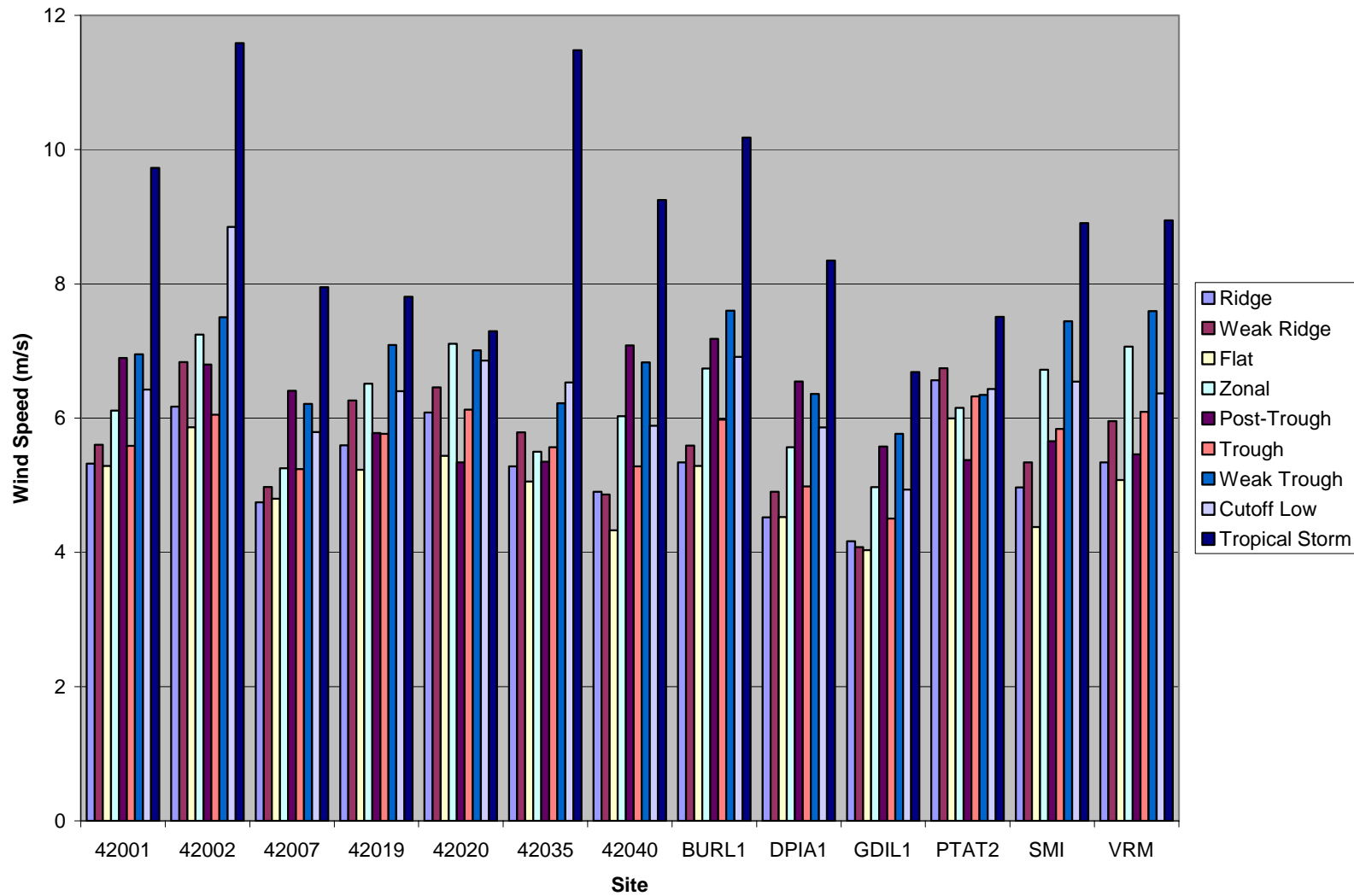


Figure 5-22. Observed average wind speed by synoptic class by site for May 1998 through October 2001.

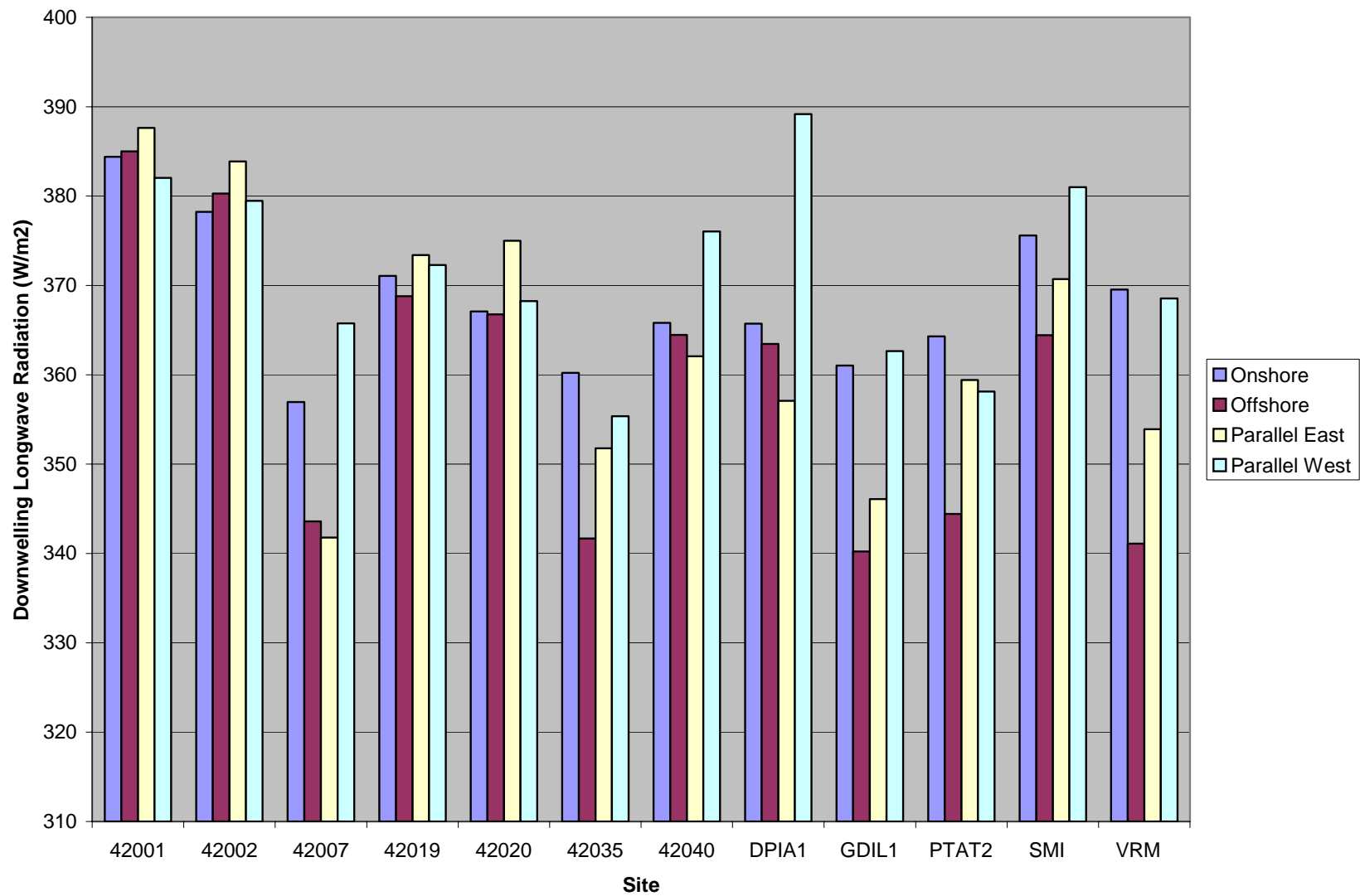


Figure 5-23. Eta average downwelling longwave radiation by general flow direction by site for May 1998 through October 2001, for the 6-to 12-hr forecast.

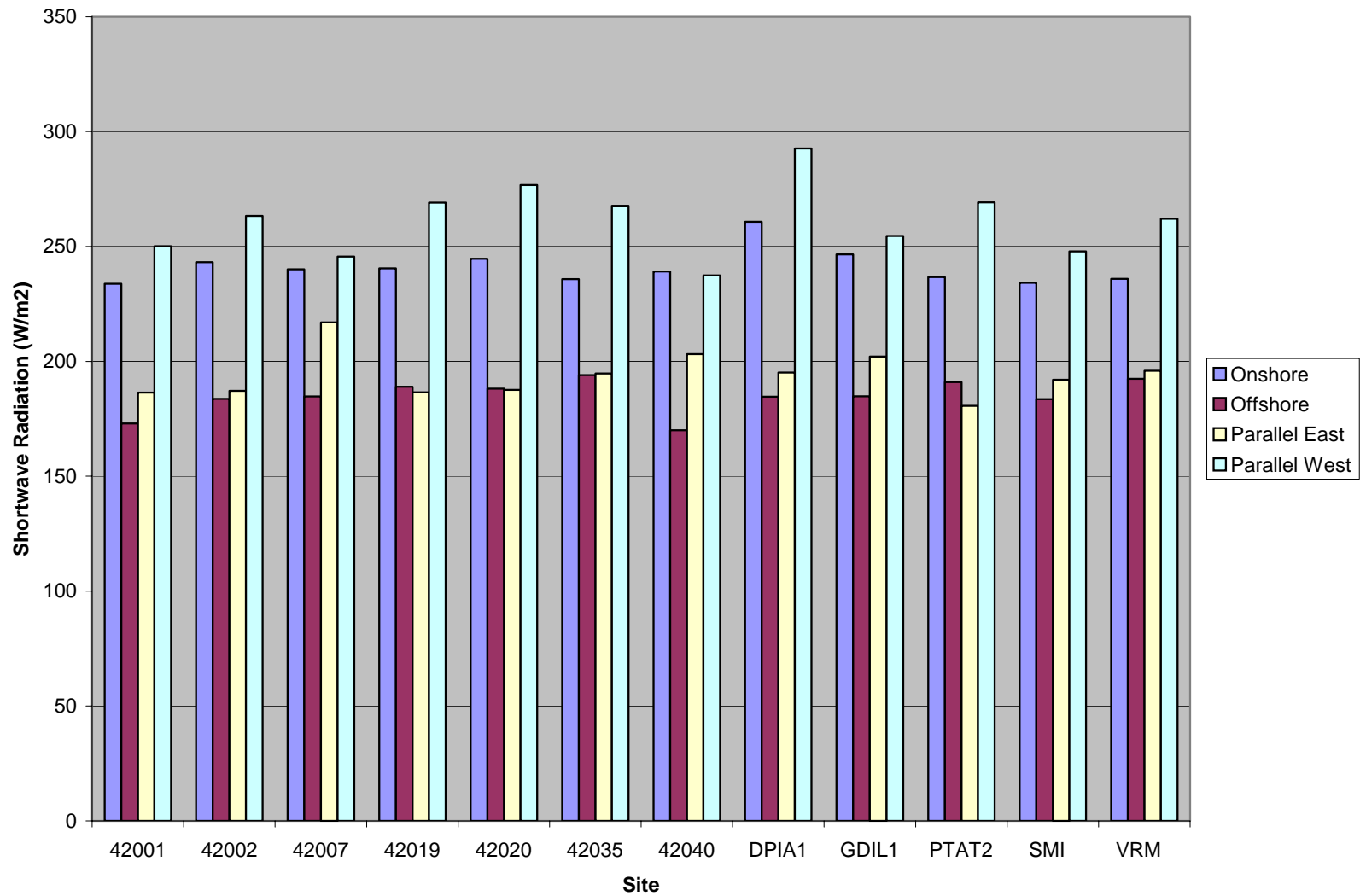


Figure 5-24. Eta average shortwave radiation by general flow direction by site for May 1998 through October 2001, for the 6-to 12-hr forecast.

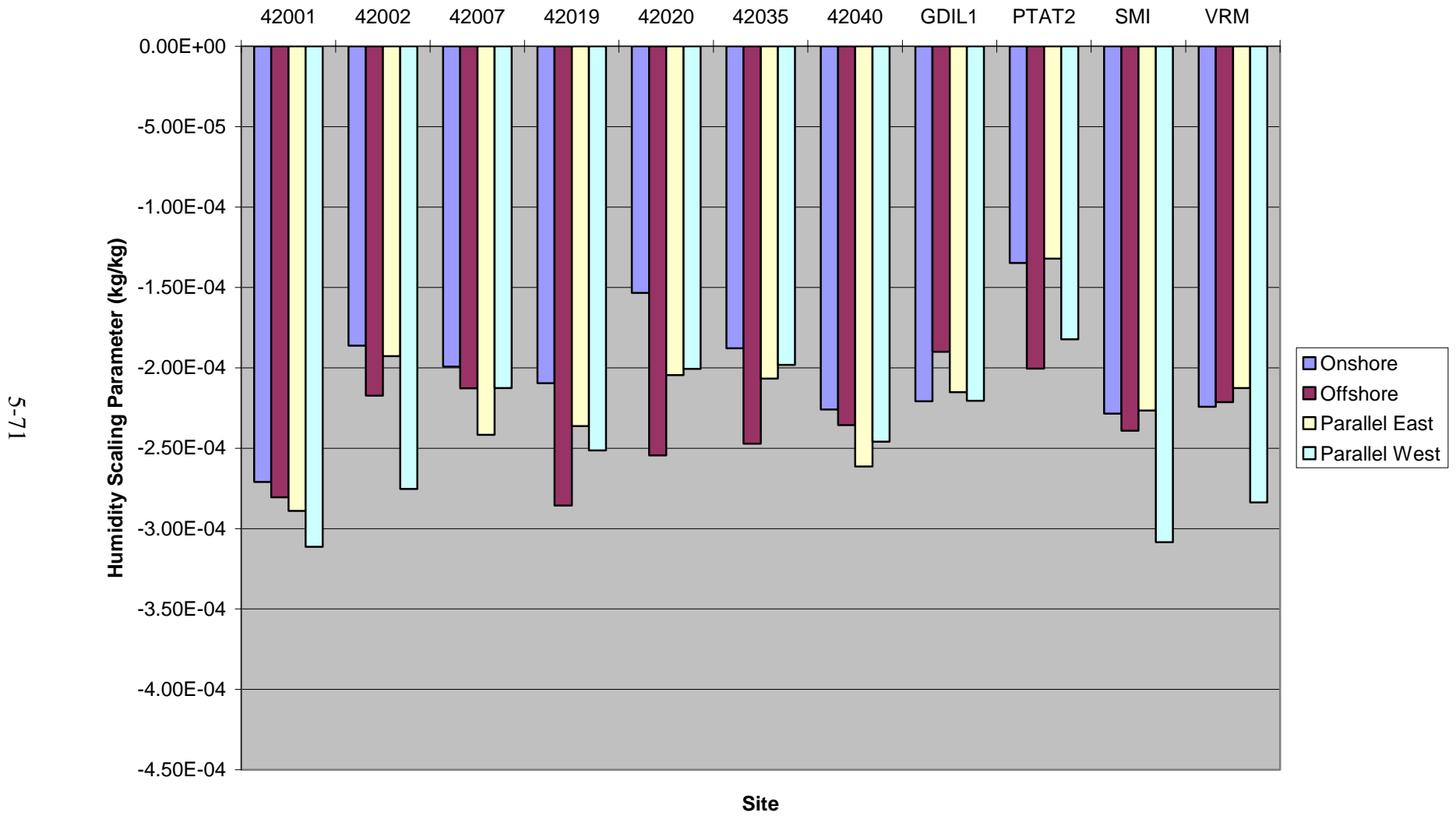


Figure 5-25a. COARE average humidity scaling parameter by general flow direction by site for May 1998 through October 2001.

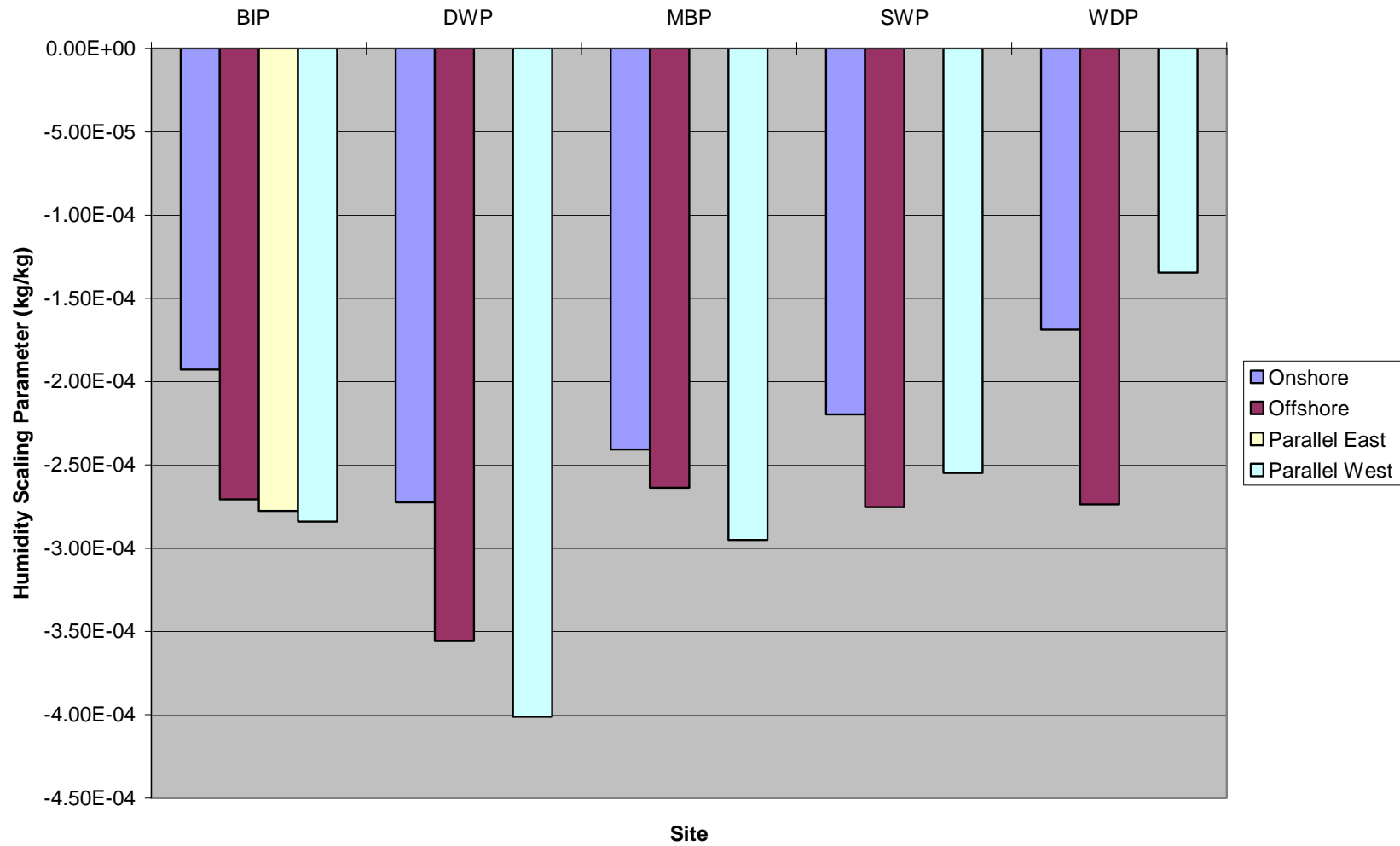


Figure 5-25b. COARE average humidity scaling parameter by general flow direction by BAMP site for September 2000 through September 2001.

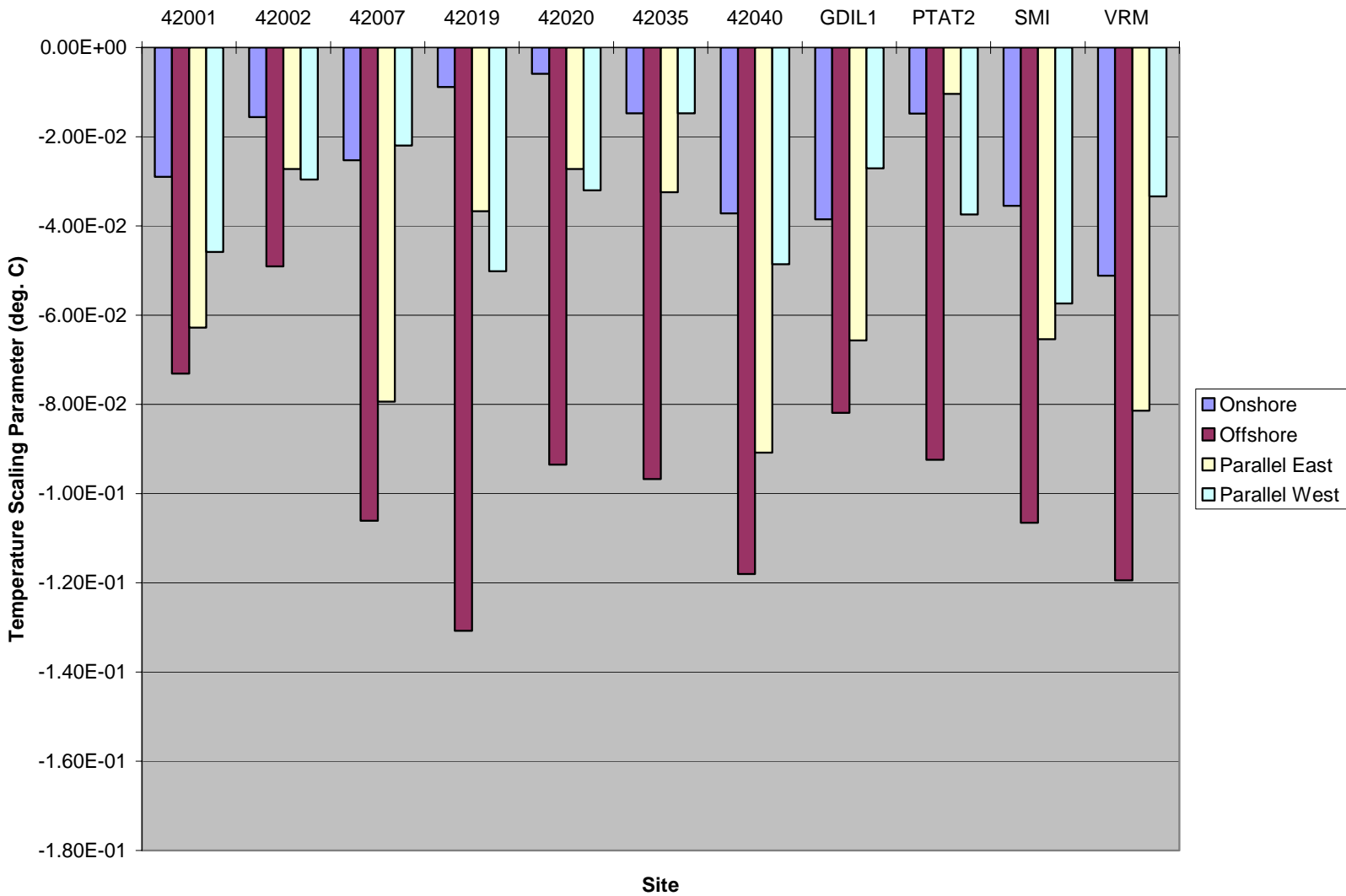


Figure 5-26a. COARE average temperature scaling parameter by general flow direction by site for May 1998 through October 2001.

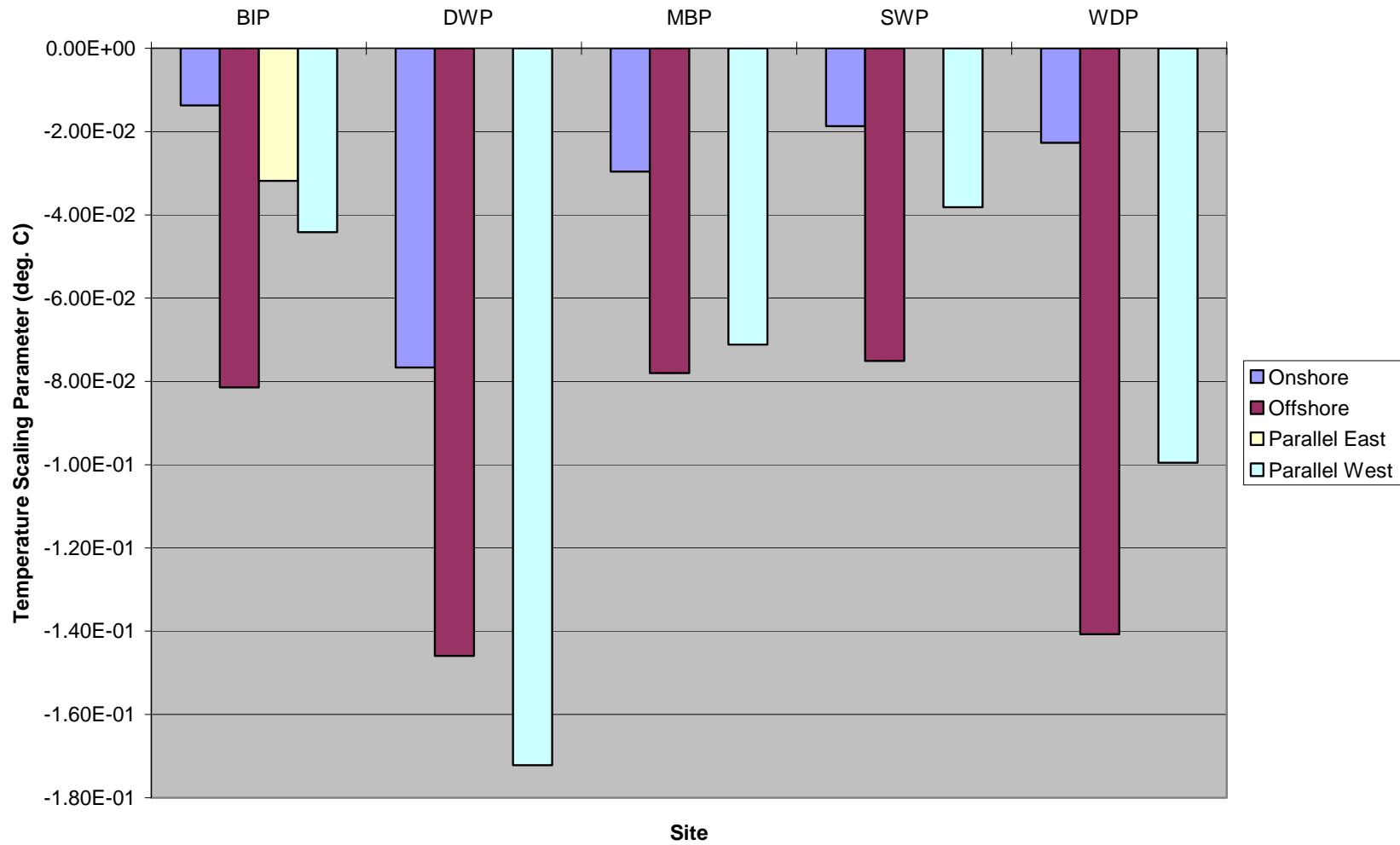


Figure 5-26b. COARE average temperature scaling parameter by general flow direction by BAMP site for September 2000 through September 2001.

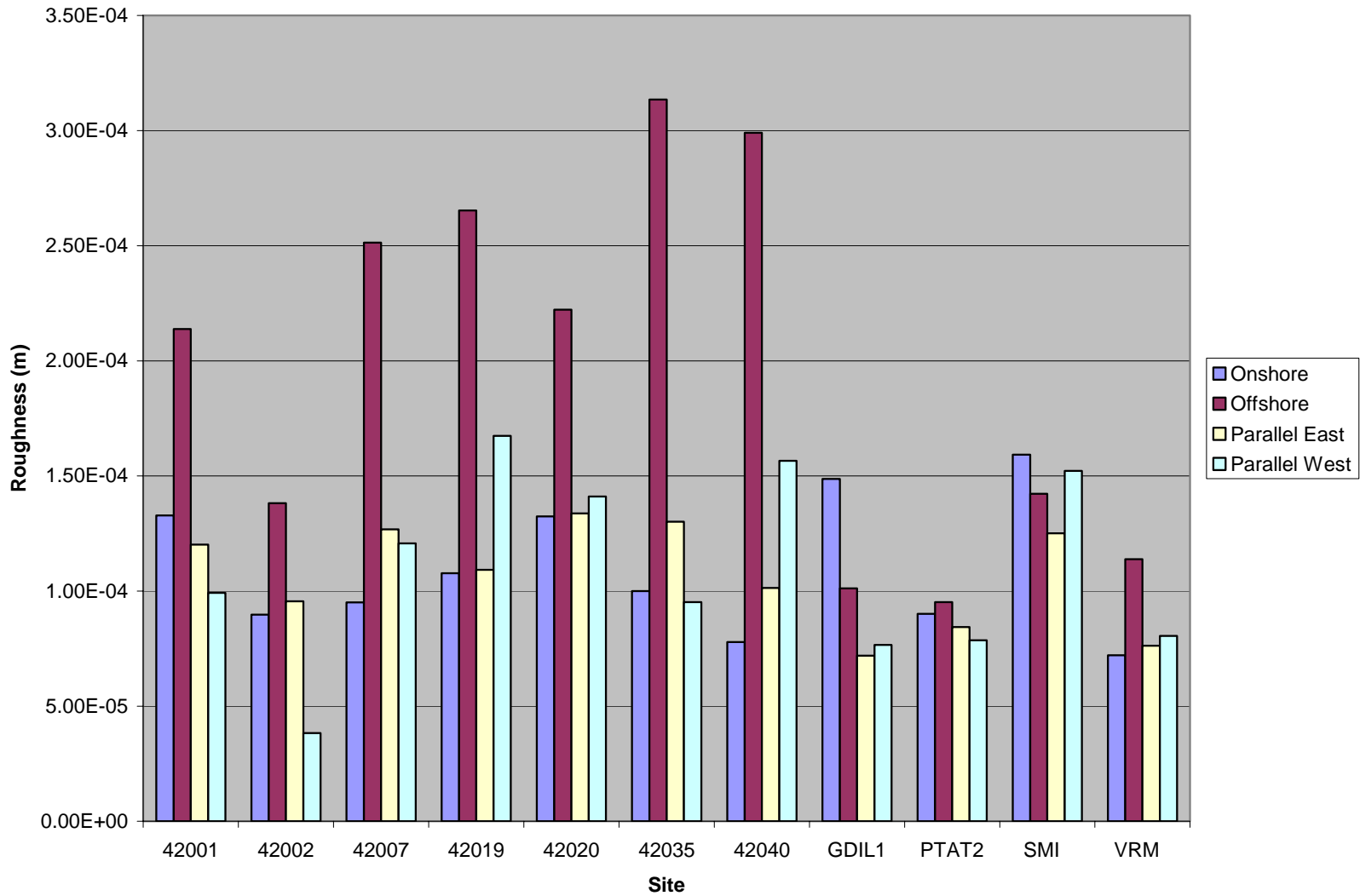


Figure 5-27a. COARE average surface roughness by general flow direction by site for May 1998 through October 2001.

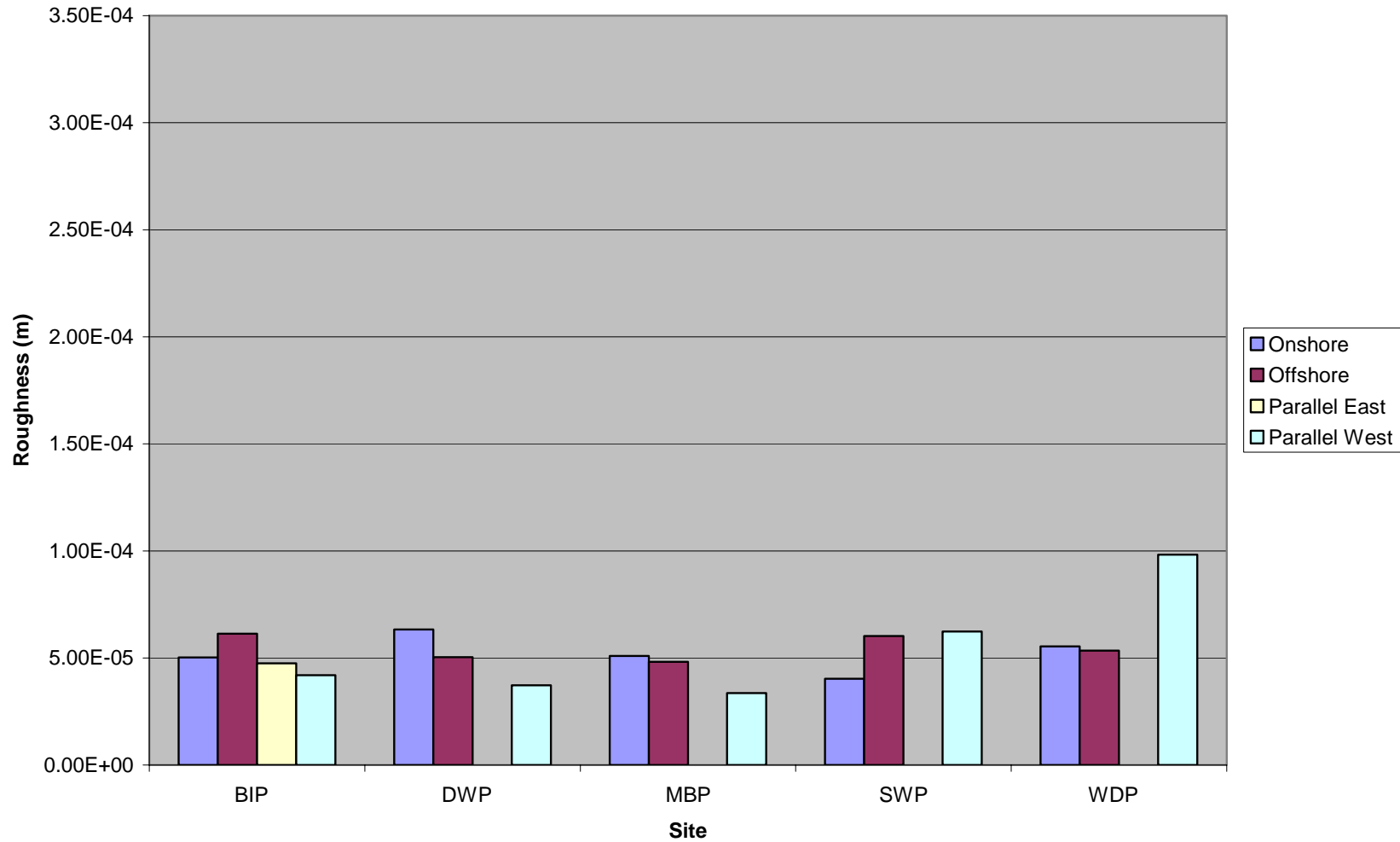


Figure 5-27b. COARE average surface roughness by general flow direction by BAMP site for September 2000 through September 2001.

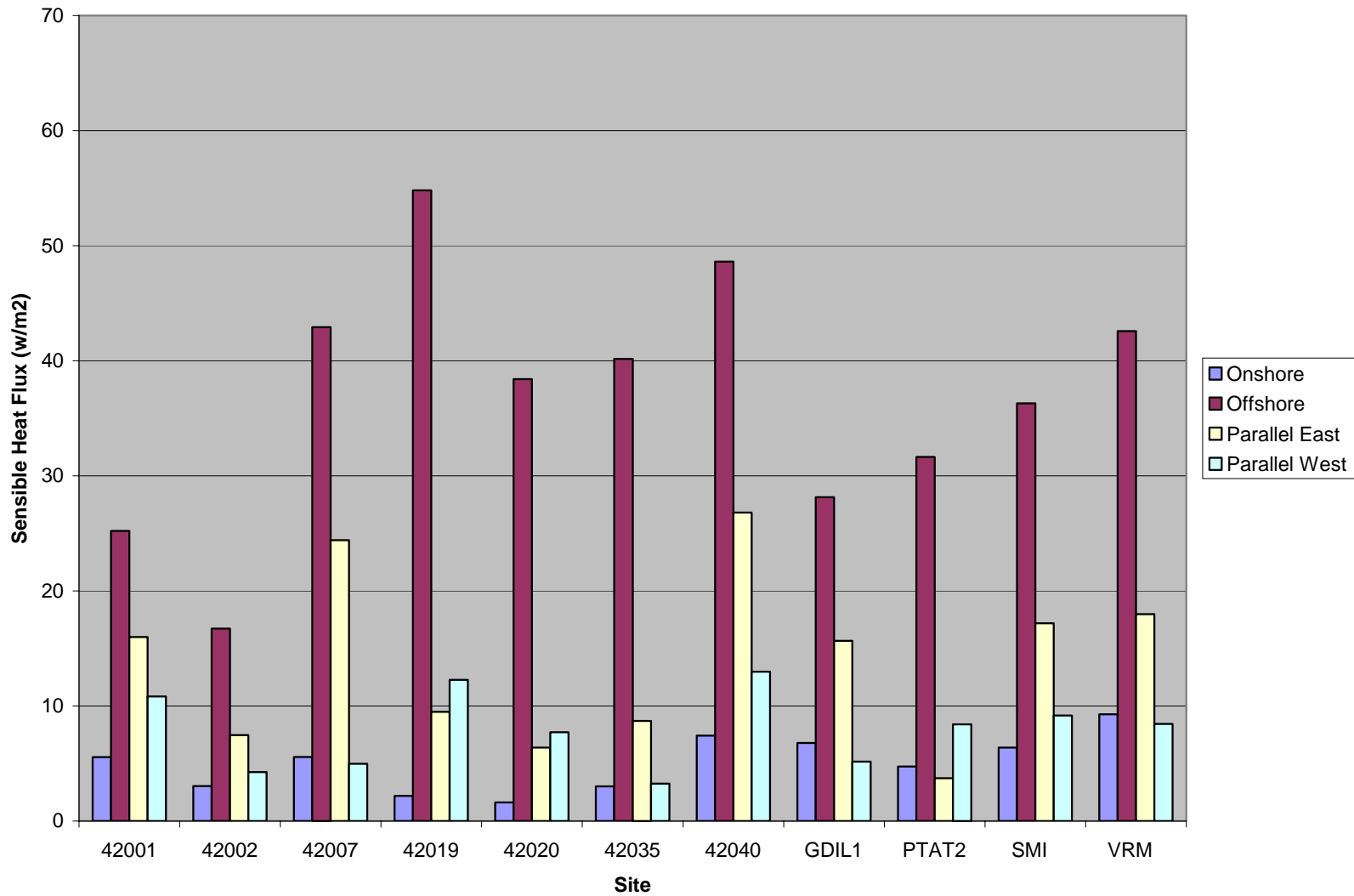


Figure 5-28a. COARE average sensible heat fluxes by general flow direction by site for May 1998 through October 2001.

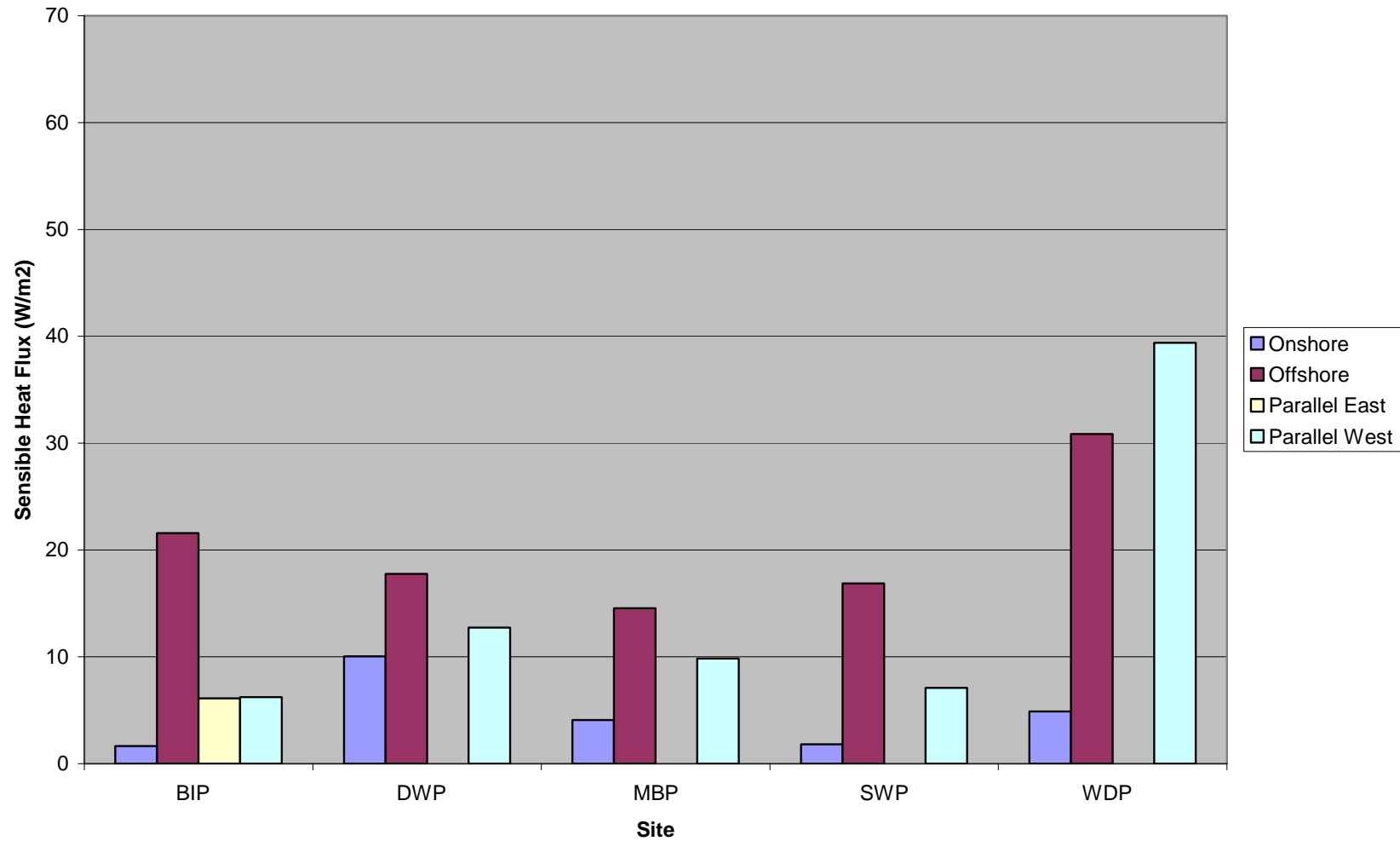


Figure 5-28b. COARE average sensible heat fluxes by general flow direction by BAMP site for September 2000 through September 2001.

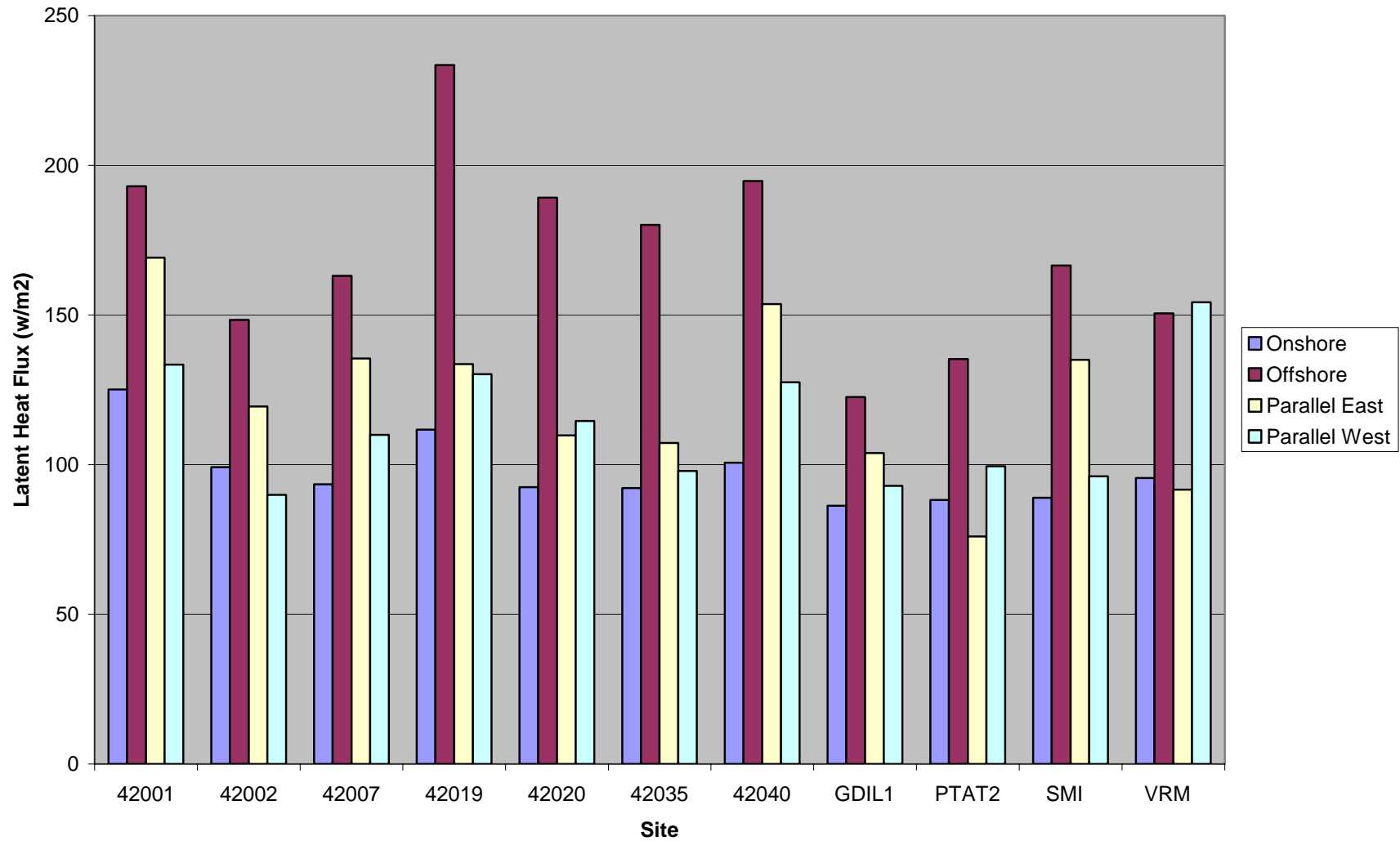


Figure 5-29a. COARE average latent heat fluxes by general flow direction by site for May 1998 through October 2001.

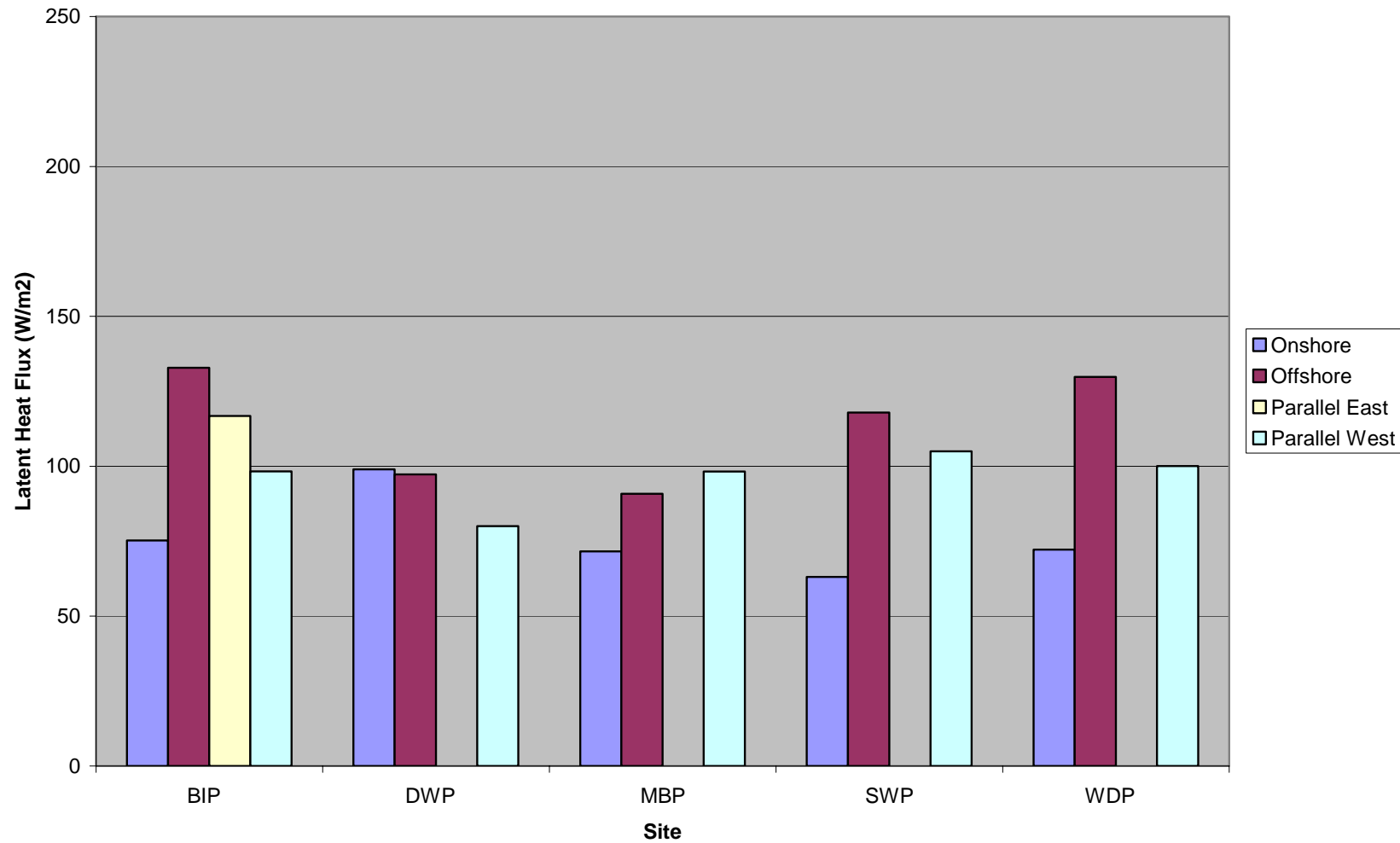


Figure 5-29b. COARE average latent heat fluxes by general flow direction by BAMP site for September 2000 through September 2001.

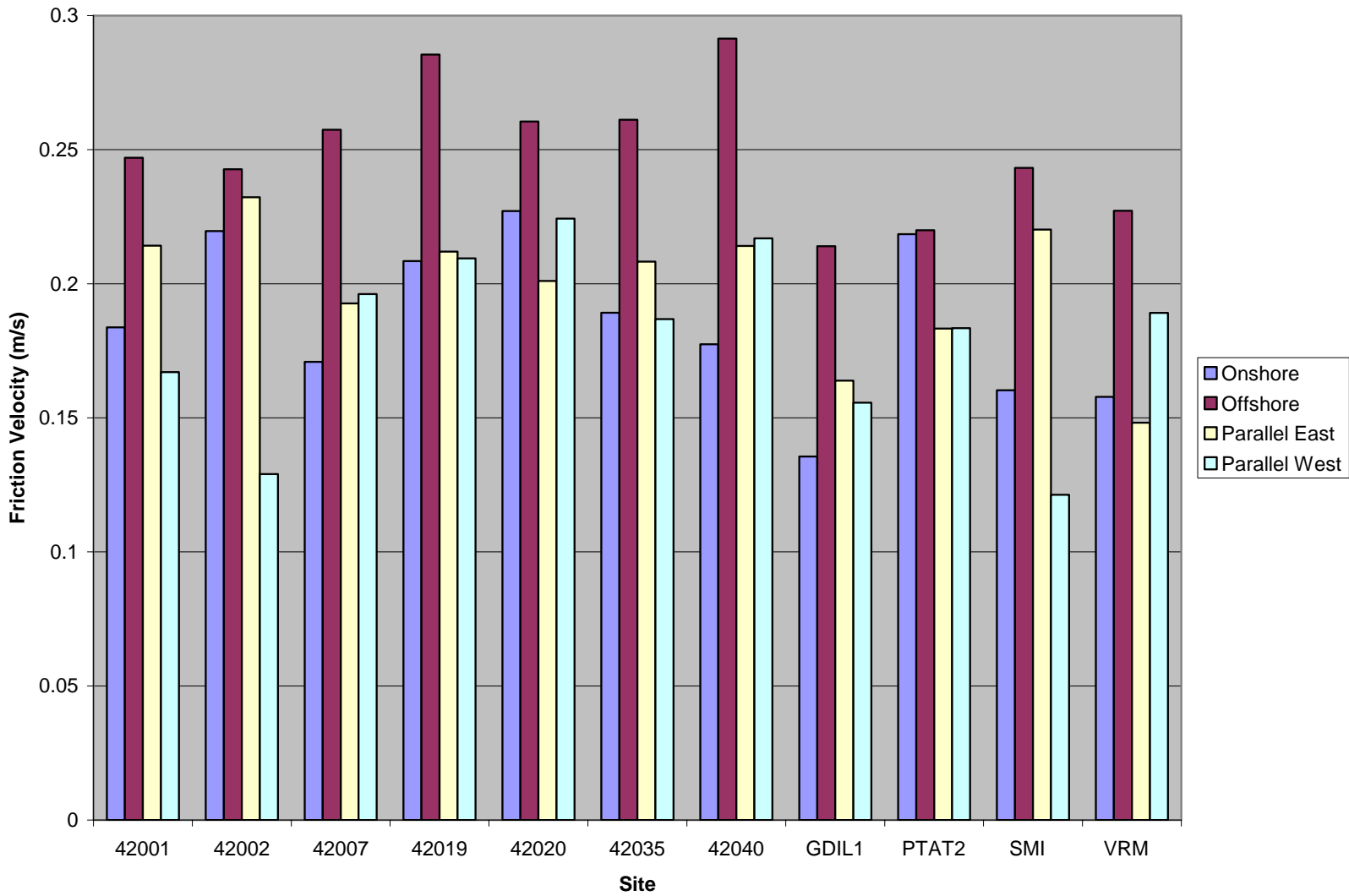


Figure 5-30a. COARE average friction velocity by general flow direction by site for May 1998 through October 2001.

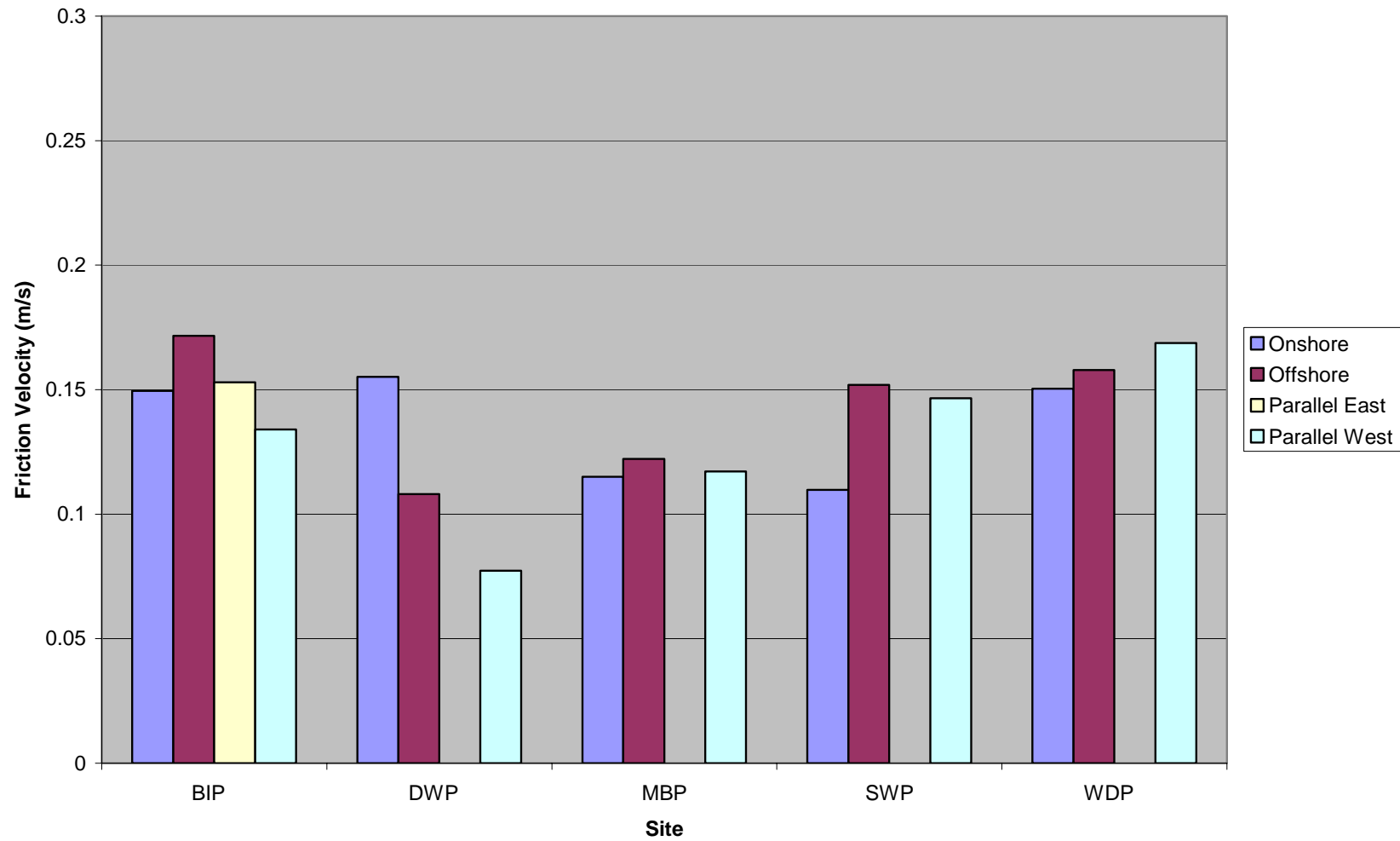


Figure 5-30b. COARE average friction velocity by general flow direction by BAMP site for September 2000 through September 2001.

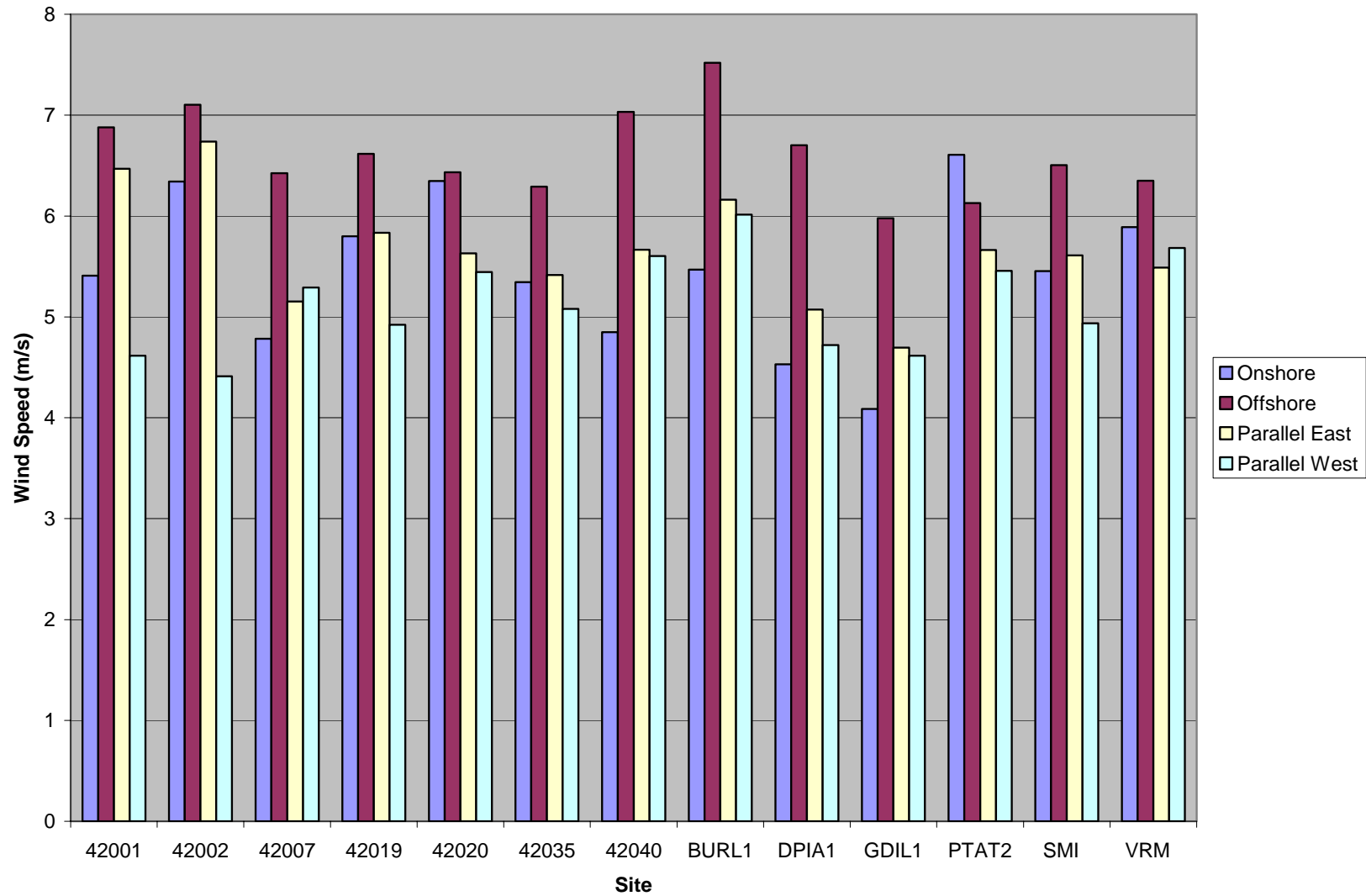


Figure 5-31. Observed average wind speed by general flow direction by site for May 1998 through October 2001.

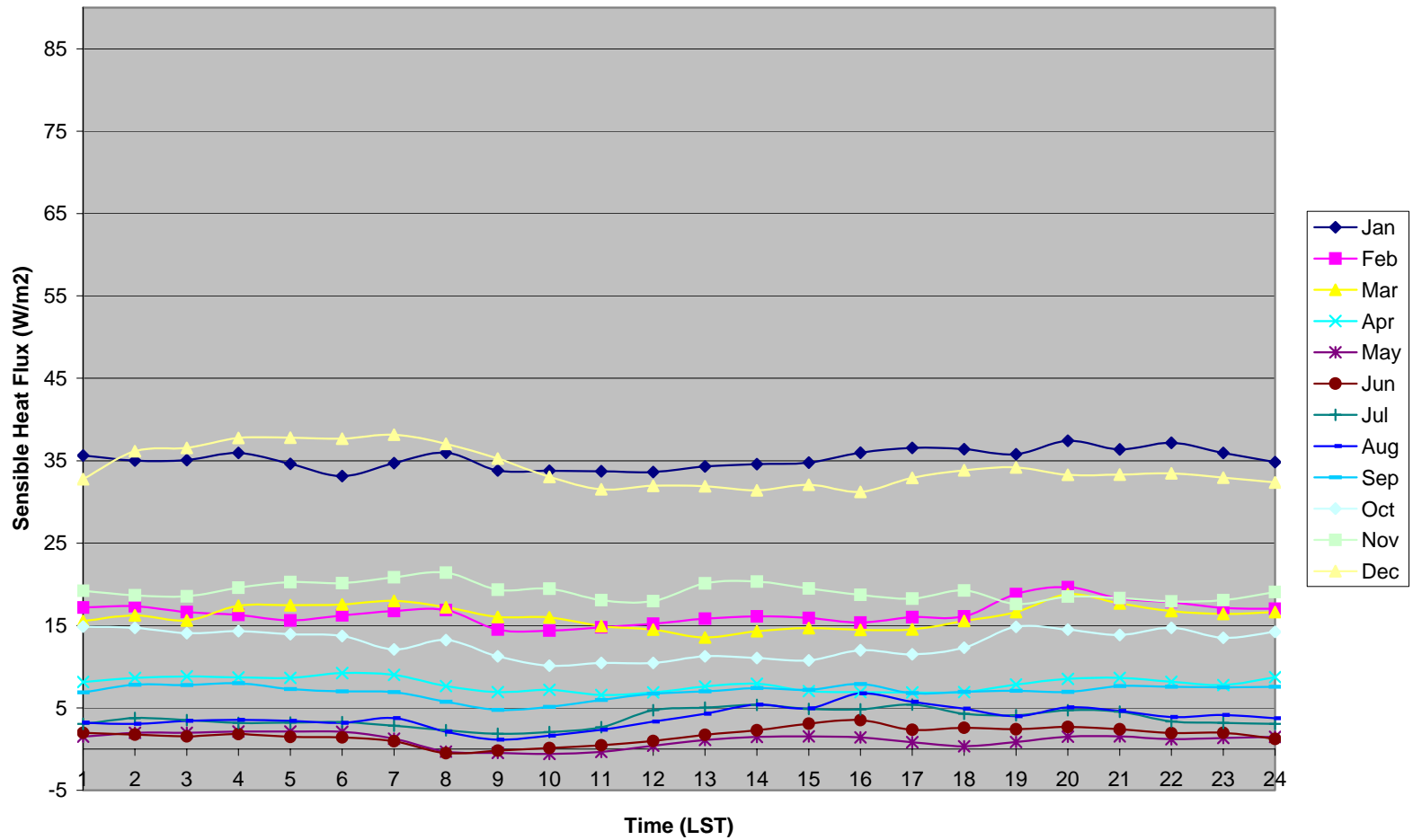


Figure 5-32. COARE hourly average sensible heat fluxes over buoy 42001 for May 1998 through October 2001.

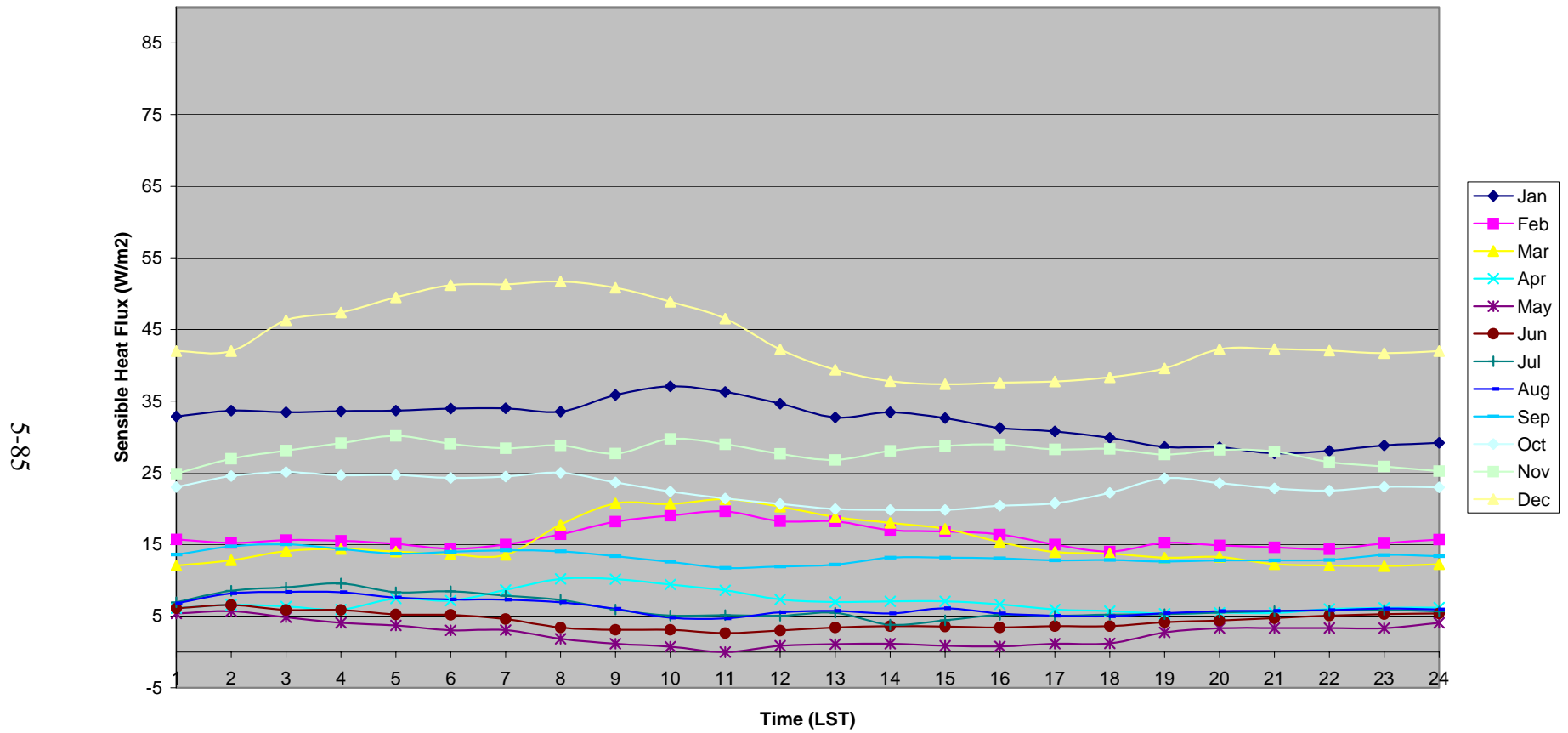


Figure 5-33. COARE hourly average sensible heat fluxes over SMI for May 1998 through October 2001.

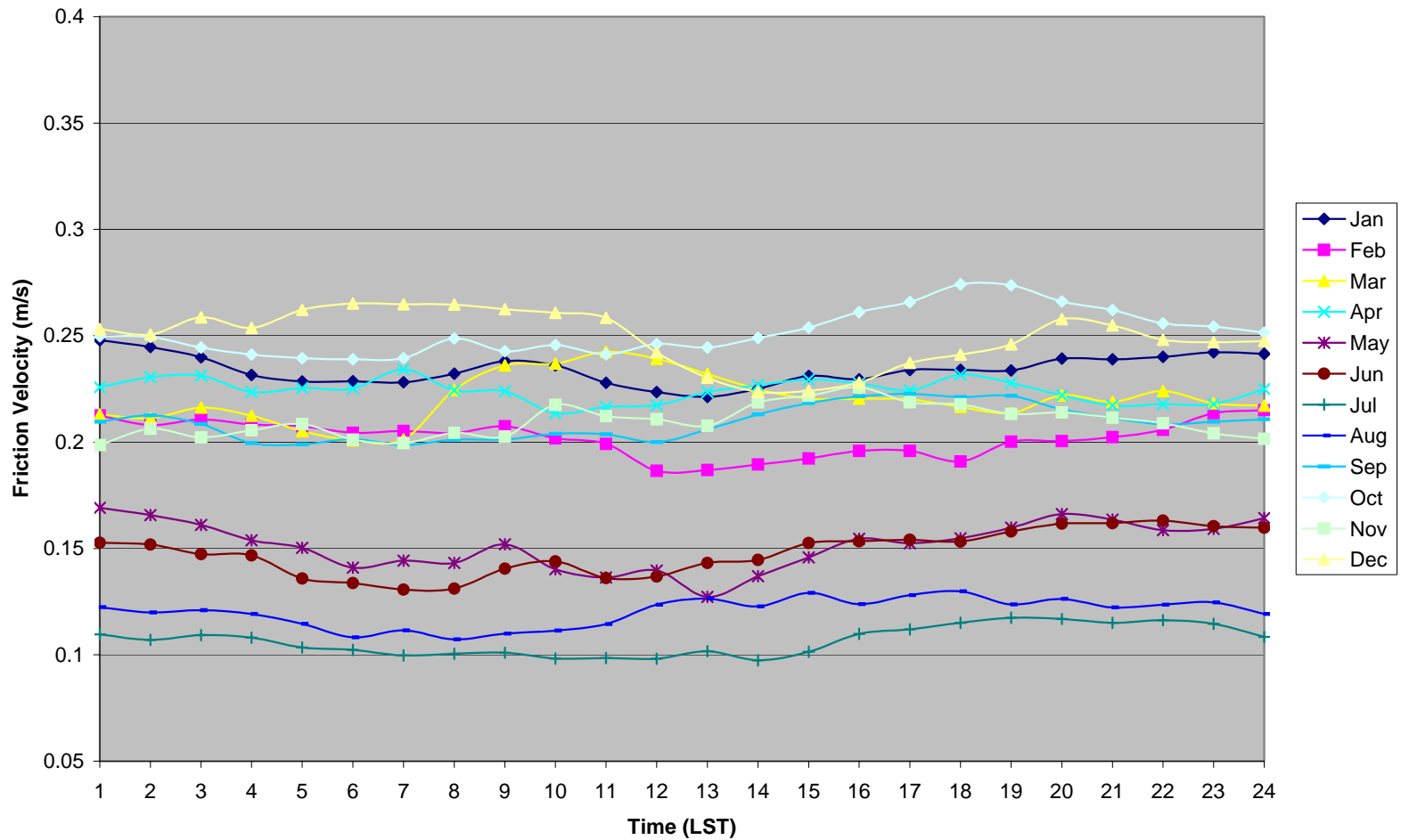


Figure 5-34. COARE hourly average friction velocity over SMI for May 1998 through October 2001.

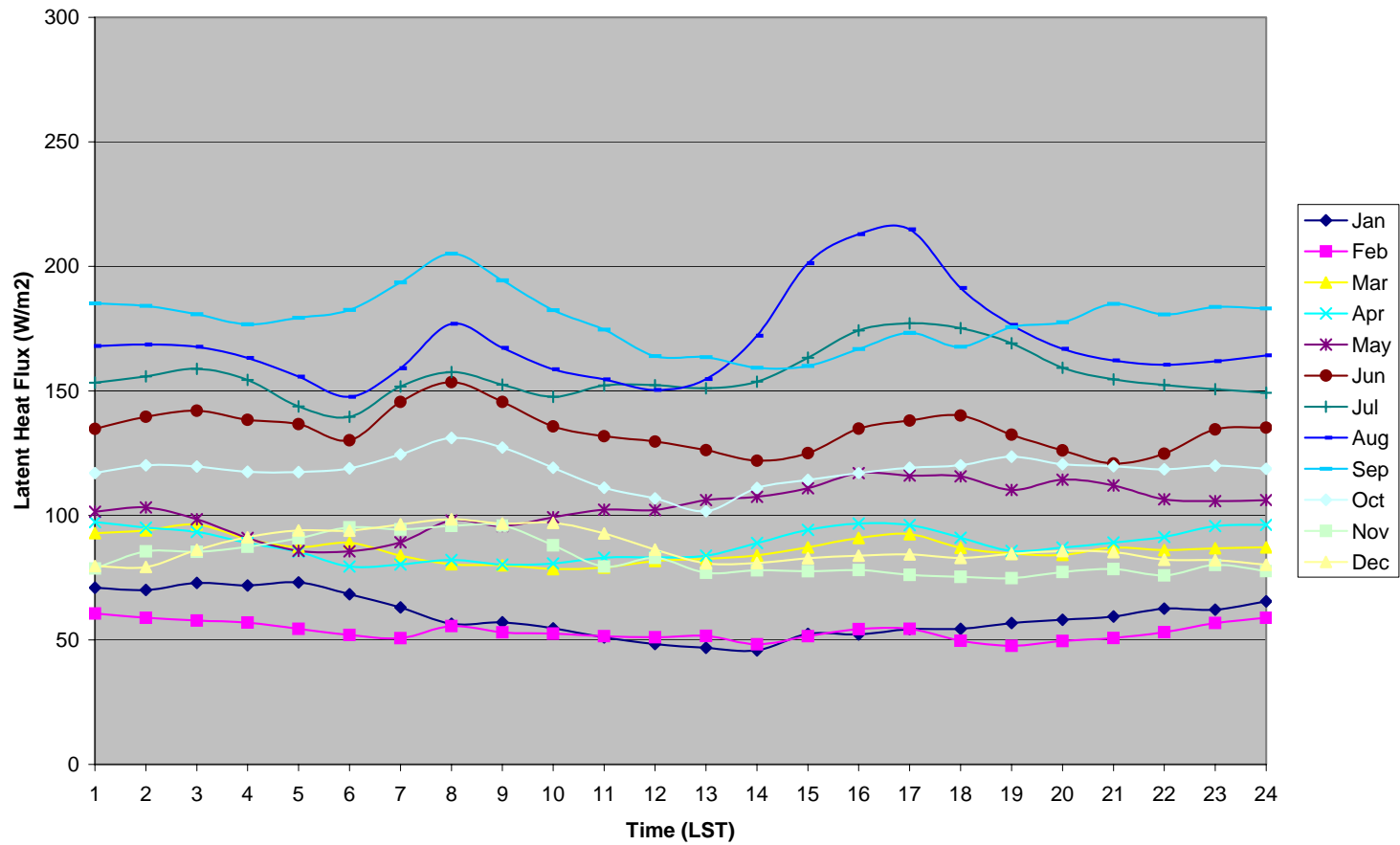


Figure 5-35. COARE hourly average latent heat fluxes over VRM for May 1998 through October 2001.

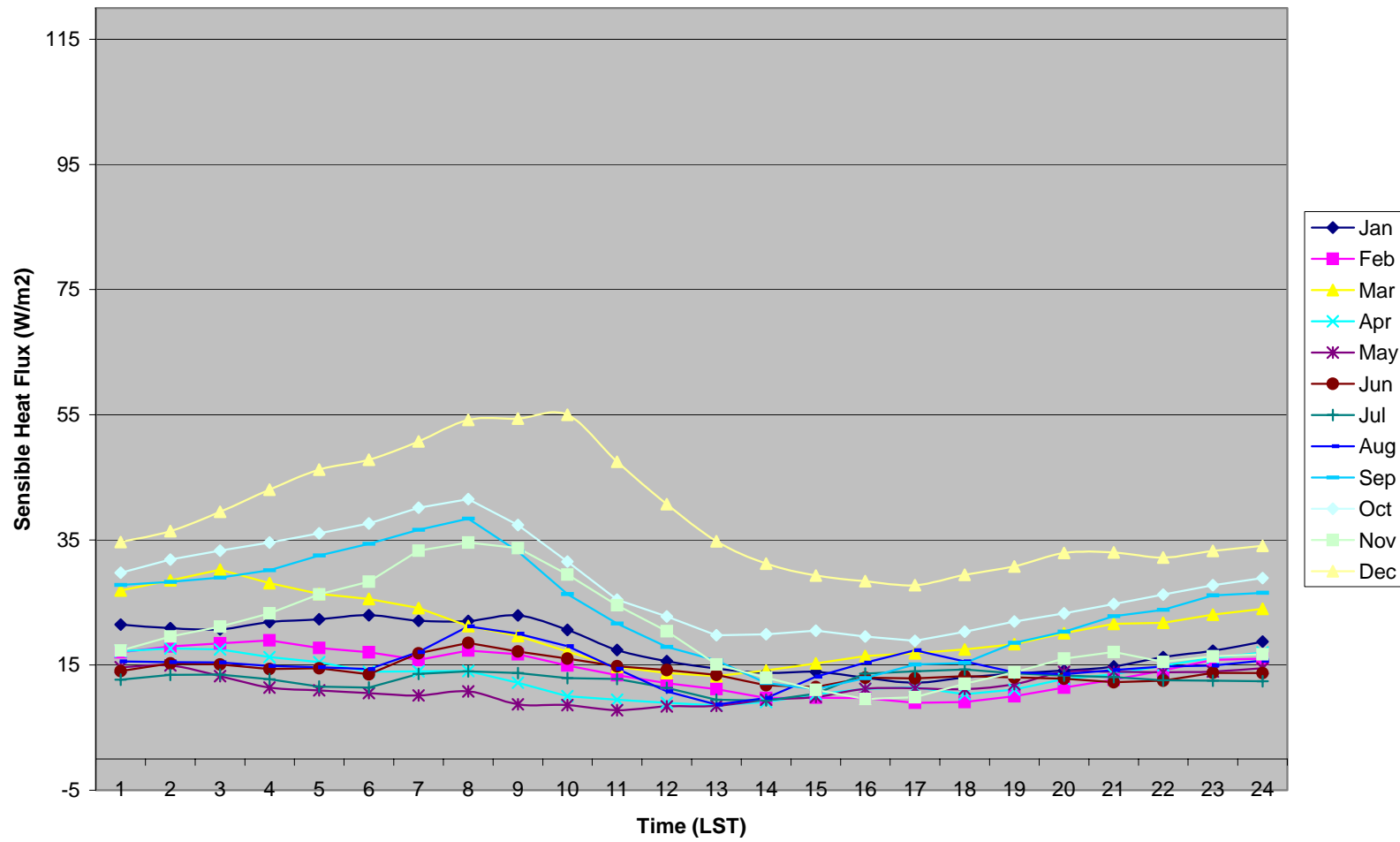


Figure 5-36. COARE hourly average sensible heat fluxes over VRM for May 1998 through October 2001.

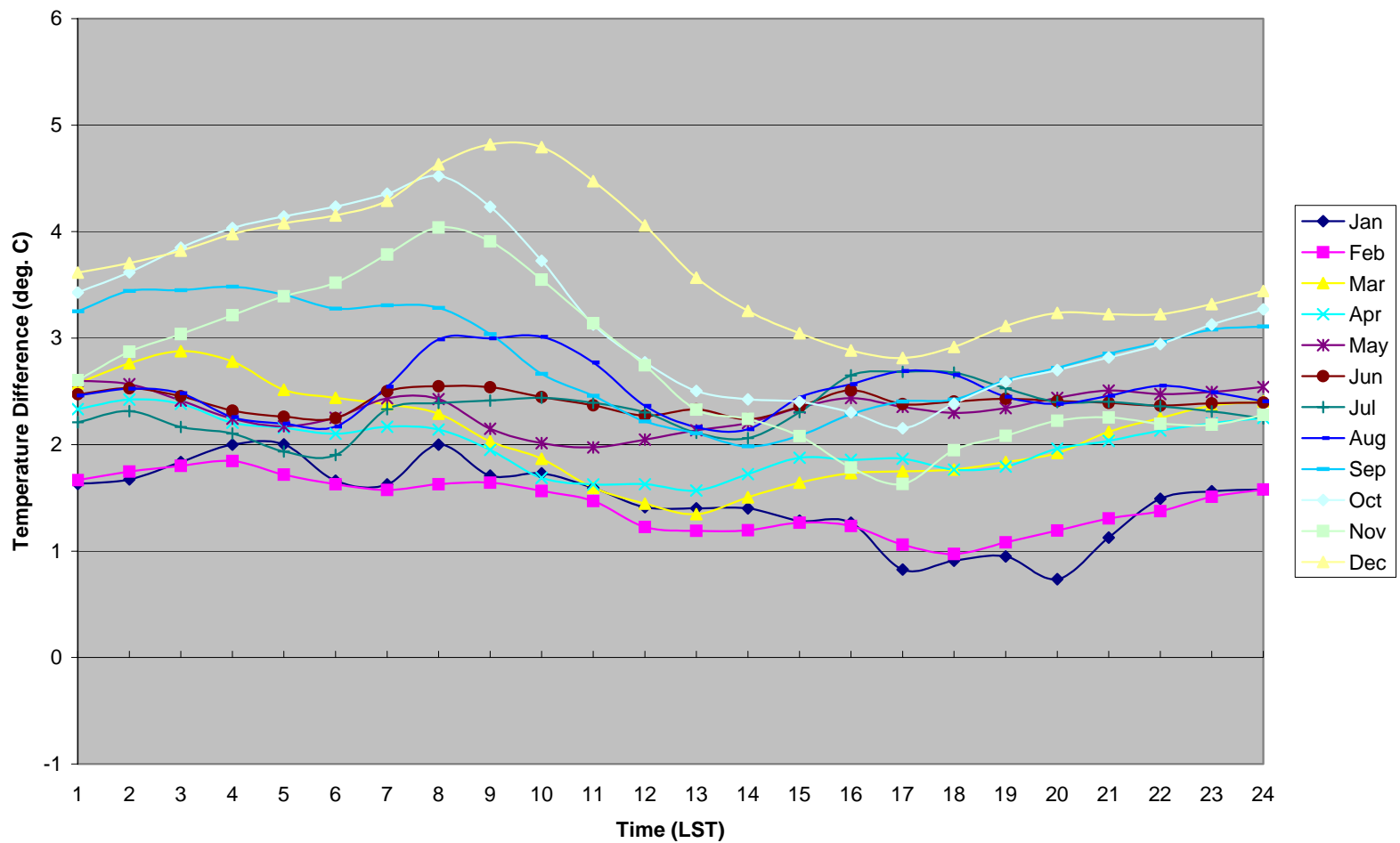


Figure 5-37. Hourly average skin temperature minus air temperature over VRM for May 1998 through October 2001.

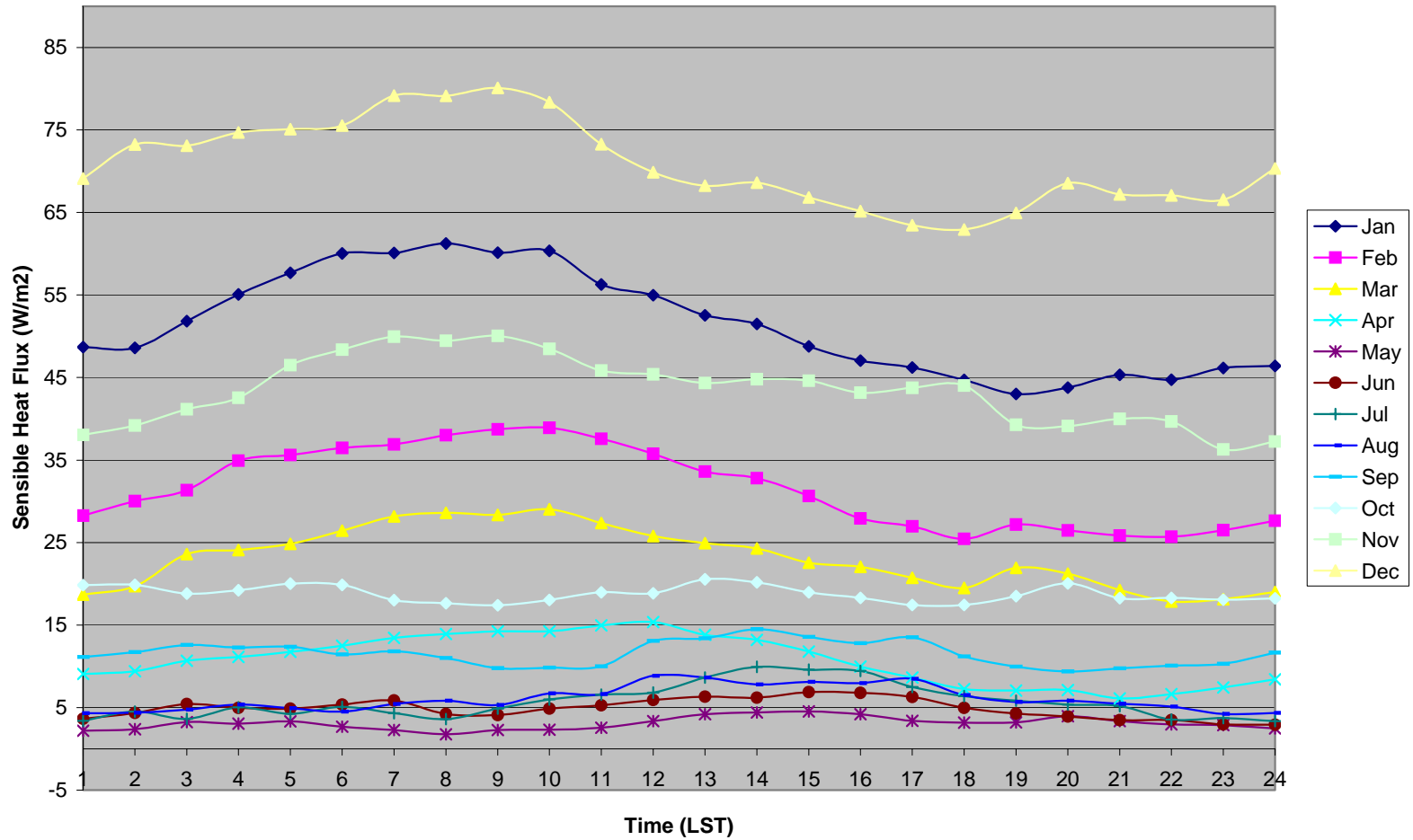


Figure 5-38. COARE hourly average sensible heat fluxes over buoy 42040 for May 1998 through October 2001.

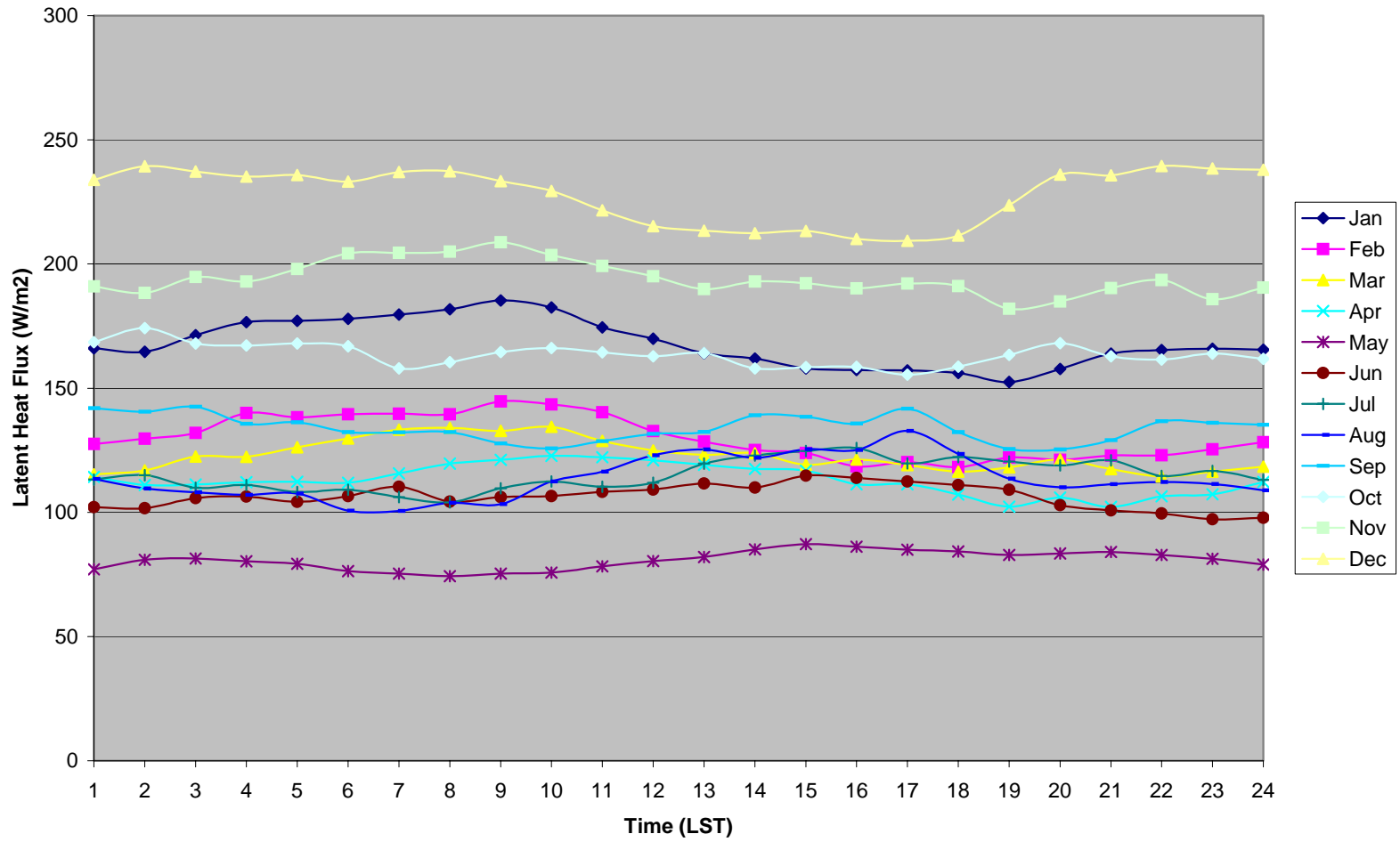


Figure 5-39. COARE hourly average latent heat fluxes over buoy 42040 for May 1998 through October 2001.

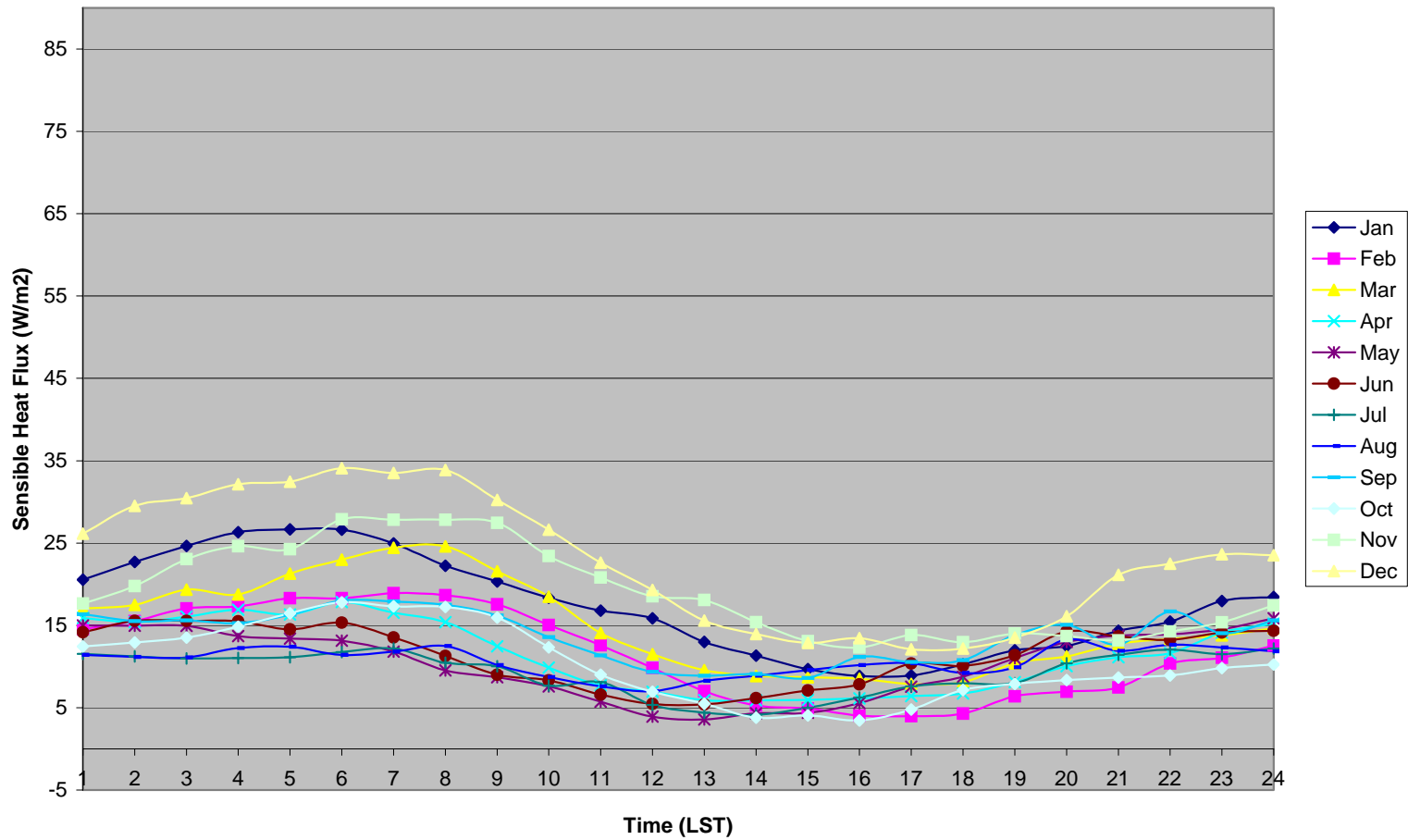


Figure 5-40. COARE hourly average sensible heat fluxes over GDIL1 for May 1998 through October 2001.

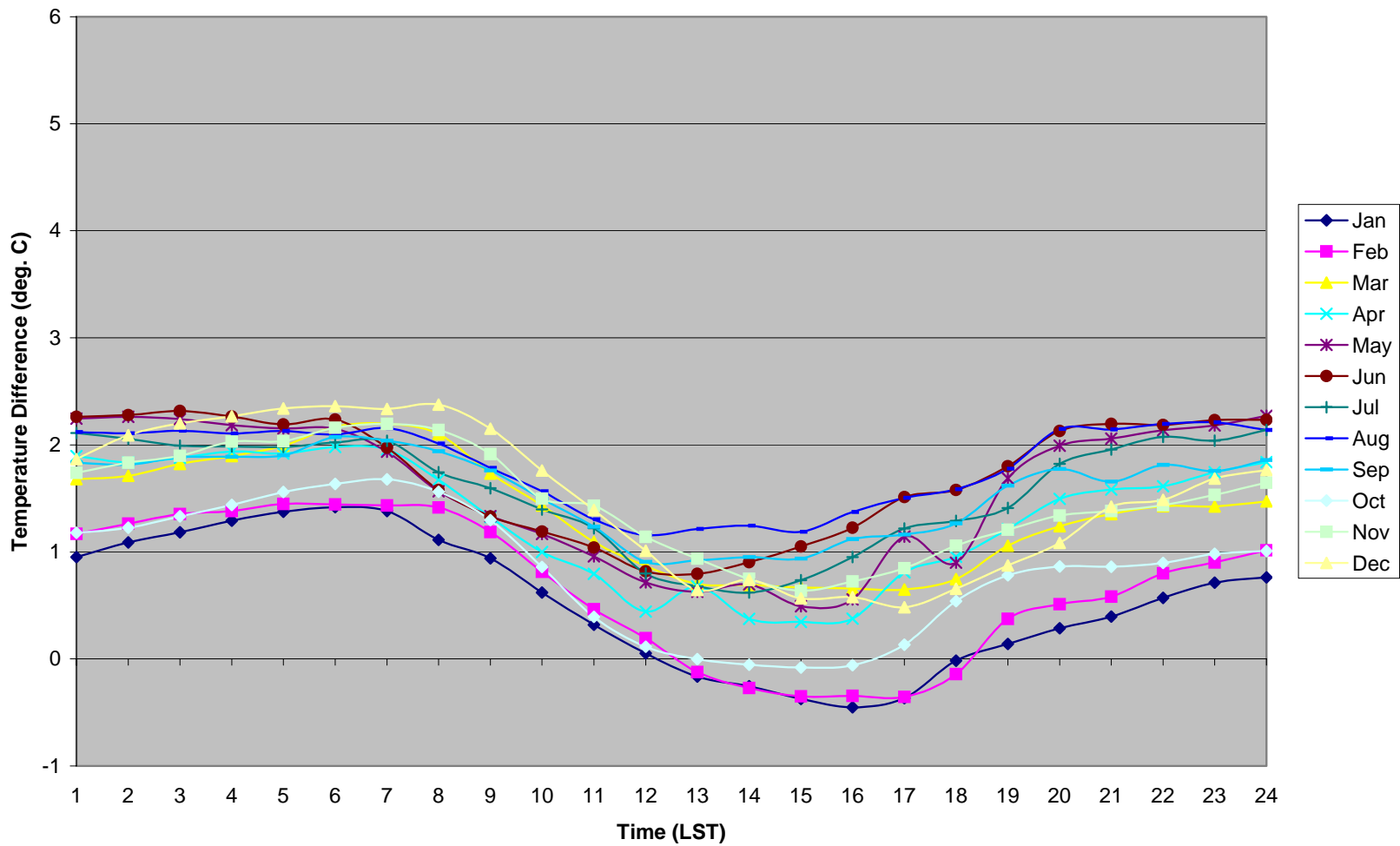


Figure 5-41. Hourly skin temperature minus air temperature over GDIL1 for May 1998 through October 2001.

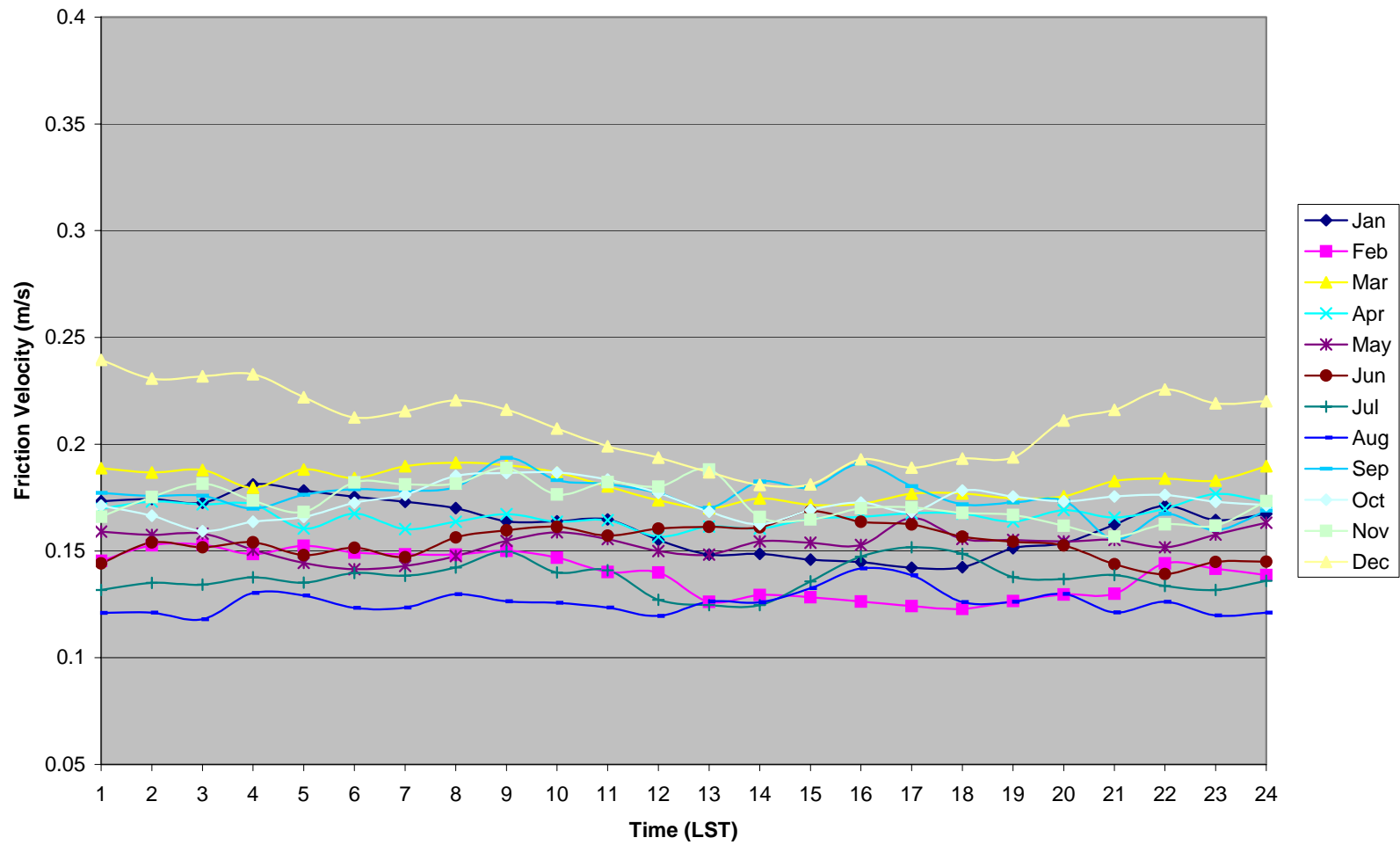


Figure 5-42. COARE hourly friction velocity over GDIL1 for May 1998 through October 2001.

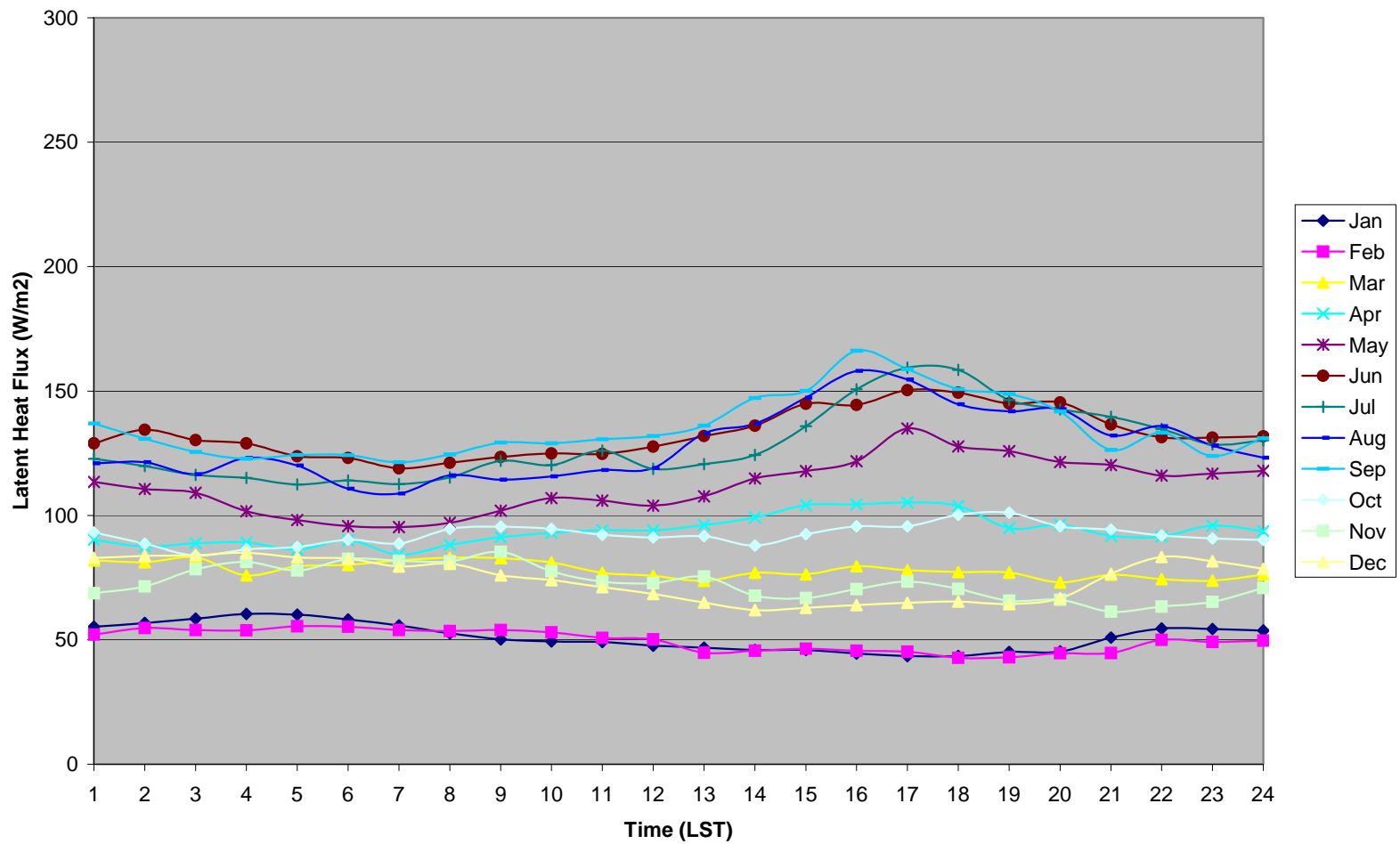


Figure 5-43. COARE hourly average latent heat fluxes over GDIL1 for May 1998 through October 2001.

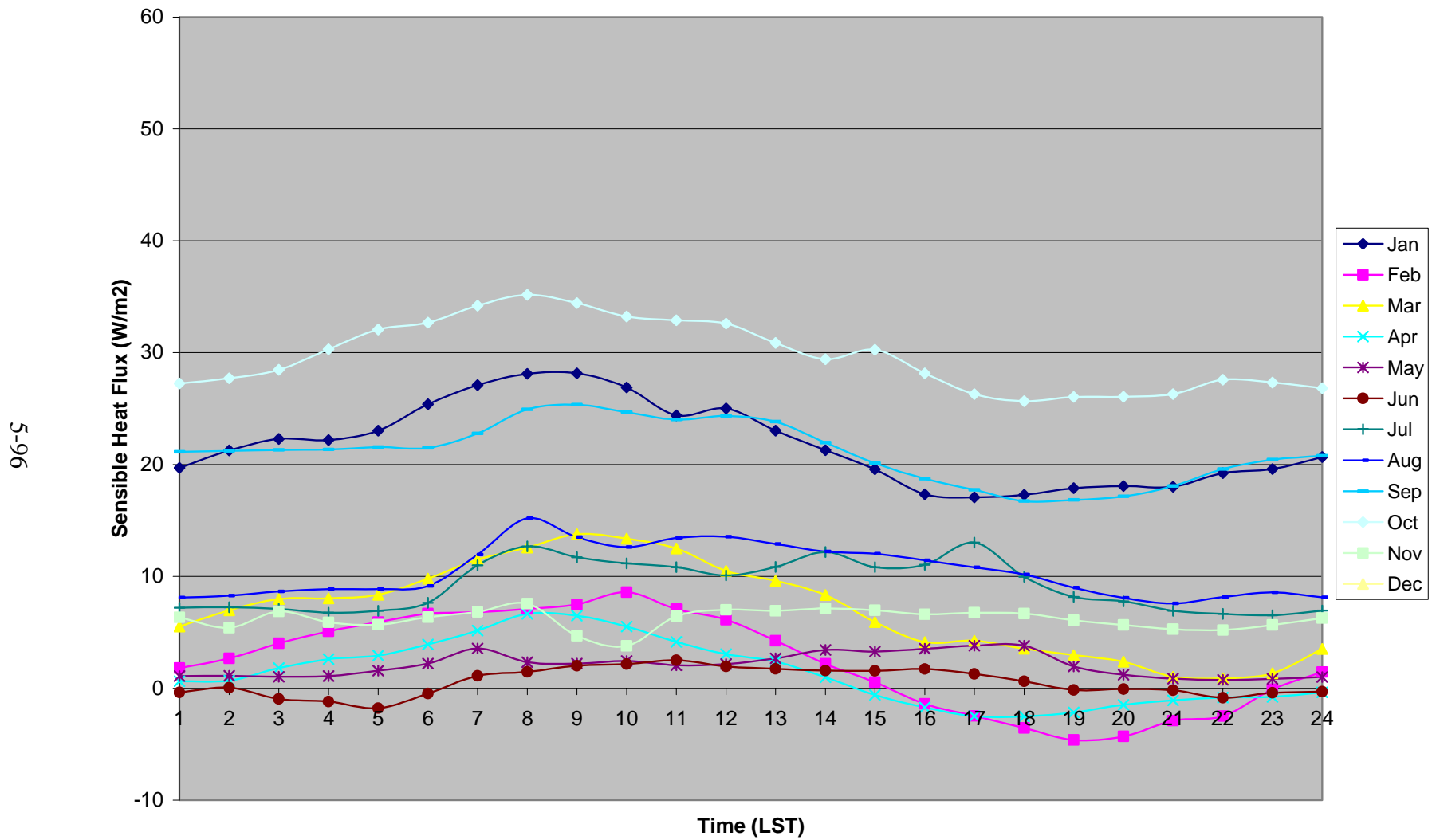


Figure 5-44. COARE hourly average sensible heat fluxes over BIP for September 2000 through September 2001.

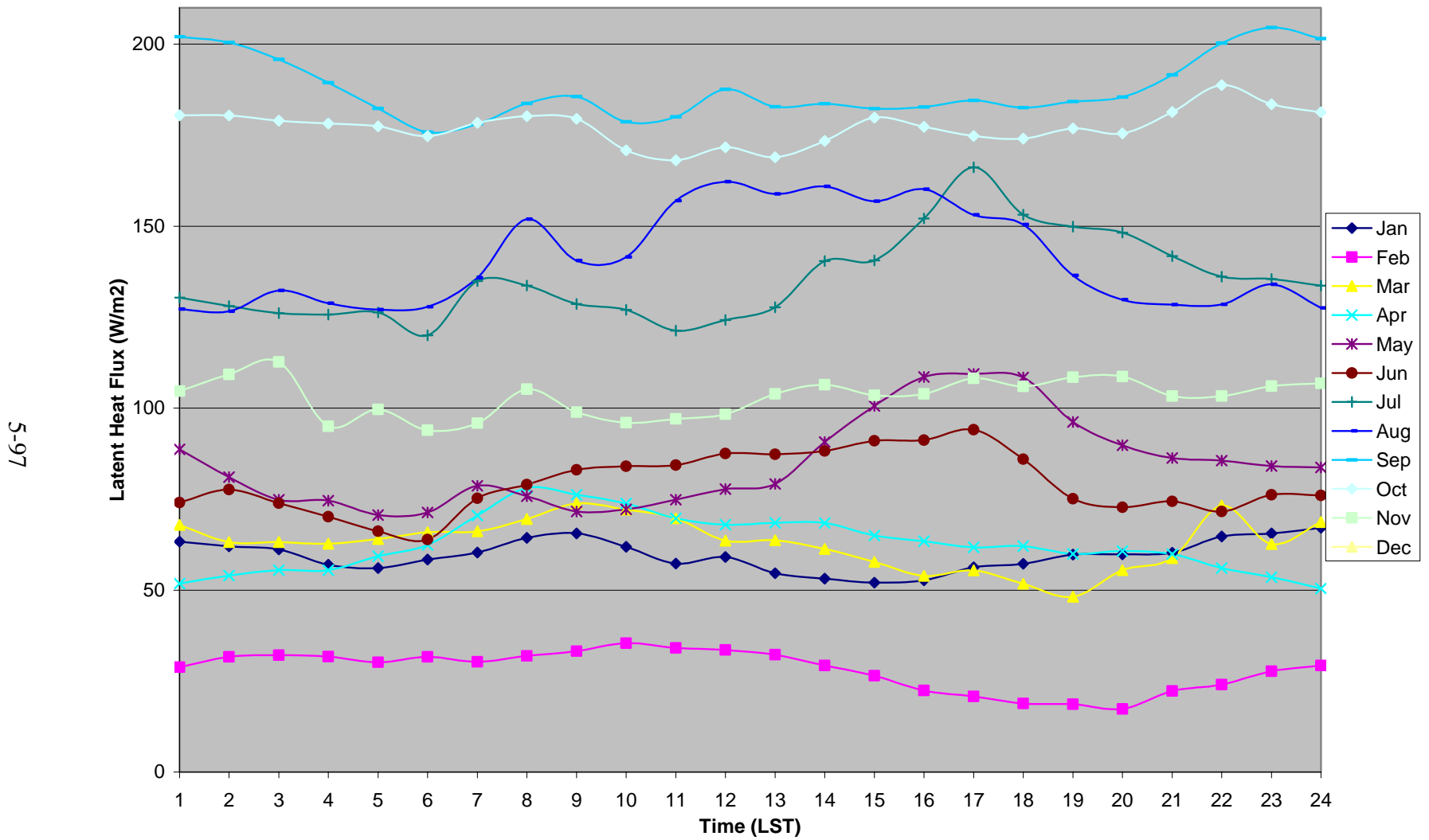


Figure 5-45. COARE hourly average latent heat fluxes over BIP for September 2000 through September 2001.

86-5

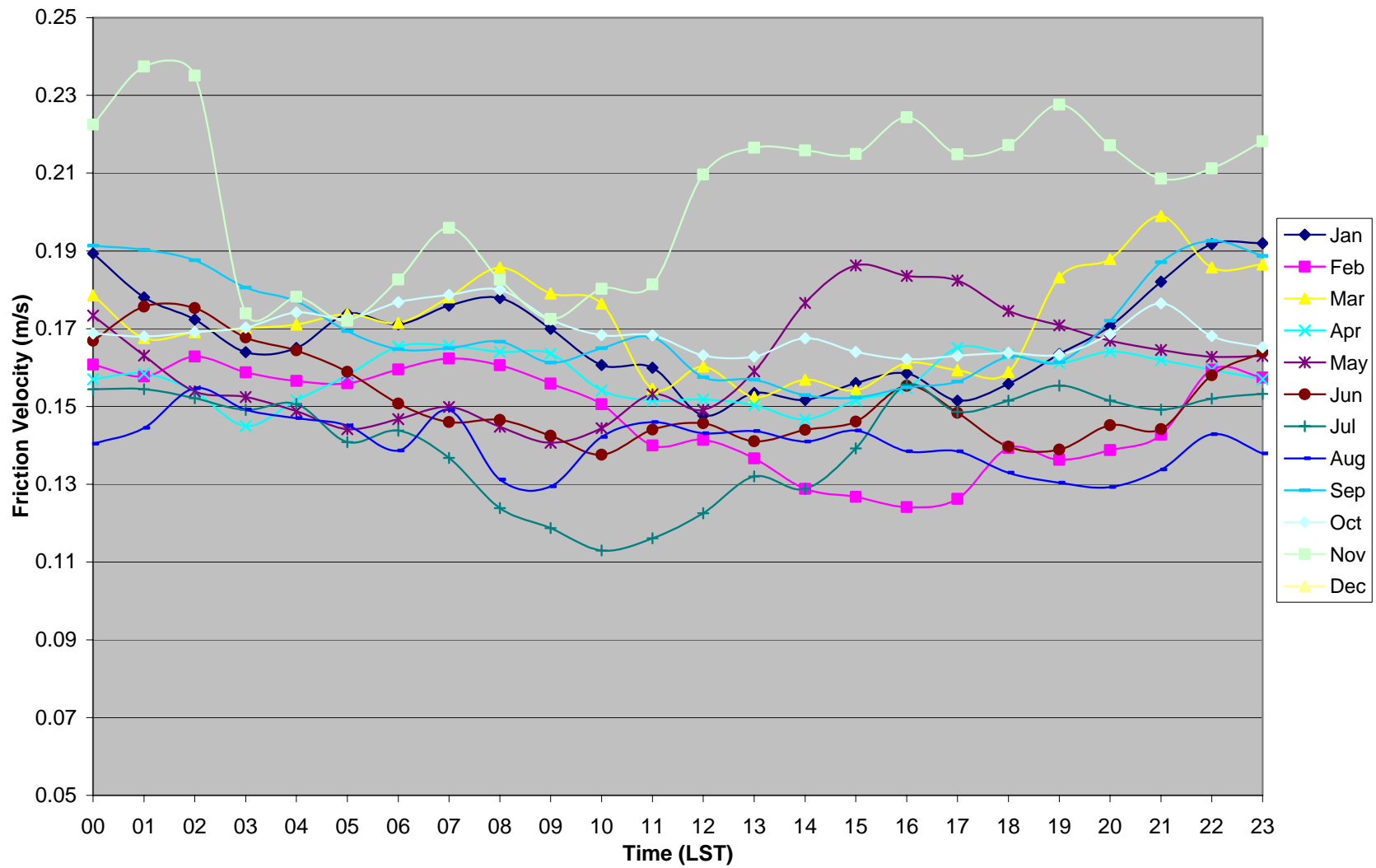


Figure 5-46. COARE hourly average friction velocity over BIP for September 2000 through September 2001.

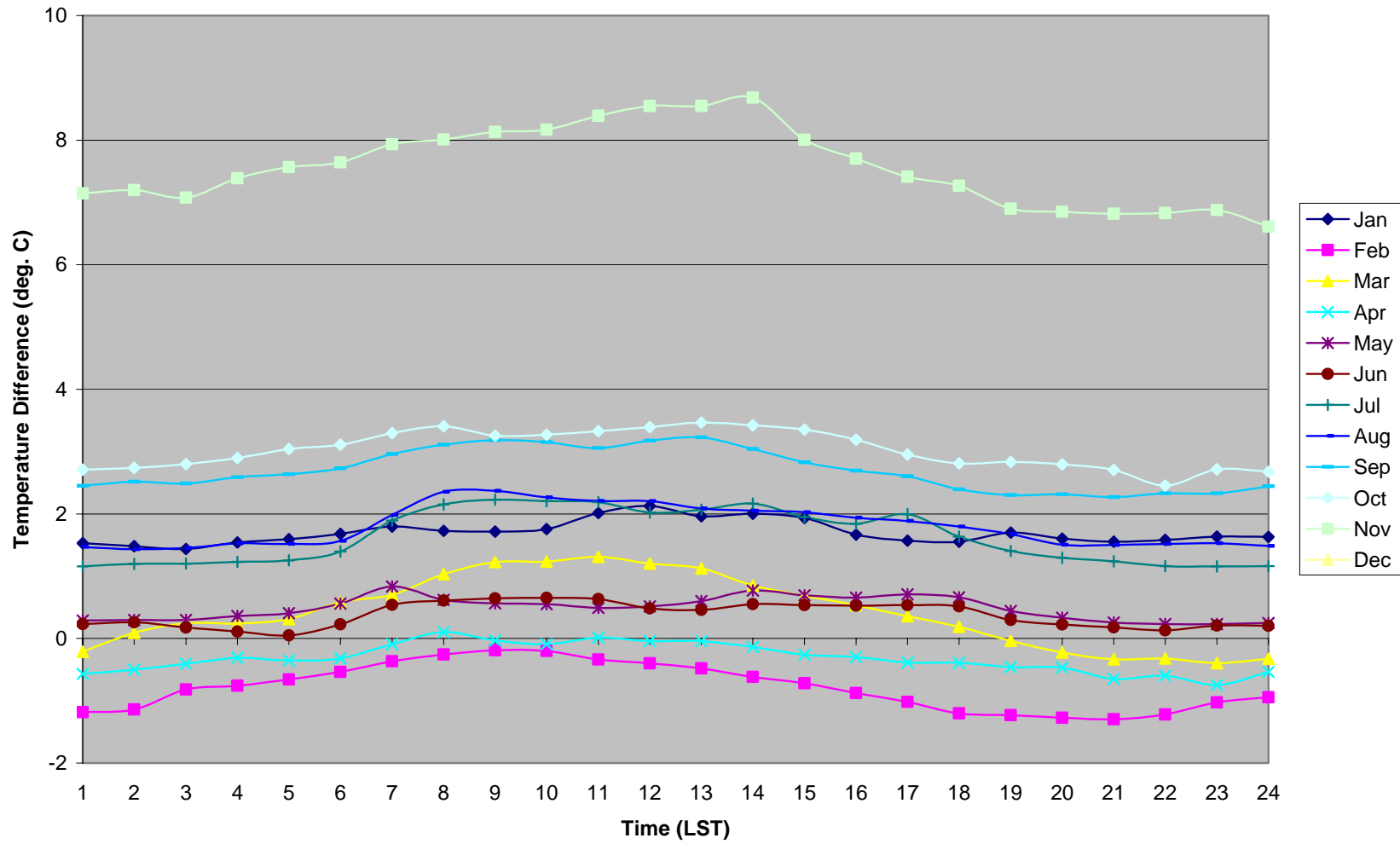


Figure 5-47. Hourly skin temperature minus air temperature over BIP for September 2000 through September 2001.

5-100

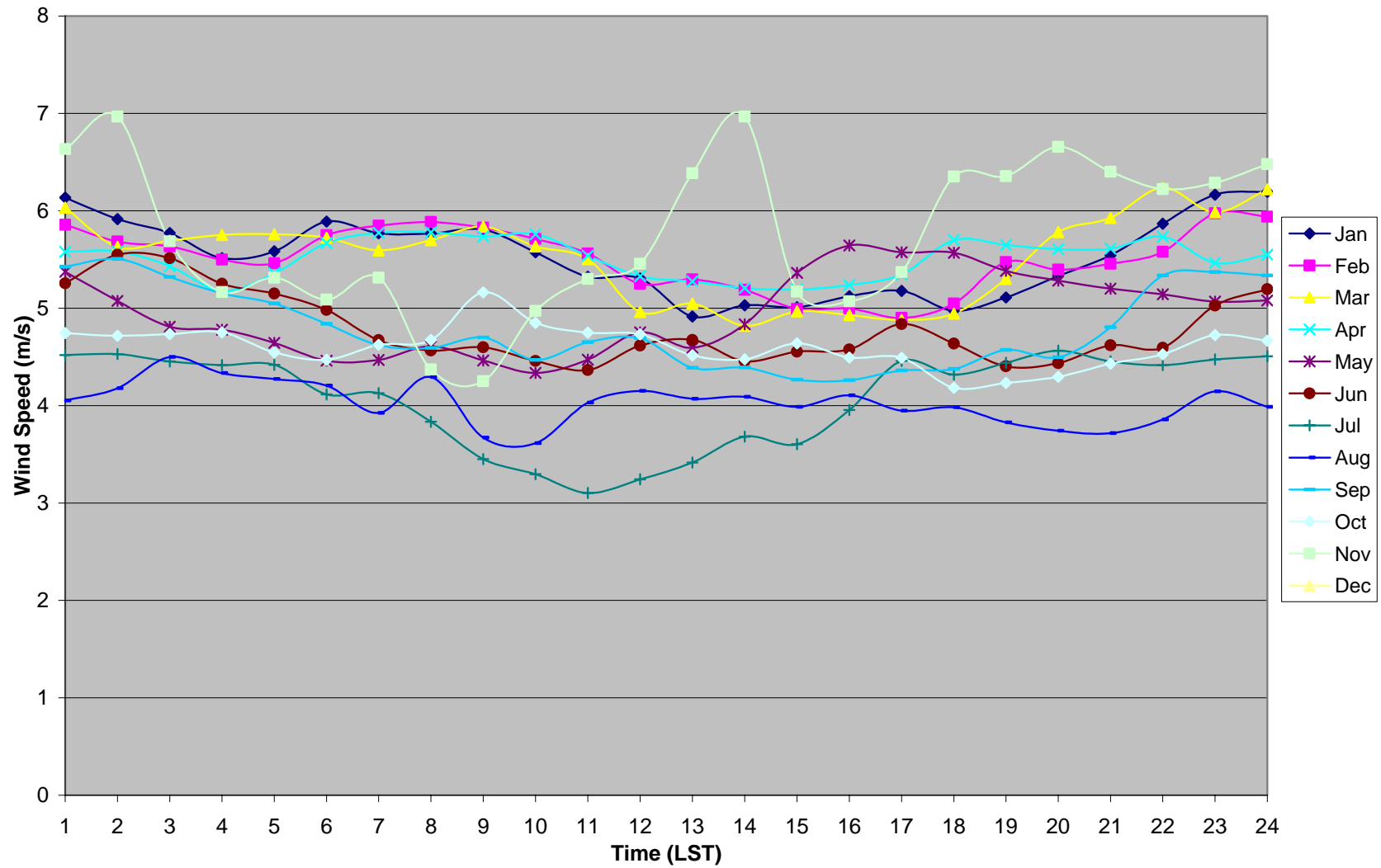


Figure 5-48. Observed hourly average wind speed over BIP for September 2000 through September 2001.

I01-5

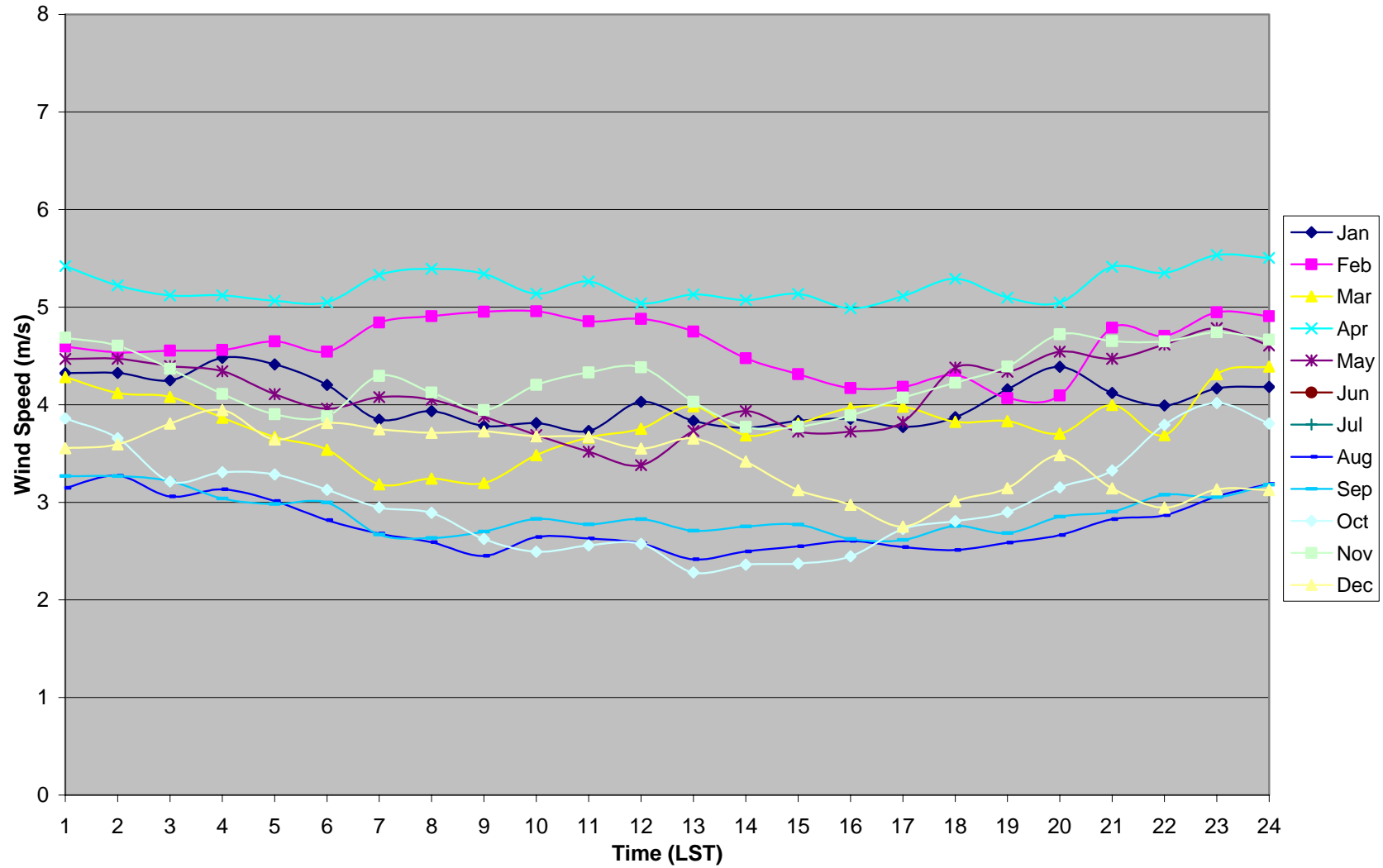


Figure 5-49. Observed hourly average wind speed over DWP for September 2000 through September 2001.

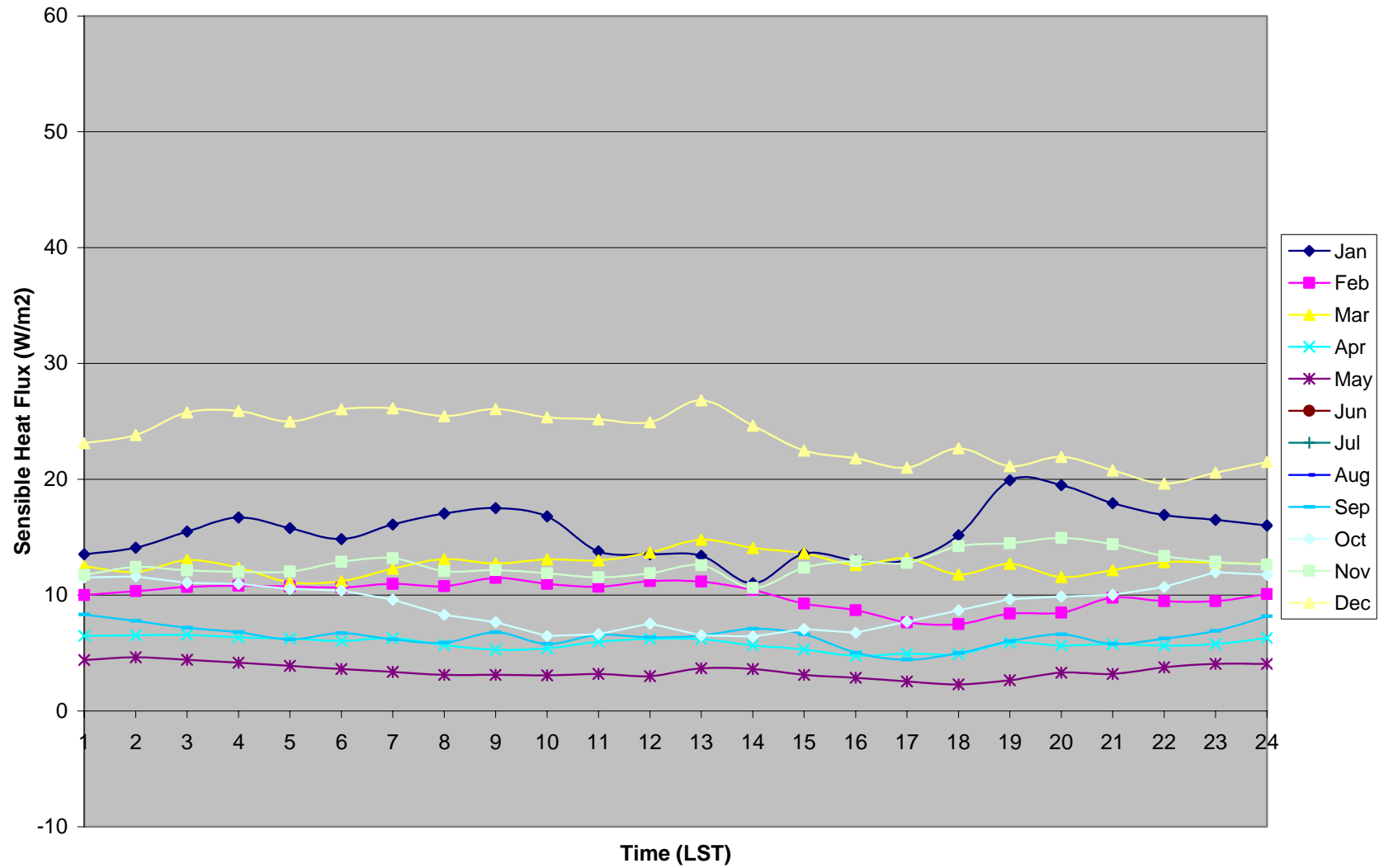


Figure 5-50. COARE hourly average sensible heat fluxes over DWP for September 2000 through September 2001.

5-103

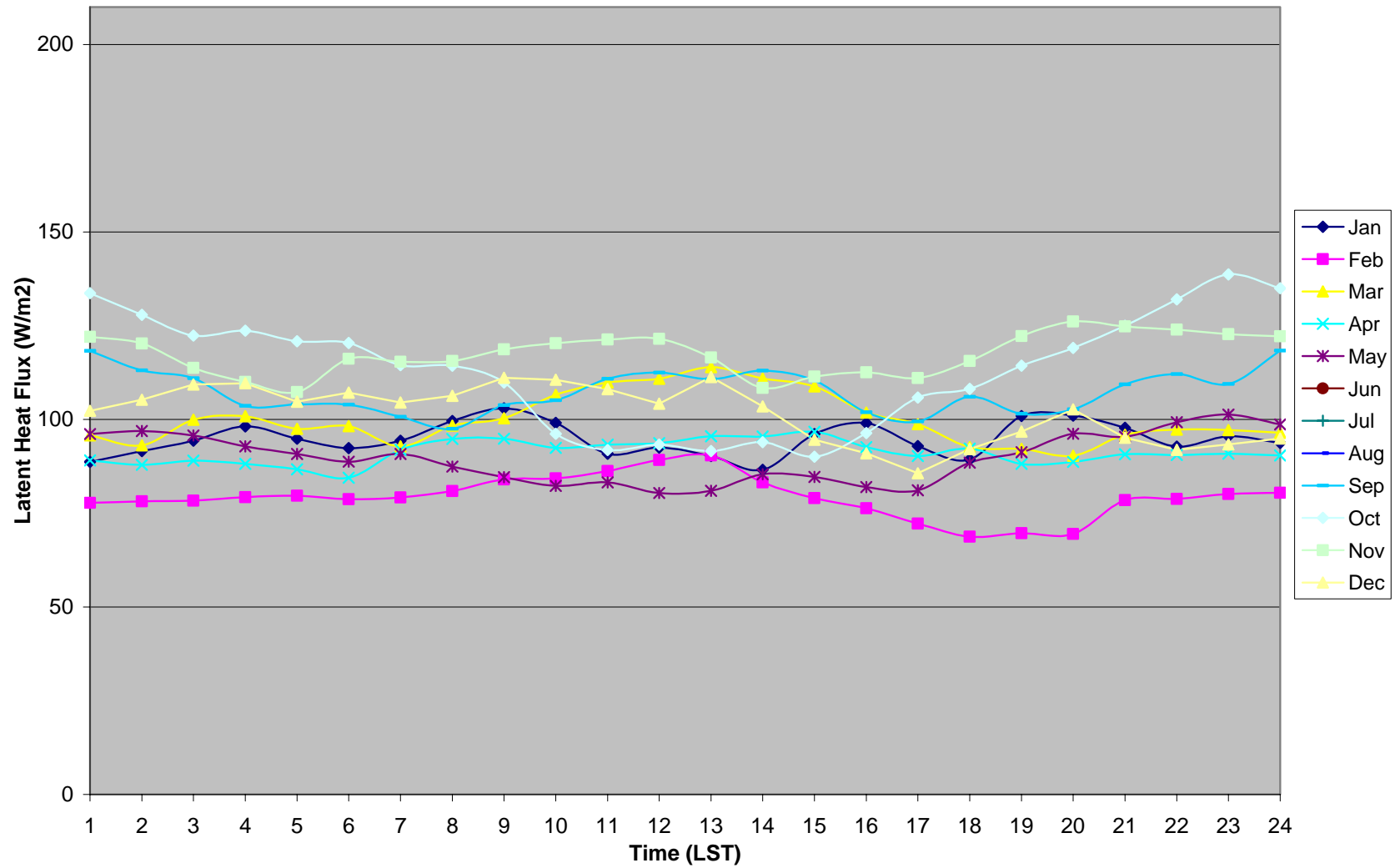


Figure 5-51. COARE hourly average latent heat fluxes over DWP for September 2000 through September 2001.

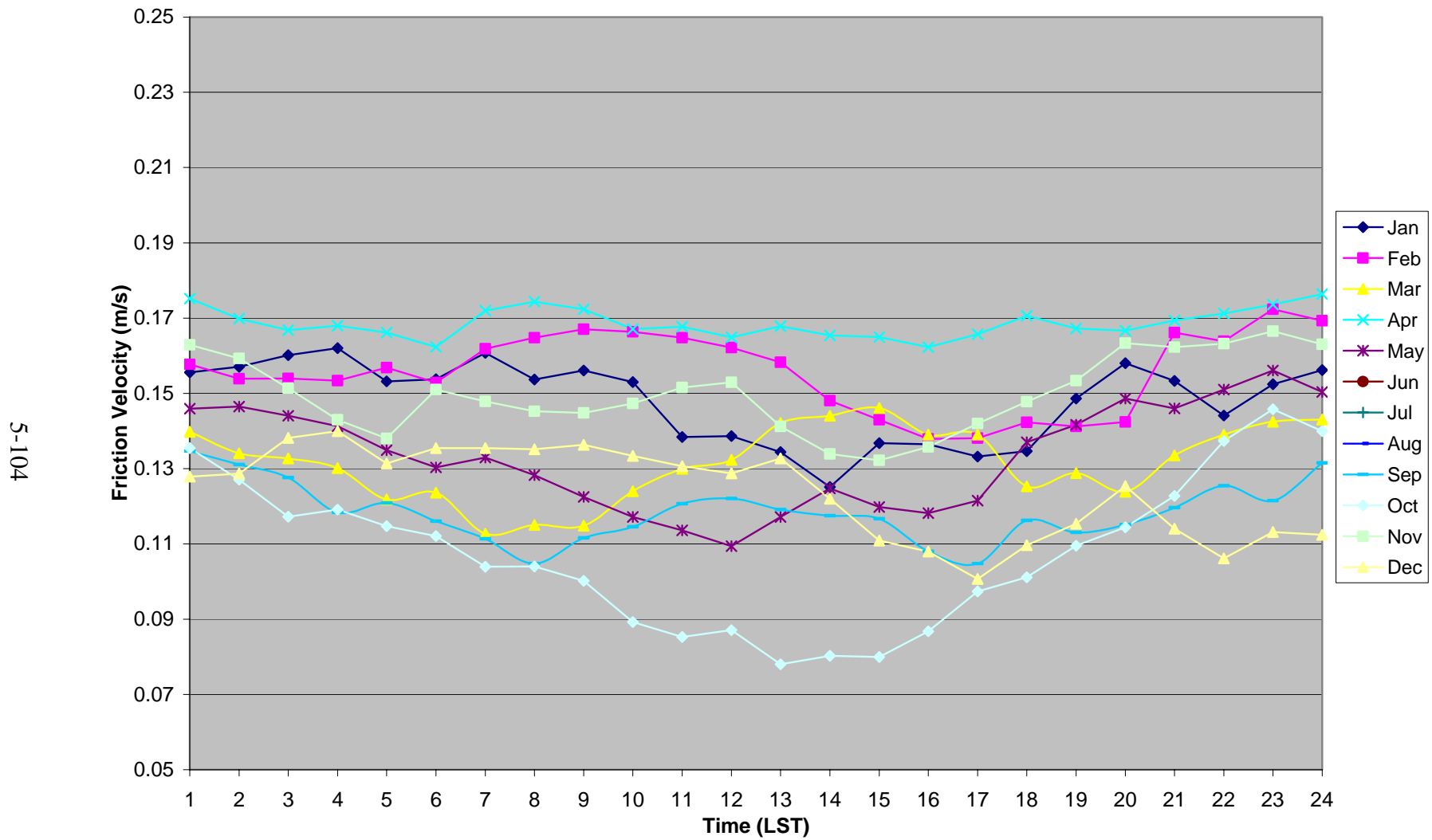


Figure 5-52. COARE hourly average friction velocity over DWP for September 2000 through September 2001.

5-105

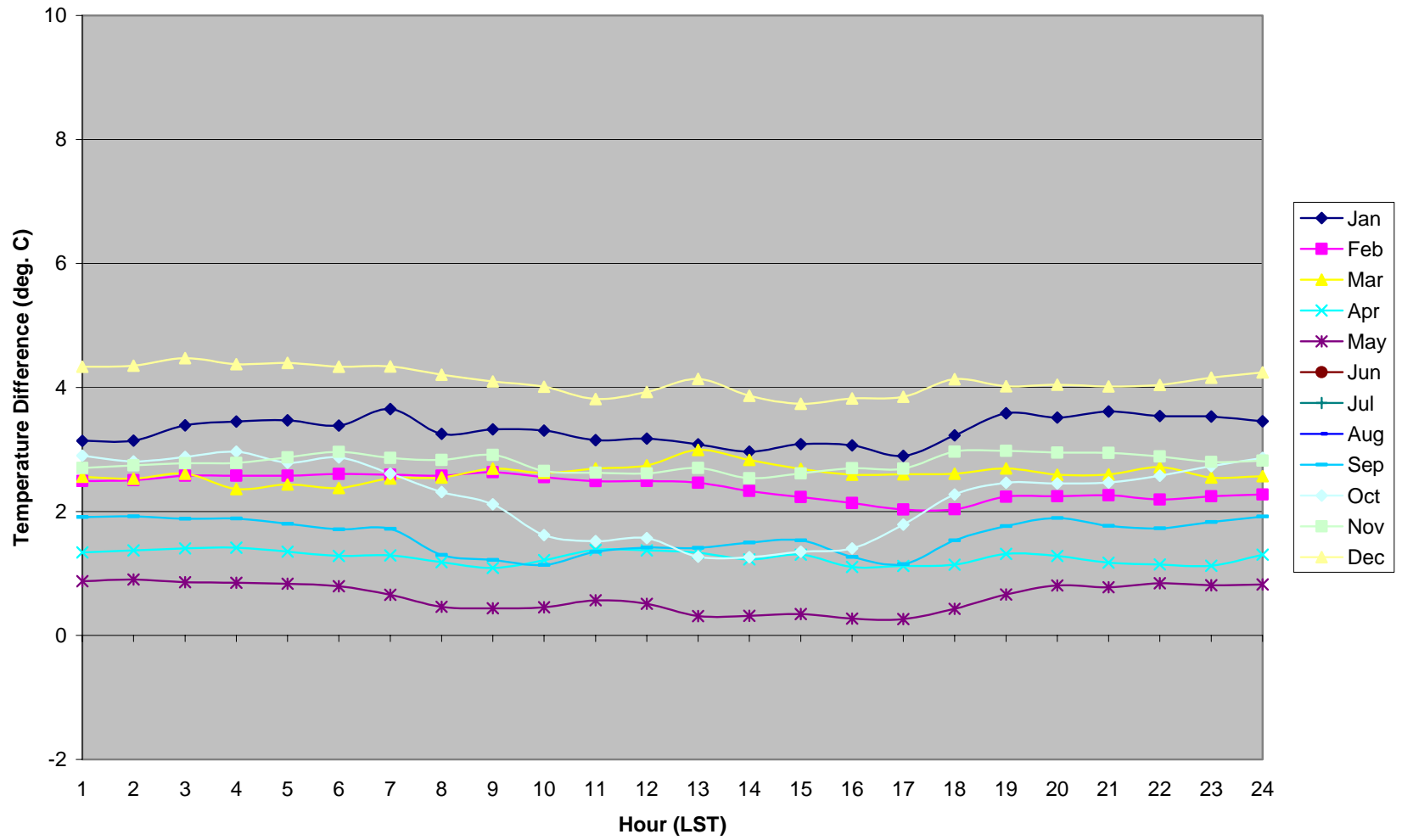


Figure 5-53. Hourly skin temperature minus air temperature over DWP for September 2000 through September 2001.

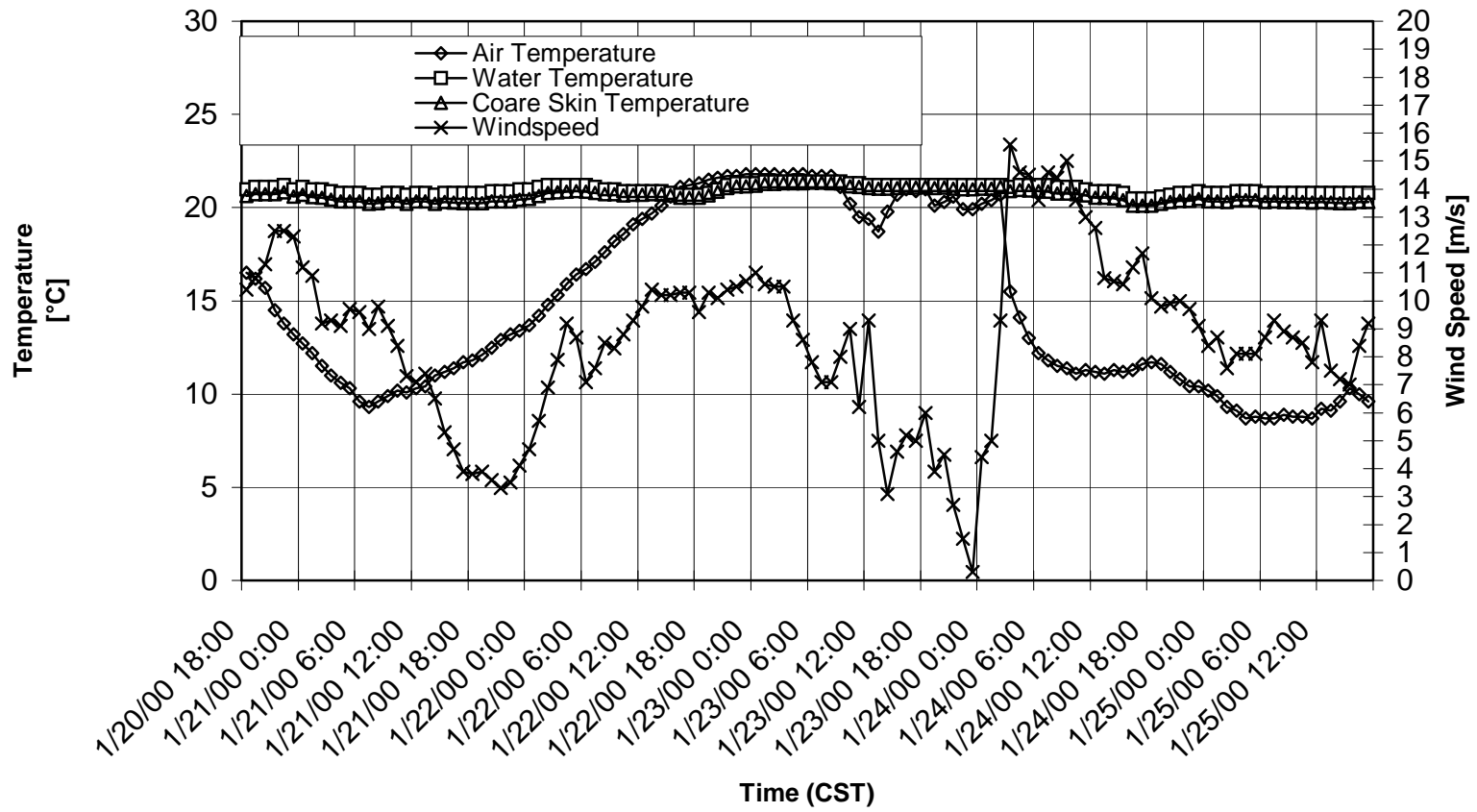


Figure 5-54. Air and skin temperatures and wind speed at buoy 42040 for January 20 through 25, 2000.

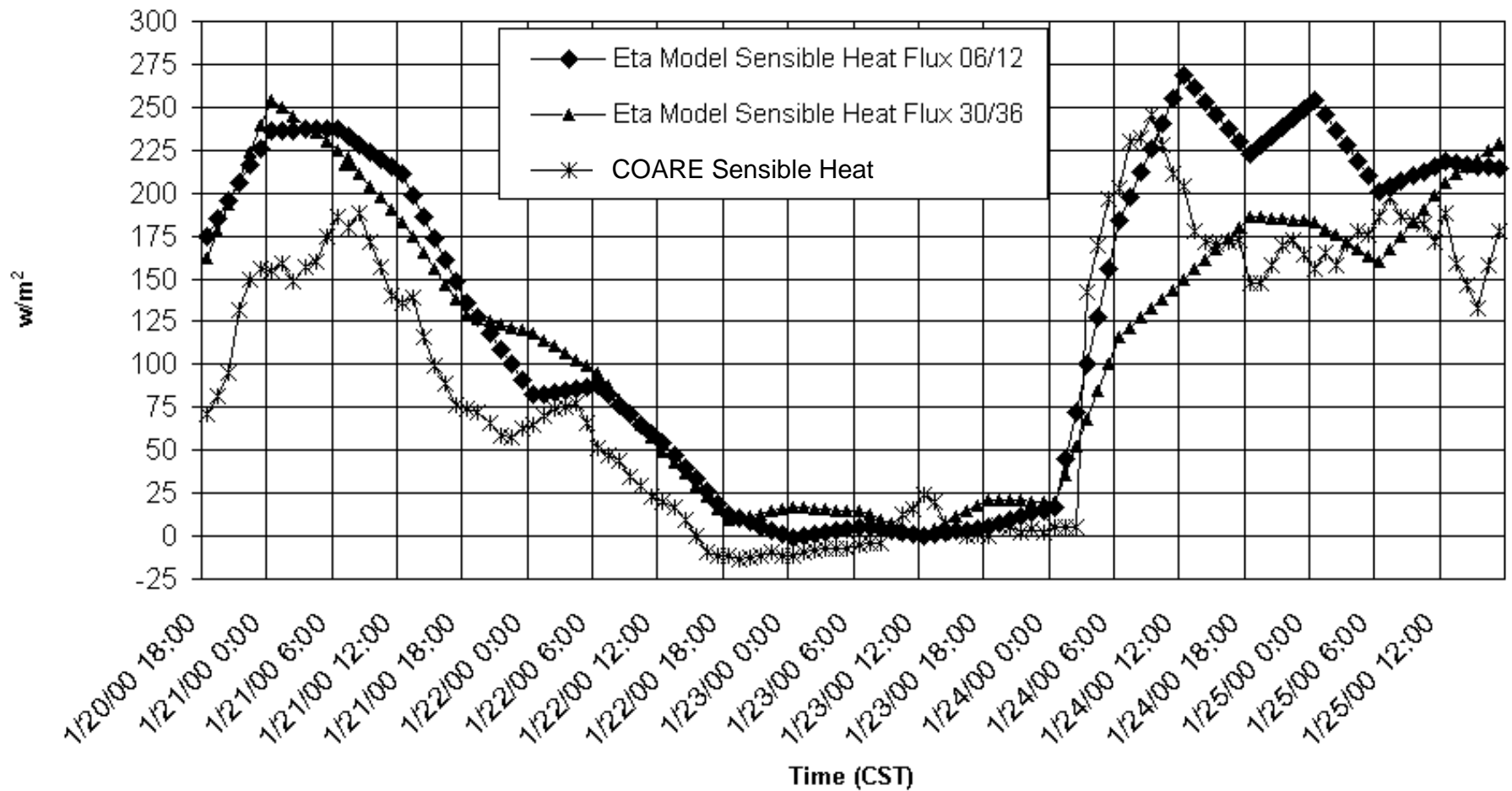


Figure 5-55. COARE and Eta hourly sensible heat fluxes at buoy 42040 for January 20 through 25, 2000. Eta-simulated sensible heat fluxes were obtained from the 6- and 12-hr (30- and 36-hr) forecasts and interpolated to hourly values between 6- and 12-hr (30- and 36-hr) forecasts.

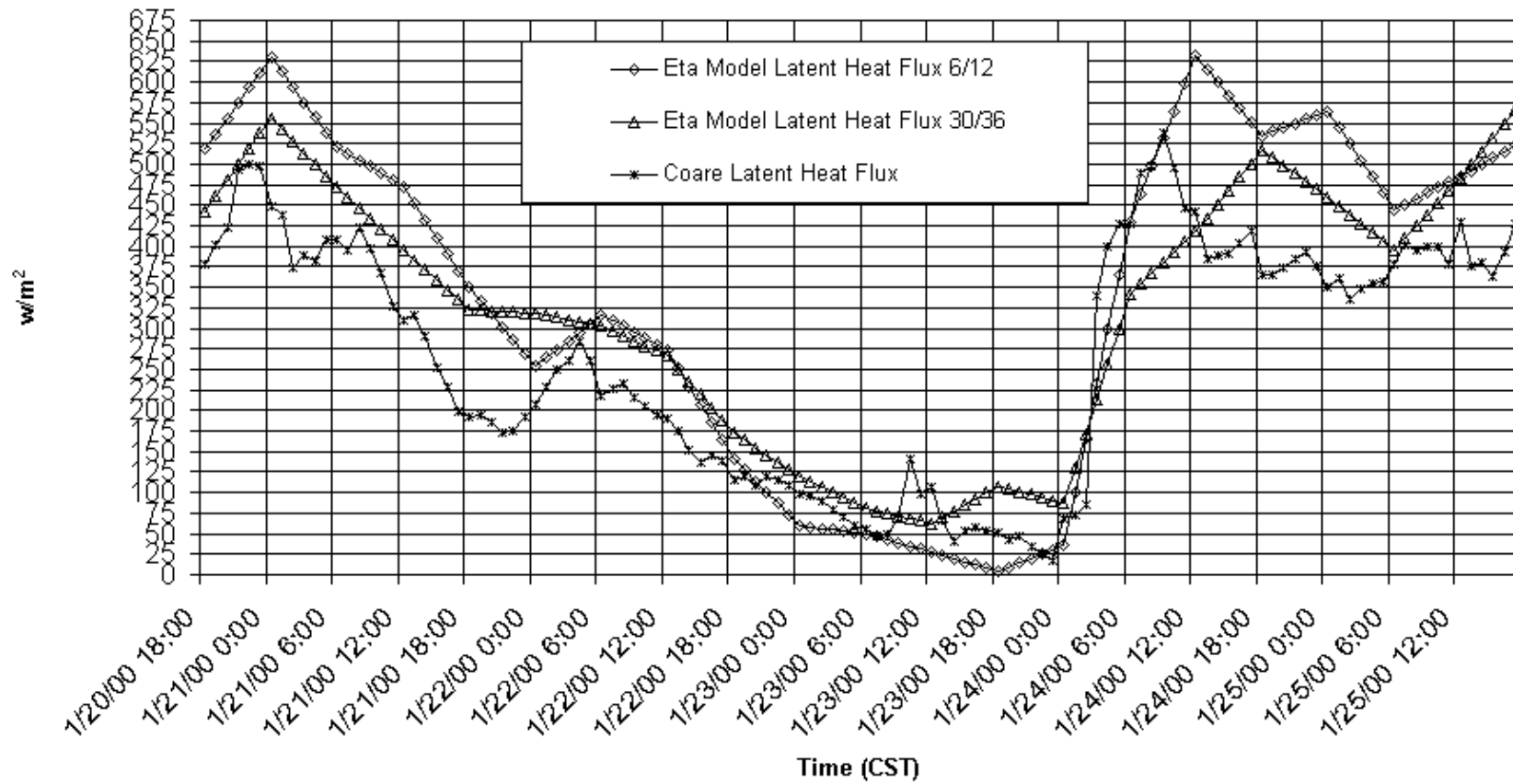


Figure 5-56. COARE and Eta hourly latent heat fluxes at buoy 42040 for January 20 through 25, 2000. Eta-simulated latent heat fluxes were obtained from the 6- and 12-hr (30- and 36-hr) forecasts and interpolated to hourly values between 6- and 12-hr (30- and 36-hr) forecasts.

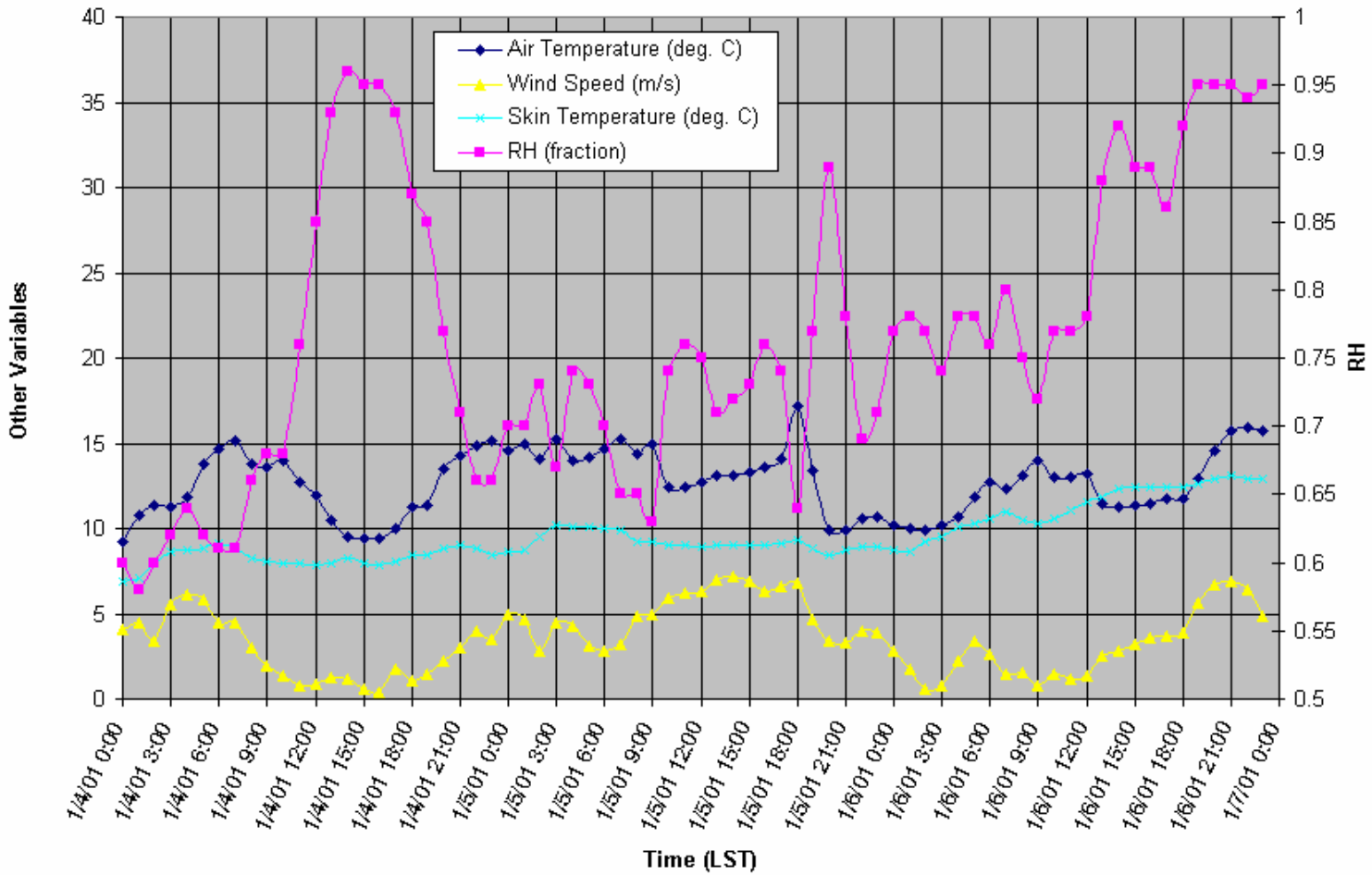


Figure 5-57. Hourly air and skin temperatures, wind speed, and relative humidity at VRM for January 4 through 6, 2001.

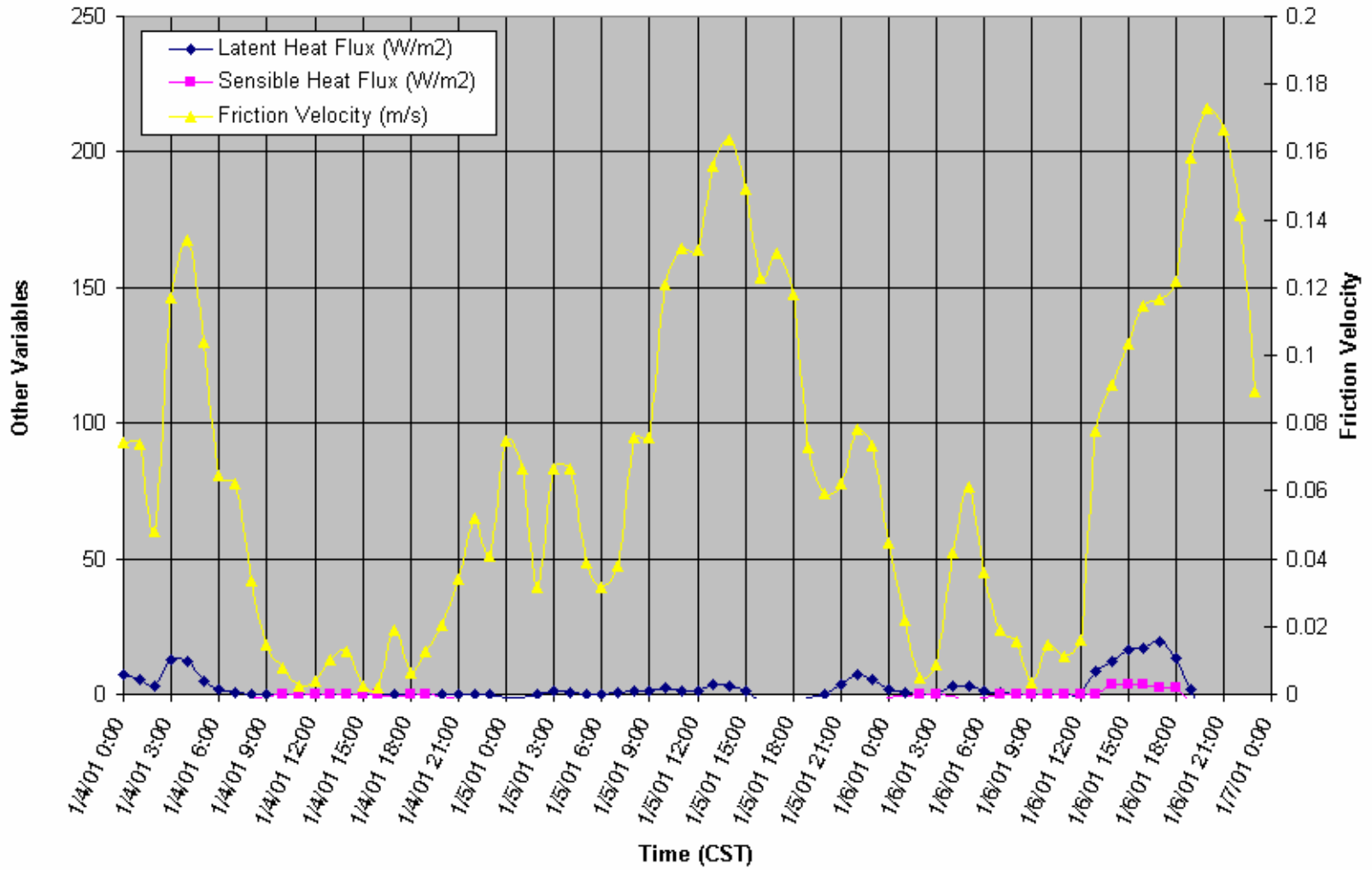


Figure 5-58. COARE hourly average latent and sensible heat fluxes and friction velocity at VRM for January 4 through 6, 2001.

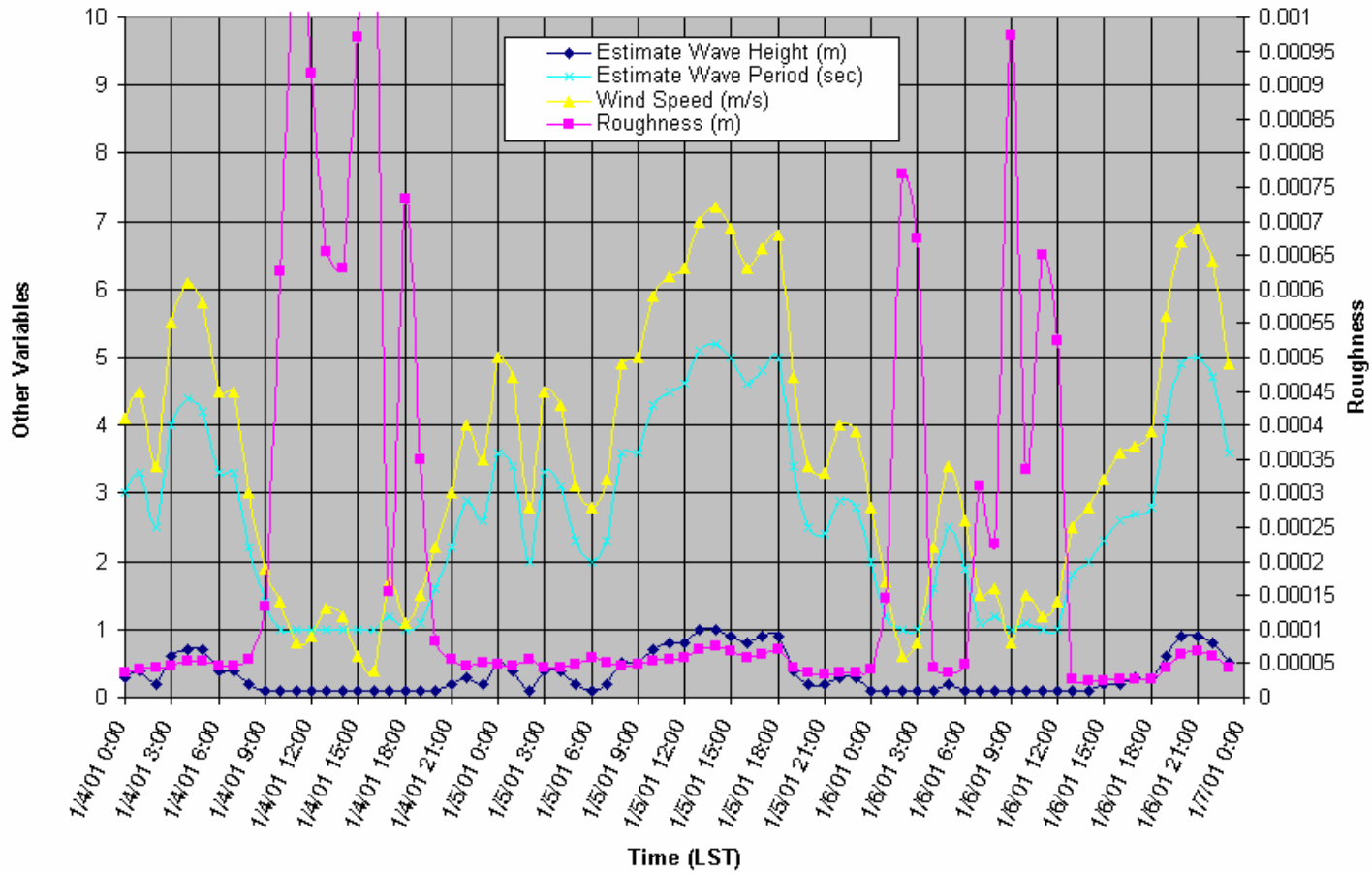


Figure 5-59. Estimated wave height and period, wind speed, and surface roughness length at VRM for January 4 through 6, 2001.

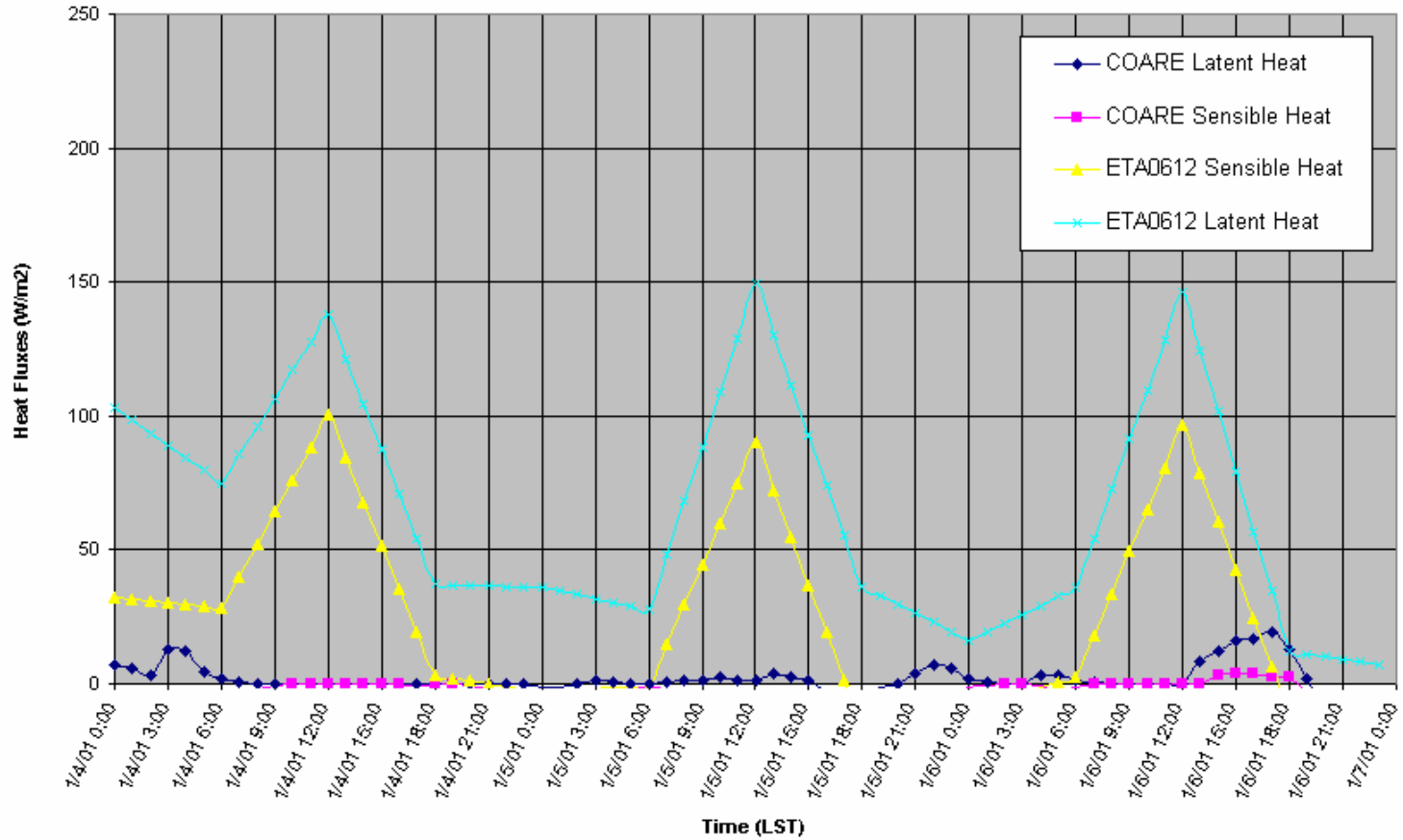


Figure 5-60. COARE and Eta latent and sensible heat fluxes at VRM for January 4 through 6, 2001. Note: the four-digit number after Eta in the key indicates the forecast period (i.e., 0612 is the -6- to 12-hr forecast).

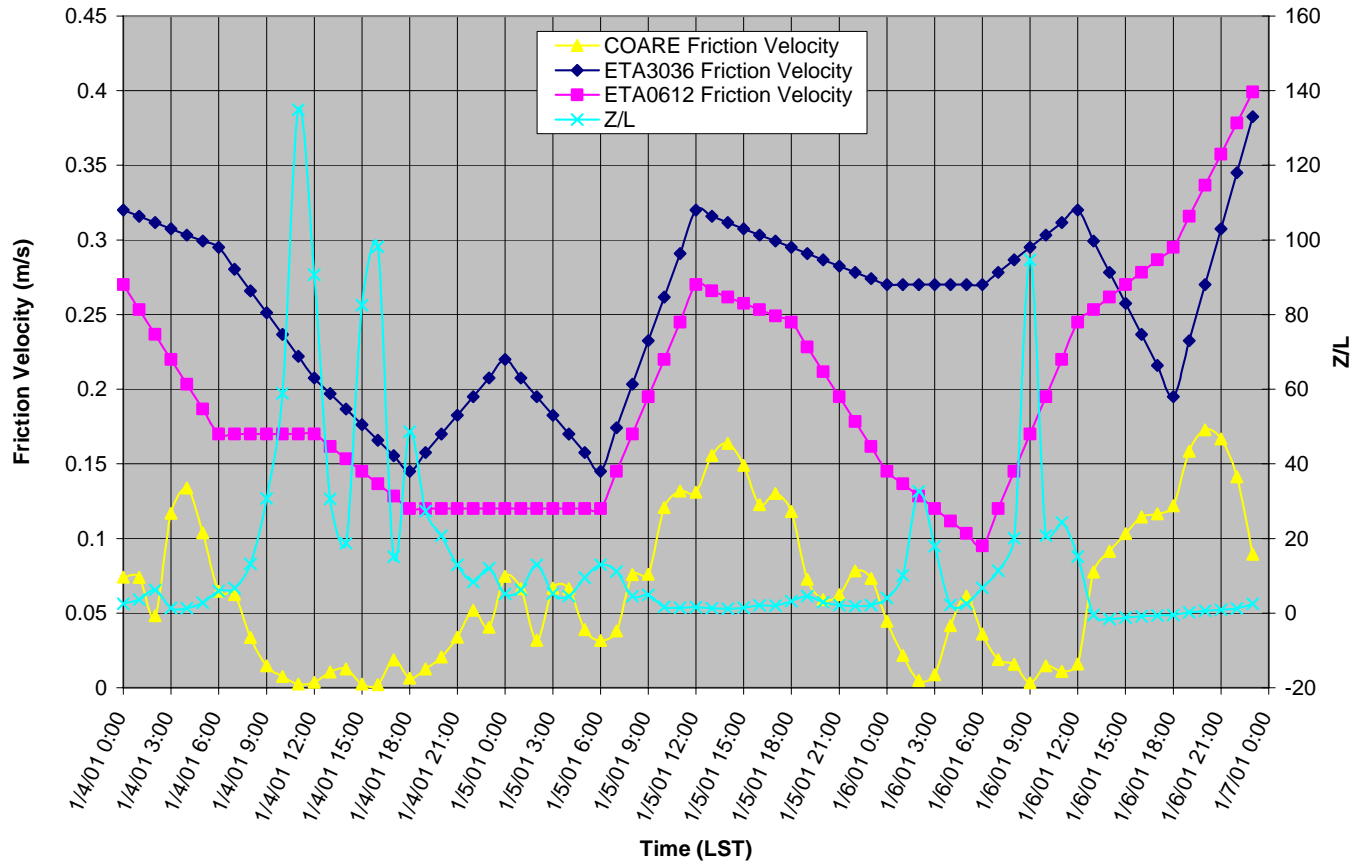


Figure 5-61. COARE and Eta friction velocity and z/L at VRM for January 4 through January 6, 2001. Note: the four-digit number after Eta in the key indicates the forecast period (i.e., 0612 is the 6- to 12-hr forecast and 3036 is the 30- to 36-hr forecast).

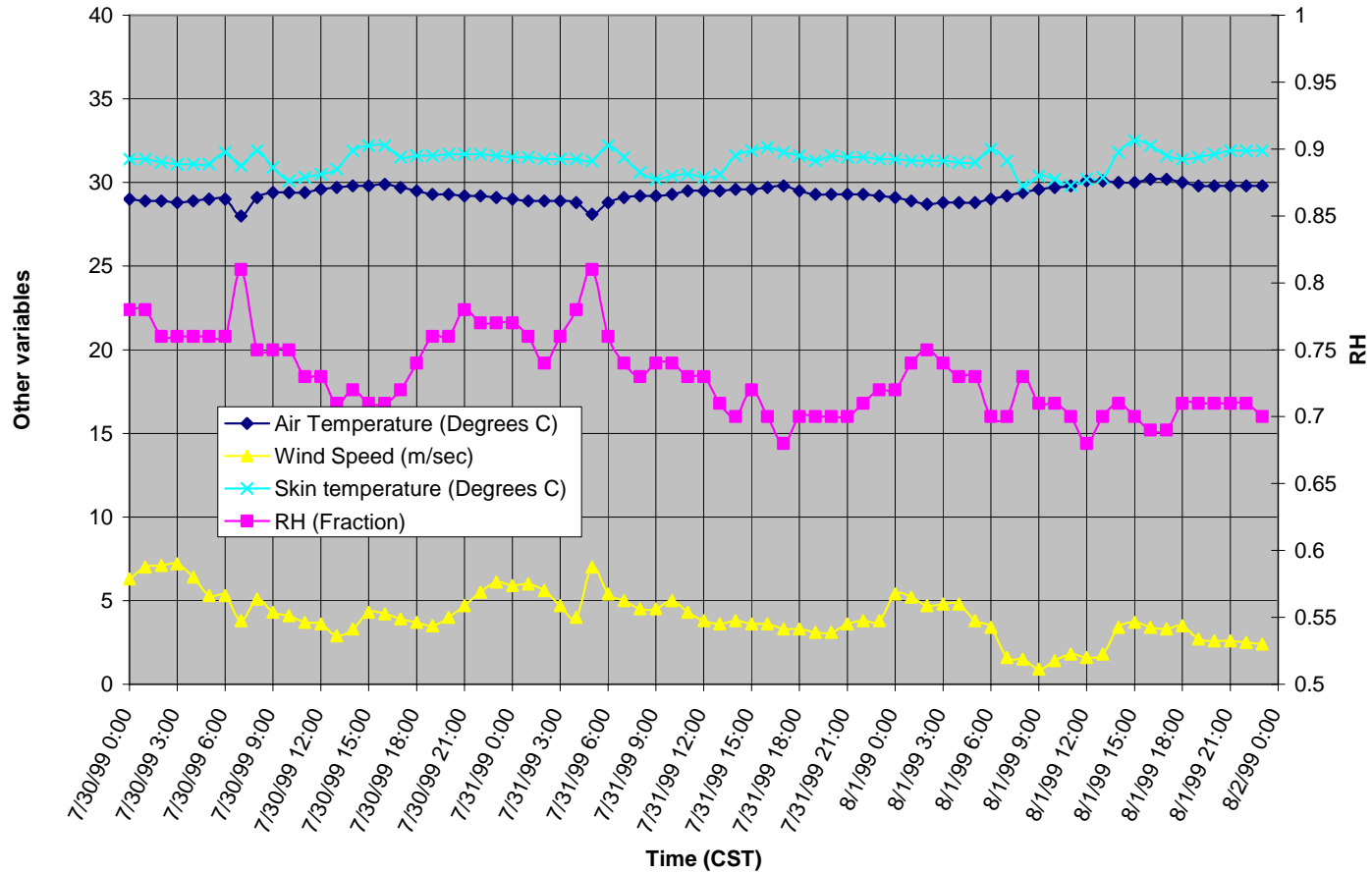


Figure 5-62a. Hourly air and skin temperatures, wind speed, and relative humidity at VRM for July 30 through August 1, 1999.

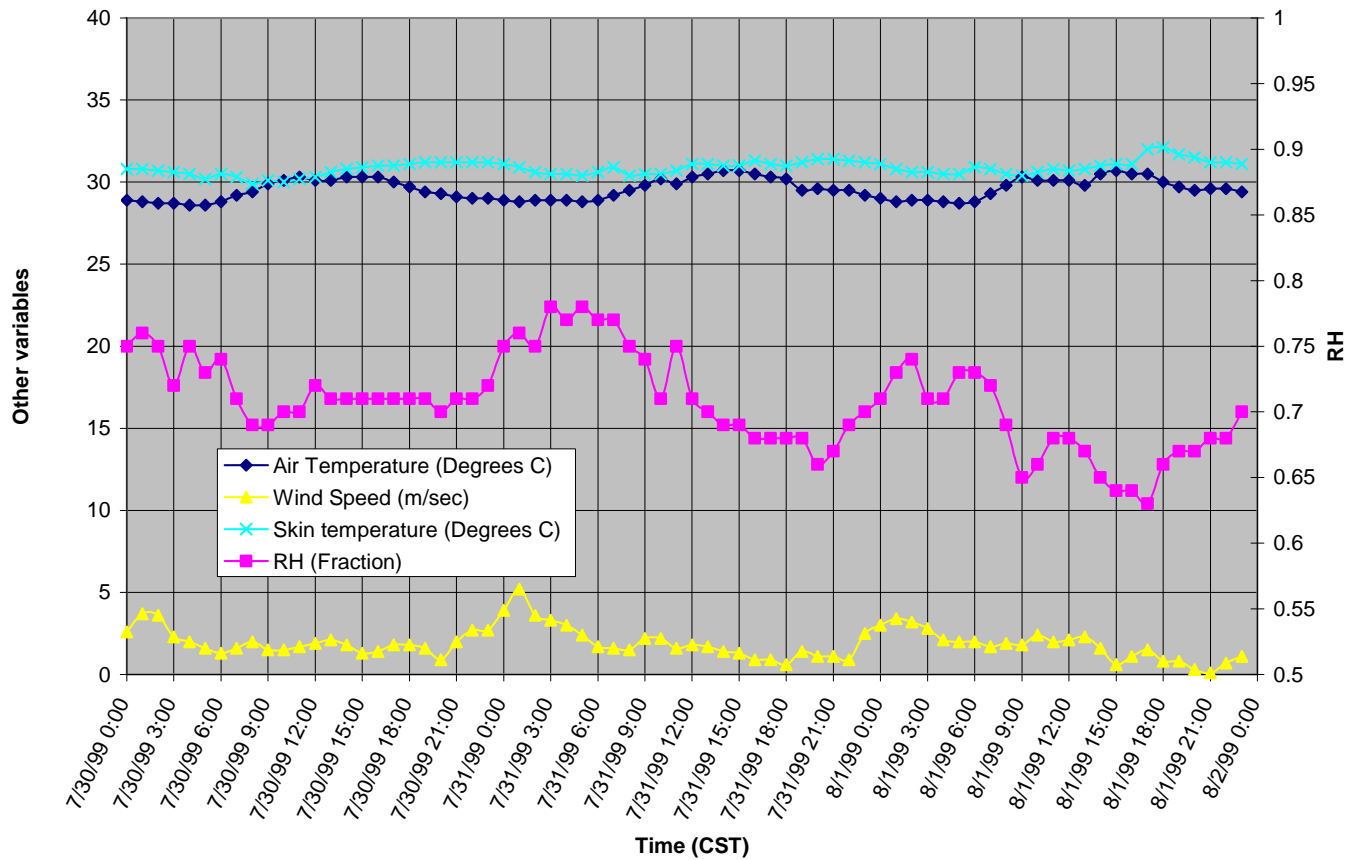


Figure 5-62b. Hourly air and skin temperatures, wind speed, and relative humidity at SMI for July 30 through August 1, 1999.

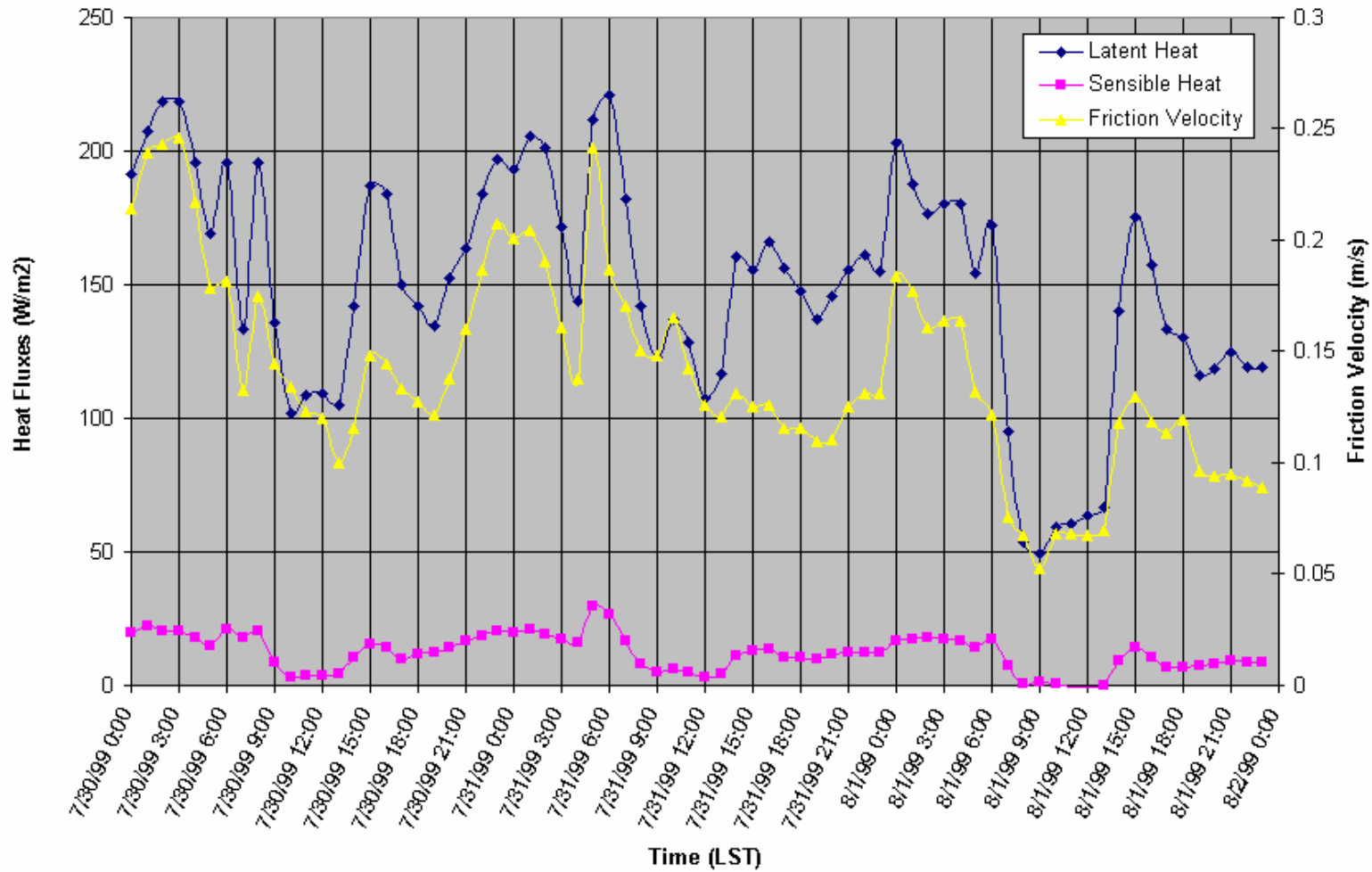


Figure 5-63a. COARE latent and sensible heat fluxes and friction velocity at VRM for July 30 through August 1, 1999.

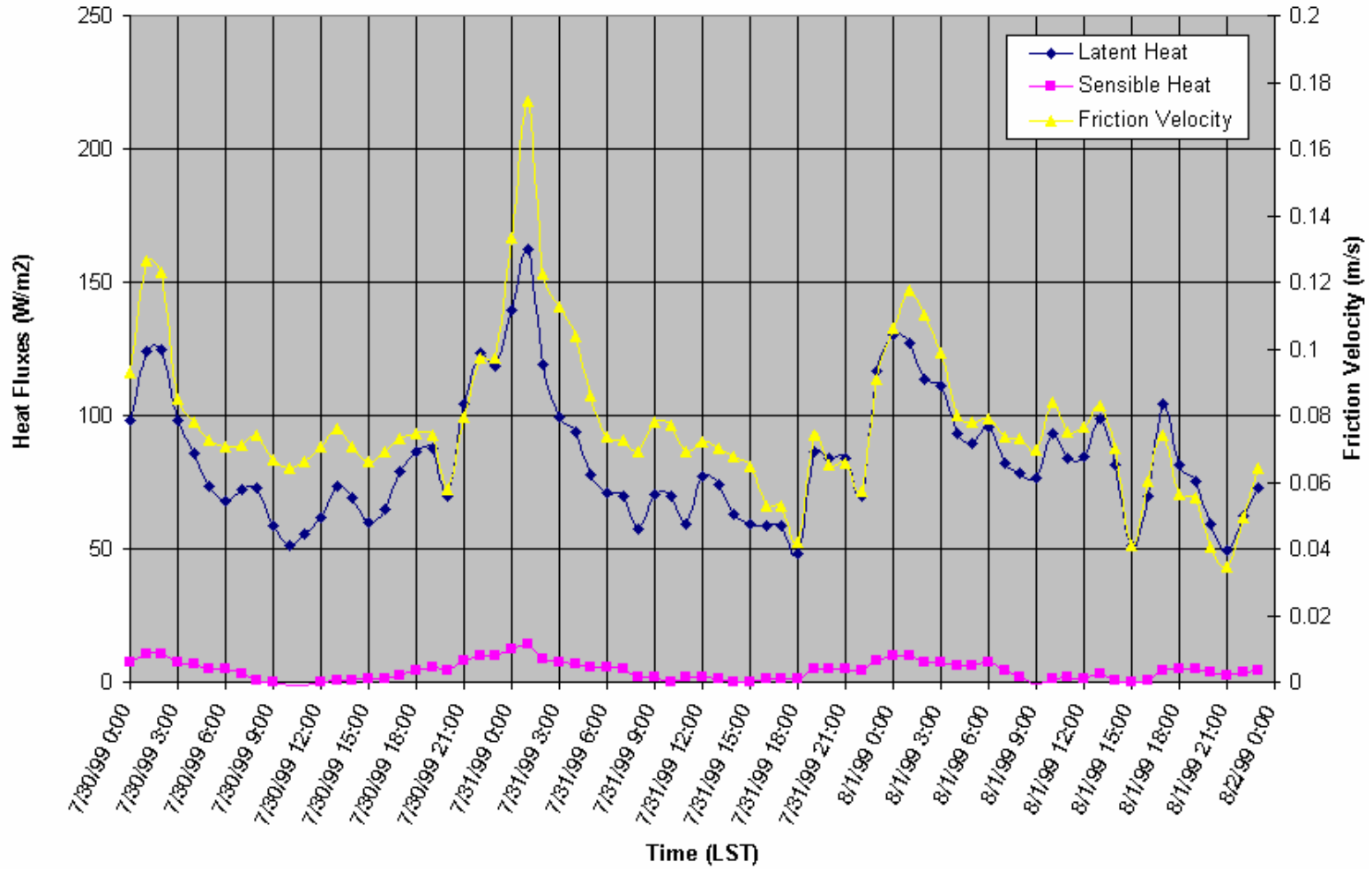


Figure 5-63b. COARE latent and sensible heat fluxes and friction velocity at SMI for July 30 through August 1, 1999.

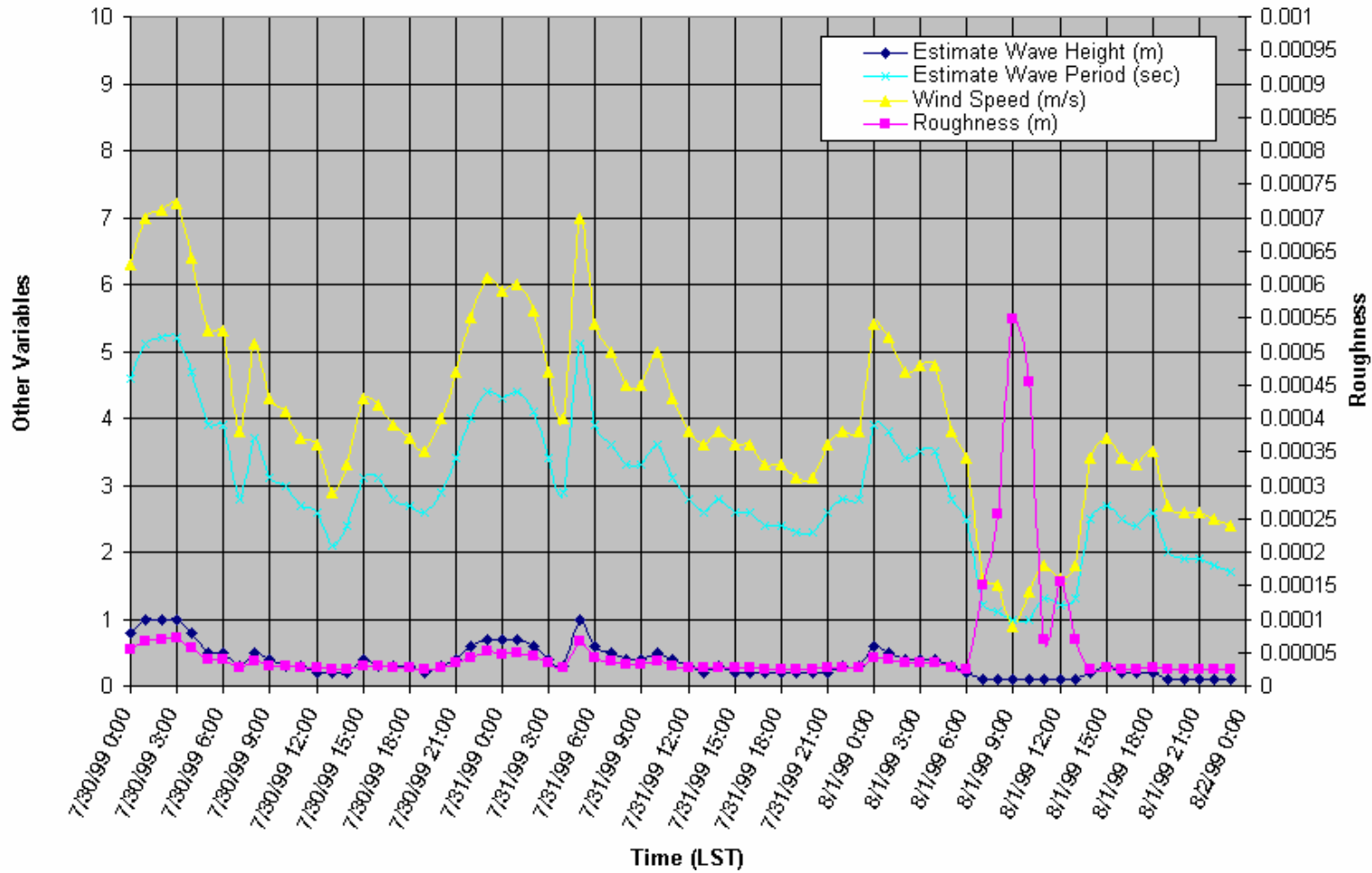


Figure 5-64a. Estimated wave height and period, and surface roughness length and wind speed at VRM for July 30 through August 1, 1999.

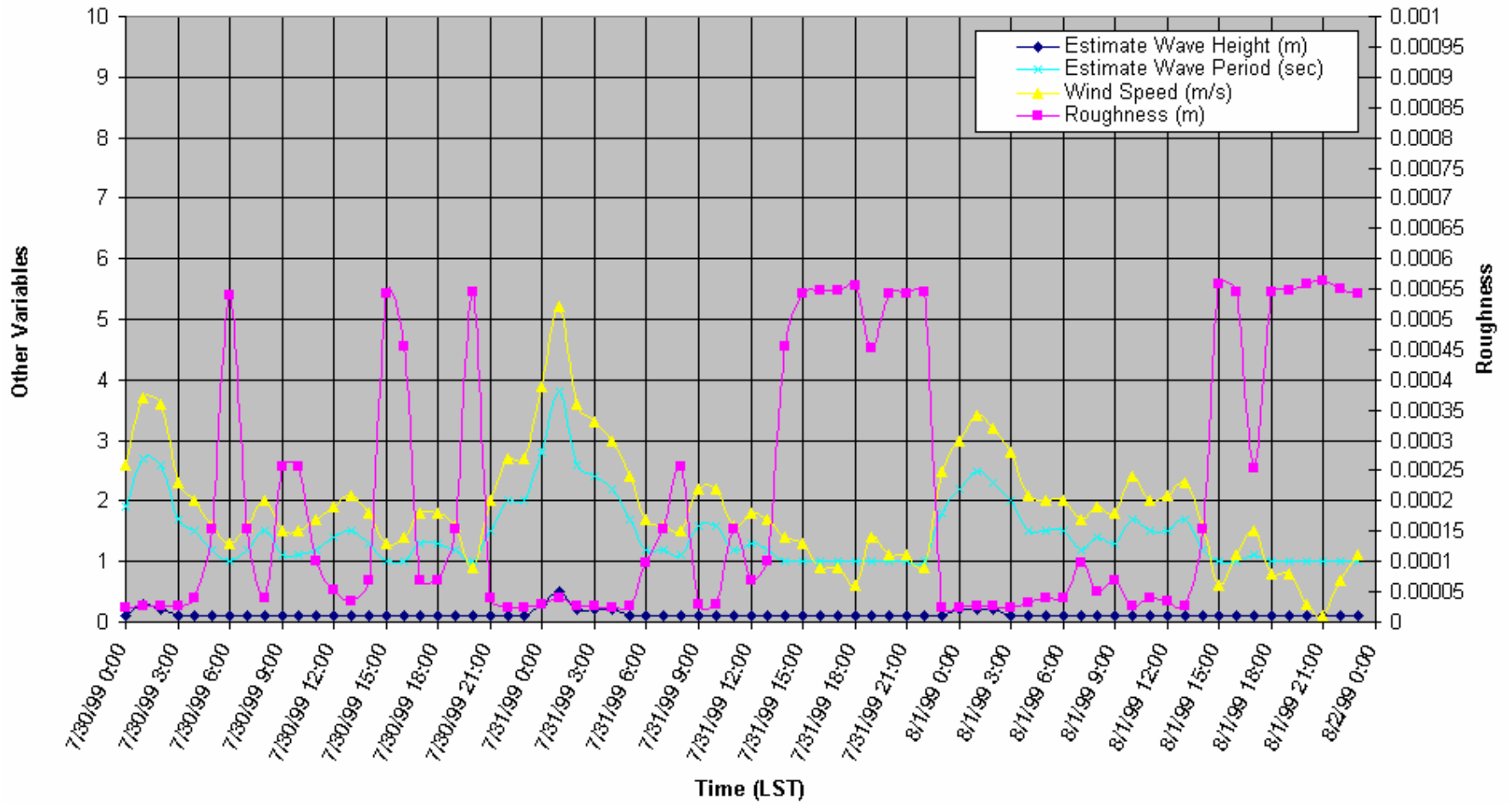


Figure 5-64b. Estimated wave height and period, and surface roughness length and wind speed at SMI for July 30 through August 1, 1999.

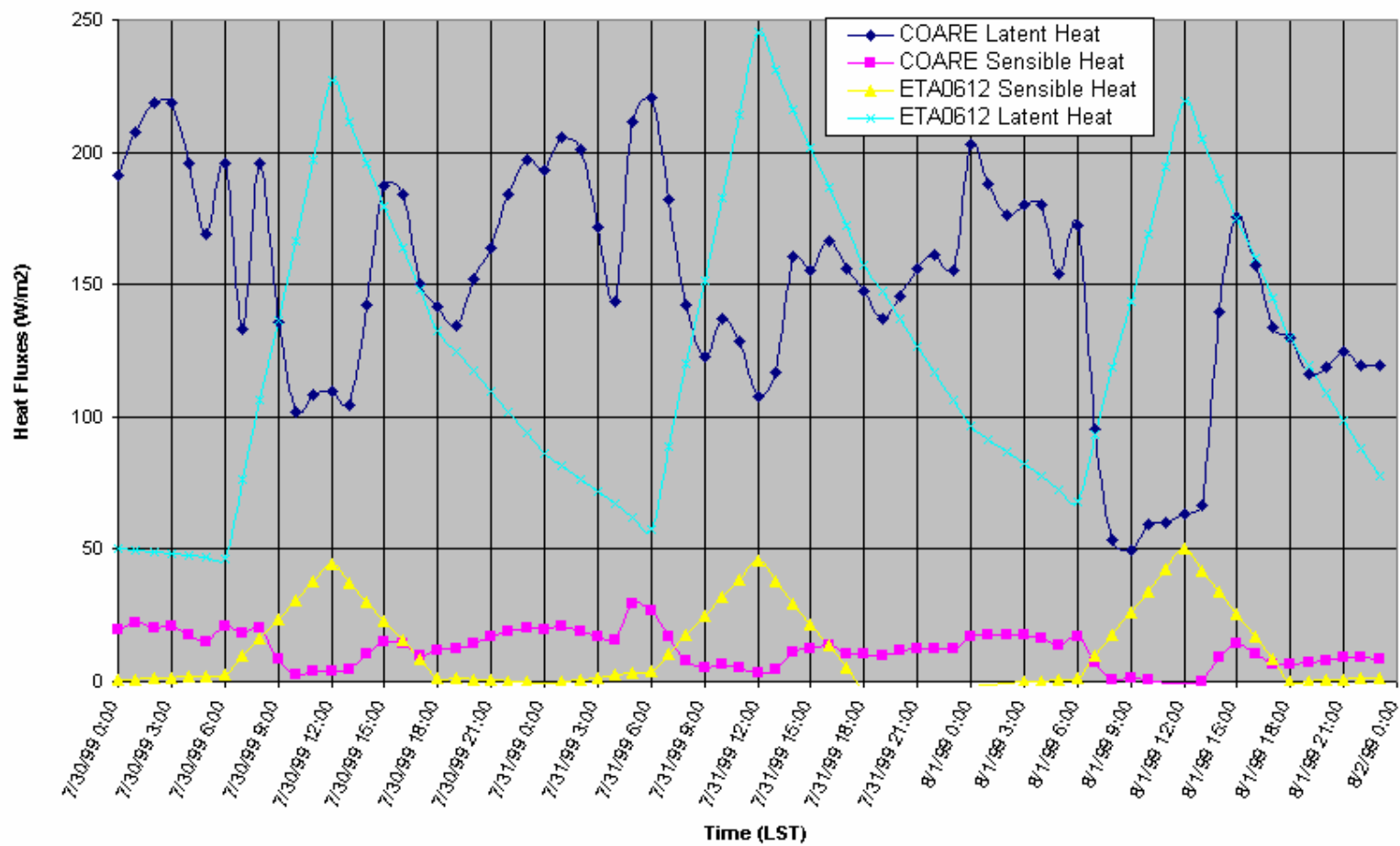


Figure 5-65a. COARE and Eta latent and sensible heat fluxes at VRM for July 30 through August 1, 1999. Note: the four-digit number after Eta in the key indicates the forecast period (i.e., 0612 is the 6- to 12-hr forecast).

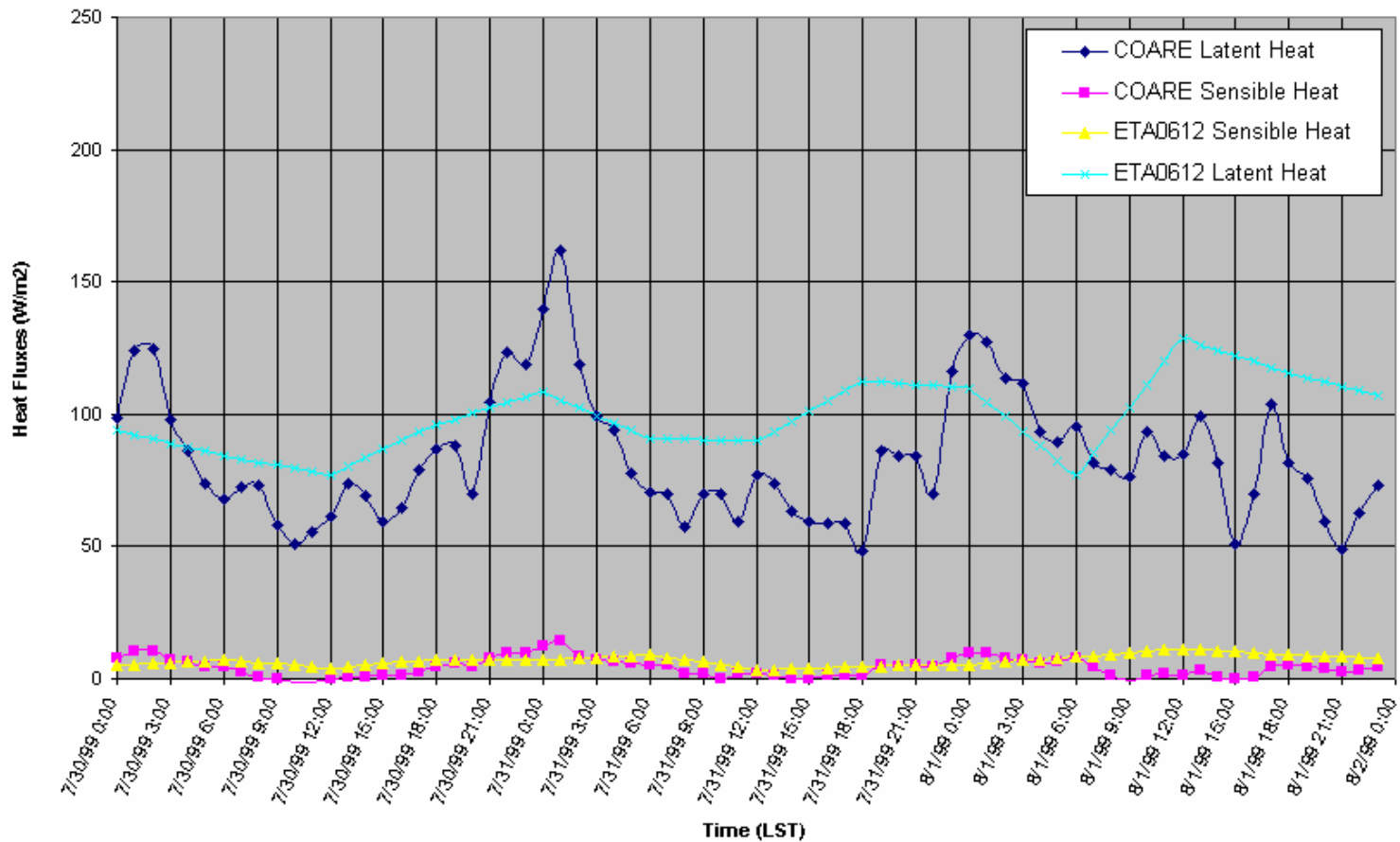


Figure 5-65b. COARE and Eta latent and sensible heat fluxes at SMI for July 30 through August 1, 1999. Note: the four-digit number after Eta in the key indicates the forecast period (i.e., 0612 is the 6- to 12-hr forecast).

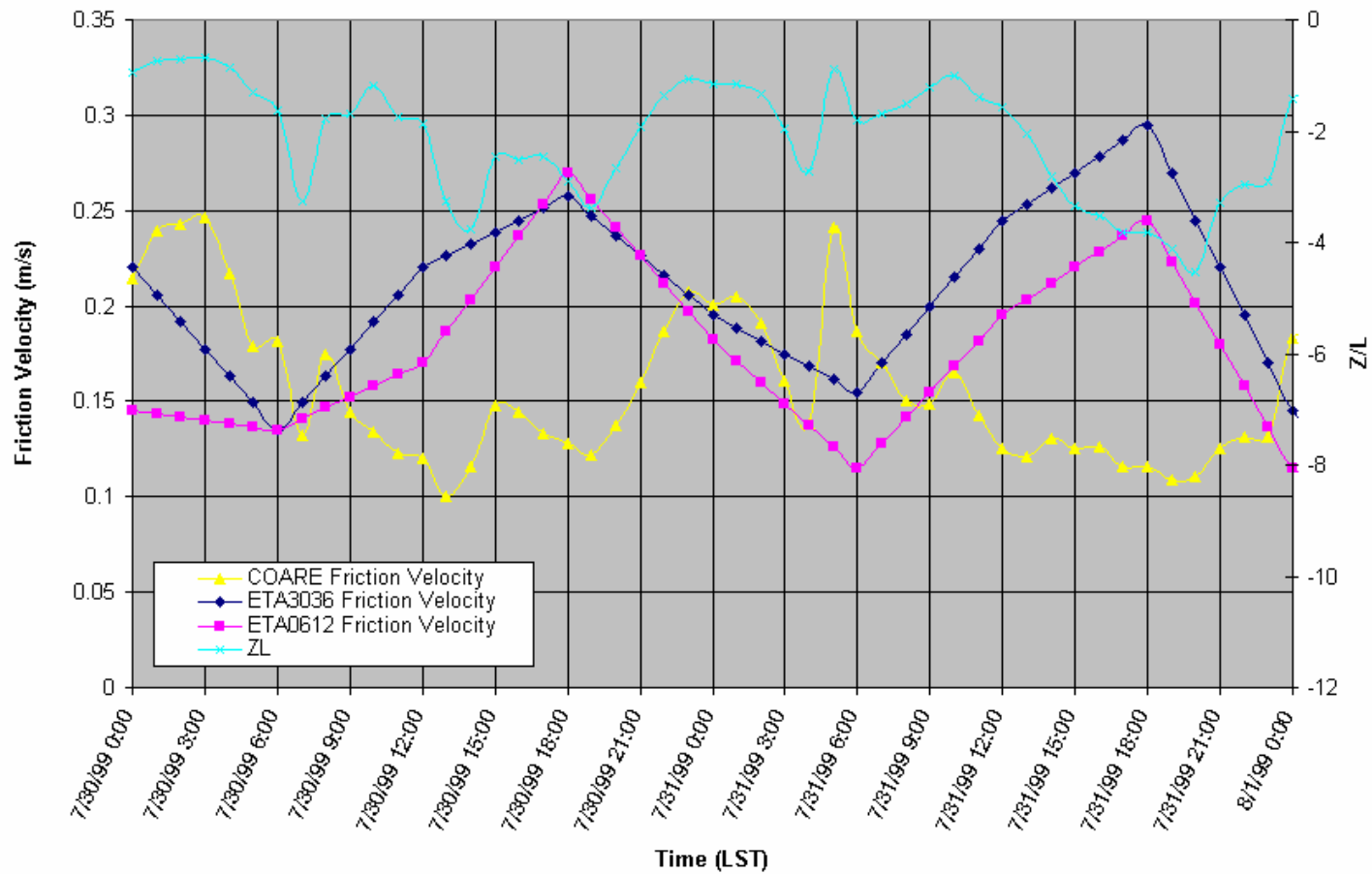


Figure 5-66a. COARE and Eta friction velocity and  $z/L$  at VRM for July 30 through August 1, 1999. Note: the four-digit number after Eta in the key indicates the forecast period (i.e., 0612 is the 6- to 12-hr forecast and 3036 is the 30- to 36-hr forecast).

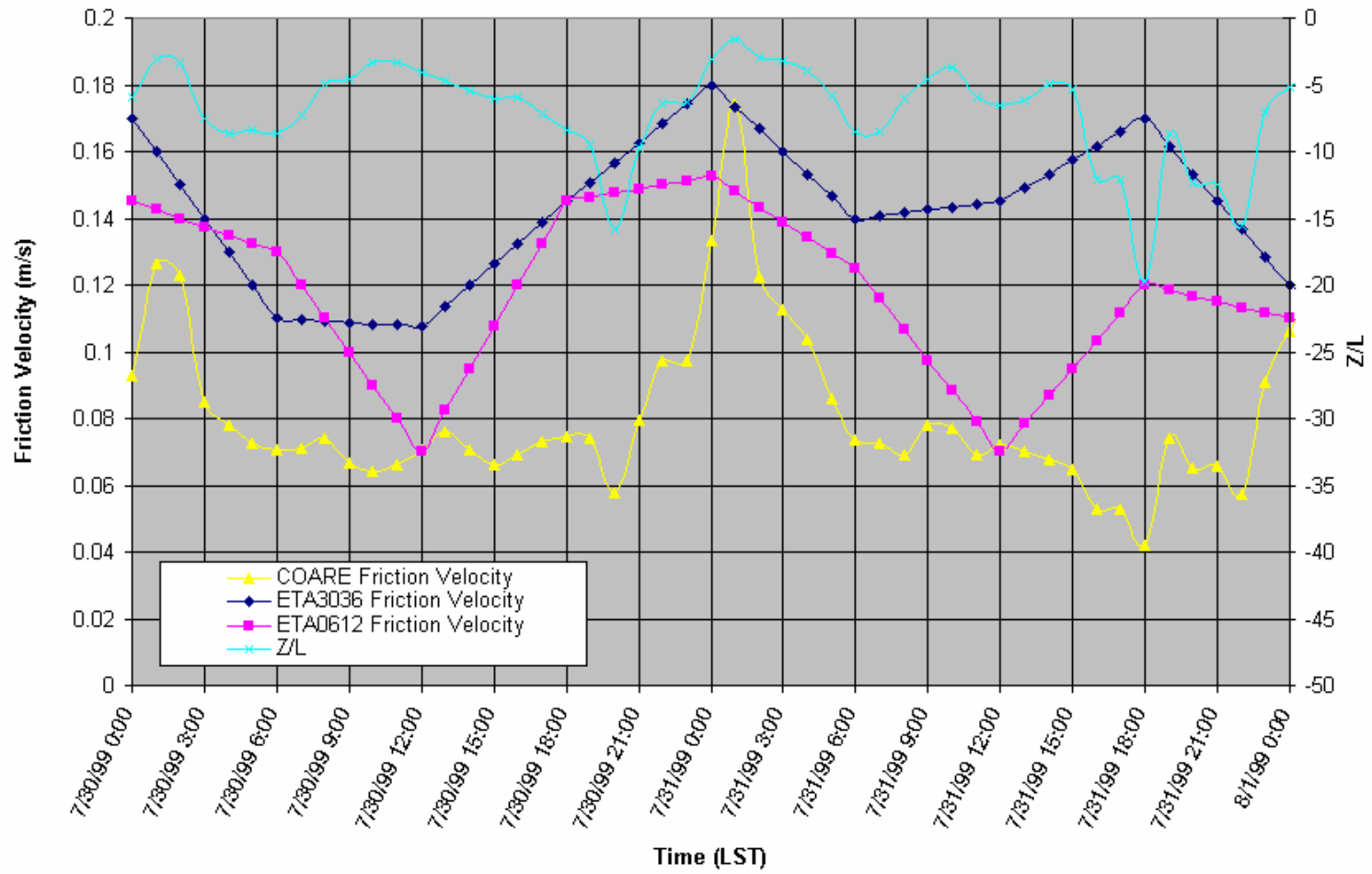


Figure 5-66b. COARE and Eta friction velocity and  $z/L$  at SMI for July 30 through August 1, 1999. Note: the four-digit number after Eta in the key indicates the forecast period (i.e., 0612 is the 6- to 12-hr forecast and 3036 is the 30- to 36-hr forecast).

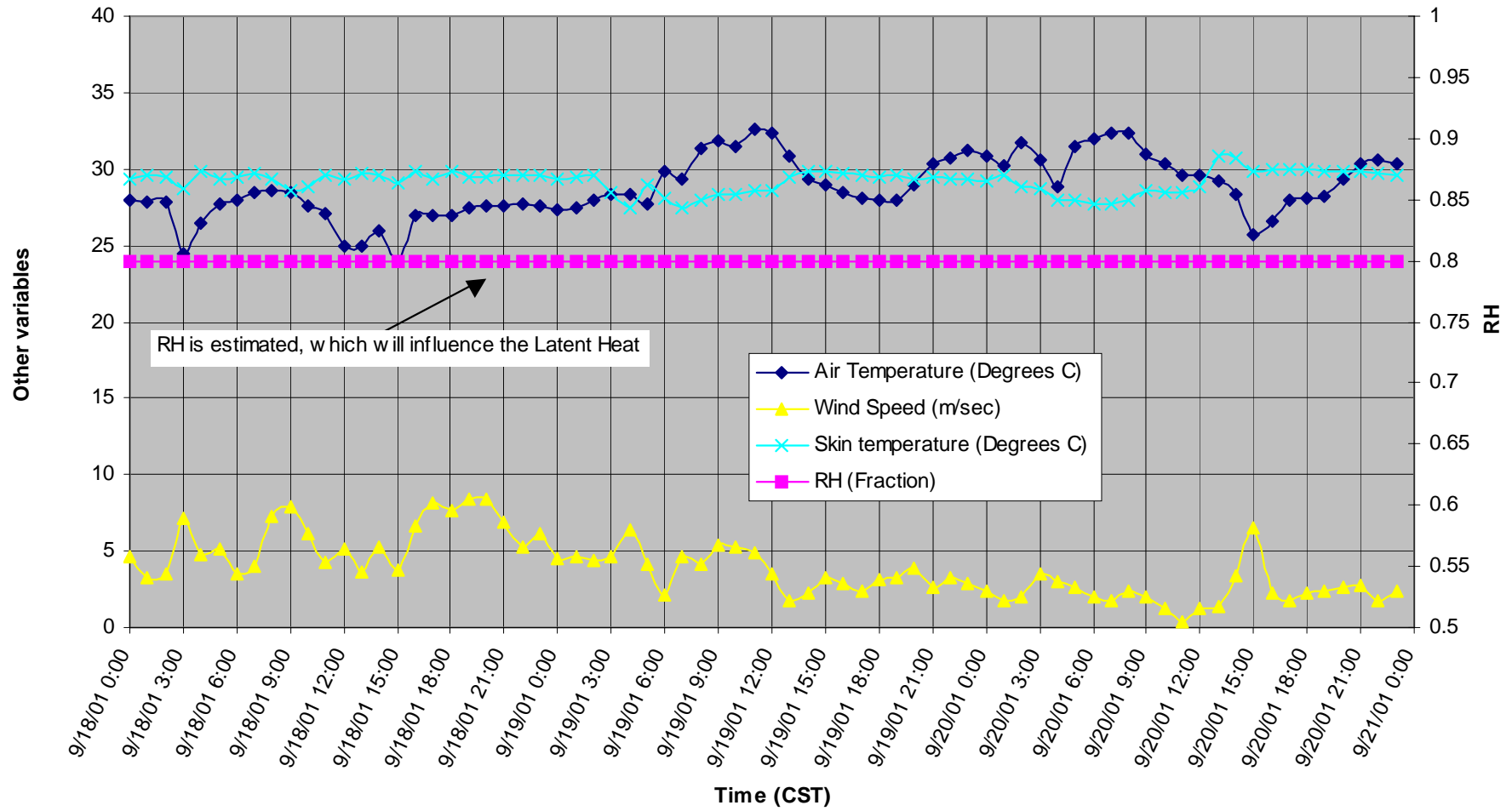


Figure 5-67a. Hourly air and skin temperatures, wind speed, and relative humidity at VRM for September 18 through 20, 2001.

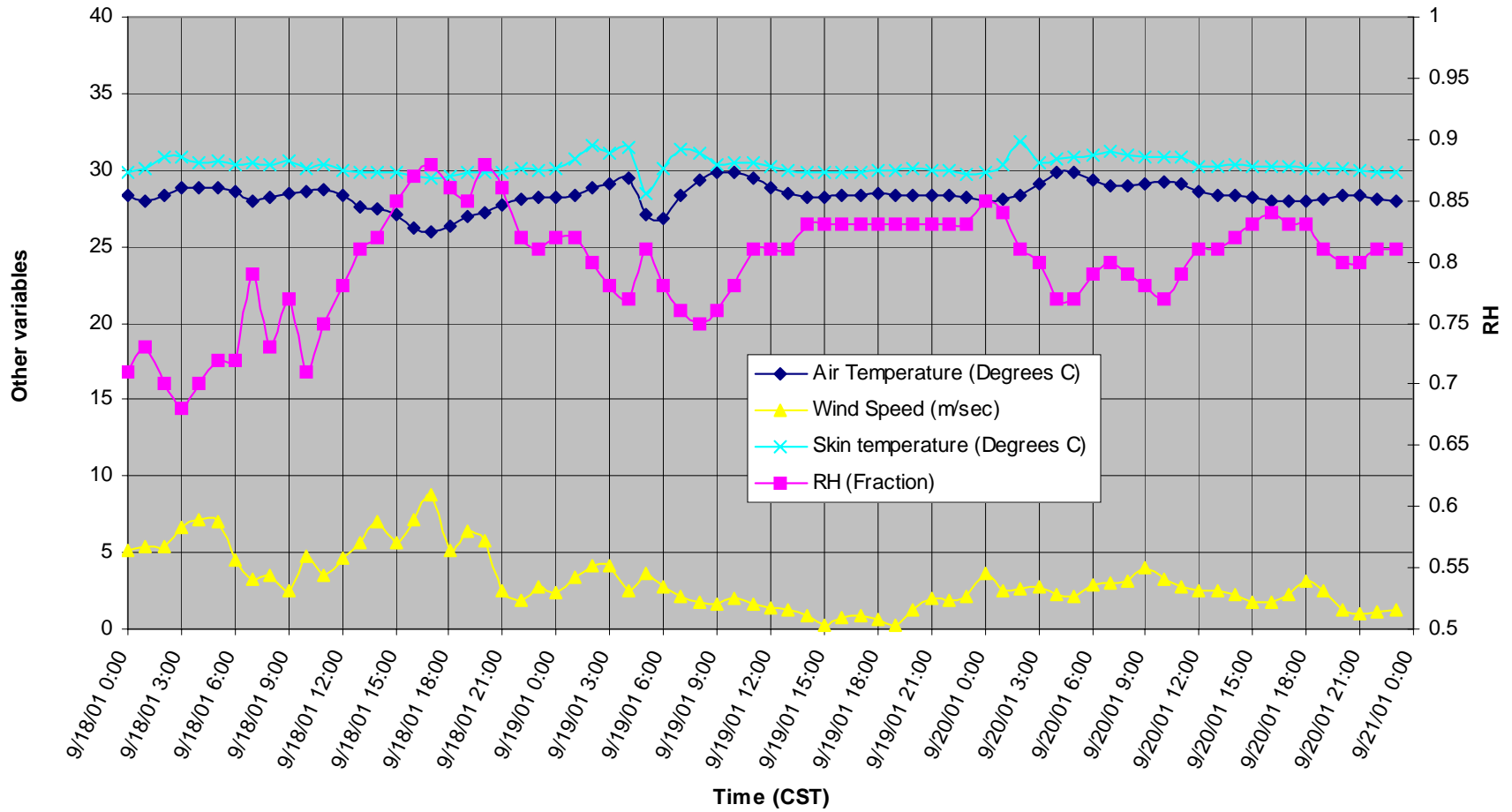


Figure 5-67b. Hourly air and skin temperatures, wind speed, and relative humidity at SMI for September 18 through 20, 2001.

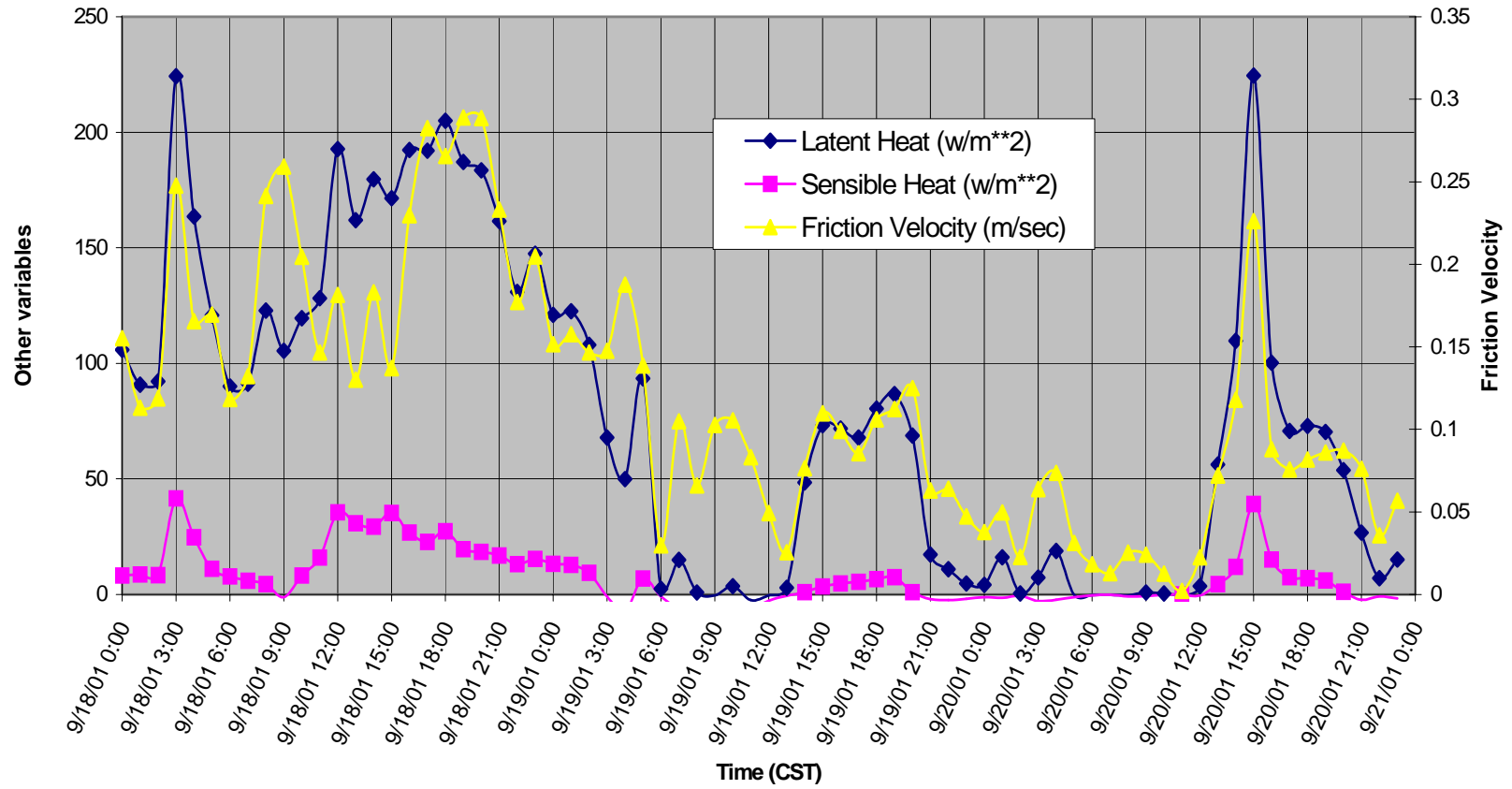


Figure 5-68a. COARE latent and sensible heat fluxes and friction velocity at VRM for September 18 through 20, 2001.

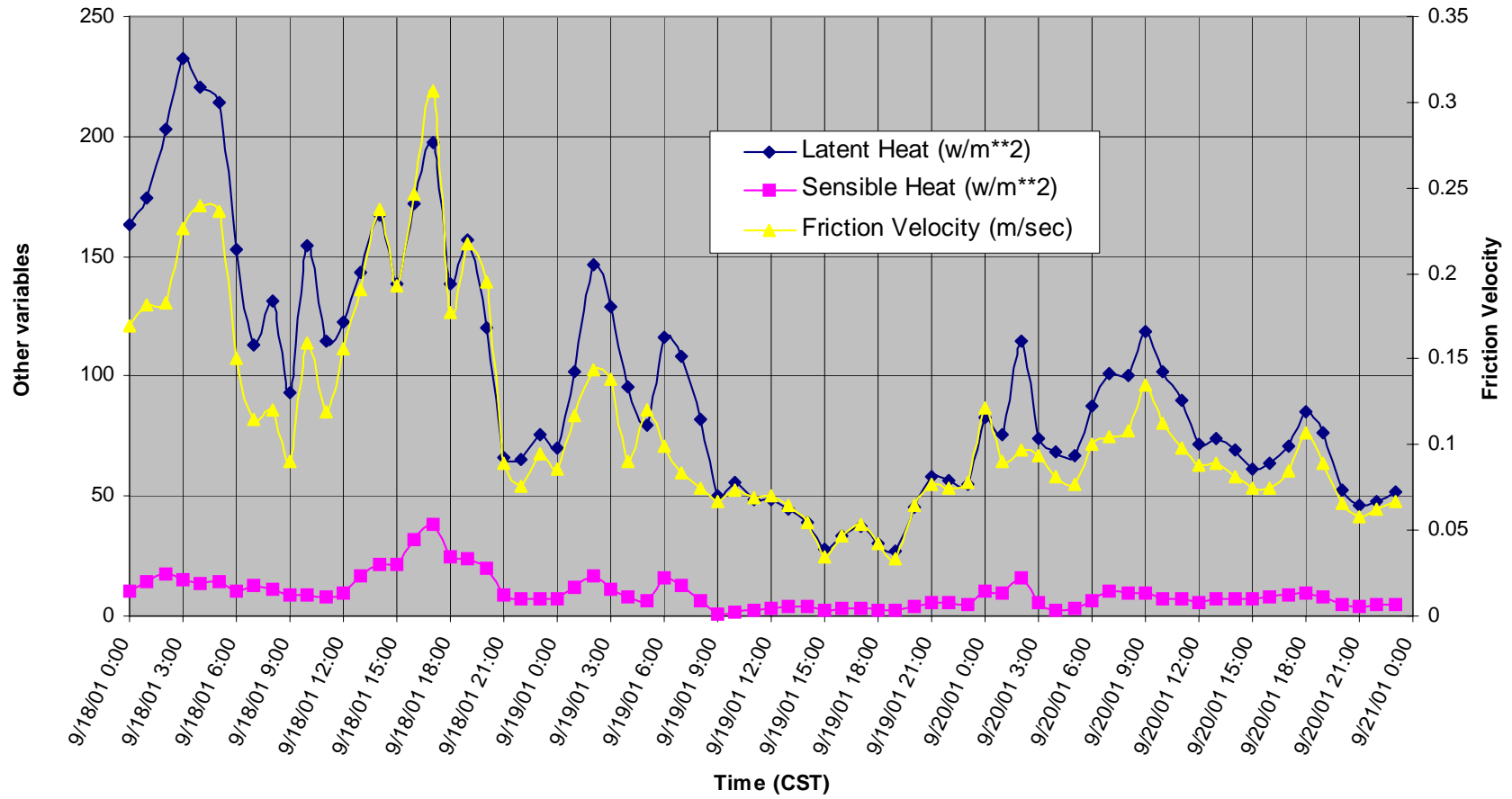


Figure 5-68b. COARE latent and sensible heat fluxes and friction velocity at SMI for September 18 through 20, 2001.

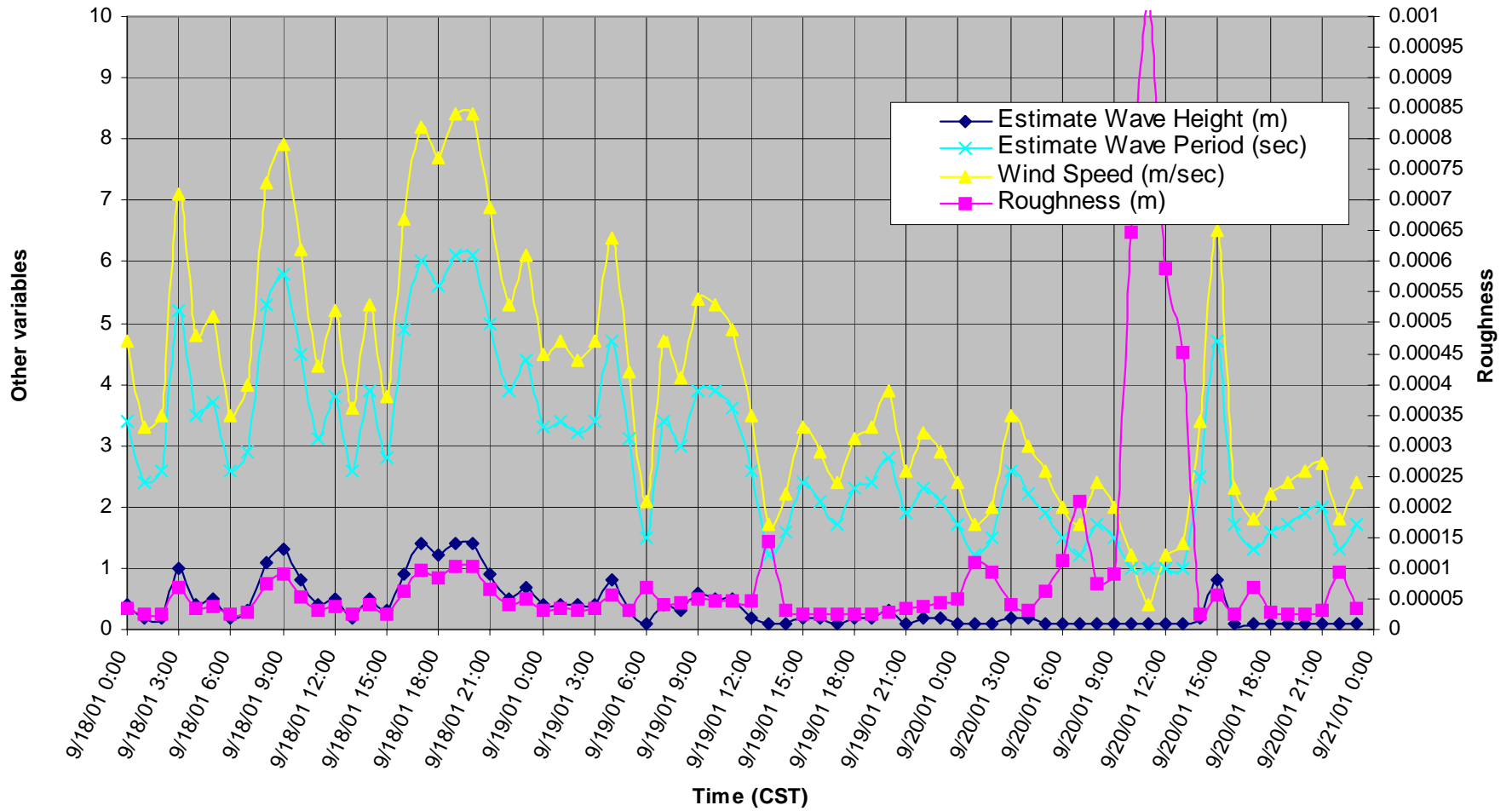


Figure 5-69a. Estimated wave height and period, wind speed, and surface roughness length at VRM for September 18 through 20, 2001.

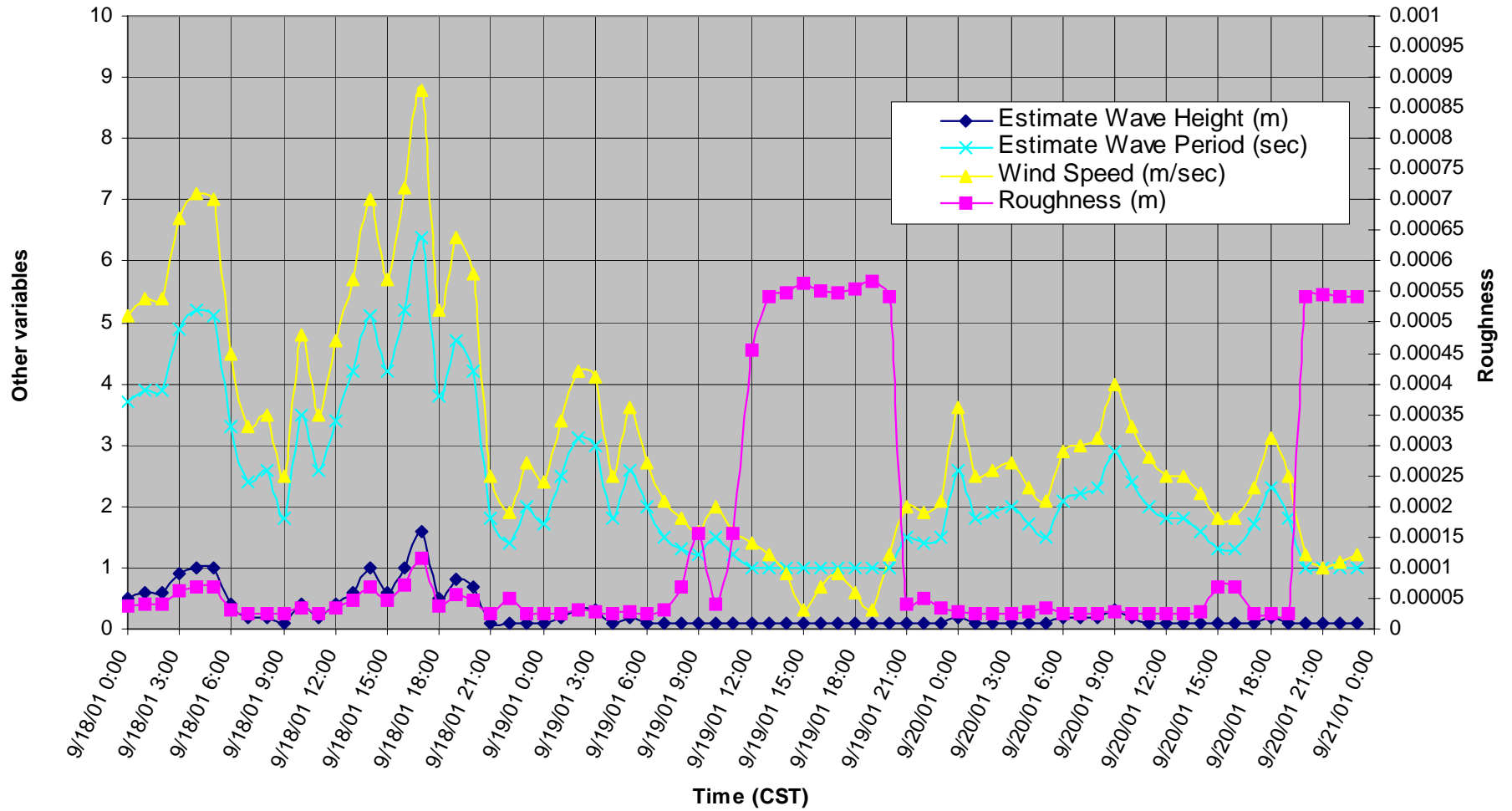


Figure 5-69b. Estimated wave height and period, wind speed, and surface roughness length at SMI for September 18 through 20, 2001.

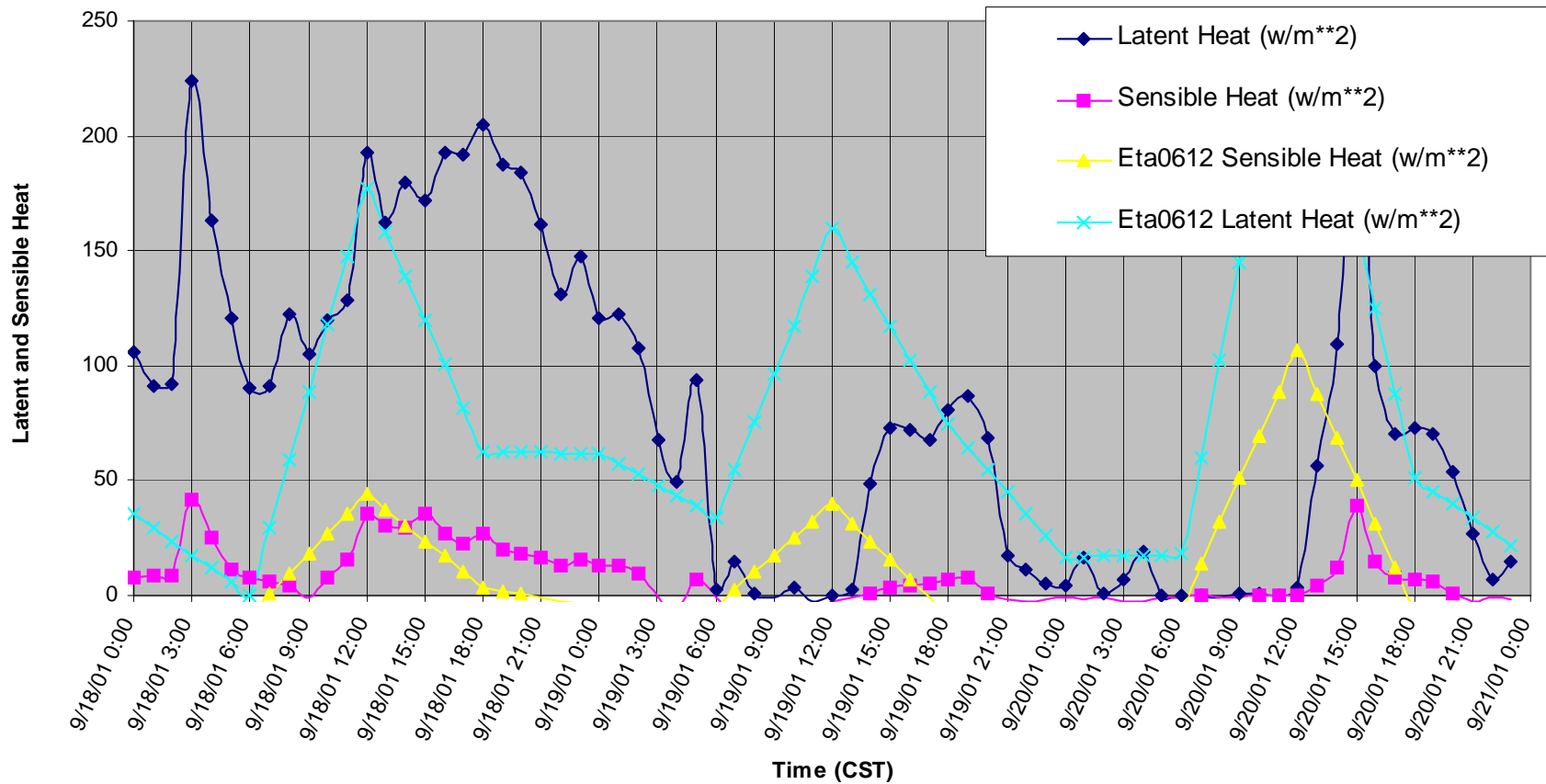


Figure 5-70a. COARE and Eta latent and sensible heat fluxes at VRM for September 18 through 20, 2001. Note: the four-digit number after Eta in the key indicates the forecast period (i.e., 0612 is the 6- to 12-hr forecast).

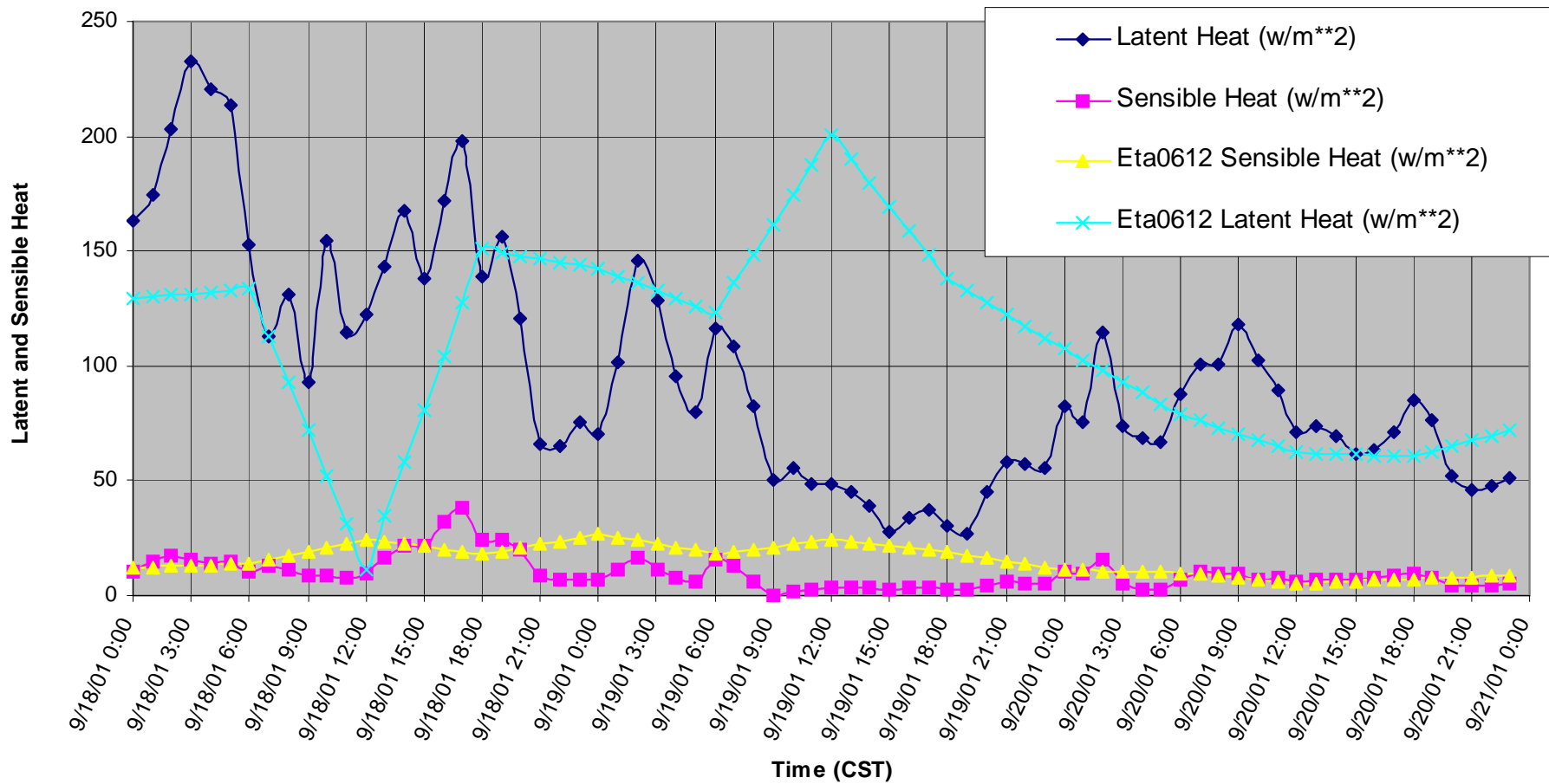
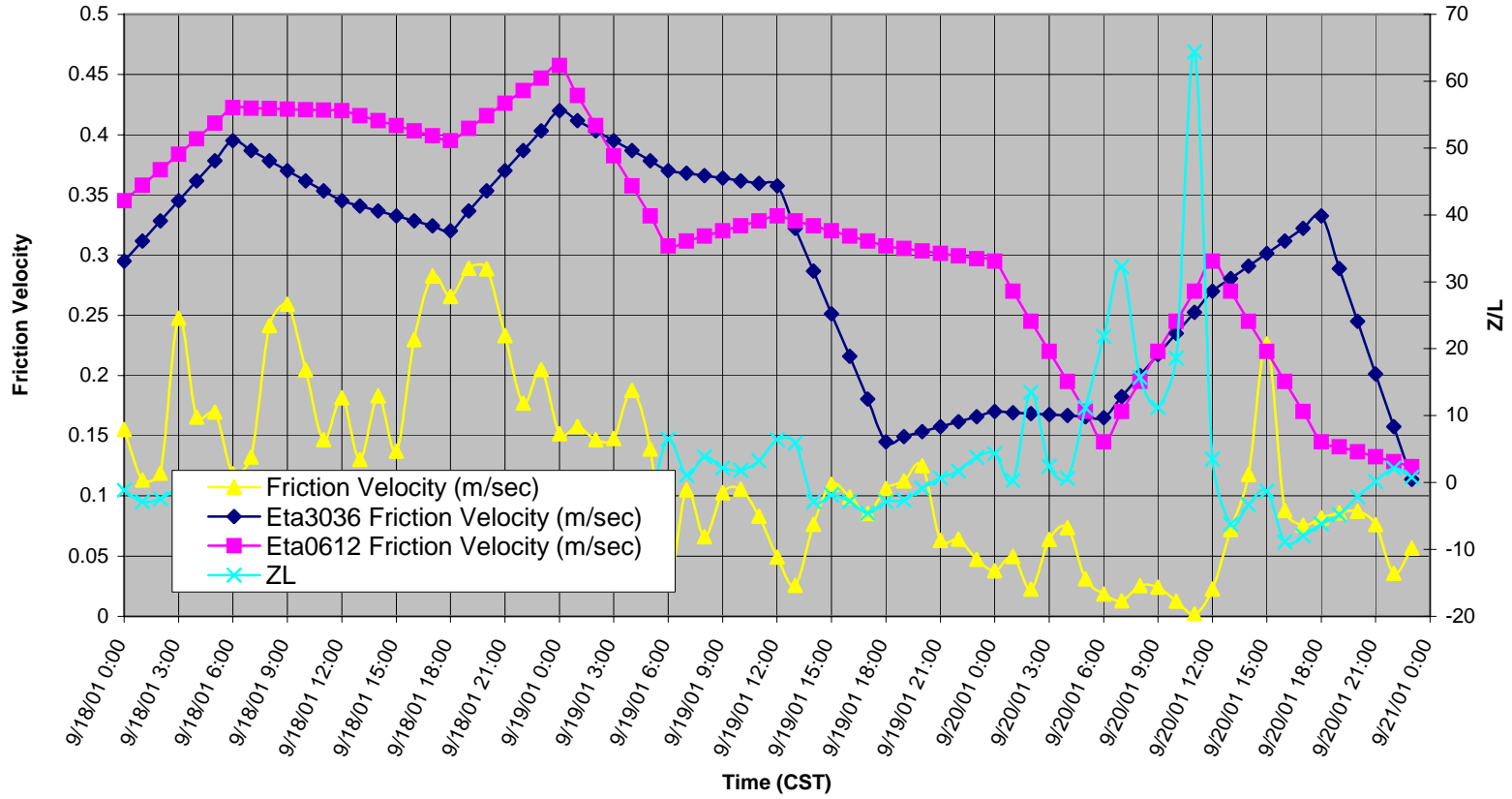


Figure 5-70b. COARE and Eta latent and sensible heat fluxes at SMI for September 18 through 20, 2001. Note: the four-digit number after Eta in the key indicates the forecast period (i.e., 0612 is the 6- to 12-hr forecast).

VRM



5-132

Figure 5-71a. COARE and Eta friction velocity and z/L at VRM for September 18 through 20, 2001. Note: the four-digit number after Eta in the key indicates the forecast period (i.e., 0612 is the 6- to 12-hr forecast and 3036 is the 30- to 36-hr forecast).

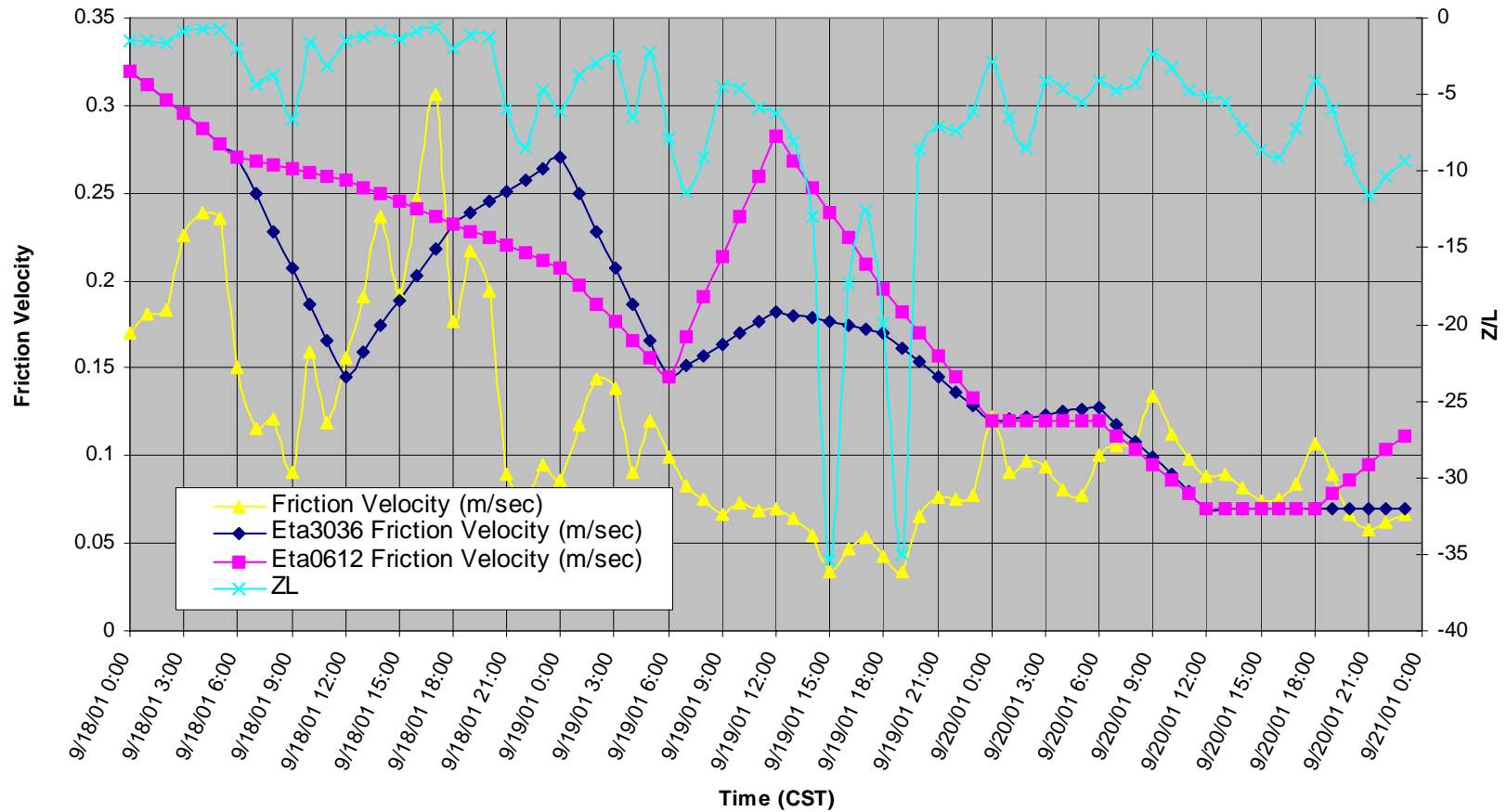


Figure 5-71b. COARE and Eta friction velocity and  $z/L$  at SMI for September 18 through 20, 2001. Note: the four-digit number after Eta in the key indicates the forecast period (i.e., 0612 is the 6- to 12-hr forecast and 3036 is the 30- to 36-hr forecast).

## **6. METEOROLOGICAL AND AIR QUALITY MODELING**

A major component of the MMS Boundary Layer Study was the development of hourly three-dimensional gridded wind fields. The wind fields were developed using the CALMET diagnostic model driven by a combination of historic Eta model simulations and observations. The wind fields, along with other ABL parameters, were used to develop three-dimensional inputs to transport and dispersion models that were used to assess dispersion and transport characteristics under multiple meteorological patterns. These patterns include onshore and offshore flow regimes, pre- and post-cold-frontal boundary passages, strong surface and upper-level high pressure systems, and upper-level flow transitioning from an area of low pressure to a weak area of high pressure. These meteorological patterns and their influence on transport and dispersion are captured in seven modeled case study periods:

- July 30 – August 1, 1999
- January 20-25, 2000
- January 4-6, 2001
- January 29, 2001
- April 14-15, 2001
- May 14-15, 2001
- September 18-20, 2001

The case studies were selected to cover a range of synoptic conditions, seasons, and wind directions.

This section contains the results of a comparison between observations and model predictions of winds; background information about the CALMET diagnostic model; discussion of the methods used to derive the three-dimensional wind fields (i.e., data sources and model settings); and discussions of the model results, trajectories, and CALPUFF dispersion runs for the above case studies. Conclusions from this discussion are set out in Section 6.6.

### **6.1 RADAR WIND PROFILER – EDAS COMPARISON**

The CALMET meteorological model can use both observations and regional-scale model predictions as input. The two data types can be weighted differently in the model, and the user must assign the weights. The weighting of observations and model predictions is of extreme importance in observationally sparse regions such as the Gulf of Mexico. To help determine the relative weighting that should be assigned to the regional scale model predictions and to the observations, horizontal wind observations collected by the six RWPs were compared with the wind predictions from the NCEP EDAS.

#### **6.1.1 Method**

The EDAS output consists of successive three-hour Eta model forecasts nudged by high frequency observing platforms, such as RWPs, hourly surface meteorological and buoy stations, aircraft observations, and winds derived from both satellite and radar measurements. However,

the RWP data used in this study and the following comparisons were not part of the routine EDAS output. The output is interpolated to a 40 km, Lambert Conformal Grid covering the continental United States. RWPs used during MMS and BAMP (**Figure 6-1**) were LAP-3000, 915-MHz boundary layer radars deployed on oil platforms. Two modes of data collection occurred at all RWP sites. The low mode represented 100-m resolution winds at heights from about 100 m above platform level (APL) to about 2000 m APL. The high mode represented 200-m resolution winds at heights from about 200 m APL up to about 4000 m APL. These RWP data were subjectively quality-controlled by STI meteorologists. Any data that were deemed incorrect were invalidated and not used in the subsequent analyses. Typical problems that led to incorrect data were the presence of clutter due to sea waves and/or platform structures.

Comparisons of EDAS-modeled and RWP-observed hourly wind speed and direction were made when EDAS wind heights were within 30 m of the RWP heights below 1000 m above ground level (agl), and within 50 m of the RWP heights above 1000 m agl. When wind speeds were less than 2 m/s, wind direction comparisons were not made.

A difference exists between the averaging volumes represented by the EDAS model and those represented by the RWP observations; this difference will manifest itself by more scatter in the observations than in the predictions. The EDAS model data are created by bilinear interpolation of the 12-km Eta model output to a 40-km grid. Vertical interpolation is performed on the 12-km Eta model (60 levels) to the EDAS grid (39 levels). On the other hand, the RWP winds are a volume-averaged measurement that is dependent on vertical resolution and beam width. Because the profiler beams diverge with height, the volume is approximately 3.5 km wide at 4 km above ground. The RWP-derived wind components are a nearly instantaneous measurement, however when averaged over an hour, the winds can be representative of a radius of 3.5 km (zero wind) or greater depending on the wind speed through the profiler beams. This issue arises whenever observations are compared with grid model predictions (see Seaman, 2000; Hanna and Yang, 2001). The grid-averaged predictions resolve only variations with scales greater than the grid dimensions. This should have little effect on the mean bias, as long as the instrument is well-sited and representative. However, the standard deviation of the RWP-observed wind will be larger than the standard deviation of the predicted wind, and this could lead to difficulties when the scatter is calculated between the observations and the predictions.

The following statistics were computed:

$$\text{Mean bias} = \frac{1}{n} \sum_{i=1}^n (P_i - M_i) \quad (6-1)$$

where:

- n = number of observations
- P<sub>i</sub> = observations by the RWP
- M<sub>i</sub> = EDAS model “predictions”

$$\text{Standard deviation} = \sqrt{\frac{1}{n} \sum_{i=1}^n \left( (P_i - M_i) - \overline{(P_i - M_i)} \right)^2} \quad (6-2)$$

$$\text{Mean absolute error} = \frac{1}{n} \sum_{i=1}^n |P_i - M_i| \quad (6-3)$$

The standard deviation defined in Equation 6-2 is a root-mean-square error, with the effect of the mean bias removed. However, the mean absolute error (MAE) defined in Equation 6-3 includes the effects of the mean bias. Consequently, it is possible to have a large MAE even though the standard deviation is small, simply because there may be a large mean bias.

Statistics were computed for those height bins containing at least 90% of the total number of RWP/EDAS possible data pairs. Sample sizes at each height and each RWP typically ranged from about 900 for the eastern sites associated with BAMP, to about 2000 for the western sites, which have been in operation for a longer period of time.

### 6.1.2 Results

**Figure 6-2** illustrates the wind speed and direction mean bias, mean standard deviation, and MAE for the entire data collection period at all sites. In general, wind speeds were overestimated by the EDAS model by a slight amount, with more mean bias at the lower heights and with gradual improvement above 1000 m. The coastal land site, FTM, had the lowest wind speed mean bias, ranging from  $-1$  to  $0$  m/s. VRM, BIP, and WDP all had wind speed mean biases generally between  $-2$  (near the surface) and  $-1$  m/s (aloft). The far offshore sites (SMI and DWP) had the highest wind speed mean biases of  $-3$  (near the surface) to  $-2$  m/s (aloft) and  $-6$  (near the surface) to  $-1$  m/s (aloft), respectively. These wind speed mean biases suggest that the EDAS model tends to overestimate wind speeds in offshore areas, with the difference increasing as distance from shore increases. The standard deviations of wind speed difference were 2 to 4 m/s and indicate little variation with altitude, which is somewhat surprising as lower standard deviations are expected aloft because the upper-level flow patterns are known to vary less than flows near the surface (Seaman, 2000).

Wind direction mean biases shown in Figure 6-2 were generally between  $-5^\circ$  and  $10^\circ$  at all sites, with higher wind direction biases observed at heights below 1000 m at DWP (as high as  $20^\circ$ ). DWP showed more wind direction mean bias near the surface, whereas the remaining sites tended to show a consistent mean bias with height. The mostly positive mean biases indicate that the EDAS model data had an overall counter-clockwise mean bias in wind direction. For example, with a  $20^\circ$  positive mean bias, if the observed mean wind direction were  $180^\circ$ , then the EDAS-predicted mean wind direction would be  $160^\circ$ . The standard deviations of wind direction differences were generally about  $25^\circ$  to  $35^\circ$  and showed little variation with height. While the wind direction mean biases at offshore sites were similar to those at the near-shore sites, the standard deviations of the wind direction differences were generally about  $40^\circ$  at the offshore sites. These standard deviation values for wind speed and wind directions (2 to 4 m/s and  $20^\circ$  to  $50^\circ$ ) found for the six RWPs in the Gulf of Mexico domain agree well with standard deviations reported by Seaman (2000) and Hanna and Yang (2001) for other models and other geographic domains.

In general, the MAE between the EDAS-predicted and the RWP-observed wind speeds at all sites was largest near the surface and increased with increasing distance from the shoreline (see Figure 6-2). The coastal site, FTM, had a MAE of 1 to 2 m/s. VRM, BIP, and WDP had MAEs of about 2 m/s, excluding the lowest height. SMI was observed to have an MAE of 2 to 3 m/s, and DWP had an MAE of 2 to 6 m/s, with the largest MAEs near the surface in both cases. Because MAE is strongly influenced by the mean bias, the large 6 m/s MAE value at DWP near the surface is primarily due to the large mean bias of approximately the same magnitude.

The wind direction MAE is generally constant with height. The wind direction MAE was found to be between 15° and 25° at the coastal and near-shore sites and 25° to 35° at the offshore sites.

### **6.1.3 Conclusions**

Comparisons between RWP-observed wind data and EDAS-modeled wind data over the Gulf of Mexico show better agreement at near-shore sites and poorer agreement at offshore sites. In general, the EDAS model tended to overstate wind speeds, especially at levels below 1500 m. The EDAS model tended to have a positive wind direction mean bias (i.e., if the observed wind direction were 180°, the predicted wind direction might be 160°); however, this mean bias was usually 10° or less. In considering these comparisons, it should be noted that the EDAS data is created by a bilinear interpolation of a fine-scale grid onto a more coarse grid resolution, whereas the RWP observations are a volume-averaged measurement in which the measurement representativeness can vary with fluctuations in the wind speed.

The results suggest that RWP data might be weighted more heavily than the EDAS model data when creating high-resolution wind fields in an area where RWP observations are available. In addition, it is suggested that the Eta model may benefit from the use of offshore RWP data at the time of initialization.

## **6.2 CALMET METEOROLOGICAL MODELING**

The CALMET meteorological model (Scire et al., 1999) is a software tool that combines objective and diagnostic analysis methods to create two- and three-dimensional meteorological fields. CALMET produces outputs of gridded meteorological fields of three-dimensional winds and air temperature; two-dimensional fields of surface friction velocity, convective velocity scale, mixing height, Monin-Obukhov length, Pasquill-Gifford-Turner stability class, and precipitation rate. CALMET also produces outputs of temperature, air density, short-wave solar radiation, and relative humidity defined at surface meteorological stations. CALMET includes a diagnostic wind field generator containing objective analysis and parameterized treatments of slope flows, kinematic terrain effects, terrain-blocking effects, a divergence minimization procedure, and a micro-meteorological model for overland and overwater boundary layers. CALMET attempts to resolve mesoscale and local-scale meteorological phenomena by blending observational data with synoptic-scale analyses.

CALMET utilizes both geophysical and meteorological data inputs in order to derive the three-dimensional wind fields and other ABL parameters. The geophysical inputs to the CALMET model consisted of 0.9-km surface terrain height and 30-m land-use data. The meteorological inputs consisted of surface observations, buoy data, rawinsonde data, RWP wind measurements (i.e., wind and  $T_v$  profiles), and EDAS wind fields. Because CALMET cannot ingest observed mixing heights, RWP-derived mixing heights were not used in the modeling. **Figure 6-3** illustrates the spatial coverage of the observed meteorological data inputs in the CALMET modeling domain used to derive three-dimensional wind fields for the MMS Boundary Layer Study. The CALMET wind fields were developed with a 5-km horizontal resolution across a modeling domain of 860 km x 560 km (NX=172 and NY=112), which includes portions of Texas, Louisiana, Mississippi, Alabama, and Florida (**Figure 6-4**). The vertical structure of the wind and temperature fields has 20 vertical layers with interfaces at: 0, 20, 50, 100, 200, 300, 400, 500, 600, 700, 800, 900, 1000, 1200, 1400, 1600, 1800, 2000, 2250, 2500, and 2750 m. This horizontal and vertical resolution was able to capture the timing, strength, and vertical structure of the important flow features, especially those important for the transport and diffusion of chemical species.

An approach used in other projects utilized gridded mesoscale model output, such as EDAS, as the initial guess wind field instead of a single point value known as the “domain mean wind”, which is often used as a default. The use of EDAS has been demonstrated to improve model performance over large domains. Therefore, for this project we used Eta and EDAS model wind field data, as well as temperature, specific humidity, and cloud data for the three-year period spanning the MMS Boundary Layer Study. The EDAS is constructed from successive 3-hr (eight analyses/day) Eta model forecasts. A bilinear interpolation of Eta model output is used to create the EDAS output on the AWIPS-212 grid. The AWIPS-212 grid is based upon a Lambert Conformal Conic Projection, which covers the contiguous United States, and consists of a horizontal resolution of 40 km (185 x 129) and twenty-six vertical levels (every 25 mb up to 850 mb; and every 50 mb up to 50 mb) (**Figure 6-5**). A three-dimensional variational analysis (3DVAR) scheme is used in the model to assimilate high frequency observations, such as RWP measurements, aircraft winds, satellite-derived winds, land-surface meteorological measurements, and oceanic-surface data from ships and buoys. However, RWP measurements made during MMS and BAMP were not integrated into the EDAS. The EDAS wind data was used as the “domain mean winds” in the CALMET model runs.

The wind-field model within CALMET is based on the Diagnostic Wind Model (DWM) (Douglas et al., 1990). The DWM has been modified within CALMET to allow the possibility of incorporation of three-dimensional meteorological fields from the Penn State/NCAR Mesoscale Models (MM4/MM5). **Figure 6-6** shows the three optional steps (A, B, and C) for input of these gridded data within CALMET. The method in CALMET for using gridded data was adapted for incorporating the gridded EDAS analyses. At a minimum, CALMET requires 00Z and 12Z NWS soundings to calculate a domain mean wind for use as the “first guess” field; however, the EDAS model output was incorporated into CALMET at Step A (**Figure 6-6**) in order to derive an initial guess field. This is particularly important, as it is difficult to represent a mean wind for larger analysis regions. Because the EDAS analysis is rather coarse (40-km grid spacing), the DWM slope flow algorithms (Allwine and Whitman, 1985) are used to estimate flows in and near complex terrain at a resolution of 1 to 4 km. The EDAS and slope flow estimates are then combined to produce the “Step 1” wind fields. This should improve the wind

fields near the coastal areas. After the Step 1 wind field was derived, an objective analysis was performed on the extensive suite of observations discussed earlier. Before the final wind field (Step 2) is created, an objective combination of the Step 1 wind field and the observations was carried out. During stable conditions, a stable layer can persist for days at the surface with little exchange of mass with the layers above. This condition has been difficult to represent with the DWM. Two modifications have been made to the model to address this issue and can be applied if the situation warrants:

- The O'Brien procedure (O'Brien, 1970) within the DWM has been modified to adjust the wind fields to minimize vertical velocities at the top of the stable layer instead of at the top of the modeling domain. This prevents the unrealistic exchange of mass between the stable layer and layers aloft that is a common problem in DWM analyses.
- The terrain-blocking adjustment scheme in DWM (Allwine and Whitman, 1985) has been moved from the Step 1 analysis to the final analysis step, which allows terrain-blocking effects to be considered after the introduction of the objective analysis. This re-ordering of the scheme prevents extrapolation of observational data into regions of complex terrain when it is physically unlikely. However, this is likely to be of little importance in the Gulf of Mexico modeling domain.

A mass-consistent wind field model in a terrain-following coordinate system which takes into account the density stratification was developed by Drake and Huang (1980); this wind field model was adopted in a mesoscale air quality modeling for complex terrain by Allwine and Whitman (1985).

### **6.2.1 High Frequency RWP and RASS Measurements and Data Manipulation for Input to CALMET**

#### **Upper-Air Files**

In the current release of CALMET, high frequency observations, such as RWP and RASS measurements, can be used as inputs but often require considerable data manipulation. This is especially true with regard to the upper-air file input to CALMET. The highest CALMET layer interface height at 2750 m was always much greater than the highest RASS  $T_v$  range gate height and occasionally greater than the height of the highest RWP wind range gate. In order for a successful CALMET model run, there needs to be an observation of wind speed, wind direction, and temperature above the highest CALMET layer interface (2750 m). Therefore, EDAS model output, matched according to the closest grid point to a particular station and the height at which a particular measurement was void, was used to fill in RWP and RASS data gaps in horizontal space and in the vertical to allow for successful CALMET runs.

As discussed above, at a minimum, CALMET requires in horizontal and vertical space that the upper-air file for each upper-air station contain a vertical profile of winds and temperature collected every twelve hours. Occasionally, NWS soundings and RWP/RASS measurements were missing for periods exceeding twelve hours. In this situation, EDAS model output was used to fill in the missing time periods and provide the vertical wind and temperature profiles needed by CALMET to derive three-dimensional wind fields and other ABL parameters.

However, when RWP wind observations and EDAS wind simulations are compared (Section 6.1), significant biases and scatter occur that could lead to discontinuities in the observed RWP wind profiles which have been “filled in” with EDAS predictions. If the time periods of the missing upper-air measurements were less than twelve hours, a linear interpolation scheme was used within CALMET.

CALMET also requires a measurement of pressure, winds, and temperature below the lowest CALMET vertical layer (10 m) each hour. Because RWP/RASS observing platforms are not capable of obtaining measurements at heights less than 50 to 100 m, collocated surface temperature and wind measurements are required. Since CALMET upper-air files rely on measurements from two different observing systems (RWP/RASS and a collocated surface instrument), the probability of missing data from one of the systems is increased. Therefore, time gaps less than twelve hours in surface meteorological measurements were subjected to a sliding  $\pm 6$ -hr window in order to obtain the next closest measurement in time. The sliding  $\pm 6$ -hr window is an attempt to obtain a reasonable and representative surface measurement that completes the vertical profiles in CALMET’s upper-air files. For time gaps greater than twelve hours, the first gate (lowest elevation) of the RWP/RASS measurements was used for the surface observation, instead of the sliding  $\pm 6$ -hr window applied to the surface observation, along with a standard atmospheric pressure value.

Because of CALMET’s limited flexibility in handling missing data in upper-air files, this complex method of accounting for missing data was undertaken. For future modeling, an alternative procedure within CALMET should be developed to handle missing upper-air measurements. Data from an upper-air station that has only one 12-hr time gap may still be usable in a CALMET model run.

### **Surface Meteorological and Over-Water Files**

Compared to the scheme used by CALMET to process upper-air files, the scheme used by CALMET to manage time gaps greater than twelve hours in high frequency surface meteorological and in over-water measurements is much more efficient. A spatial interpolation using the non-missing observations is performed to account for missing surface data.

Some important CALMET model settings used to derive the three-dimensional wind fields and other ABL parameters are listed below:

- Sea-surface temperature was inut for buoy, C-MAN, and platform sites only. No satellite-derived sea temperature data were used.
- Extrapolation of surface winds into the upper levels was not allowed because surface observations can be influenced by local terrain and other siting issues and we did not want to extrapolate the surface winds aloft where they would then be used to represent more regional-scale flows.
- The maximum radius of influence over land in the surface layer was 20 km.
- The maximum radius of influence over land in the aloft layers was 150 km.
- The maximum radius of influence over water was 50 km

The three threshold levels used to characterize the radius of influence of the observations were based on initial experiments designed to minimize the radius of influence, yet retain the ability to interpolate to every grid cell in the CALMET modeling domain. Maintaining the smaller-scale flows in the surface analysis fields was the goal. Utilizing too large a radius of influence can result in the elimination of mesoscale features.

- Equal weighting of the “initial guess” field (EDAS) and observations in the surface layer occurs at 40 km from the observation.
- Equal weighting of the “initial guess” field (EDAS) and observations in the aloft layers occurs at 150 km from the observation.

These two settings were based on experiments. For the surface, allowing observations to dominate the analysis out to about two times the radius of influence enables a blending of objective analysis and EDAS fields.

- One smoothing pass below 400 m and two smoothing passes elsewhere were utilized. This limited smoothing was performed to reduce any artifacts in the analysis fields due to variations in density and distribution of observations, while not to eliminate important mesoscale features, particularly in the boundary layer where the greatest variations are expected.

### 6.3 CALPUFF DISPERSION MODELING

CALPUFF is a multi-layer, multi-species, non-steady-state puff dispersion model that can simulate the effects of time- and space-varying meteorological conditions on pollutant transport, transformation, and removal. CALPUFF contains algorithms for near-source effects such as building downwash, transitional plume rise, partial plume penetration, subgrid scale terrain interactions as well as longer-range effects such as pollutant removal (wet scavenging and dry deposition), chemical transformation, vertical wind shear, over-water transport, and coastal interaction effects. It can accommodate arbitrarily varying point source and gridded area source emissions. Most of the algorithms contain options to treat the physical processes at different levels of detail depending on the model application.

The CALPUFF dispersion model utilizes geophysical gridded data as well as the three-dimensional diagnostic gridded wind fields and other ABL parameters (Section 6.1) that are output from the CALMET model. CALPUFF was applied with an arbitrary hypothetical emission rate from three platform sites in the Gulf of Mexico (SMI, DWP, BIP); the locations of the three platforms are shown in **Figure 6-7**. The goal of the CALPUFF simulations was to characterize, in a preliminary manner, the potential impact of offshore emission sources on coastal areas along the Gulf of Mexico. The CALPUFF simulations were intended to predict relative rather than absolute concentrations. The resulting patterns and extent of transport, and the diffusion of the plume, were compared for the three release locations, and for the days within case study periods, and for days under different synoptic regimes.

The following source characteristics were assumed:

- The stack heights above the platforms were set to 10 m.

- The stack diameter was set to 10 m for each platform.
- The exit velocity was assumed to equal 0.005 m/s.
- The exit temperature was based on the ambient temperature measured at each platform site.
- A continuous emission rate of 2000 g/sec was used at all platform locations.

The results from the dispersion model are discussed in Section 6.5.

## 6.4 TRANSPORT ANALYSIS

The transport analysis was carried out by computing forward trajectories calculated over a duration of 24 hours and originating at heights of 10 m, 75 m, and 350 m from the SMI, DWP, and BIP platforms (see Figure 6-7 for the locations of the platforms). The goal of the transport analysis was to characterize the influence of the large-scale and local-scale meteorology on transport from the potential emission sources and analyze the potential impact of this transport on coastal regions. The forward trajectories were computed using the derived wind fields output from the CALMET meteorological model as input into an STI in-house trajectory model (TRAJMOD), and also using EDAS model output as input into the HYbrid Single-Particle Lagrangian Integrated Trajectory (HYSPLIT) model. The results from the transport analysis are discussed in Section 6.5.

## 6.5 CASE STUDIES

To assess the impact of offshore emissions on onshore areas along the Gulf Coast, three-dimensional gridded wind fields and other ABL parameters (i.e., mixing heights) were calculated using the CALMET diagnostic meteorological model for seven case studies. The case studies were chosen to represent the variety of weather patterns that influence regional meteorological conditions, which have a direct impact on the transport and dispersion characteristics of pollutants in the western and central Gulf of Mexico. The boundary layer characteristics (i.e., heat flux, friction velocity, etc.) were also analyzed for these particular case studies and the results are presented in Section 5.

The three-dimensional wind fields created by CALMET are a combination of observations and gridded EDAS output. Trajectories were calculated using the gridded wind fields generated by CALMET and were compared to trajectories calculated by the HYSPLIT model, which utilized EDAS output. It should be noted that the CALMET modeling domain was limited so the entire 24-hr forward trajectory may not have been completely calculated. Dispersion runs were calculated using the CALPUFF air quality model, which utilized the three-dimensional diagnostic gridded fields output by CALMET. The dispersion plots that follow show the accumulation of material from the start of each case study to the time indicated on the plot. Accurate mixing heights are a critical parameter in transport and dispersion modeling. One important note regarding the scheme that the CALMET model utilizes to derive over-water mixing heights is that mixing height growth is entirely driven by mechanical mixing, negating any growth due to convective processes (buoyancy). This resulted in the underestimation of

daytime mixing heights by CALMET when compared to mixing heights derived from RWP measurements. Therefore, the stand-alone dispersion results presented in each of the following case studies may be inaccurate; however, a comparison of the relative dispersion patterns and characteristics between episode types is still useful.

### **6.5.1 July 30–August 1, 1999: Summer Period with Strong Upper-Level Ridge and Surface High Causing Weak Winds**

**Overview:** This case study period was chosen because it is typical of summer light wind conditions. The region was dominated by a large upper-level ridge of high pressure and a surface area of high pressure throughout July 30–August 1, 1999. Winds across the region lacked a significant onshore component because a surface area of high pressure was centered directly south of Louisiana. As a result, the hypothetical tracer emissions from the platforms did not have a major influence along the Gulf coast. The only exception was a brief period on July 31, when tracers emitted from the SMI platform would have been transported toward the Mississippi River Delta.

**Large-Scale Aloft (500 mb):** A large upper-level area of high pressure was in place across the Gulf of Mexico throughout the entire case study period.

**Large-Scale Surface:** A large surface area of high pressure was located in the central Gulf of Mexico throughout the case study period. General flow across the Gulf of Mexico consisted of light southerly/southwesterly flow across the western regions of the Gulf and light west-northwesterly flow along the Gulf Coast of Louisiana, Mississippi, and Alabama on July 30. As time progressed, the center of the area of high pressure moved closer to the modeling domain and winds became lighter and more variable.

**Modeled 24-hr Forward Trajectories:** Trajectories calculated from both the CALMET wind fields (using TRAJMOD) and EDAS wind fields (using HYSPLIT) during the period, 0000 CST on July 30 through 0800 CST on August 1, 1999, were predominantly from a westerly direction. This flow direction observed near the platforms was caused by the anticyclonic circulation around an area of high pressure centered in the central Gulf of Mexico (**Figures 6-8 through 6-13**). As time progressed, the trajectories began to shift more out of the northwest. Consequently, the trajectories and the associated tracer plumes had little if any interaction with areas along the Gulf Coast. The CALMET and EDAS trajectories were quite similar.

**Modeled Dispersion:** On July 30, the westerly flow influencing the DWP and BIP platforms caused the hypothetical emissions to be transported eastward over open water where they had no impact on onshore areas (**Figure 6-14**). The simulated plume from the SMI platform contained more of a southerly component, which allowed a very minimal amount of the hypothetical emissions to impact areas along the immediate Louisiana coastline. As the center of the area of high pressure moved northward on July 31, the associated winds across the Gulf lightened considerably, which in turn produced less dilution of the plumes and also produced lower mixing heights derived by CALMET. Consequently, the hypothetical emissions slowly accumulated near the platforms. Winds near SMI on July 31 contained a slight onshore component, which caused hypothetical emissions to impact areas of the Mississippi River Delta in Louisiana

**(Figure 6-15).** BIP and DWP experienced west-northwesterly flow on July 31, which kept hypothetical emissions from having an immediate impact along the Gulf Coast (Figure 6-15). On August 1, light and variable winds and low mixing heights across the Gulf of Mexico allowed the tracer to accumulate around all platform sites (**Figure 6-16**). However, with no onshore wind component the enhanced hypothetical emissions had no impact along the Gulf Coast. The CALPUFF dispersion results should be compared only in a relative sense, since the same emissions were released from all platforms at all times. It was concluded earlier that, because the CALMET-estimated mixing heights do not account for convection and are much too low over water, actual concentrations would be about a factor of three or four lower if correct mixing heights were used (i.e., the current estimated mixing heights are 100 m to 200 m, whereas the actual mixing heights are known to be 500 m to 600 m).

A comparison of the dispersion contours in this case study with the contours from the January 20-24 case study, when winds were much higher, provides insight as to how transport and dispersion are influenced by the different meteorological conditions. The maximum relative concentrations are higher by a factor of four or five in the light-wind summer period.

### **6.5.2 January 20-25, 2000: Winter Case Study with Shift in Wind Direction**

**Overview:** This case study period was characterized by post-frontal strong offshore flow on January 20 and 21, followed by strong onshore flow on January 22 and 23, and strong offshore flow again on January 24 and 25 after a frontal passage late on January 23. The two periods with strong offshore winds were marked by cold air temperatures and very large skin-air temperature differences, resulting in very large sensible and latent heat fluxes from the water surface. In contrast, the onshore flow was marked by more stable conditions. The strong winds resulted in persistent narrow calculated plumes with relatively low concentrations for the hypothetical tracer releases from the three platforms.

**Large-Scale Aloft (500 mb):** Northwesterly flow aloft across the Gulf region on January 20 and 21 was the result of a large upper-level area of low pressure centered in Ontario, Canada, whose influence extended south through the eastern half of the United States. An upper-level ridge extended throughout the Mountain West. On January 22, zonal flow was evident over the United States, as the result of the upper-level ridge over the Mountain West breaking down and the upper-level trough pushing off the eastern seaboard. However, on January 22, a shortwave trough was analyzed over the eastern Gulf of Mexico, while a shortwave ridge strengthened in the western Gulf of Mexico. By January 23 an upper-level trough began to strengthen across the eastern two-thirds of the United States. The trough remained in place over the Gulf of Mexico on January 24 before beginning to exit on January 25.

**Large-Scale Surface:** On January 20, strong offshore, northerly flow was associated with a strong pressure gradient located between an area of high pressure moving through the Plains, centered in Kansas, and a low pressure area located over the eastern seaboard. As the area of high pressure moved toward the east, the flow over the Gulf of Mexico rotated from northerly-to-northeasterly-to-easterly on January 21. On that day, the Gulf region was located on the southern edge of the surface high, now centered in Tennessee. Strong southerly flow developed on January 22, and was associated with cyclonic circulation around an approaching surface low

moving across the Central Plains. Southwesterly flow continued across the Gulf of Mexico on January 23 as the surface low pressure area became centered in Alabama, with an associated stationary front analyzed along the Gulf Coast. However, a surface high was building into the region from the Central Plains, behind the departing area of low pressure and its stationary frontal boundary. The anticyclonic flow around the approaching high pressure area drove strong northerly flow across the Gulf of Mexico from January 24-25.

**Modeled 24-hr Forward Trajectories:** As noted, the period, 0000 CST on January 20 through 0000 CST on January 25, 2000, consisted of offshore transport, followed by onshore transport, and ending with a period of strong offshore transport, which is depicted by trajectories calculated from both the CALMET wind fields (using TRAJMOD) and EDAS wind fields (using HYSPLIT). TRAJMOD-derived trajectories (including the RWP observations) and HYSPLIT-derived trajectories (utilizing EDAS wind fields and no Gulf of Mexico RWP observations) were calculated at 10 m, 75 m, and 350 m originating from the SMI, DWP, and BIP platforms and are shown in **Figures 6-17 through 6-22** for the period from 0000 CST on January 19 through 1600 CST on January 22. The trajectories between January 20 and early on January 21 of the analysis period are shown originating at the platform sites and moving out into the Gulf of Mexico due to the northerly wind component. Figures 6-17 through 6-22 also show onshore transport beginning later on January 21 and continuing through the afternoon hours on January 23, with the trajectories from the latter part of the period shown in **Figures 6-23 through 6-28**. The onshore flow occurred at all heights, as a result of cyclonic circulation around the surface area of low pressure moving across the Central Plains. Because of the surface area of high pressure that built into the region on January 24 and 25, trajectories regained a strong, offshore northerly component at all heights (see Figures 6-23 through 6-28). Generally the same general time variations were seen at all heights (10 m, 75 m, and 350 m). However, as expected, winds and transport distances increased with height. Both the TRAJMOD- and HYSPLIT-calculated trajectories agree for the most part throughout the case study period. The HYSPLIT trajectories seem to indicate faster speeds, as found earlier when RWP winds (used to create CALMET wind fields for TRAJMOD) were compared with EDAS winds (used in HYSPLIT). Note, however, that because the TRAJMOD trajectories often truncated due to the limited CALMET modeling domain and the HYSPLIT trajectories had no such boundary limit, the lengths of the trajectories should not be compared for those cases.

**Modeled Dispersion:** The strong northerly flow on January 20 (**Figure 6-29**) transported the hypothetical tracer emissions from the platforms over open waters of the Gulf of Mexico, causing no onshore impact. The strong winds contributed to the increased dilution of the hypothetical tracer, resulting in relatively low hypothetical concentrations. The estimated mixing heights were slightly higher on this day due to the higher wind speed (**Figure 6-30**). However, if the model had properly accounted for the influence of convection on the mixing height, the mixing heights would have been larger and more realistic, since the large water-air temperature differences led to extremely large heat fluxes. On January 21, the strong east-northeasterly flow (**Figure 6-31**) caused the hypothetical plume released from BIP to pass over Breton Island, while hypothetical emissions from SMI and DWP caused no onshore impact because they were transported out over open water (Figure 6-31). **Figure 6-32** shows that the estimated mixing heights remained relatively low at about 200 m or less over water, which is likely to be a large underestimate. On January 22 (**Figure 6-33**) strong southerly flow from all platform locations allowed the hypothetical emissions to impact onshore locations to a certain degree, although

relative concentrations were low because of the dilution effects of the strong winds. The mixing heights on January 22 are shown in **Figure 6-34**, which illustrates patterns similar to the other days. Southwesterly flow ahead of the frontal passage on January 23 is evident in **Figure 6-35**; onshore locations in Louisiana were directly influenced by tracers emitted at the SMI platform and onshore locations in Alabama were directly influenced by tracers emitted from BIP. The hypothetical concentrations on January 23 were higher than on January 22 due to lighter winds and lower mixing heights (**Figure 6-36**), which decreased dilution and mixing of pollutants. Strong northerly flow behind the cold front late on January 23 resulted in the transport of hypothetical emissions released at the platforms on January 24 (**Figure 6-37**) and January 25 (**Figure 6-38**) away from the shore, with relatively low concentrations due to the strong dilution. The strong winds increased CALMET's estimated mixing heights to about 400 m or 500 m in the area surrounding the RWP sites, as shown in **Figures 6-39 and 6-40**; but at distances beyond about 50 km from the RWP sites, the mixing heights dropped down to the usual unrealistically low values of 100 m or 200 m over the water. The observed mixing heights are likely to be much greater at these times, due to the extremely strong convective heat fluxes over water.

### **6.5.3 January 4-6, 2001: Winter Period Post Upper-level Trough Transitioning into Weak Upper-level Ridge**

**Overview:** A strong surface pressure gradient existed across the Gulf of Mexico on January 4, which drove moderate northwesterly flow and kept hypothetical emissions from impacting onshore areas. Transitioning from January 4 to January 5, the pressure gradient gradually weakened and allowed a brief period of west-southwesterly surface flow, which caused hypothetical emissions calculated by CALPUFF to impact areas along the immediate coastline. Later on January 5 and into January 6, winds were moderate from a west-northwest direction and hypothetical emissions were simulated to remain offshore.

**Large-Scale Aloft (500 mb):** An upper-level trough had passed through the region and was located along the eastern seaboard on the January 4. By January 5 an upper-level ridge building in the west and the eastward movement of the upper-level area of low pressure began to produce nearly zonal flow across the Gulf of Mexico in the upper levels for January 5 and 6.

**Large-Scale Surface:** Moderate northwesterly flow across the Gulf of Mexico occurred on January 4 due to the strong pressure gradients between a high pressure system to the west and a low pressure system on the east coast. Late on January 4 and early on January 5, the pressure gradient began to weaken. A surface anticyclone developed just to the north of the Bay of Campeche, west of the Yucatan Peninsula, and began to influence flow across the Gulf. Westerly winds, with a brief period of west-southwesterly winds across the modeling domain on January 5, were the result of the anticyclonic circulation around the area of high pressure to the south. By January 6, the winds shifted more to the northwest and weakened. During the entire case study period, the winds were much stronger over the Gulf of Mexico than over the adjacent land areas.

**Modeled 24-hr Forward Trajectories:** Trajectories calculated from both the CALMET wind fields (using TRAJMOD) and EDAS wind fields (using HYSPLIT) during the period, 0000 CST on January 4 through 0000 CST on January 6, 2001, generally were westerly and contained an

offshore component. Initially on January 4 the trajectories indicate northwesterly flow, which transitioned midday to westerly on January 4 into January 5, before returning to northwesterly on January 6 (**Figures 6-41 through 6-46**). The trajectories were consistent with the large-scale meteorology discussed above. Both the TRAJMOD- and HYSPLIT-calculated trajectories were similar throughout the period. However, comparisons of the more distant portions of the TRAJMOD trajectories with HYSPLIT trajectories are not possible because the TRAJMOD trajectories truncate when they reach the boundary of the CALMET modeling domain.

**Modeled Dispersion:** As seen in **Figure 6-47**, the northwesterly flow that persisted throughout January 4 caused the hypothetical emissions being released from the designated offshore source platforms to be transported southward, away from the Gulf Coast toward the southern part of the Gulf of Mexico. As the general flow rotated from northwesterly to west-southwesterly in the early morning of January 5 (**Figure 6-48**), the southern tip of the Mississippi River Delta was influenced by some of the hypothetical emissions from the SMI platform and the Alabama coastline was influenced by hypothetical emissions from BIP. As westerly flow strengthened throughout January 5 (**Figure 6-49**), most of the hypothetical emissions were transported eastward, causing little influence on the Gulf Coast. As seen in **Figure 6-50**, the light west-northwesterly flow on January 6, transported hypothetical emissions from the platforms away from the Gulf Coast and into the southern part of the Gulf of Mexico.

#### **6.5.4 January 29, 2001: Winter Case with Strong Southerly Winds**

**Overview:** January 29, 2001, was characterized by strong southerly winds ahead of an approaching frontal boundary. Despite the fact that the simulated tracer plumes were transported directly toward coastal areas, relative concentrations were not predicted by CALPUFF to be large because of the strong dilution.

**Large-Scale Aloft (500 mb):** Prior to January 29, the Gulf of Mexico was under the influence of a large upper-level area of high pressure. A strengthening upper-level area of low pressure moving out of the West toward the Central Plains aided in breaking down the upper-level ridge over the Gulf of Mexico. By January 30, the upper-level ridge influencing the Gulf region was eventually replaced by an upper-level trough.

**Large-Scale Surface:** On January 28, a large area of high pressure covered the entire eastern third of the United States. A developing surface area of low pressure moved into the Central Plains on January 29, with an associated frontal boundary extending into the northwestern section of the Gulf of Mexico. Because the study region was located between the surface area of high pressure centered along the eastern seaboard and the approaching surface low, a strong pressure gradient existed that produced strong southerly flow across the entire Gulf of Mexico on January 29.

**Modeled 24-hr Forward Trajectories:** As seen in **Figures 6-51 through 6-56**, the period, 0000 CST on January 27 through 0000 CST on January 30, 2001, generally was characterized by strong onshore trajectories from the south at 10 m, 75 m, and 350 m across the Gulf of Mexico at all three platform sites. Some of the 24-hr HYSPLIT trajectories passed completely across the United States and entered Canada, reflecting an average wind speed of 30 m/s. Toward the end

of the case study period, the influence of the approaching frontal passage on the trajectories was beginning to be observed, as the trajectories began to take on more of a westerly component. The strong, onshore trajectories were consistent with the large-scale synoptic patterns discussed above. The trajectories calculated from both the CALMET winds fields (using TRAJMOD) and EDAS wind fields (using HYSPLIT) were similar in transport direction and agreed in transport distance over the first few hours, but comparisons were not possible for times after the TRAJMOD-calculated trajectories truncated at the arbitrary boundaries.

**Modeled Dispersion:** Figure 6-57 shows CALPUFF-estimated plume contours for hypothetical tracer releases from the SMI, DWP, and BIP platforms. The plumes generally were transported by the strong southerly winds toward the coast, although concentrations were relatively low because of the large dilution by the strong wind. The CALMET wind interpolation procedure can be seen in the area around DWP because the DWP RWP was recording more west-southwesterly winds in the midst of generally southerly winds. CALMET causes the observed west-southwesterly wind direction to strongly influence grids out to about 50 km from the platform. Outside 50 km to 100 km, the winds do not deviate much from the southerly direction.

### 6.5.5 April 14-15, 2001: Onshore Wind Case Study

**Overview:** The April 15, 2001, case study was selected because the wind was onshore during the period. The moderate surface winds caused the hypothetical tracers emitted from the offshore platforms to be transported directly toward shore with relatively small lateral spreading. As a result, the impact on onshore areas was confined to small areas.

**Large-Scale Aloft (500 mb):** The Gulf region was under a broad, weak upper-level ridge of high pressure on April 14, which gave way to zonal flow across the Gulf Coast on April 15.

**Large-Scale Surface:** A nearly-stationary frontal boundary extended from northern Texas to southern Georgia, with a weak area of low pressure developing in Texas on April 14 and 15. An area of high pressure was also centered off of the western coast of Florida. Moderate southerly/southwesterly winds on the April 14 and 15 were associated with the pressure gradients between this area of high pressure and the lower pressure to the west.

**Modeled 24-hr Forward Trajectories:** The period, 0000 CST on April 13 through 0000 CST on April 15, 2001, was dominated by southerly winds and consequently onshore transport from all platforms in the Gulf of Mexico as depicted by trajectories calculated from both the CALMET wind fields (using TRAJMOD) and EDAS wind fields (using HYSPLIT). At later times, the onshore transport weakened and changed to nearly calm and then northerly and easterly transport. As noted above, the onshore transport was caused by the anticyclonic circulation of air around the high pressure centered off the western coast of Florida. Southerly transport from each platform is seen at the 10-m level during the onshore transport period (Figures 6-58 and 6-59). At 75 m, the onshore transport period indicated consistent southerly transport from the SMI platform, but a more southwesterly component from the BIP and DWP platforms (Figure 6-60 and 6-61). At 350 m, the onshore transport period was dominated by southwesterly flow at all the sites (Figure 6-62 and 6-63). There was fair agreement (i.e., usually the directions agreed within about 20 or 30 degrees) between the TRAJMOD- and

HYSPLIT-derived trajectories at the 10-m, 75-m, and 350-m levels. However, the HYSPLIT trajectories suggest faster speeds than the TRAJMOD trajectories, consistent with the findings in Section 6.1 that the EDAS model wind speeds (used for HYSPLIT) are a few m/s higher than the RWP wind speeds (used by CALMET and TRAJMOD), with the difference increasing as distance from shore increases.

**Modeled CALPUFF Dispersion:** The moderate southerly/southwesterly onshore flow on April 14 caused the hypothetical emissions released from the SMI and BIP platforms to impact onshore coastal areas (**Figure 6-64**). Emissions from DWP do not impact the coastline in the domain shown on the figure. The estimated concentrations were higher in the DWP plume than in the SMI or BIP plumes (Figure 6-64), probably due to lower mixing heights simulated by CALMET at DWP (**Figure 6-65**). On April 15, the continued south/southwesterly flow near the platforms caused the hypothetical emissions released from SMI and BIP to impact onshore coastal areas, while emissions from DWP remained well offshore (**Figure 6-66**). The concentrations in the simulated plumes from SMI and DWP were higher than in the plume from BIP, probably due to lower wind speeds and lower mixing heights (**Figure 6-67**). The mixing heights,  $z_i$ , shown over water in Figures 6-65 and 6-67 are only 100 m or 200 m, which are much lower than the observed values of 500 m or 600 m. The discrepancy is due to the fact that CALPUFF uses only the mixing height formula for neutral conditions, where  $z_i$  is proportional to wind speed, and unrealistically ignores the contributions of convection over the water.

#### **6.5.6 May 14-15, 2001: Spring Case Study with Light Winds and Regional High Ozone**

**Overview:** This case study period was chosen because it featured high observed concentrations of ozone across the coastal region. As is typical of high ozone scenarios, the period was characterized by a surface high pressure area and light and variable winds. The hypothetical tracers released from the platforms as a test of CALPUFF tended to be transported very slowly and remain within 50 km to 100 km of the platforms during a 24-hr period. As a result the concentrations were relatively high but remained offshore for the most part. The estimated plume from BIP showed some coastal impact on both days, while the SMI plume impacted the areas across the Mississippi River Delta on May 15.

**Large-Scale Aloft (500 mb):** The large-scale synoptic pattern for May 14-15 was dominated by an upper-level ridge of high pressure. On May 14 the ridge was in place across the Central Plains with the ridge axis extending into Texas. By May 15 the upper-level ridge of high pressure began to weaken and move into the midwestern United States with the ridge axis extending into Louisiana.

**Large-Scale Surface:** The light northeasterly/east-northeasterly surface winds across the Gulf of Mexico on May 14 were associated with a large area of high pressure that encompassed the entire east coast with the center located over eastern Kentucky and Tennessee. By May 15, the region was still under the influence of the large, weak area of high pressure, which was now centered over the southeastern United States. Wind speeds were weak at the beginning of the period and weakened even more by May 15. However, a small anticyclonic circulation centered south of the Louisiana/Texas border caused weak westerly flow for most of May 15.

**Modeled 24-hr Forward Trajectories:** As seen in **Figures 6-68 through 6-73**, the trajectories calculated from both the CALMET wind fields (using TRAJMOD) and EDAS wind fields (using HYSPLIT) for the analysis period, May 14 at 0000 CST through 1600 CST on May 15, 2001, indicated light and variable flow as a result of the large area of high pressure in place across the Gulf of Mexico. During the period, flow was first from the northeast quadrant, then became variable, and finally was from the west quadrant; the flow was weak at all times. However, very weak winds were present during the middle of the period. As a result of the weak winds, the calculated 24-hr trajectories remained in the Louisiana coastal area. The TRAJMOD- and HYSPLIT-derived trajectories are in fair agreement, although, as seen in all the case studies and described in Section 6.1, the speeds of the HYSPLIT trajectories are as much as a factor of two larger than those calculated by TRAJMOD using the CALMET wind fields because CALMET assimilates the RWP observations. On average, the RWP speeds are less than the EDAS speeds (used in HYSPLIT), with the difference increasing as distance from the shore increases.

**CALPUFF Modeled Dispersion:** Light and variable winds (**Figure 6-74**), combined with low mixing depths (**Figure 6-75**) contributed to the accumulation of hypothetical emissions near each source platform on May 14 (**Figure 6-74**). A period of light winds from the northeast near BIP caused hypothetical emissions to impact coastal regions of the Mississippi River Delta (**Figure 6-74**). In fact, the dense part of the plume is very close to New Orleans. On May 15, the flow remained very light with a slight onshore component due to the development of the small anticyclonic circulation south of the Louisiana/Texas border. The combination of light winds (**Figure 6-76**) and low mixing heights (**Figure 6-77**) again on May 15, along with minimal dispersion of hypothetical emissions from the previous day, caused plumes containing high concentrations of the hypothetical tracer to cover large areas and eventually impact coastal areas of Louisiana and Alabama (**Figure 6-76**). In particular, the estimated path of the plume from BIP could result in impact of relatively high concentrations on the Alabama coastal area. These results suggest that, during light and variable wind conditions, plumes from the three platforms would have high concentrations but would usually remain offshore. However, in a few instances, it is possible that a persistent on-shore light wind for a few hours could cause relatively high impact on a coastline or on an offshore island, although the underestimate of mixing heights in CALMET produces higher relative pollutant concentrations than it should.

### **6.5.7 September 18-20, 2001: Nearly Stationary Front Along the Gulf Coast**

**Overview:** Moderate south-southeasterly flow occurred in the Gulf of Mexico along the Louisiana coast region on September 18, associated with a surface high located along the eastern seaboard, and an approaching surface low. Consequently, hypothetical emissions released at offshore locations impacted onshore areas on September 18. Later on September 19 and 20, a stationary front developed over the coast and winds became light and variable, but with generally an east to northeast drift. Consequently, the hypothetical tracer emissions were transported to the northeast toward shore on September 19, but remained mostly offshore on September 20. Concentrations were relatively high in the plumes on September 19 and 20 because of the light winds. High concentrations were also due to the unrealistically low overwater mixing heights estimated by CALMET, as discussed in previous case studies.

**Large-Scale Aloft (500 mb):** The aloft pattern for this case study period was characterized by a weak upper-level trough that moved out of the Rockies, across the Central Plains, and toward the eastern seaboard. At the same time, an upper-level area of high pressure developed over Mexico/western Gulf of Mexico and gradually began to influence the region throughout the case study period.

**Large-Scale Surface:** The entire east coast was under the influence of a large area of high pressure, while a surface area of low pressure began to develop over the Central Plains. South-southeasterly flow across the region on September 18 was associated with the pressure gradient between the surface high that was centered in Georgia and the surface low pressure over the Central Plains. The area of low pressure began to move northeastward away from the Gulf region on September 19, and the associated frontal boundary pushed closer to the region. By September 20, the frontal boundary nearly stagnated along the Louisiana and Mississippi coastline and an area of high pressure moved in behind the frontal boundary. This caused weak and variable surface flow as the front boundary slowly passed to the south.

**Modeled 24-hr Forward Trajectories:** As seen in **Figures 6-78 through 6-83**, the trajectories calculated from both the CALMET wind fields (using TRAJMOD) and the EDAS wind fields (using HYSPLIT) for the analysis period, 0000 CST on September 18 through 1600 CST on September 20, 2001, were consistent with the large-scale meteorological patterns influencing the Gulf of Mexico as discussed above. The trajectories at all sites and heights on September 18 indicate onshore transport (due to the moderate southeast winds) originating at the platforms and moving toward the Gulf Coast. As the frontal boundary approached the region on September 19 and the pressure gradients and winds weakened, the trajectories still had a slight onshore component as the winds became southwesterly (**Figures 6-78 through 6-83**). As the nearly stationary front slowly moved to the south, weak northerly winds occurred on September 20. The general flow directions and transport speeds for the TRAJMOD- and HYSPLIT-derived trajectories were quite similar, although the TRAJMOD-derived trajectory speeds were slightly less than the HYSPLIT-derived trajectory speeds for offshore locations, as discussed in Section 6.1.

**CALPUFF Modeled Dispersion:** The moderate south-southeasterly flow that was present on September 18 allowed the hypothetical emissions released from all three platforms (BIP, DWP, SMI) to impact onshore areas (**Figure 6-84**). On that day, the hypothetical tracer emissions from SMI and DWP affected coastal areas of Louisiana, while those emitted from BIP affected Mississippi. The light southerly and southwesterly flow ahead of the approaching weak frontal boundary on September 19 also caused hypothetical emissions from offshore platforms to impact onshore coastal areas (**Figure 6-85**). The emissions from BIP and DWP reached the Mississippi coastline on September 19, while lighter winds near SMI contributed to a broader plume with higher concentrations which influenced parts of Louisiana (**Figure 6-85**). As the flow on September 20 adopted more of a westerly component before giving way to flow with more of a northerly component later in the day as a result of the passage of the weak front boundary, the hypothetical emissions were transported offshore for the most part, with little influence on onshore areas (**Figure 6-86**). Again, light wind speeds allowed the accumulation of emissions near the platforms, which resulted in broad plumes being calculated by CALPUFF out over the open waters of the Gulf of Mexico.

## 6.6 CONCLUSIONS

This section summarizes the results discussed in Section 6. Sections 6.1 to 6.3 summarized the comparisons of RWP and EDAS winds and the procedures for running CALMET and CALPUFF. Subsequent sections summarized the results of the seven case studies:

1. The EDAS-simulated wind fields and the observed RWP winds from six sites were compared. EDAS is based on a combination of Eta model forecast winds and diagnostic interpolations of observed winds but does not include RWP data. The comparison is complicated because the EDAS simulations represent averages over a grid volume of size about 40 km by 40 km by 100 m whereas the RWP observations represent an average over a much smaller grid volume with a radius about 5 m; consequently, more turbulent variations are expected in the observations than in the EDAS simulations. The mean wind speed (WS) bias was near zero close to the shore but increased with offshore distance, such that the EDAS mean WS exceeded the RWP mean wind speed by 1 to 2 m/s at 50 km offshore and by 2 to 6 m/s at 100 to 200 km offshore. Mean wind direction (WD) bias was relatively small, with about a 10° to 20° difference (e.g., if the RWP WD was 180°, then the EDAS WD would be 160°). Standard deviations of the differences (with mean bias removed) were 1 to 2 m/s for WS and 20 to 40° for WD, in agreement with findings for other domains and models (Hanna and Yang, 2001).
2. The CALMET diagnostic wind model was applied to the Gulf of Mexico domain using RWP and other observations. Methods were devised for interpolating between missing observations, especially for the vertical profiles of winds and temperature, since CALMET has stringent requirements for data continuity. Furthermore, recommendations were made for assumptions concerning length scales related to spatial interpolations. For example, based on the evaluations of EDAS simulations and RWP observations (see Item 1), a distance scale of 150 km from the observing location was chosen for the point where RWP and EDAS simulations would have equal weight.
3. The procedure for applying the CALPUFF transport and dispersion model was described in Section 6.3. Since actual source emission data were not available and no tracer studies had been done, the CALPUFF runs were made using arbitrary assumptions for hypothetical tracers from the three oil platforms, BIP, SMI, and SWP. The major model outputs for analysis were contour plots of 24 hr average concentration.
4. Twenty-four hour trajectories of hypothetical emissions released from the three oil platforms were calculated for several times at heights of 10 m, 75 m, and 350 m, using (1) CALMET wind fields and an in-house STI trajectory model (TRAJMOD), and (2) EDAS wind fields and the HYSPLIT trajectory model. However, the trajectory comparisons were hampered by the truncation of the CALMET trajectories at the domain boundary.
5. Seven multi-day case studies were analyzed using EDAS, HYSPLIT, CALMET, and CALPUFF. These seven periods covered the range of representative synoptic conditions and seasons, such as strong-wind January days and light-wind July days. Some general conclusions may be drawn:

- The CALMET trajectories and the EDAS-HYSPLIT trajectories agree within 20° to 30° most of the time, although the speeds of the EDAS trajectories are larger by as much as a factor of two (see the evaluations of mean biases under Item 1 above). However, because the CALMET trajectories often truncate at the edges of the CALMET domain, the comparisons with HYSPLIT trajectories are limited.
- The CALPUFF-simulated plumes from the three oil platforms sometimes impact the shoreline or the offshore islands, depending on wind direction. The concentrations are higher during light winds, when dilution is less. It is fortunate that the most persistent winds, associated with onshore impact near the same location for several hours, are nearly always marked by high winds and consequently lower concentrations. When winds are light and variable, the local centerline concentration may be higher, but the plume does not remain long over a specific point.
- The CALMET-CALPUFF estimates of overwater mixing depth were low, 100 to 200 m, in contrast to observed mixing depths of about 600 m. This factor of a three to six difference causes overpredictions in relative pollutant concentrations because the plume is constricted to the mixing layer. The underpredictions of mixing depth appear to be due to the neglect of convective mixing processes offshore, where CALMET currently assumes that the mixing depth is due solely to mechanical mixing and is, therefore, proportional to wind speed.

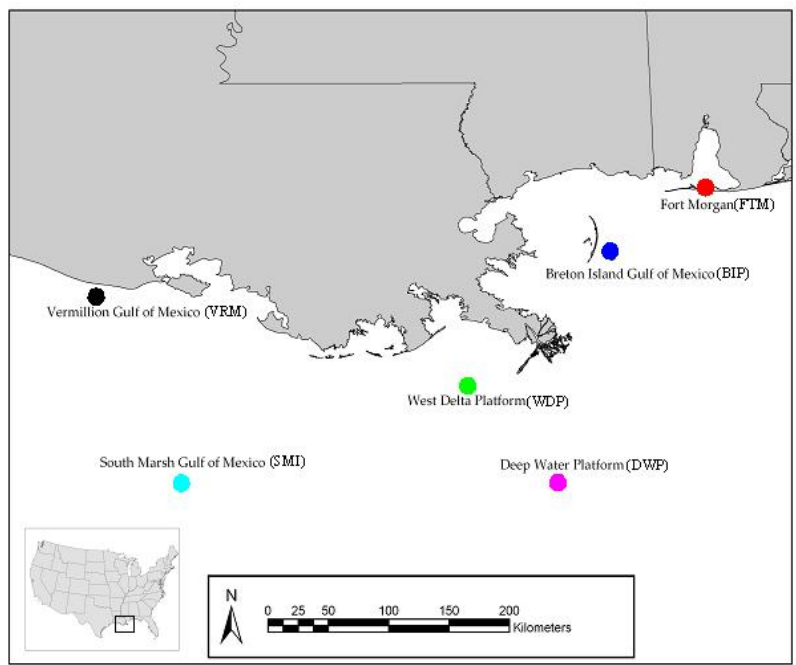


Figure 6-1. Gulf of Mexico study region with site locations for the six RWPs.

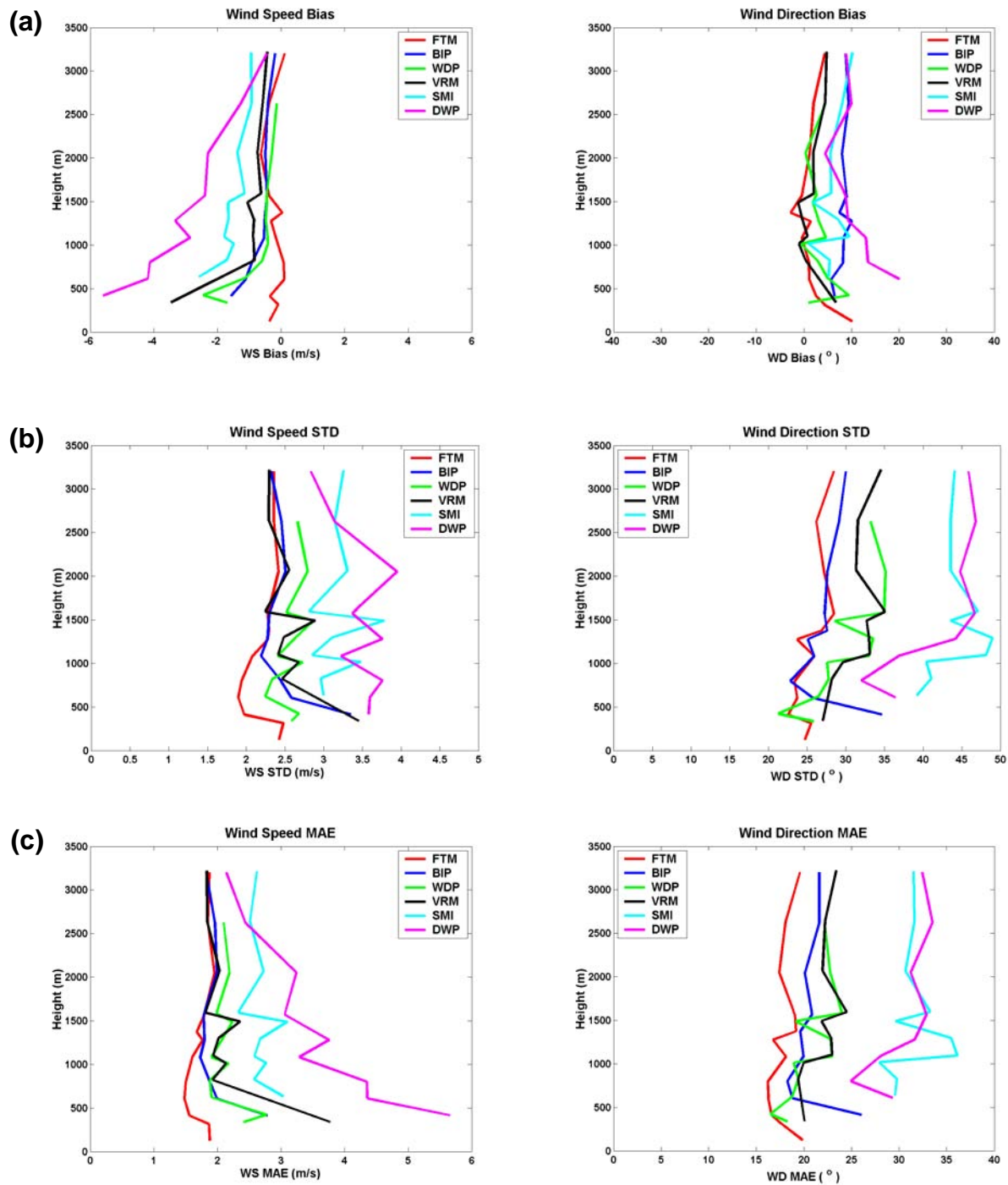


Figure 6-2. Comparison of RWP wind speeds and directions with EDAS simulations: (a) wind speed and direction mean bias, (b) mean standard deviation (STD), and (c) mean absolute error (MAE) for all RWP sites shown in Figure 6.1.

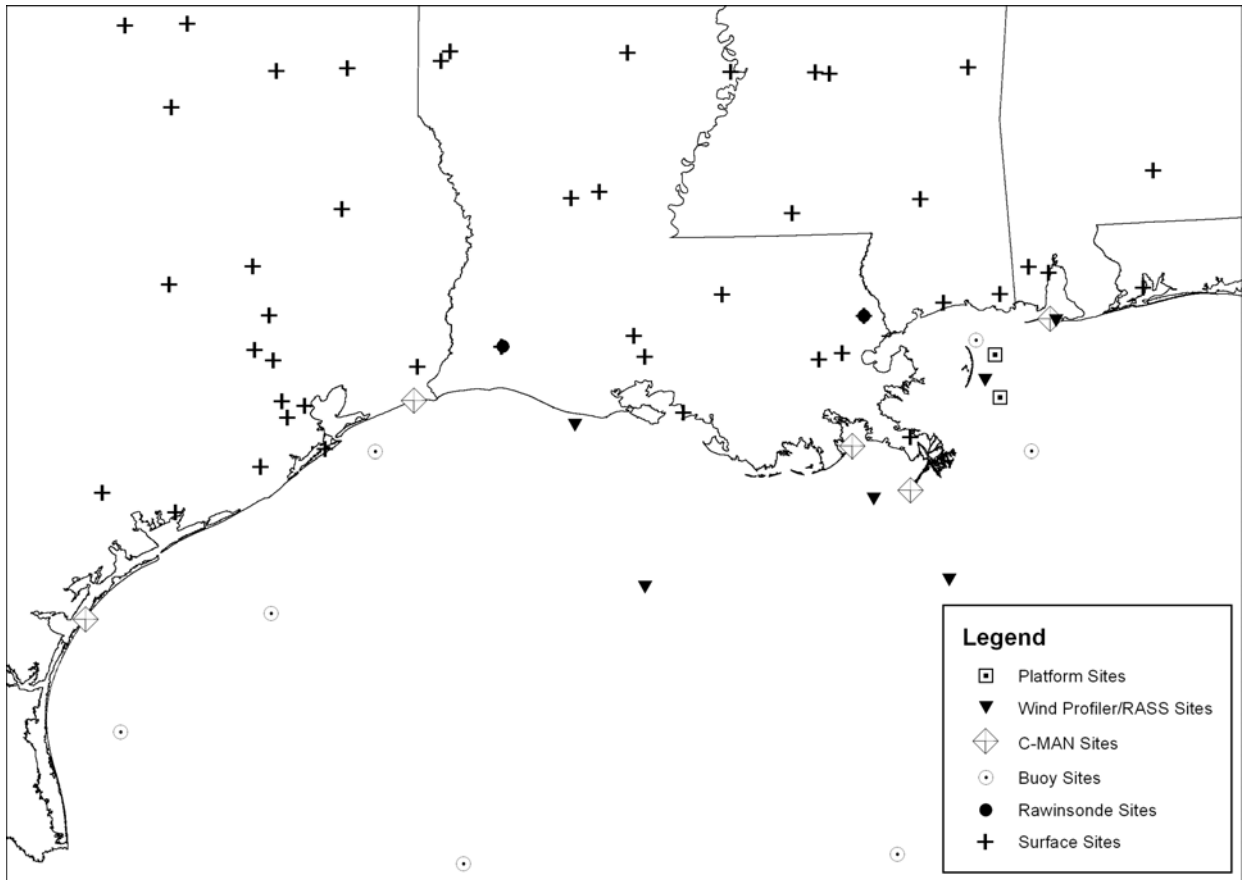


Figure 6-3. Locations of meteorological stations used to provide inputs to the CALMET diagnostic meteorological model to derive three-dimensional wind fields and other ABL parameters.

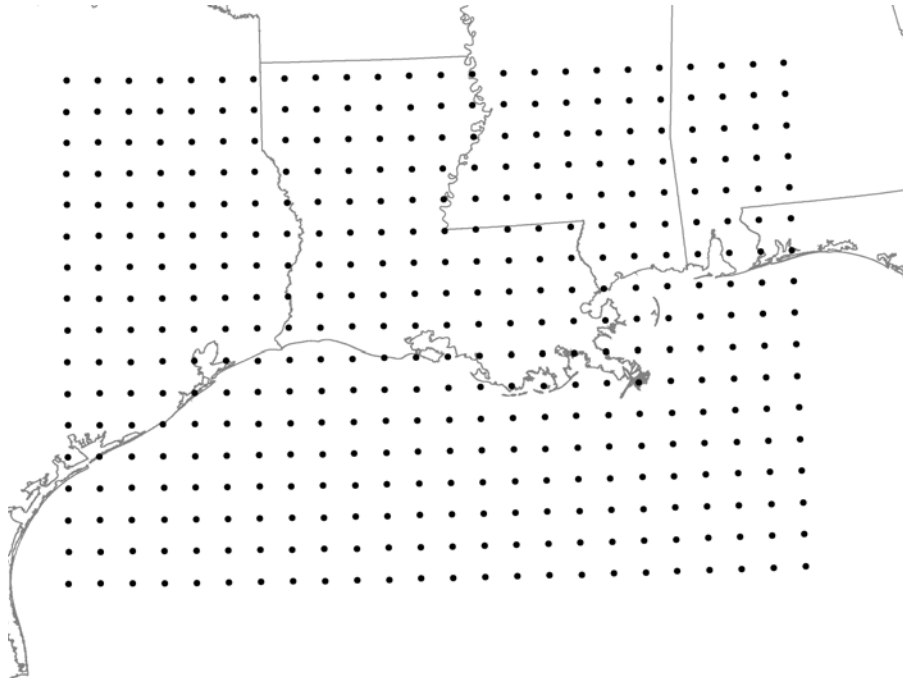


Figure 6-4. CALMET modeling domain for the Gulf of Mexico coastal region from mid-Texas to western Florida; 860 X 560 km (NX=172 and NY=112); 5-km horizontal grid resolution.

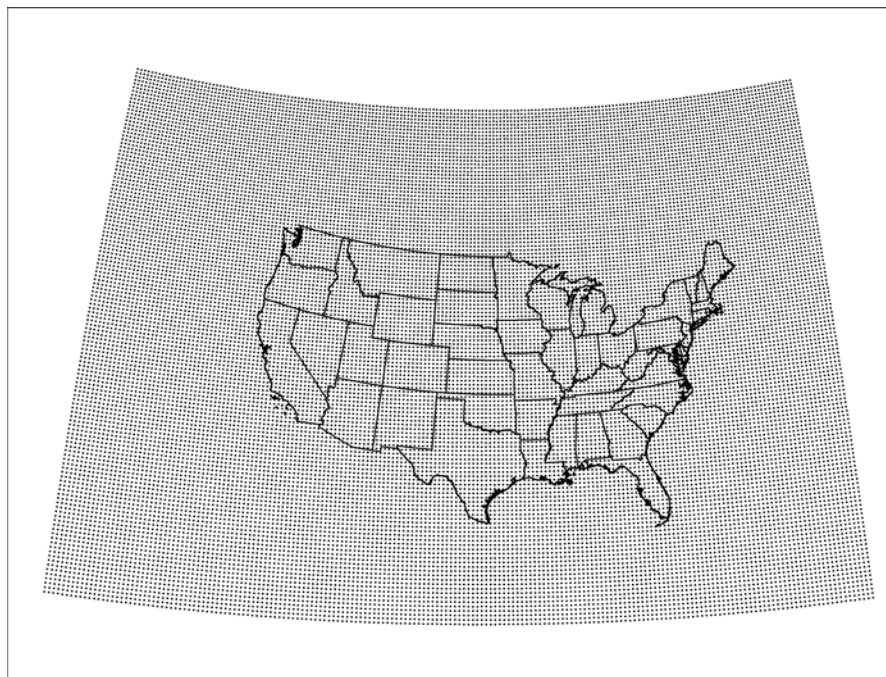


Figure 6-5. EDAS modeling domain using a horizontal resolution of 40 km (NX=185 X NY=129)

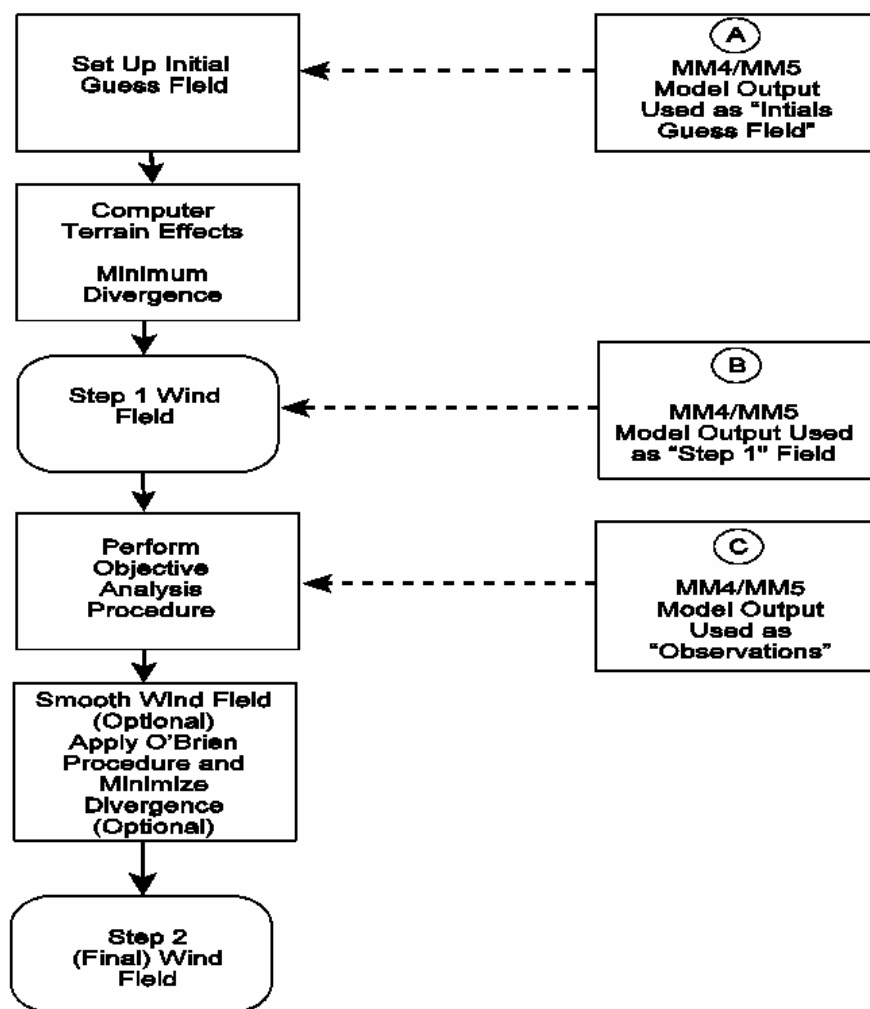


Figure 6-6. Standard options for incorporating gridded model output into a CALMET analysis (from Scire et al., 1999).

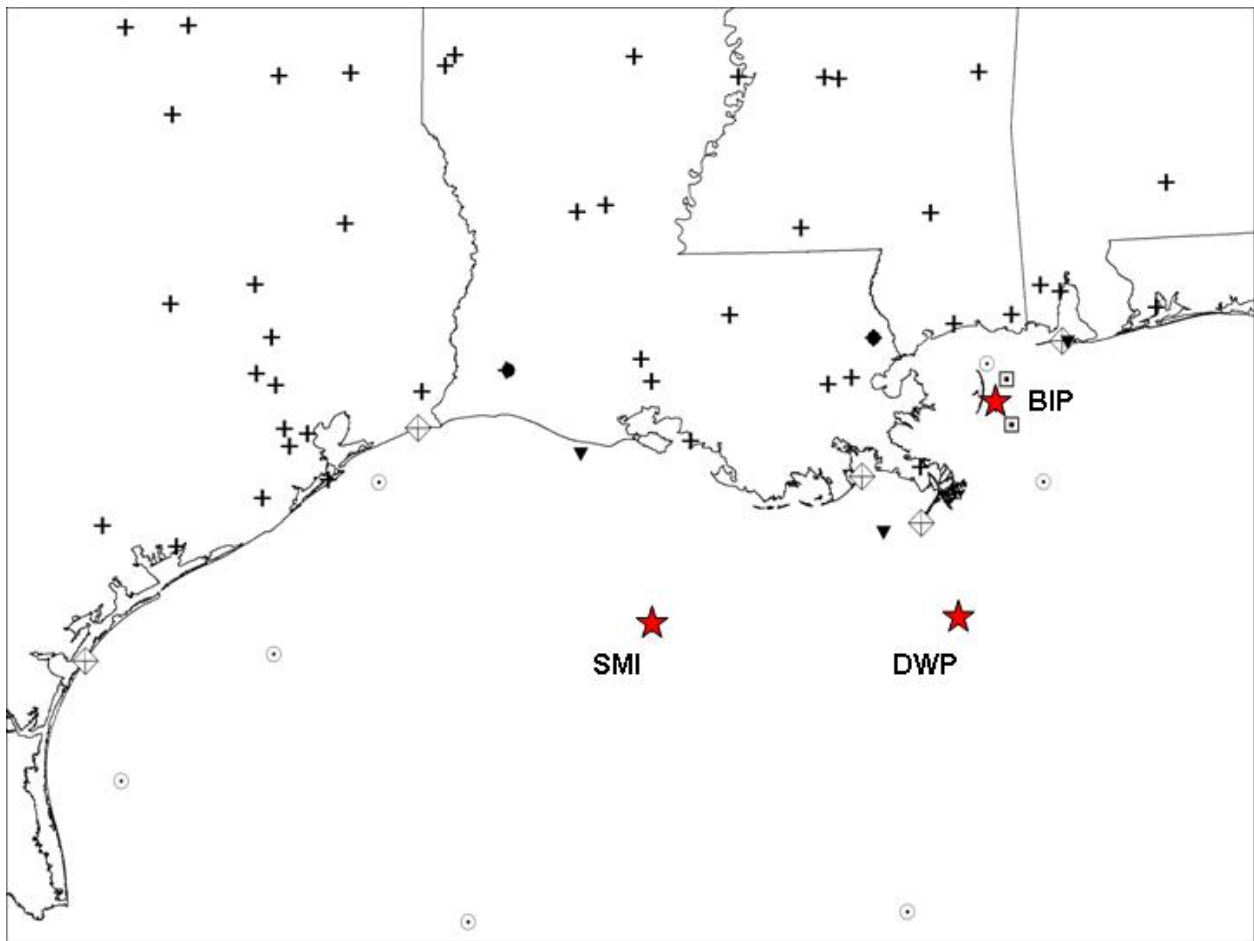


Figure 6-7. Locations of oil platform (red stars) where the arbitrary hypothetical tracers were assumed to be emitted for the air quality modeling exercise. The other symbols represent CALPUFF meteorological measuring stations.

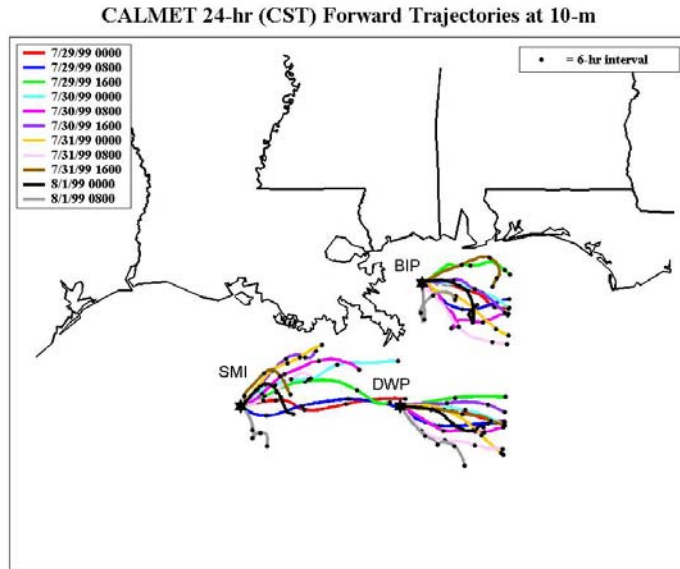


Figure 6-8. CALMET 24-hr forward trajectory at 10 m based on CALMET diagnostic wind fields for July 29 at 0000 CST through August 1, 1999, at 0800 CST. The RWP observations are used in CALMET. Note that the trajectories terminate when they reach the arbitrary boundary of the CALMET domain, even though the total time period has not elapsed.

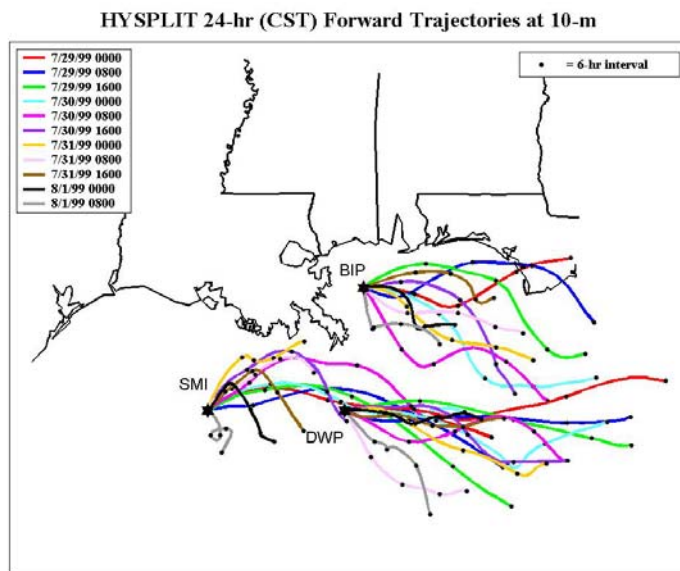


Figure 6-9. HYSPLIT 24-hr forward trajectory at 10 m based on EDAS wind fields for July 29 at 0000 CST through August 1, 1999, at 0800 CST. RWP observations are not used in EDAS.

CALMET 24-hr (CST) Forward Trajectories at 75-m

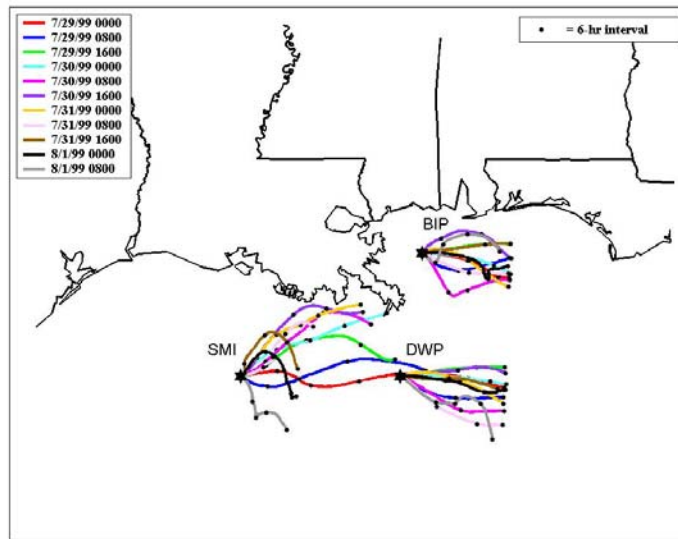


Figure 6-10. CALMET 24-hr forward trajectory at 75 m based on CALMET diagnostic wind fields for July 29 at 0000 CST through August 1, 1999, at 0800 CST. The RWP observations are used in CALMET. Note that the trajectories terminate when they reach the arbitrary boundary of the CALMET domain, even though the total time period has not elapsed.

HYSPLIT 24-hr (CST) Forward Trajectories at 75-m

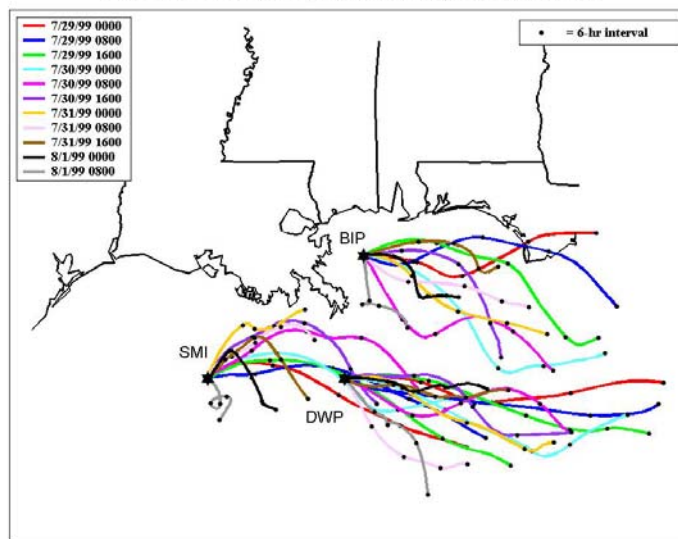


Figure 6-11. HYSPLIT 24-hr forward trajectory at 75 m based on EDAS wind fields for July 29 at 0000 CST through August 1, 1999, at 0800 CST. RWP observations are not used in EDAS.

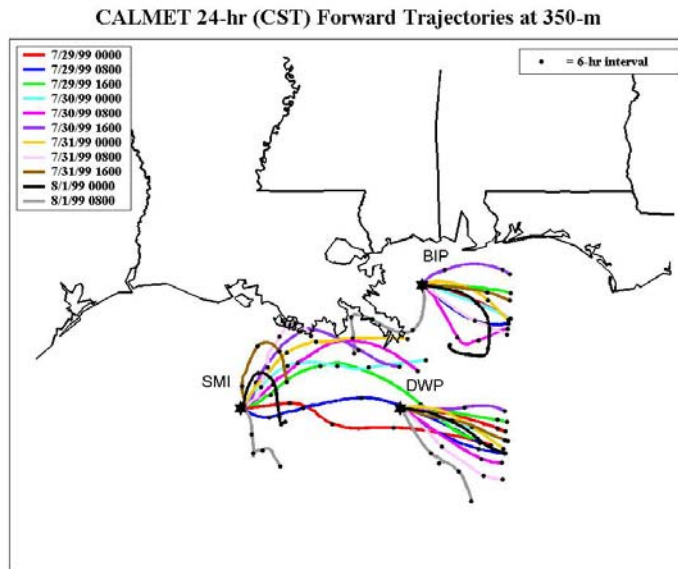


Figure 6-12. CALMET 24-hr forward trajectory at 350 m based on CALMET diagnostic wind fields for July 29 at 0000 CST through August 1, 1999, at 0800 CST. The RWP observations are used in CALMET. Note that the trajectories terminate when they reach the arbitrary boundary of the CALMET domain, even though the total time period has not elapsed.

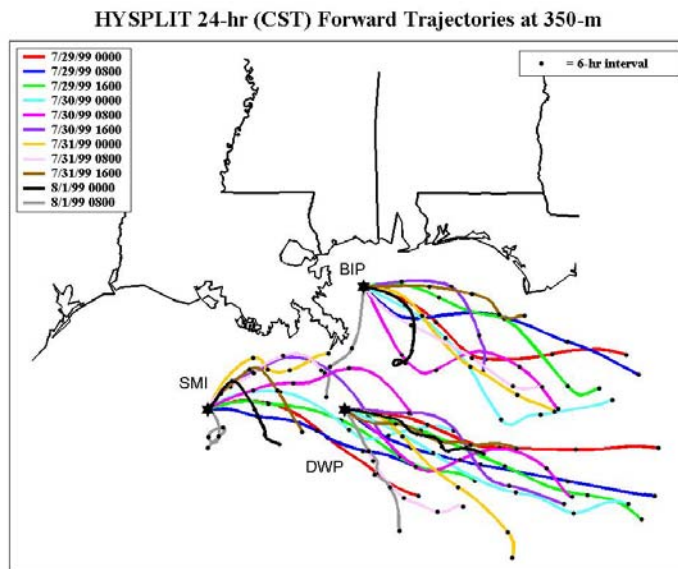


Figure 6-13. HYSPLIT 24-hr forward trajectory at 350 m based on EDAS wind fields for July 29 at 0000 CST through August 1, 1999, at 0800 CST. RWP observations are not used in EDAS.

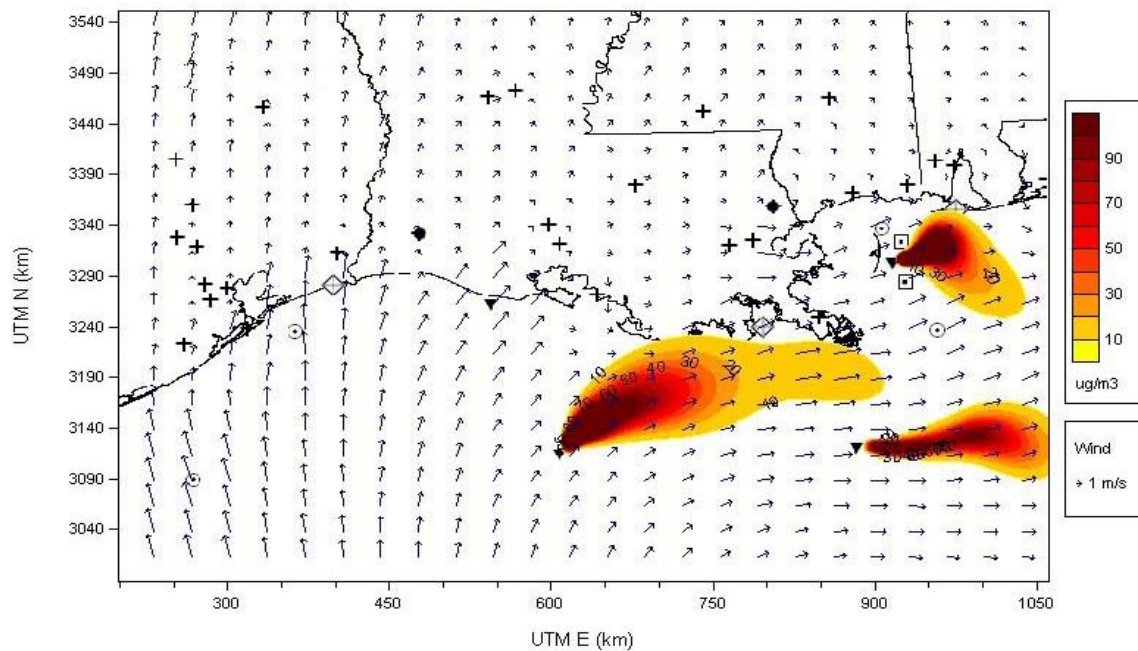


Figure 6-14. CALPUFF dispersion simulations for hypothetical tracers originating from SMI, DWP, and BIP ending on July 30, 1999, at 2200 CST. The same amount of tracer is assumed to be released from each source.

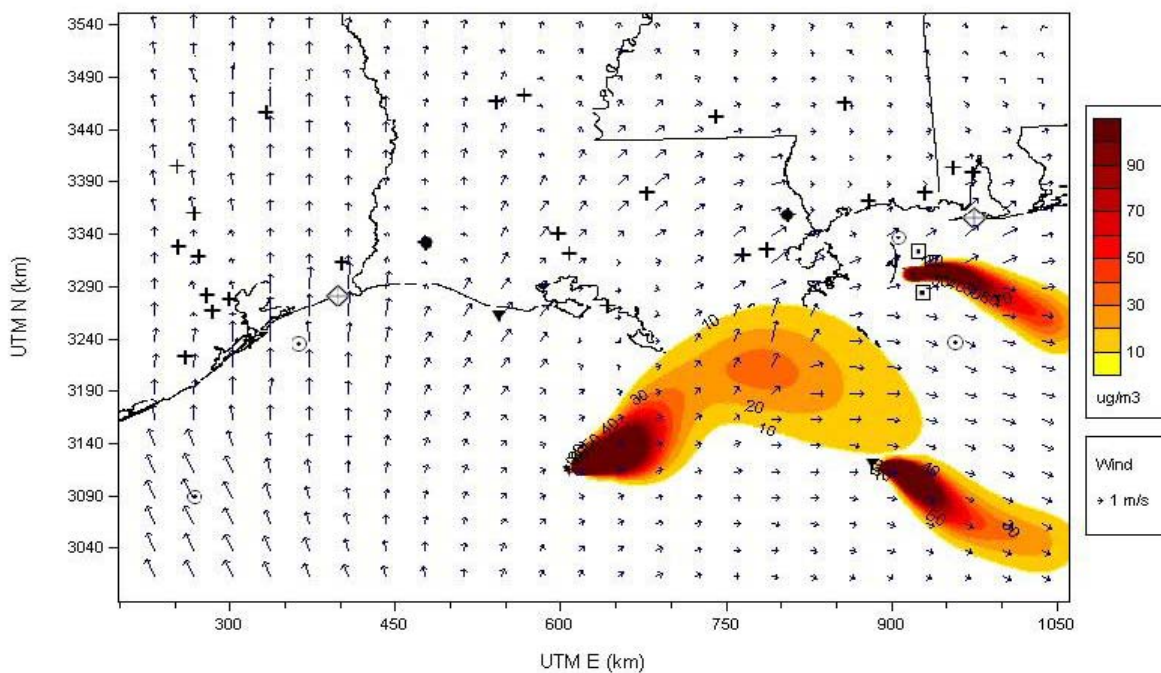


Figure 6-15. CALPUFF dispersion simulations for hypothetical tracers originating from SMI, DWP, and BIP ending on July 31, 1999, at 1600 CST. The same amount of tracer is assumed to be released from each source.

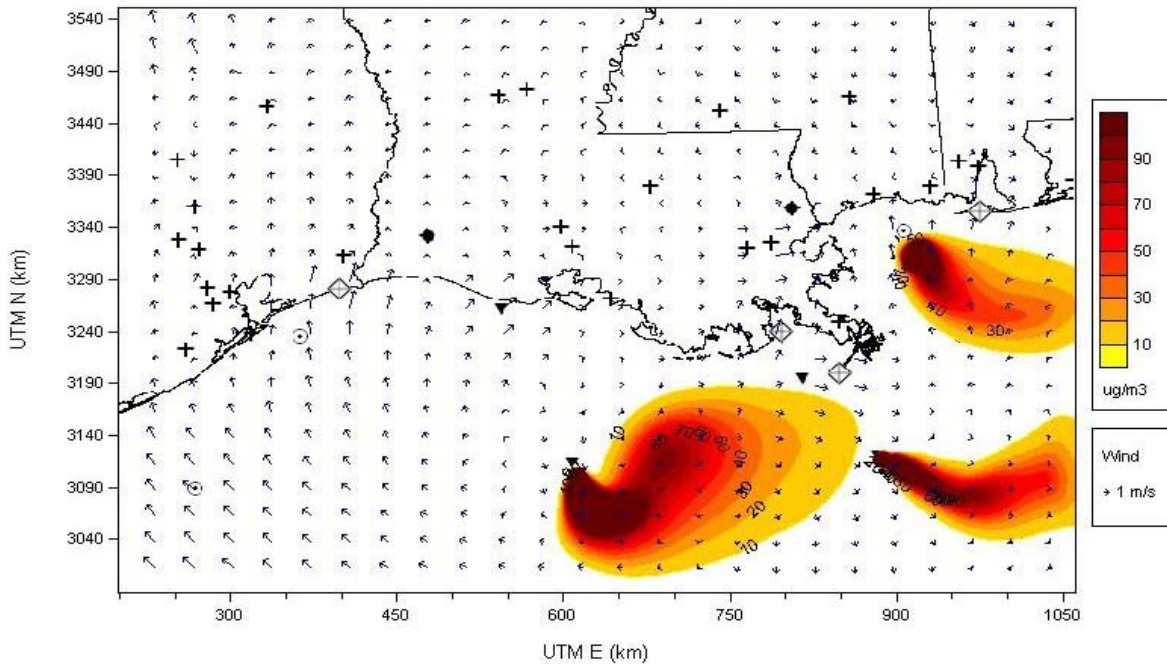


Figure 6-16. CALPUFF dispersion simulations for hypothetical tracers originating from SMI, DWP, and BIP ending on August 1 at 1700 CST. The same amount of tracer is assumed to be released from each source.

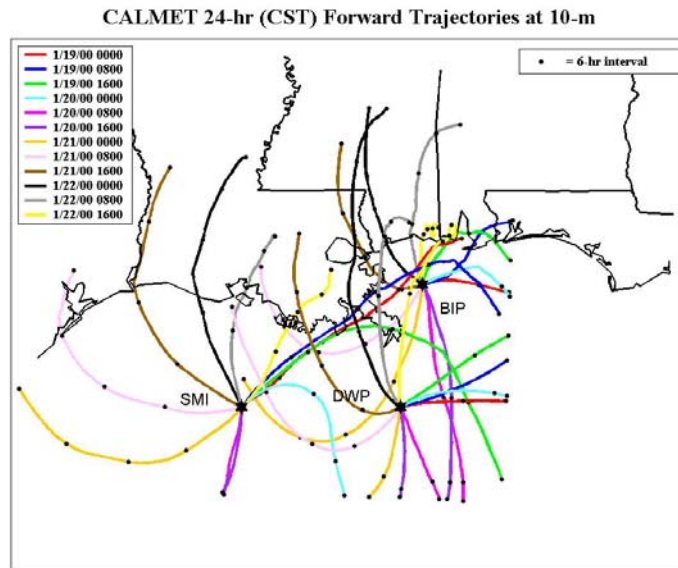


Figure 6-17. CALMET 24-hr forward trajectory at 10 m based on CALMET diagnostic wind fields for January 19 at 0000 CST through January 22, 2000, at 1600 CST. The RWP observations are used in CALMET. Note that the trajectories terminate when they reach the arbitrary boundary of the CALMET domain, even though the total time period has not elapsed.

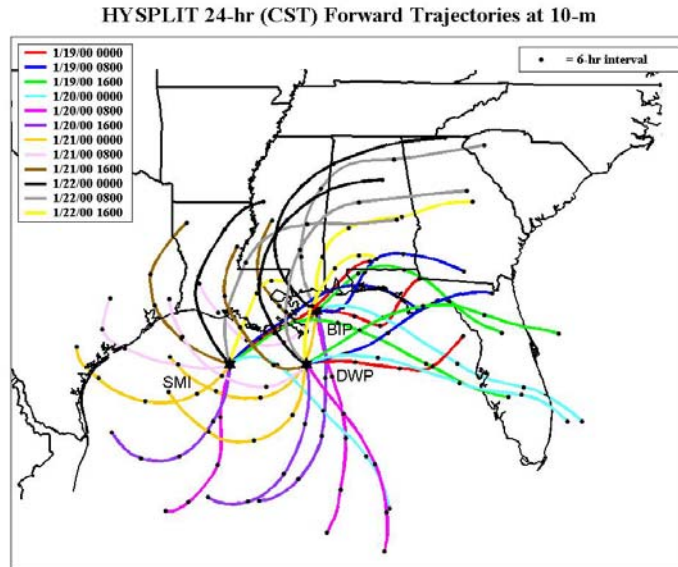


Figure 6-18. HYSPLIT 24-hr forward trajectory at 10 m based on EDAS wind fields for January 19 at 0000 CST through January 22, 2000, at 1600 CST. RWP observations are not used in EDAS.

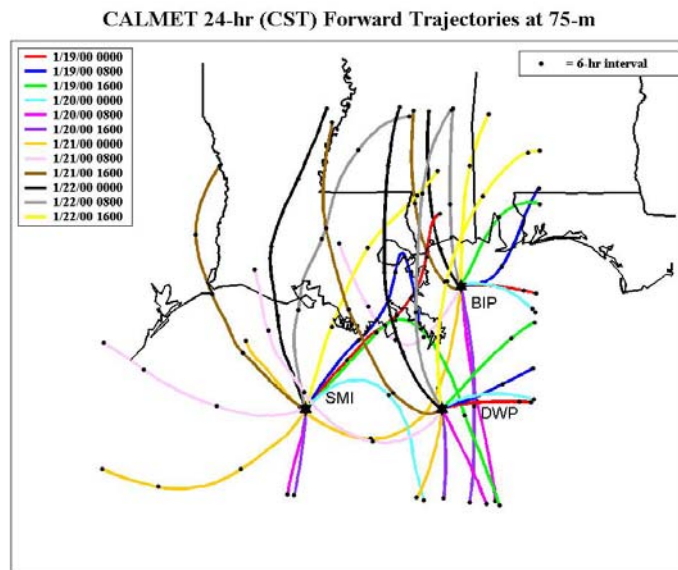


Figure 6-19. CALMET 24-hr forward trajectory at 75 m based on CALMET diagnostic wind fields for January 19 at 0000 CST through January 22, 2000 at 1600 CST. The RWP observations are used in CALMET. Note that the trajectories terminate when they reach the arbitrary boundary of the CALMET domain, even though the total time period has not elapsed.

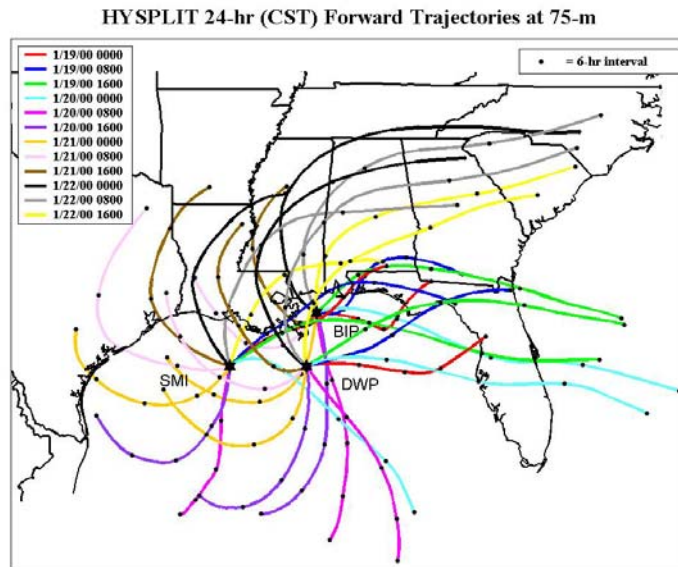


Figure 6-20. HYSPLIT 24-hr forward trajectory at 75 m based on EDAS wind fields for January 19 at 0000 CST through January 22, 2000 at 1600 CST. RWP observations are not used in EDAS.

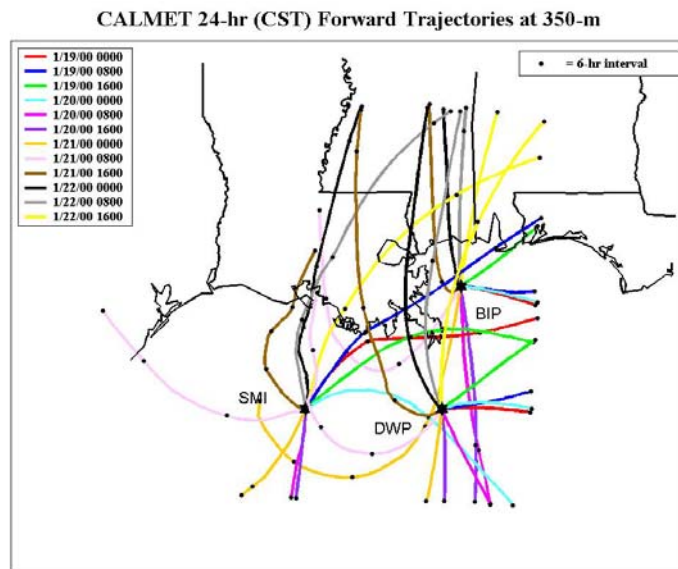


Figure 6-21. CALMET 24-hr forward trajectory at 350 m based on CALMET diagnostic wind fields for January 19 at 0000 CST through January 22, 2000, at 1600 CST. The RWP observations are used in CALMET. Note that the trajectories terminate when they reach the arbitrary boundary of the CALMET domain, even though the total time period has not elapsed.

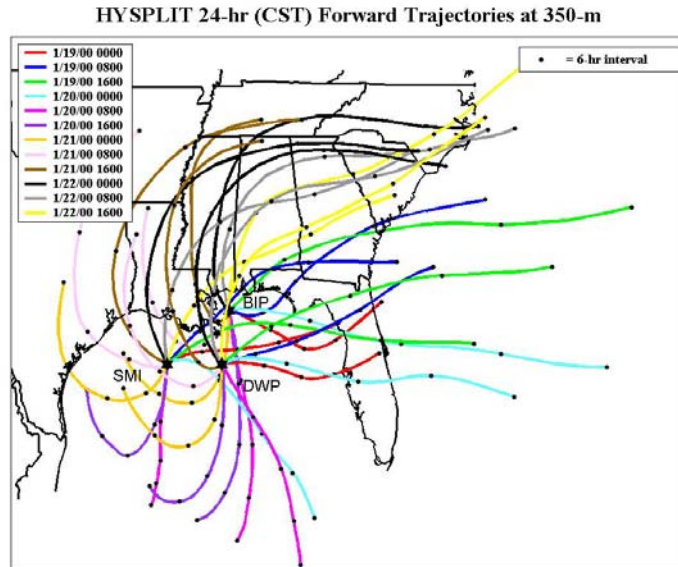


Figure 6-22. HYSPLIT 24-hr forward trajectory at 350 m based on EDAS wind fields for January 19 at 0000 CST through January 22, 2000, at 1600 CST. RWP observations are not used in EDAS.

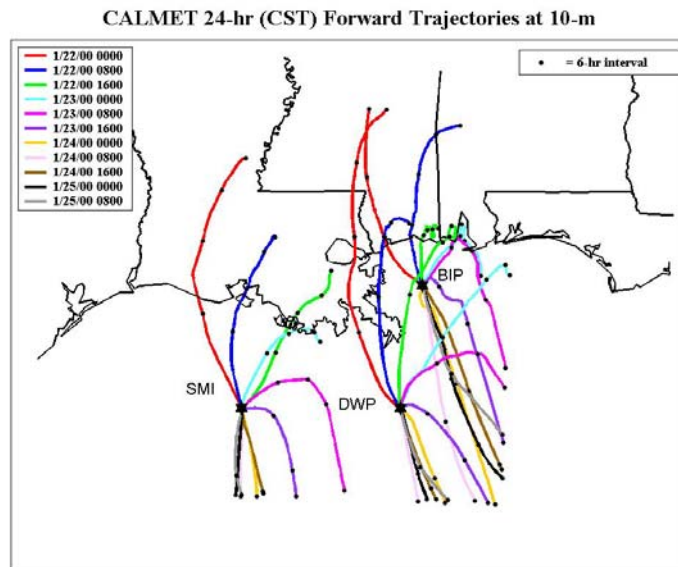


Figure 6-23. CALMET 24-hr forward trajectory at 10 m based on CALMET diagnostic wind fields for January 22 at 0000 CST through January 25, 2000, at 0800 CST. The RWP observations are used in CALMET. Note that the trajectories terminate when they reach the arbitrary boundary of the CALMET domain, even though the total time period has not elapsed.

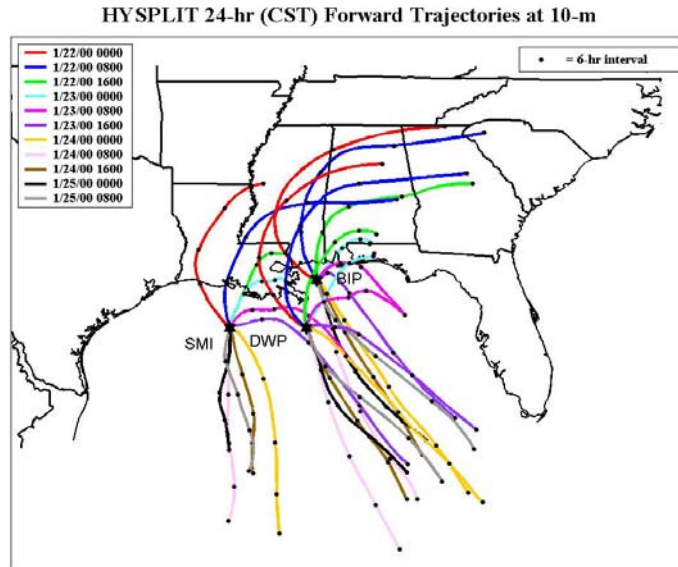


Figure 6-24. HYSPLIT 24-hr forward trajectory at 10 m based on EDAS wind fields for January 22 at 0000 CST through January 25, 2000, at 0800 CST. RWP observations are not used in EDAS.

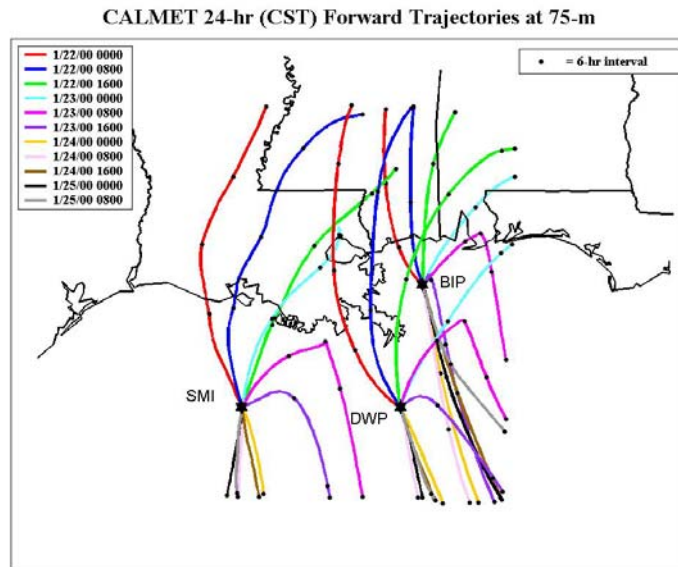


Figure 6-25. CALMET 24-hr forward trajectory at 75 m based on CALMET diagnostic wind fields for January 22 at 0000 CST through January 25, 2000, at 0800 CST. The RWP observations are used in CALMET. Note that the trajectories terminate when they reach the arbitrary boundary of the CALMET domain, even though the total time period has not elapsed.

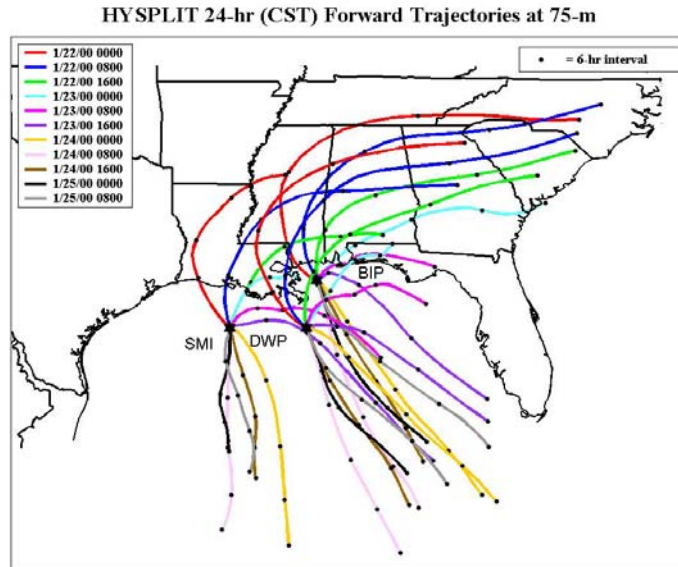


Figure 6-26. HYSPLIT 24-hr forward trajectory at 75 m based on EDAS wind fields for January 22 at 0000 CST through January 25, 2000, at 0800 CST. RWP observations are not used in EDAS.

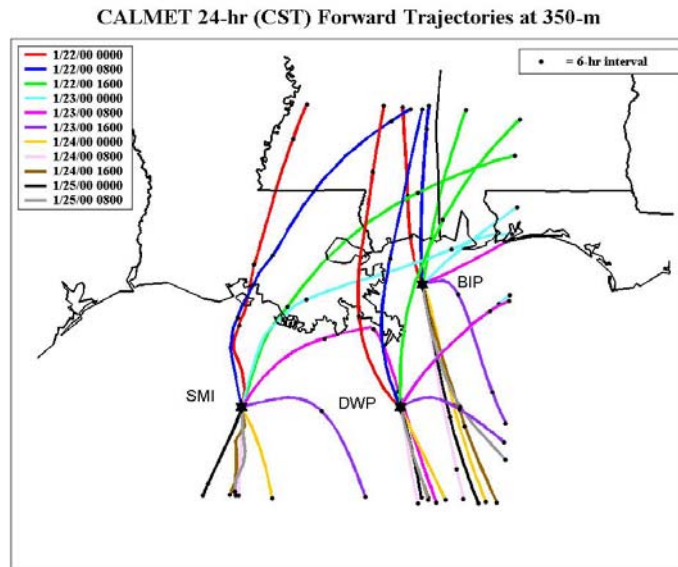


Figure 6-27. CALMET 24-hr forward trajectory at 350 m based on CALMET diagnostic wind fields for January 22 at 0000 CST through January 25, 2000, at 0800 CST. The RWP observations are used in CALMET. Note that the trajectories terminate when they reach the arbitrary boundary of the CALMET domain, even though the total time period has not elapsed.

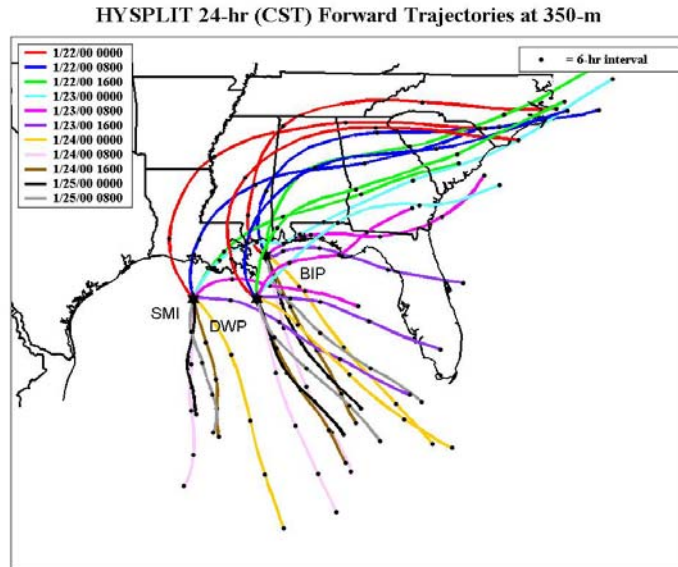


Figure 6-28. HYSPLIT 24-hr forward trajectory at 350 m based on EDAS wind fields for January 22 at 0000 CST through January 25, 2000, at 0800 CST. RWP observations are not used in EDAS.

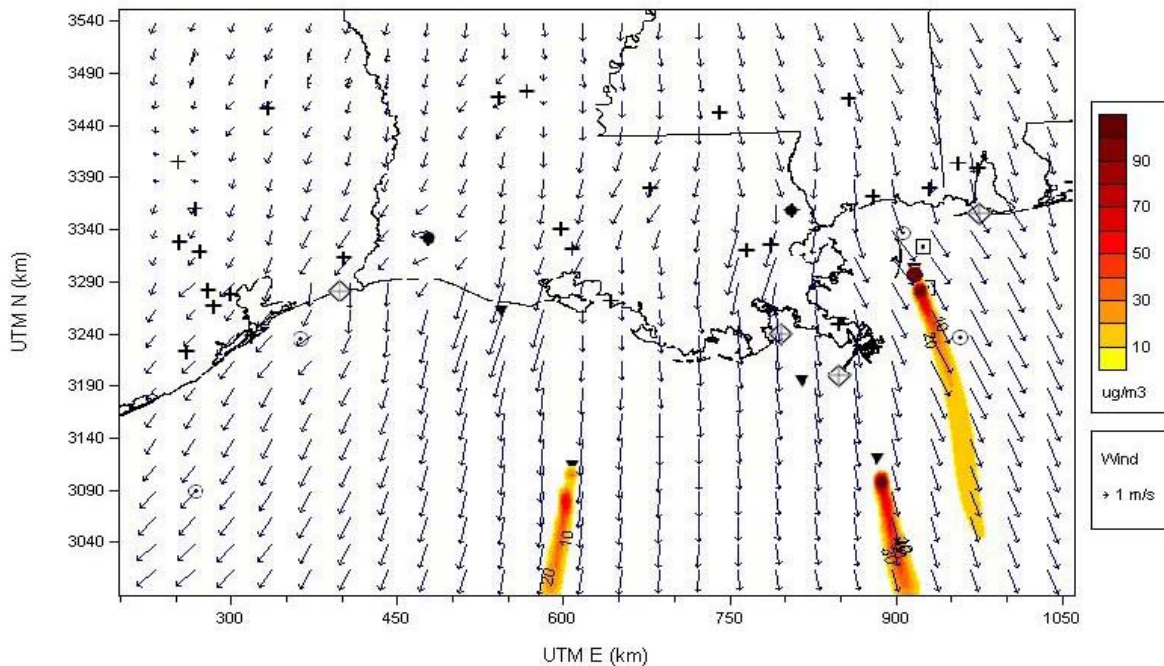


Figure 6-29. CALPUFF dispersion simulations for hypothetical tracers originating from SMI, DWP, and BIP ending on January 20, 2000, at 1600 CST. The same amount of tracer is assumed to be released from each source.

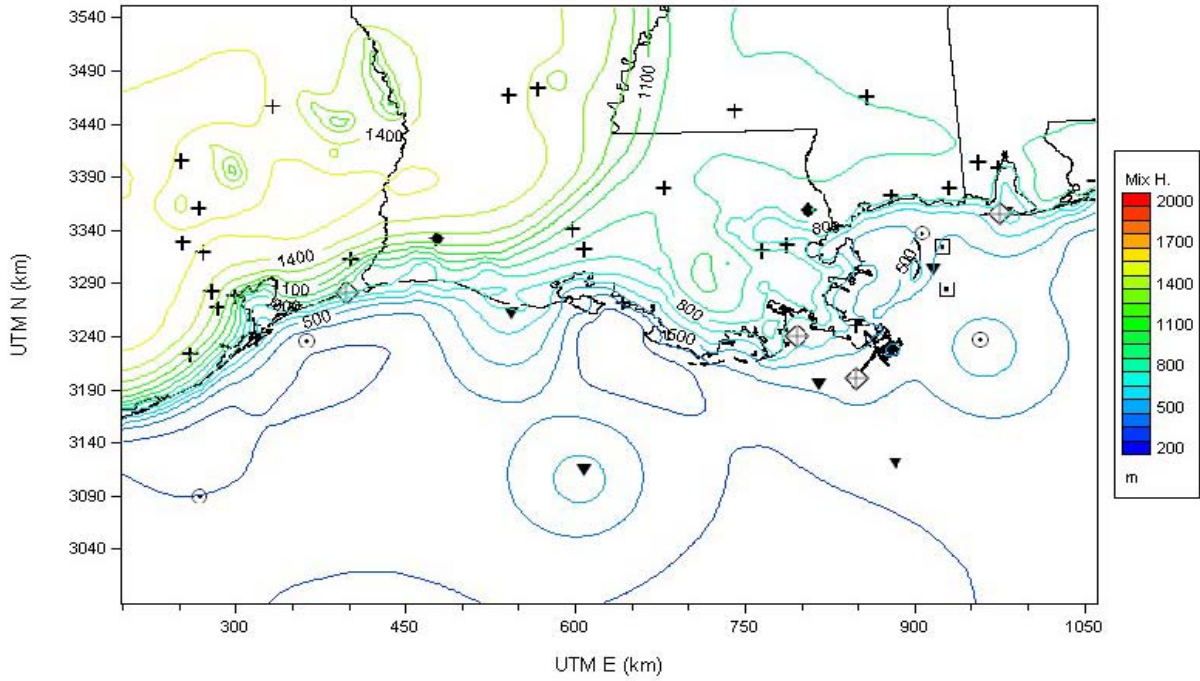


Figure 6-30. CALMET-derived mixing heights for January 20, 2000, at 1400 CST.

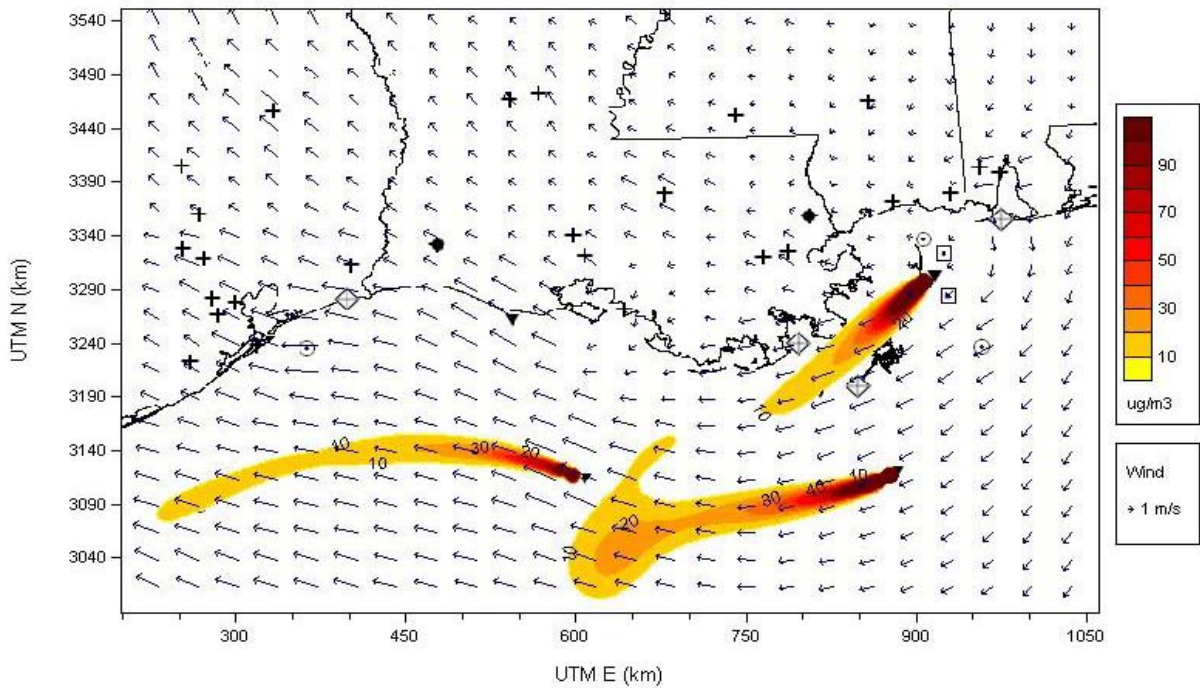


Figure 6-31. CALPUFF dispersion simulations for hypothetical tracers originating from SMI, DWP, and BIP ending on January 21, 2000, at 1600 CST. The same amount of tracer is assumed to be released from each source.

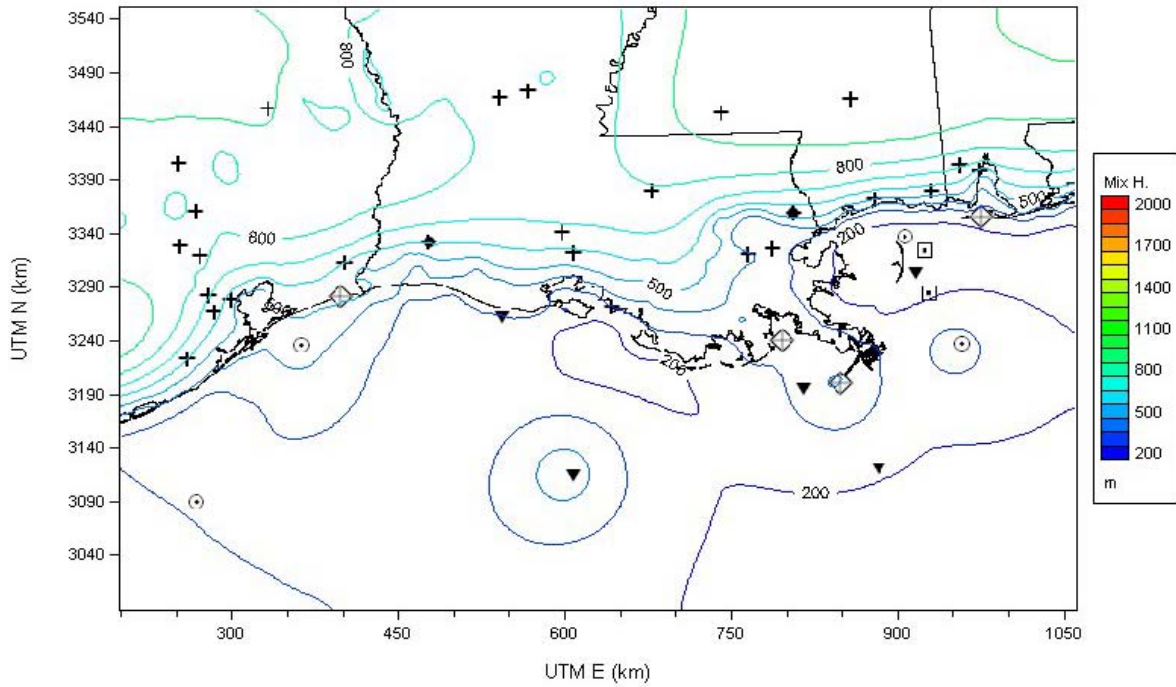


Figure 6-32. CALMET-derived mixing heights for January 21, 2000, at 1400 CST.

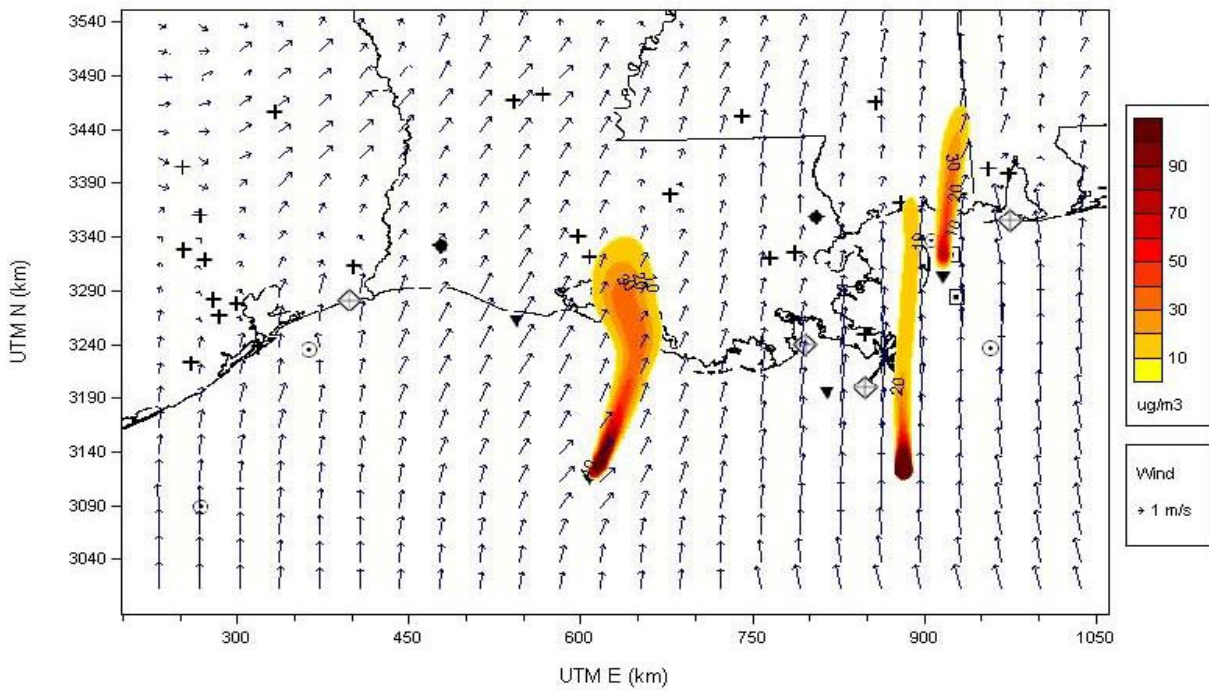


Figure 6-33. CALPUFF dispersion simulations for hypothetical tracers originating from SMI, DWP, and BIP ending on January 22, 2000, at 1900 CST. The same amount of tracer is assumed to be released from each source.

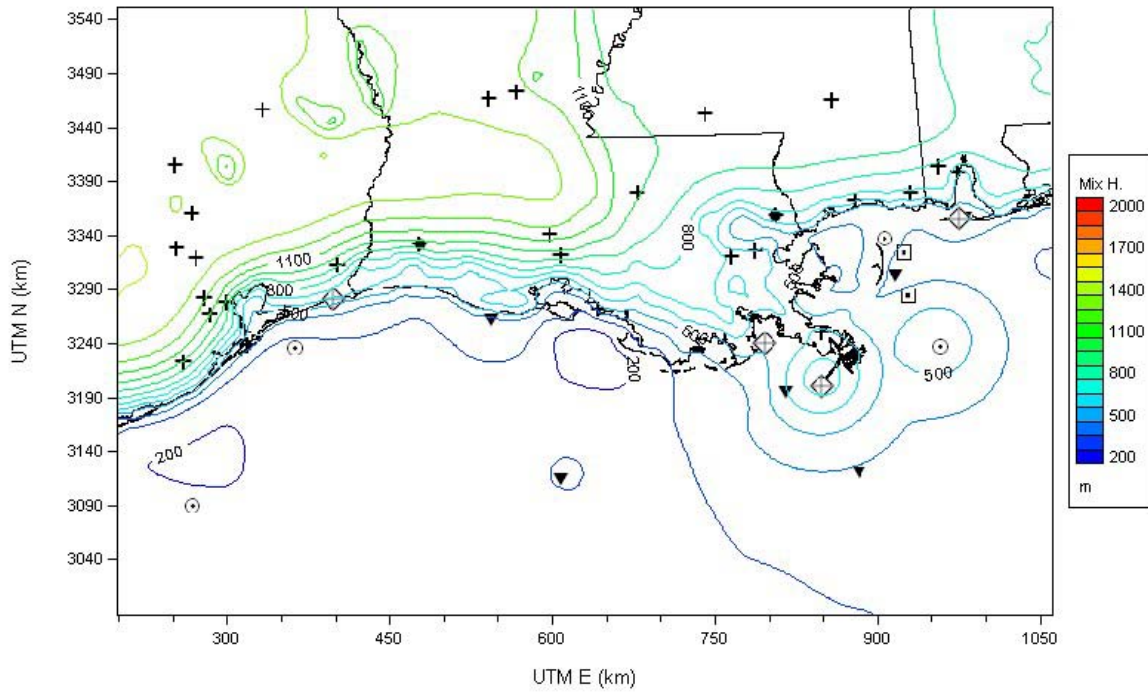


Figure 6-34. CALMET-derived mixing heights for January 22, 2000, at 1400 CST.

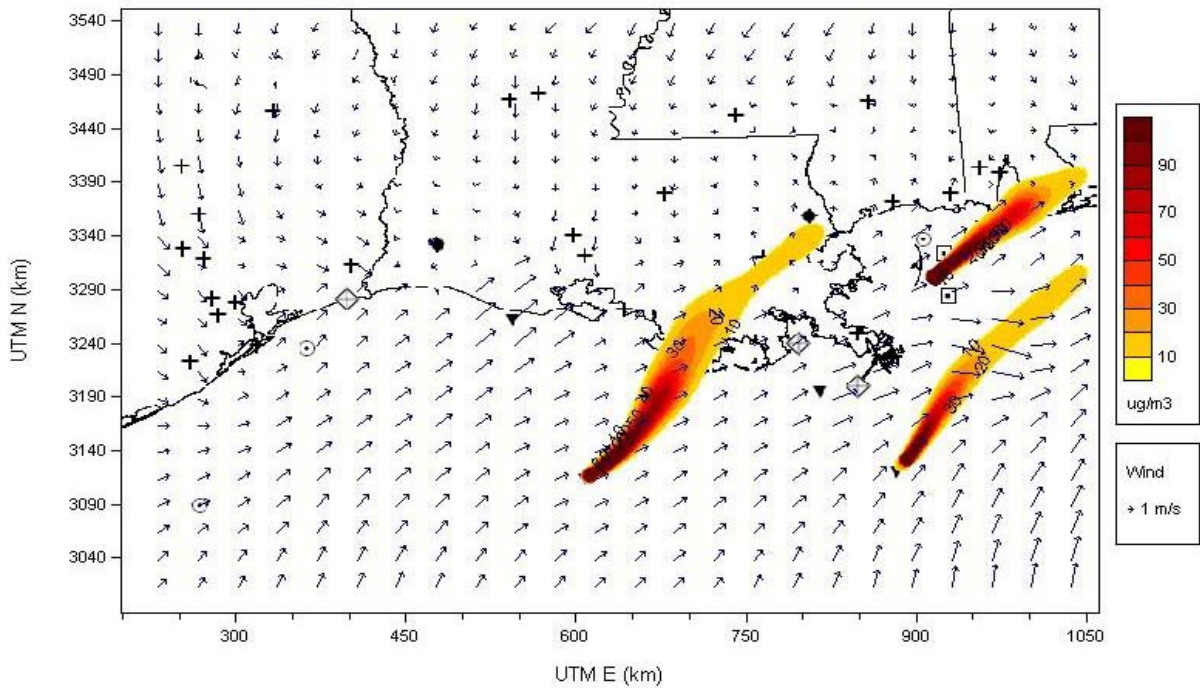


Figure 6-35. CALPUFF dispersion simulations for hypothetical tracers originating from SMI, DWP, and BIP ending on January 23, 2000, at 1200 CST. The same amount of tracer is assumed to be released from each source.

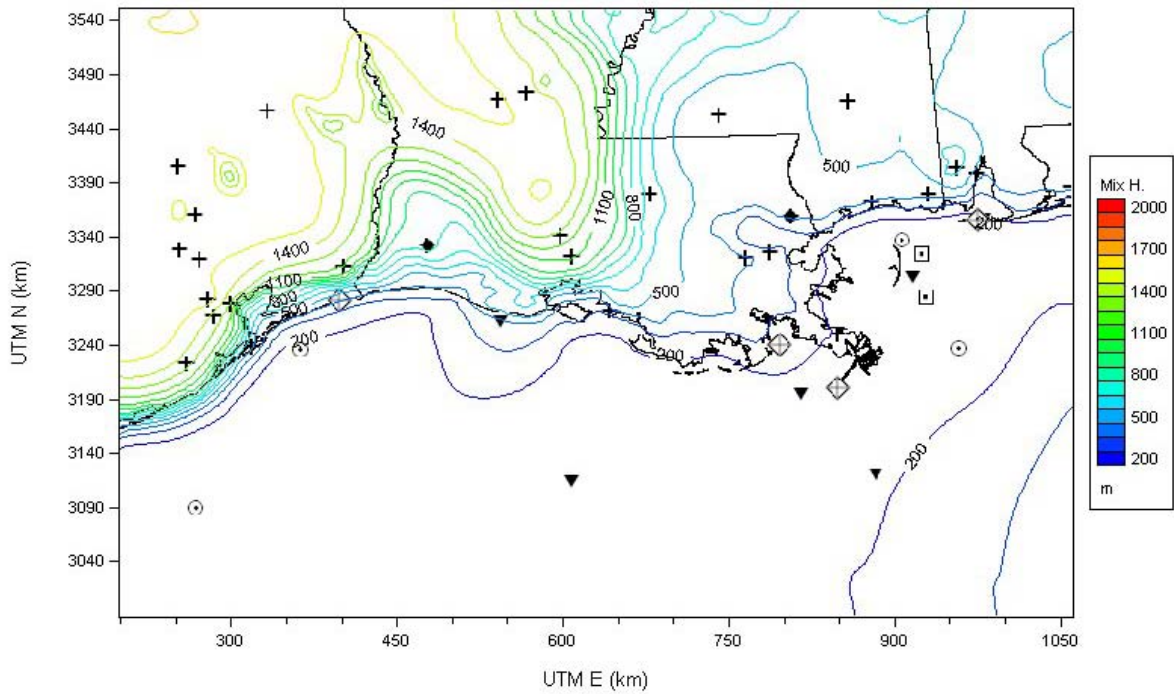


Figure 6-36. CALMET-derived mixing heights for January 23, 2000, at 1400 CST.

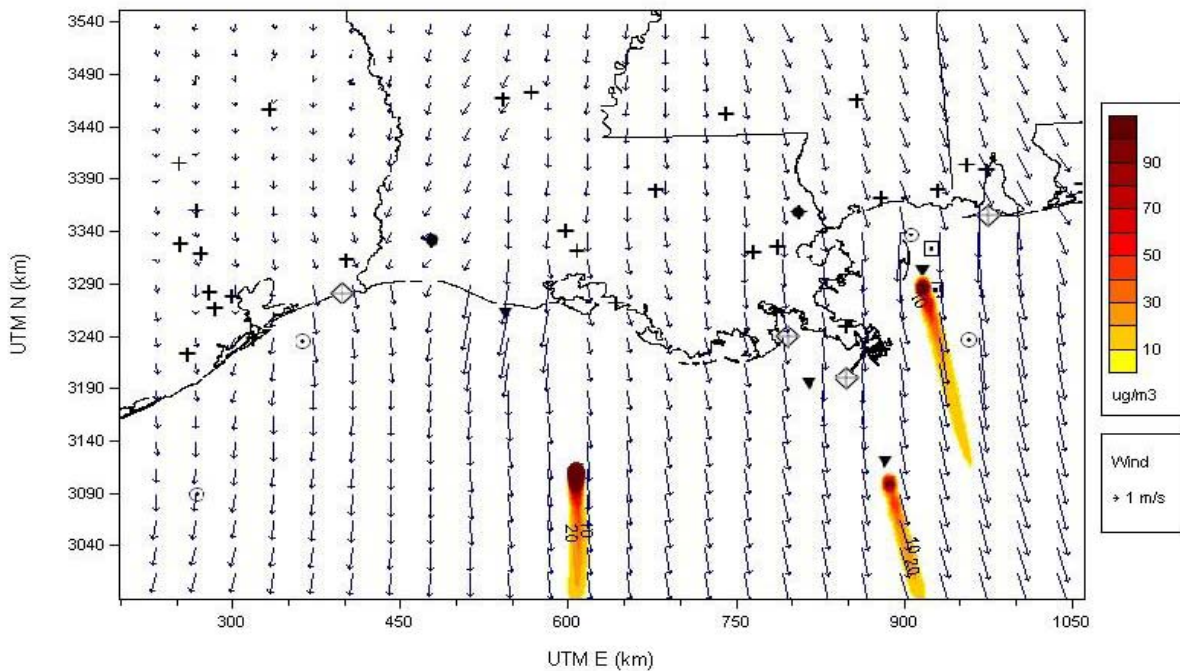


Figure 6-37. CALPUFF dispersion simulations for hypothetical tracers originating from SMI, DWP, and BIP ending on January 24, 2000, at 1200 CST. The same amount of tracer is assumed to be released from each source.

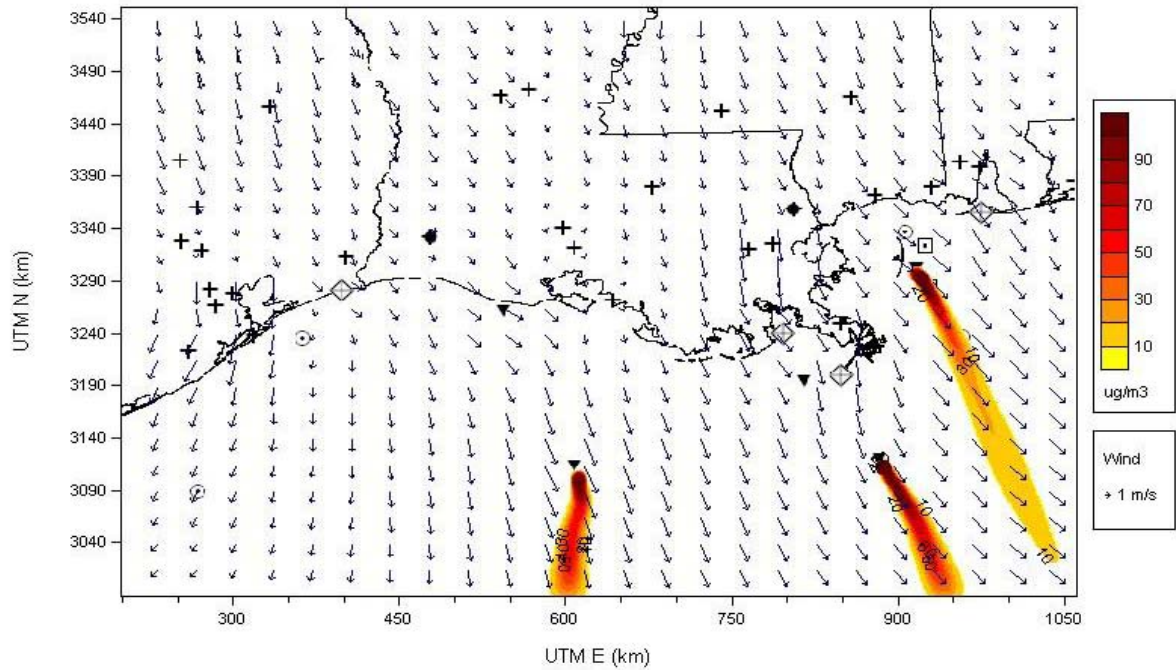


Figure 6-38. CALPUFF dispersion simulations for hypothetical tracers originating from SMI, DWP, and BIP ending on January 25, 2000, at 1400 CST. The same amount of tracer is assumed to be released from each source.

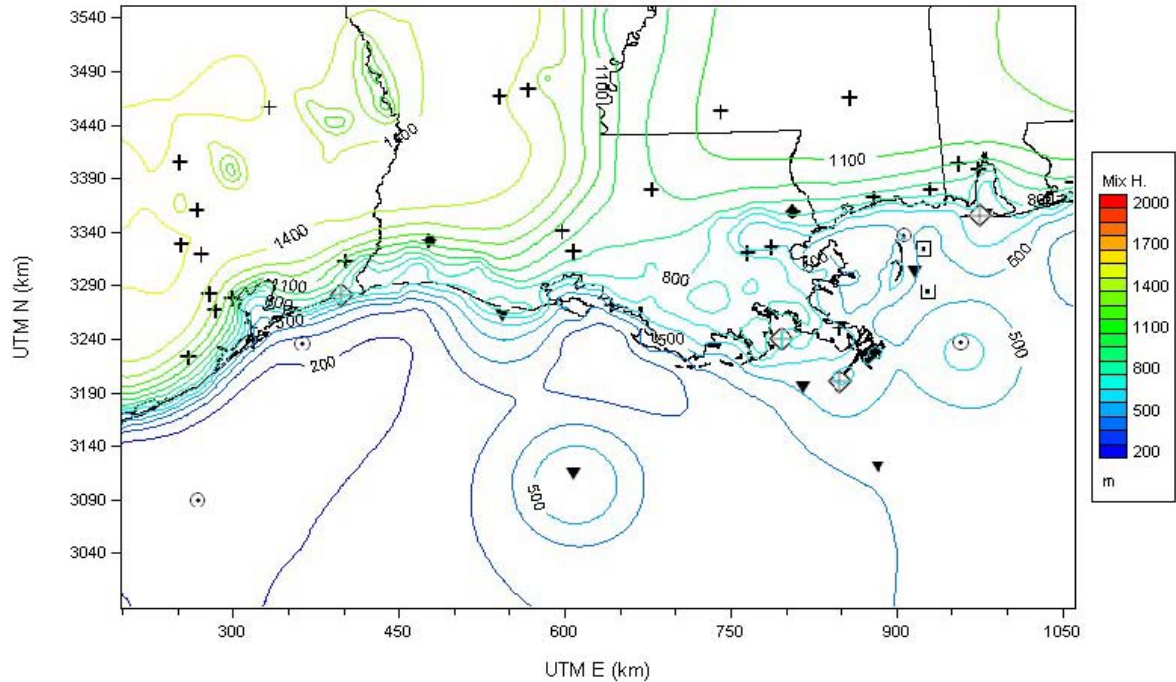


Figure 6-39. CALMET-derived mixing heights for January 24, 2000, at 1400 CST.

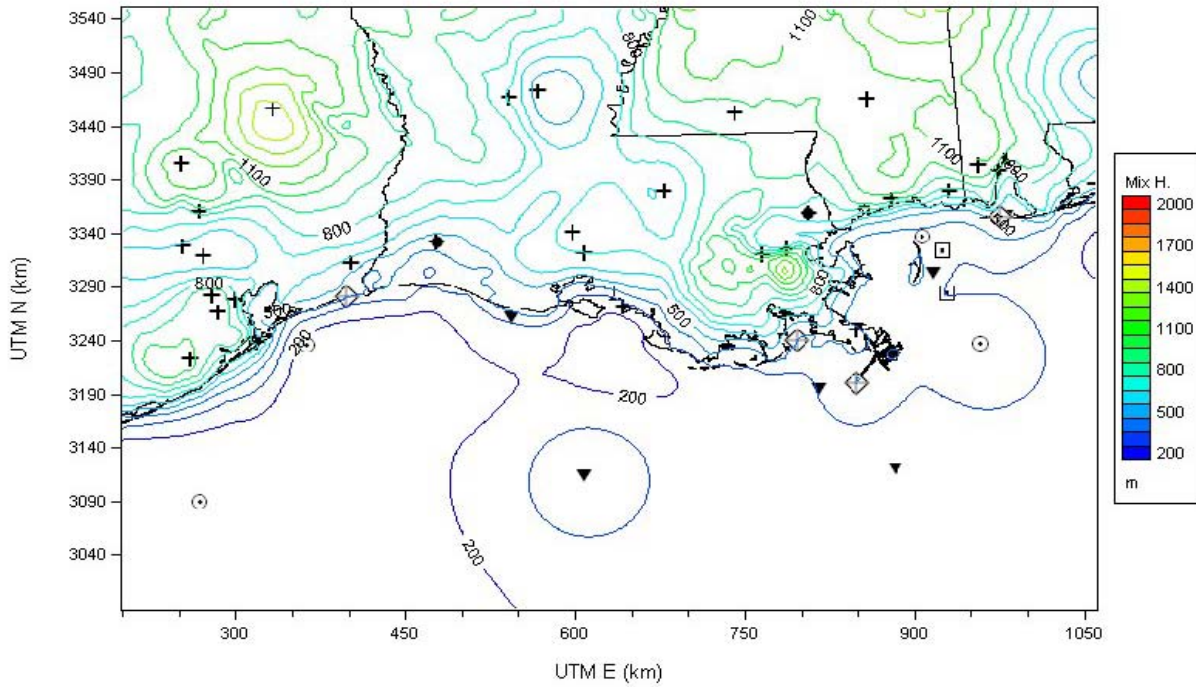


Figure 6-40. CALMET-derived mixing heights for January 25, 2000, at 1400 CST.

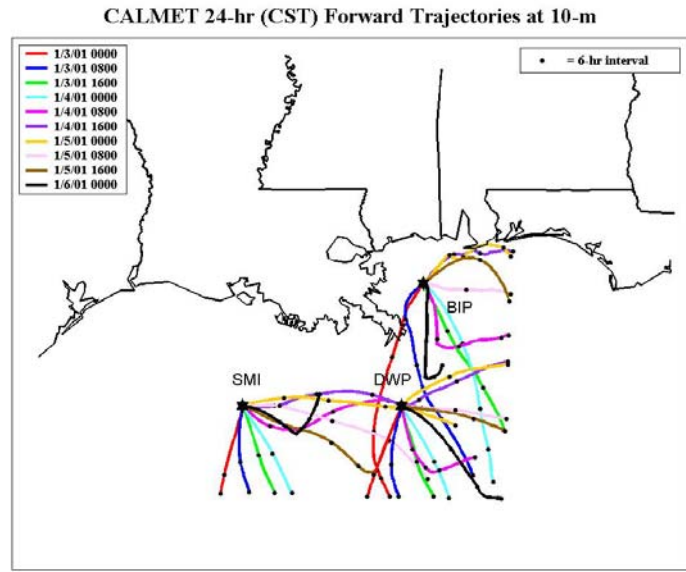


Figure 6-41. CALMET 24-hr forward trajectory at 10 m based on CALMET diagnostic wind fields for January 3, at 0000 CST through January 6, 2001, at 0000 CST. The RWP observations are used in CALMET. Note that the trajectories terminate when they reach the arbitrary boundary of the CALMET domain, even though the total time period has not elapsed.

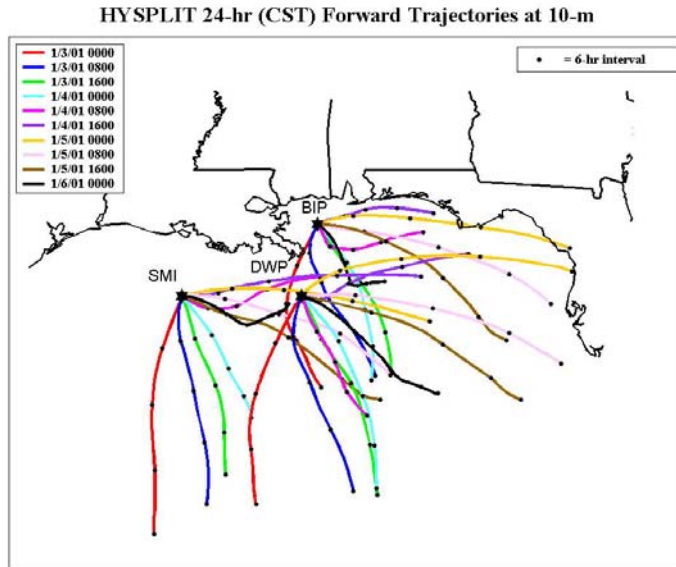


Figure 6-42. HYSPLIT 24-hr forward trajectory at 10 m based on EDAS wind fields for January 3 at 0000 CST through January 6, 2001, at 0000 CST. RWP observations are not used in EDAS.

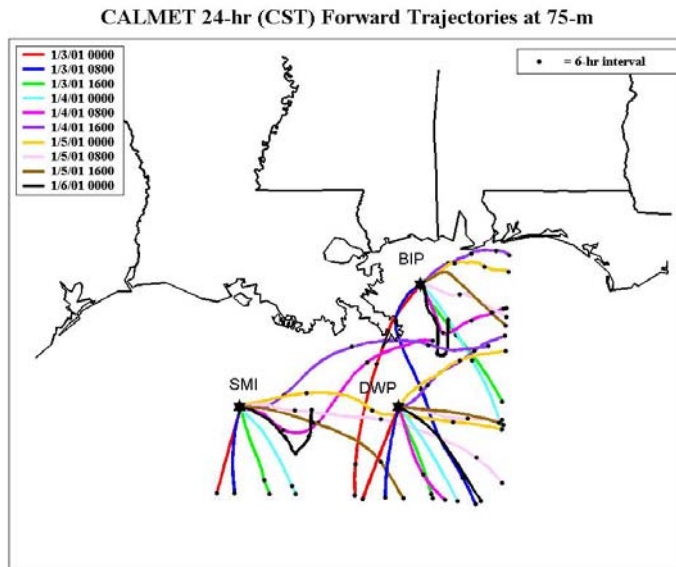


Figure 6-43. CALMET 24-hr forward trajectory at 75 m based on CALMET diagnostic wind fields for January 3 at 0000 CST through January 6, 2001, at 0000 CST. The RWP observations are used in CALMET. Note that the trajectories terminate when they reach the arbitrary boundary of the CALMET domain, even though the total time period has not elapsed.

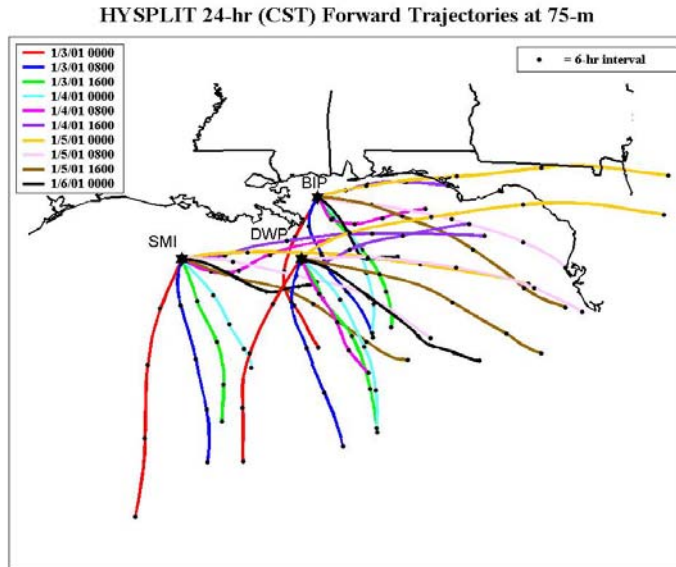


Figure 6-44. HYSPLIT 24-hr forward trajectory at 75 m based on EDAS wind fields for January 3 at 0000 CST through January 6, 2001, at 0000 at 0800 CST. RWP observations are not used in EDAS.

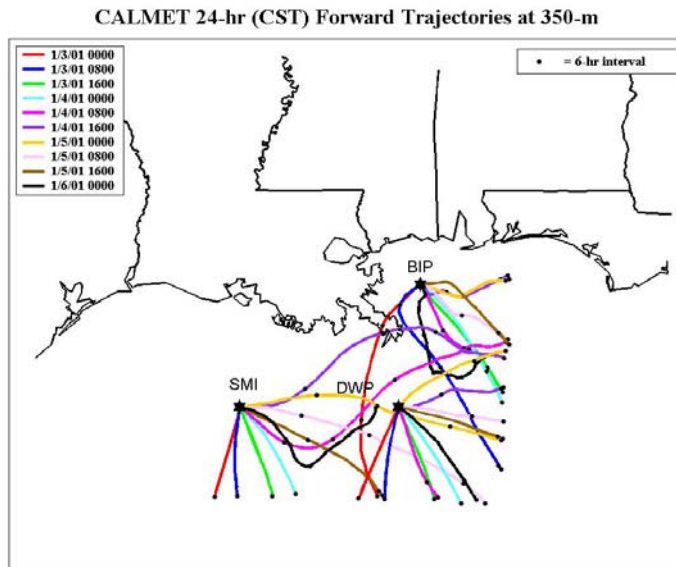


Figure 6-45. CALMET 24-hr forward trajectory at 350 m based on CALMET diagnostic wind fields for January 3 at 0000 CST through January 6, 2001, at 0000 CST. The RWP observations are used in CALMET. Note that the trajectories terminate when they reach the arbitrary boundary of the CALMET domain, even though the total time period has not elapsed.

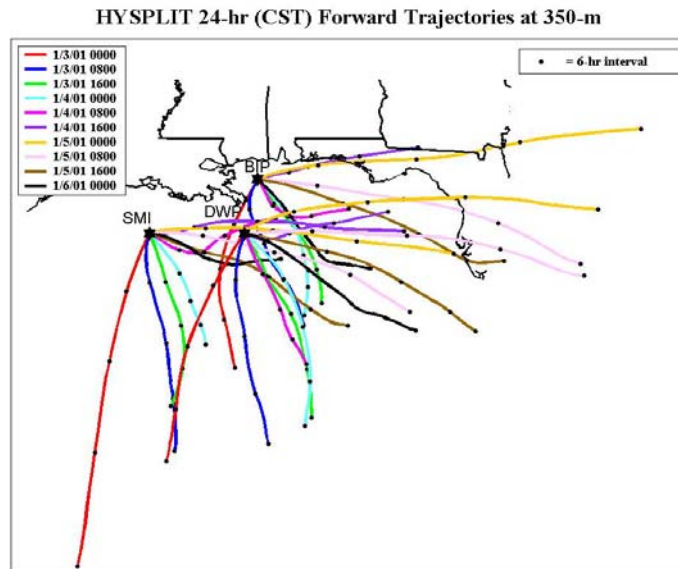


Figure 6-46. HYSPLIT 24-hr forward trajectory at 350 m based on EDAS wind fields for January 3 at 0000 CST through January 6, 2001, at 0000 CST. RWP observations are not used in EDAS.

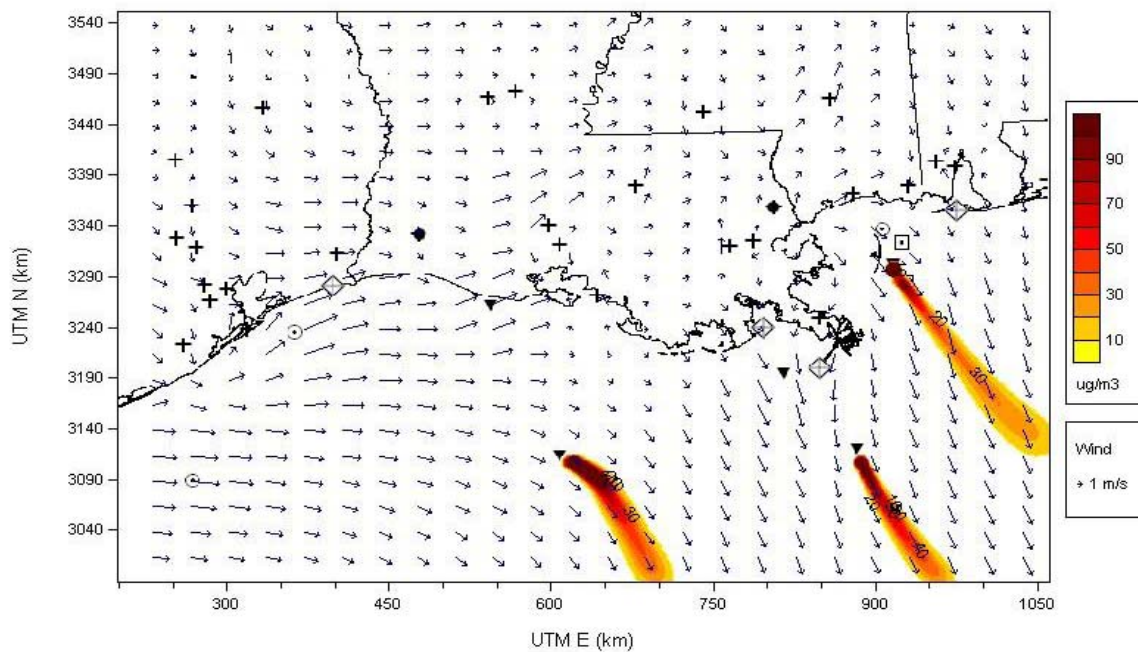


Figure 6-47. CALPUFF dispersion simulations for hypothetical tracers originating from SMI, DWP, and BIP ending on January 4, 2001, at 0800 CST. The same amount of tracer is assumed to be released from each source.

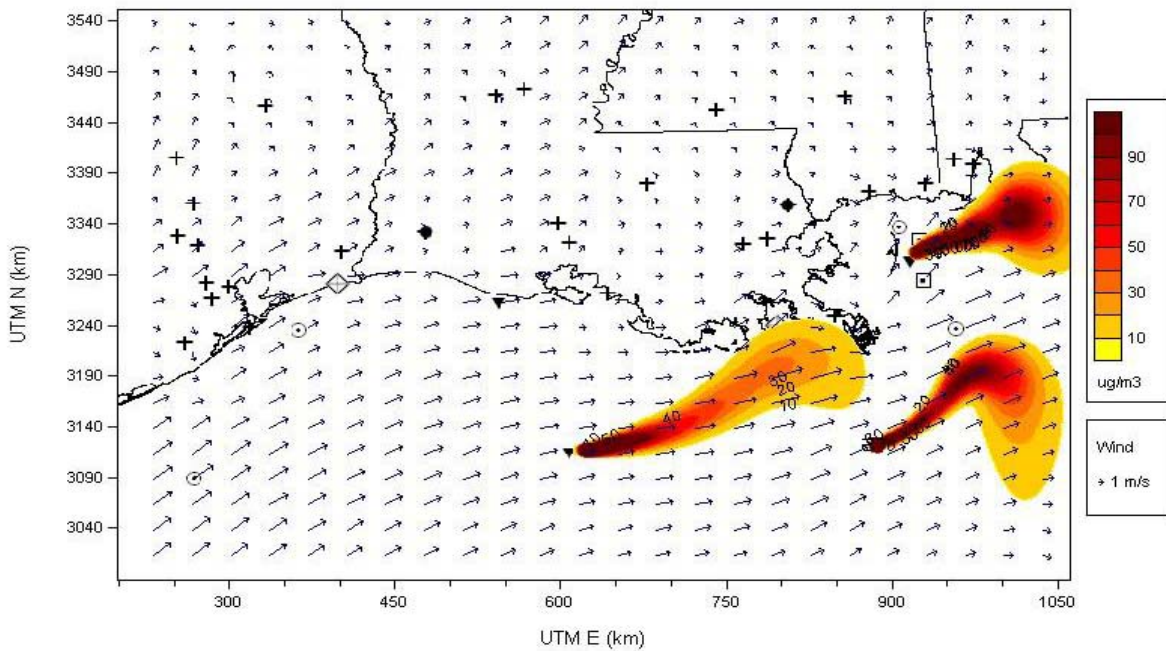


Figure 6-48. CALPUFF dispersion simulations for hypothetical tracers originating from SMI, DWP, and BIP ending on January 5, 2001, at 0300 CST. The same amount of tracer is assumed to be released from each source.

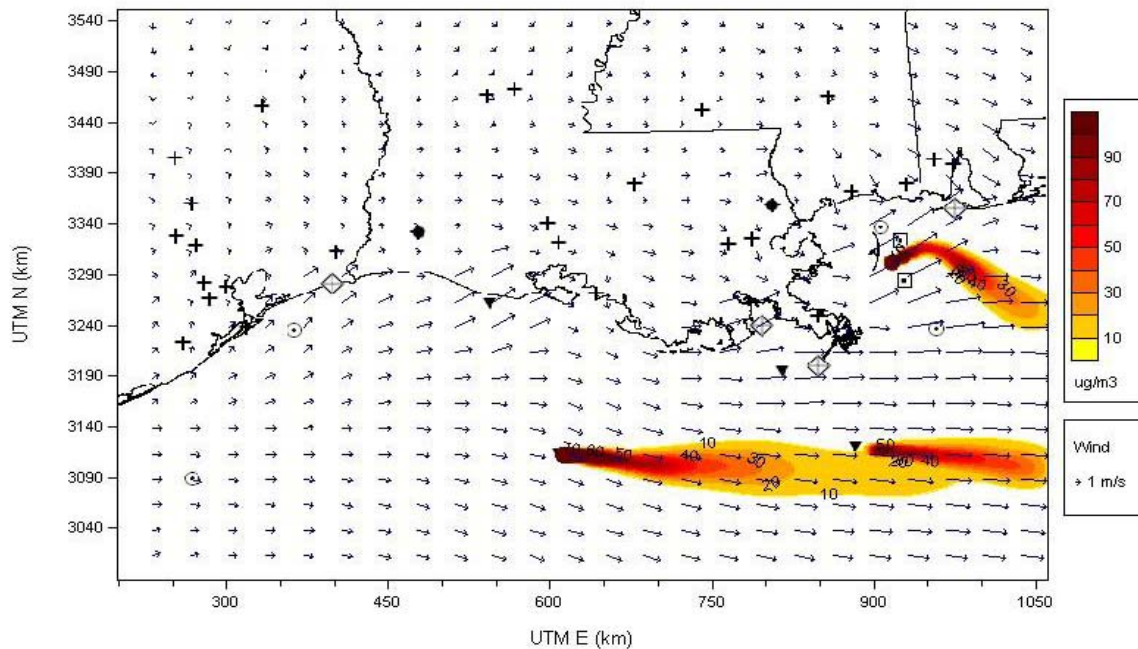


Figure 6-49. CALPUFF dispersion simulations for hypothetical tracers originating from SMI, DWP, and BIP ending on January 5, 2001, at 1700 CST. The same amount of tracer is assumed to be released from each source.

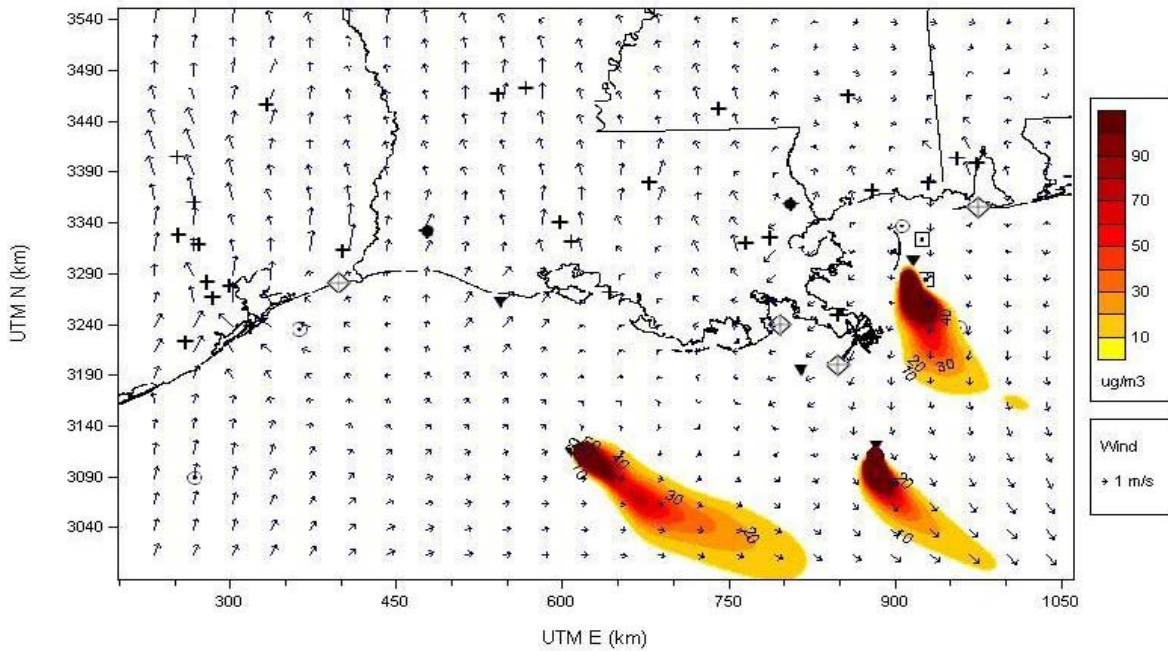


Figure 6-50. CALPUFF dispersion simulations for hypothetical tracers originating from SMI, DWP, and BIP ending on January 6, 2001, at 1000 CST. The same amount of tracer is assumed to be released from each source.

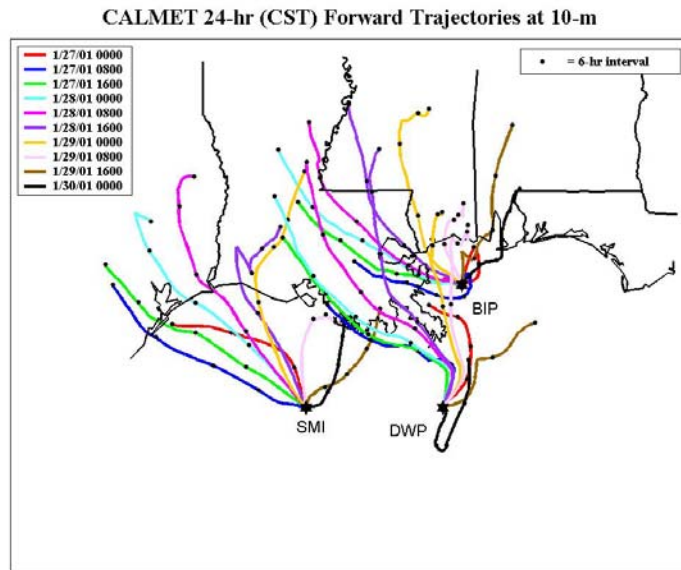


Figure 6-51. CALMET 24-hr forward trajectory at 10 m based on CALMET diagnostic wind fields for January 27 at 0000 CST through January 30, 2001, at 0000 CST. The RWP observations are used in CALMET. Note that the trajectories terminate when they reach the arbitrary boundary of the CALMET domain, even though the total time period has not elapsed.

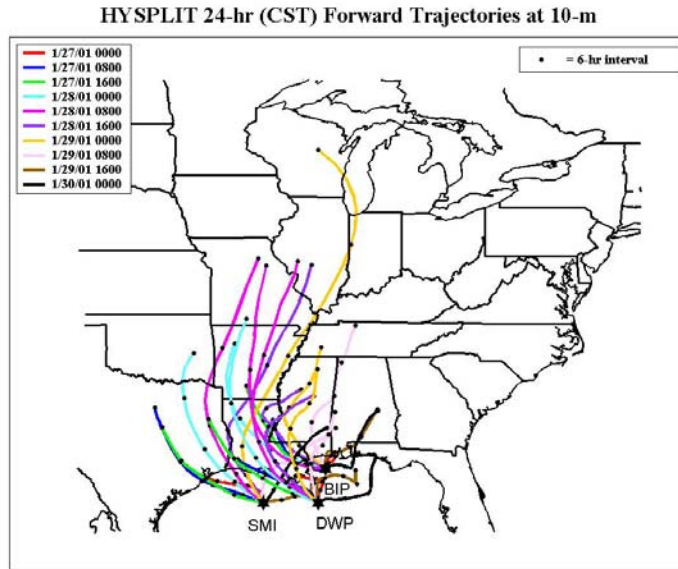


Figure 6-52. HYSPLIT 24-hr forward trajectory at 10 m based on EDAS wind fields for January 27 at 0000 CST through January 30, 2001, at 0000 CST. RWP observations are not used in EDAS.

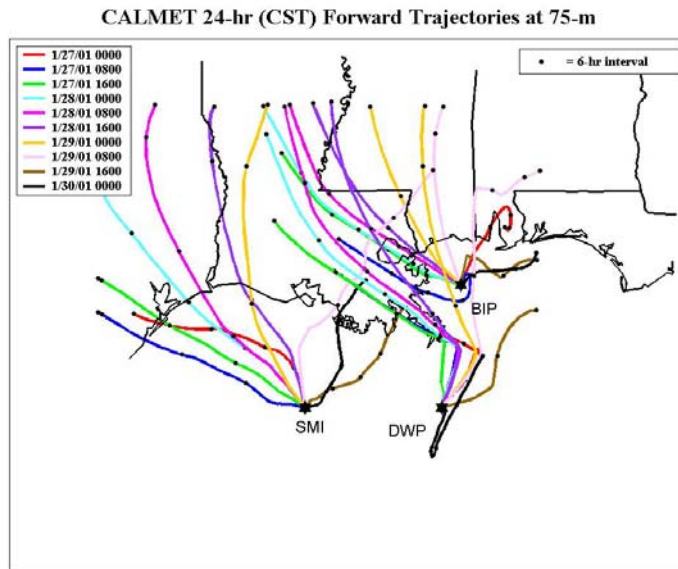


Figure 6-53. CALMET 24-hr forward trajectory at 75 m based on CALMET diagnostic wind fields for January 27 at 0000 CST through January 30, 2001, at 0000 CST. The RWP observations are used in CALMET. Note that the trajectories terminate when they reach the arbitrary boundary of the CALMET domain, even though the total time period has not elapsed.

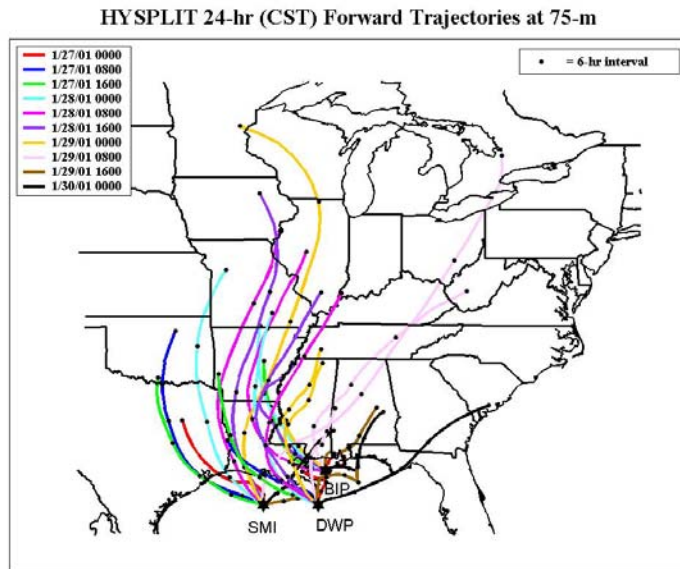


Figure 6-54. HYSPLIT 24-hr forward trajectory at 75 m based on EDAS wind fields for January 27 at 0000 CST through January 30, 2001, at 0000 CST. RWP observations are not used in EDAS.

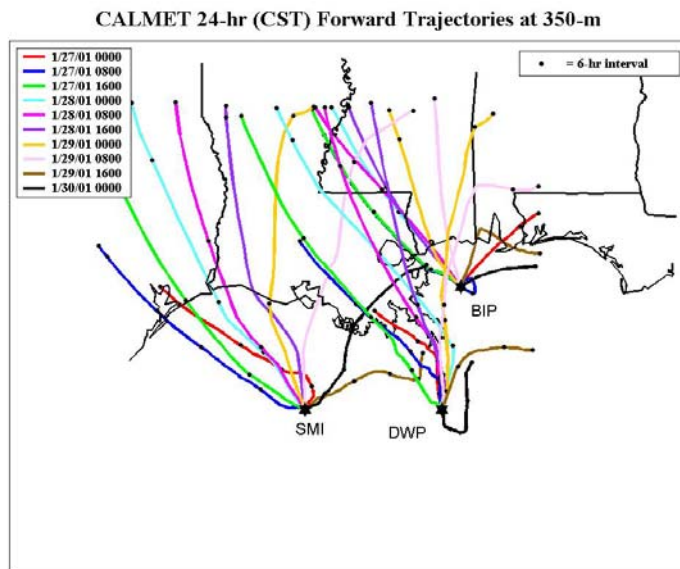


Figure 6-55. CALMET 24-hr forward trajectory at 350 m based on CALMET diagnostic wind fields for January 27 at 0000 CST through January 30, 2001, at 0000 CST. The RWP observations are used in CALMET. Note that the trajectories terminate when they reach the arbitrary boundary of the CALMET domain, even though the total time period has not elapsed.

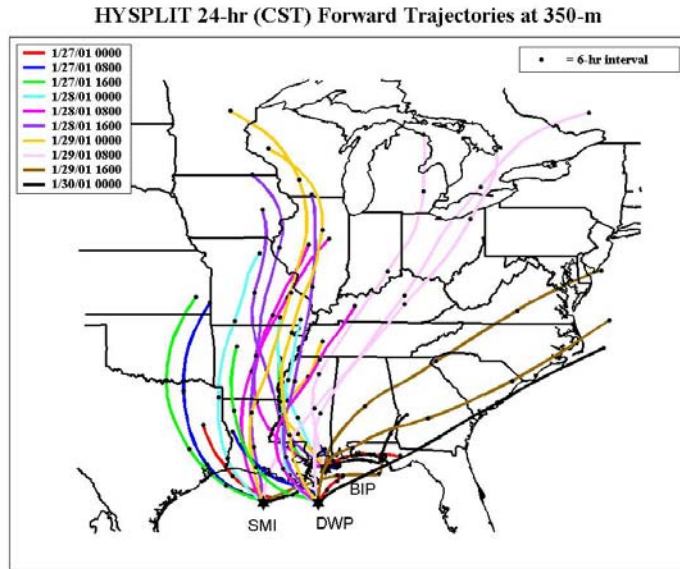


Figure 6-56. HYSPLIT 24-hr forward trajectory at 350 m based on EDAS wind fields for January 27 at 0000 CST through January 30, 2001, at 0000 CST. RWP observations are not used in EDAS.

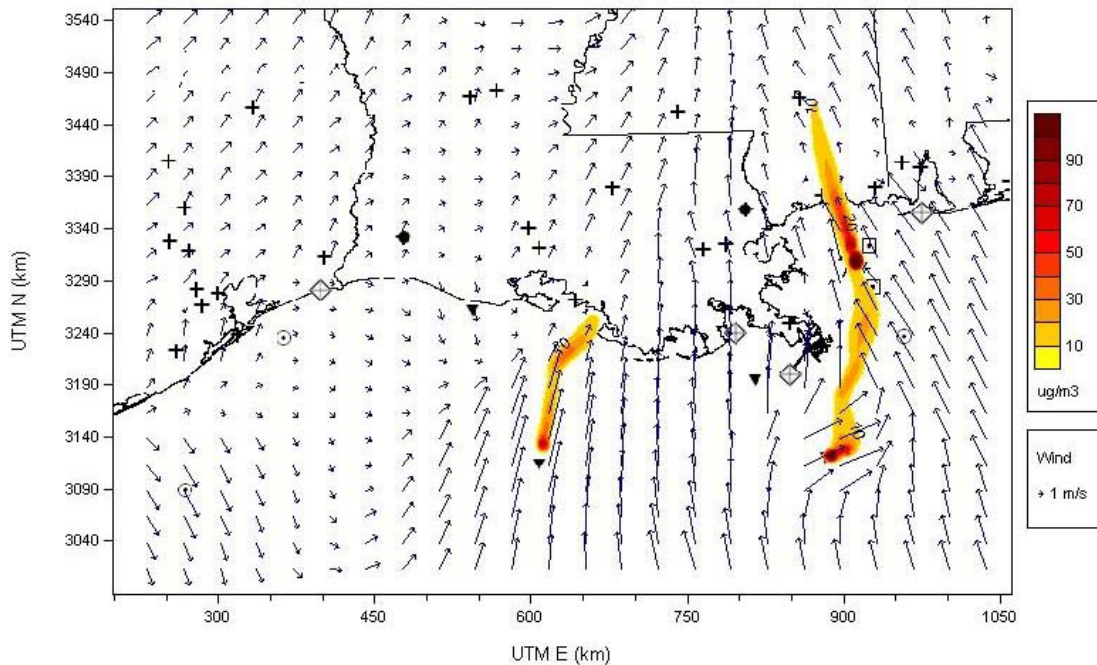


Figure 6-57. CALPUFF dispersion simulations for hypothetical tracers originating from SMI, DWP, and BIP ending on January 29, 2001, at 1200 CST. The same amount of tracer is assumed to be released from each source.

CALMET 24-hr (CST) Forward Trajectories at 10-m

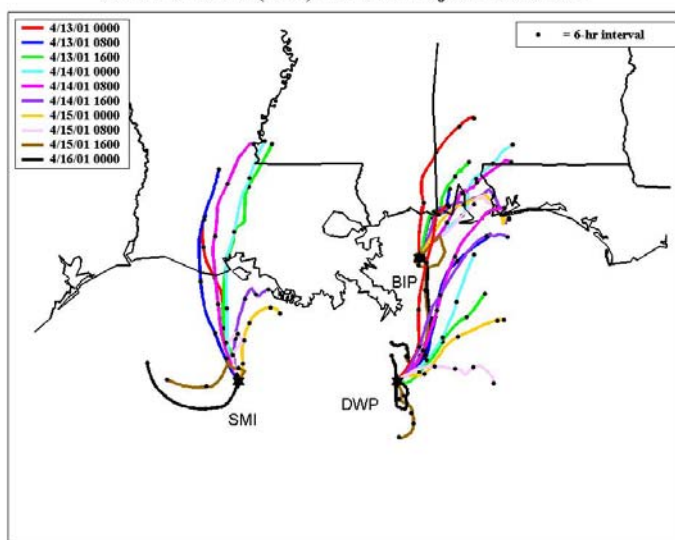


Figure 6-58. CALMET 24-hr forward trajectory at 10 m based on CALMET diagnostic wind fields for April 13 at 0000 CST through April 16, 2001, at 0000 CST. The RWP observations are used in CALMET. Note that the trajectories terminate when they reach the arbitrary boundary of the CALMET domain, even though the total time period has not elapsed.

HYSPLIT 24-hr (CST) Forward Trajectories at 10-m

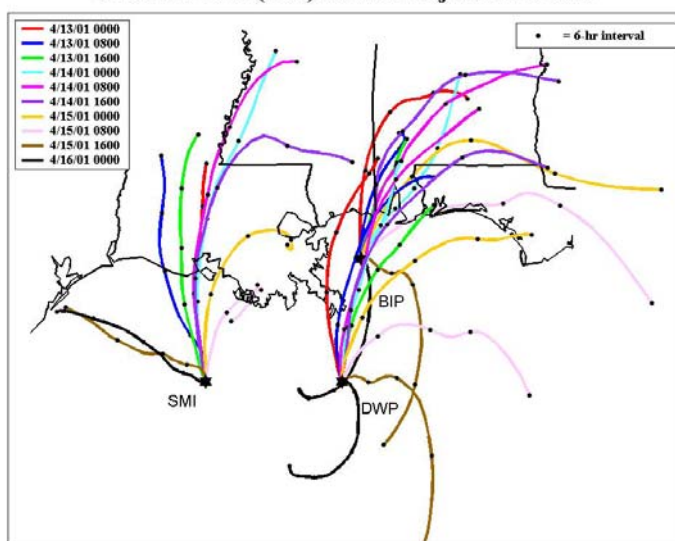


Figure 6-59. HYSPLIT 24-hr forward trajectory at 10 m based on EDAS wind fields for April 13 at 0000 CST through April 16, 2001, at 0000 CST. RWP observations are not used in EDAS.

CALMET 24-hr (CST) Forward Trajectories at 75-m

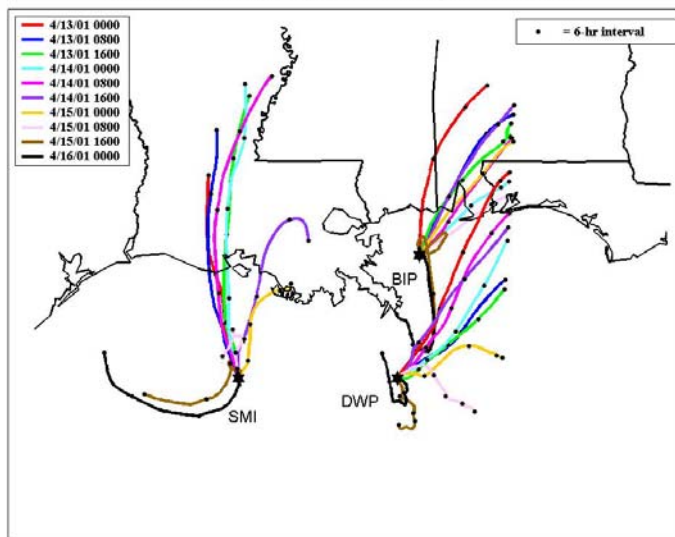


Figure 6-60. CALMET 24-hr forward trajectory at 75 m based on CALMET diagnostic wind fields for April 13 at 0000 CST through April 16, 2001, at 0000 CST. The RWP observations are used in CALMET. Note that the trajectories terminate when they reach the arbitrary boundary of the CALMET domain, even though the total time period has not elapsed.

HYSPLIT 24-hr (CST) Forward Trajectories at 75-m

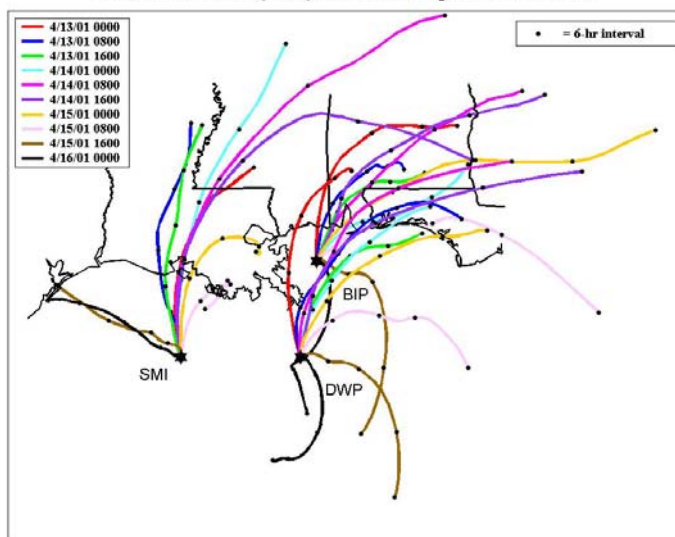


Figure 6-61. HYSPLIT 24-hr forward trajectory at 75 m based on EDAS wind fields for April 13 at 0000 CST through April 16, 2001, at 0000 CST. RWP observations are not used in EDAS.

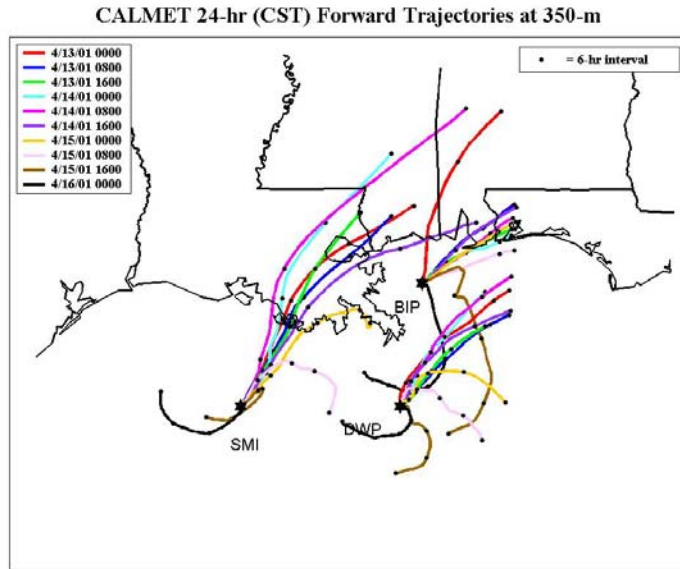


Figure 6-62. CALMET 24-hr forward trajectory at 350 m based on CALMET diagnostic wind fields for April 13 at 0000 CST through April 16, 2001, at 0000 CST. The RWP observations are used in CALMET. Note that the trajectories terminate when they reach the arbitrary boundary of the CALMET domain, even though the total time period has not elapsed.

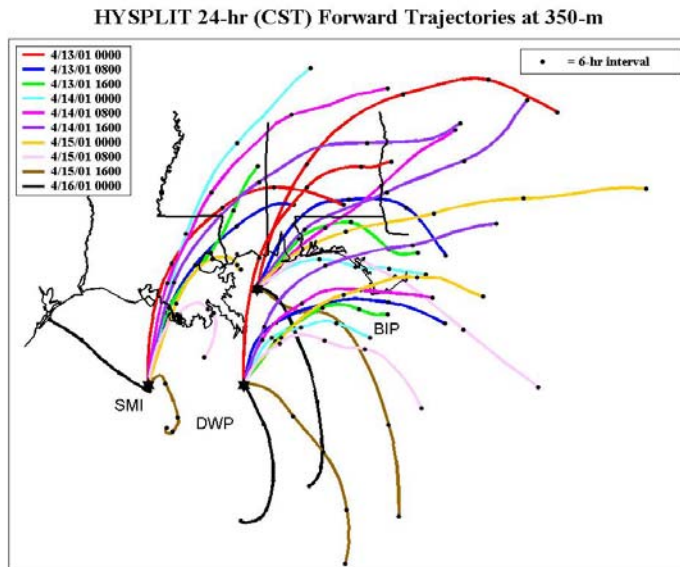


Figure 6-63. HYSPLIT 24-hr forward trajectory at 350 m based on EDAS wind fields for April 13 at 0000 CST through April 16, 2001, at 0000 CST. RWP observations are not used in EDAS.

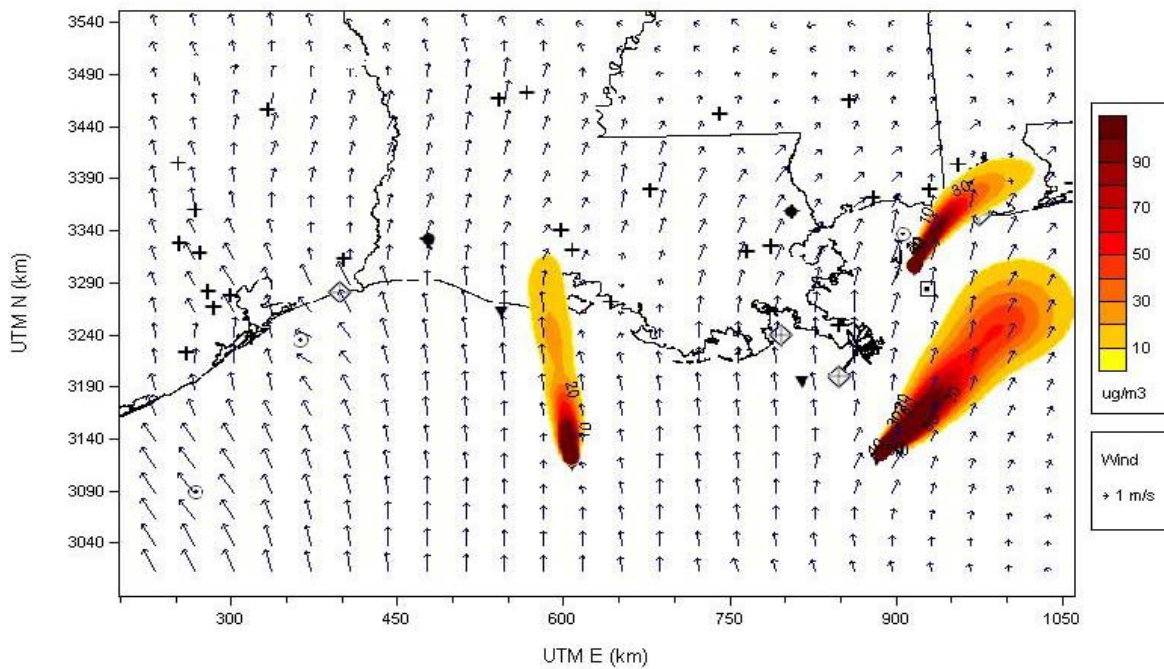


Figure 6-64. CALPUFF dispersion simulations for hypothetical tracers originating from SMI, DWP, and BIP ending on April 14, 2001, at 1900 CST. The same amount of tracer is assumed to be released from each source.

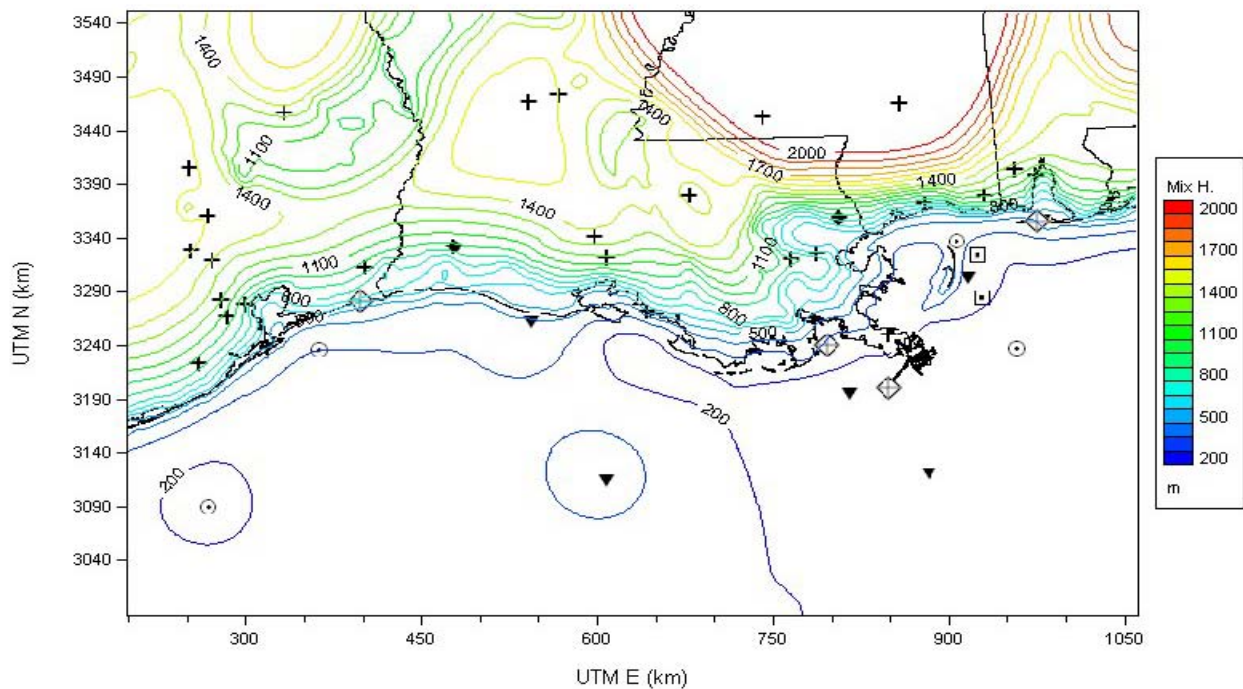


Figure 6-65. CALMET-derived mixing heights for April 14, 2001, at 1400 CST.

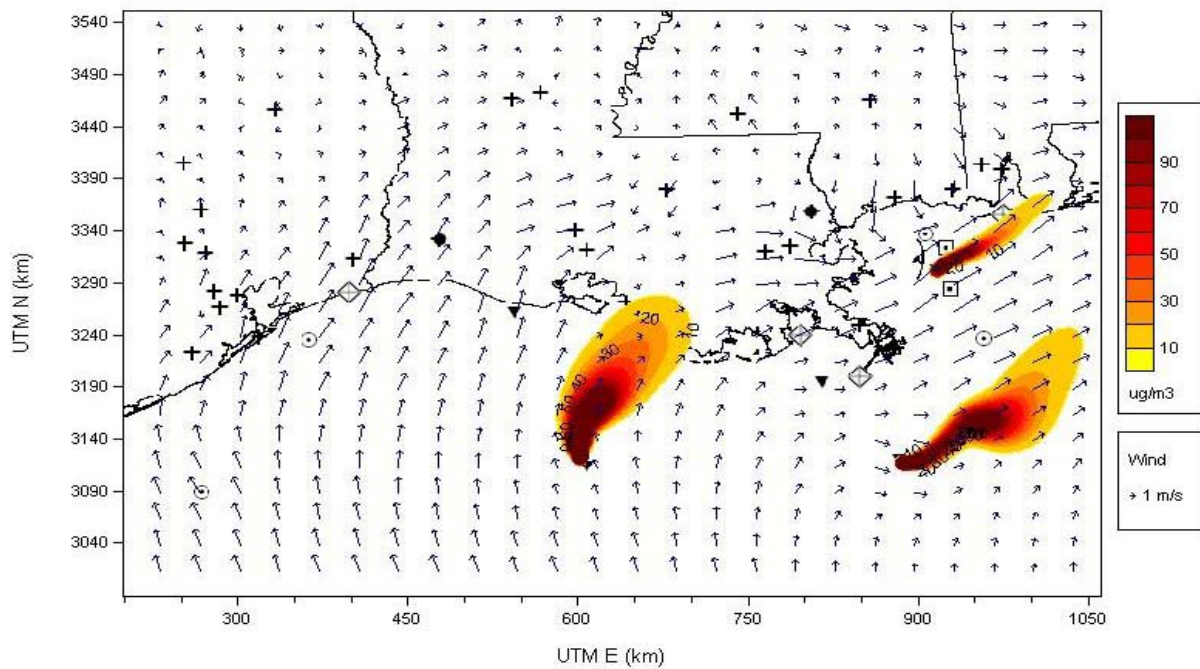


Figure 6-66. CALPUFF dispersion simulations for hypothetical tracers originating from SMI, DWP, and BIP ending on April 15, 2001, at 1100 CST. The same amount of tracer is assumed to be released from each source.

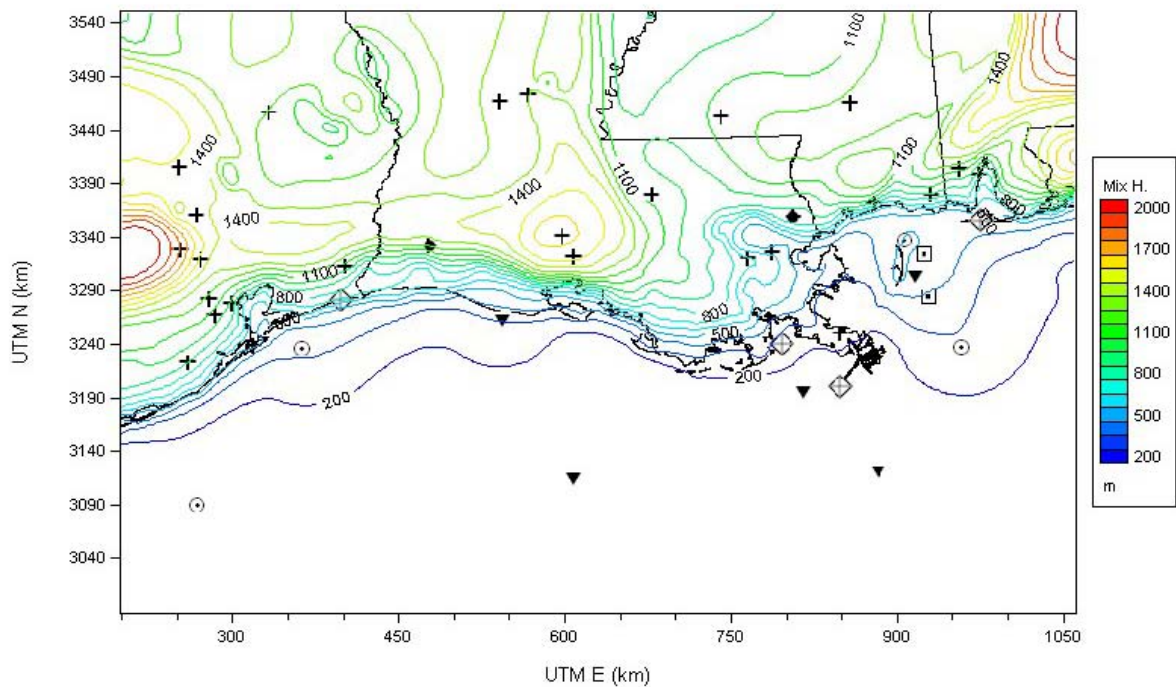


Figure 6-67. CALMET-derived mixing heights for April 15, 2001, at 1400 CST.

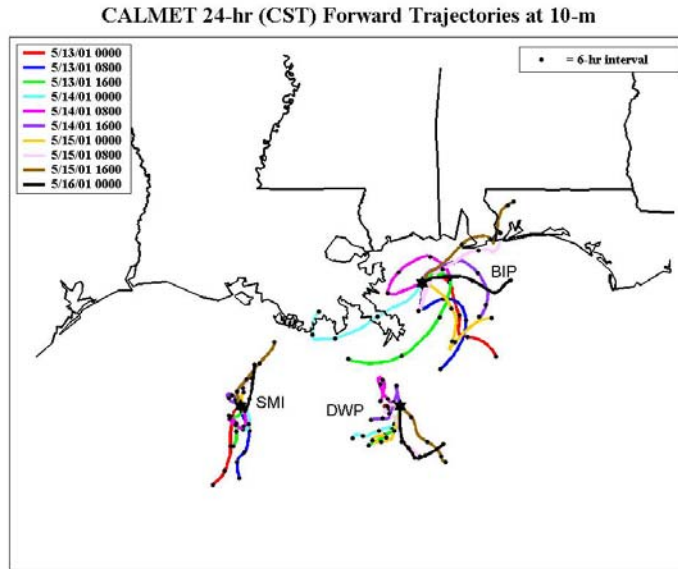


Figure 6-68. CALMET 24-hr forward trajectory at 10 m based on CALMET diagnostic wind fields for May 13 at 0000 CST through May 16, 2001, at 0000 CST. The RWP observations are used in CALMET. Note that the trajectories terminate when they reach the arbitrary boundary of the CALMET domain, even though the total time period has not elapsed.

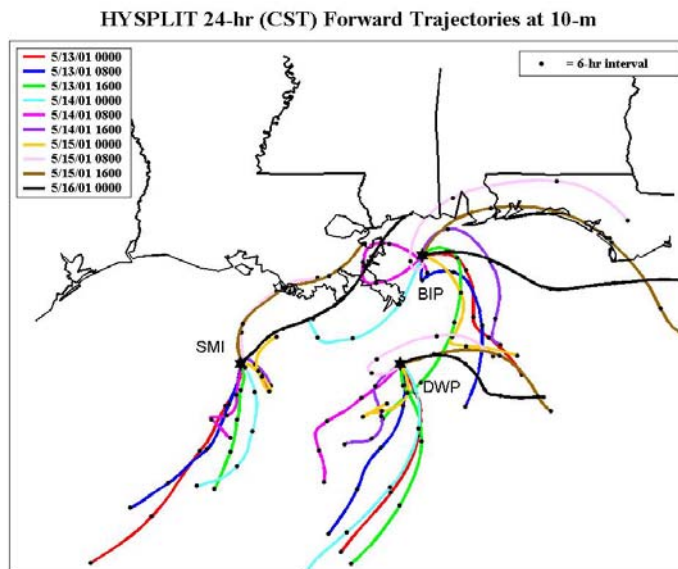


Figure 6-69. HYSPLIT 24-hr forward trajectory at 10 m based on EDAS wind fields for May 13 at 0000 CST through May 16, 2001, at 0000 CST. RWP observations are not used in EDAS.

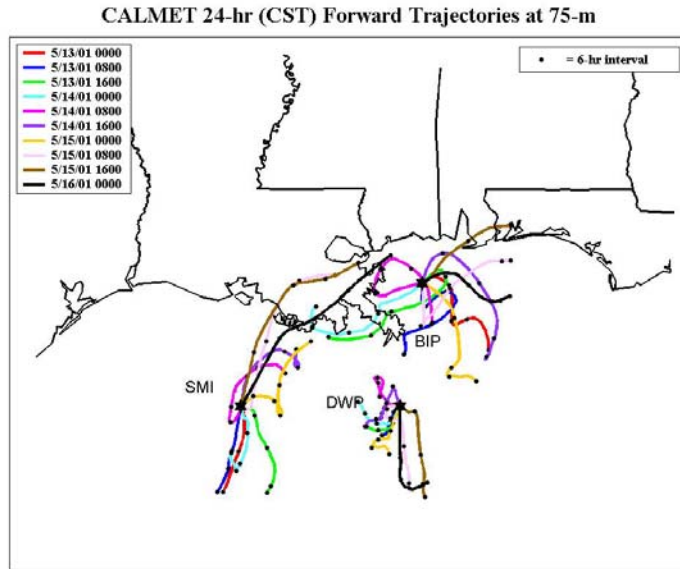


Figure 6-70. CALMET 24-hr forward trajectory at 75 m based on CALMET diagnostic wind fields for May 13 at 0000 CST through May 16, 2001, at 0000 CST. The RWP observations are used in CALMET. Note that the trajectories terminate when they reach the arbitrary boundary of the CALMET domain, even though the total time period has not elapsed.

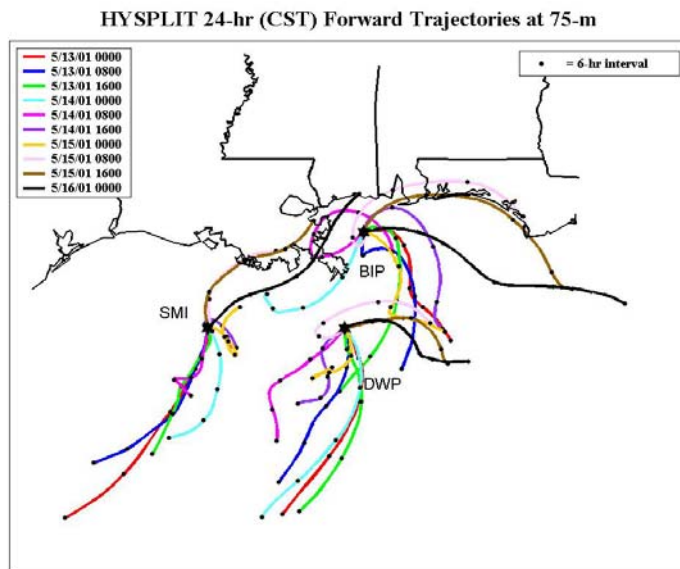


Figure 6-71. HYSPLIT 24-hr forward trajectory at 75 m based on EDAS wind fields for May 13 at 0000 CST through May 16, 2001, at 0000 CST. RWP observations are not used in EDAS.

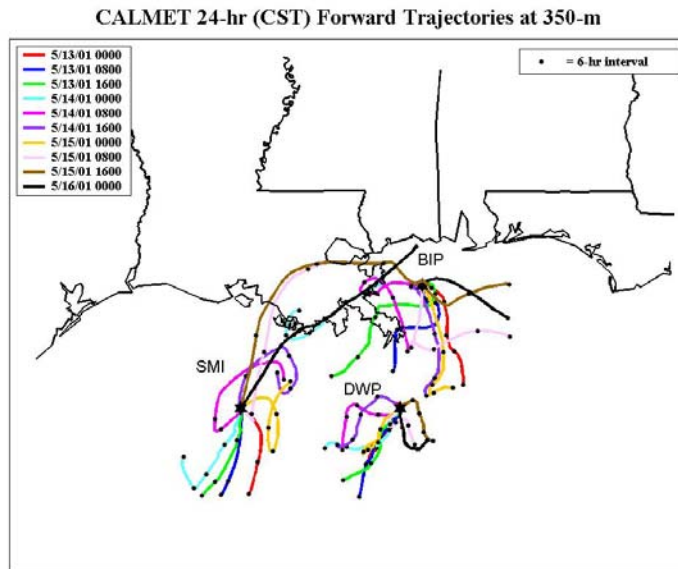


Figure 6-72. CALMET 24-hr forward trajectory at 350 m based on CALMET diagnostic wind fields for May 13 at 0000 CST through May 16, 2001, at 0000 CST. The RWP observations are used in CALMET. Note that the trajectories terminate when they reach the arbitrary boundary of the CALMET domain, even though the total time period has not elapsed.

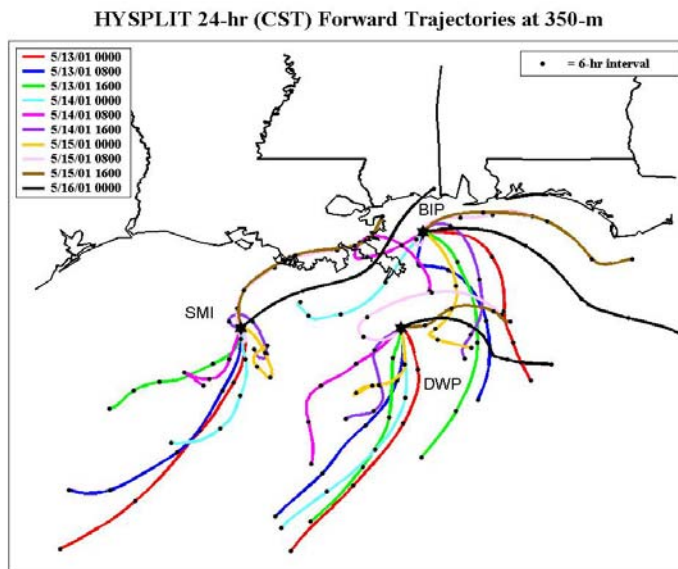


Figure 6-73. HYSPLIT 24-hr forward trajectory at 350 m based on EDAS wind fields for May 13 at 0000 CST through May 16, 2001, at 0000 CST. RWP observations are not used in EDAS.

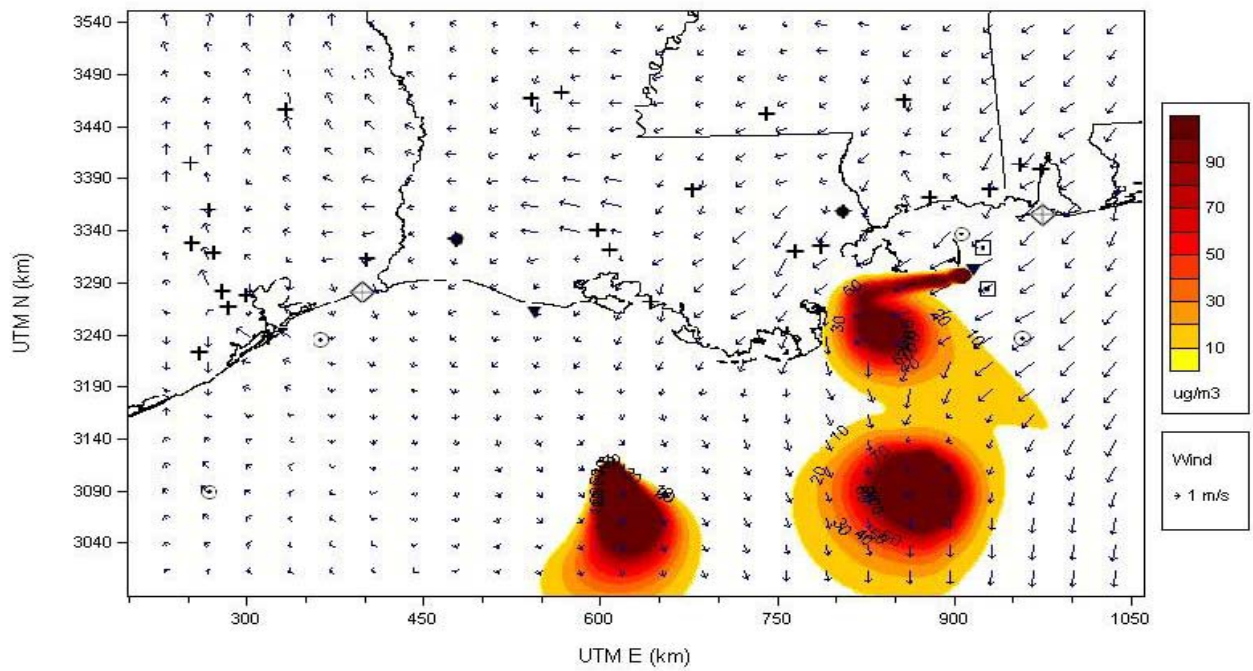


Figure 6-74. CALPUFF dispersion simulations for hypothetical tracers originating from SMI, DWP, and BIP ending on May 14, 2001, at 0600 CST. The same amount of tracer is assumed to be released from each source.

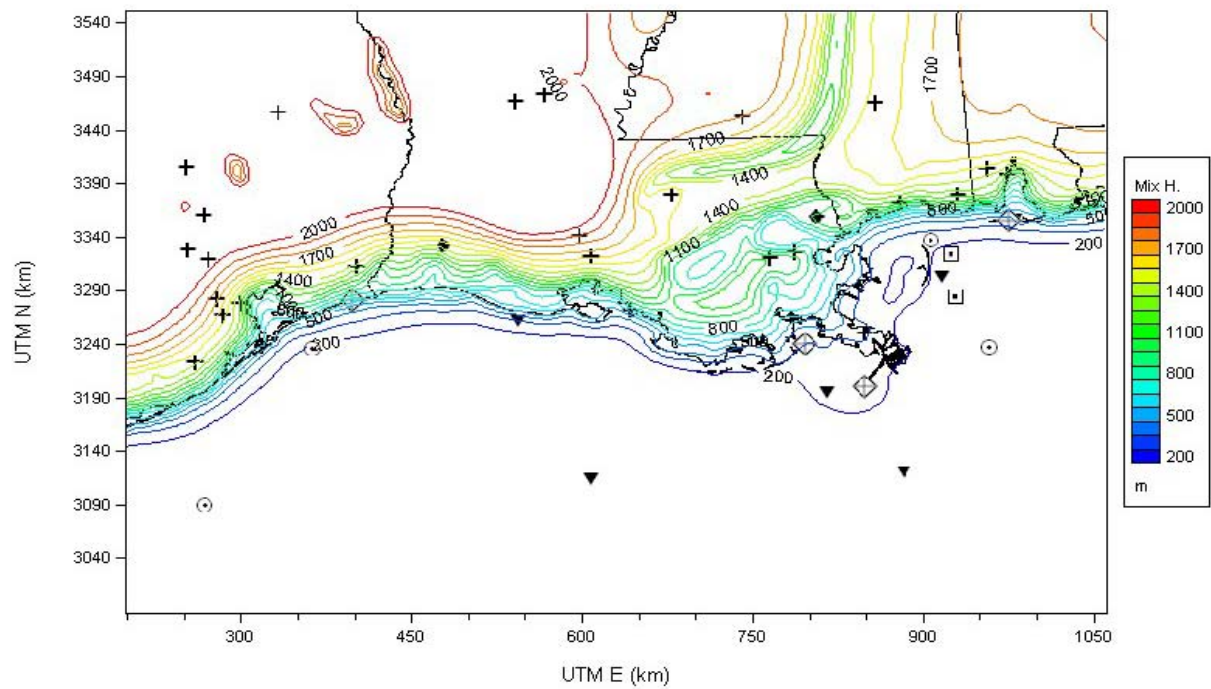


Figure 6-75. CALMET-derived mixing heights for May 14, 2001, at 1400 CST.

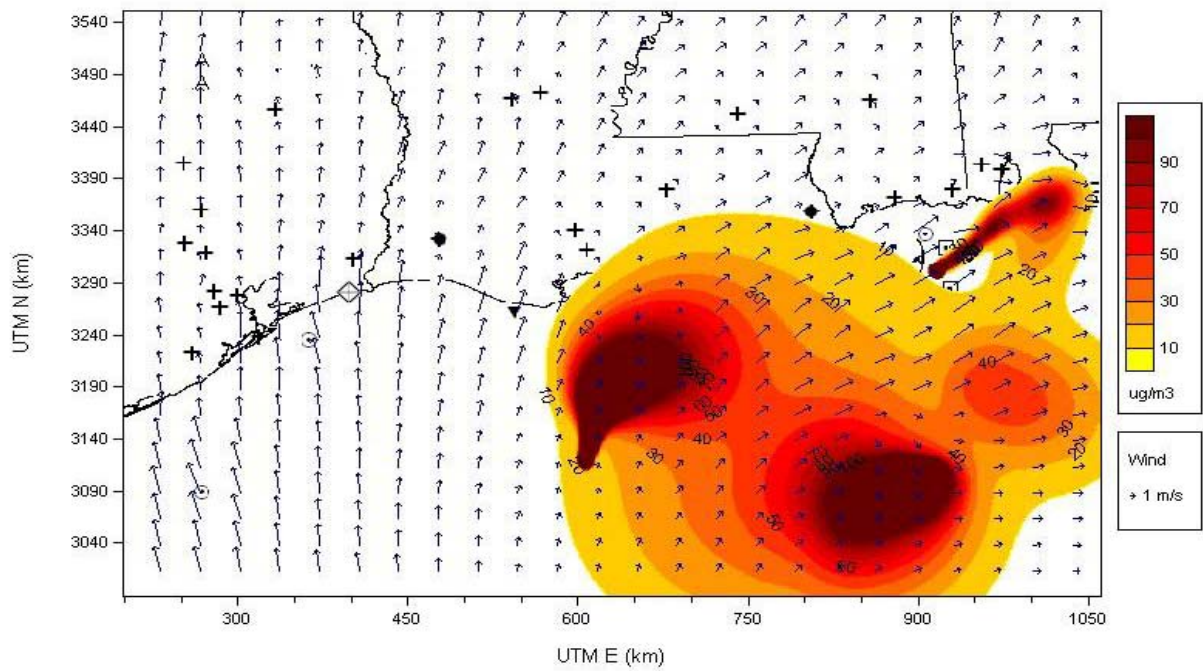


Figure 6-76. CALPUFF dispersion simulations for hypothetical tracers originating from SMI, DWP, and BIP ending on May 15, 2001, at 2200 CST. The same amount of tracer is assumed to be released from each source.

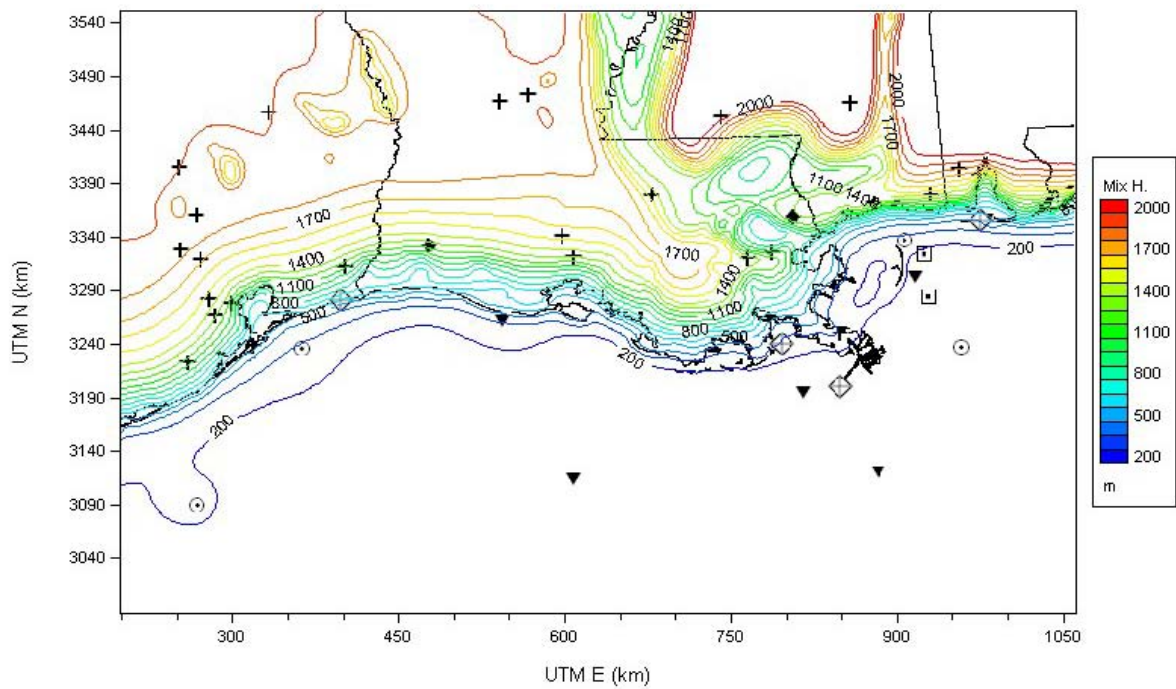


Figure 6-77. CALMET-derived mixing heights for May 15, 2001, at 1400 CST.

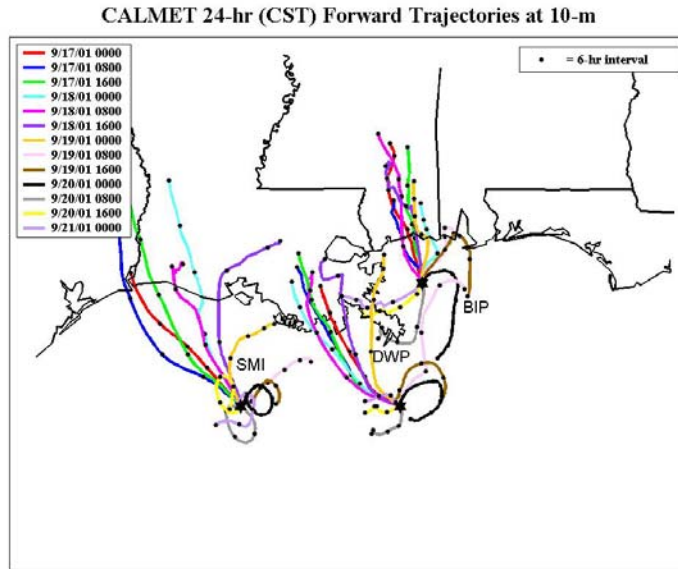


Figure 6-78. CALMET 24-hr forward trajectory at 10 m based on CALMET diagnostic wind fields for September 17 at 0000 CST through September 21, 2001, at 0000 CST. The RWP observations are used in CALMET. Note that the trajectories terminate when they reach the arbitrary boundary of the CALMET domain, even though the total time period has not elapsed.

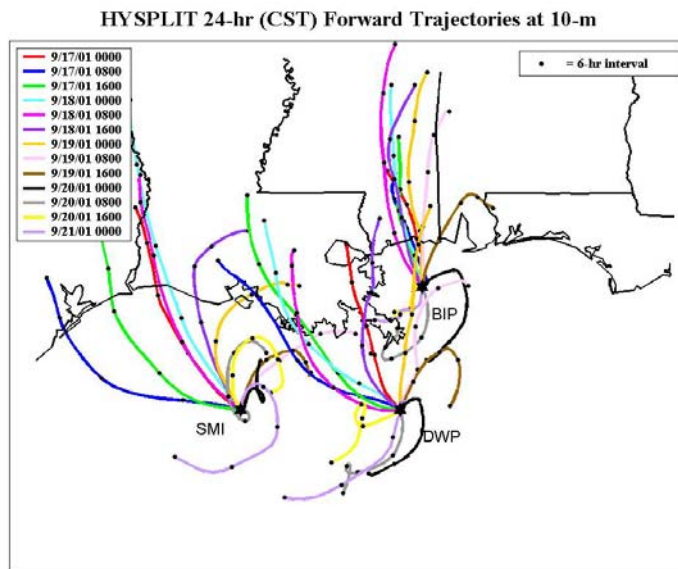


Figure 6-79. HYSPLIT 24-hr forward trajectory at 10 m based on EDAS wind fields for September 17 at 0000 CST through September 21, 2001, at 0000 CST. RWP observations are not used in EDAS.

CALMET 24-hr (CST) Forward Trajectories at 75-m

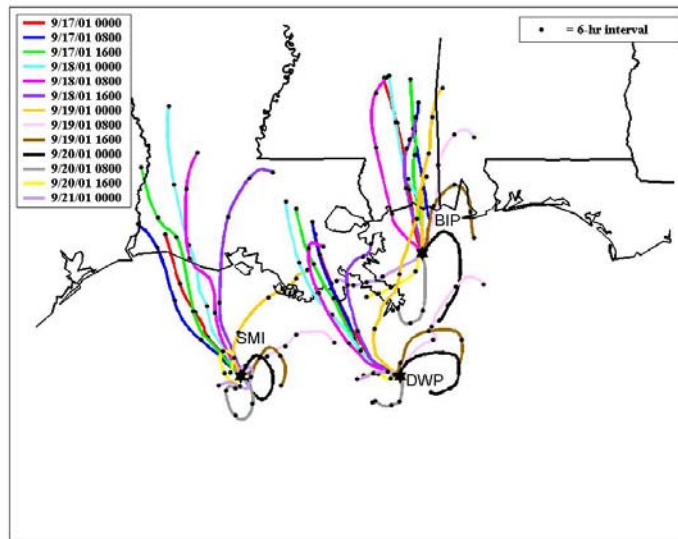


Figure 6-80. CALMET 24-hr forward trajectory at 75 m based on CALMET diagnostic wind fields for September 17 at 0000 CST through September 21, 2001, at 0000 CST. The RWP observations are used in CALMET. Note that the trajectories terminate when they reach the arbitrary boundary of the CALMET domain, even though the total time period has not elapsed.

HYSPLIT 24-hr (CST) Forward Trajectories at 75-m

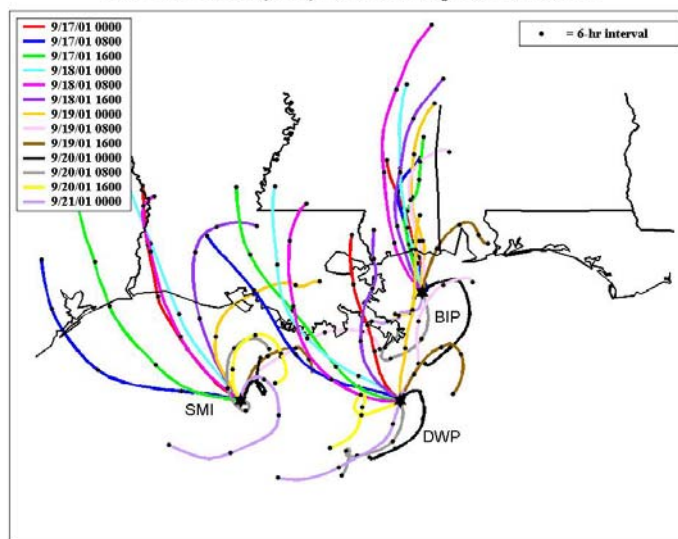


Figure 6-81. HYSPLIT 24-hr forward trajectory at 75 m based on EDAS wind fields for September 17 at 0000 CST through September 21, 2001, at 0000 CST. The RWP observations are not used in EDAS.

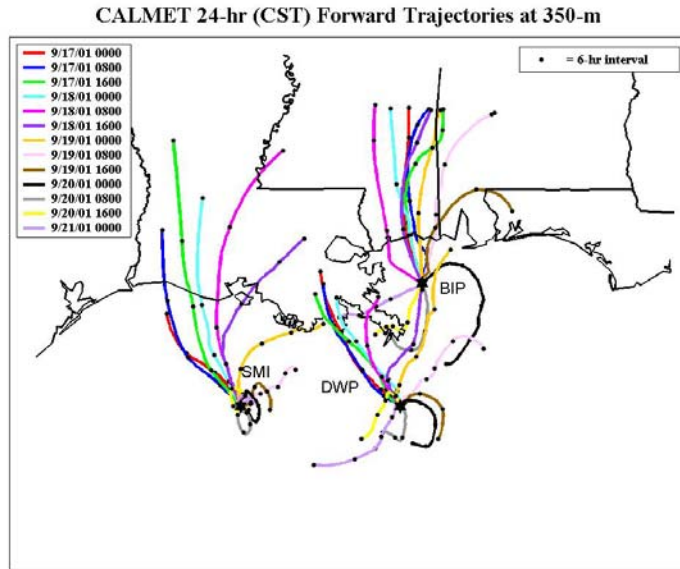


Figure 6-82. CALMET 24-hr forward trajectory at 350 m based on CALMET diagnostic wind fields for September 17 at 0000 CST through September 21, 2001, at 0000 CST. The RWP observations are used in CALMET. Note that the trajectories terminate when they reach the arbitrary boundary of the CALMET domain, even though the total time period has not elapsed.

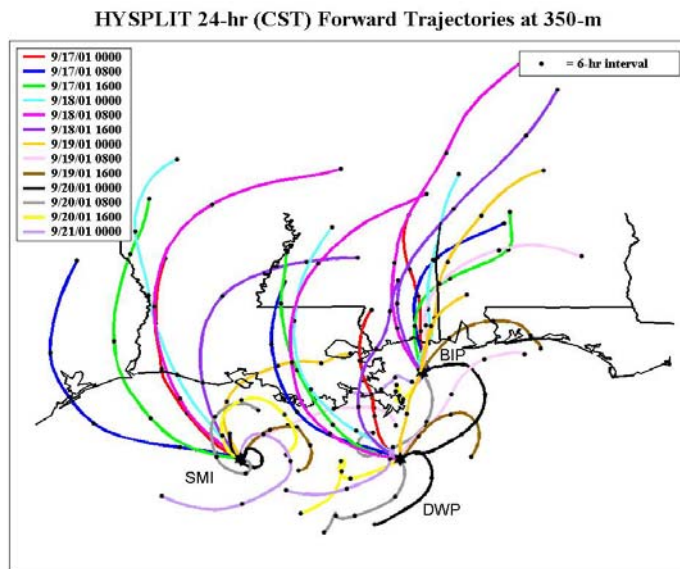


Figure 6-83. HYSPLIT 24-hr forward trajectory at 350 m based on EDAS wind fields for September 17 at 0000 CST through September 21, 2001, at 0000 CST. RWP observations are not used in EDAS.

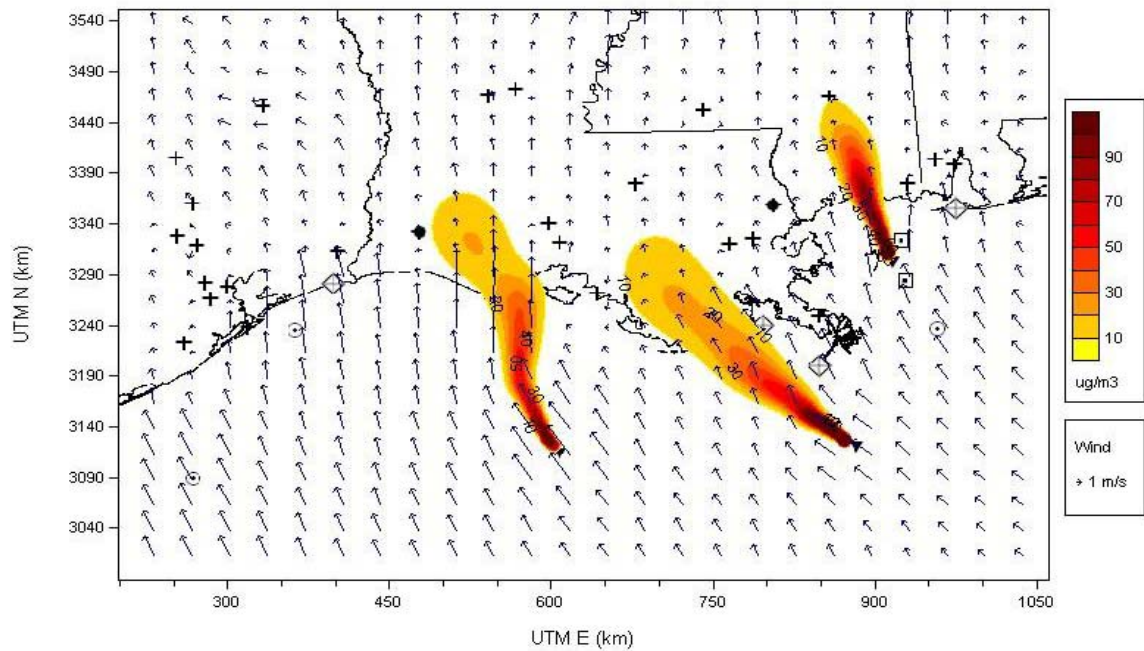


Figure 6-84. CALPUFF dispersion simulations for hypothetical tracers originating from SMI, DWP, and BIP ending on September 18, 2001, at 2200 CST. The same amount of tracer is assumed to be released from each source.

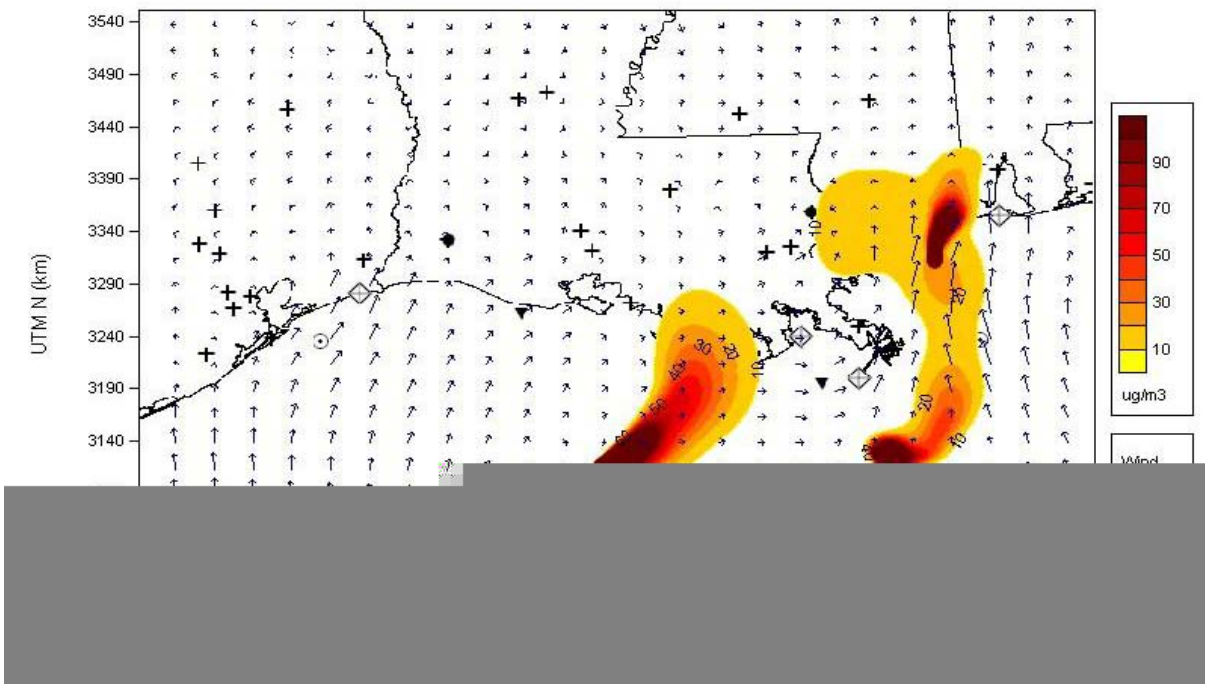


Figure 6-85. CALPUFF dispersion simulations for hypothetical tracers originating from SMI, DWP, and BIP ending on September 19, 2001, at 1900 CST. The same amount of tracer is assumed to be released from each source.

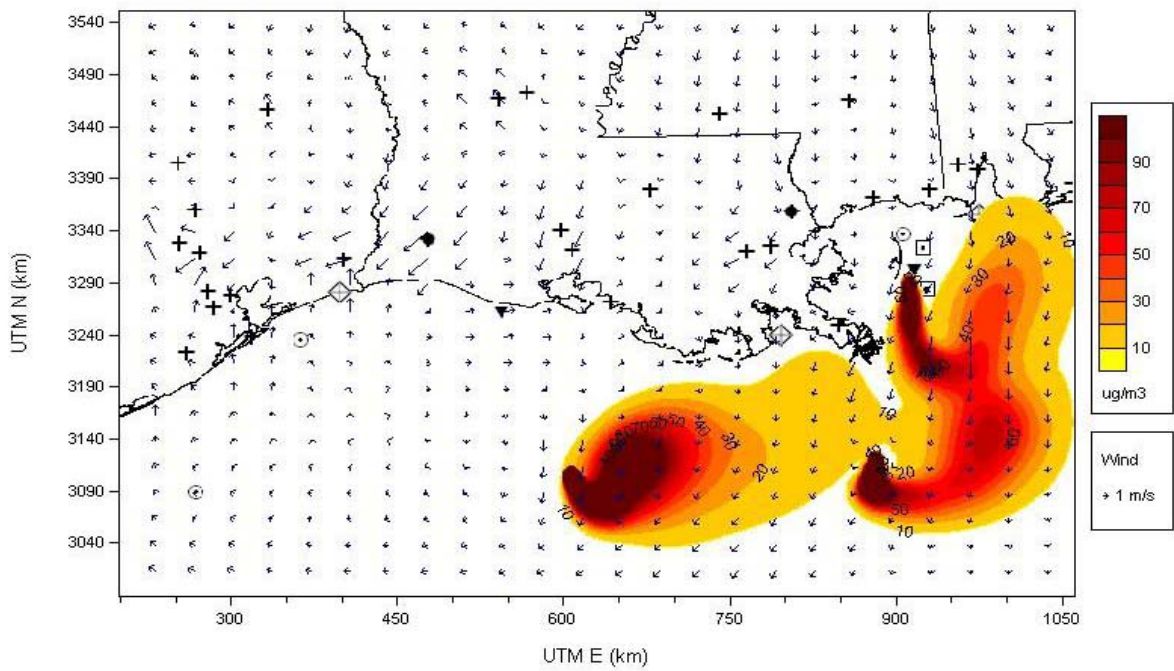


Figure 6-86. CALPUFF dispersion simulations for hypothetical tracers originating from SMI, DWP, and BIP ending on September 20, 2001, at 1300 CST. The same amount of tracer is assumed to be released from each source.

## **7. SUMMARY OF MAJOR FINDINGS AND RECOMMENDATIONS**

The project objectives were described in Section 1: (1) creating a quality-controlled data inventory and tools to view the data; (2) understanding the annual, seasonal, and diurnal variations in the ABL's structure; (3) understanding the processes governing variations in the ABL's structure; (4) creating three-dimensional gridded wind fields; and (5) characterizing the variation of transport and dispersion under different weather conditions. Sections 2 through 6 provided detailed analyses of the ABL data from the Gulf of Mexico to satisfy these objectives. This section summarizes the major findings and provides a set of recommendations for further research with the data that have been collected. The recommendations also include some suggestions for future routine meteorological measurements.

### **7.1 SUMMARY OF FINDINGS**

Major project findings are discussed in the following subsections. Each subsection references the report section in which the specific information is available and, when appropriate, a deliverable that accompanies this report.

#### **7.1.1 Data and Data Viewer (Section 2)**

All data collected as part of this study, as well as other relevant data, have been placed in a common Microsoft SQL Server database. In addition, the data are contained in quarterly Microsoft Access databases. These data sets were delivered to MMS. The data are generally available for the period May 1998 through September 2001. The data have been validated and are ready for immediate use by data analysts and modelers. The data include

- Hourly RWP and RASS  $T_v$  data collected at five platforms and one coastal site. Note that data from four RWP sites (WDP, DWP, BIP, and FTM) are available only from September 2000 through September 2001.
- Rawinsonde data collected from Lake Charles and Slidell, Louisiana, at 0000 UTC and 1200 UTC, for each day during the study.
- Hourly surface meteorological data collected at the RWP sites and from buoy and C-MAN sites. The routine data collected at most sites include wind speed and direction, temperature, relative humidity, station pressure, and skin temperature. The buoy sites also collected wave height and wave period data.
- Hourly surface meteorological data collected at land-based surface sites throughout the Gulf of Mexico region. These data were input into a Microsoft SQL Server database; however, they were not quality-controlled.
- Hourly boundary layer parameters such as heat fluxes and scaling parameters derived for all over-water sites using the COARE model.
- Eta forecast model geopotential height, friction velocity, latent heat flux, sensible heat flux, low, middle, and high cloud cover, and EDAS model wind speed and wind direction at grid points nearest each over-water site location.

- Daily aloft synoptic weather classifications and surface flow classifications.
- Averages of RWP wind and RASS  $T_v$  data. Averages were created for the entire 1998-2001 study period by year, season, month, and aloft classification.

In addition to the data contained in the database, CALMET wind fields derived for seven selected case studies are also available in their native binary format.

To effectively display this diverse set of data for use in data analysis, the Environmental Data Analysis Tool (EDAT) was developed and delivered to MMS. EDAT is designed to work with environmental data sets such as RWP, RASS, rawinsonde, air quality, surface meteorological, and modeling data sets. EDAT reads from a Microsoft Access database or a Microsoft SQL Server database. EDAT can produce four types of plots including time series, time-height cross-sections, vertical profiles, and spatial plots, and can display images.

### **7.1.2 Atmospheric Boundary Layer Characteristics (Sections 3-5)**

To understand the characteristics of the meteorology in the Gulf of Mexico, several types of data were studied that capture a variety of phenomena that occur over time and space. The data analyzed include aloft synoptic weather, surface flow speed and direction, vertical profiles of wind and temperature, near-surface stability, mixing heights, and boundary layer parameters such as heat fluxes, friction velocity, surface roughness, and Monin-Obukhov length. Both statistical and case study analyses of these data were performed, and the major findings from these analyses are presented below.

#### **ABL Characteristics Related to Aloft Synoptic Weather (Section 3)**

For the purposes of this project, “aloft” is defined as anything above the surface layer. It is obvious that synoptic-scale, upper-air weather patterns have a strong impact on local and regional weather conditions, especially in the ABL. To understand the relationship between synoptic-scale weather and local ABL conditions, upper-level patterns over the Gulf of Mexico were classified for each day during the study (May 1998 through September 2001). The classification patterns are ridge, weak ridge, flat, zonal, trough, weak trough, post-trough, cut-off low, and tropical storm.

The ridge of high pressure was the dominant aloft upper-air pattern, occurring approximately one-third of the time. This is important because the ridge pattern is often associated with ABL characteristics (e.g., light winds with low mixing depths) that lead to high pollutant concentrations. The trough was the second most predominant aloft or upper-air feature and was observed about one-fourth of the time. This is important because the ABL characteristics under trough scenarios typically lead to periods with relatively low air pollution concentration episodes, because of stronger winds and strong vertical mixing. Weak troughs occurred less frequently, observed on about one of every six days. The other patterns were found to occur far less frequently; tropical storms were rare. A summary of the influence of the aloft patterns on local boundary layer parameters follows; the local parameters are derived from observations using the COARE algorithm.

The Longwave Radiation is a component of the surface energy balance. It has little variation by synoptic class or by site, ranging from 290 to 420 W/m<sup>2</sup>. The magnitude is less for post-trough synoptic conditions since such periods are generally cool and clear. The magnitude of longwave radiation is largest for tropical storms, which are marked by warm temperatures, high humidity, and a maximum amount of natural aerosols (i.e., fog, clouds, and rain).

The Shortwave (Solar) Radiation is another component of the surface energy balance and reaches a maximum during ridge conditions, which are usually clear and sunny, and a minimum during weak troughs or tropical storms, which are more likely characterized by clouds and rain.

The Humidity Scaling Parameter is a key parameter in Monin-Obukhov similarity theory and is proportional to the latent heat flux divided by the friction velocity. The latent heat flux tends to be maximized during periods with a low dew point in the air and/or periods when the skin temperature is much higher than the air temperature, for example, after a cold front passes or in the middle of a large high pressure system. The humidity scaling parameter is, therefore, also expected to be largest during low humidity periods or hot high pressure periods. As expected, the humidity scaling factor is larger during post-trough and ridge periods. It is smallest during tropical storms, when the air is likely to be saturated and the same temperature as the water.

The Temperature Scaling Parameter is also a key parameter in Monin-Obukhov similarity theory and is proportional to the sensible heat flux divided by the friction velocity. The sensible heat flux is largest during periods when the air is much cooler than the water, such as after a cold front passes. As expected, the temperature scaling factor is much larger during post-trough periods with cold air advection. It is smallest during tropical storms, when the air is likely to be the same temperature as the water.

The Sensible Heat Flux is another component of the surface energy balance and is calculated using observations of wind speed and the skin-air temperature difference. It increases as the wind speed and/or skin-air temperature difference increases. Sensible heat flux is maximized for post-trough synoptic conditions, which are likely to be marked by above average wind speeds and by low air temperature relative to water temperature. There is a factor of ten variability across the nine synoptic classes. There are some differences among the sites but they are not consistent and need further investigation.

The Latent Heat Flux is also a component of the surface energy balance and, over water at the latitude of the Gulf of Mexico, is about an order of magnitude greater than the sensible heat flux. Over water, the variability in the latent heat flux is less than that in the sensible heat flux, perhaps because the latent heat flux (calculated from observations of wind speed, air-skin temperature difference, and relative humidity) tends to be nearly always positive, since the air at the water surface is always saturated with water vapor. In contrast, the sensible heat flux can sometimes be negative, when air temperature is greater than skin temperature. The latent heat flux is largest during post-trough synoptic condition, due to the higher wind speeds and the relatively low dew points that follow a cold front.

The Friction Velocity is calculated using the log wind profile relation, given the observed wind speed near the surface. The wind speed averages 6 m/s, ranging from 4 m/s for ridge and flat classes to 11.5 m/s for the tropical storm class. Since friction velocity is proportional to wind

speed, the friction velocity values are largest during high-wind periods during tropical storms. Aside from the anomaly during tropical storms, there is little variability in friction velocity from site to site or by synoptic class. The friction velocity averages 0.2 m/s.

### **ABL Characteristics Related to Surface Flow (Section 3)**

Surface wind speed and direction data collected at the C-MAN, buoy, and platform surface monitors were analyzed to characterize the surface flow patterns in the Gulf of Mexico. The analysis involved creating wind rose plots for all sites to characterize surface flows and classifying the flow at selected sites on each day of the study period as a function of four wind direction classes relative to the local orientation of the shoreline: onshore, offshore, parallel west, or parallel east. The daily surface wind speed and direction flow classifications are included in the database. The buoy and platform sites are separated by large distances, stretching from buoy 42019, located about 200 km southwest of Houston, to buoy 42040 near southern Alabama, to as far as 100 km offshore. These distances alone will cause variability in the nature of the onshore and offshore flow characteristics.

An onshore flow that was light to moderate in speed was observed most of the time for the entire study period at the four sites used for analyzing the daily flow characteristics. Onshore flow occurred about twice as often as offshore flow. In 1999, less onshore flow was observed at buoy 42019 and VRM compared to 1998 and 2000. This pattern was not observed at buoy 42035 or SMI. This difference is important because it can impact the ABL characteristics listed below. The dominance of onshore flow was evident for all of the upper-air patterns. Annual and seasonal results were similar. Stronger winds were observed under the trough pattern as opposed to the ridge pattern.. In general, stronger winds were observed more often at the offshore sites. A summary of the influence of the surface flow patterns on local boundary layer parameters follows, using the same surface energy balance and similarity parameters discussed in the previous subsection:

The Downwelling Longwave Radiation shows little variation by flow direction or by station, ranging from 340 to 390 W/m<sup>2</sup>. The magnitude is slightly less for offshore flow directions since such periods are generally associated with post-frontal northerly wind directions that are cool and clear.

The Shortwave Radiation does not vary much with site or with flow direction, since the minimum and maximum values in the figures are 170 and 290 W/m<sup>2</sup>, respectively. The behavior at each of the 14 monitoring sites is consistent, with higher values (averaging about 240 W/m<sup>2</sup>) for onshore and parallel west flow directions, and lower values (averaging about 190 W/m<sup>2</sup>) for offshore and parallel east flow directions. The difference may be caused by differences in cloud cover.

The Humidity Scaling Parameter shows little (less than factor of two) variability across the 14 sites and the four flow directions. No obvious trends are apparent.

The Temperature Scaling Parameter is largest during offshore flow periods because the sensible heat flux tends to be maximized during periods when the air temperature is cooler than the water temperature, such as for northerly offshore wind flow patterns. It is smallest during onshore

flow periods at the buoy sites, when the air is likely to be at the same temperature as the water. At the oil platform and C-MAN sites, the temperature scaling parameter is smallest during either onshore or parallel west flow directions.

The Sensible Heat Flux increases as the wind speed and the skin-air temperature difference increase. Sensible heat flux is maximized for northerly offshore flow directions, which are more likely to be marked by above average wind speeds and by low air temperatures. The sensible heat flux is lowest for onshore flow directions, when the boundary layer air temperatures are in balance with the water surface. The average difference in sensible heat flux for offshore and onshore flow directions across the nine stations is about a factor of ten. There are some differences between the sites but they are not consistent and the reasons for the differences are not obvious.

The Latent Heat Flux shows some differences at most sites between offshore and onshore wind directions. The latent heat flux is largest during offshore (northerly) flows, which tend to be associated with post-trough synoptic conditions, when higher wind speeds and relatively low dew points follow a cold front. With any offshore flow, the dew point in the air is likely to be less than that usually found over water. Minimum latent heat fluxes occur with onshore flows, which tend to be boundary layer flows when nearly saturated air is in balance with the water surface.

Friction Velocity is proportional to wind speed; thus, it is highest when winds are offshore since offshore winds have larger speeds than onshore or parallel winds. These high winds are often associated with post-cold-front conditions from the north quadrant. Minimum friction velocity occurs during parallel west wind directions.

### **Aloft Winds and Temperature (Section 4 and Appendix D)**

The aloft winds and temperature data consist of quality-controlled RWP and RASS data from six sites. As part of the analysis, these data were averaged over several intervals to determine their characteristics and patterns. For example, averaging was performed by month, season, year, upper-air class, and entire operational period. In addition, surface wind and  $T_v$  data were averaged and analyzed along with the aloft data to give a more complete picture of the lower levels of the ABL. The winds were vector-averaged, which inherently produces lighter wind speeds than the scalar averages that are more typically reported .

Wind data were averaged by hour and height to create an average diurnal profile for a given interval.  $T_v$  data were grouped by height and into day (0600 to 1800 CST) or night (1800 to 0600 CST) categories before averaging to yield a daytime and nighttime  $T_v$  profile for each averaging period. Averages were only calculated if at least 50% of the possible measurements contributing to that average were valid.

Average wind profiles from the platform height of 25 m to the top of the RWP range (about 3500 m) are characterized by the following conclusions:

- Southwest through easterly flows were dominant throughout all seasons and years; the most frequent flow direction was southeasterly.

- In the fall, easterly flows occurred at lower levels and southwesterly flows occurred aloft, with the transition height near 1000 m.
- In the winter, easterly surface flows occurred and were decoupled from south to southwesterly flows that were observed aloft.
- In the spring, southerly winds were observed up to 1000 m and southwesterly winds above 1000 m.
- In the summer, winds ranged from easterly to southwesterly below 2000 m. The most diurnal variability occurred at VRM.
- With a ridge pattern, winds were south to southeasterly below 1100 m, and southwest to easterly aloft.
- With a trough pattern, winds were mostly southwesterly aloft, with southeasterly to northeasterly flow in the low levels. Stronger troughs had a more defined shear layer.

The following conclusions were reached for the RASS data. The average  $T_v$ , observed by RASS were analyzed for elevations ranging from 131 m (above the level of the instrument on the oil platform) to about 700 m. The RASS data were combined with  $T_v$  observations collected by thermometers on short towers on the oil platforms at heights of about 25 msl to obtain “complete” vertical profiles that show the following:

- A discontinuity often occurs in the temperature gradient at the lower two or three RASS levels (e.g., 131 m) due to a known cold bias in the measurement system.
- The average profiles, which extend to about 700 m, do not show an elevated inversion or mixing height, despite the fact that a mixing depth of 500 to 700 m is expected and often observed in the reflectivity ( $C_n^2$ ) data.
- The differences in temperature between the surface and RASS measurements showed variability inconsistent with scientific expectations. Because the surface and 131-m temperatures are measured by two types of instruments, biases may occur that influence the diagnosis of stable or unstable temperature gradients.

### **Near-Surface Stability (Final Presentation in Appendix D)**

Near-surface stability was calculated by skin temperature minus surface air temperature. Average diurnal profiles of near-surface stability were averaged by month and show the following characteristics:

- Most sites are unstable most of the time (80%) and are, therefore, stable about 20% of the time.
- January and February are the most stable months, which may be due to non-representative stability created during the day by platform heating by the sun.

## **RWP- and RASS-Estimated Mixing Heights (Section 5)**

RWP/RASS-estimated  $C_n^2$  and  $T_v$  data are often used to estimate mixing heights at overland sites. Mixing heights are important in air quality issues because the mixing height defines the maximum vertical extent to which surface- (or platform-) based emissions can mix. A goal of the project was to use automatic mixing height detection algorithms to produce hourly mixing heights at the RWP sites. The automatic system is needed when there are thousands of soundings that must be analyzed, as was the case with this study. However, frequent sea clutter in the lowest 600 m contaminated the reflectivity data. Furthermore, the aloft inversion that caps the ABL was rarely observed in the RASS data, since the RASS could not “see” high enough. It was not possible to automatically calculate the mixing heights for nearly all of the hours of this study. Instead, mixing heights were manually estimated (by a meteorologist), but only for case study periods. For the seven case studies, manually estimated mixing heights ranged from 400 m to 1000 m and were usually around 600 m above ground level.

## **Boundary Layer Parameterization by COARE (Section 5)**

To characterize the ABL surface fluxes and scaling parameters, the COARE algorithm was used to estimate hourly surface fluxes of momentum (also called the surface stress), sensible heat, and latent heat from observations of wind speed, air temperature, and water vapor mixing ratio at some standard reference height near the water surface and the skin temperature at the water surface. The COARE algorithm was originally derived from the TOGA-COARE research project.

When COARE was applied to the first portions of the data, a problem sometimes occurred with the evaporative cooling calculation due to unrealistically high amounts of solar energy estimated to reach the ocean surface. To solve this problem, the first coefficient in the equation for the net absorption by the ocean (Equation 7-1) was changed from 0.137 to 0.060, based on tests performed by Dr. Christopher Fairall, a COARE developer. This change provided a more realistic representation of the actual absorption, which caused the evaporative cooling calculations to better agree with observations.

$$\text{Net} = \text{SW} * (.137 + 11 * \text{CST} - 6.6\text{e-}5 / (\text{CST} * (1 - \exp(-\text{CST}/8.0\text{e-}4)))) \quad (7-1)$$

where:

- Net = Net absorption by the ocean (watts per square meter)
- SW = Incoming short wave radiation (watts per square meter)
- CST = Cool skin thickness (meters)

During early daylight hours, under light wind conditions when the air temperature was warmer than skin temperature (i.e., a stable near-surface layer), COARE calculated unrealistic rapid increases in skin temperature (up to 500°C). A lack of heat removal due to very small accumulated stress (surface momentum flux) and a very thin (almost zero) warm layer thickness caused this condition. To correct this problem, a minimum stress of 0.002 N/m<sup>2</sup> was imposed for this calculation. This value was chosen after analysis of measured stresses during TOGA-COARE (personal communication with Dr. Christopher Fairall, July 2002).

In addition to the change in the basic calculations, the COARE program was changed to incorporate Eta model analyzed fields and/or predictions. The capability of flagging COARE output based on the validity of the incoming data was also incorporated.

Statistical and case study analyses were carried out with the COARE input and output data, and the following results are summarized:

Fluxes and Scaling Parameters. The fluxes and scaling parameters calculated by the COARE algorithm in the Gulf of Mexico are physically consistent with expectations and are similar in magnitude to the observations and COARE calculations for TOGA, which took place in the warm western Pacific Ocean near the equator. Calculated monthly average sensible heat fluxes in the Gulf of Mexico ranged from 5 to 30 W/m<sup>2</sup>, typical of other over-water areas. Similarly, calculated monthly average latent heat fluxes ranged from 50 to 150 W/m<sup>2</sup>, also typical of other over-water areas. Both the latent and sensible heat fluxes were highest in the late fall and early winter and lowest in the late spring and summer, although the yearly cycle in latent heat values is less pronounced than the seasonal cycle. Sensible heat flux is maximized for post-trough synoptic conditions, which are likely to be marked by above average wind speeds and by low air temperature. The latent heat flux is consistently large during the post-trough synoptic condition, due to the higher wind speeds and the low dew points that follow a cold front. It can also be large during tropical storms because of the high temperatures and strong winds.

The study of the estimates of annual variations of latent and sensible heat fluxes reveal smaller fluxes in the summer. These results are consistent with lighter winds and smaller skin-air temperature differences in the summer compared to other times of year. Calculated monthly average sensible heat fluxes were about one-fifth the calculated monthly average latent heat fluxes, and the differences between the two were generally greater in the summer and smaller in the late fall and winter.

The calculated fluxes are generally in good agreement with the monthly average Eta model latent and sensible heat fluxes. However, the Eta model fluxes did not show as much variation between sites as the calculated fluxes. In addition, the Eta model fluxes were about 20% greater than the calculated fluxes in the fall and early winter, but were very similar during the spring and summer.

Friction Velocity. The COARE-calculated monthly average friction velocity for the buoys, the C-MAN sites, and the SMI platform shows agreement among these sites well within a factor of two and often within 20%. This agreement is important because the monthly average friction velocity is the key scaling velocity for estimating transport speeds and dispersion rates. However the VRM, BIP, DWP, MBP, SWP, and WDP platforms (part of BAMP) suggest mean friction velocities that are 30% to 40% less than the other sites. Possible explanations are that the wave height and frequency are estimated from empirical relations given observations of wind speed at the platforms, whereas they are directly measured at the buoys. Also, the platform wind observations are corrected from a height of >20 m to 10 m and are, on average, less (at the 10-m height) than at the other non-BAMP sites. All data show that the calculated monthly average friction velocity was slightly lower from May through August and peaked in late fall and early winter. The monthly average Eta model friction velocity showed the same yearly pattern as the calculated friction velocity. However, the Eta model friction velocity was 10% to 20%

higher than the calculated friction velocity in the fall and early winter. This is most likely the reason why the Eta model fluxes were slightly high during the same period.

Temperature and Humidity Scaling Parameter. The COARE-calculated monthly average temperature scaling parameter and humidity scaling parameter generally showed a factor of two or better agreement among sites. The monthly average temperature scaling parameter and the humidity scaling parameter tended to be smaller in April and May, when the difference between the skin and air temperatures was at its minimum, and tended to be larger in November through January, when the difference between the skin and air temperatures was at its maximum.

Skin and Air Temperature Differences. The differences between the skin and air temperatures were, on average, +1 to +3°C at most sites all year. The differences were fewer in late spring and greater in late fall and early winter. This persistent positive temperature difference has been noted by Dr. Christopher Fairall at most other sites located on warm-water oceans.

Surface Wind Speed. Scalar monthly average wind speeds showed good agreement among sites. The lowest speeds occurred in July and August and the highest in December and January. For some years, there was a transition from lower wind speeds in August to higher wind speeds in September and October. Weather maps indicate that the high wind speeds in September and October on some years were probably a result of tropical storms.

### **7.1.3 Wind Fields, Transport, and Dispersion (Section 6)**

Wind fields were developed using the CALMET diagnostic model driven by a combination of historic Eta model simulations and observations. The wind fields, along with other ABL parameters, were used to develop three-dimensional inputs to the CALPUFF transport and dispersion model. Trajectories from the CALMET wind fields and the EDAS wind fields were compared. CALPUFF was used to assess dispersion and transport characteristics under several types of meteorological patterns. These patterns include onshore and offshore flow regimes, pre- and post-cold-frontal boundary passages, strong surface and upper-level high pressure systems, and upper-level flow transitioning from an area of low pressure to a weak area of high pressure. The conclusions from this study are summarized:

1. The EDAS-simulated wind fields and the observed RWP winds from six sites were compared. EDAS is based on a combination of Eta model forecast winds and diagnostic interpolations of observed winds but does not include the RWP data. The comparison is complicated because the EDAS simulations represent averages over a grid volume size of 40 km by 40 km by 100 m whereas the RWP observations represent an average over a much smaller grid volume with a radius of 1 km to 2 km; consequently, more turbulent variations are expected in the observations than in the EDAS simulations. The mean wind speed (WS) bias was near zero close to the shore but increased with offshore distance, so that the EDAS mean wind speed exceeded the RWP mean wind speed by 1 to 2 m/s at 50 km offshore and by 2 to 6 m/s at 100 to 200 km offshore. Mean wind direction (WD) bias was small, about a 10° to 20° difference (e.g., if the RWP WD was 180°, then the EDAS WD would be 160°). Standard deviations of the differences (with mean bias removed) were 1 to 2 m/s for WS and 20° to 40° for WD, in agreement with findings for other domains and models (Hanna and Yang, 2001).

2. The CALMET diagnostic wind model was applied to the Gulf of Mexico domain using RWP and other observations. Methods had to be devised for interpolating between missing observations, especially for the vertical profiles of winds and temperature, since CALMET has stringent requirements for data continuity. Furthermore, recommendations were made for assumptions concerning length scales related to spatial interpolations. For example, based on the evaluations of EDAS simulations and RWP observations (see Item 1), a distance scale of 150 km from the observing location was chosen for the point where RWP and EDAS simulations would have equal weight.
3. The procedure for applying the CALPUFF transport and dispersion model was described. Since actual source emission data were not available and no tracer studies were performed, the CALPUFF runs were made using arbitrary assumptions for hypothetical tracers from the three oil platforms, BIP, SMI, and SWP. The major model outputs for analysis were contour plots of 24-hr average concentrations.
4. Twenty-four-hour trajectories were calculated for releases of hypothetical emissions from the three oil platform at several times and at heights of 10 m, 75 m, and 350 m using (1) the CALMET wind fields and an in-house STI trajectory model (TRAJMOD) and (2) the EDAS wind fields and the HYSPLIT trajectory model. However, the trajectory comparisons were hampered by the truncation of the CALMET trajectories at the domain boundary.
5. Seven multi-day case studies were analyzed using EDAS, HYSPLIT, CALMET, and CALPUFF. These seven periods covered the range of representative synoptic conditions and seasons, such as strong-wind January days and light-wind July days. Some general conclusions follow:
  - The CALMET trajectories and the EDAS-HYSPLIT trajectories agree within 20° to 30° most of the time, although the speeds of the EDAS trajectories are larger by as much as a factor of two (see the evaluations of mean biases under Item 1). However, since the CALMET trajectories are often truncated at the edges of the CALMET domain, the comparisons with HYSPLIT trajectories are limited.
  - The CALPUFF-simulated plumes from the three oil platforms sometimes impact the shoreline or offshore islands, depending on wind direction. The concentrations are higher during light winds, when dilution is less. It is fortunate that the most persistent winds, associated with onshore impact near the same location for several hours, are nearly always marked by high winds and consequently lower concentrations. When winds are light and variable, the local centerline concentration may be higher, but the plume does not remain for long over a specific point.
  - The CALMET-CALPUFF estimates of over-water mixing depth were low, about 100 to 200 m, in contrast to observed mixing depths of about 600 m. This factor of three to six difference causes model overpredictions in concentrations, since the plume is constricted to the mixing layer. The underpredictions of mixing depth appear to be due to the neglect of convective mixing processes offshore, where CALMET currently assumes that the mixing depth is due solely to mechanical mixing and is therefore proportional to wind speed.

## 7.2 RECOMMENDATIONS

Based on the conclusions listed in Section 7.1, several recommendations can be made for future studies with the existing data set to enhance the research already completed. A few recommendations require the collection of additional data. The recommendations are arranged into five categories: Collaboration, Publication, Analysis, Modeling, and Measurements.

**Collaboration** – Follow-on work involving collaboration with outside organizations:

- Work with NCEP to better understand over-water wind differences between the Eta model and observed RWP winds. Analysis has shown that Eta model winds are biased compared to RWP winds.
- Compare Eta 12-km gridded predictions to observed data; compare to the comparisons made with EDAS 40-km predictions/observations. The results will help guide how finer-resolution Eta model data should be used in high-resolution modeling efforts.
- Work with NOAA ETL to design a scheme to remove sea-clutter from profiler data so that mixing heights can be automatically estimated for data from the ABL study and future studies using existing mixing-height algorithms.
- Work with Dr. Christopher Fairall at NOAA to improve COARE predictions at high surface roughness. Roughness increases under very low wind speeds, which influences estimations of the ABL parameters.
- Conduct a joint meeting on COARE to further improve the model for use in the Gulf of Mexico. Participants might include MMS representatives, Dr. Christopher Fairall of NOAA, STI, Earth Tech, and Hanna Consultants.
- Make better use of ABL measurements and analyses in other MMS-sponsored projects by reviewing plans and progress and recommending ways to incorporate ABL data and analysis and modeling results.

**Publication** – Plan a special issue (of, for example, *Journal of Applied Meteorology*, *Journal of Geophysical Research*, or *Boundary Layer Meteorology*) on ABL issues in the Gulf and prepare specific papers on the following:

- Eta/RWP wind comparisons.
- Three-year climatology of surface ABL parameters calculated using COARE in a shallow water ocean and modifications made to COARE (jointly with NOAA?).
- Modeled and estimated mixing heights in the Gulf of Mexico.
- Results from related MMS-sponsored projects.

**Analysis**

- Compare satellite-derived sea-surface temperatures to radiometer temperatures and buoy temperatures measured during this study. Accurate spatial sea-surface temperatures are important for accurate modeling.

- Compare estimates of sea-surface temperatures to the radiometer temperatures when clouds obscure the satellite's view of the Gulf (currently estimated using hole-filling techniques).
- Identify several additional periods of super-stable conditions in the existing data set (i.e., a period of southerly flow after a cold outbreak has cooled the water in the shallow portion of the Gulf) and perform a ABL case study similar to other case studies.
- Determine the best method for estimating wave height and frequency as a function of water depth from wind speed alone. When wave data is not available at the platforms, inaccurate estimations of wave characteristics can result in inaccurate estimations of surface roughness, which influence ABL parameterizations. Evaluate the roughness estimations from wind speed alone; compare to observed wave data.
- Integrate onshore and offshore air quality data into the meteorological data set and analyses performed during this project. This will expand the applicability of the results and provide further evaluation of the methods used.
- Revise the North-East Gulf of Mexico Meteorological Statistical Expert System to use improved model output and now-available data; this will result in a more accurate tool for visualization of meteorological data and of estimates of transport and dispersion from specific locations offshore.
- Use buoyancy flux to estimate mixing heights when winds are less than 6 m/sec and compare to RWP-derived mixing heights.

## **Modeling**

- Update the CALMET model to better estimate mixing heights; perform additional comparisons of observation-based estimations of mixing heights to model mixing heights. Currently, CALMET does a poor job estimating mixing heights in the Gulf of Mexico, primarily because it ignores convective mixing over water.
- Run CALMET using the pseudo-shoreline of 3-m water depth to represent marshland. Compare results to prior modeling.
- Update the CALPUFF dispersion runs using new CALMET output created with an improved mixing-height scheme. Compare the results from the new runs to those created as part of the current project.
- Compare CALMET diagnostic model runs to MM5 prognostic model runs and observational data and create best estimates of gridded mixing heights and winds.
- Modify the way diagnostic and prognostic models treat the diffuse shoreline of the Gulf of Mexico; operate the models and compare results with observations.
- Quantify the differences between the CALMET and HYSPLIT trajectories and the differences between the CALPUFF-calculated concentrations. The current conclusions use subjective statements such as “the trajectories were similar” or “the plume impacts were different”. In other trajectory comparisons, two trajectories were compared by calculating the difference in the two positions after certain travel times. The differences can then be expressed as function of time for that trajectory and a root mean square error

(rmse) calculated for a group of trajectories. The difference can be categorized by its components (e.g., radial distance and angular distance). The studies by Kahl and Samson (1986) usually found an rmse difference of 100 to 200 km after one day. Much of this difference is ascribed to stochastic variations. It would be of interest to determine if the rmse's that could be calculated with model output from the current study were similar to those found by others and if they differed with synoptic condition or wind speed.

- Compare CALPUFF concentration predictions quantitatively because the same amount of tracer was released in each case. For example the following outputs could be compared:
  - Maximum concentration at the point the shoreline is hit.
  - Maximum (centerline) concentration at specific downwind times (e.g., 3 hrs, 6 hrs, etc.) and distances (50 km, 100 km, etc.)
  - Penetration distance (downwind distance) for a given concentration.
  - Width of plume for a given concentration contour at a given travel time or distance.
- Develop an alternative procedure within CALMET to handle missing upper-air measurements.

**Measurements** – Conduct continuous measurements to (1) support routine source-based modeling for lessees and special-research MMS objectives; (2) provide long-term information on spatial and temporal ABL characteristics; and (3) support routine comparisons with Eta model predictions for routine estimates of ABL characteristics, for real-time modeling, and for special research studies involving ABL gradients on- and off-shore, etc.

- Collocate a radiometer and underwater temperature sensor to better determine the relationship and accuracy of the COARE-estimated warm-layer and cool-skin effect. This effect is used to estimate skin temperature at buoys, an important parameter for the estimation of ABL parameters and for model initial conditions. Work with NOAA to adjust COARE as needed.
- On a platform, operate temperature, relative humidity, and wind sensors at two heights within the surface layer, as well as a solar radiometer. Use this data to verify COARE estimations of ABL parameters that used surface ABL data at only one level.
- Continue routine operations of surface and upper-air meteorological measurements at the Lumcon site near the Mississippi River Delta.
- Routinely operate a measurement system on an offshore platform that measures a range of meteorological parameters at several depths of the surface layer and boundary layer. Such a system could include a mini-Sodar, an RWP/RASS system, and a surface meteorological monitoring system on a platform to obtain wind and temperature measurements. The addition of the mini-Sodar would fill the measurement void that exists from 30 m to 200 m; this hole is often the location of plumes.
- Improve the RWP and RASS sounders so that they are not so susceptible to interference from waves and nearby objects (e.g., oil platforms).

## 8. REFERENCES

- Allwine K.J. and Whiteman D. (1985) MELGAR: a mesoscale air quality model for complex terrain: volume 1 – overview, technical description and user's guide. Report prepared by Pacific Northwest Laboratory, Richland, WA.
- Arya S. P. (1999) *Air Pollution Meteorology and Dispersion*. Oxford University Press, New York, NY, 98-100.
- Blackadar A.K. (1997) Turbulence and diffusion in the atmosphere. Springer, New York, NY, 73-76 and Appendix C.
- Bradley E.F. and Weller R.A. (1995) Third Workshop of the TOGA COARE Air-Sea Interaction (Flux) Working Group. Honolulu, HI, August 2-4, 1995. UCAR/TCIPO, UCAR Communications, Boulder, CO.
- Bradley E.F, Moncrieff M.W., and Weller R.A. (1997) Joint workshop of the TOGA COARE Flux and Oceans Working Groups, and the GEWEX GCSS Working Group 4. Boulder, CO, May 14-16, 1997. UCAR/TCIPO, UCAR Communications, Boulder, CO.
- Bradley E.F. and Weller R.A. (1997) Fourth Workshop of the TOGA COARE Air-Sea Interaction (Flux) Working Group. Woods Hole, October 9-11, 1996. UCAR/TCIPO. UCAR Communications, Boulder, CO.
- Brooks I.M. and Rogers D.P. (1999) Observations of the turbulence structure of a well-developed internal boundary layer over the Persian Gulf. *13<sup>th</sup> Symposium on Boundary Layers and Turbulence*, American Meteorology Society, Boston, MA, pp. 367-370.
- Businger J.A. (1982) The fluxes of specific enthalpy, sensible heat, and latent heat near the earth's surface. *J. Atmos. Sci.* **39**, 1889-1892.
- Caldwell D.R. and Elliott W.H. (1971) Surface stresses produced by rainfall, *J. Phys. Oceanog.* **1**, 145-148.
- Carson D.J. (1973) The development of a dry inversion-capped convectively unstable boundary layer. *Quart. J. Roy. Meteorol. Soc.*, **99**, 450-467.
- Charnock H. (1955) A note on empirical wind-wave formulae. *Quart. J. Roy. Meteorol. Soc.*, **84**, 443-447.
- Curry J.A., Clayson C.A., Rossow W.B., Reeder R., Zhang Y.-C., Webster P.J., Liu G. and Sheu R.-S. (1999) High-resolution satellite-derived dataset of the surface fluxes of heat, freshwater, and momentum for the TOGA-COARE IOP. *Bull. Am. Meteorol. Soc.* **80**, 2059-2080.
- Doneland M. (1990) Air-Sea Interactions. *Ocean Engin. Sci.* (B. LeMehaute and D.M. Hanes, eds.), John Wiley, 239-291.
- Douglas S.G., Kessler R.C., and Carr E.L. (1990) User's guide for the urban airshed model. Volume III: user's manual for the diagnostic wind model. Office of Air Quality Planning and Standards, U.S. Environmental Protection Agency, Research Triangle Park, NC, EPA-450/4-90-007C.

- Drake R.L. and Huang C.H. (1980) Mass-consistent, interpolated wind fields for complex terrain. Presented at the *Symposium on Intermediate Range Atmospheric Transport Processes and Technical Assessment, Gatlinburg, TN, October 1-3*.
- Edwards K.A. and Rogers D.P. (1999) Scaled mean profiles of the MBL during coastal waves 96. *13<sup>th</sup> Symposium on Boundary Layers and Turbulence*, American Meteorology Society, Boston, MA, pp. 413-416.
- Fairall C.W., Bradley E.F., Rogers D.P., Edson J.B., and Young G.S. (1996a) Bulk parameterization of air-sea fluxes for TOGA-COARE. *J. Geophys. Res.*, **101**, 3747-3764.
- Fairall C.W., Bradley E.F., Godfrey J.S., Wick G.A., Edson J.B., and Young G.S. (1996b) The cool skin and the warm layer in bulk flux calculations. *J. Geophys. Res.* **101**, 1295-1308.
- Garratt J.R. and Ryan F.B. (1989) The structure of the stable internal boundary layer in offshore flow over the sea. *Bound. Lay. Meteorol.*, **47**, 17-40.
- Garratt, J.R. (1992) *The Atmospheric Boundary Layer*. Cambridge University Press, UK.
- Godfrey J.S. and Beljaars (1991) On the turbulent fluxes of buoyancy, heat and moisture at the air-sea interface at low wind speeds. *J. Geophys. Res.* **96**, 22043-22048.
- Gosnell R., Fairall C.W., and Webster P.J. (1995) The sensible heat flux of rainfall in the tropical ocean. *J. Geophys. Res.* **100**, 18437-18442.
- Hanna S.R. (1969) The thickness of the planetary boundary layer. *Atmos. Environ.* **3**, 519-536.
- Hanna S.R., Briggs G.A. and Hosker R.P. (1982) *Handbook on Atmospheric Diffusion*. DOE/TIC-11223 (DE82-002045). NTIS/USDOC, Springfield, VA.
- Hanna S.R., Paine R.J. and Schulman L.L. (1984) Overwater dispersion in coastal regions. *Bound. Lay. Meteorol.* **30**, 389-411.
- Hanna, S.R., Schulman L.L., Paine R.J., Pleim J.E., and Baer M. (1985) Development and evaluation of the Offshore and Coastal Diffusion Model. *J. Air Poll. Control Assoc.* **35**, 1039-1047.
- Hanna S.R. (1987) An empirical formula for the height of the coastal internal boundary layer. *Bound. Lay. Meteorol.* **40**, 205-207.
- Hanna S.R. and Paine R.J. (1989) Hybrid Plume Dispersion Model (HPDM) development and evaluation. *J. Appl. Meteorol.* **28**, 206-224.
- Hanna S.R. and Chang J.C. (1992a) Boundary layer parameterizations for applied dispersion modeling over urban areas. *Bound. Lay. Meteorol.* **58**, 229-259.
- Hanna S.R. and Chang J.C. (1992b) Representativeness of wind measurements on a mesoscale grid with station separations of 312 m to 10000 m. *Bound. Lay. Meteorol.* **60**, 309-324.
- Hanna S.R. and Chang J.C. (1995) Relations between meteorology and ozone in the Lake Michigan region. *J. Appl. Meteorol.* **34**, 670-678.
- Hanna S.R. and Britter R.E. (2001) Wind flow and vapor cloud dispersion at industrial and urban sites. AICHE, New York, NY.

- Hanna S.R., Roberts P.T., and MacDonald C.P. (2001) Estimation of boundary layer fluxes and profiles over the Gulf of Mexico using new observations and using the COARE program. Paper 1-7 in *American Meteorological Society Conference on Air-Sea Interaction*, 8 pages.
- Hanna S.R. and Yang R. (2001) Evaluations of mesoscale model predictions of near-surface winds, temperature gradients, and mixing depths. *J. Appl. Meteorol.* **42**, 453-466.
- Hare J.E., Persson P.O.G., Fairall C.W., and Edson J.B. (1999) Behavior of Charnock's relationship for high wind conditions. *13<sup>th</sup> Symposium on Boundary Layers and Turbulence*, American Meteorology Society, Boston, MA, pp. 252-255.
- Hsu S.A. (1988) *Coastal Meteorology*. Academic Press, San Diego, CA, 260 pages.
- Hsu S.A. (1989) The relationship between the Monin-Obukhov stability parameter and the Bulk Richardson Number at sea. *J. Geophys. Res.* **94**, 8053-8054.
- Hsu S.A. (1997) Estimating overwater convective boundary layer height from routine meteorological measurements for diffusion applications at sea. *J. Appl. Meteorol.* **36**, 1245-1248.
- Kazanski A.B. and Monin A.S. (1961) On the dynamical interaction between the atmosphere and the earth's surface. *Bull. Acad. Sci. USSR, Series Geophysics*, Number 5, 786-788.
- Kahl J.D. and Samson P.J. (1986) Uncertainty in trajectory calculations due to low resolution meteorological data, *J. Clim. Appl. Meteorol.* **25**, 1816-1831.
- Lambert D., Durand P., Thoumieux F., Benech B., and Druilhet A. (1999) The marine atmospheric boundary layer during SEMAPHORE. II: Turbulence profiles in the mixed layer. *Q. J. R. Meteorol. Soc.* **125**, 513-528.
- Ledvina D.V., Young G.S., Miller R.A., and Fairall C.W. (1993) The effect of averaging on bulk estimates of heat and momentum fluxes for the tropical western Pacific Ocean. *J. Geophys. Res.* **98**, 20211-20217.
- Lindsey C.G., Ray S.E., Dye T.S., Arthur M., Roberts P.T., and Stuart C. (1997a) Data collected by 915-MHZ radar profilers and surface meteorological stations during the 1996 Paso Del Norte ozone study. Data volume prepared for the U.S. Environmental Protection Agency, Research Triangle Park, NC by Sonoma Technology, Inc., Santa Rosa, CA, STI-996293-1729-DV, EPA Work Assignment III-101, Contract No. 68-D3-0030, July.
- Lindsey C.G., Ray S.E., Schoell B.M., Dye T.S., and Arthur M. (1997b) Meteorological data collected at the Walnut Grove Tower facility during IMS95. Letter report prepared for the California Air Resources Board, Sacramento, CA, by Sonoma Technology, Inc., Petaluma, CA, May.
- Liu W.T, Katsaros K.B., and Businger J.A. (1979) Bulk parameterization of the air-sea exchange of heat and water vapor including the molecular constraints at the interface. *J. Atmos. Sci.* **36**, 1722-1735.

- MacDonald C.P., Roberts P.T., Knoderer C.A., Miller D.S., Lilly M.R., and Hanna S.R. (2003) Boundary layer study in the western and central Gulf of Mexico. Presented at the Final Meeting of the Technical Review Group, Minerals Management Group, New Orleans, LA, October (STI-998555-2265).
- Mahrt L., Vickers D., Edson J., Sun J., Hojstrup J., Hare J., and Wilczac J. (1998) Heat flux in the coastal zone. *Bound. Lay. Meteorol.* **86**, 421-446.
- Mahrt L., Vickers D., Sun J., Crawford T.L., Vogel C., and Dumas E. (1999) Coastal zone boundary layers. *13<sup>th</sup> Symposium on Boundary Layers and Turbulence*, American Meteorology Society, Boston, MA, pp. 403-406.
- Nieuwstadt F.T.M. (1981) The steady-state height and resistance laws of the nocturnal boundary layer: Theory compared with CABAUX observations. *Boundary-Layer Meteorol.* **20**, 3-17.
- O'Brien J.J. (1970) Alternative solutions to the classical vertical velocity problem. *J. Appl. Meteorol.* **9**, 197-203.
- Oost W.A., Komen G.J., Jacobs C.M.J., and van Wort C. (2001) New evidence for a relation between wind stress and wave age from measurements during ASGAMAGE. Tech. Report 2001-5, Royal Dutch Meteorological Institute (KNMI), De Bilt, The Netherlands.
- Price J.F., Weller R.A., and Pinkel R. (1986) Diurnal cycling: Observations and models of the upper ocean response to diurnal heating, cooling, and wind mixing. *J. Geophys. Res.* **91**, 8411-8427.
- Saunders P.M. (1967) The temperature at the ocean-air interface. *J. Atmos. Sci.* **24**, 269-273.
- Scire S.S., Robe F.R., Fernau M.F., and Yamartino R.J. (1999) A user's guide for the CALMET Meteorological model (Version 5.0). EarthTech, Inc., Concord, MA, September.
- Seaman N.L. (2000) Meteorological modeling for air quality assessments. *Atmos. Environ.* **34**, 2231-2259.
- Smedman A.-S., Bergstrom H., and Grisogono B. (1997) Evolution of the stable boundary layer over a cold sea. *J. Geophys. Res.* **102**, 1091-1099.
- Smith S.D. (1988) Coefficients for sea surface wind stress, heat flux, and wind profiles as a function of wind speed and temperature. *J. Geophys. Res.* **93**, 15467-15472.
- Stull R.B. (1988) *An Introduction to Boundary Layer Meteorology*. Kluwer Academic Publishers, Boston, MA.
- Sun J., Mahrt L., Vickers D., Wong J., Crawford T.L., Vogel C., Dumas E., Mourad P., and Vandemark D. (1999) Air-sea interaction in the coastal shoaling zone. *13<sup>th</sup> Symposium on Boundary Layers and Turbulence*, American Meteorology Society, Boston, MA, pp. 343-346.
- Taylor P. K. and Yelland M. J. (2001) The dependence of sea surface roughness on the height and steepness of the waves. *J. Phys. Oceanography*, **31**, 572-590.
- Ternstrom M. and Smedman A.-S. (1992) The vertical turbulent structure of the coastal marine atmospheric boundary layer. *J. Geophys. Res.* **98**, 4809-4826.

- Vaisala Meteorological Systems, Inc. and Sonoma Technology, Inc. (2002) Profilers and data collection for the MMS boundary layer study in the western and central Gulf of Mexico: final performance report. Prepared for the U.S. Department of the Interior, Minerals Management Service, Gulf of Mexico OCS Region, New Orleans, LA, OCS Study MMS 2002-028.
- Verkaik J.W. (1999) Estimation of form drag using satellite data. *13<sup>th</sup> Symposium on Boundary Layers and Turbulence*, American Meteorology Society, Boston, MA, pp. 286-287
- Vickers D. and Mahrt L. (1999) Monin-Obukhov similarity in the coastal zone. *13<sup>th</sup> Symposium on Boundary Layers and Turbulence*, American Meteorology Society, Boston, MA, pp. 407-410.
- Vogel C.A., Crawford T.L., Sun J., and Mahrt L. (1999) Spatial variation of the atmospheric surface drag coefficient within a coastal shoaling zone. *13<sup>th</sup> Symposium on Boundary Layers and Turbulence*, American Meteorology Society, Boston, MA, pp. 347-348.
- Webb E.K., Pearman G.I., and Leuning R. (1980) Correction of flux measurements for density effects due to heat and water vapour transfer. *Q.J.R. Meteorol. Soc.* **106**, 85-100.
- Webster P.J. and Lukas R. (1992) TOGA-COARE: The coupled ocean-atmosphere response experiment. *Bull. Am. Meteorol. Soc.* **73**, 1377-1416.
- Yelland M. and Taylor P. K. (1996) Wind stress measurements from the open ocean. *J. Phys. Oceanogr.* **26**, 541-558.
- Zeng X., Zhao M., and Dickenson R.E. (1997) Intercomparison of bulk aerodynamic algorithms for the computation of sea surface fluxes using the TOGA-COARE and TAO data. *J. Climat.* **11**, 2628-2644.

# **APPENDIX A**

## **EDAT DATABASE FORMAT**

Appendix A contains information on the format and structure of the MMS EDAT database.

# EDAT DESIGN DOCUMENT

1.	EDAT DATABASE TABLES .....	4
1.1	Table Class.....	4
1.2	Table Data.....	4
1.3	Table Parameter .....	4
1.4	Table QCCode .....	5
1.5	Table QCLevel.....	5
1.6	Table Site .....	5
2.	EDAT DATABASE RELATIONS DIAGRAMS .....	6

## 1. EDAT DATABASE TABLES

### 1.1 Table Class

Surface, Model, Profiler, RASS are current classes.

Name	Type	Description	Constraints
<b><i>uClassID</i></b>	<i>tinyint</i>	<i>Surrogate PK</i>	<i>Unique auto increment integer</i>
sName	varchar(50)	Class name	Unique

### 1.2 Table Data

Contains observed or modeled data.

Name	Type	Description	Constraints
<b><i>uDataID</i></b>	<i>integer</i>	<i>Surrogate PK</i>	<i>Unique auto increment integer</i>
<i>uSiteID</i>	<i>smallint</i>	<i>FK to Site Table's PK</i>	<i>Referential Integrity</i>
<i>uClassID</i>	<i>tinyint</i>	<i>FK to Class Table's PK</i>	<i>Referential Integrity</i>
<i>uParameterID</i>	<i>smallint</i>	<i>FK to Parameter Table's PK</i>	<i>Referential Integrity</i>
dUTC	smalldatetime	Greenwich Mean Time (GMT) for which data was collected.	
rValue	float		
rHeight	float		
<i>uQCLevelID</i>	<i>tinyint</i>	<i>FK to QCLevel Table's PK</i>	<i>Referential Integrity</i>
<i>uQCCodeID</i>	<i>tinyint</i>	<i>FK to QCCode Table's PK</i>	<i>Referential Integrity</i>

### 1.3 Table Parameter

Contains all of the information about each air quality parameter stored and used in the database. Many of the fields are printed in the header sections of each data group in the exported OBS files.

Name	Type	Description	Constraints
<b><i>uParameterID</i></b>	<i>smallint</i>	<i>Surrogate PK</i>	<i>Unique auto increment integer</i>
sCode	varchar(50)	Parameter short code	May be NULL
sName	varchar(100)		
sUnit	varchar(50)		
<i>uAIRSPParameterID</i>	<i>integer</i>	<i>Natural AIRS parameter number</i>	
sAIRSUnitID	varchar(50)	AIRS Units	

#### 1.4 Table QCCode

Name	Type	Description	Constraints
<b><i>uQCCodeID</i></b>	<i>tinyint</i>	<i>Natural PK</i>	<i>Unique</i>
sName	varchar(50)		Unique

#### 1.5 Table QCLevel

Name	Type	Description	Constraints
<b><i>uQCLevelID</i></b>	<i>tinyint</i>	<i>Natural PK</i>	<i>Unique</i>
sName	varchar(50)		Unique

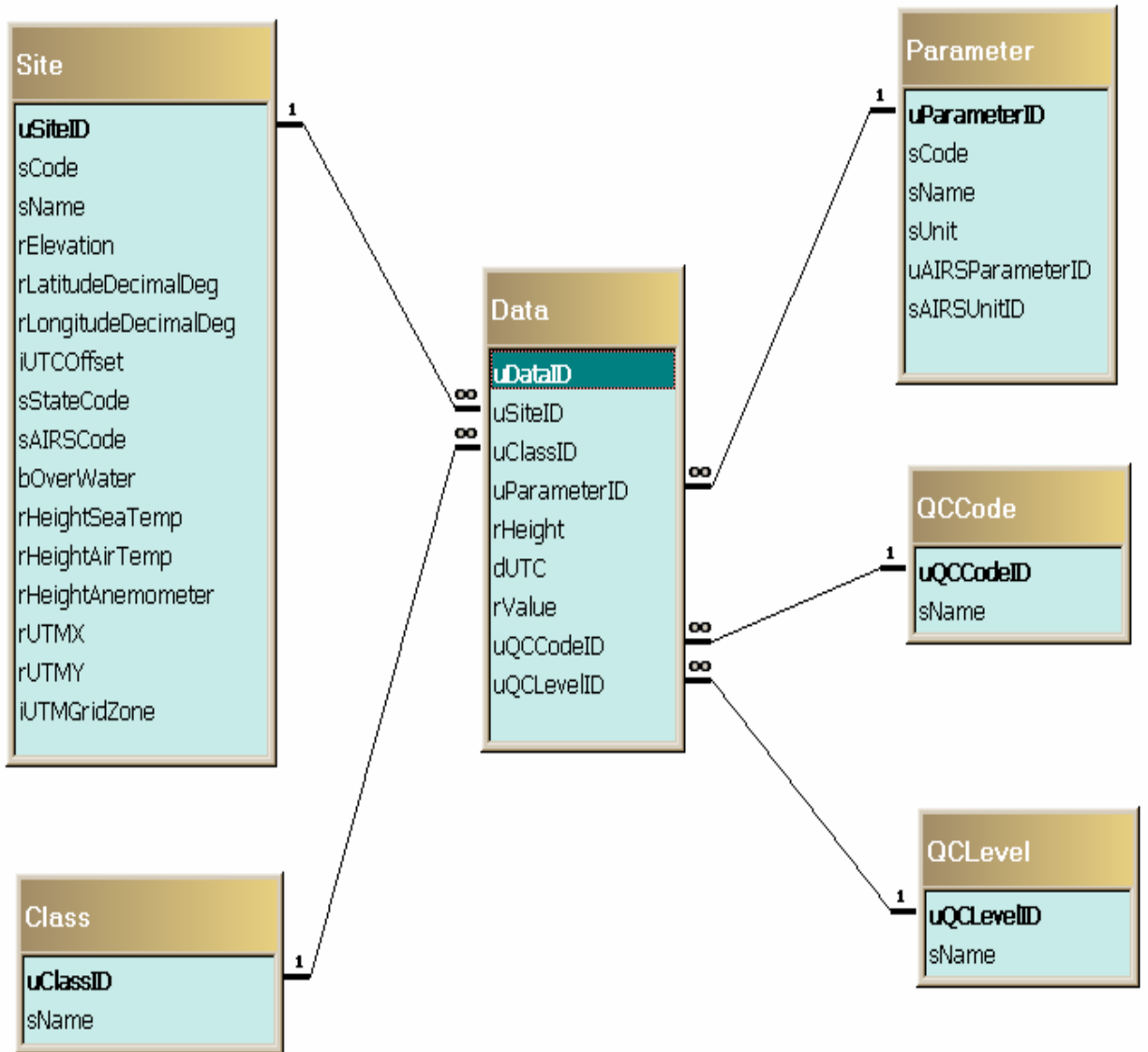
#### 1.6 Table Site

Contains information about each of the air quality monitoring sites.

Name	Type	Description	Constraints
<b><i>uSiteID</i></b>	<i>smallint</i>	<i>Surrogate PK</i>	<i>Unique auto increment integer</i>
<u>sCode</u>	varchar(50)		
<u>sName</u>	varchar(50)	Site name	
rElevation	real	Elevation of monitoring site purposes only	
rLatitudeDecimalDeg	float	Latitude of site in decimal degrees	0 to 360
rLongitudeDecimalDeg	float	Longitude of site in decimal degrees	-180 to 180
iUTCOffset	tinyint	Time zone offset of monitoring site from GMT	
sStateCode	char(2)	State Abbreviation	
<u>sAIRSCde</u>	char(9)		Candidate Key
bOverWater	bit		
rHeightSeaTemp	real		
rHeightAirTemp	real		
rHeightAnemometer	real		
rUtmX	real		
rUtmY	real		
iUTMGridZone	smallint		

## 2. EDAT DATABASE RELATIONS DIAGRAMS

Figure 1 – EDAT Database Diagram



## **APPENDIX B**

### **COARE DOCUMENTATION FROM NOAA'S FTP SITE**

Appendix B contains information about the COARE program from NOAA's ftp site at <ftp://ftp.etl.noaa.gov/et7/anonymous/cfairall/bulkalg/>

## COARE BULK AIR-SEA FLUX ALGORITHM

January 1, 2000

C. Fairall (NOAA/ERL)

E.F. Bradley (CSIRO Land and Water)

### History

In 1993, Chris Fairall, Frank Bradley and David Rogers began development of a bulk air-sea flux algorithm for use by the COARE community. Based on the model of Liu, Katsaros and Businger (1979, LKB), it took account of the light wind, strongly convective conditions over tropical oceans. **Version 1.0** was released in November 1993, and included modifications to the basic LKB code for wind roughness length (Smith, 1988), Monin-Obukhov profile functions for strong convection, and low-wind "gustiness" (Godfrey and Beljaars, 1991). **Version 2.0** (August 1994) included code to model the cool skin physics (Saunders, 1967), and also daytime near-surface warming based on a simplified version of the Price, Weller and Pinkel (1986) ocean mixing model (Fairall et al., 1996a). These optional features enable conversion from bulk to true skin temperature for calculating the fluxes. Calculation of fluxes of momentum (Caldwell and Elliott, 1971) and sensible heat (Gosnell, Fairall and Webster, 1995) due to rainfall are incorporated in the code, as is the so-called Webb correction to latent heat flux which arises from the requirement that the net dry mass flux be zero (Webb et al., 1980). The formalism of the algorithm is fully described in Fairall et al. (1996b).

The next major modifications to the algorithm were made at the COARE Air-Sea Interaction (Flux) Group Workshop in Honolulu, 2-4 August 1995 (Bradley and Weller, 1995). Transfer coefficients were adjusted by six percent to give better average agreement with covariance latent heat fluxes from several COARE ships. This produced version 2.5b, which has been used successfully on various ocean-atmosphere field campaigns by members of the Flux Group, at various locations and from a variety of platforms. At the Woods Hole workshop, 9-11 October 1996 (Bradley and Weller, 1997) it was agreed that no further development would be attempted to the community version of the COARE Bulk Flux Algorithm, and that a **version 2.5b** bulk algorithm "package" would be made available, consisting of the Fortran source code and a test data set. This was released at a meeting of the Flux Group at NCAR, 14-16 May 1997 (Bradley, Moncrieff and Weller, 1997), and was made available from the following archive sites:

1. The Florida State University COAPS (Center for Ocean Atmospheric Prediction Studies)

[http://www.coaps.fsu.edu/COARE/flux\\_algor/](http://www.coaps.fsu.edu/COARE/flux_algor/)

OR

[ftp://coaremet.fsu.edu/pub/coare/flux\\_algor/](ftp://coaremet.fsu.edu/pub/coare/flux_algor/)

2. Scripps Institution of Oceanography Physical Oceanography Research Division

<http://penarth.ucsd.edu/coare/>

OR

<ftp://penarth.ucsd.edu/coare/>

3. NCAR (National Center for Atmospheric Research) Data Support Section

<http://www.scd.ucar.edu/dss/datasets/ds606.1.html>

In December of 1999, Bradley and Fairall made available **version 2.6a** in both Fortran and matlab forms. The new version of the model has several changes that are summarized as follows:

1. The empirical constants in the convective portion of the profile functions have been changed for improved matching to direct profile observations (Grachev et al., 1999). These are referred to as `psiu_26` and `psit_26`; the original forms are referred to as `psiu_25` and `psit_25`.
2. The Kansas stable profile functions have been replaced by those from Beljaars and Holtslag (1991) which is a better fit to new profile data taken over the Arctic ice cap in the SHEBA project.
3. A fixed value of the Charnock parameter ( $\alpha=0.011$ ) has been replaced by a formulation with a simple wind-speed dependence above 12 m/s based on data from Yelland and Taylor (1996) and Hare et al. (1999).
4. The Liu et al. (1979) scalar roughness relationship [  $f_x(R_p)$  ] has been replaced with a much simpler one that fits both the COARE, several additional ETL flux data sets, and HEXMAX data base (DeCosmo et al., 1996).
5. The stability iteration loop has been reduced from 20 to 3 using bulk Richardson number parameterization for an improved first guess (Grachev and Fairall, 1997).
6. The latent heat flux has been reformulated in terms of mixing ratio,  $q$ , instead of water vapor density,  $Q$ , to eliminate the need for a Webb et al. (1980) correction. This change is not apparent in the input variables, which used mean mixing ratio (as does version 2.6). However, the original transfer coefficients were fit to the measurements of fluxes in the form  $\langle w'Q' \rangle / \rho_a$  rather than the correlation of vertical velocity with mixing ratio, because  $\langle w'Q' \rangle$  was the actual measured quantity. In the new version of the model, we have fit the transfer coefficients to  $\langle w'Q' \rangle / \rho_a + \text{Webb} = \langle w'q' \rangle$  because the mixing ratio is the quantity that is fundamentally conserved during mixing.

In January of 2000, Bradley and Fairall made available **version 2.6a** in both Fortran and matlab forms. That version of the model was described in the `coare26a_readme` file. A new edition that incorporates surface gravity wave information, **version 2.6bw**, has been produced in June 2001. We recommend using 2.6bw; there will be no further 2.6 versions. If you are not interested in the wave aspects, just set the wave switch to 0 and put in dummy numbers for the wave properties.

Version 2.6bw has three small changes relative to 2.6a in addition to the wave effects:

- (1). The `zoq` parameterization has been changed to

```
zoq=min(1.15e-4,5.5e-5/rr^.6);
```

This slightly reduces the moisture and heat transfer coefficients at low winds.

- (2) The `xlamx` parameter limit has been changed from 30 to 6 in the 'warm skin' regime to eliminate unreasonable values in very light winds.

- (3) The date is input in Y2K format (YYYY instead of YY).

It .has simple additions for waves as follows:

The data inputs have been expanded to allow three additional parameters: a switch coded 0,1, or 2 to designate the wave model used, wave period and significant wave height.

wave=0: No wave model, just use the specified Charnock parameter in the version 2.6a code.

wave=1: Use the Oost et al. (2001) wave age parameterization. In this case you must specify wave period

wave=2: Use the Taylor and Yelland (2000) wave slope/height model. In this case you must specify wave period and significant wave height.

## Description of the bulk algorithm "package"

The "package" consists of a input data, bulk algorithm program, and output data files:

### Input data

test2\_5b.dat (Test data set, with headers)

test2\_6b.txt (Test data set, without headers, Y2K)

### Programs

*cor2\_6bw.for* (Fortran source code) and *.m* (matlab source code). This is the new version 2.6b setup to use the Fairall near-surface temperature sensor for Ts bulk.

### Output files (sea surface T source X=f or h)

tst2\_6bX.out Fortran output file from test data using Charnock formula

oea2\_6bw.out Output file using the Oost et al. formula and fully developed sea

tay2\_6bw.out Output file using the Taylor and Yelland formula and fully developed sea

## Bulk algorithm program

A full description of the code and the test data set appears at the head of the Fortran file. We provide some notes here:

1. The input "read" statement is set up for the test data file test2\_5b.dat . This consists of four days of Moana Wave COARE data, 26-29 Nov 1992, prepared from Chris Fairall's hourly data file wavhr2\_5.asc dated 31/10/96. A full description of the Moana Wave operations, instruments and data set is given at

[http://www.ncdc.noaa.gov/coare/catalog/data/air\\_sea\\_fluxes/moana\\_flux.html](http://www.ncdc.noaa.gov/coare/catalog/data/air_sea_fluxes/moana_flux.html)

2. Only those observations required by the flux algorithm were extracted from Chris' lines of data, excepting that his independently calculated bulk fluxes are included for comparison.

3. Some parameters are not input, but must be redefined in the code if necessary (e.g., the height of sensors (hum, htm), the bulk temperature sensor depth (ts\_depth), needed for calculation of the warm layer effect, and pressure and mixed layer height (pp and zi) if available).

4. Because Chris' Tsea was measured at only 0.05m depth, we have added Ts at 6m depth from Mike Gregg's Advanced Microstructure Profiler (AMP, but called MSP in the file) to demonstrate the warm layer code. The Profiler was operated from the Moana Wave during leg 1, and the data was kindly provided in suitable form for the test file by Hemantha Wijesekera (Oceanography Dept., Oregon State University).

5. The warm layer and/or cool skin code may be bypassed by setting jwarm and/or jcool to zero in the code. Note that if jcool or jwarm are set to zero, then values for dt\_cool and dt\_warm are still computed and passed back by the code, but are not used in calculations of the flux.

6. To demonstrate the warm layer and cool skin, we output the respective delta-temperatures and the warm layer thickness. Note that dt\_warm is the warming across the entire warm layer--only if tk\_pwp is less than the sensor depth (ts\_depth = 6m in the test case) will  $T0=ts-dt\_cool*jcool+dt\_warm*jwarm$ . Otherwise, a linear profile is assumed, and the appropriate fraction of warming above the bulk sensor calculated. Chris' Tsea at 0.05m depth will generally include most of the warm layer but not the cool skin effect.

7. The Webb correction to latent heat flux is now included because we have adjusted the transfer coefficient to include it. Instead of the correction to the latent heat flux, the new version of the code returns the mean vertical velocity appropriate for applying the Webb correction to any measurements of scalar concentration flux. The sensible heat flux due to rainfall is NOT added internally in the code. This is output separately, and may be accounted for at the user's discretion.

We provide some notes on just the wave aspects here.

1. The Oost et al. (2001) formula has been written in the form:

$$zo=50/2/pi*lwave*(usr/cwave)^{4.5+0.11*visa/usr}$$

2. The Taylor and Yelland (2000) formula is

$$zo=1200*hwave*(hwave/lwave)^{4.5+0.11*visa/usr}$$

Note, lwave (wave length) and cwave (phase speed) are computed in the code from twave using standard deep water wave formulae. If you have shallow water, you will have to put in the depth and use the appropriate formulae.

Test input file

- 1 Date: YYYYMMDDHHmmss, YYYY=year, MM=month, DD=day, HH=hour, mm=minute,ss=sec
- 2 U: true wind speed at 15-m height m/s
- 3 Tsea: sea surface temp (at about 0.05m depth) deg.C

- 4 Tair: Vaisala air temperature (about 15 m) deg.C
- 5 qair: Vaisala air specific humidity (about 15 m) g/kg
- 6 Hsb: Fairall's original BASIC code bulk sensible heat flux W/m2
- 7 Hlb: Fairall's original BASIC code bulk latent heat flux W/m2
- 8 Taub: Fairall's original BASIC code bulk surface stress N/m2
- 9 Rs: solar irradiance W/m2
- 10 Rl: downwelling longwave irradiance W/m2
- 11 Rain: precipitation mm/hr
- 12 Lat: Latitude
- 13 Lon: Longitude
- 14 MSP: MSP temperature at 6m depth deg.C

Because the test input file does not contain wave information, we have added formulae in the master program to estimate typical wave parameters for a fully developed sea:

```
b=.729;
Twave=b*u;
hwave=0.018*u.^2.*(1+.015*u);
```

The programs are presently setup with wave=0, so no wave data is used.

Test output file

- 1 index: data line number
- 2 xtime: YYYYMMDDHHmmss, date and time as read in
- 3 hsb: Fairall's bulk sensible heat flux as read in W/m2
- 4 hlb: Fairall's bulk latent heat flux as read in W/m2
- 5 taub: Fairall's bulk surface stress as read in N/m2
- 6 ts: Bulk water temperature: MSP at 6m depth (h version) or Fairall at 0.05 m depth (f version) as read in deg.C
- 7 HF: calculated sensible heat flux W/m2
- 8 EF: calculated latent heat flux W/m2
- 9 TAU: calculated surface stress N/m2
- 10 T0: calculated sea skin temperature deg.C
- 11 Webb mean vertical velocity (2.6) m/s
- 12 RainF: sensible heat flux due to precipitation W/m2
- 13 rain: precipitation mm/hr as read in
- 14 dt\_cool: cool skin effect deg.C
- 15 dt\_warm: total warming across warm layer thickness deg.C
- 16 tk\_pwp: warm layer thickness m

## MATLAB Programs

*cor2\_5bf.m* and *cor2\_5bh.m*

Read the data, do the warm layer calculations, draw some graphs, write the new files

Calls the flux and cool skin subroutine *cor25.m*

This routine operates of the data vector

$x=[u \text{ us } ts \ t \ qs \ q \ Rs \ Rl \ rain \ zi \ P \ zu \ zt \ zq \ lat \ jcool]$

and returns a long data vector of 21 quantities described at the end of the routine.

Other subroutines used: *psiu\_25.m*, *psit\_25.m*, *qsee.m*, *grv.m*

*cor2\_6af.m* and *cor2\_6ah.m*

Read the data, do the warm layer calculations, draw some graphs, write the new files

Calls the flux and cool skin subroutine *cor26.m*

This routine operates of the data vector

$x=[u \text{ us } ts \ t \ qs \ q \ Rs \ Rl \ rain \ zi \ P \ zu \ zt \ zq \ lat \ jcool]$

and returns a long data vector of 21 quantities described at the end of the routine.

Other subroutines used: *psiu\_26.m*, *psit\_26.m*, *qsee.m*, *grv.m*

Note: if you are not interested in the warm layer, then fluxes can be computed by calling *cor25(x)* or *cor26a(x)* as a simple function.

*cor2\_6bfw.m*. This is the new version 2.6b setup to use the Fairall near-surface temperature sensor for Ts bulk.

Read the data, do the warm layer calculations, draw some graphs, write the new files

Calls the flux and cool skin subroutine *cor26w.m*

This routine operates of the data vector

$x=[u \text{ us } ts \ t \ qs \ q \ Rs \ Rl \ rain \ zi \ P \ zu \ zt \ zq \ lat \ jcool \ wave \ twave \ hwave]$

and returns a long data vector of 21 quantities described at the end of the routine. Other

subroutines used: *psiu\_26.m*, *psit\_26.m*, *qsee.m*, *grv.m*

*cor2\_6bhw.m*. This is the new version 2.6b setup to use the MSP temperature at a depth of 6 m for Ts bulk. This implies greater dependence on the warm layer code for flux calculations.

Note: if you are not interested in the warm layer, then fluxes can be computed by calling  $y=cor26bw(x)$  as a simple function.

Output files (sea surface T source  $X=f$  or  $h$ )

*tst2\_6bXw\_out.txt* Matlab output file from test data in ascii format

*tst2\_6bXw\_out.mat* Matlab output file from test data as matlab mat file

## References

Beljaars, A. C. M., and A. A. M. Holtslag, 1991: Flux parameterization over land surfaces for atmospheric models. *J. Appl. Meteor.*, **30**, 327-341.

Bradley, E.F., and R.A. Weller, 1995: Third Workshop of the TOGA COARE Air-Sea Interaction (Flux) Working Group. Honolulu, 2-4 Aug 1995. UCAR/TCIPO. UCAR Communications, PO Box 3000, Boulder CO 80307-3000 USA.

- Bradley, E.F., and R.A. Weller, 1997: Fourth Workshop of the TOGA COARE Air-Sea Interaction (Flux) Working Group. Woods Hole, 9-11 Oct 1996. UCAR/TCIPO. UCAR Communications, PO Box 3000, Boulder CO 80307-3000 USA.
- Bradley, E.F, M.W. Moncrieff and R.A. Weller, 1997: Joint workshop of the TOGA COARE Flux and Oceans Working Groups, and the GEWEX GCSS Working Group 4. Boulder, Colorado, 14-16 May 1997. NCAR/MMM, PO Box 3000, Boulder CO 80307-3000 USA.
- Caldwell, D.R. and W.H. Elliott, 1971: Surface stresses produced by rainfall. *J. Phys. Oceanog.* 1, 145-148.
- DeCosmo, J., K. B. Katsaros, S. D. Smith, R. J. Anderson, W. A. Oost, K. Bumke, and H. Chadwick, 1996: Air-sea exchange of water vapor and sensible heat: The Humidity Exchange Over the Sea (HEXOS) results. *J. Geophys. Res.*, 101, 12001-12016.
- Fairall, C.W., E.F. Bradley, J.S. Godfrey, G.A. Wick, J.B. Edson, and G.S. Young, 1996a: The cool skin and the warm layer in bulk flux calculations. *J. Geophys. Res.* 101, 1295-1308.
- Fairall, C.W., E.F. Bradley, D.P. Rogers, J.B. Edson, G.S. Young, 1996b: Bulk parameterization of air-sea fluxes for TOGA COARE. *J. Geophys. Res.* 101, 3747-3764.
- Godfrey, J.S., and Beljaars, 1991: On the turbulent fluxes of buoyancy, heat, and moisture at the air-sea interface at low wind speeds. *J. Geophys. Res.* 96, 22043-22048.
- Gosnell, R., C.W. Fairall, and P.J. Webster, 1995: The sensible heat flux of rainfall in the tropical ocean. *J. Geophys. Res.* 100, 18437-18442.
- Grachev, A.A., and C.W. Fairall, 1997: Dependence of the Monin-Obukhov stability parameter on the bulk Richardson number for unstable conditions over the ocean. *J. Appl. Meteorol.*, **36**, 406-414.
- Grachev, A. A., C. W. Fairall, and E. F. Bradley, 1999: Convective profile constants revisited. *Bound.-Layer Meteorol.*, to appear.
- Hare, J. E., P. O. G. Persson, C. W. Fairall, and J. B. Edson, 1999: Behavior of Charnock's relationship for high wind conditions. Proc. 13<sup>th</sup> Symposium of Boundary Layers and Turbulence. AMS. Dallas, TX, Jan. 15-20, paper 5B.8.
- Liu, W.T, K.B. Katsaros and J.A. Businger, 1979: Bulk parameterization of the air-sea exchange of heat and water vapor including the molecular constraints at the interface, *J. Atmos. Sci.* 36, 1722-1735.
- Price, J.F., R.A. Weller and R. Pinkel, 1986: Diurnal cycling: Observations and models of the upper ocean response to diurnal heating, cooling, and wind mixing, *J. Geophys. Res.* 91, 8411-8427.

Oost, W. A., G. J. Komen, C. M. J. Jacobs, and C. van Wort, 2001: New evidence for a relation between wind stress and wave age from measurements during ASGAMAGE. Tech. Report 2001-5, Royal Dutch Meteorological Institute (KNMI), De Bilt, The Netherlands, pp30.

Saunders, P.M., 1967: The temperature at the ocean-air interface. *J. Atmos. Sci.* 24, 269-273.

Smith, 1988: Coefficients for sea surface wind stress, heat flux, and wind profiles as a function of wind speed and temperature. *J. Geophys. Res.* 93, 15467-15472.

Taylor, P. K., and M. J. Yelland, 2000: The dependence of sea surface roughness on the height and steepness of the waves. *J. Phys. Oceanography*, **31**, 572-590.

Webb, E.K., G.I. Pearman and R. Leuning, 1980: Correction of flux measurements for density effects due to heat and water vapour transfer, *Q.J.R. Meteorol. Soc.* 106, 85-100.

Yelland, M. and P. K. Taylor, 1996: Wind stress measurements from the open ocean. *J. Phys. Oceanogr.*, **26**, 541-558.

For more information, please contact:

Chris Fairall  
NOAA/ERL/WPL  
325 Broadway  
Boulder, CO 80303 USA  
e-mail: cwf@etl.noaa.gov  
Phone: (303)497-3253  
Fax: (303)497-6101

OR

E. Frank Bradley  
CSIRO Land and Water  
GPO Box 1666  
Canberra, ACT 2601 AUSTRALIA  
e-mail: frank.bradley@cbr.clw.csiro.au  
Phone: (61) 2 6246 5575  
Fax: (61) 2 6246 5560

## **APPENDIX C**

### **COARE FORTRAN CODE**

Appendix C contains Fortran code of COARE 26bw.for that was modified for use in the MMS ABL project. This version of the COARE program was used to make estimates of fundamental boundary layer scaling parameters such as the surface roughness length,  $z_o$ , the friction velocity,  $u^*$ , the scaling temperature,  $T^*$ , the scaling water vapor mixing ratio,  $q^*$ , and the Monin-Obukhov length,  $L$  from routine surface meteorological observations in the Gulf of Mexico.

```

c $debug
c.....
c PROGRAM: bulk_v2.6
c
c 16/5/01 in San Diego. This is cor2_6aw.for with wave state options
c Made from cor2_6af.for i.e. uses Chris' SST sensor. zoq modification
c
c COARE bulk flux version 2.6a was made from 2.5b by Frank Bradley 3/12/99
c Replace 20 iterations with Grachev and Fairall first guess z/L routine
c J. App. Meteor. 36, 406-414, 1997
c
c Add Chris' mods as used in Jasmine of rr-zoq,charnock,cool skin
c
c Untangle some complexity which had crept into 2.5b
c Use separate phiu,phit functions with Grachev et al (2000) constants
c Stable functions according to Beljaars and Holtslag
c J. Appl. Meteor. 30, 327-341, 1991
c Return Webb Wbar because Webb flux correction already included in QE
c
c THIS version cor2_6af.for uses Chris' seasnake for Ts
c Another version cor2_6ah.for uses Hemantha's 6m depth MSP data for Ts
c Set up to read COARE test data set, see Bradley, Moncrieff and Weller,
c Proceedings of the COARE Flux Group workshop, May 14-16 1997,
c NCAR/MMM, PO Box 3000, Boulder, CO 80307-3000, USA
c COARE test data file is test2_5b.dat
c This routine outputs tst2_6af.out
c
c Output compared with Chris Fairall's Matlab version - OK
c.....
c input data - converted for subroutine call because of conflict with COMMON:
c xtime (COARE convention yymnddhhmmss.ssss GMT)
c zu (wind measurement height) m
c zt (T&rh measurement height) m
c zus (wind standard height) m - changes to different ref. height.
c zts (T&rh standard height) m
c ts_depth (depth of sst instrument) - positive m - for cool skin/warm layer correction
c u (wind speed relative to the sea surface) m/s
c ts (sea surface temp.) deg. C
c t (air temperature) deg. C
c q (specific humidity) g/kg or qq (RH as decimal) - code works internally in kg/kg!!
c rs (shortwave radiation) W/m2
c rl (downwelling longwave) W/m2
c rain (average rainrate in timestep) mm/hour
c p (pressure) mb; use 1008mb if data unavailable
c zi (boundary-layer depth; use 600m if data unavailable) m
c jcool (=1 for cool skin calculation; =0 if SST measured by IR radiometer)

```

```

c  jwarm (=1 for warm layer calculation; =0 if SST measured by IR radiometer)
c  xlat (latitude) degrees [latitude north +ve, latitude south -ve]
c  xlon (longitude) degrees [Longitude east +ve, longitude west -ve]
c.....
c  output:
c  QH W/m**2   (Sensible heat flux) - turbulent part only
c  QE W/m**2   (Latent heat flux) - turbulent part only
c  QR W/m**2   (Rainfall heat flux)
c  TAU N /m**2 (wind stress) - turbulent part only
c  Ustar m/s   (velocity scaling parameter - friction velocity)
c  Qstar kg/kg (humidity scaling parameter)
c  Tstar C     (temperature scaling parameter)
c  CDN - neutral drag coefficient
c  CHN - neutral transfer coefficient for heat
c  CEN - neutral transfer coefficient for moisture
c  RR - Roughness Reynolds number
c  RT - Roughness Reynolds number for temperature
c  RQ - Roughness Reynolds number for moisture
c  ZL - height/L where L is the Obukhov length
c  Z0 - roughness length
c  zot - roughness length for temperature
c  zoq - roughness length for humidity
c  dt_wrm - total warm layer temperature difference C
c  tk_pwp - thickness of warm layer
c  dter - cool skin temperature difference C
c  T0 - skin temperature C (T0 = sst - dter + dt_wrm*ts_depth/tk_pwp)
c  wg - gustiness factor m/s
c  Taur - momentum flux due to rain N/m**2
c  Wbar - Webb mean vertical velocity m/s
c
c  program fluxes
c  real*8 ws_h,Ta_h,qq_h
c  real*8 zu,zt,zus,zts,u,ts,t,q,p,zi,rain,xlat,xlon,tt
c  real*8 QH,QE,TAU,Ustar,Qstar,Tstar
c  real*8 rl,rs,QR,T0,ts_depth,wg
c  real*8 CDN,CEN,CHN,RR,RT,RQ,ZL
c  real*8 Zo,zot,zoq,dt_wrm,dter,S
c  real*8 Wbar,Tau_r,glat
c  real*8 time_old,qcol_ac,tau_ac,tau_old,rf_old,hf_old,ef_old
c  real*8 intime,sol_time,tk_pwp,fxp,Tsin
c  real*8 hwave,twave
c  integer hh,yy,dd,ss
c
c  real*8 HEeta0612,HEeta1824
c  real*8 HEeta3036,HEeta4248

```

real\*8 HSeta0612,HSeta1824  
real\*8 HSeta3036,HSeta4248

real\*8 Fricveta0612,Fricveta1824  
real\*8 Fricveta3036,Fricveta4248

real\*8 Lowcloud,Midcloud,Highcloud

Integer Heflag0612  
Integer Heflag1824,Heflag3036  
Integer Heflag4248

Integer HSflag0612,HSflag1824  
Integer HSflag3036,HSflag4248  
Integer Fricvflag0612,Fricvflag1824  
Integer Fricvflag3036, Fricvflag4248

Integer Lowflag,Midflag,Highflag  
Integer shortflag,longflag

integer Uflag,tsflag,tflag,qflag  
integer rsflag,rflag, rainflag, xlatflag  
integer xlonflag, pflag, ziflag,outflag,hwaveflag,twaveflag

character\*17 chtime  
character\*12 xtime  
character\*5 site

COMMON /old/time\_old,qcol\_ac,tau\_ac,tau\_old,rf\_old,hf\_old,  
& ef\_old,jamset,jump,fxp,tk\_pwp,index

c

c initialize variables

qcol\_ac=0.  
tau\_ac=0.  
time\_old=0.  
jamset=0.  
tau\_old=0.  
hf\_old=0.  
ef\_old=0.  
rf\_old=0.  
jamset=0  
jump=0

c

c

```

open (unit=15,file='config.dat') !info on tdepth,jwarm,jcool
open(unit=3,file='indata.dat') ! original coare2.5b input data
open(unit=9,file='coare.out') ! output file from this program
c   open(unit=10,file='exch2_6c.out') ! CDN,CHN and CEN from this program
c
write(9,500)
c ADD variables (MMS)
500 format('SITE xtime xlat xlon
1 t tflag q qflag u uflag ts tsflag tsin tsflag
1 rs shortflag rl longflag p pflag Zi Ziflag
& outflag QH QE TAU T0 rain rainflag dter dt_wrm tk_pwp
& ZL RR ZO ustar tstar qstar
1 Fricveta0612 Fricvflag0612 Fricveta1824 Fricvflag1824
1 Fricveta3036 Fricvflag3036 Fricveta4248 Fricvflag4248
1 Heeta0612 Heflag0612 Heeta1824 Heflag1824
1 Heeta3036 Heflag3036 Heeta4248 Heflag4248
1 HSeta0612 HSflag0612 HSeta1824 HSflag1824
1 HSeta3036 HSflag3036 HSeta4248 HSflag4248
1 lowcloud lowflag midcloud midflag highcloud highflag')

c
c Sensor heights zu and zt and ts_depth to be read in from indata (MMS)
c
c   zu=15.           !height of wind measurement
c   zt=15.           !height of air temp. and RH
c   zus=10.          !10m standard levels
c   zts=10.
c   ts_depth=0.05    !Chris Fairall's floating sensor
c   ts_depth=0.45    !from IMET buoy
c   ts_depth=6.0     !Hemantha's 6m data
c
c default values for pressure and mixed layer height
c read in from input file instead
c   p=1008.
c   zi=600.
c
c initial guesses to the warm layer parameters, these values simulate what is expected
c in early morning: fxp=0.5 implies a shallow heating layer to start the integration;
c tk_pwp=19.0 implies the thickness is a maximum from the day before and is not meant to
c match this timestep's fxp.
c   fxp=0.5
c   tk_pwp=19.0

c   if SST sensed by IR radiometer, set jwarm and jcool to zero
c read in config (MMS)
c   jwarm=1 (MMS readin)

```

```

c   jcool=1 (MMS readin)
c   jwave=1 ! (MMS readin) 0=Charnock,1=Oost et al,2=Taylor and Yelland. Also choose
output file name
    READ (15,505)ADUM      ! READ IN CONFIG HEADER
    READ (15,431)ZU,ZT,TS_DEPTH,JCOOL,JWARM,jwave !READ IN
JCOOL,JWARM,TS_DEPTH
    print *, ZU,ZT,TS_DEPTH,JCOOL,JWARM,jwave
431  FORMAT (F4.1,1X,F4.1,1X,F4.2,1X,I1,1X,I1,1X,I1)

c loop through data
c
    index=0
    READ(3,505)ADUM      ! skip header line of test data
c   READ(4,505)ADUM      ! skip header line of test output data
505  FORMAT(A1)
    do ijk=1,1000000 !start of loop
    index=index+1      !count data records (hours)
c
c Read in data where Ts is either skin or underwater. If underwater Jcool and Jwarm = 1

700  READ (3,705,end=910) site,xtime,u,uflag,ts,tsflag,
    1  t,tflag, q,qflag,rs,shortflag,
    1  rl,longflag,
    1  rain,rainflag,xlat,xlon,
    1  p,pflag,zi, ziflag,
    1  Fricveta0612, Fricvflag0612,
    1  Fricveta1824, Fricvflag1824,
    1  Fricveta3036, Fricvflag3036,
    1  Fricveta4248, Fricvflag4248,
    1  Heeta0612, Heflag0612,
    1  Heeta1824, Heflag1824,
    1  Heeta3036, Heflag3036,
    1  Heeta4248, Heflag4248,
    1  HSeta0612, HSflag0612,
    1  HSeta1824, HSflag1824,
    1  HSeta3036, HSflag3036,
    1  HSeta4248, HSflag4248,
    1  lowcloud, lowflag,
    1  midcloud, midflag,
    1  highcloud, highflag,
    1  hwave, hwaveflag,
    1  twave, twaveflag

```

```

705  FORMAT(a5,1x,a12,3x,3(F9.1,3x,i1,3x),F11.3,3x,i1,3x,
1    3(F9.1,3x,i1,3x),2(F8.2,4x),f9.1,3x,i1,3x,f9.0,3x,i1,3x
1    4(f10.5,3x,i1,3x),8(f9.2,3x,i1,3x),3(f6.2,3x,i1,3x),
1    2(f7.1,3x,i1,3x)) !wave formats

```

c Set ts orig so can see warm and cool effect

```
tsin=ts
```

c

c set u=.1 and hwave to .1 and twave to 7 when 0 to avoid crash

```
if (u .eq. 0.) then
```

```
u=0.1
```

```
endif
```

```
if (hwave .eq. 0.) then
```

```
hwave=0.1
```

```
endif
```

```
if (twave .eq. 0.) then
```

```
twave=1
```

```
endif
```

c IF pressure is missing and read in as -999. set pp=1008. (MMS)

```
if (p .lt. 0.) then
```

```
p=1008.
```

```
endif
```

c IF mixing height is missing and read in as -999. set zi=600. (MMS)

```
if (zi .lt. 0.) then
```

```
zi=600.
```

```
endif
```

c

c

```
glat=xlat
```

c check warm layer, cool skin switches

c

```
if(Jwarm.gt.0) then
```

```
if(index.eq.1) then
```

```
  Jwarm=2
```

```
else
```

```
  Jwarm=1
```

```

        endif
    endif
c
c convert time to decimal hours (e.g. yymn ddhhmmss -> hh. hhhh)
c
        read(xtime,12) yy,mn,dd,hh,mm,ss
12    format(6i2)

        intime=(float(hh)+float(mm)/60.+float(ss)/3600.) !eg 18.4833

c
c and convert to local solar time in seconds xlon/15 is UTC offset = 6.12
c ex. intime=00 leaves 6.12*3600 = 22032 for lon=90.10
c seconds past midnight
        sol_time=mod(xlon/15+intime+24.,24.)*3600. !eg 17580
c

c Set dummy values when -999 so program continues to run (MMS)
c set flags
c set outflag =8, leave uflag =9 etc
        outflag=0
        if (u .lt. 0.) then
            u=3.
            outflag=8
        endif

        if (t .lt. 0.) then
            t=30.
            outflag=8
        endif

        if (ts .lt. 0.) then
            ts=31.
            outflag=8
        endif

        if (q .lt. 0.) then
            q=.80
            outflag=8
        endif
c c default values for wave height and period for equilibrium sea
        if (hwave.eq.-999.) then
            hwave=0.018*u*u*(1+.015*u)
            hwave=max(hwave,.1) !Set minimum hwave to .1 CPM 7/4/2002

```

```
hwaveflag=2
endif
```

```
if (twave.eq.-999.) then
twave=0.729*u
twave=max(twave,1)    !Set minimum twave to 1 CPM 7/4/200
twaveflag=2
endif
```

```
c  set dummy's for missing rs and rl only if warm effect ie jwarm=1
if (jwarm .gt. 0 .and. rs .eq. -999.) then
  temptime=sol_time*3600
  if (sol_time .lt. 21600. .or. sol_time .gt. 64800)then
    rs = 0.
    rl=400.
  else
    rs =sin((3.14/2)*(sol_time/3600-6)/6)*1380
    rl=400.
  endif
  if (outflag .ne. 8) then !set outflag to 7 if jwarm is on, all obs available, but rs estimated
  outflag =7
endif
```

```
endif
```

```
c  Set flag=3 for COARE calculated parmeters if from interpolated data i.e input flag=3
```

```
c  But if rs estimated and data interp flag=6
```

```
c
```

```
if (tflag .eq. 3 .or. qflag .eq. 3 .or. uflag .eq. 3
1   .or. tsflag .eq. 3) then
```

```
  if (outflag .eq. 7) then    ! But if rs estimated and data interp flag=6
    outflag=6
  endif
```

```
  if (outflag .eq. 8 .or. outflag .eq. 6) then    ! Don't want to reset to 3 if rs is dummy and
jwarm is on                                     !
```

```
    goto 2333
```

```
  else
```

```
    outflag=3
```

```
  endif
```

```
2333 continue
```

```
endif
```

```

c
c call bulk flux routine
c
    call bulk_flux(sol_time,xlat,zu,zt,zus,zts,Jwave,hwave,twave,
& u,ts,t,q,ws_h,Ta_h,qq_h,rs,rl,rain,p,zi,Jcool,Jwarm,
& QH,QE,QR,TAU,Ustar,Tstar,Qstar,
& CDN,CHN,CEN,RR,RT,RQ,ZL,Zo,zot,zoq,S,
& dt_wrm,dter,T0,ts_depth,wg,TAU_r,Wbar)
c output results
c
    write(9,200)SITE,xtime,xlat,xlon,
1 t,tflag,q,qflag,u,uflag,ts,tsflag,tsin,tsflag,
1 rs,shortflag,rl,longflag, p,pflag ,Zi,Ziflag,
& outflag,QH,QE,TAU,T0,rain,rainflag,dter,dt_wrm,tk_pwp,
& ZL,RR,ZO,ustar,tstar,qstar,
1 Fricveta0612, Fricvflag0612,
1 Fricveta1824, Fricvflag1824,
1 Fricveta3036, Fricvflag3036,
1 Fricveta4248, Fricvflag4248,
1 Heeta0612, Heflag0612,
1 Heeta1824, Heflag1824,
1 Heeta3036, Heflag3036,
1 Heeta4248, Heflag4248,
1 HSeta0612, HSflag0612,
1 HSeta1824, HSflag1824,
1 HSeta3036, HSflag3036,
1 HSeta4248, HSflag4248,
1 lowcloud, lowflag,
1 midcloud, midflag,
1 highcloud, highflag,
1 hwave, hwaveflag,
1 twave, twaveflag

200 format(A5,a16,2(f8.2),9(f9.2,1x,i1,1x),i1,1x
1 2(f11.1),f11.4,f11.2,f9.2,1x,i1,1x,4(f11.2),5(f14.7),
1 3x,4(f10.5,3x,i1,3x),8(f9.2,3x,i1,3x),3(f6.2,3x,i1,3x),
1 2(f6.1,3x,i1,3x)) !wave formats
c
c the following write is useful to monitor various other outputs of interest
c write(10,202)index,u,cdn,chn,cen !to check with Chris' figures
c202 format(i4,2x,f7.2,3(1pe10.2)) !take care p affects everything following

    write(*,*) index
c

```

```

        enddo          !return to beginning of loop
910 continue
c
c end of loop
c
    stop
    end
c
c*****
    subroutine bulk_flux(sol_time,glat,zux,ztx,zusx,ztsx,Jwave,hwavex,
& twavex,ux,tsx,tx,qx,U_hs,T_hs,Q_hs,rs,rl,rainx,px,zix,Jcool,
& Jwarm,HF,EF,RF,TAU,Ustar,Tstar,Qstar,
& CD,CH,CE,RRx,RTx,RQx,ZLx,ZOx,zotx,zoqx,S,
& dt_wrmx,dterx,T0,ts_depthx,wgx,TAU_r,Wbar)
c
    real*8 zux,ztx,zusx,ztsx,U_hs,T_hs,Q_hs,ts_depthx
    real*8 ZU,ZT,ZQ,ZUs,ZTs,ZQs,glat
    real*8 ux,tsx,tx,qx,rainx,px,zix,wgx
    real*8 U,TS,QS,T,Q,rl,rs,rain,p,zi,QA,S,DU_Wg,Wg,Wbar
    real*8 HF,EF,TAU,RF,Ustar,Qstar,Tstar,TAU_r,ef_webb
    real*8 CD,CE,CH,USR,TSR,QSR
    real*8 Zox,zotx,zoqx,RRx,RTx,RQx,Zlx
    real*8 ZO,zot,zoq,RR,RT,RQ,RI,zL
    real*8 T0,ee,rns,rnl
c various constants
    real*8 al,beta,cpa,cpw,grav,xlv,rhoa,rhow,rgas,toK,visa
    real*8 visw,von,fdg
c rain heat variables
    real*8 alfac,dqs_dt,dwat,dtmp
c warm layer variables
    real*8 sol_time,newtime,time_old,ctd1,ctd2,rich
    real*8 qcol_ac,tau_ac,tau_old,rf_old,hf_old,ef_old
    real*8 fxp,tk_pwp,dsea,dt_wrmx,dterx,qjoule,qr_out,dtime
    real*8 dt_wrm,dter,dqer,tk
    real*8 hwave,twave,hwavex,twavex
c
    COMMON /old/time_old,qcol_ac,tau_ac,tau_old,rf_old,hf_old,
&      ef_old,jamset,jump,fxp,tk_pwp,index
    COMMON/PIN/U,T,Q,TS,QS,rns,rnl,ZU,ZT,ZQ,zi,P,ID
    COMMON/POUT/USR,TSR,QSR,ZO,zot,zoq,ZL,RR,RT,RQ,RI,
&      dter,dqer,tk,DU_Wg,Wg
    COMMON/const/al,beta,cpa,cpw,grav,xlv,rhoa,rhow,rgas,toK,
&      visa,visw,von,fdg
    COMMON/wave/hwave,twave      ! pass to ASL
c
    Data dt_wrm /0.d0/          !set undefined variable to zero

```

```
Data RTdefault /0.d0/
Data RQdefault /0.d0/
RT=RTdefault
RQ=RQdefault
```

```
c
c convert back variables that appear in COMMON
```

```
c
ZU=zux      !height of wind measurement
ZT=ztx      !height of temperature measurement
ZQ=ztq      !height of water vapor measurement
ZUs=zusx    !standard height of wind measurement
ZTs=ztsx    !standard height of temperature measurement
ZQs=ztsx    !standard height of water vapor measurement
U=ux        !wind speed m/s
TS=tsx      !surface temp. Celsius
T=tx        !air temp. Celsius
q=qx
P=px        !pressure mb
zi=zix      !atmospheric boundary layer depth
hwave=hwavex
twave=twavex
```

```
c
toK=273.16
Rnl= 0.97*(5.67e-8*(TS+toK)**4-r1)  !Net longwave (up = +)
Rns=0.945*rs                        !Net shortwave (into water)
rain=rainx                          !rainfall
ts_depth=ts_depthx                 !depth of sst measurement
call gravity(glat,grav)
```

```
c  grav=9.72  ! gravity equatorial value (ref. IGPP-SIO)
```

```
c
c Warm Layer
```

```
c
if(Jwarm.ne.0) then
  newtime=sol_time                !run time in secs JUMP=1 first go or missing chunk of data
  if(Jwarm.eq.2) then              !jwarm=2 for first run need to set dt_wrm to 0.0
    jump=1
    goto 16                        !set time_old and pass thru' ASL
  elseif(newtime.gt.21600.and.jump.eq.1) then
    goto 16                        !6 am too late to start
  elseif(newtime.lt.time_old) then !reset all var. at midnight
    jump=0                          !test threshold q morning only
    jamset=0
    fxp=0.5
    tk_pwp=19.0
    tau_ac=0.0
    qcol_ac=0.0
```

```

dt_wrm=0.0
goto 16
else
rich=.65                !critical Rich. No.
ctd1=sqrt(2*rich*cpw/(al*grav*rhow))    !u^2 integrated so
ctd2=sqrt(2*al*grav/(rich*rhow))/(cpw**1.5) !has /rhow in both
dtime=newtime-time_old    !delta time
qr_out=rnl+hf_old+ef_old+rf    !flux out from previous pass
q_pwp=fxp*rns-qr_out    !effective net warming
if(q_pwp.lt.50.and.jamset.eq.0) go to 16    !integration threshold
jamset=1
tau_ac=tau_ac+(max(tau_old,.001)*dtime)    !tau from previous pass CPM ADD
minimum stress .002 to prevent dt_wrm blowup
c
if(qcol_ac+q_pwp*dtime.gt.0) then
do 10 iter1=1,5    !iterate for warm layer thickness
fxp=1.-(0.28*0.014*(1-dexp(-tk_pwp/0.014))    !
&    +0.27*0.357*(1-dexp(-tk_pwp/0.357))    !
&    +.45*12.82*(1-dexp(-tk_pwp/12.82)))/tk_pwp    !solar absorb. prof
qjoule=(fxp*rns-qr_out)*dtime
if((qcol_ac+qjoule.gt.0.0))
&    tk_pwp=min(19,ctd1*tau_ac/sqrt(qcol_ac+qjoule))
10 continue
else
fxp=.76
tk_pwp=19
qjoule=(fxp*rns-qr_out)*dtime
endif
c
qcol_ac=qcol_ac+qjoule    !integrate heat input
if(qcol_ac.gt.0) then
dt_wrm=ctd2*(qcol_ac)**1.5/tau_ac    !pwp model warming
else
dt_wrm=0.
endif
endif
if(tk_pwp.lt.ts_depth) then    !sensor deeper than pwp layer
dsea=dt_wrm    !all warming must be added to ts
else    !warming deeper than sensor
dsea=dt_wrm*ts_depth/tk_pwp    !assume linear temperature profile
endif
ts=ts+dsea    !add warming above sensor for new ts
16 time_old=newtime
endif
c
c end of warm layer

```

```

c
15 call humidity(T,P,QA)      !Teten's formula returns sat. air in mb
if(q.lt.2.) then            !checks whether humidity in g/Kg or RH
  R=q
  ee=QA*R                    !convert from RH using vapour pressure
  Q=.62197*(ee/(P-0.378*ee)) !Spec. humidity kg/kg
else
  Q=q/1000.                  !g/kg to kg/kg
endif
QA=.62197*(QA/(P-0.378*QA)) !convert from mb to spec. humidity kg/kg
call humidity(TS,P,QS)      !sea QS returned in mb
QS=QS*0.98                  !reduced for salinity Kraus 1972 p. 46
QS=.62197*(QS/(P-0.378*QS)) !convert from mb to spec. humidity kg/kg
Rnl= 0.97*(5.67e-8*(TS+toK)**4-rl) !Recompute net longwave (up = +)
c
c calculate atmospheric surface layer
c
  call ASL(Jcool,Jwave,IER,index) ! pass Jwave option
  if(IER.ge.0) then
c
c compute surface stress (TAU), sensible heat flux (HF),
c latent heat flux (EF) & other parameters
c
  S=sqrt(u*u + wg*wg)        !velocity incl. gustiness param.
  TAU=rhoa*USR*usr*u/S       !kinematic units
  HF=-cpa*rhoa*USR*TSR
  EF=-xlv*rhoa*USR*QSR
  tau_old=tau
  ef_old=ef
  hf_old=hf
c compute heat flux due to rainfall
  dwat=2.11e-5*((T+toK)/toK)**1.94      !water vapour diffusivity
  dtmp=(1.+3.309e-3*T-1.44e-6*T*T)*0.02411/(rhoa*cpa) !heat diffusivity
  dq_s_dt=QA*xlv/(rgas*(T+toK)**2)      !Clausius-Clapeyron
  alfac= 1/(1+0.622*(dq_s_dt*xlv*dwat)/(cpa*dtmp)) !wet bulb factor
  RF= rain*alfac*cpw*((TS-T-dter*jcool)+(QS-Q-dqer)*xlv/cpa)/3600.
c compute momentum flux due to rainfall
  TAU_r=0.85*rain/3600*u
c Webb correction to latent heat flux already in EF via zoq/rr function so return Wbar
  Wbar=-1.61*usr*qsr/(1+1.61*q)-usr*tsr/(T+toK)
c compute transfer coefficients
c  CD=(USR/S)**2
c  CH=USR*TSR/(S*(T-TS+.0098*zt+dter*jcool)) !revise 2e to 2f to include '+dter'
c  CE=USR*QSR/(S*(Q-QS+dqer))
c compute neutral transfer coefficients and met variables at standard height
  CD=(0.4/dlog(zus/zo))**2

```

```

CH=0.4*0.4/(dlog(zus/zo)*dlog(zts/zot))
CE=0.4*0.4/(dlog(zus/zo)*dlog(zqs/zoq))
T0=ts-dter*jcool
ihumid=0
c Bypass attempt to accommodate q as RH. Don't have time to fix it. Bradley
c   if(q .lt. 2) ihumid=1
   call h_adjust(ZUs,ZTs,ZQs,U_hs,T_hs,Q_hs,ihumid)
c   ws_h=U_hs
c   Ta_h=T_hs
c   qq_h=Q_hs
c Convert a few things back to pass through parameter list
  dterx=dter      !cool skin parameters
  tktx=tkt
  dt_wrmx=dt_wrm    !warm layer parameter
  Ustar=USR
  Tstar=TSR
  Qstar=QSR
  RRx=RR
  RTx=RT
  RQx=RQ
  ZLx=ZL
  Zox=Zo
  zotx=zot
  zoqx=zoq
  wgx=wg
else      !input parameters out of range
  EF=-999.
  HF=-999.
  TAU=-999.
  TAUr=-999.
  EF_webb=-999.
  Ustar=-999.
  Tstar=-999.
  Qstar=-999.
  RRx=-999.
  RTx=-999.
  RQx=-999.
  ZLx=-999.
  ZOx=-999.
  ws_h=-999.
  Ta_h=-999.
  qq_h=-999.
  wg=-999.
endif
return    !return to main program
end

```

```

c
c -----
c      subroutine ASL(Jcool,Jwave,IER,index)
c
c      TO EVALUATE SURFACE FLUXES, SURFACE ROUGHNESS AND STABILITY OF
c      THE ATMOSPHERIC SURFACE LAYER FROM BULK PARAMETERS BASED ON
c      LIU ET AL. (79) JAS 36 1722-1735
c
c      real*8 U,T,Q,TS,QS,rms,rnl,ZU,ZT,ZQ,zi,P,DU_Wg,Wg
c      real*8 USR,TSR,QSR,Zo,zot,zoq,ZL,RR,RT,RQ,RI,zetu,L10,L,zet
c constants
c      real*8 al,beta,cpa,cpw,grav,xlv,rhoa,rhow,rgas,toK,visa
c      real*8 visw,von,fdg,charn,psiu,psit
c cool skin quantities
c      real*8 wetc,bigc,be,cpv,dq,dt,dter,dqer,tkf,Bf,tew
c      real*8 hsb,hlb,alq,qcol,qout,dels,xlamx,pr,du,ta
c Grachev and Fairall variables
c      real*8 u10,zo10,cd10,ch10,ct10,zot10,cd,ct,cc,ribcu,ribu
c      real*8 hwave,twave,cwave,lwave,twopi
c
c      COMMON/PIN/U,T,Q,TS,QS,rms,rnl,ZU,ZT,ZQ,zi,P,ID
c      COMMON/POUT/USR,TSR,QSR,ZO,zot,zoq,ZL,RR,RT,RQ,RI,
c      &      dter,dqer,tkf,DU_Wg,Wg
c      COMMON/const/al,beta,cpa,cpw,grav,xlv,rhoa,rhow,rgas,toK,
c      &      visa,visw,von,fdg
c      COMMON/wave/hwave,twave
c Factors
c      Beta=1.2      !Given as 1.25 in Fairall et al.(1996)
c      Von=0.4      ! von Karman's "constant"
c      fdg=1.00     ! Fairall's LKB rr to von karman adjustment
c      fdg=1.00     !based on results from Flux workshop August 1995
c      toK=273.16  ! Celsius to Kelvin
c      twopi=3.14159*2.
c
c Air constants and coefficients
c      Rgas=287.1      !J/kg/K   gas const. dry air
c      xlv=(2.501-0.00237*TS)*1e+6 !J/kg latent heat of vaporization at TS
c      Cpa=1004.67     !J/kg/K specific heat of dry air (Businger 1982)
c      Cpv=Cpa*(1+0.84*Q) !Moist air - currently not used (Businger 1982)
c      rhoa=P*100./(Rgas*(T+toK)*(1+.61*Q)) !kg/m3 Moist air density ( " )
c      visa=1.326e-5*(1+6.542e-3*T+8.301e-6*T*T-4.84e-9*T*T*T) !m2/s
c      !Kinematic viscosity of dry air - Andreas (1989) CRREL Rep. 89-11
c
c
c Cool skin constants
c      al=2.1e-5*(ts+3.2)**0.79 !water thermal expansion coefft.
c      be=0.026                !salinity expansion coefft.

```

```

cpw=4000.          !J/kg/K specific heat water
rhow=1022.         !kg/m3 density water
visw=1.e-6        !m2/s kinematic viscosity water
tcw=0.6           !W/m/K Thermal conductivity water
bigc=16.*grav*cpw*(rhow*visw)**3/(tcw*tcw*rhoa*rhoa)
wetc=0.622*xlv*QS/(rgas*(TS+toK)**2) !correction for dq;slope of sat. vap.
c
c Wave parameters
  cwave=grav*twave/twopi
  lwave=cwave*twave
c
c Initial guesses
c
  IER=0
  Dter=0.3*jcool   !cool skin Dt
  Dqer=0.          !cool skin Dq
  Zo=0.0001
  Wg=0.5          !Gustiness factor initial guess
  tkt= 0.001      ! Cool skin thickness first guess
  DU=U            !assumes U is measured rel. to current
  DU_Wg=(DU**2.+Wg**2. )**0.5 !include gustiness in wind spd. difference
                          !equivalent to S in definition of fluxes
  DT=Ts-T-0.0098*zt !potential temperature diff. Changed sign
  DQ=Qs-Q         ! from Coar2_5b
c
c ***** neutral coefficients *****
c
  u10=DU_Wg*dlog(10/Zo)/dlog(zu/Zo)
  usr=0.035*u10
  zo10=0.011*usr*usr/grav+0.11*visa/usr
  Cd10=(von/dlog(10/zo10))**2
  Ch10=0.00115
  Ct10=Ch10/sqrt(Cd10)
  zot10=10/dexp(von/Ct10)
  Cd=(von/dlog(zu/zo10))**2
c
c ***** Grachev and Fairall (JAM, 1997) *****
c
  Ct=von/dlog(zt/zot10) ! Temperature transfer coefficient
  CC=von*Ct/Cd         ! z/L vs Rib linear coefficient
  Ribcu=-zu/(zi*0.004*Beta**3) ! Saturation or plateau Rib
  TA=T+toK
  Ribu=-grav*zu*((DT-dter)+0.61*TA*DQ)/(TA*DU_Wg**2)
  if (Ribu.lt.0.) then
    zetu=CC*Ribu/(1+Ribu/Ribcu) ! Unstable G and F
  else

```

```

    zetu=CC*Ribu*(1+27/9*Ribu/CC) ! Stable, Chris forgets origin
endif
L10=zu/zetu ! MO length
thing=psiu(zetu)
if (zetu.gt.50) then
  nits=1
else
  nits=3 ! number of iterations
endif
c
c ***** First guess stability dependent scaling params. *****
c
  usr= DU_Wg*von/(dlog(zu/zo10)-psiu(zu/L10))
  tsr=-(DT-dter)*von*fdg/(dlog(zt/zot10)-psit(zt/L10))
  qsr=-(DQ-wetc*dter)*von*fdg/(dlog(zq/zot10)-psit(zq/L10))
c
  charn=0.011 !then modify Charnock for high wind speeds Chris' data
  if(DU_Wg.gt.10) charn=0.011+(0.018-0.011)*(DU_Wg-10)/(18-10)
  if(DU_Wg.gt.18) charn=0.018
c
c ***** bulk loop *****
c
  do 10 iter=1,nits
    zet= von*grav*zu/ta*(tsr+0.61*ta*qsr)/(usr*usr)
    ZL=zet
    if(Jwave.eq.0) then
      zo=charn*USR*USR/grav + 0.11*visa/usr !after Smith 1988
    else if(Jwave.eq.1) then
      zo=(50./twopi)*lwave*(usr/cwave)**4.5+0.11*visa/usr !Oost et al.
    else if(Jwave.eq.2) then
      zo=1200.*hwave*(hwave/lwave)**4.5+0.11*visa/usr !Taylor and Yelland
    endif
    rr=zo*usr/visa
c
c *** zoq and zot fitted to results from several Chris cruises *****
c
  zoq=min(1.15e-4,5.5e-5/rr**0.6) !was 0.63, changed 15/05/01
  zot=zoq
c
  L=zu/zet
  psu=psiu(zu/L)
  pst=psit(zt/L)
  usr=DU_Wg*von/(dlog(zu/zo)-psiu(zu/L))
  tsr=-(DT-dter*jcool)*von*fdg/(dlog(zt/zot)-psit(zt/L))
  qsr=-(DQ-wetc*dter*jcool)*von*fdg/(dlog(zq/zoq)-psit(zq/L))
  Bf=-grav/ta*usr*(tsr+0.61*ta*qsr)

```

```

if (Bf.gt.0) then
  Wg=Beta*(Bf*zi)**.333
else
  Wg=0.2
endif
c
c ***** break into coare2.5b code again *****
c
  DU_Wg=sqrt(DU**2.+Wg**2.)      !include gustiness in wind spd.
  hsb=-rhoa*cpa*usr*tsr
  hlb=-rhoa*xlv*usr*qsr
  qout=rnl+hsb+hlb
  dels=rns*(.06+11*tkl-6.6e-5/tkl*(1-dexp(-tkl/8.0e-4))) ! Eq.16 changed .137 to .060
CPM from CF 7/3/02
  qcol=qout-dels
  alq=A1*qcol+be*hlb*cpw/xlv      !Eq. 7 Buoy flux water
  if(alq.gt.0) then                !originally (qcol.gt.0)
    xlamx=6/(1+(bigc*alq/usr**4)**.75)**.333 !Eq 13 Saunders coeff.
  else
    pr=bigc*abs(alq)/usr**4        !new from Chris
    if(pr.lt.1) then
      xlamx=6/(1-pr**.75)**.333    !Eq 13 Saunders coeff.
    else
      xlamx=6.                    !was 30 - caused excessive warm skins
    endif
  endif
  tkt=xlamx*visw/(sqrt(rhoa/rhow)*usr) ! Eq.11 Sublayer thickness
  dter=qcol*tkl/tcw                ! Eq.12 Cool skin
  dqer=wetc*dter
10 continue      ! end Chris iterations
c
  idum=index      ! avoids warning on compilation
  return          !to main subroutine, bulk_flux
end
c
c-----
subroutine humidity(T,P,Qsat)
c
c Tetens' formula for saturation vp Buck(1981) JAM 20, 1527-1532
c
  real*8 T,P,Qsat
c
  Qsat = (1.0007+3.46e-6*P)*6.1121*dexp(17.502*T/(240.97+T))
  return
end
c

```

```

c-----
function psiu(zL)
c
c psiu and psit evaluate stability function for wind speed and scalars
c matching Kansas and free convection forms with weighting f
c convective form follows Fairall et al (1996) with profile constants
c from Grachev et al (2000) BLM
c stable form from Beljaars and Holtslag (1991)
c
real*8 zL,x,y,psik,psic,f,psiu,c
if(zL.lt.0) then
  x=(1-15.*zL)**.25          !Kansas unstable
  psik=2.*dlog((1.+x)/2.)+dlog((1.+x*x)/2.)-2.*atan(x)+2.*atan(1.)
  y=(1.-10.15*zL)**.3333    !Convective
  psic=1.5*dlog((1.+y+y*y)/3.)-sqrt(3.)*atan((1.+2.*y)/sqrt(3.))
&   +4.*atan(1.)/sqrt(3.)
  f=zL*zL/(1.+zL*zL)
  psiu=(1.-f)*psik+f*psic
else
  c=min(50.,0.35*zL)        !Stable
  psiu=-((1.+1.*zL)**1.+0.6667*(zL-14.28)/dexp(c)+8.525)
endif
return
end

```

```

c-----
function psit(zL)
real*8 zL,x,y,psik,psic,f,psit,c
if(zL.lt.0) then
  x=(1-15.*zL)**.5          !Kansas unstable
  psik=2.*dlog((1.+x)/2.)
  y=(1.-34.15*zL)**.3333    !Convective
  psic=1.5*dlog((1.+y+y*y)/3.)-sqrt(3.)*atan((1.+2.*y)/sqrt(3.))
&   +4.*atan(1.)/sqrt(3.)
  f=zL*zL/(1.+zL*zL)
  psit=(1.-f)*psik+f*psic
else
  c=min(50.,0.35*zL)        !Stable
  psit=-((1.+2.*zL/3.)**1.5+0.6667*(zL-14.28)/dexp(c)+8.525)
endif
return
end

```

```

c-----
subroutine ZETA(T,Q,USR,TSR,QSR,Z,ZL)

```

C

C TO EVALUATE OBUKHOVS STABILITY PARAMETER Z/L FROM AVERAGE  
 C TEMP T IN DEG C, AVERAGE HUMIDITY Q IN GM/GM, HEIGHT IN M,  
 C AND FRICTIONAL VEL,TEMP.,HUM. IN MKS UNITS  
 C SEE LIU ET AL. (1979)

```

C
  real*8 T,Q,OB,TVSR,TV,TA,sgn
  real*8 USR,TSR,QSR,Z,ZL
  real*8 al,beta,cpa,cpw,grav,xlv,rhoa,rhow,rgas,toK,visa
  real*8 visw,von,fdg
  COMMON/const/al,beta,cpa,cpw,grav,xlv,rhoa,rhow,rgas,toK,
&      visa,visw,von,fdg
  TA=T+toK
  TV=TA*(1.+0.61*Q)
  TVSR=TSR*(1.+0.61*Q)+0.61*TA*QSR
  sgn=sign(1.,tvsr)      !added this to avoid program
  if(abs(tvsr) .lt. 1.e-3) then !failure when TVSR is very small
    tvsr=sgn*tvsr
  endif
  OB=TV*USR*USR/(grav*VON*TVSR)
  ZL=Z/OB
c   if(ZL .gt. 1000) ZL=1000.
    goto 99
  10 ZL=0.
  99 return
  end

```

```

c-----
  subroutine H_ADJUST(ZUs,ZTs,ZQs,U_hs,T_hs,Q_hs,IHUMID)

```

```

c
c This subroutine adjusts the U,T,Q variables to the specified
c standard height (ZUs,ZTs,ZQs) using the loglayer profiles.
c The DELTA correction (adjustment) is relative to the surface
c measurement. Cronin 4/13/94
c Modified to use new profile relations psiu,psit Bradley 26/10/99

```

```

c
  real*8 ZUs,ZTs,ZQs,U_hs,T_hs,Q_hs,ZUsL,ZTsL,ZQsL
  real*8 U,T,Q,TS,QS,rms,rml,ZU,ZT,ZQ,zi,P,PUZs,PTZs,PQZs
  real*8 U_wg_hs,Rho_hs,Rho_avg,QA,Rho,P_hs,ee
  real*8 USR,TSR,QSR,ZO,zot,zoq,ZL,RR,RT,RQ,RI,dter,dqer,tk
  real*8 al,beta,cpa,cpw,grav,xlv,rhoa,rhow,rgas,toK,visa
  real*8 visw,von,fdg,DU_Wg,Wg,S,D,psit,psiu
c
  COMMON/PIN/U,T,Q,TS,QS,rms,rml,ZU,ZT,ZQ,zi,P,ID
  COMMON/POUT/USR,TSR,QSR,ZO,zot,zoq,ZL,RR,RT,RQ,RI,
&      dter,dqer,tk,DU_Wg,Wg
  COMMON/const/al,beta,cpa,cpw,grav,xlv,rhoa,rhow,rgas,toK,

```

```

&      visa,visw,von,fdg
c
call ZETA(T,Q,USR,TSR,QSR,ZUs,ZUsL)
call ZETA(T,Q,USR,TSR,QSR,ZTs,ZTsL)
call ZETA(T,Q,USR,TSR,QSR,ZQs,ZQsL)
PUZs= PSIfu(ZUsL)
PTZs= PSIfT(ZTsL)
PQZs= PSIfT(ZQsL)

S = (dlog(ZTs/zot)-PTZs)/(von*fdg)
D = (dlog(ZQs/zoq)-PQZs)/(von*fdg)
T_hs =TSR*S +TS - dter -.0098*ZTs
Q_hs =(QSR*D + QS - dqr)*1000
U_wg_hs = USR*(dlog(ZUs/ZO) - PUZs)/0.4
if(U_wg_hs.ge.Wg) then
  U_hs = SQRT(U_wg_hs**2 - Wg**2)
else
  U_hs = U_wg_hs
endif
c
if(IHUMID.eq.1) then  ! then need to convert sp hum into rh
  Q_hs = Q_hs/1000  ! sh kg/kg
  RHO=1./(287.*(T+273.16)*(1.+.61*Q))*P*100.
  P_hs = P - (RHO*grav*(ZTs - ZT))/100 !Approx hydrost.Pressure mb
  RHO_hs=1./(287.*(T_hs+273.16)*(1.+.61*Q_hs))*P_hs*100
  RHO_avg = (RHO + RHO_hs)/2
  P_hs = P -(RHO_avg*grav*(ZTs - ZT))/100 !hydrostatic Pressure
  call humidity(T_hs,P_hs,QA)  !Teten's formula for Pvp,sat
  ee=Q_hs*P_hs/(.62197 + .378*Q_hs) !to get vapor pressure
  Q_hs = ee/QA  !to get relative humidity
endif
return
end
c-----
Subroutine gravity(lat,g)
c  calculates g as a funccton of latitude using the 1980 IUGG formula
c
c  Bulletin Geodesique, Vol 62, No 3, 1988 (Geodesist's Handbook)
c  p 356, 1980 Gravity Formula (IUGG, H. Moritz)
c  units are in m/sec^2 and have a relative precision of 1 part
c  in 10^10 (0.1 microGal)
c  code by M. Zumberge.
c
c  check values are:
c
c  g = 9.780326772 at latitude 0.0

```

```

c   g = 9.806199203 at latitude 45.0
c   g = 9.832186368 at latitude 90.0
c
real*8 gamma, c1, c2, c3, c4, phi, lat, g
gamma = 9.7803267715
c1 = 0.0052790414
c2 = 0.0000232718
c3 = 0.0000001262
c4 = 0.0000000007
phi = lat * 3.14159265358979 / 180.0
g = gamma * (1.0
$ + c1 * ((sin(phi))**2)
$ + c2 * ((sin(phi))**4)
$ + c3 * ((sin(phi))**6)
$ + c4 * ((sin(phi))**8))
c
return
end

```

## **APPENDIX D**

### **BOUNDARY LAYER STUDY IN THE WESTERN AND CENTRAL GULF OF MEXICO FINAL MEETING**

**PRESENTED TO:  
MINERALS MANAGEMENT SERVICE  
TECHNICAL REVIEW GROUP**

**OCTOBER 15-16, 2003**

## **Boundary Layer Study in the Western and Central Gulf of Mexico Final Meeting**

By:

Clinton P. MacDonald, Paul T. Roberts  
Charley A. Knoderer, Dianne S. Miller, Mark R. Lilly  
Sonoma Technology, Inc.  
Petaluma, CA

Steven R. Hanna  
Hanna Consultants  
Kennebunkport, ME

Presented to:  
Minerals Management Service  
Technical Review Group

October 15-16, 2003



998555-2265

## **Project Objectives**

- Focus on atmospheric boundary layer (ABL) in the western and central Gulf of Mexico, 1998-2002
- Produce quality-controlled data inventory and tools to view data
- Evaluate annual, seasonal, and diurnal variations in the ABL's structure
- Describe the processes governing the variations in the ABL's structure
- Provide three-dimensional gridded wind fields for study period
- Evaluate transport and mixing characteristics



## **MMS Uses of Study Results** (1 of 2)

- Estimate impact of Outer Continental Shelf (OCS) oil and gas activities
- Provide quality-controlled data set for use in other MMS research studies
- Provide access to, and statistical summaries of, quality controlled data set
- Synthesize ABL characteristics and pollutant transport and dispersion



## **MMS Uses of Study Results** (2 of 2)

- Provide a conceptual model summary, with examples, of processes that influence ABL characteristics and variability
- Provide a conceptual model summary, with examples, of processes that influence pollutant transport and dispersion



## Main Tasks

- Data Collection and Inventory
- Data Base
- Data Analysis Tool (EDAT)
- Analysis of the ABL structure
  - Observed data
  - COARE
- Modeling, Transport, and Dispersion Analysis



## Data

So much data: 68,000,000+ records!

- Data and sources
- Data validation
- Database
- Graphical user interface
  - Environmental Data Analysis Tool (EDAT)



915-MHz radar wind profiler, RASS, and surface meteorological station at the South Marsh Island site



## Data – Types

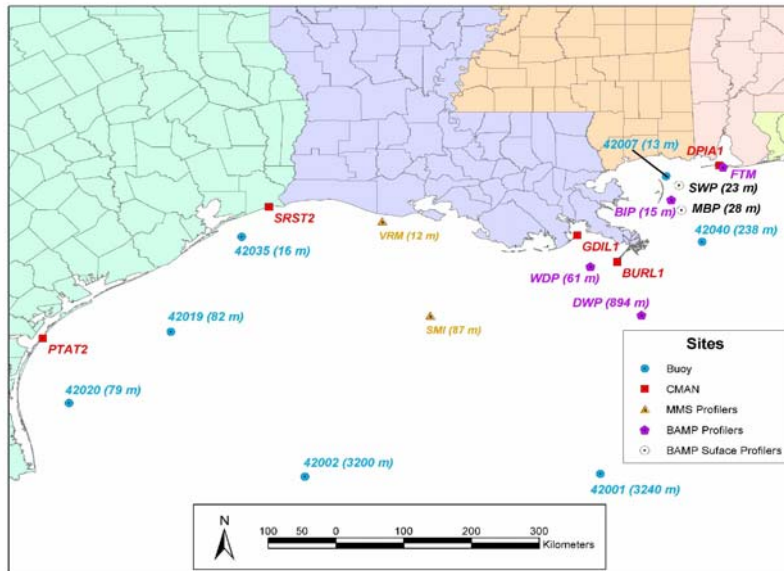
May 1998 through October 2001

- Upper Air
- Surface
- Derived
- Eta Model
- Statistical
- Meteorological Classes
- CALMET



STI

## Data – Site Map

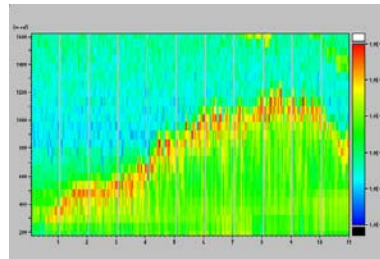
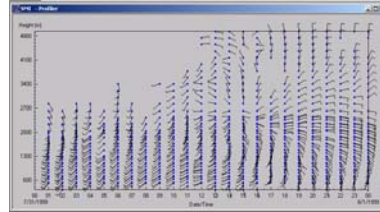


STI

## Data – Upper Air (1 of 2)

### Profiler/RASS (6 sites)

- Hourly virtual temperature profiles
  - 100 m to 1500 m agl
  - 60-m resolution
  - Reality 160 m to 800 m agl
- Hourly wind profiles
  - 100 m to 2000 m agl at 60-m resolution
  - 100 m to 4000 m agl at 120-m resolution
  - Reality 300 m to 2000+ m agl
- $C_n^2$ 
  - Changes of the index of refraction
  - Two-minute
- Vertical velocity



## Data – Upper Air (2 of 2)

### Rawinsonde

- National Climatic Data Center
- Lake Charles, Louisiana
- Slidell, Louisiana
- 0000 and 1200 UTC



## Data – Surface

- Buoy (7) and C-MAN (5)
  - National Buoy Data Center
- Collocated with profilers (6)
  - ABL field program
  - BAMP field program
- Surface land sites (40)
  - National Climatic Data Center



**Dauphin Island**



## Data – Surface Over Water (1 of 3)

Site	Site ID	Air Temperature	Near-Sea Surface Temperature	Skin Temperature	Relative Humidity	Wind	Pressure	Wave Height and Period
Mid Gulf 180 nm South of Southwest Pass LA	42001	✓	✓		✓	✓	✓	✓
West Gulf 240 nm South-Southeast of Sabine TX	42002	✓	✓		✓	✓	✓	✓
Biloxi 22 nm South-Southeast of Biloxi MS	42007	✓	✓		✓	✓	✓	✓
Freeport TX. 60 nm South of Freeport TX	42019	✓	✓		✓	✓	✓	✓
Corpus Christi TX 50 nm Southeast of Corpus Christi	42020	✓	✓		✓	✓	✓	✓
Galveston 22 nm East of Galveston TX	42035	✓	✓		✓	✓	✓	✓
Mobile South 64 nm South of Dauphin Island AL	42040	✓	✓		✓	✓	✓	✓
Southwest Pass LA	BURL11	✓			✓	✓	✓	
Dauphin Island AL	DPIA11	✓			✓	✓	✓	
Grand Isle LA	GDIL11	✓	✓		✓	✓	✓	
Port Aransas TX	PTAT21	✓	✓		✓	✓	✓	
South Marsh Gulf of Mexico	SMI	✓		✓	✓	✓	✓	
Sabine TX	SRST21	✓			✓	✓	✓	
Vermillion Gulf of Mexico	VRM	✓		✓	✓	✓	✓	
Breton Island Platform	BIP	✓		✓	✓	✓	✓	
Deep Water Platform	DWP	✓		✓	✓	✓	✓	
Shallow Water Platform	SWP	✓		✓	✓	✓	✓	
Mid Buoy Platform	MBP	✓		✓	✓	✓	✓	
West Delta Platform	WDP	✓		✓	✓	✓	✓	



## Data – Surface Over Water (2 of 3)



Port Aransas TX Site, adjusted location in yellow  
Jan. 7, 1995 Digital Orthophotoquad



## Data – Surface Over Water (3 of 3)

### Locations and Measurement Heights

Site Name	Site	Latitude (degrees N)	Longitude (degrees W)	Elevation (m msl)	Air Temperature Height Above Site (m)	Anemometer Height Above Site (m)	Sea Temperature Height (m)
Mid Gulf 180 nm South of Southwest Pass LA	42001	25.93	89.65	0.0	10.0	10.0	-1.0
West Gulf 240 nm South-Southeast of Sabine TX	42002	25.89	93.57	0.0	10.0	10.0	-1.0
Biloxi 22 nm South-Southeast of Biloxi MS	42007	30.10	88.78	0.0	4.0	5.0	-0.6
Freeport TX, 60 nm South of Freeport TX	42019	27.92	95.35	0.0	4.0	5.0	-0.6
Corpus Christi TX 50 nm Southeast of Corpus Christi	42020	26.92	96.70	0.0	4.0	5.0	-0.6
Galveston 22 nm East of Galveston TX	42035	29.25	94.41	0.0	4.0	5.0	-0.6
Mobile South 64 nm South of Dauphin Island AL	42040	29.18	88.30	0.0	4.0	5.0	-0.6
Southwest Pass LA	BURL1	28.90	89.43	0.0	11.9	30.5	-0.5
Dauphin Island AL	DPIA1	30.25	88.07	0.0	9.1	17.4	-0.5
Grand Isle LA	GDIL1	29.27	89.96	1.8	15.2	15.8	-0.5
Port Aransas TX	PTAT2	27.83	97.05	0.0	9.1	14.9	-0.5
Sabine TX	SRST2	29.67	94.05	0.9	11.9	12.5	-0.5
Breton Island Platform	BIP	29.77	88.71	20.0	2.0	3.0	0.0
Deep Water Platform	DWP	28.15	89.10	41.0	2.0	3.0	0.0
Shallow Water Platform	SWP	29.98	88.60	20.0	2.0	2.0	0.0
Mid Buoy Platform	MBP	29.62	88.57	20.0	2.0	3.0	0.0
West Delta Platform	WDP	28.83	89.78	20.0	2.0	3.0	0.0
Vermillion Gulf of Mexico	VRM	29.47	92.55	21.0	2.0	3.0	0.0
South Marsh Gulf of Mexico	SMI	28.15	91.91	25.0	2.0	3.0	0.0



## Data – Derived

- COARE algorithm: originally derived from the Tropical Ocean-Global Atmosphere Coupled-Ocean Atmosphere Response Experiment (TOGA COARE) research project
- Calculates fundamental boundary layer scaling parameters over water using routine surface observation
  - Heat fluxes
  - Surface roughness length
  - Friction velocity
  - Scaling temperature
  - Scaling water vapor mixing ratio
  - Monin-Obukhov length, etc.



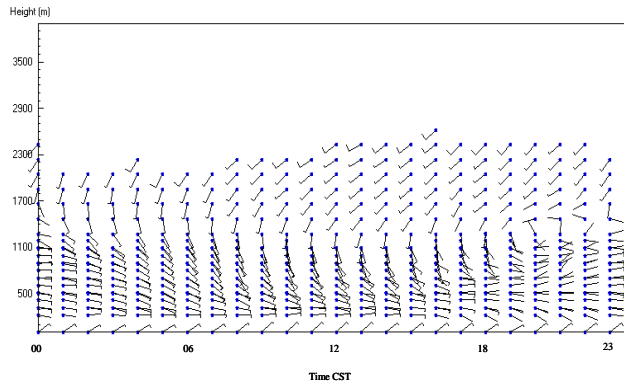
## Data – Model Predictions

- Six-hourly Eta and three-hourly Eta Data Assimilation System (EDAS) predictions
  - Eta forecasts have many more parameters such as friction velocity, heat fluxes, etc.
  - EDAS has nudged data from observations.
- University Corporation for Atmospheric Research (UCAR)
- 00 and 12 UTC model runs out to 48 hours
- Resolutions 40-km x 40-km with 38 vertical levels
- Data at grid points nearest to site stored in database
- Other data in GRIB format



## Data – Statistical

Monthly, yearly, and seasonal average wind and temperature profiles



Fall average winds at VRM from 0000 to 2300 CST, September 24 to December 22



## Data – Meteorological Classifications

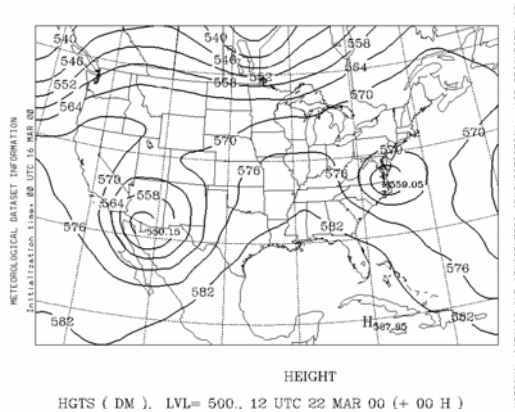
- Daily upper-air synoptic classifications — Based on 12 UTC 500-mb charts
- Daily surface-flow speed and direction classifications for each site
- Wind roses
- 1998-2001
- Western/central Gulf of Mexico

Classifications
Ridge
Weak ridge
Flat
Zonal
Post-trough
Weak post-trough
Weak trough
Trough
Cut-off low
Tropical storm

Flow Direction	Flow Speed (m/sec)
Onshore	Light (0 to 5)
Offshore	Moderate (5 to 10)
Parallel east	Strong (10 +)
Parallel west	



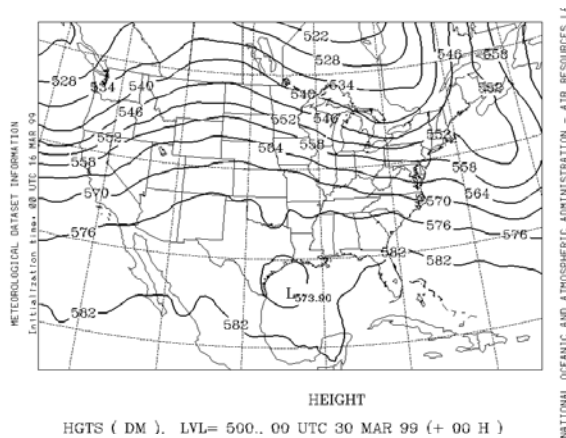
## Meteorological Classifications Upper Air (1 of 4)



Example of an upper-air ridge pattern for the Gulf of Mexico region on March 22, 2000, at 1200 UTC (0600 CST). Solid lines indicate height contours (decameters).



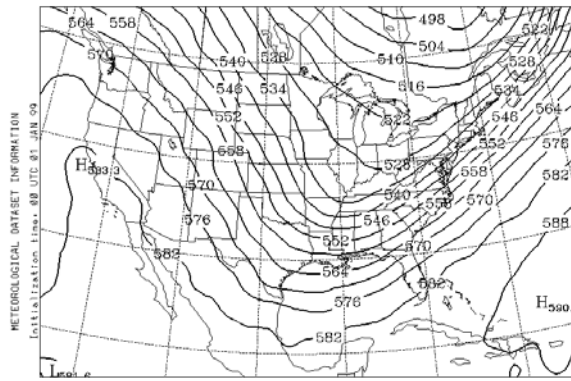
## Meteorological Classifications Upper Air (2 of 4)



Example of an upper-air cut-off low pattern for the Gulf of Mexico region on March 30, 1999, at 0000 UTC (March 29, 1999, at 1800 CST). Solid lines indicate height contours (decameters).



## Meteorological Classifications Upper Air (3 of 4)



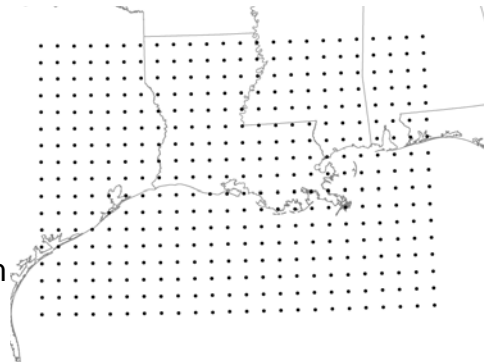
## Data – CALMET Modeling

- Seven case studies
  - September 18–20, 2001
  - January 20–25, 2000
  - January 4–6, 2001
  - July 30–August 1, 1999
  - May 14–15, 2001
  - April 15, 2001
  - January 29, 2001
- Range of meteorological and transport conditions
- Data stored as binary CALMET files



## Data – CALMET Modeling

- Vertical resolution included 20 interfaces (21 levels in meters)  
(0, 20, 50, 100, 200, 300, 400, 500, 600, 700, 800, 900, 1000, 1200, 1400, 1600, 1800, 2000, 2250, 2500, 2750 m)
- Horizontal resolution of 5 km
- Modeling domain, 860 km x 560 km



## Data Validation (1 of 2)

- Objectives
  - Evaluate the internal, spatial, temporal, and physical consistency of the data
  - Produce a working Microsoft SQL database with values that are validated and of known quality
  - Save quarterly subsets of Microsoft SQL database in MS Access databases
  - Determine the suitability of the data for analysis and modeling

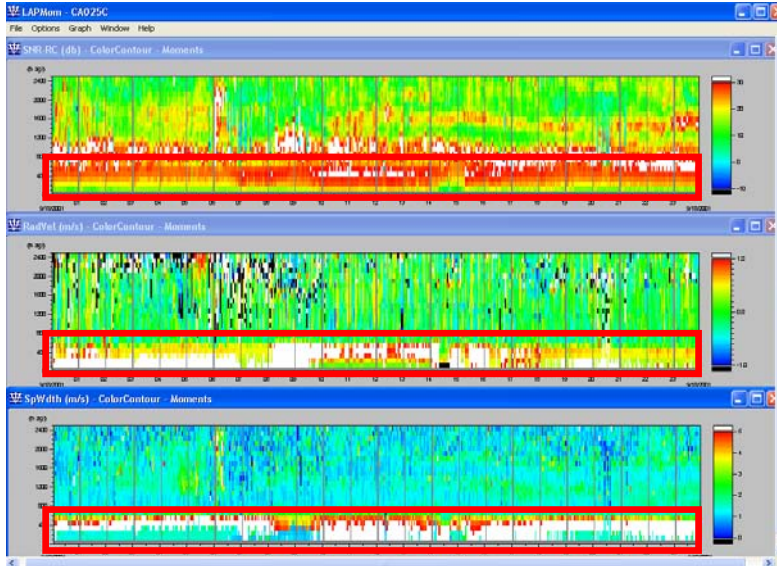


## Data Validation (2 of 2)

- Platform data previously validated by STI as part of the data collection process
  - Issue with data recovery rates at higher altitude
  - Issue with sea clutter at lower altitude
- Buoy, C-MAN, and COARE output data visually and range-checked
- Secondary QC performed during analysis and CALMET modeling, resulting in changes to the COARE software and data reprocessing

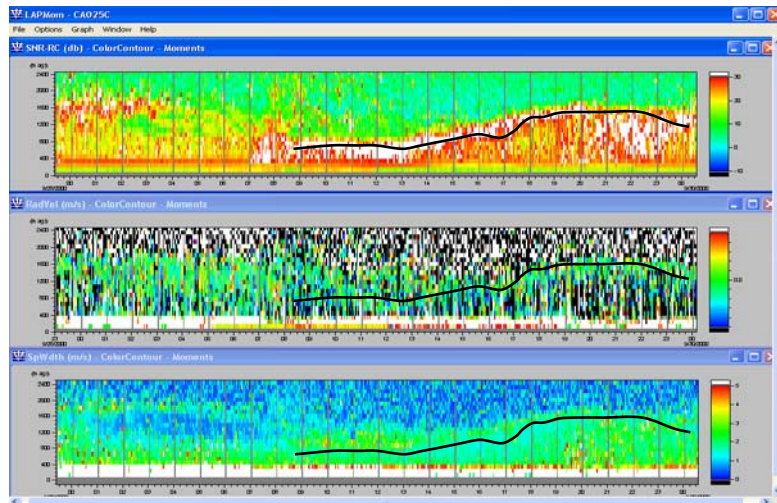


## Profiler Data Issues – Sea Clutter (1 of 2)



BIP profiler data on September 18, 2001

## Profiler Data Issues – Sea Clutter (1 of 2)



BIP profiler data on September 29, 2000

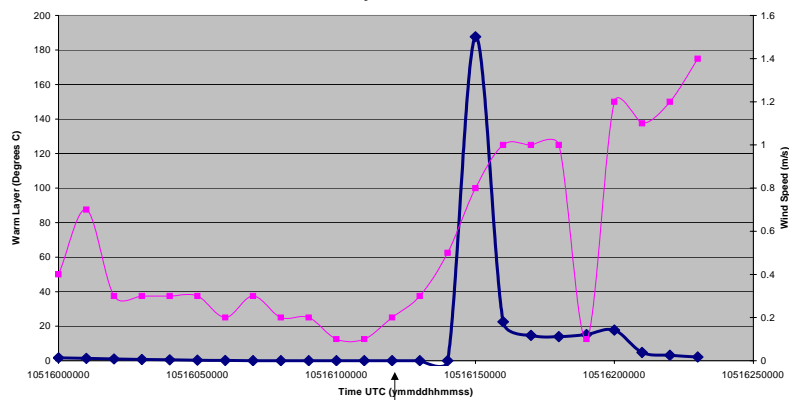
## Data Validation – Flags

- Valid = 0
- Invalid data = 8. Observations judged inaccurate or in error
- Missing data = 9. Observations not collected (the data were assigned a value of -999.0)
- Coare output flags
  - Out flag = 0: Radiation predictions from Eta model cloud data and all observations needed by COARE are available.
  - Out flag = 3: Observations were interpolated in time, and radiation data exist from Eta model cloud data.
  - Out flag = 6: Observations were interpolated in time; radiation was estimated by time of year, day, and latitude.
  - Out flag = 7: Observations exist; radiation was estimated by time of year, day, and latitude.



## Data Validation – Problems (1 of 4)

Warm layer error at SMI



Sunrise  
May 16, 2001



## Data Validation – Problems (2 of 4)

- Problem: unrealistic sea surface warming
  - Daylight hours
  - Light wind conditions
  - Stable vertical temperature gradient
- Cause: lack of heat removal due to the very small accumulated stress (surface momentum flux) and the very thin (almost zero) warm layer thickness
- Solution: a minimum stress of  $0.002 \text{ N/m}^2$  imposed for this calculation only (Christopher Fairall, Steve Hanna, and STI)



## Data Validation – Problems (3 of 4)

- Problem
  - The representation in COARE follows from laboratory measurements with artificial light sources
  - Unrealistic evaporative cooling calculation due to unrealistic amounts of solar energy reaching the ocean surface
- Solution: for the net absorption equation, coefficient changed from 0.137 to 0.060 (based on calculational tests by Christopher Fairall)

$$\text{Net} = \text{SW} * (0.060 + 11 * \text{CST} - 6.6\text{e-}5 / \text{CST} * (1 - \exp(-\text{CST}/8.0\text{e-}4)))$$

where

Net = Net absorption by the ocean  
SW = Incoming short wave radiation  
CST = Cool skin thickness



## Data Validation – Problems (4 of 4)

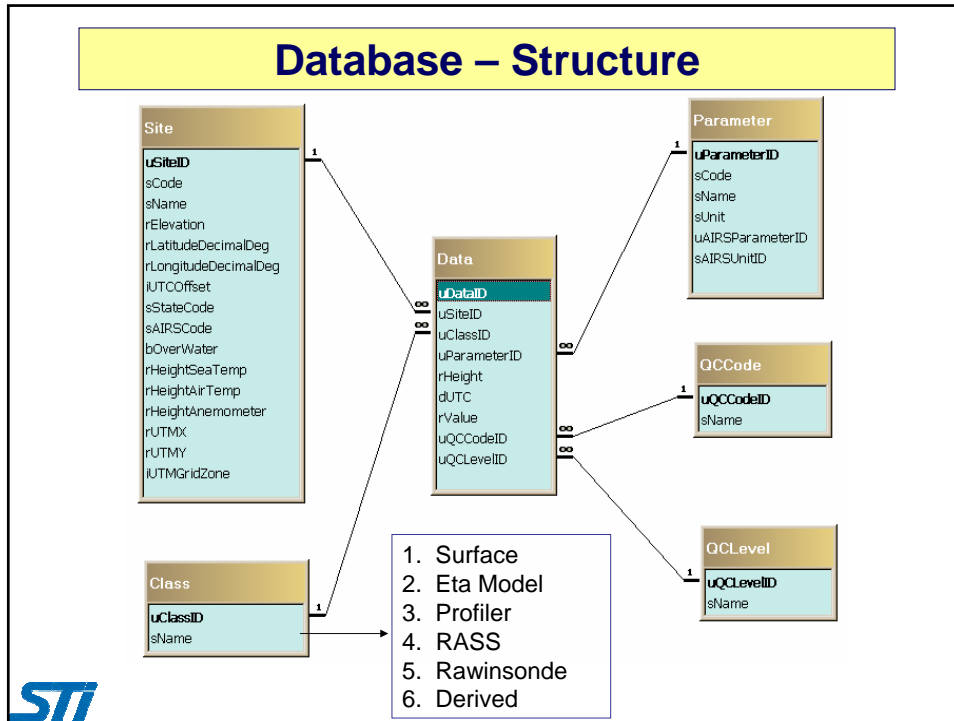
- Problem: when wave period is very short (< 4 seconds) and waves are greater than 1 m, surface roughness becomes large.
- Solution: further investigation is needed.



## Database

- 68,000,000+ records stored in a MS SQL database
- Quarterly MS Access databases
- Scalable data structure, handles most environmental data types



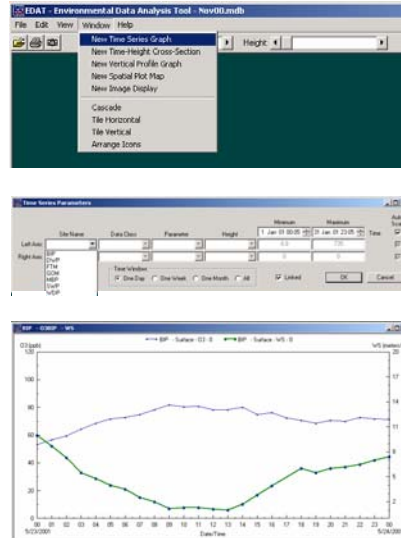


## EDAT

- Environmental Data Analysis Tool
- Displays data from MS SQL or MS Access database including the profiler/RASS, rawinsonde, surface meteorological, modeling, and COARE data sets
  - time series
  - time-height cross-sections
  - vertical profiles
  - spatial plots
- Exports to EPA's WRLPlot wind rose program
- Allows users to save data subsets

## EDAT – Time Series

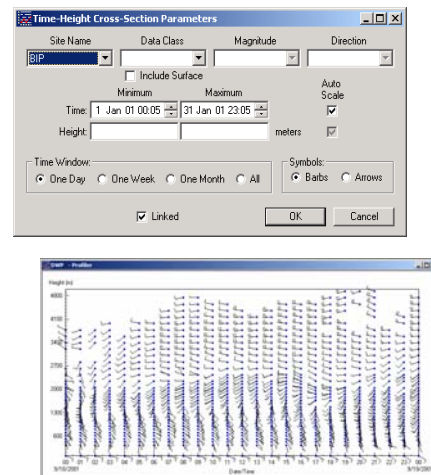
- *Time-series plots* can display any type of data. For example, this display enables the user to analyze hourly or diurnal changes in a single variable.



STI

## EDAT – Time-Height Cross Sections

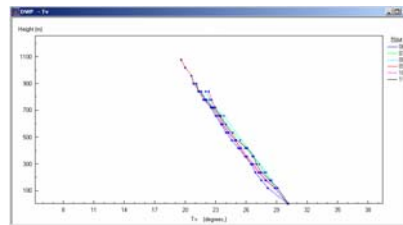
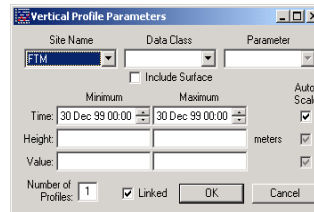
- *Time-height cross-sections* are ideal for displaying radar wind profiler data. For example, this display enables the user to identify regions of vertical and horizontal wind shear from the profiler data.



STI

## EDAT – Vertical Profiles

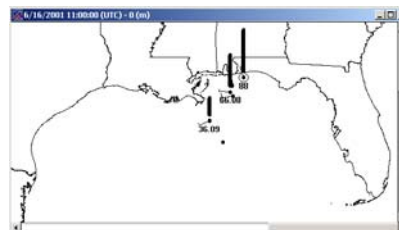
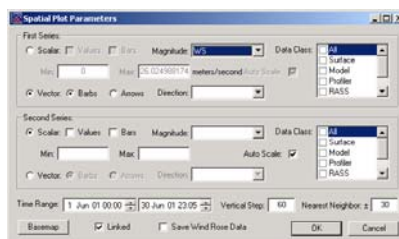
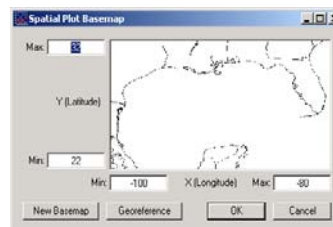
- *Vertical profiles* are ideal for displaying RASS data.



STI

## EDAT – Spatial

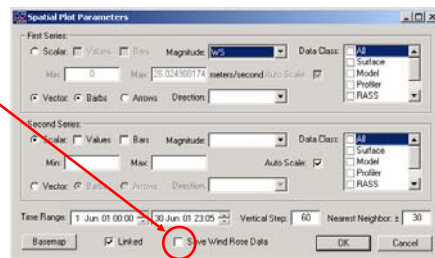
- *Spatial plot maps* can display any type of data in the database on a user-selected base map



STI

## EDAT – Wind Rose Data

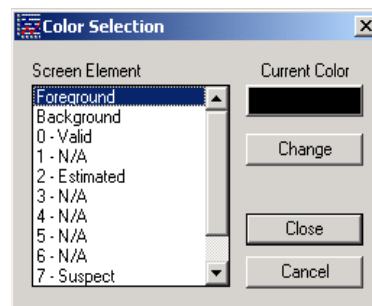
- On the **Spatial Plot Map** selection menu, there is a checkbox option to save wind rose data. When the box is checked, EDAT will extract all surface wind speed and direction data and format them to work with the wind rose program, WRPLOT View, a program available at no charge on the Intranet at <http://www.lakes-environmental.com>.



STI

## EDAT – Display Options Color Selection

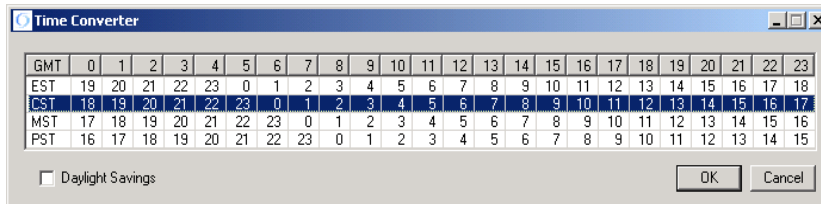
- The user may define some of the color settings on the graphs. The foreground and background colors may be changed, and the colors based on QC code may be changed.



STI

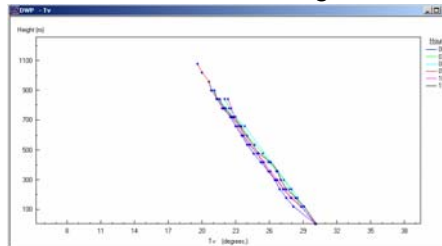
## EDAT – Display Options Time Zone

- The user may define the time zone in which the data should be displayed. All the data in the database are in UTC, but for analysis purposes, local time may be more useful. All time zones within the continental United States are available.



## EDAT – Display Options Lines and Points

- Lines and points
  - When a time series or vertical profile plot is created, the data are displayed as points, with a line connecting them as a default.
  - The points are the only way to visually discern (by color) the QC code. The line colors are determined by the series number; for example, a time series plot may have two series displayed. The first series is a blue line, and the second series is a green line. For vertical profile plots, each hour of data is displayed as a different color line.



## EDAT – Display Options Toolbar and Status Bar

- The toolbar and status bar may be turned on or off.
  - The toolbar displays the time and height scrollbars and the buttons to open a new file, print the current graph, and save the current graph.



- The status bar displays the details of the data point selected: site, data class, parameter, height, date-time, value, and QC code.



## Profiler, RASS, and Surface Data Summary

- Statistical averages
  - Surface wind roses
  - Profiler wind time-height cross-sections
  - RASS virtual temperature profiles
- EDAS profiler comparison
  - Case examples
  - Statistical
- Estimated mixing heights
  - Issues
  - Comparison with CALMET



## Meteorological Classifications

- Daily upper-air synoptic classifications — Based on 12 UTC 500-mb charts

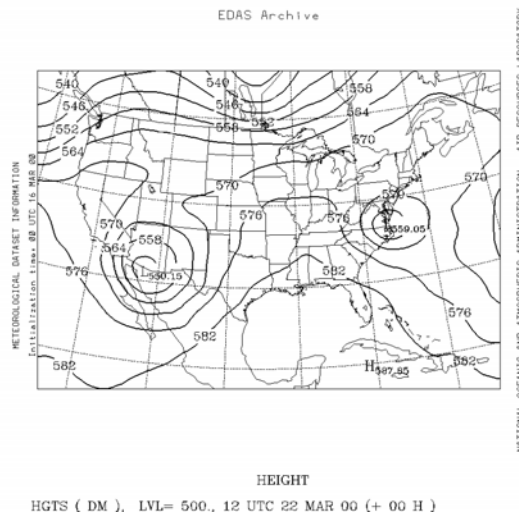
Classifications
Ridge
Weak ridge
Flat
Zonal
Post-trough
Weak post-trough
Weak trough
Trough
Cut-off low
Tropical storm

- Daily surface flow speed and direction classifications for each site
- Wind roses

Flow Direction	Flow Speed (m/sec)
Onshore	Light (0 to 5)
Offshore	Moderate (5 to 10)
Parallel east	Strong (10 +)
Parallel west	



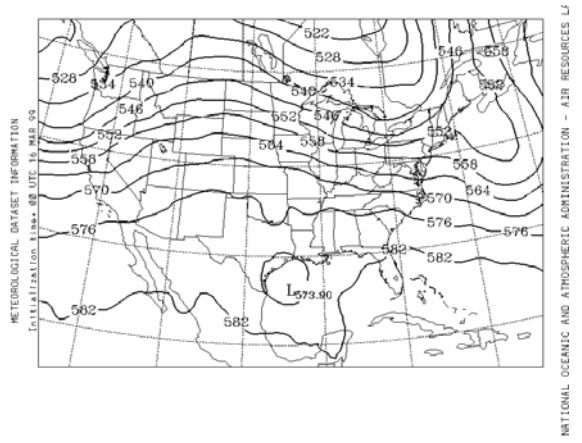
## Meteorological Classifications – UA (1 of 9)



Example of an upper-air ridge pattern for the Gulf of Mexico region for March 22, 2000, at 1200 UTC (0600 CST). Solid lines indicate height contours (decameters).



## Meteorological Classifications – UA (2 of 9)



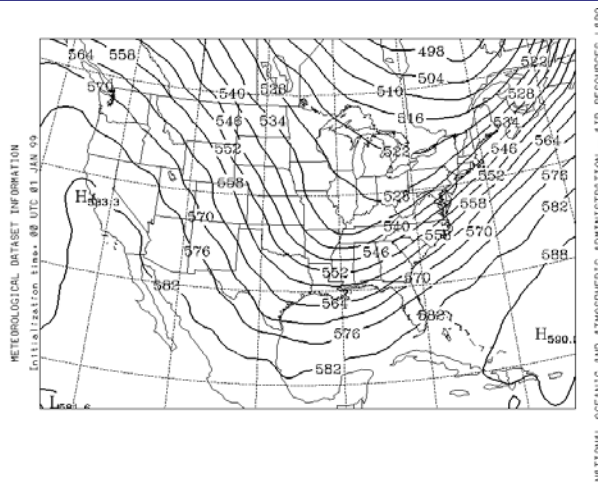
HEIGHT

HGTS ( DM ). LVL= 500.. 00 UTC 30 MAR 99 (+ 00 H )

Example of an upper-air cut-off low pattern for the Gulf of Mexico region for March 30, 1999, at 0000 UTC (March 29, 1999, at 1800 CST). Solid lines indicate height contours (decameters).



## Meteorological Classifications – UA (3 of 9)



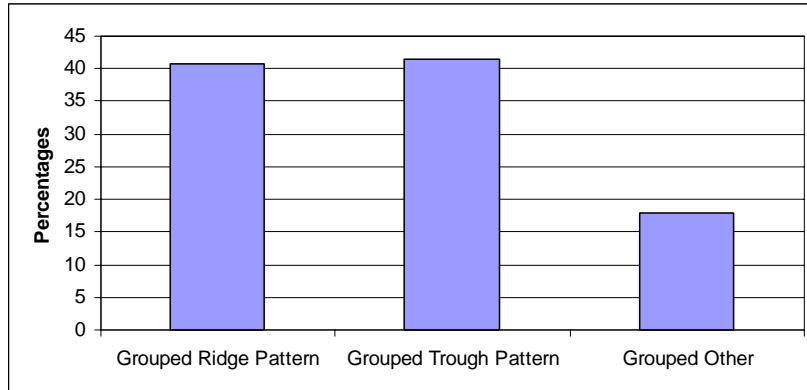
HEIGHT

HGTS ( DM ). LVL= 500.. 00 UTC 05 JAN 99 (+ 00 H )

Example of an upper-air trough pattern for the Gulf of Mexico region for January 05, 1999, at 0000 UTC (January 4, 1999 at 1800 CST). Solid lines indicate height contours (decameters).



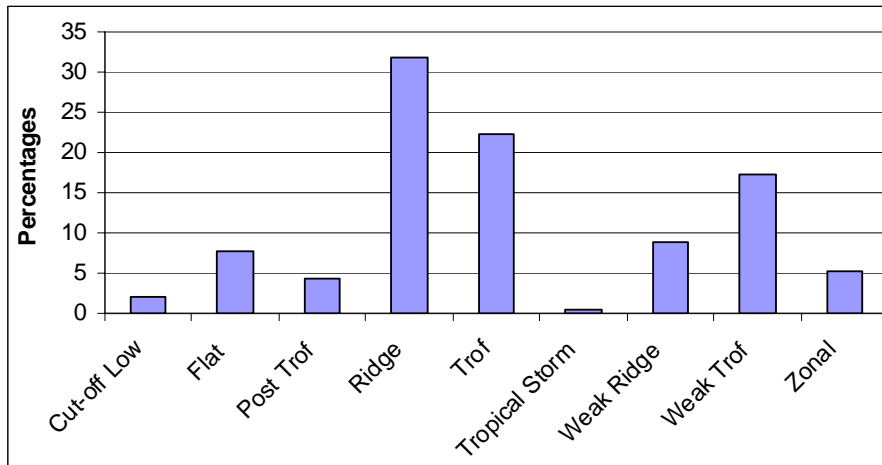
## Meteorological Classifications – UA (4 of 9)



Overall frequency distribution of grouped upper-air patterns observed for the entire study period



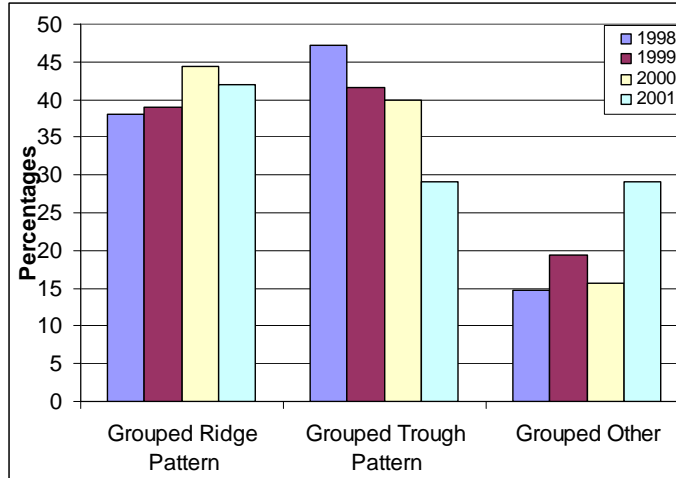
## Meteorological Classifications – UA (5 of 9)



Frequency distribution of upper-air patterns observed for the entire study period



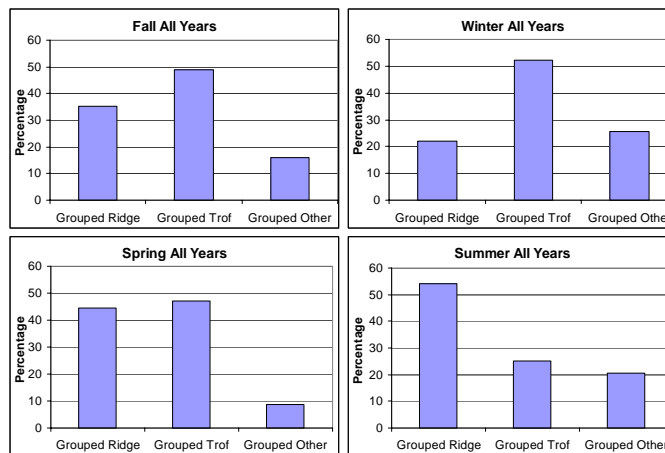
## Meteorological Classifications – UA (6 of 9)



Frequency distribution of grouped upper-air patterns observed for each MMS year, June through May, during the study period



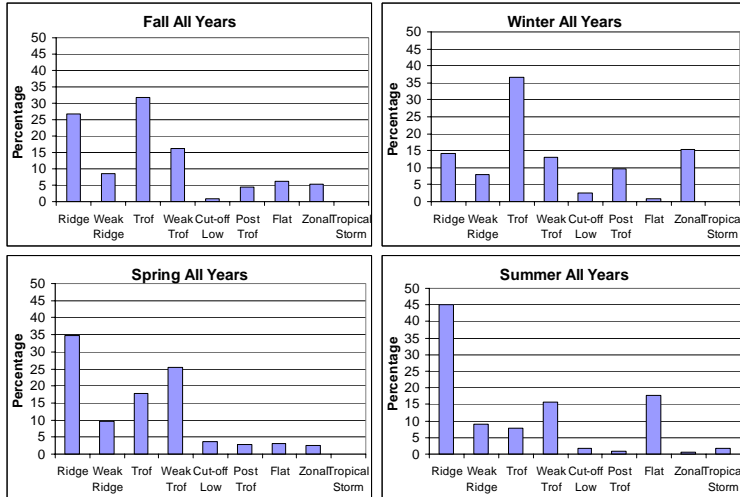
## Meteorological Classifications – UA (7 of 9)



Frequency distribution of grouped upper-air patterns observed for each season for all years during the MMS study period



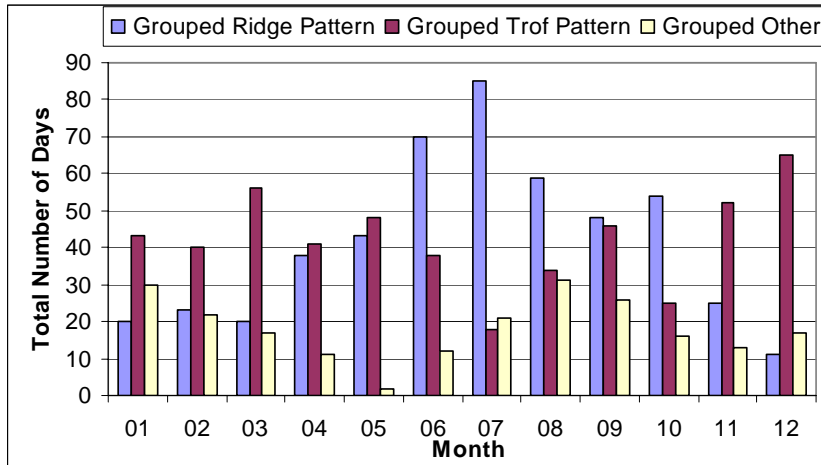
## Meteorological Classifications – UA (8 of 9)



Frequency distribution upper-air pattern observed for each season for all years during the MMS study period



## Meteorological Classifications – UA (9 of 9)



Frequency distribution of grouped upper-air patterns observed for each month for all years during the MMS study period

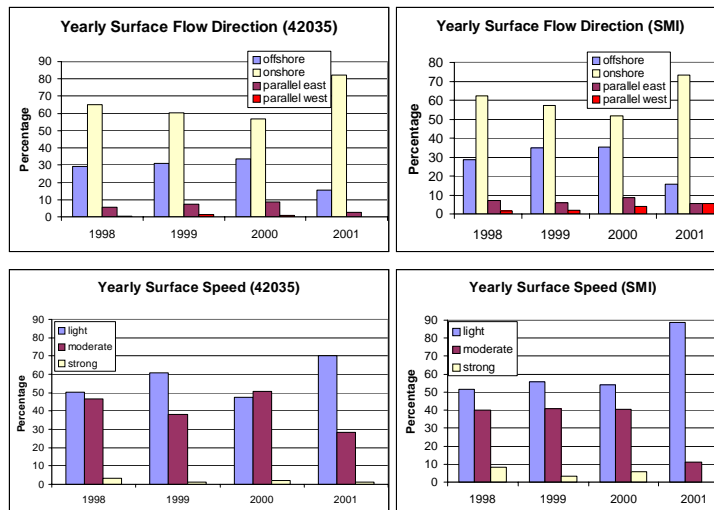


## Meteorological Classifications – Surface (1 of 4)

- Buoy 42035 and the VRM platform site represent near-shore characteristics.
- Buoy 42019 and the SMI platform site represent offshore characteristics.



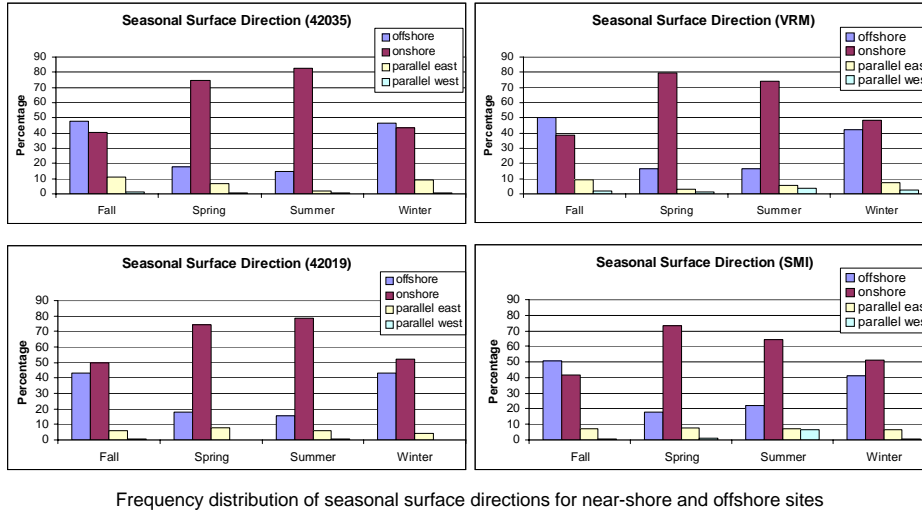
## Meteorological Classifications – Surface (2 of 4)



Yearly frequency distributions of surface direction and speed (top graphs show direction, bottom graphs show speed) for the near-shore site, buoy 42035, and the offshore site, SMI. These two sites are about 200 km apart.

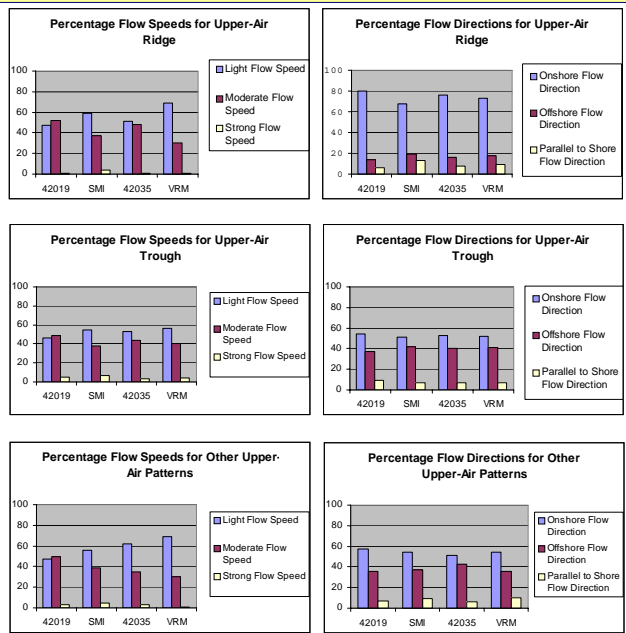


## Meteorological Classifications – Surface (3 of 4)

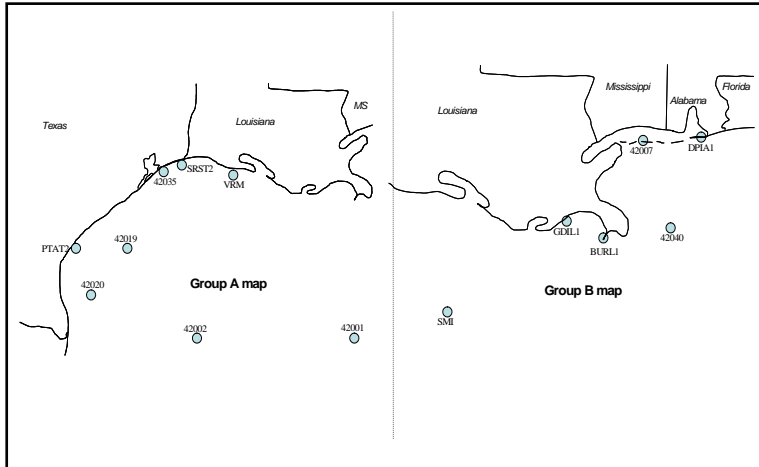


## Meteorological Classifications – Surface (4 of 4)

Frequency distribution for MMS study period of surface flow typing for upper-air ridge, upper-air trough, and other upper-air patterns



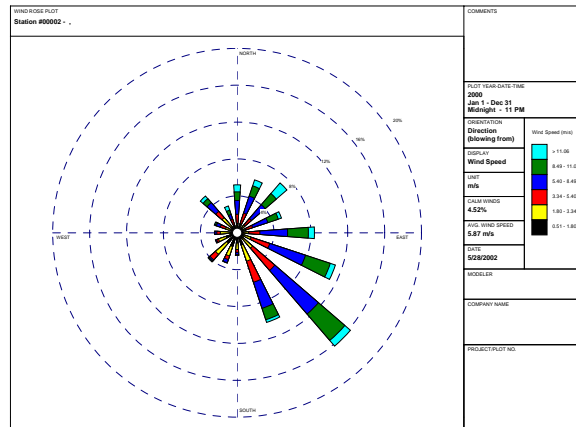
## Wind Rose (1 of 3)



Data suggested two site groups.



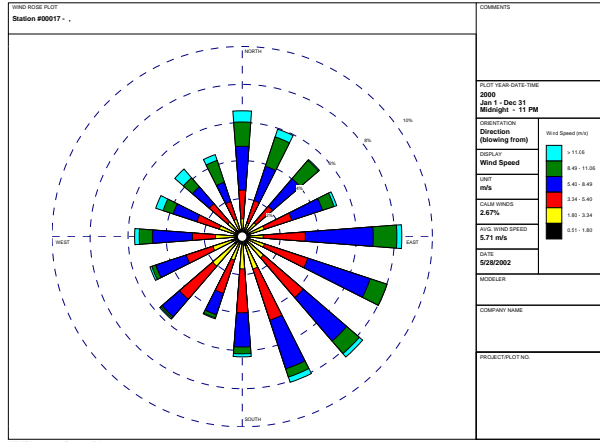
## Wind Rose (2 of 3)



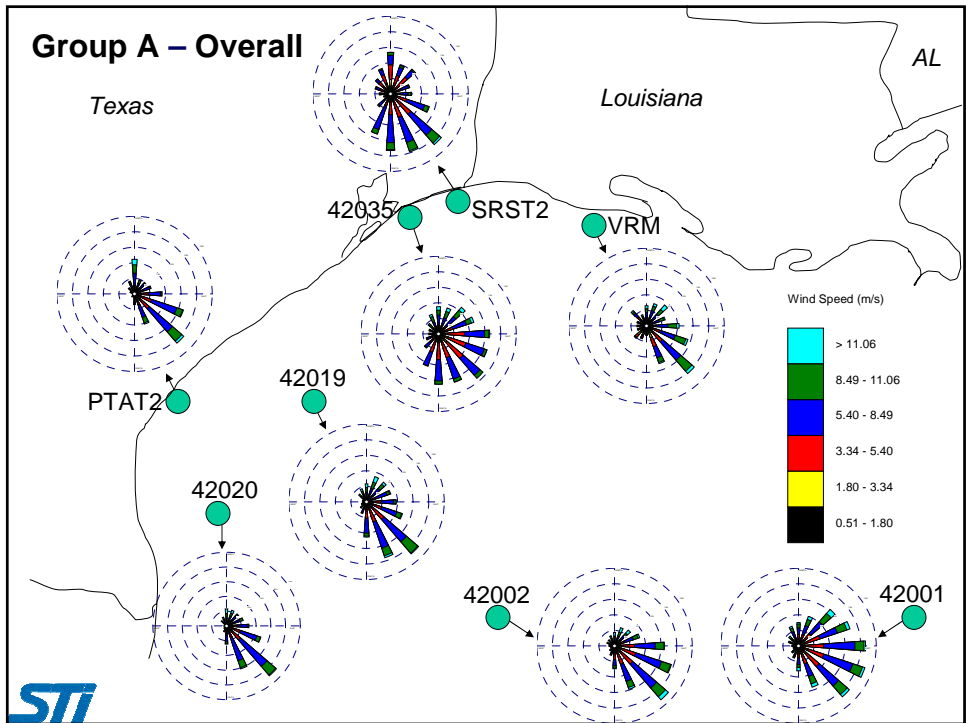
The VRM wind rose is representative of the wind rose plots at group A sites.

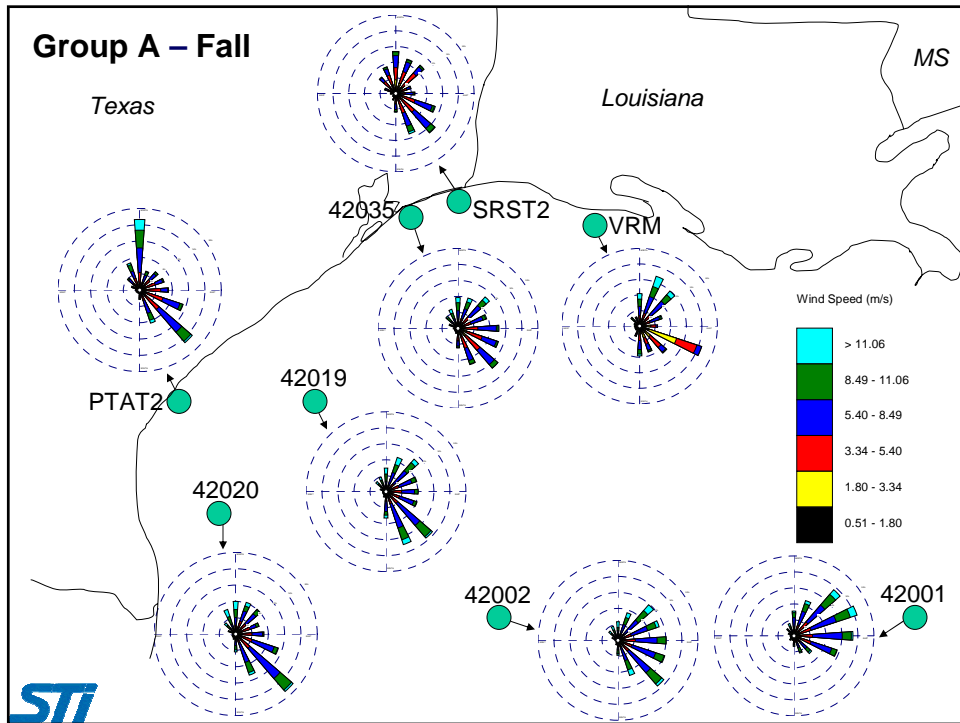
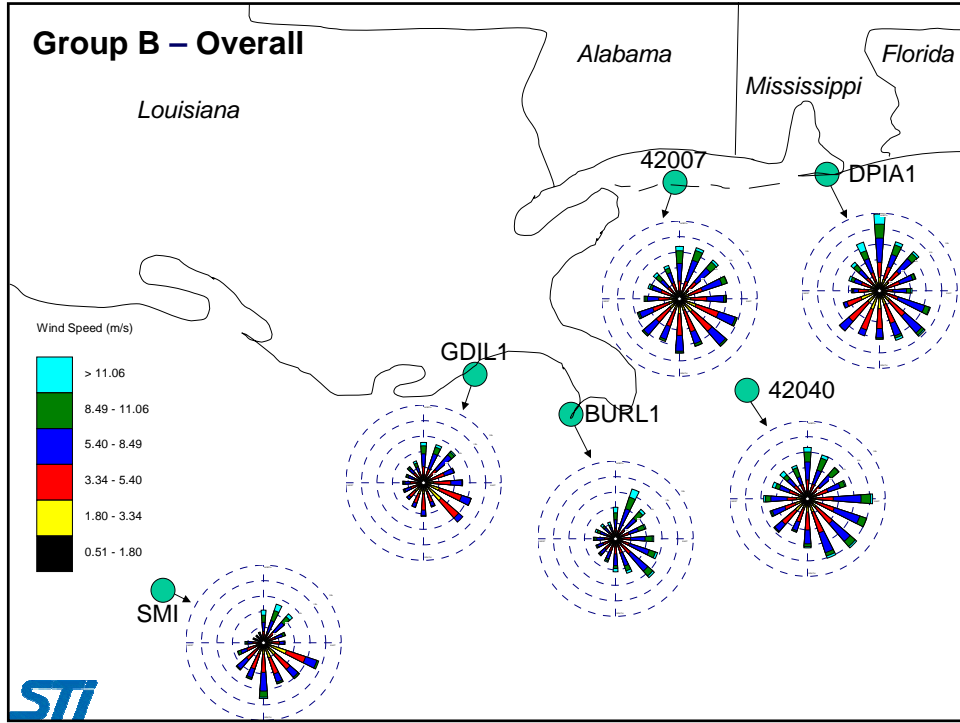


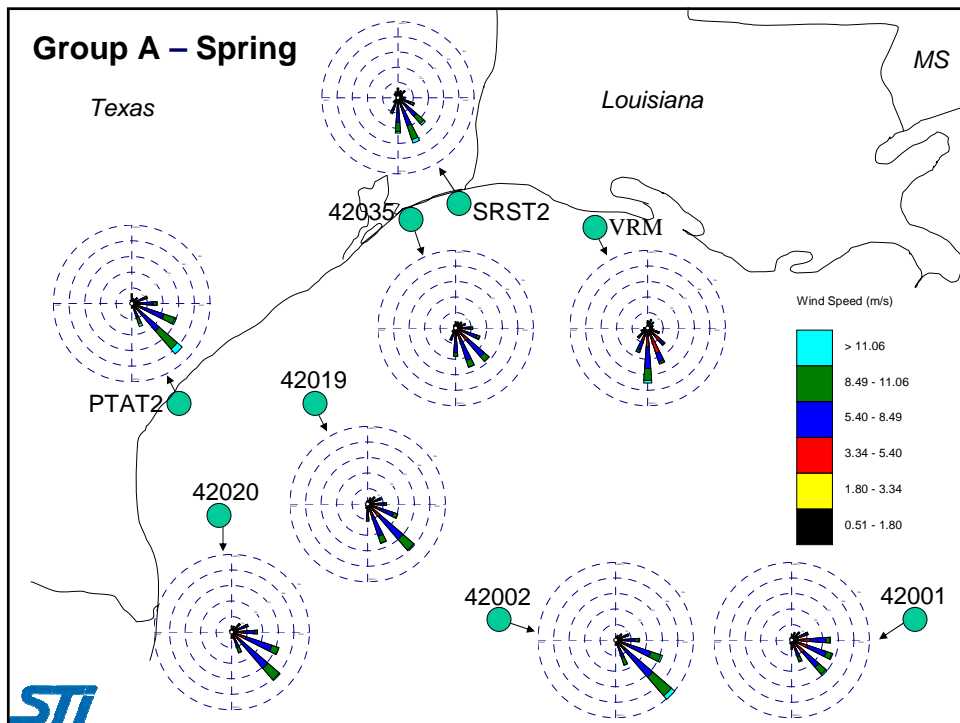
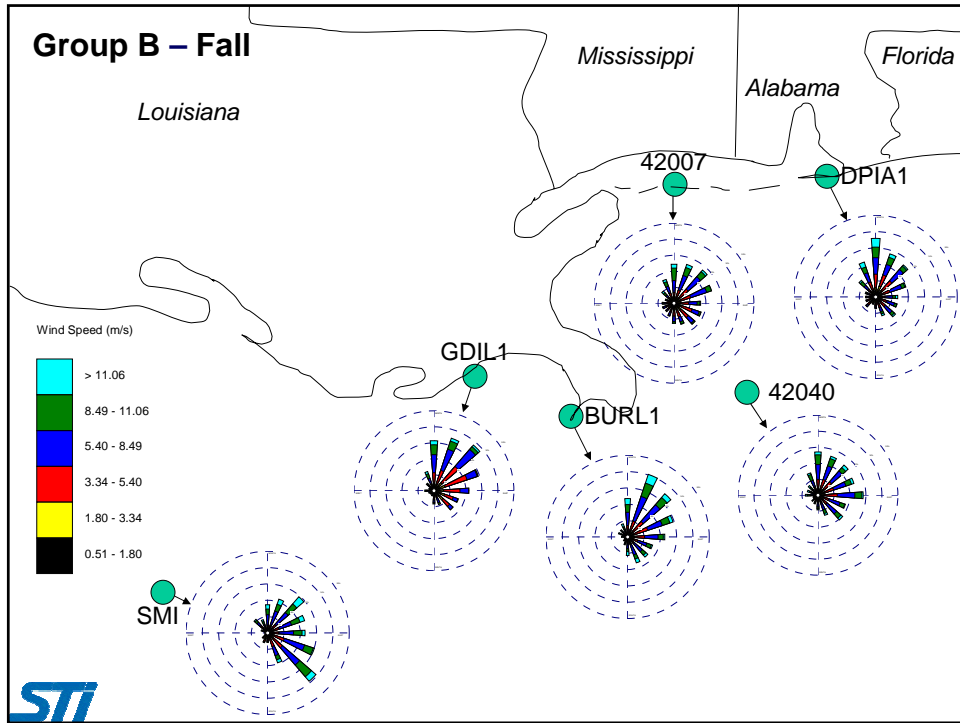
## Wind Rose (3 of 3)

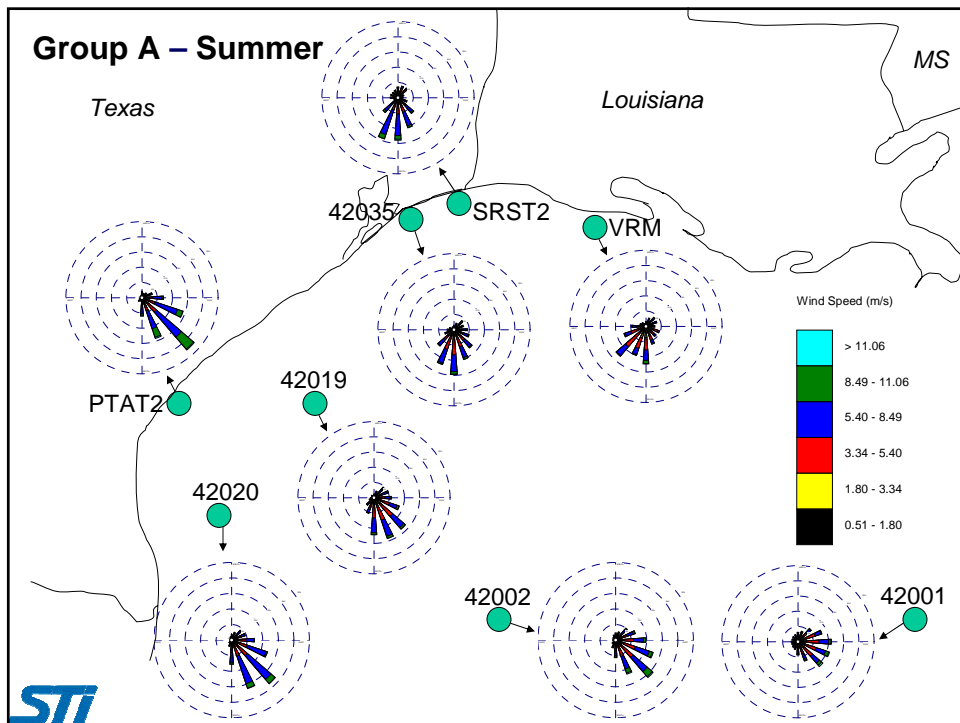
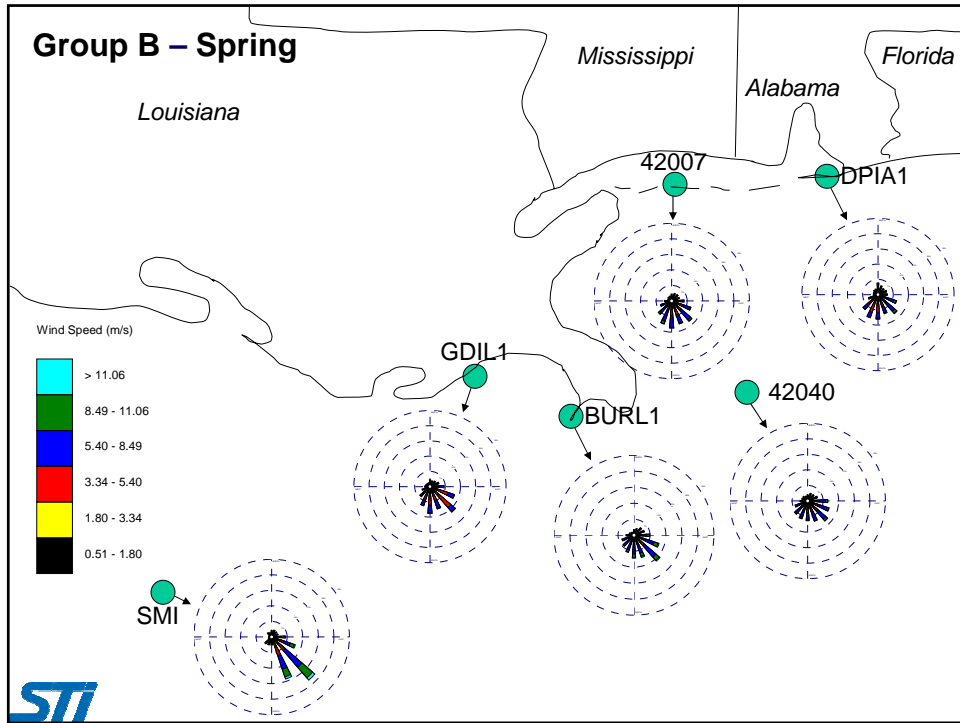


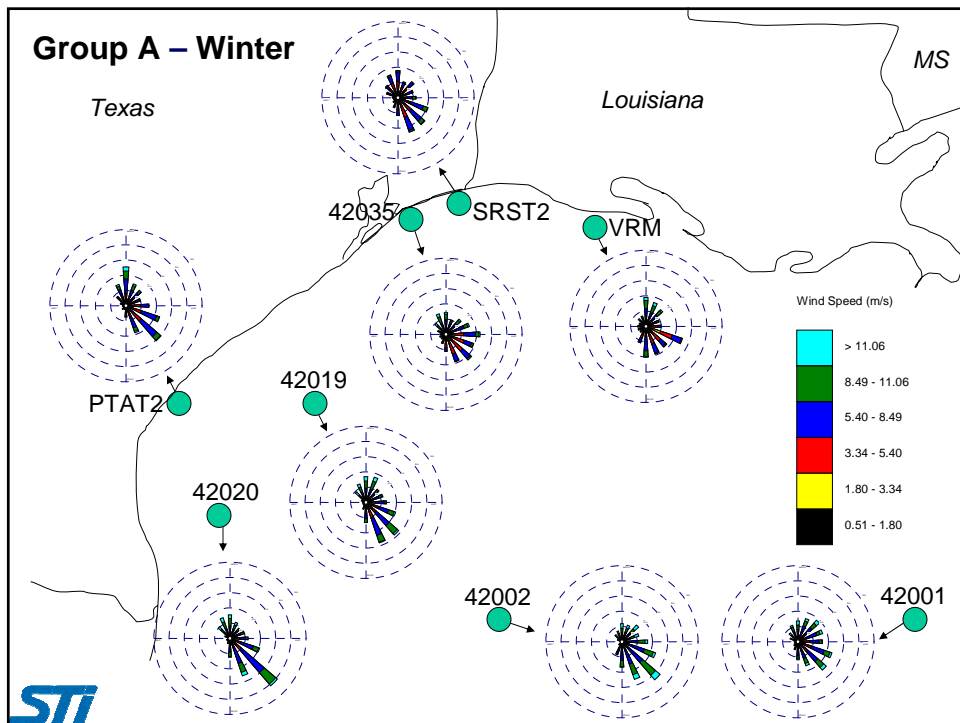
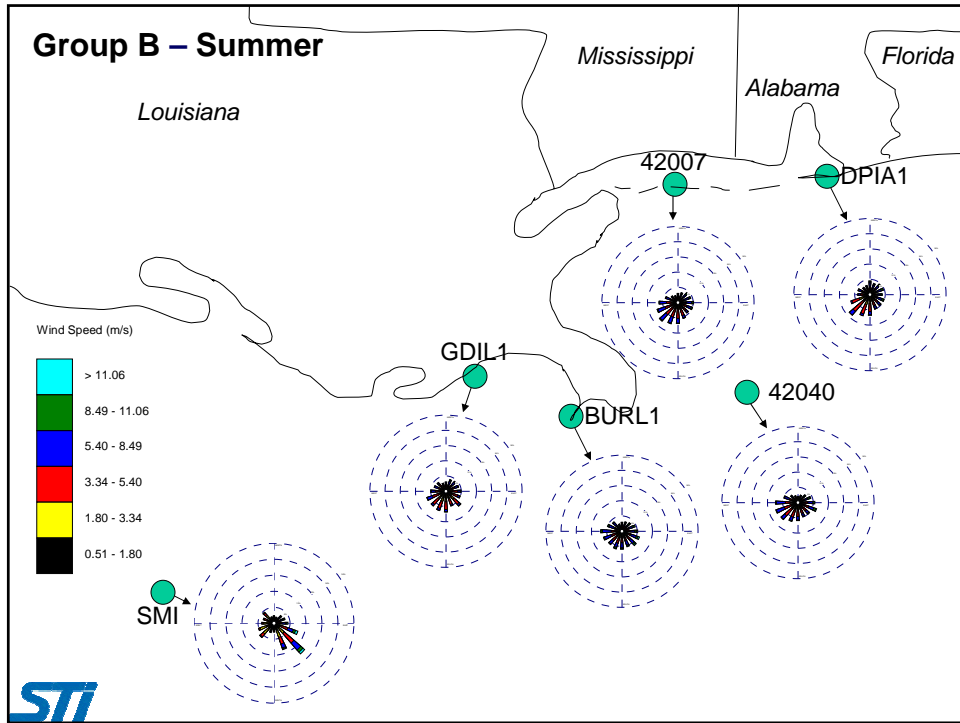
Buoy 42040 is representative of the wind rose plots at Group B sites.

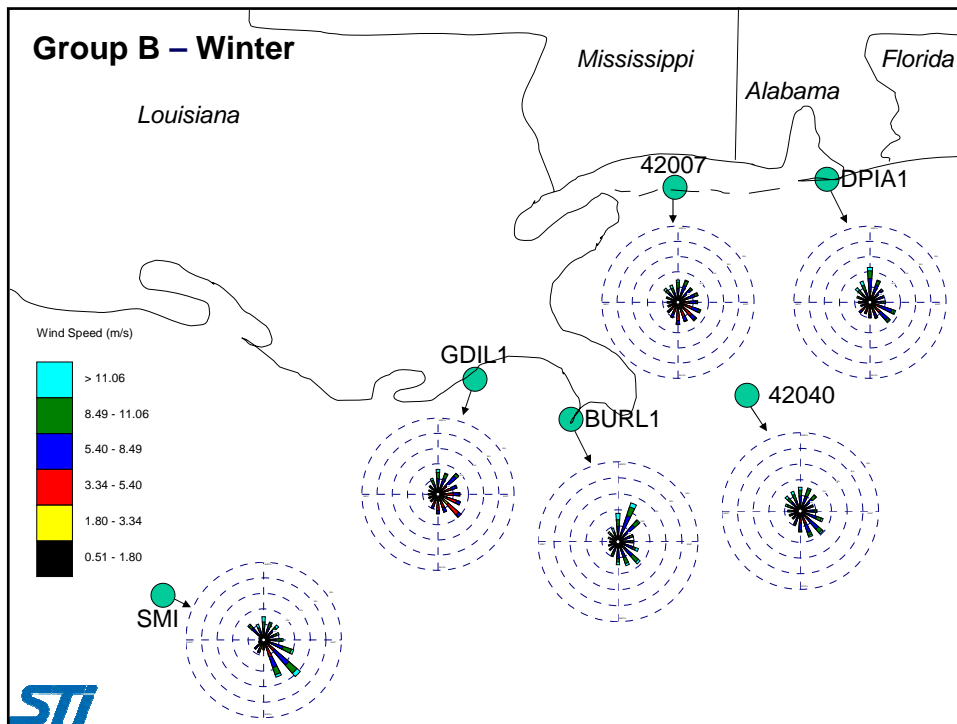












## Wind Rose – Overall

- Dominant southeasterly flow, with a secondary flow from the northeast
- Almost non-existent westerly flow within the region
- Group A
  - Strong southeasterly flow
  - Very little southwest through northeast wind flow
  - Southeasterly flow likely a reflection of the predominant weather feature, the Bermuda High, as well as the sea breeze. The northeasterly flow is likely a result of continental high pressure systems.
- Group B
  - Dominated by southeasterly flow
  - More evenly distributed throughout other directions than Group A

STI

## Wind Rose – Seasons

- Fall
  - Group B sites: predominantly north-northeast flow and very little southwesterly flow
  - Group A sites: predominantly southeasterly flow with secondary flows from the north-northeast
- Winter
  - Similar to fall, except stronger southeast flow at the Group B sites



## Wind Rose – Seasons

- Spring
  - Very different at both site groups compared to fall and winter
  - Predominant southeasterly flow with very little northerly flow at the Group A sites
  - Group B sites dominated by a broad peak from the east-southeast to the southwest
- Summer
  - Group A sites: similar to spring with a dominant southeast peak
  - Near-shore sites: more frequent southerly peak, likely due to the land/sea breeze circulation
  - Group B sites: evenly distributed peak from east through south to west, with the exception of SMI, which only had a southwest peak



## Profiler and RASS Statistics

- Characteristics of boundary layer winds and temperature profiles at VRM and SMI
- How these characteristics change by year, season, month, and upper-air classification and between sites



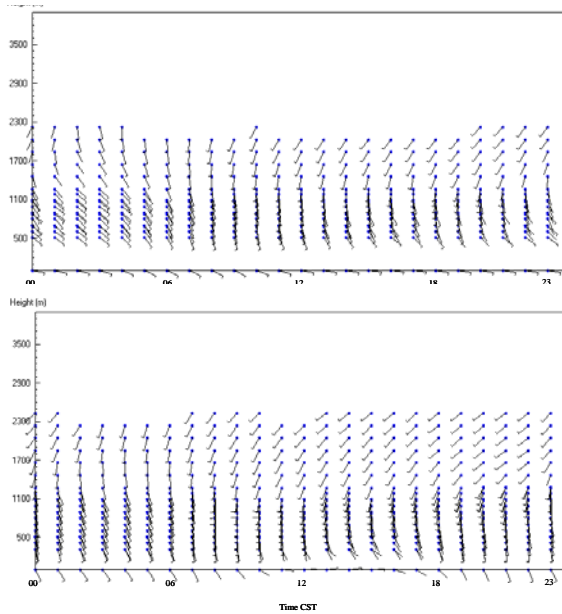
## Profiler and RASS Statistics – Method

- Winds were vectorially averaged.
- Virtual temperature data were grouped into “day” (0600 to 1800 CST) and “night” (1800 to 0600 CST).
- Averages were only calculated if at least 50% of the possible measurements contributing to that average were valid.
- Note: SMI and VRM provided three years of data, whereas BAMP sites provided one year of data.

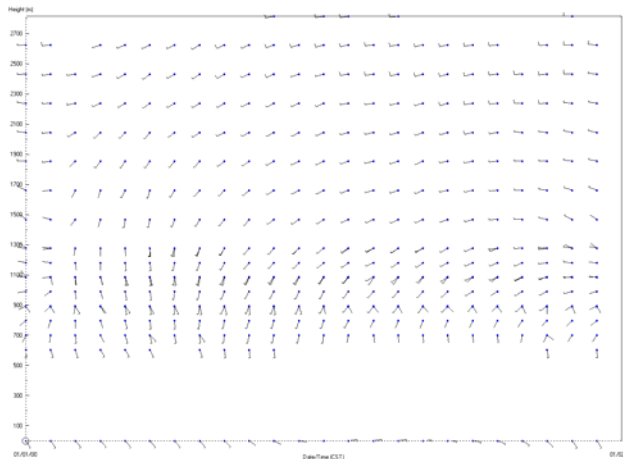


## VRM and SMI Overall

Overall average winds at SMI (top) and VRM (bottom) from 0000 to 2300 CST, June 1, 1998, to May 31, 2001



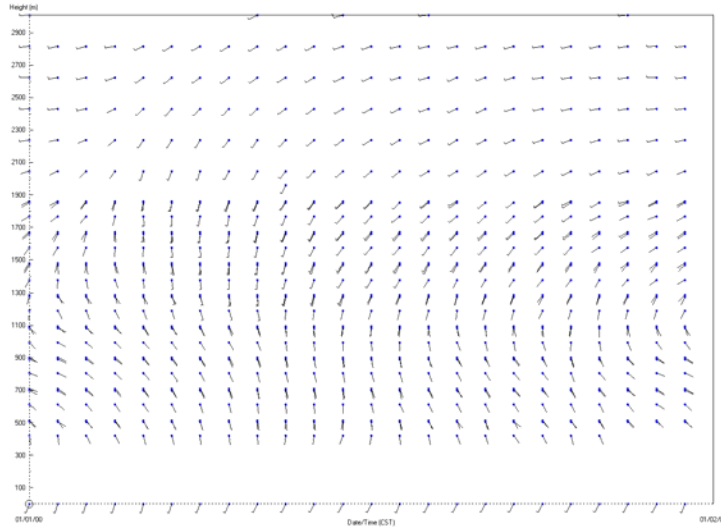
## BIP Overall Mean Winds



Overall average winds at BIP from 0000 to 2300 CST, September 2000 to September 2001



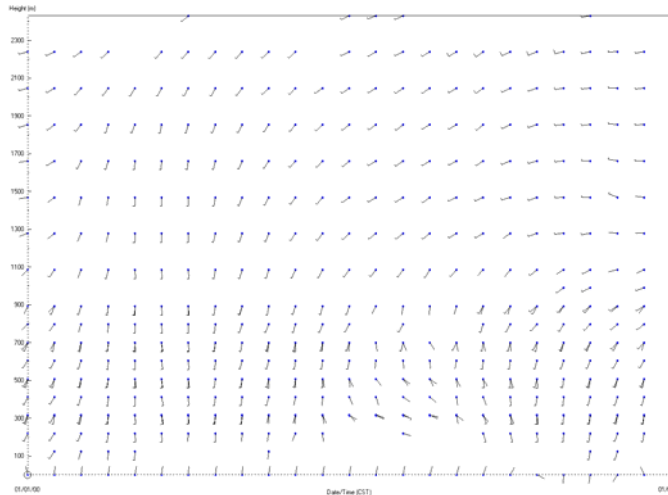
## DWP Overall Mean Winds



Overall average winds at DWP from 0000 to 2300 CST, September 2000 to September 2001



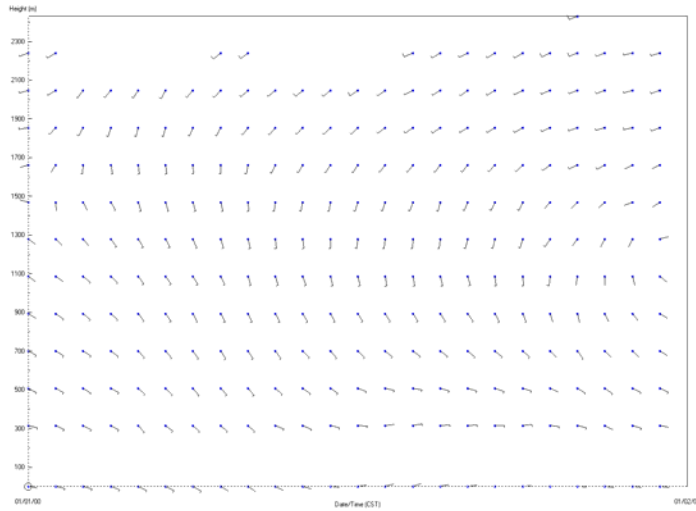
## FTM Overall Mean Winds



Overall average winds at FTM from 0000 to 2300 CST, September 2000 to September 2001



## WDP Overall Mean Winds

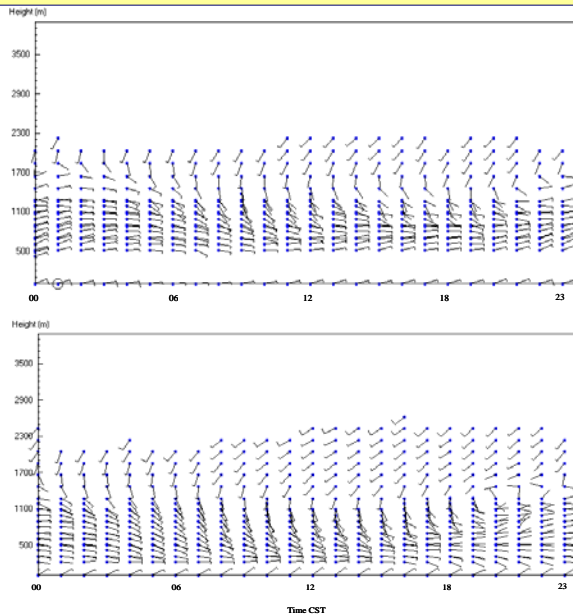


Overall average winds at WDP from 0000 to 2300 CST, September 2000 to September 2001

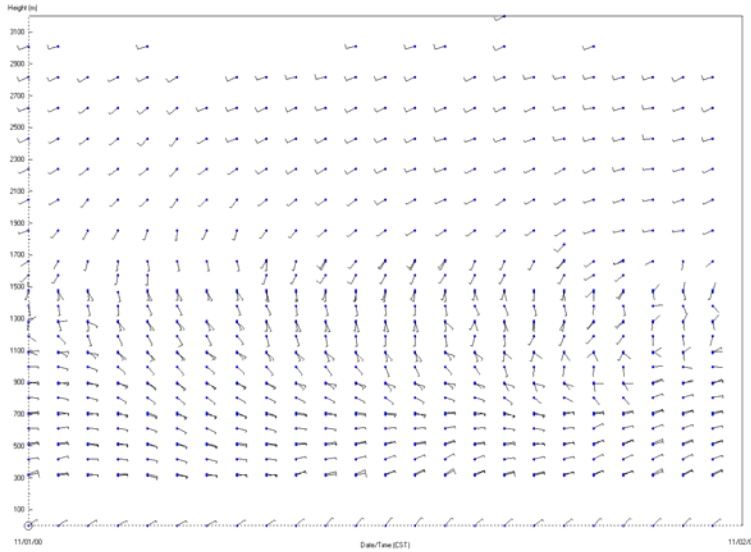


## Profiler Winds – Fall

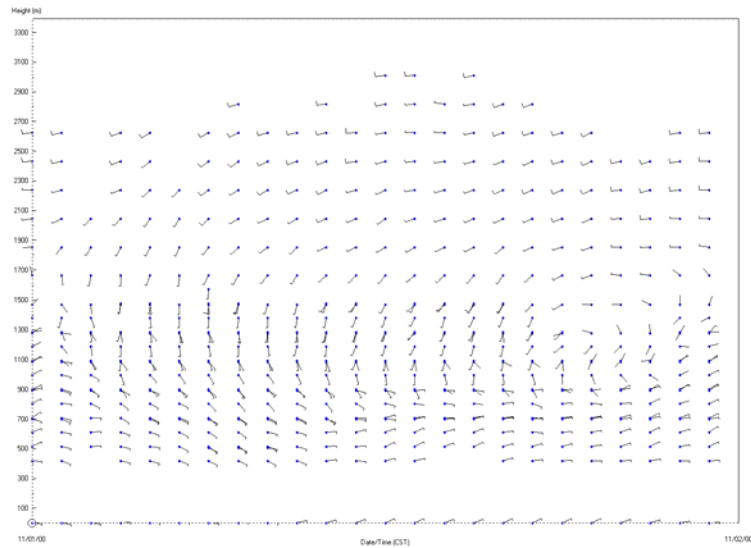
Fall average winds at  
SMI (top) and VRM (bottom)



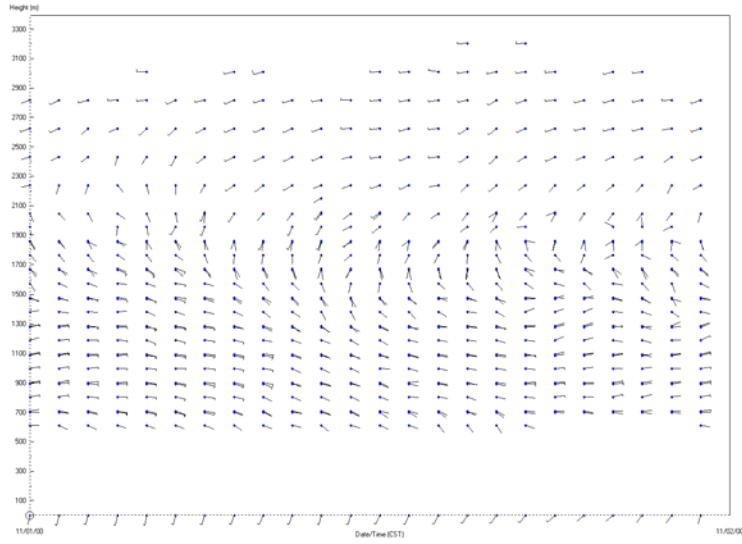
## WDP Mean Winds – Fall



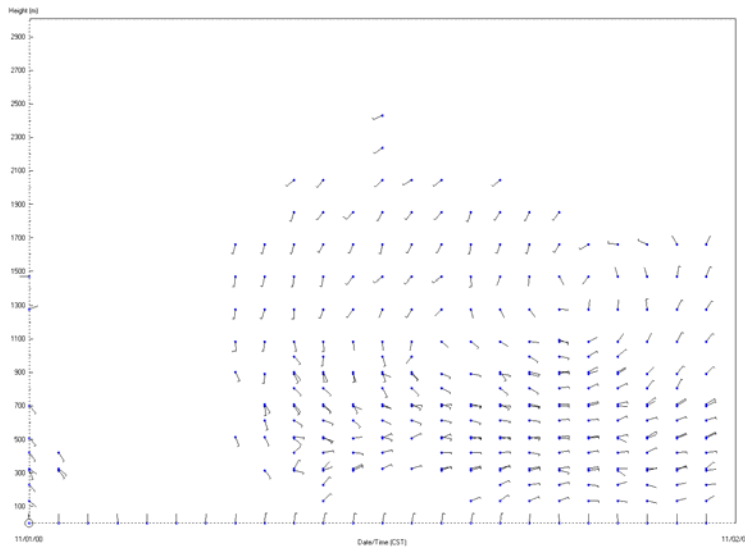
## BIP Mean Winds – Fall



## DWP Mean Winds – Fall

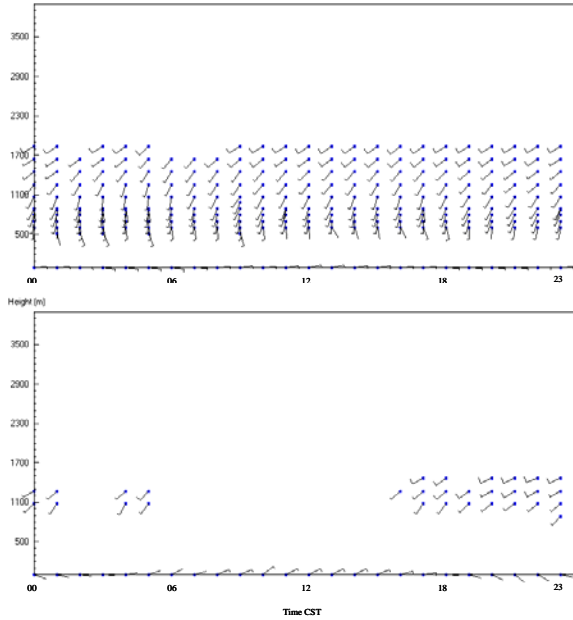


## FTM Mean Winds – Fall

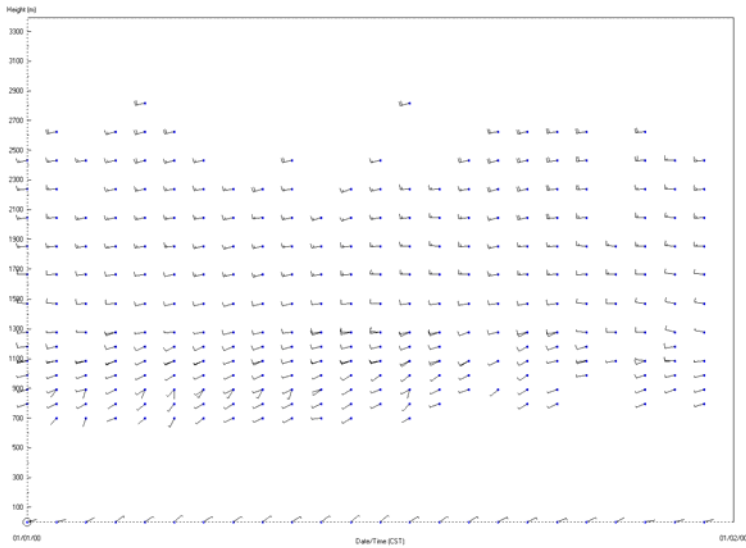


## Profiler Winds – Winter

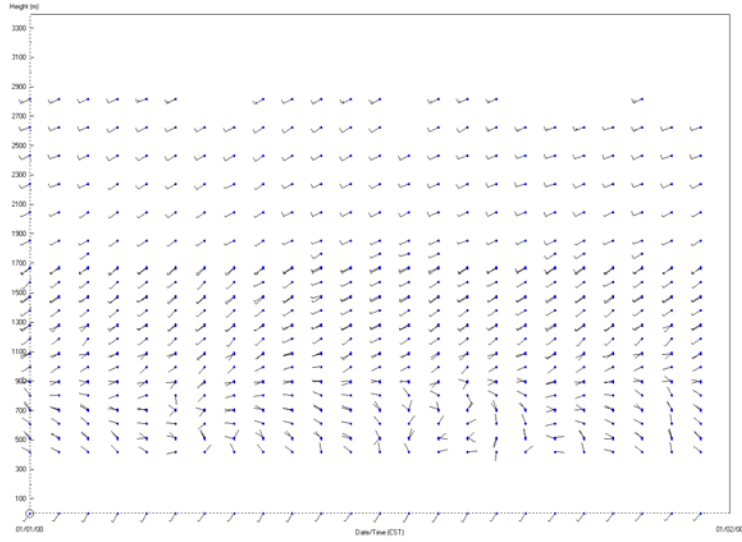
Winter average winds at  
SMI (top) and VRM (bottom)



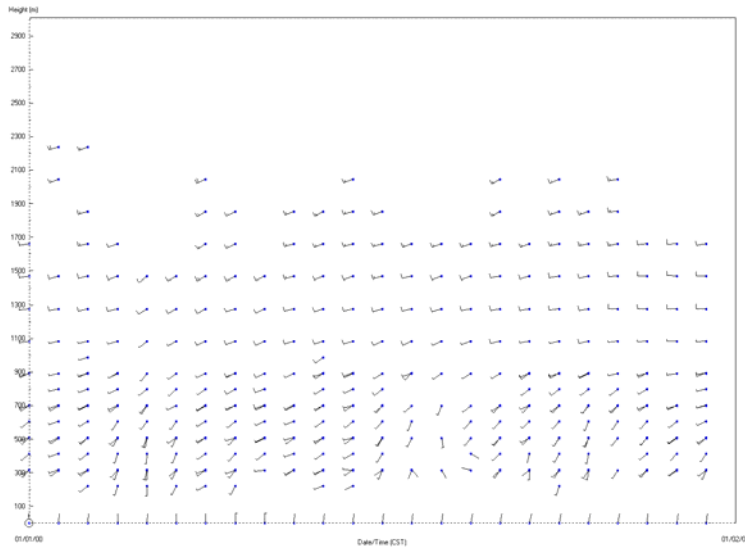
## BIP Mean Winds – Winter



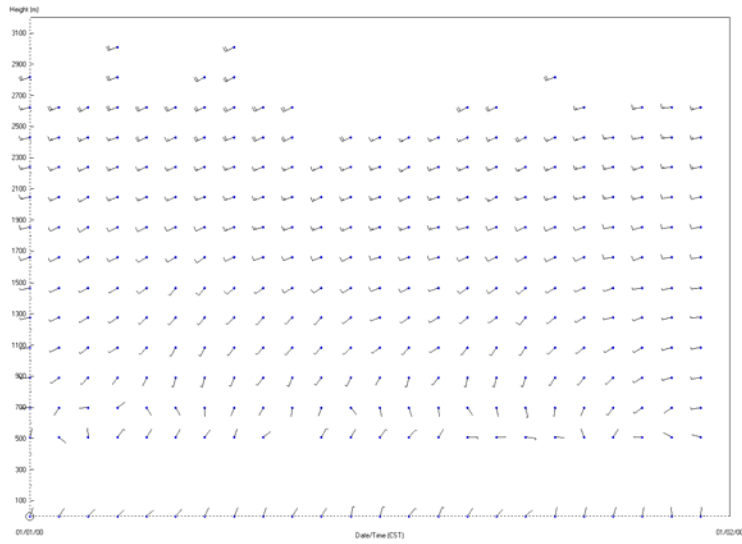
## DWP Mean Winds – Winter



## FTM Mean Winds – Winter

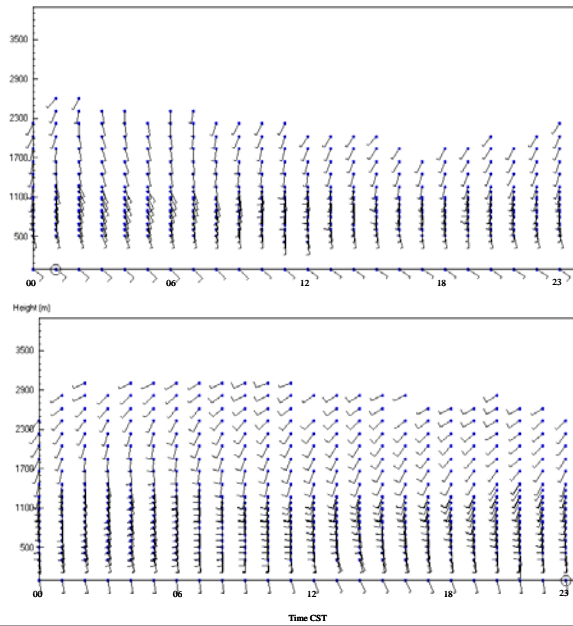


## WDP Mean Winds – Winter

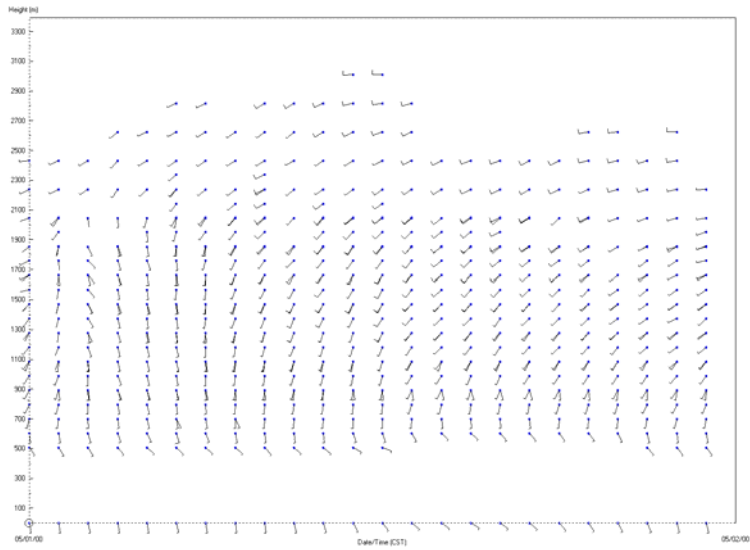


## Profiler Winds – Spring

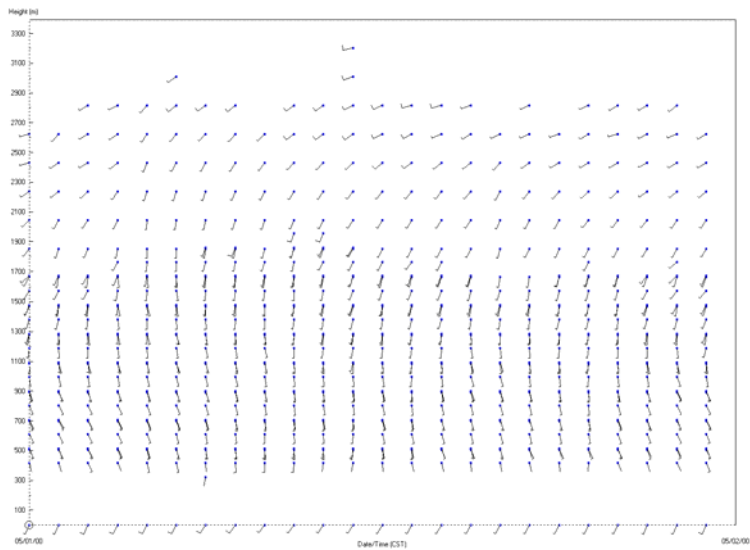
Spring average winds at  
SMI (top) and VRM (bottom)



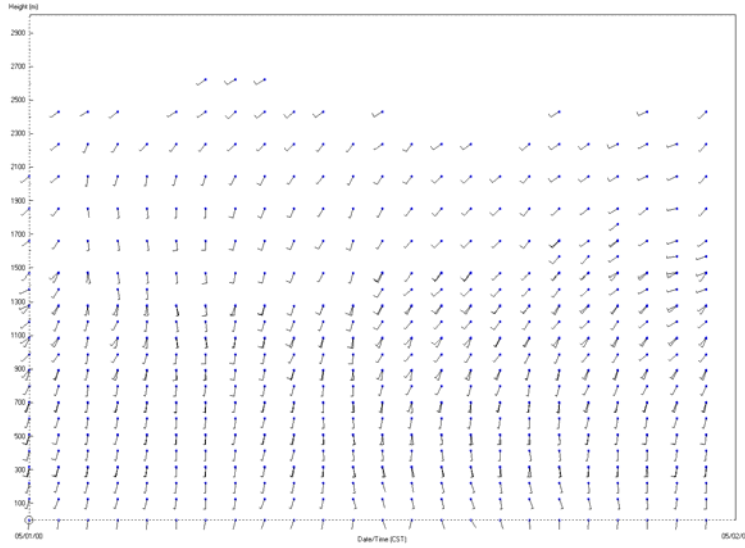
## BIP Mean Winds – Spring



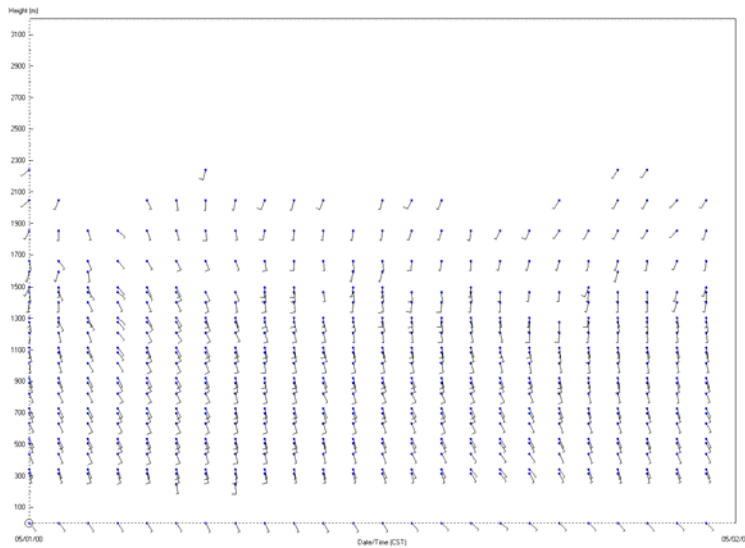
## DWP Mean Winds – Spring



## FTM Mean Winds – Spring

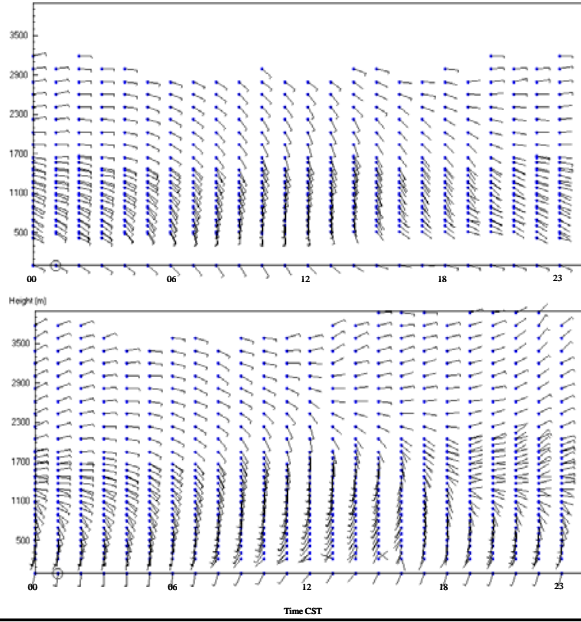


## WDP Mean Winds – Spring

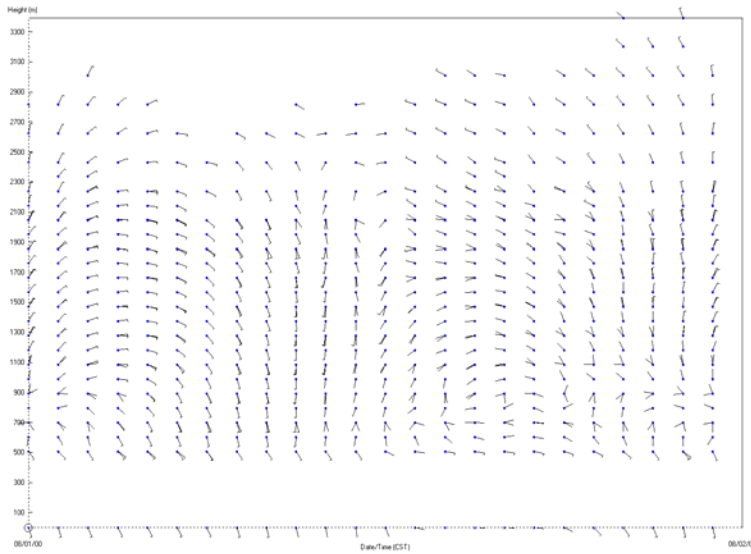


## Profiler Winds – Summer

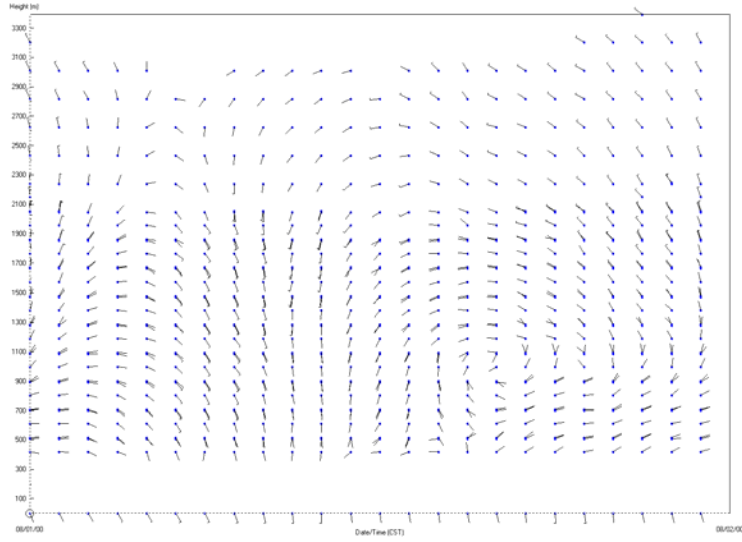
Summer average winds at  
SMI (top) and VRM (bottom)



## BIP Mean Winds – Summer

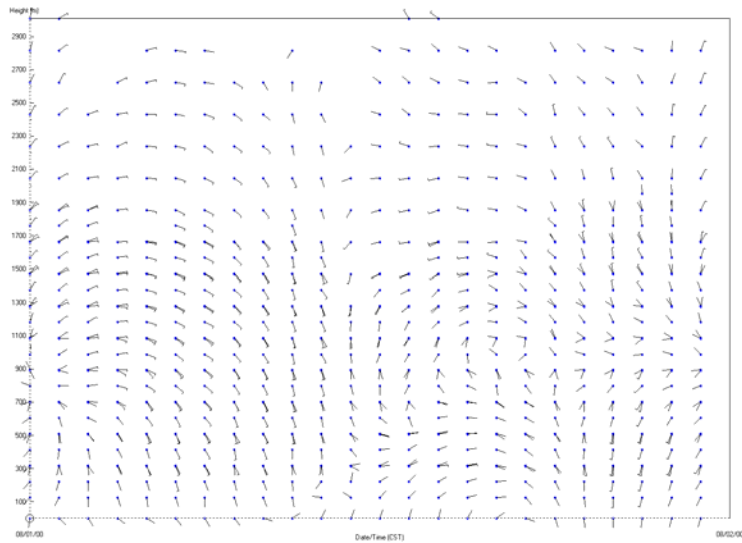


## DWP Mean Winds – Summer



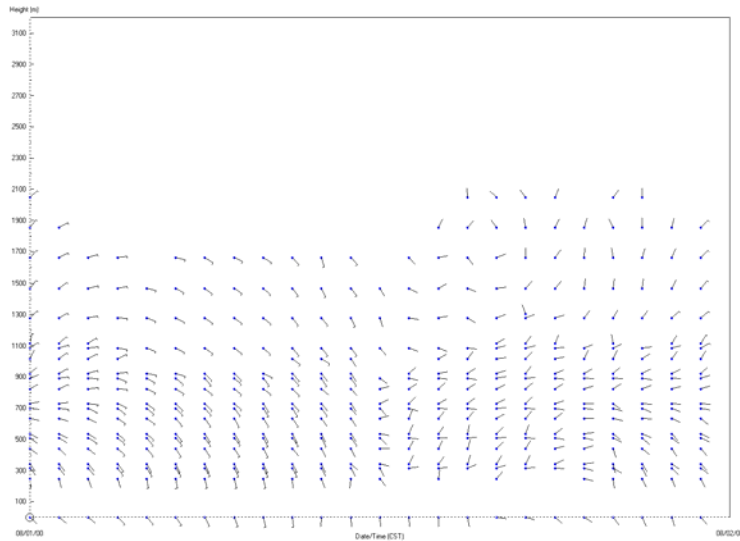
STI

## FTM Mean Winds – Summer



STI

## WDP Mean Winds – Summer



STI

## Profiler Winds – Summary (1 of 2)

- Overall
  - Southwest through easterly flow throughout all seasons, years, and sites; southeasterly flow the most frequent direction
  - At WDP winds were more easterly in the lowest 500 m compared to southerly at the other sites.
- Ridge (not shown here)
  - South to southeasterly below 1100 m and southwest to easterly aloft
- Trough (not shown here)
  - Mostly southwesterly flow aloft
  - Southeast to northeasterly flow in the low levels, with strong troughs having a more defined shear layer

STI

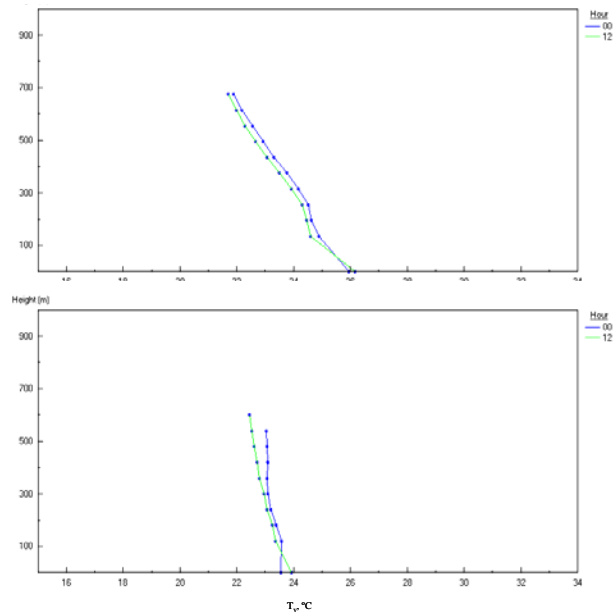
## Profiler Winds Summary (2 of 2)

- Fall
  - Easterly flow at lower levels
  - Southwesterly flow aloft
- Winter
  - Easterly surface flow very decoupled from south to southwesterly flow aloft
  - Northerly flow at the surface at near-shore sites
- Spring
  - Coupled surface and aloft flow with southerly flow up to 1000 m
  - Southwesterly flow above 1000 m
- Summer
  - Easterly to southwesterly flow below 2000 m
  - Most diurnal variability at VRM compared to all seasons and sites

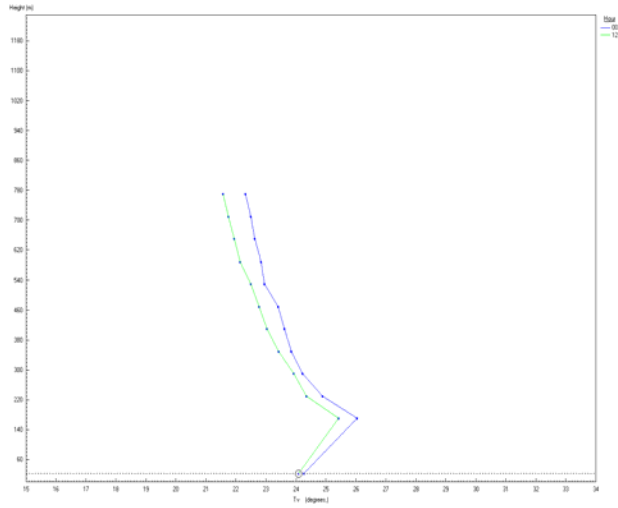


## VRM and SMI Overall

Average overall daytime and nighttime temperature profiles at SMI (top) and VRM (bottom).

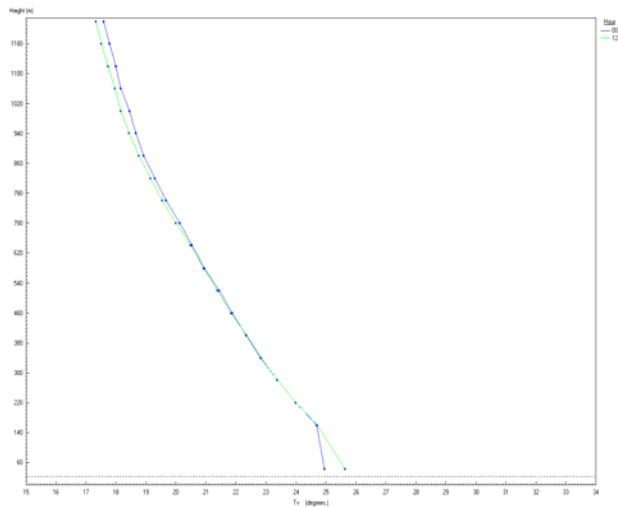


## BIP Overall



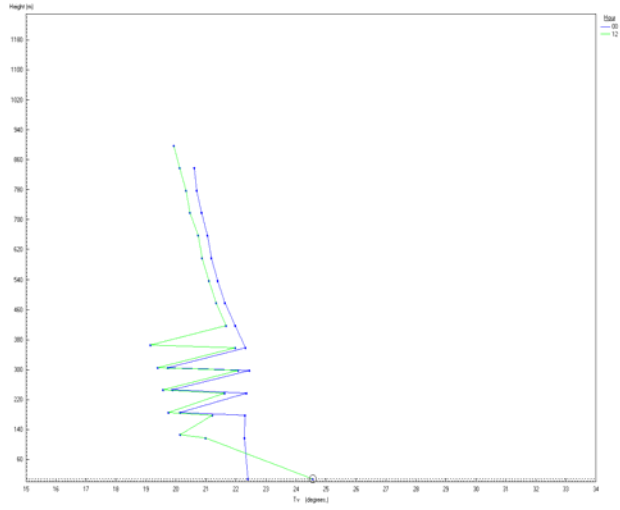
STI

## DWP Overall



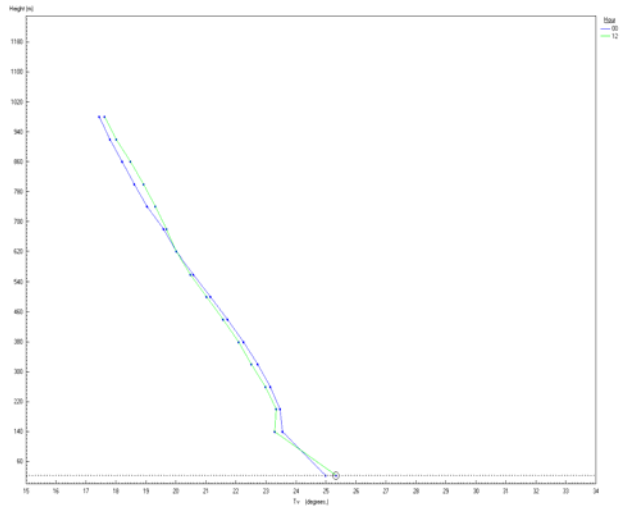
STI

## FTM Overall



STI

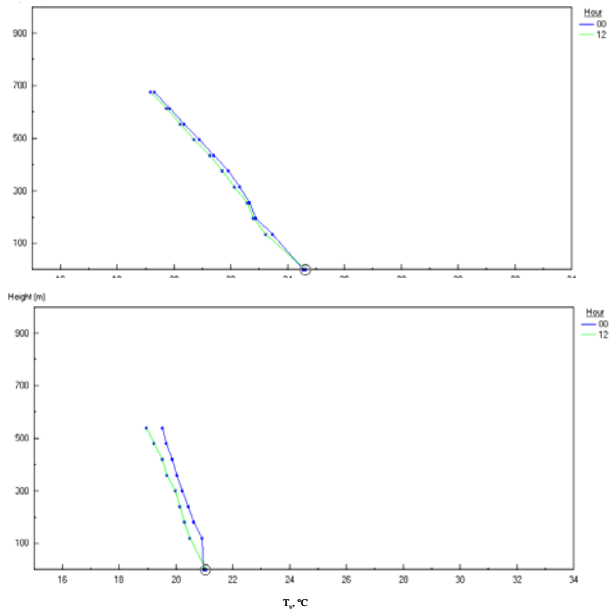
## WDP Overall



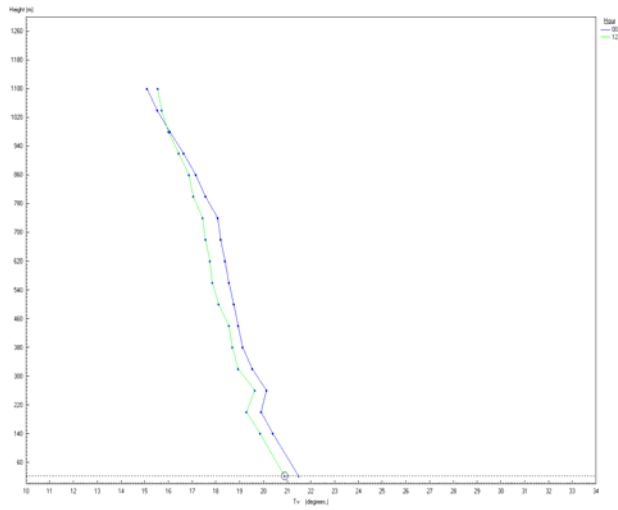
STI

## SMI and VRM – Fall

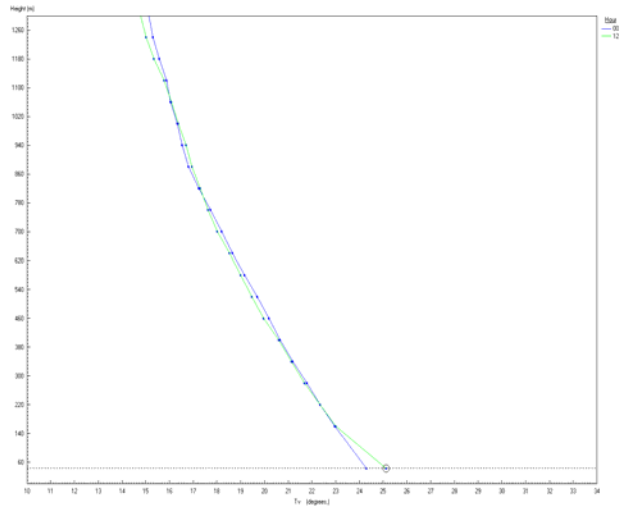
Fall overall daytime and nighttime temperature profiles at SMI (top) and VRM (bottom).



## BIP – Fall

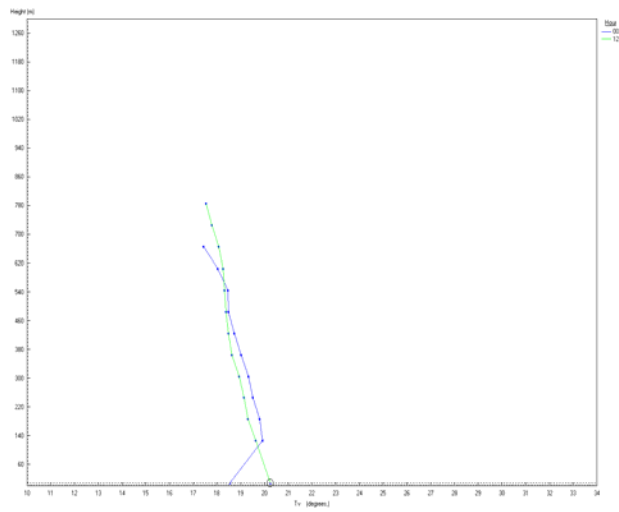


## DWP – Fall



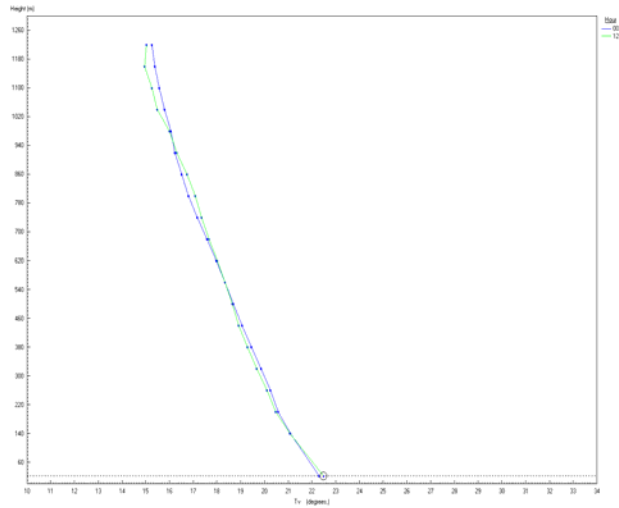
STI

## FTM – Fall



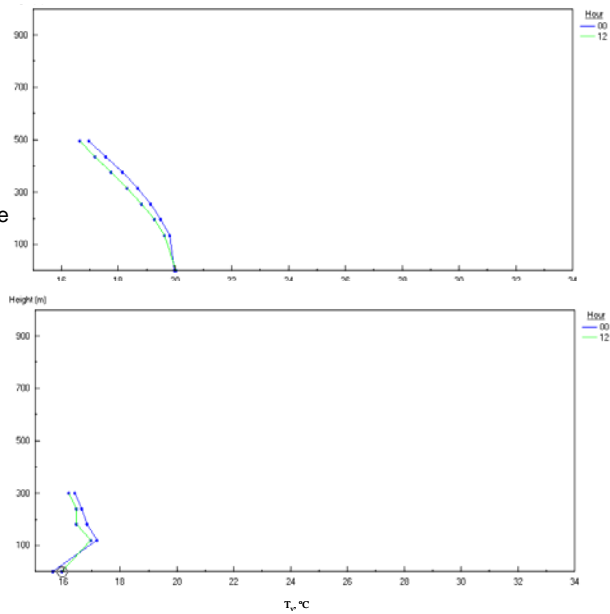
STI

## WDP – Fall

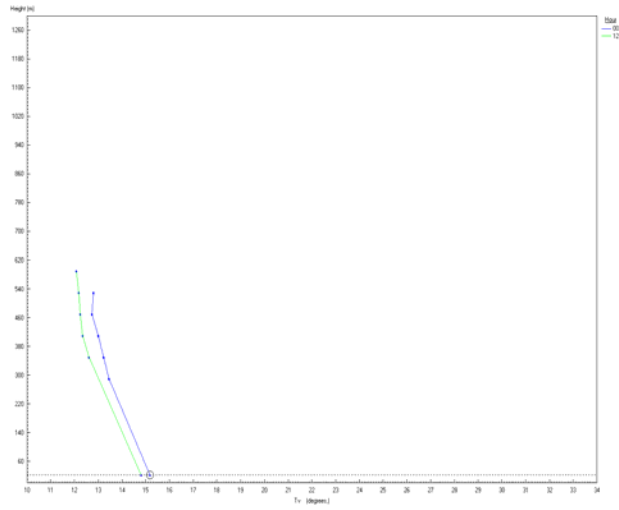


## SMI and VRM – Winter

Winter overall daytime and nighttime temperature profiles at SMI (top) and VRM (bottom), June 1, 1998, to May 31, 2001. Hour 12 is the daytime profile and hour 00 is the nighttime profile.

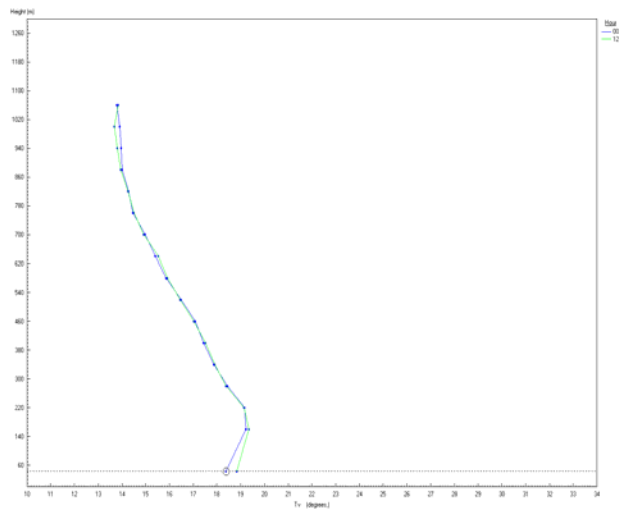


## BIP – Winter



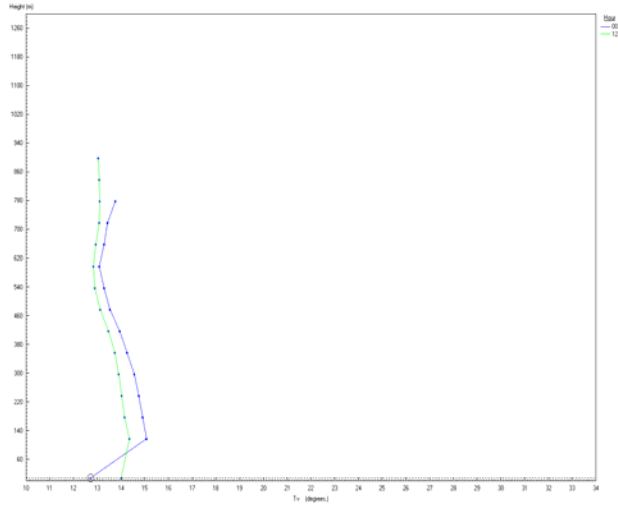
STI

## DWP – Winter



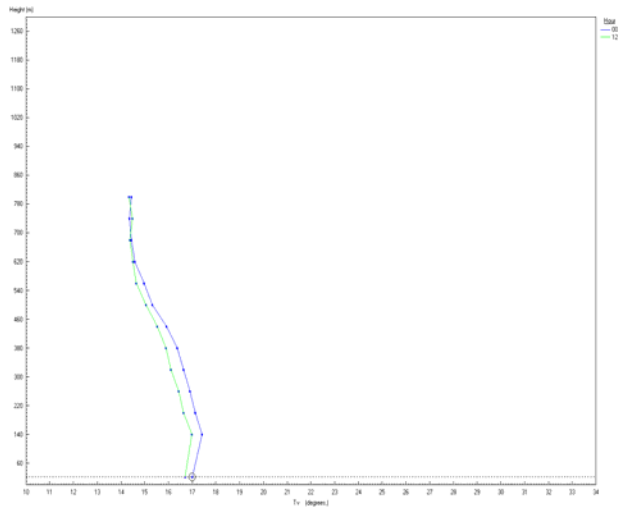
STI

## FTM – Winter



STI

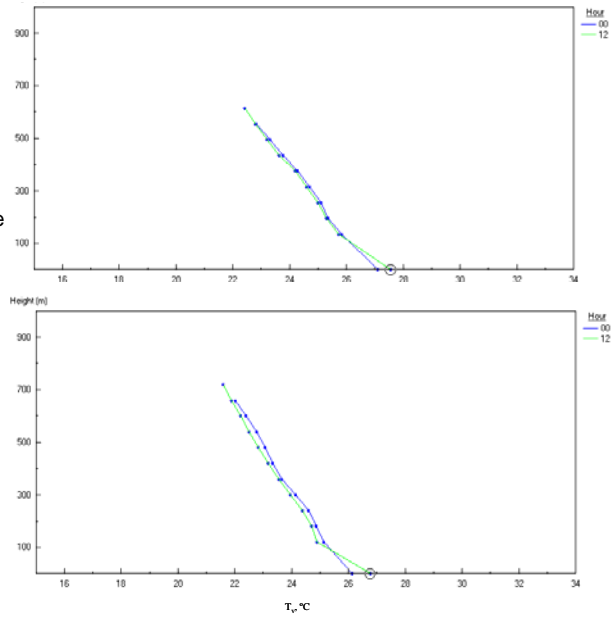
## WDP – Winter



STI

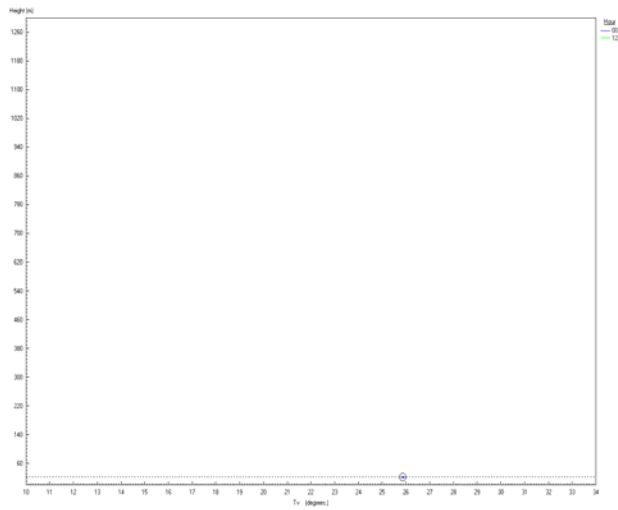
## SMI and VRM – Spring

Spring overall daytime and nighttime temperature profiles at SMI (top) and VRM (bottom), June 1, 1998, to May 31, 2001. Hour 12 is the daytime profile and hour 00 is the nighttime profile.



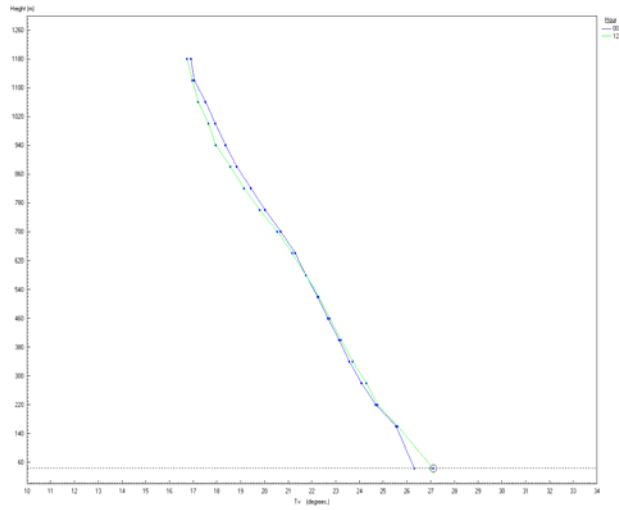
STI

## BIP – Spring



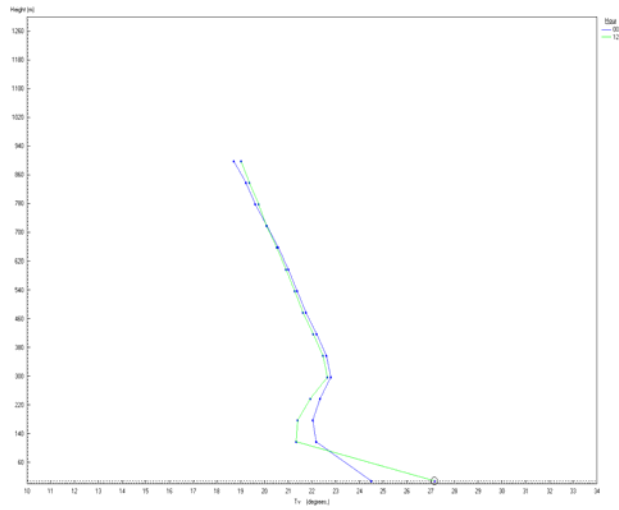
STI

## DWP – Spring



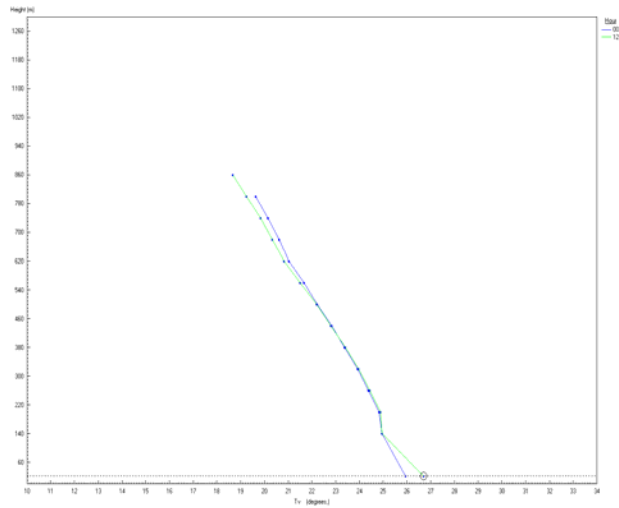
STI

## FTM – Spring



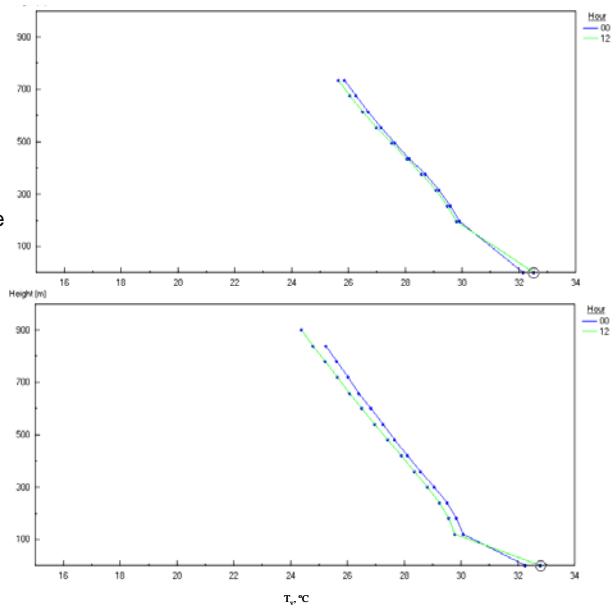
STI

## WDP – Spring

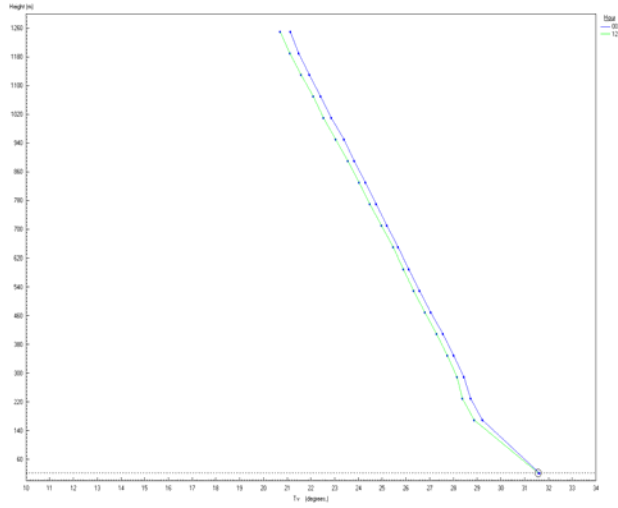


## SMI and VRM – Summer

Summer overall daytime and nighttime temperature profiles at SMI (top) and VRM (bottom), June 1, 1998, to May 31, 2001.

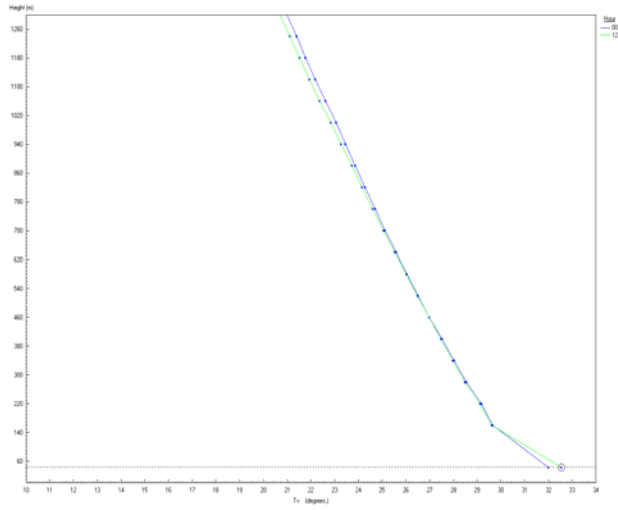


## BIP – Summer



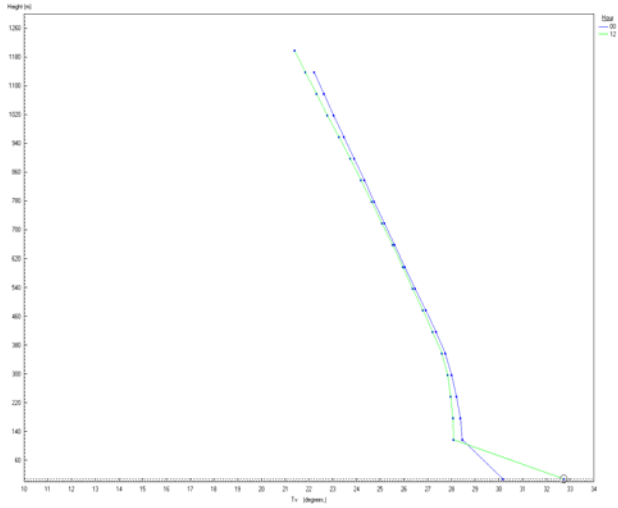
STI

## DWP – Summer

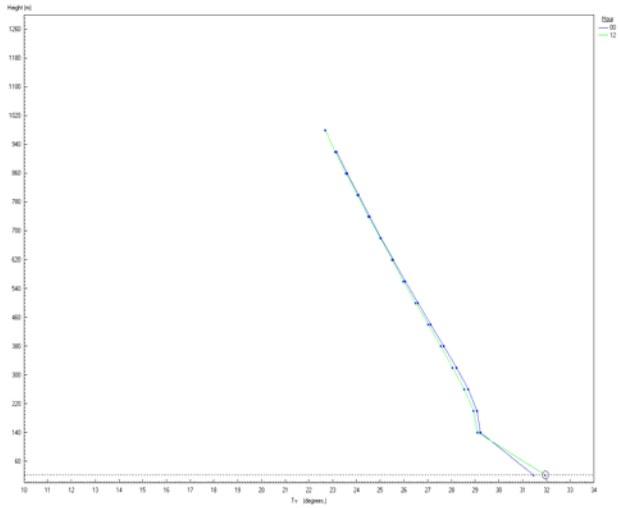


STI

## FTM – Summer



## WDP – Summer



## RASS Virtual Temperature – Summary (1 of 2)

- There is often a discontinuity in temperature gradient at the lower two or three RASS levels (e.g., 131 m), due to a known cold bias.
- The surface temperature and the 131-m temperature are measured by two types of instruments, which may influence the diagnosis of stable or unstable temperature gradients.
- The average profiles, which extend to about 700 m, do not show an elevated inversion or mixing height, despite the fact that a mixing depth of 500 to 700 m is expected and often observed in the  $C_n^2$  data.



## RASS Virtual Temperature – Summary (2 of 2)

- Overall
  - VRM is more stable than other sites.
  - BIP has strong stable inversion in lowest layer, other sites do not.
- Fall
  - FTM has surface inversion at night, others do not.
- Winter
  - All sites have an inversion during the day and night except VRM and BIP. Inversion may be a result of platform radiational cooling.
- Spring and Summer
  - All sites are about adiabatic.



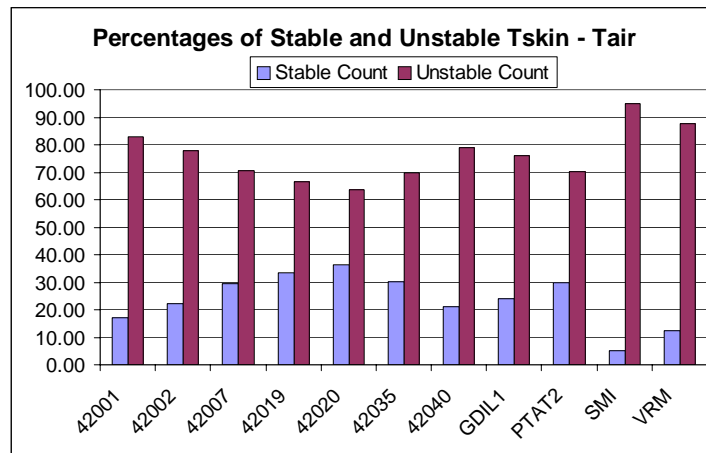
## Near-Surface Stability

- Skin temperature ( $T_s$ ) minus surface temperature ( $T_{\text{surface}}$ ).
- Diurnal profiles by month
- Stable defined as when  $T_s$  minus  $T_{\text{surface}}$  is less than zero.



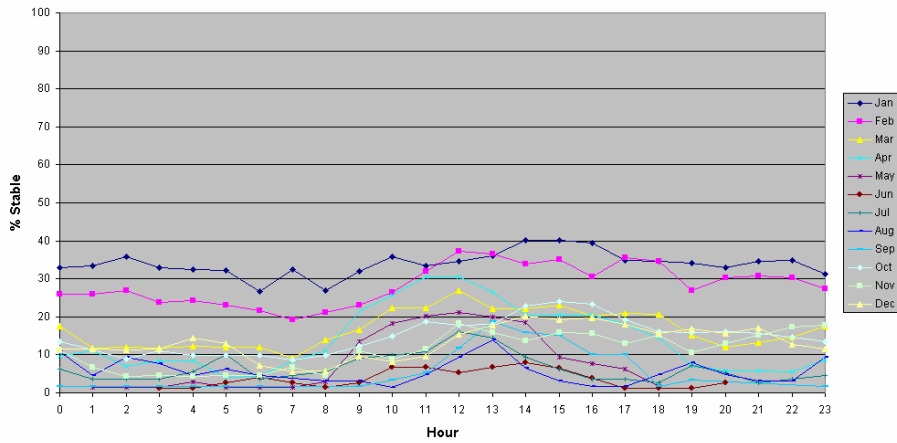
## Annual Average

$T_s$  at the buoys is estimated from the underwater temperature in COARE.



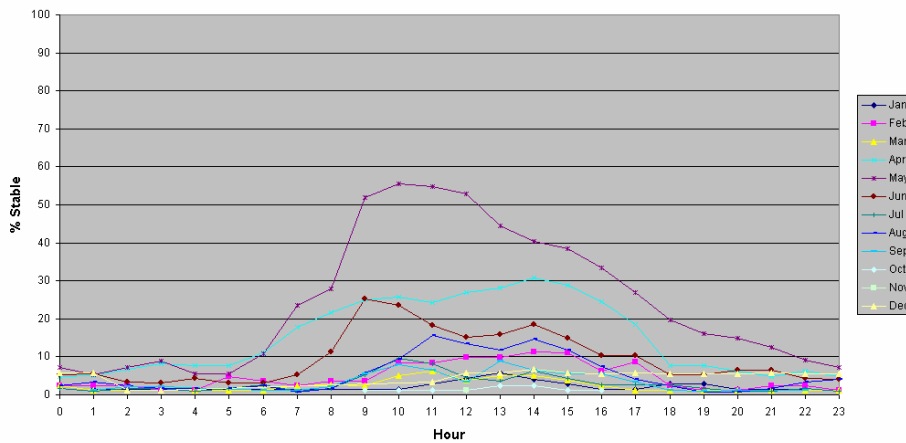
## VRM – Monthly Average Diurnal Profiles

Percent Stable Days by Hour - VRM

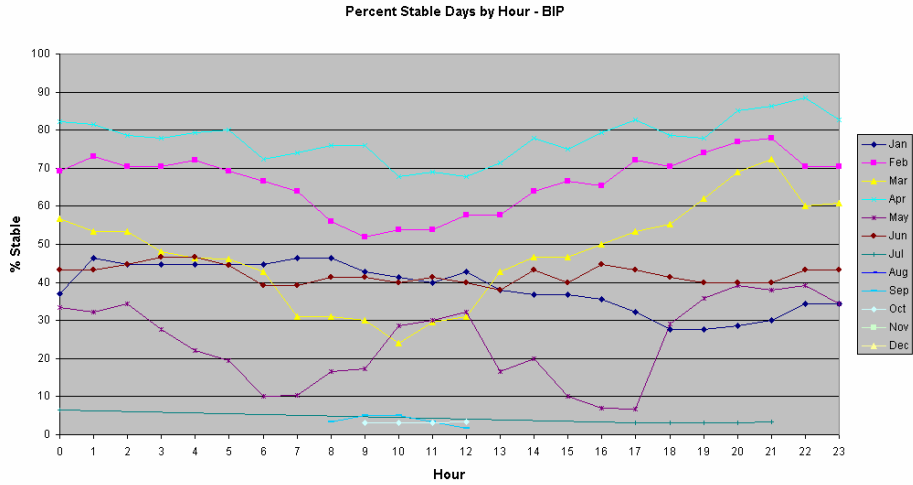


## SMI – Monthly Average Diurnal Profiles

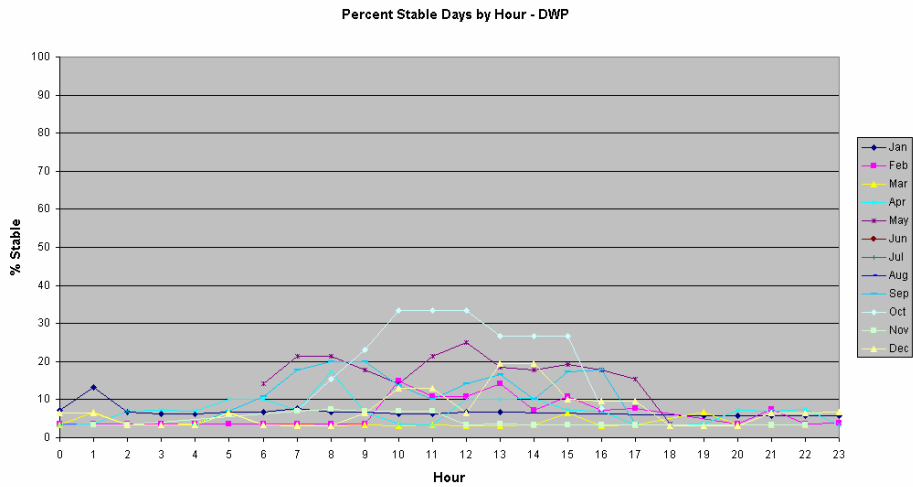
Percent Stable Days by Hour - SMI



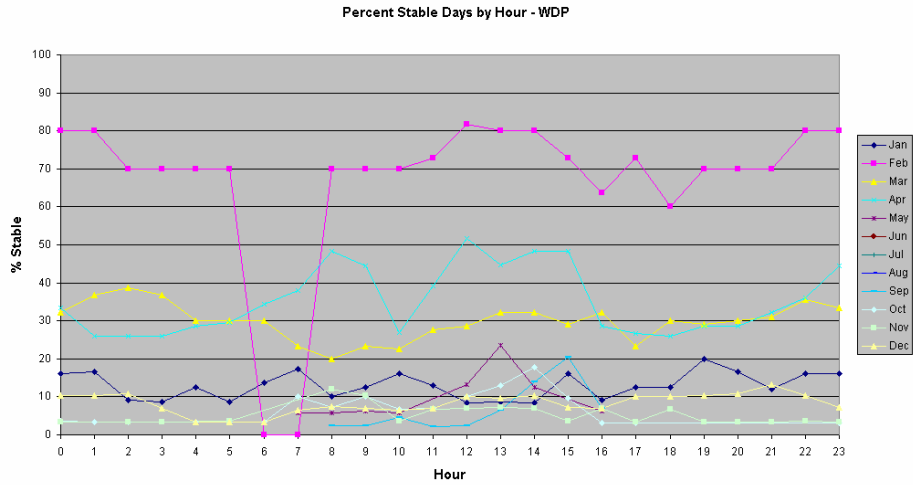
## BIP – Monthly Average Diurnal Profiles



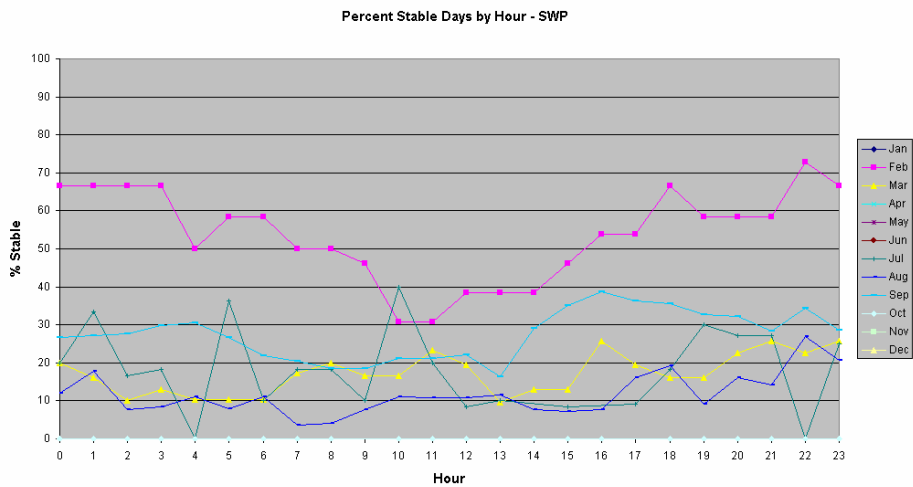
## DWP – Monthly Average Diurnal Profiles



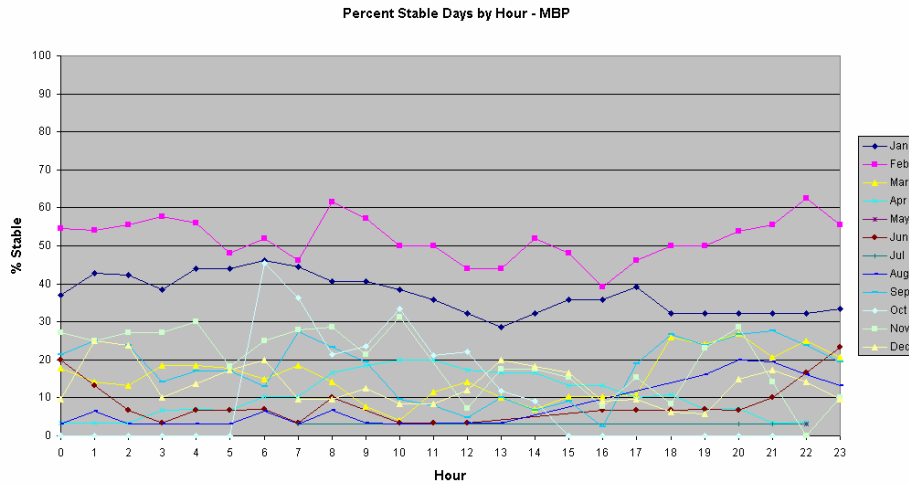
## WDP – Monthly Average Diurnal Profiles



## SWP – Monthly Average Diurnal Profiles



## MBP – Monthly Average Diurnal Profiles



## Stability Summary

- Most sites are about 20% stable and 80% unstable.
- January and February are the most stable months.
- Possible non-representative daytime stability created by platform heating.



## Estimated Mixing Heights

- Goal – Automatically produce hourly mixing heights using observed data
  - RASS virtual temperature and surface temperature
  - Profiler reflectivity and vertical velocity
- Findings
  - Sea clutter in lowest 600 m contaminated reflectivity data
  - Aloft inversion capping boundary layer was rarely observed in RASS data
- Conclusion – Automatic processing difficult over warm water
- Solution – Case study mixing heights



## Mixing Depth – RWP (1 of 2)

- Reflectivity
  - Measures variations in the refractive index of the atmosphere
  - Turbulence produces variations in atmospheric temperature, humidity, and pressure, which in turn cause variations in the refractive index.
  - Reflectivity largest at inversion capping convective or marine boundary
  - CBL height-finding algorithms (Angevine et al., 1994; Dye et al., 1995; Bianco and Wilczak, 2002)

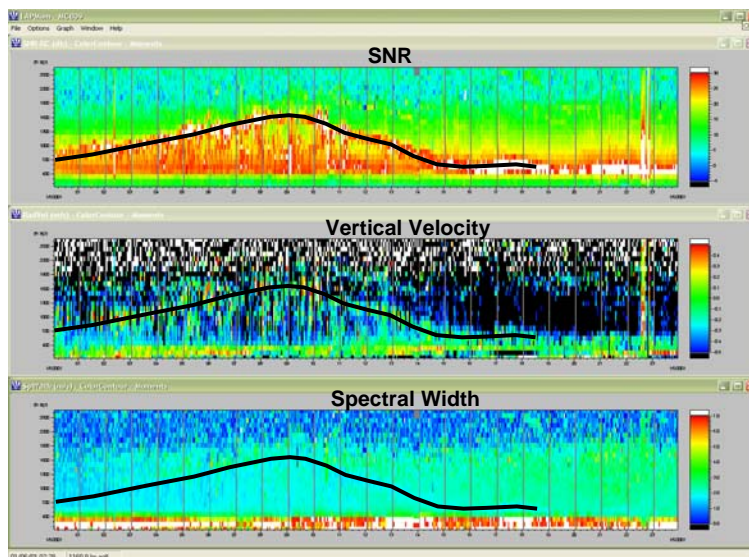


## Mixing Depth – RWP (2 of 2)

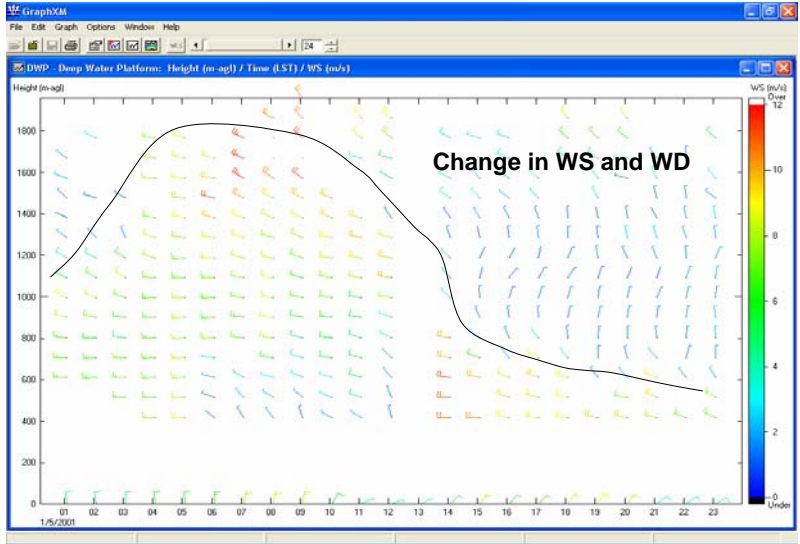
- Vertical Velocity
  - The radial velocity measured by the RWP vertical beam is a direct measure of vertical velocity
  - Convective thermals within the CBL act to vertically redistribute heat, moisture, and momentum
  - Identification of the vertical extent of convective thermals helps obtain an estimate of mixing depth
- Spectral Width
  - The range of radial velocities measured within the scatter volume is illustrated by spectral width
  - Locating the gradient in the spectral width (variability in the scales of turbulence) can be used as a reasonable estimate of mixing depth



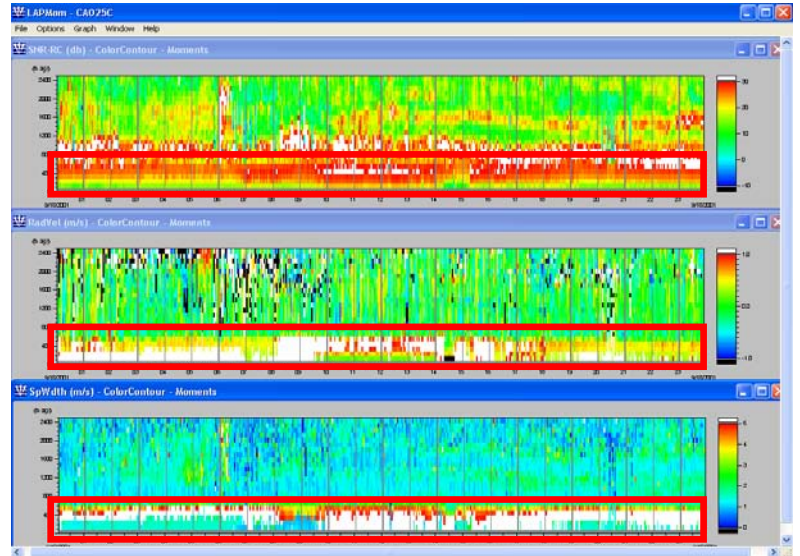
## RWP Mixing Heights – Moments



## RWP Mixing Heights – Wind Profiles

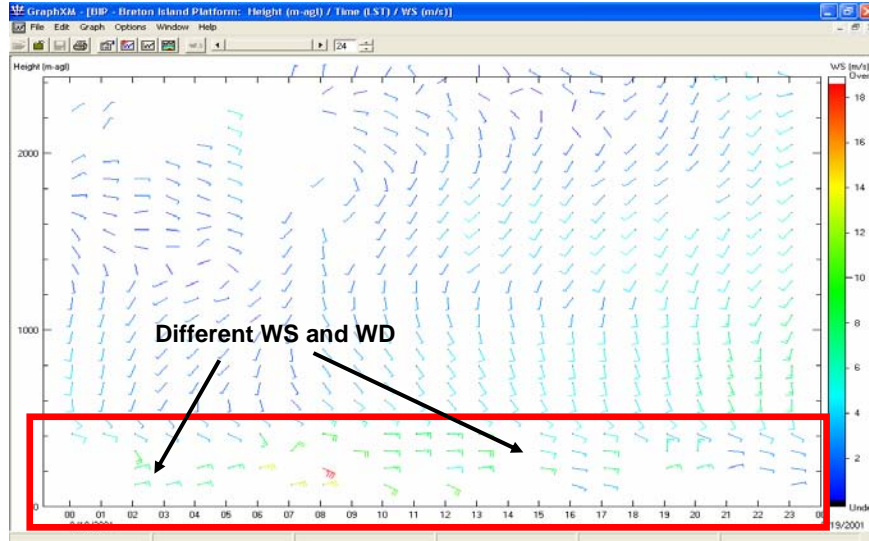


## Profiler Data Issues – Sea Clutter



BIP profiler data on September 18, 2001

## RWP Mixing Heights – Sea Clutter



STI

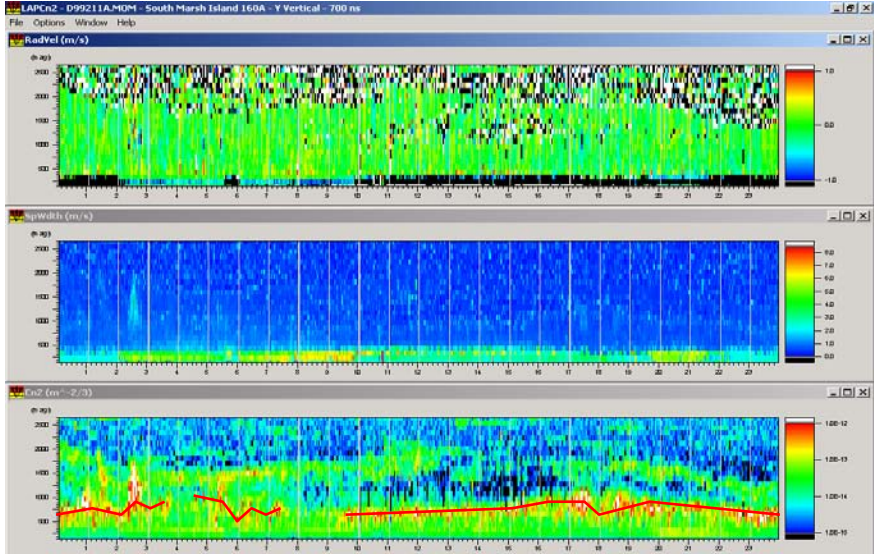
## Mixing Height – Case Examples

SMI  
July 30 to August 1, 1999

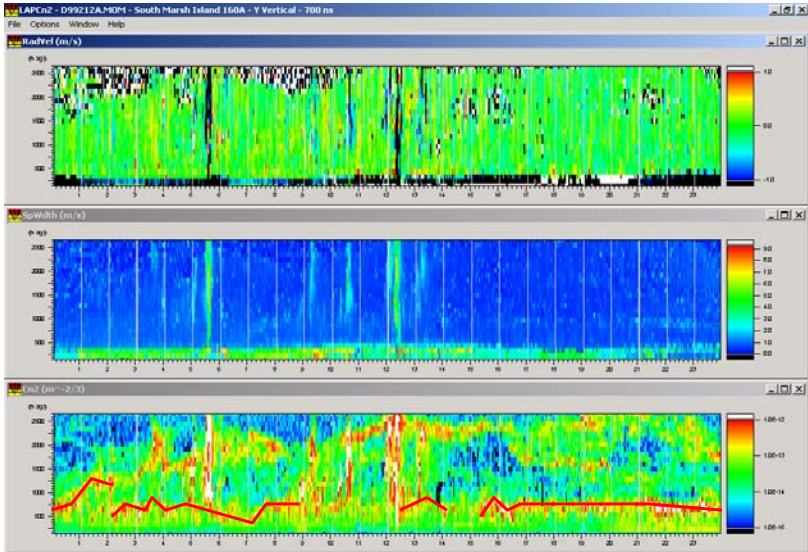
VRM  
September 18, 2001

STI

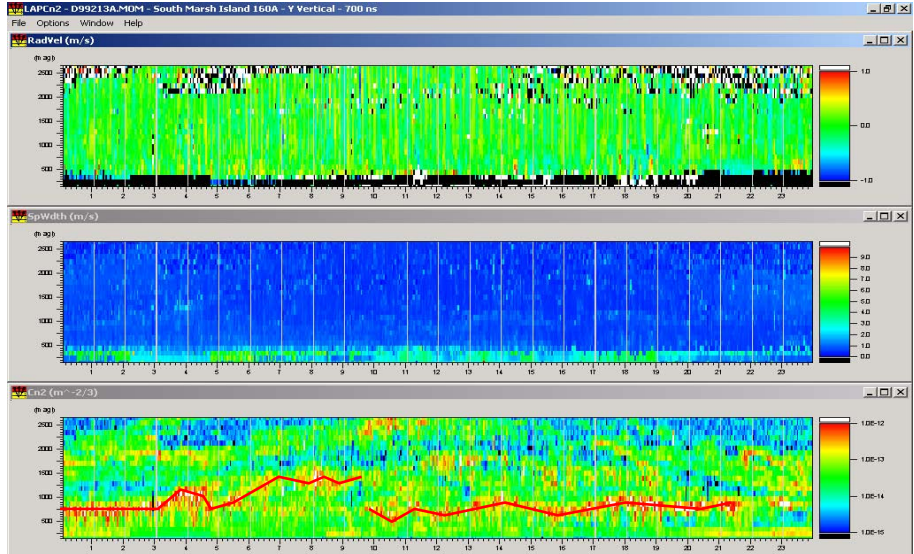
# SMI – July 30, 1999



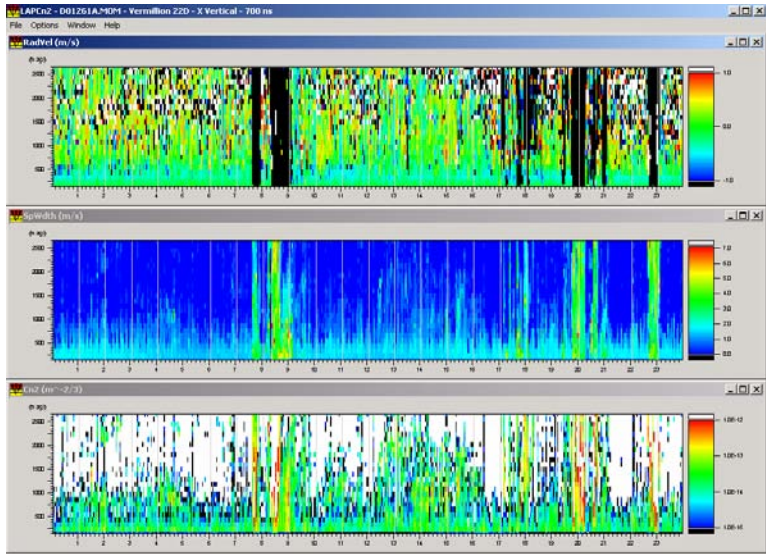
# SMI – July 31, 1999



# SMI – August 1, 1999



# VRM – September 18, 2001



## CALMET Mixing Heights

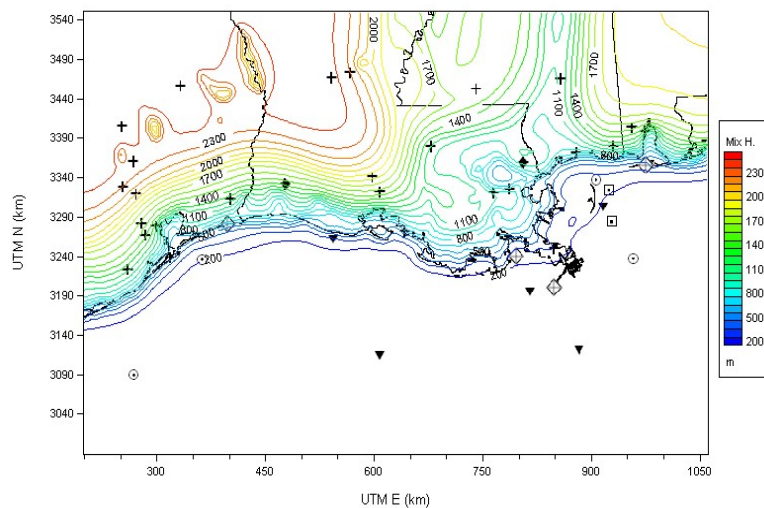
CALMET uses two different schemes to model the boundary layer

1. Overland – determined from observed temperature soundings and the computed hourly surface heat fluxes using a modified Carson (1973) method based on Maul (1980).
2. Overwater
  - “Calculated using the neutral barotropic scaling relationship” (Blackadar and Tennekes, 1968).
  - This relationship takes into account only mechanical mixing and not convective mixing (neglects the surface heat flux).



## CALMET Mixing Heights – Example

CALMET Mixing Heights - May 14, 2001 1700 CST



## CALMET Mixing Heights

To create a mixing height of 800 m, the current CALMET overwater mixing height scheme, requires a surface wind speed of ~24.5 knots (12.5 m/s).



## Mixing Height Comparison

### Goal:

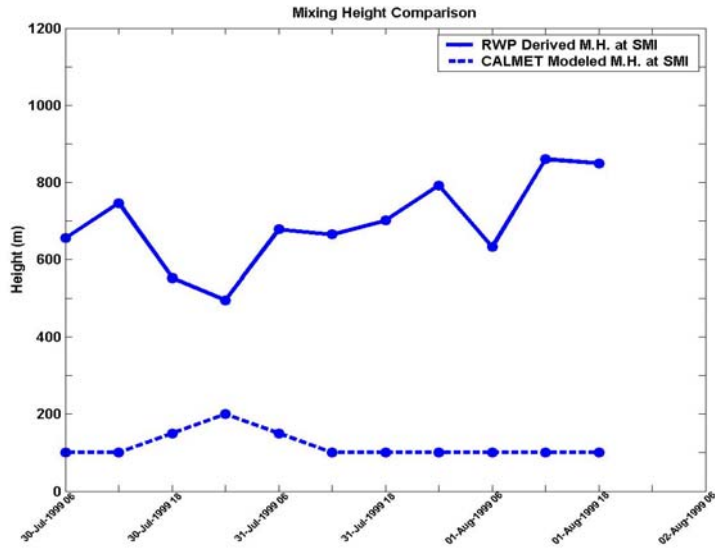
- Distinguish whether any difference exists between mixing height estimates derived from RWP moments data and mixing heights modeled by CALMET for case study periods.

### Method:

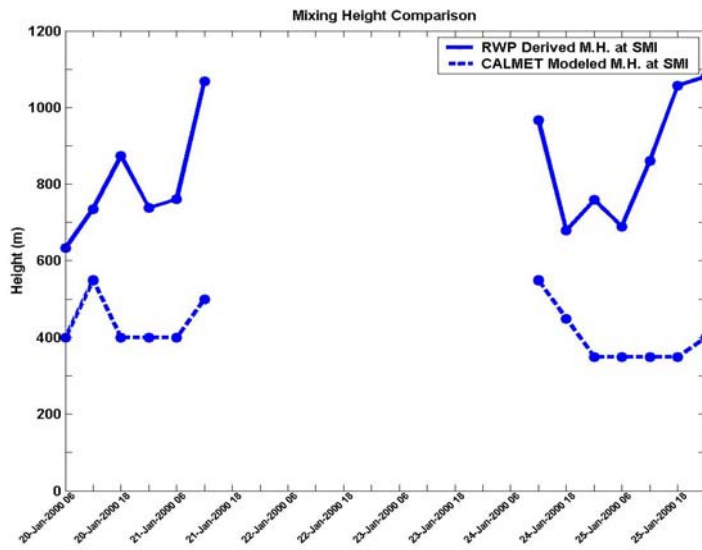
- Subjective and limited statistical comparison was carried out on case study periods when the mixing heights could be determined from the RWP moments data.



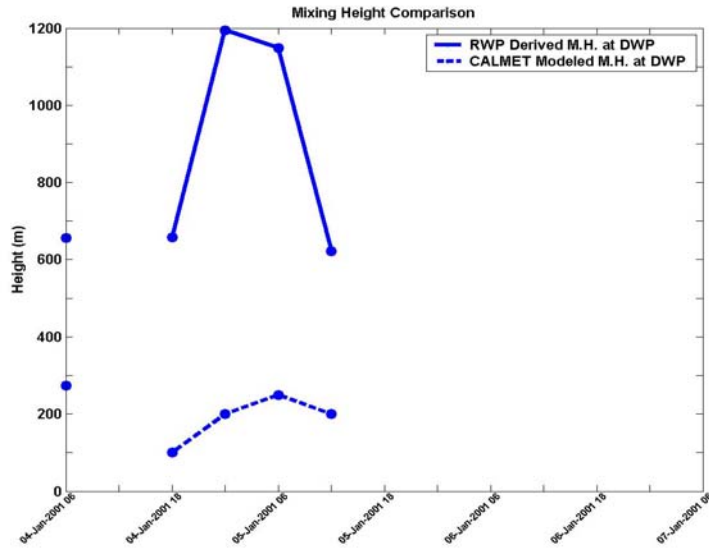
## Mixing Height Comparison July 31 – August 1, 2001



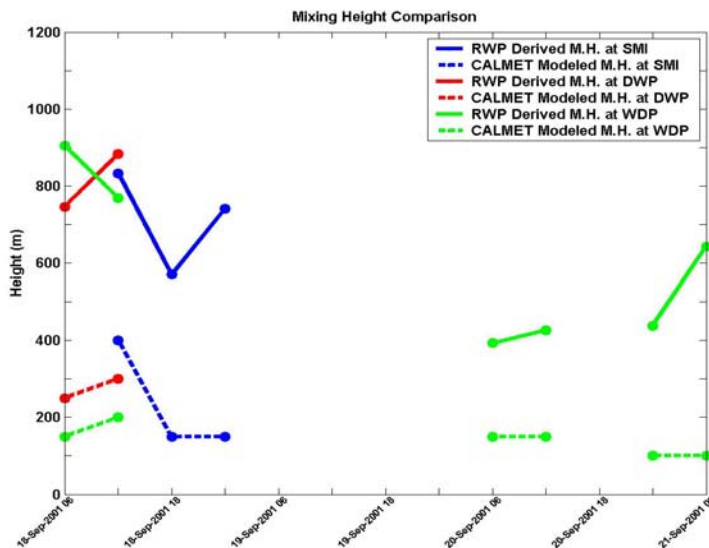
## Mixing Height Comparison January 20-25, 2000



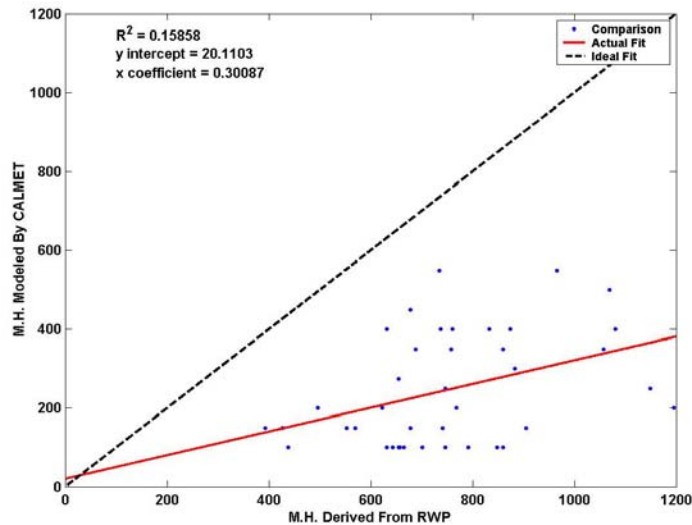
## Mixing Height Comparison January 4-7, 2001



## Mixing Height Comparison September 15-21, 2001



## Mixing Height Comparison All Case Studies



STI

## Mixing Summary (1 of 2)

- Mixing heights were created for selected episodes when data permitted
  - September 18-20, 2001
  - January 20-25, 2000
  - January 4-6, 2001
  - July 30 – August 1, 1999
  - May 14-15, 2001
  - April 15, 2001
  - January 29, 2001
- Estimated mixing heights can be used to verify mixing heights generated by MM5

STI

## Mixing Summary (2 of 2)

Because CALMET underestimates mixing heights compared to estimates derived from RWP measurements, the following recommendation should be considered:

When surface wind speeds are below a specified threshold at overwater sites, a convective scheme should be used to calculate mixing heights at these sites. This will enable more realistic modeling of mixing over the ocean



## Wind Field Comparisons (1 of 2)

- Goal: Determine if Eta Data Assimilation System (EDAS) winds properly represent observations.
- Method: Compare three-hourly historic EDAS winds (horizontal grid resolution of 40 km) to observations.
- Poster presented at the International Symposium on Tropospheric Profiling Needs and Technologies.



## Wind Field Comparisons (2 of 2)

- EDAS
  - Horizontal grid of 40 km x 40 km
  - Vertical resolution of 25 constant pressure surfaces from 1000 mb to 25 mb at intervals of 50 mb (in the lowest 2 km, the interval is 25 mb)
- Profilers
  - VRM and SMI plus four BAMP profilers



## RWP/EDAS Comparison – Method

- Statistical and limited subjective comparisons were made
- The closest EDAS model grid point were compared to the location of the RWP sites
- Wind direction (WD) comparisons were not made when wind speeds (WS) were less than 2 m/s
- Comparisons of WS and WD were carried out when the heights of EDAS winds were within
  - 30-m of a RWP measurement below 1000-m
  - 50-m of a RWP measurement above 1000-m
- Point-to-point time matching was used

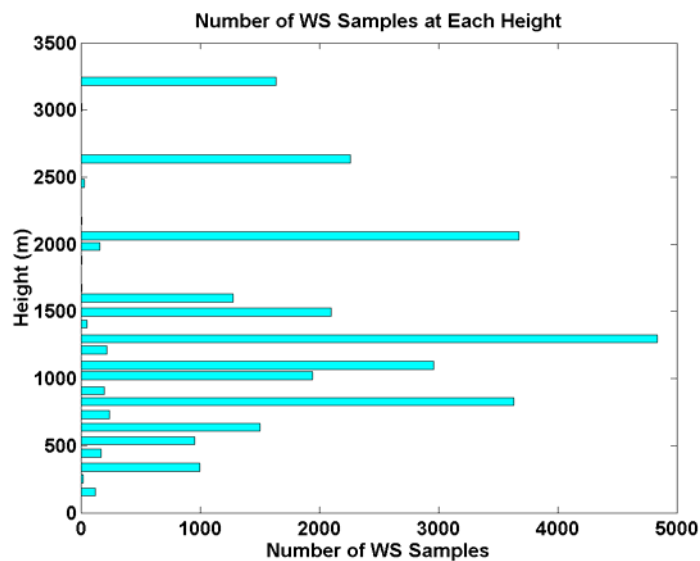


## RWP/EDAS Comparison – Statistics

- Statistics were computed on height bins that, when sorted by number of samples, comprised 90% of the total number of samples
- Statistics were calculated for the total period, by synoptic class, and by flow pattern



## RWP/EDAS Comparison – Sample Selection Example for SMI



## RWP/EDAS Comparison – Statistics

$$\text{Bias} = \frac{1}{n} \sum_{i=1}^n (P_i - M_i)$$

$$\text{Standard Deviation} = \sqrt{\frac{1}{n} \sum_{i=1}^n [(P_i - M_i) - \overline{(P_i - M_i)}]^2}$$

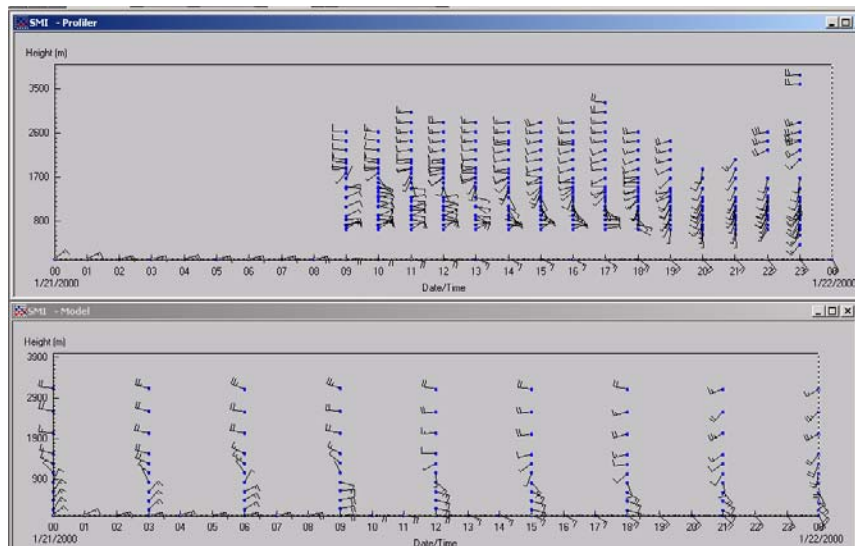
$$\text{Mean Absolute Error (MAE)} = \frac{1}{n} \sum_{i=1}^n |P_i - M_i|$$

Where:

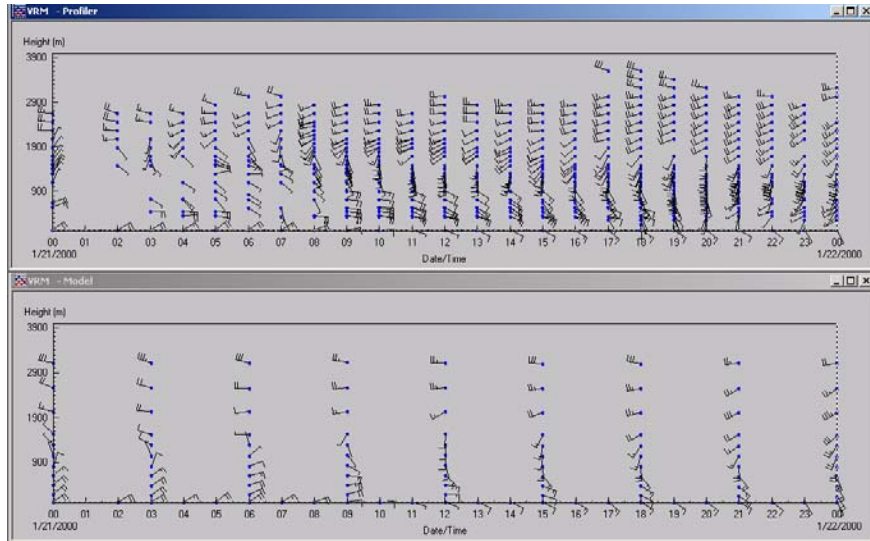
- n = number of observations
- P = ith observation by the RWP
- M<sub>i</sub> = ith EDAS model “observation”



## RWP Winds and Eta Model Winds at SMI, January 21, 2000

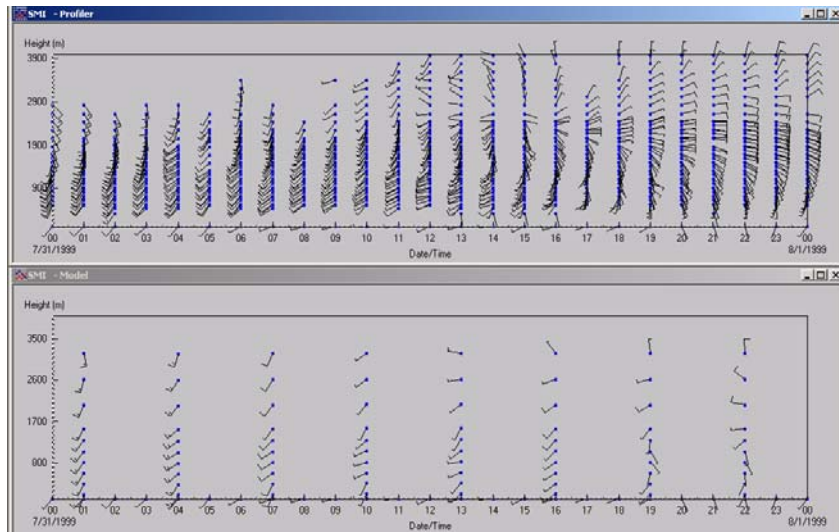


## RWP Winds and Eta Model Winds at SMI, January 21, 2000



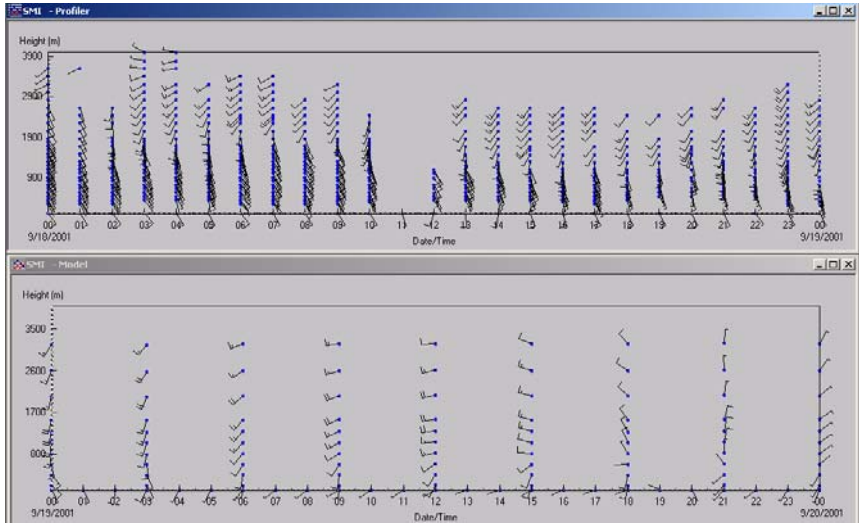
STI

## RWP Winds and Eta Model Winds at SMI, July 31, 1999

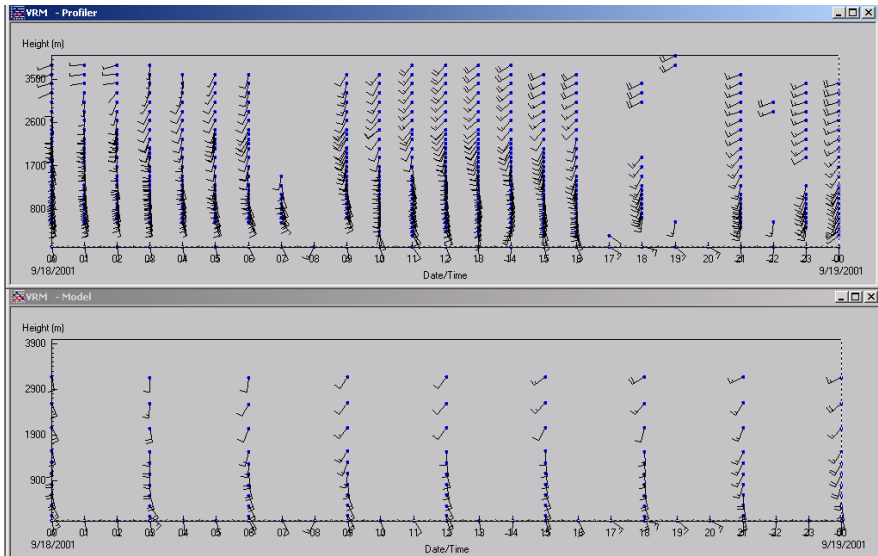


STI

**RWP Winds and Eta Model Winds at SMI, September 18, 2001**

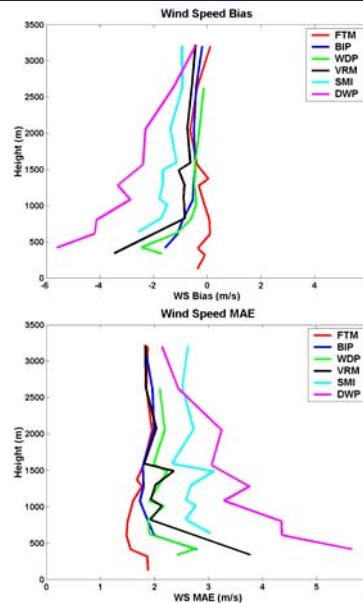


**RWP Winds and Eta Model Winds at VRM, September 18, 2001**



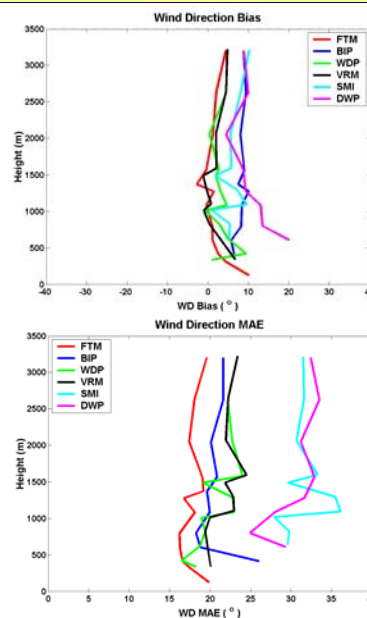
## RWP/EDAS Comparison - Results

- Wind speed – entire period
  - Overestimated by EDAS model output
  - Greater negative bias and larger MAE were observed in the lower levels; however, bias and MAE improved with height
  - Sites further offshore illustrated greater bias (negative) and had larger MAE than sites closer to the shoreline
- When sorted by synoptic class and flow direction, the statistics were similar



## RWP/EDAS Comparison - Results

- Wind direction – entire period
  - Generally, bias were between  $0^\circ$  and  $10^\circ$
  - The overall positive bias illustrates that the EDAS model output had a counter-clockwise bias
  - MAE was  $15^\circ - 25^\circ$  at sites closer to shore, while sites further offshore exhibited a  $25^\circ - 35^\circ$
- When sorted by synoptic class and flow direction the statistics were similar



## RWP/EDAS Comparison - Conclusions

- Results suggest that RWP measurements should be given considerable weight when creating high-resolution wind fields
- Meteorological and air quality models may undergo considerable improvement from the use of RWP measurements
- More case study comparisons would provide more guidance on when EDAS and RWP data agree and disagree.



## Modeling Overview

- Overall Goals
- CALMET
  - Background
  - Data (data manipulation, missing data)
  - Model Settings
  - Example
- CALPUFF
  - Background
  - Data inputs
  - Source characteristics
  - Example
- Trajectory Calculation
- Final Thoughts



## Overall Goals

### Goals:

- Assess dispersion and transport characteristics under multiple meteorological patterns and determine the effect of large-scale meteorology on transport and dispersion
- Investigate potential impact of offshore oil platform emissions on onshore areas



## CALMET – Background

- What is CALMET?
  - CALMET is a meteorological model, which includes a diagnostic wind field generator containing objective analysis and parameterized treatments of slope flows, kinematic terrain effects, terrain-blocking effects, a divergence minimization procedure, and a micro-meteorological model for overland and overwater boundary layers
- Why use CALMET?
  - To resolve mesoscale and local-scale meteorological phenomena by blending observational data with synoptic-scale analyses

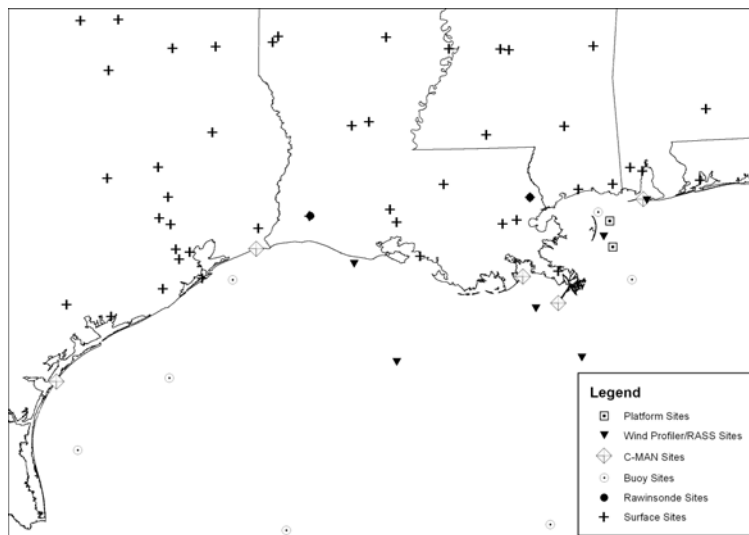


## Observational Meteorological Data Sources (1 of 2)

- 2 NWS rawinsonde sites – Sidell, Lake Charles
- 2 RWP with surface meteorological measurements – Vermillion, South Marsh Island (5/98 – 8/00)
- 6 RWP with surface meteorological measurements – Vermillion, South Marsh Island, Breton Island, Fort Morgan, Deep Water Platform, West Delta Platform (9/00 – 9/01)
- 2 Platforms with surface meteorological measurements – Mid Buoy Platform, Shallow Water Platform
- 7 NDBC buoys
- 5 NDBC C-Man stations
- 45 stations reporting METAR observations



## Observational Meteorological Data Sources (2 of 2)



## Geophysical Data Sources

- 0.9-km resolution terrain data
- 30-m resolution land use data

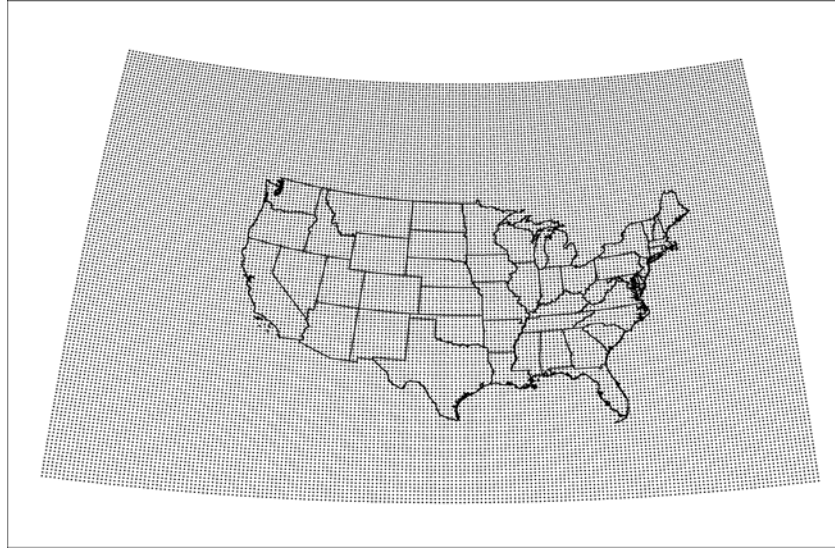


## Eta Data Assimilation System (EDAS)

- EDAS output is constructed from successive 3-hr (eight analyses/day) ETA model forecasts (Black, 1994)
- Bilinear interpolation of ETA model output is used to create the EDAS output on the AWIPS-212 grid
- AWIPS-212 grid
  - Lambert Conformal Projection
  - 40-km horizontal resolution (185 X 129)
  - 26 vertical levels (every 25 mb up to 850 mb, every 50 mb up to 50 mb)
- Three-dimensional variational analysis (3DVAR) scheme to assimilate surface and upper-air observations (Rogers et al., 1997):
  - Pibals
  - GOES satellite data
  - radar wind profilers
  - aircraft soundings
  - NEXRAD derived winds



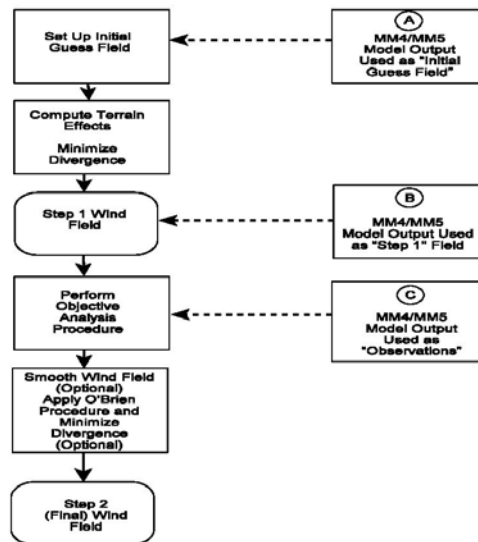
## EDAS Domain



STI

## CALMET Diagnostic Wind Model

Standard options for incorporating gridded model output into a CALMET analysis (Scire et al., 1999)



STI

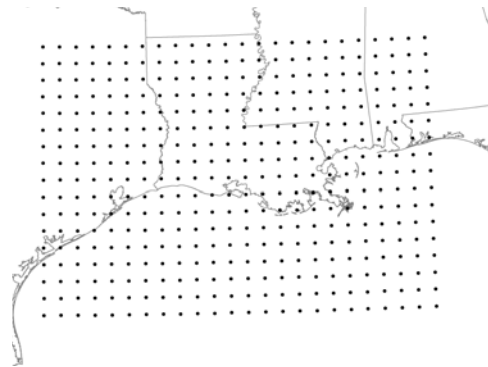
## CALMET Initialization

- Typical “Initial Guess” Field
  - At a minimum, CALMET requires 00Z and 12Z NWS soundings to calculate a domain mean wind for use as the “first guess” field.
- MMS “Initial Guess” Field
  - Instead, the EDAS three-dimensional wind fields on the AWIPS-212 grid were used as the “initial guess” field and interpolated to a 5-km CALMET grid.

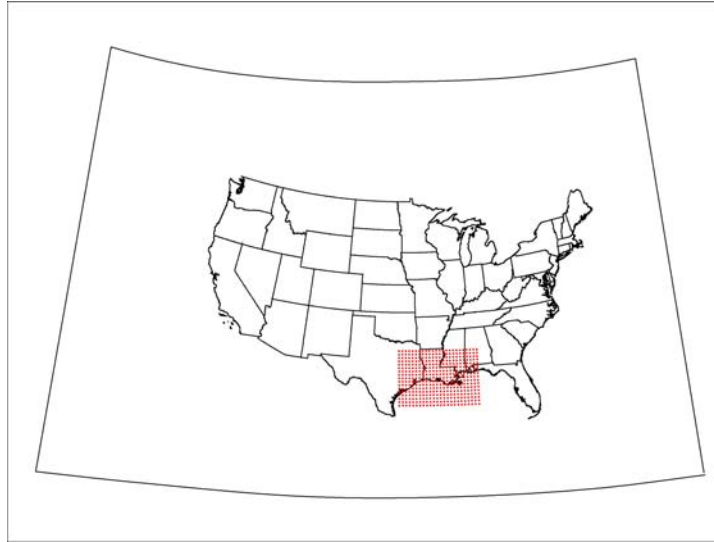


## CALMET Grid Resolution

- 20 vertical layers with interfaces at 0, 20, 50, 100, 200, 300, 400, 500, 600, 700, 800, 900, 1000, 1200, 1400, 1600, 1800, 2000, 2250, 2500, and 2750 m
- Horizontal resolution of 5 km
- Modeling domain  $NX = 172$  &  $NY = 112$  (860 x 560 km)



## EDAS and CALMET Domain



STI

## CALMET Data Manipulation

- Upper-air files
  - Convert  $T_v \rightarrow T$

$$T = \left( \frac{T_v}{1 + (.61 * q)} \right) \text{ where } q \text{ is the EDAS specific humidity; } T_v \text{ is measured by RASS}$$

- Surface files
  - Closest observation to the top of the hour used
  - Cloud cover and derived ceiling height from 6-hr and 12-hr ETA forecasts

STI

## Missing Data

- Upper-air files
  - RWP/RASS data
    - Filled in top of vertical WS, WD, and  $T_v$  profiles with EDAS as needed
    - Time gaps > 12 hrs filled with EDAS
    - Time gaps < 12 hrs CALMET linear interpolation
  - NWS rawinsonde data
    - Time gaps > 12 hrs filled with EDAS
  - Surface data
    - Time gap < 12 hrs filled by moving +/- 6-hr window (no interpolation)
    - Time gap > 12 hrs first gate of RWP/RASS used at surface
- Surface meteorology and over-water files
  - Surface meteorology and buoy data
    - Time gaps > 12 hrs CALMET spatial interpolation



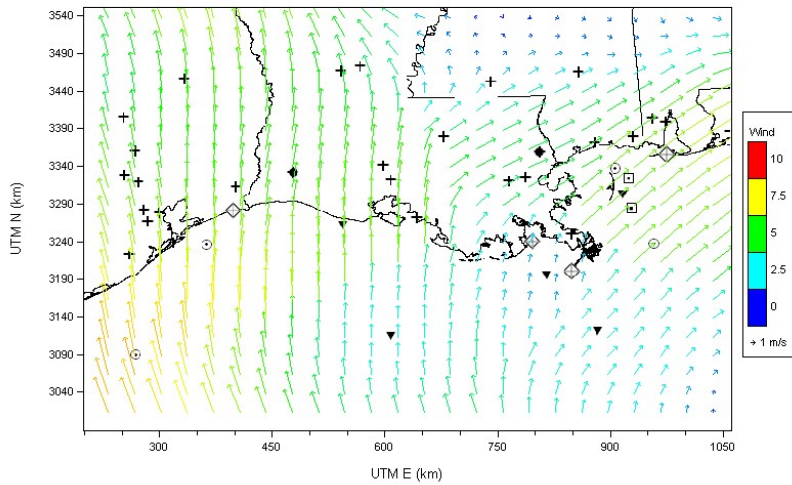
## Model Settings

- No extrapolation of surface winds to upper levels
- Maximum radius of influence over land in the surface layer – 20 km
- Maximum radius of influence over land aloft – 150 km
- Maximum radius of influence over water – 50 km
- Equal weighting of the “initial guess” field and observations in the surface layer occurs at 40 km from the observation
- Equal weighting of the “initial guess” field and observations in aloft layers occurs at 150 km from the observation
- One smoothing pass below 400 m and two smoothing passes elsewhere



## Example - CALMET

Modeled Winds - April 13, 2001 2300 CST



STI

## CALPUFF – Background

- What is CALPUFF?
  - CALPUFF is a multi-layer, multi-species, non-steady-state puff dispersion model that can simulate the effects of time- and space-varying meteorological conditions on pollutant transport, transformation, and removal.

Note: An arbitrary emission rate was utilized, and the goal is not to predict absolute concentrations, but to predict relative concentrations.
- What were the inputs?
  - Geophysical and meteorological data from CALMET
  - Emissions inputs

STI

## Data Inputs

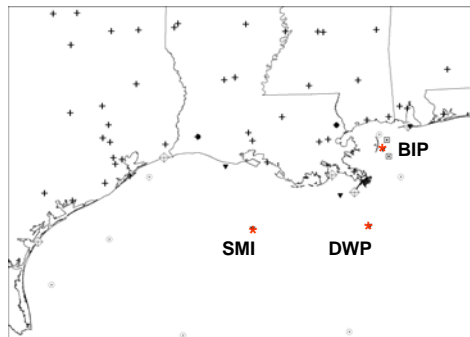
- Geophysical data – gridded fields of
  - surface roughness lengths
  - Land use categories
  - Terrain elevations
  - Leaf area indices
- Meteorological Data
  - Gridded fields of
    - u, v, w wind components (3-D)
    - Air temperature (3-D)
    - Surface friction velocity
    - Convective velocity scale
    - Mixing height
    - Monin-Obukhov length
    - PGT stability class
    - Precipitation rate
  - Hourly values of the following parameters at surface met stations
    - Air density
    - Air temperature
    - Short-wave solar radiation
    - Relative humidity
    - Precipitation type



## Emissions Inputs

Inert tracers were emitted from three offshore platforms in the Gulf of Mexico to assess potential onshore impact:

- South Marsh Island (SMI)
- Breton Island Platform (BIP)
- Deep Water Platform (DWP)



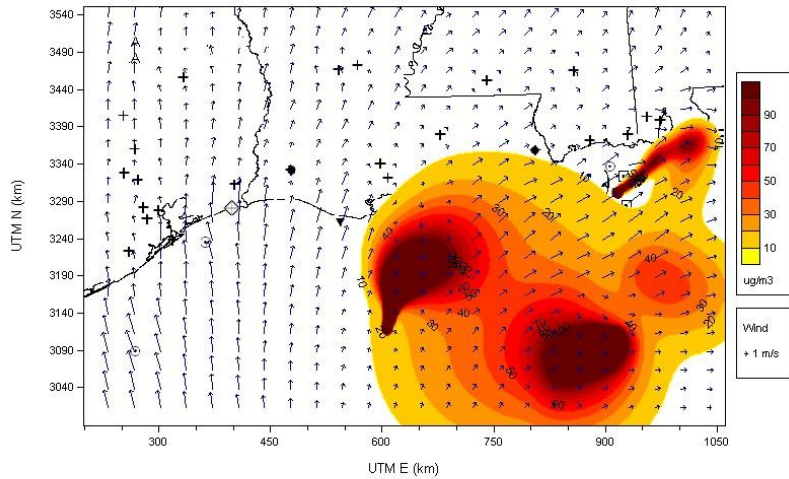
## Source Characteristics

- Stack heights and stack diameters set to 10 m agl
- Exit velocity of .005 m/s
- Exit temperature based on the temperature measured on each platform
- Continuous emission rates of 2000 g/sec used for all three platforms



## Example - CALPUFF

Modeled Dispersion - May 15, 2001 2200 CST



## Trajectory Calculation

- HYSPLIT (EDAS)
- TRAJMOD (CALMET)



## Final Thoughts

- High frequency data requires considerable data manipulation of upper-air files
- EDAS may impose synoptic features on the local scale, particularly when local observations are missing
- Mixing heights are buoyancy driven



## References

- Black T. (1994) The new NMC mesoscale Eta model: description and forecast examples. *Wea. Forecasting*. **9**, 265-278.
- Rogers E., Baldwin M., Black T., Brill K., Chen F., DiMego G., Gerrity J., Manikin G., Mesinger F., Mitchell K., Parrish D., and Zhao Q. (1997) Changes to the NCEP operational "Early" Eta Analysis/Forecast System. Technical Procedures Bulletin, Series No. 447, National Weather Service, Office of Meteorology, December. Available on the Internet at <<http://www.nws.noaa.gov/om/tpb/447.htm>>
- Scire J.S., Robe F.R., Fernau M.E., and Yamartino R.J. (1999) Auser's guide for the CALMET meteorological model (version 5.0). Prepared by Earth Tech, Inc., Concord, MA, September.



## CALMET/CALPUFF Modeling Case Studies

- September 18–20, 2001
- \*January 20-25, 2000 – Winter Case Study with Shift in Wind Direction
- January 4-6, 2001
- July 30 – August 1, 1999
- \*May 14-15, 2001 – Spring Case Study with Regional High Ozone
- \*April 15, 2001 – Onshore Flow Case Study
- January 29, 2001

\*Cases in red are discussed today



## Onshore Wind Case Study April 15, 2001



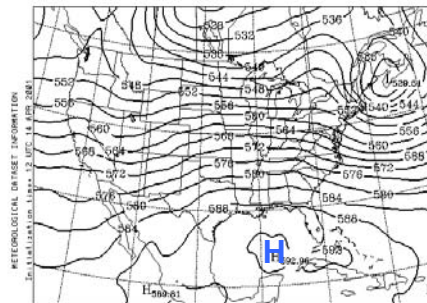
## Onshore Wind Case Study April 14, 2001: 12Z – 500-mb Heights



NOAA Air Resources Laboratory  
This product was produced by an Internet user on the NOAA Air Resources Laboratory's web site. See the disclaimer for further information (<http://www.arl.noaa.gov/ready/disclaimer.html>).

EDAS Archive

The region was under a broad, weak upper-level ridge of high pressure at 500-mb

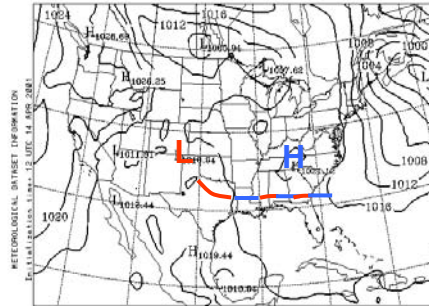


## Onshore Wind Case Study April 14, 2001: 12Z – Sea-level Pressure

- Stationary frontal boundary oriented east-west across the Gulf Coast
- South/southwesterly winds at the surface


 NOAA Air Resources Laboratory  
 This product was produced by an Internet user on the NOAA Air Resources Laboratory's web site. See the disclaimer for further information. (<http://www.arl.noaa.gov/ready/disclaimer.html>).

EDAS Archive



MEAN SEA-LEVEL PRESSURE  
 MSLP (HPA). LVL= SFC. 12 UTC 14 APR 2001 (+ 00 H)



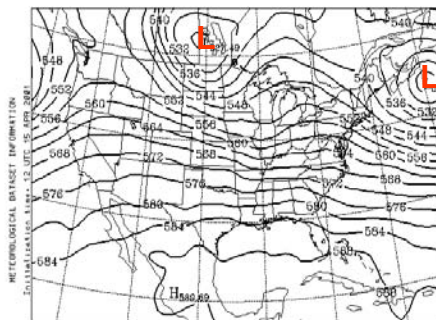
NATIONAL OCEANIC AND ATMOSPHERIC ADMINISTRATION - AIR RESOURCES LABORATORY

## Onshore Wind Case Study April 15, 2001: 12Z – 500 mb Heights

Zonal flow at 500 mb across the Gulf region


 NOAA Air Resources Laboratory  
 This product was produced by an Internet user on the NOAA Air Resources Laboratory's web site. See the disclaimer for further information. (<http://www.arl.noaa.gov/ready/disclaimer.html>).

EDAS Archive



HEIGHT  
 HGTS ( DM ). LVL= 500. 12 UTC 15 APR 2001 (+ 00 H)

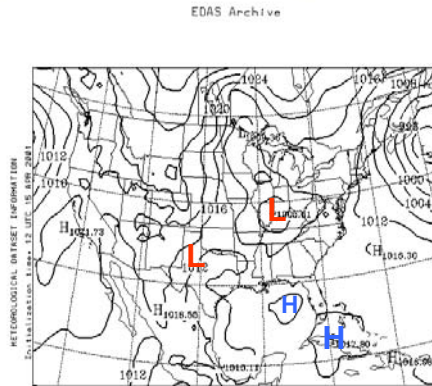


NATIONAL OCEANIC AND ATMOSPHERIC ADMINISTRATION - AIR RESOURCES LABORATORY

## Onshore Wind Case Study April 15, 2001: 12Z – Sea-level Pressure


 NOAA Air Resources Laboratory  
 This product was produced by an Internet user on the NOAA Air Resources Laboratory's web site. See the disclaimer for further information (<http://www.arl.noaa.gov/ready/disclaim.html>).

- Southerly winds at the surface across the central and western part of the domain
- Southwesterly surface winds across the eastern part of the domain

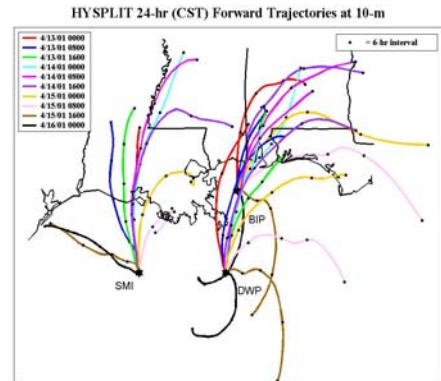
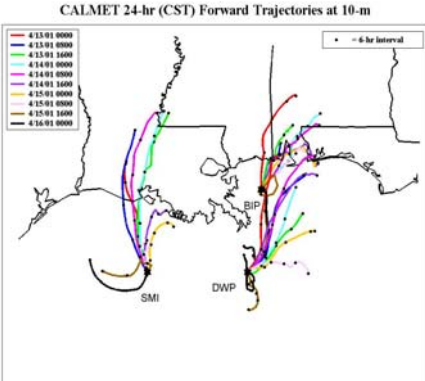


NATIONAL OCEANIC AND ATMOSPHERIC ADMINISTRATION - U.S. DEPARTMENT OF COMMERCE



MEAN SEA-LEVEL PRESSURE  
 MSLP (HPA), LVL = SFC, 12 UTC 15 APR 2001 (+00 H)

## Forward Trajectories (10 m) from SMI, BIP, and DWP on April 13-16, 2001



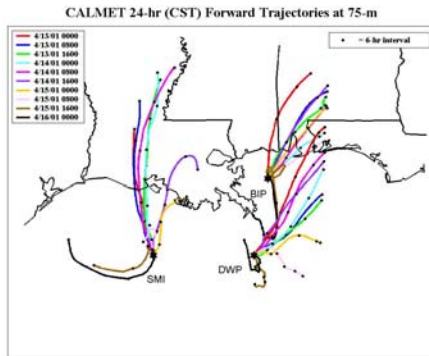
CALMET 24-hr forward trajectories based on CALMET diagnostic wind fields (4/13/01 0000 – 4/16/01 0000 CST)

HYSPLIT 24-hr forward trajectories based on EDAS wind fields (4/13/01 0000 – 4/16/01 0000 CST)

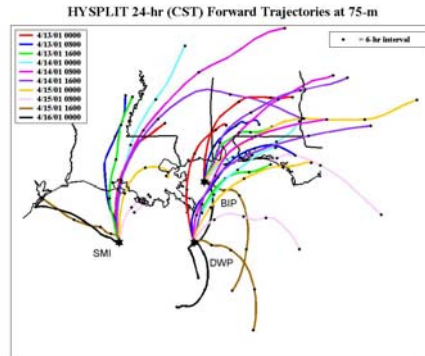
Onshore transport from each of the platforms at 10 m from 4/13/01 at 0000 CST – 4/15/01 at 0000 CST. Fair agreement between CALMET and EDAS wind fields.



## Forward Trajectories (75 m) from SMI, BIP, and DWP on April 13-16, 2001



CALMET 24-hr forward trajectories based on CALMET diagnostic wind fields (4/13/01 0000 – 4/16/01 0000 CST)

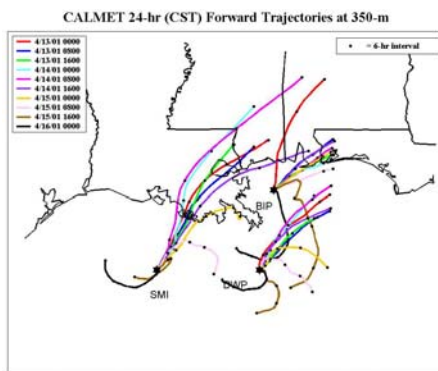


HYSPLIT 24-hr forward trajectories based on EDAS wind fields (4/13/01 0000 – 4/16/01 0000 CST)

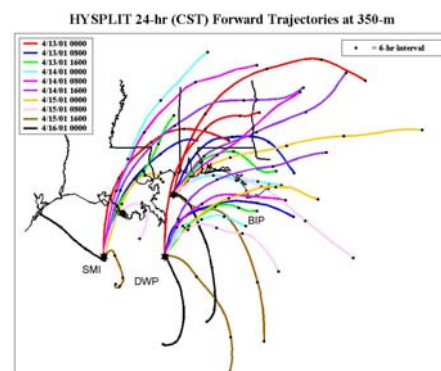
- Onshore, southerly transport from SMI and onshore transport out of the southwest from BIP and DWP at 75 m
- Onshore transport changed to near-calm or north or east transport toward the end of the case study period



## Forward Trajectories (350 m) from SMI, BIP, and DWP on April 13-16, 2001



CALMET 24-hr forward trajectories based on CALMET diagnostic wind fields (4/13/01 0000 – 4/16/01 0000 CST)



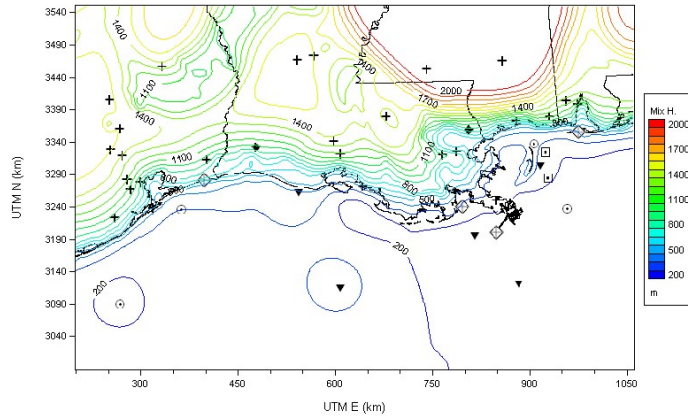
HYSPLIT 24-hr forward trajectories based on EDAS wind fields (4/13/01 0000 – 4/16/01 0000 CST)

- Onshore transport out of the southwest at 350 m from each of the platforms from 4/13/01 at 0000 CST – 4/15/01 at 0000 CST
- Onshore transport changed to near-calm or north or east transport toward the end of the case study period



## CALMET Derived Mixing Heights April 14, 2001

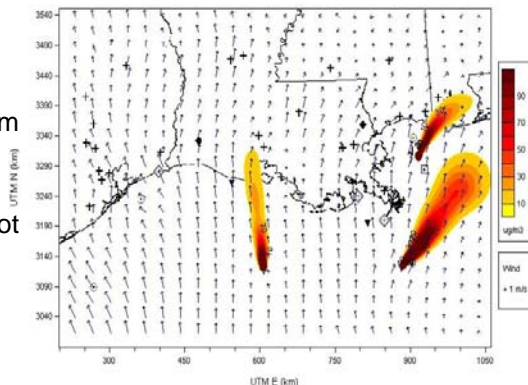
4/14/01 1400 CST - Mixing Heights



## Dispersion Patterns from SMI, BIP, and DWP – April 14, 2001

Same source emission rate assumed at each platform

- Hypothetical emissions from SMI and BIP impact onshore coastal areas
- Emissions from DWP do not impact the coastline even though the concentrations are higher than at SMI and BIP, probably due to lower mixing heights at DWP

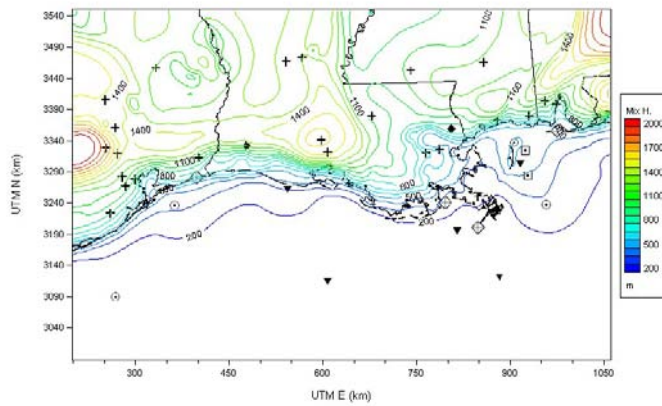


Start time 1900 CST



## CALMET Derived Mixing Heights April 15, 2001

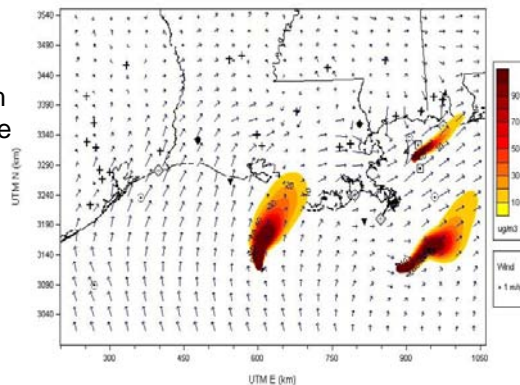
4/15/01 1400 CST - Mixing Heights



## Dispersion Patterns from SMI, BIP, and DWP – April 15, 2001

Same source emission rate assumed at each platform

- Hypothetical emissions from SMI and BIP impact onshore coastal areas
- Emissions from DWP do not impact coastal areas
- Concentrations from SMI and DWP are higher, probably due to lower wind speeds and lower mixing heights



Start time 1100 CST



## Winter Case Study with Shift in Wind Direction January 20-25, 2000

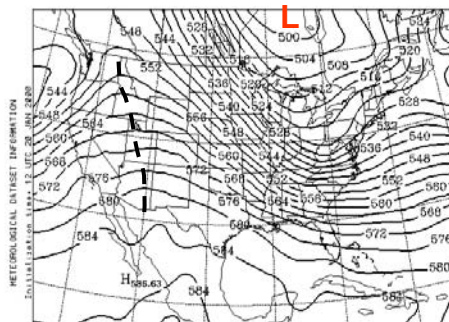


### Winter Case Study with Shift in Wind Direction January 20, 2000: 12Z – 500-mb Heights

NOAA Air Resources Laboratory  
This product was produced by an Internet user on the NOAA Air Resources Laboratory's web site. See the disclaimer for further information (<http://www.arl.noaa.gov/read/disclaimer.html>).

EDAS Archive

- Strong upper-level area of low pressure at 500 mb was centered in Ontario and extended south through the eastern half of the U.S.
- 500-mb ridge in place across the Mountain West



HEIGHT

HGTS ( DM ). LVL= 500.. 12 UTC 20 JAN 2000 (+ 00 H )

NATIONAL OCEANIC AND ATMOSPHERIC ADMINISTRATION - AIR RESOURCES LABORATORY

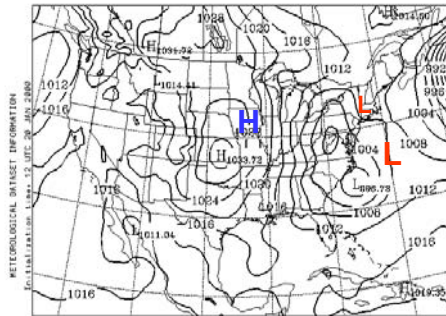


## Winter Case Study with Shift in Wind Direction January 20, 2000: 12Z – Sea-level Pressure

NMRR Air Resources Laboratory  
This product was produced by an Internet user on the NMRR Air Resources Laboratory's web site. See the disclaimer for further information (<http://www.arl.noaa.gov/read/disclaimer.html>).

EDAS Archive

Surface high-pressure area centered over the Central Plains and low-pressure area located over the eastern seaboard drove strong, offshore, northerly flow across the modeling domain



MEAN SEA-LEVEL PRESSURE

MSLP (HFA). LVL= SFC. 12 UTC 20 JAN 2000 (+ 00 H)



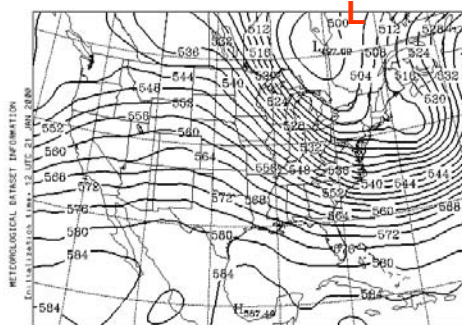
NATIONAL OCEANIC AND ATMOSPHERIC ADMINISTRATION - AIR RESOURCES LABORATORY

## Winter Case Study with Shift in Wind Direction January 21, 2000: 12Z – 500-mb Heights

NMRR Air Resources Laboratory  
This product was produced by an Internet user on the NMRR Air Resources Laboratory's web site. See the disclaimer for further information (<http://www.arl.noaa.gov/read/disclaimer.html>).

EDAS Archive

- Strong upper-level area of low pressure at 500 mb continued to dominate the eastern half of the United States
- Upper-level ridge at 500 mb began to weaken across the western United States



HEIGHT

HGTS ( DM ). LVL= 500. 12 UTC 21 JAN 2000 (+ 00 H)



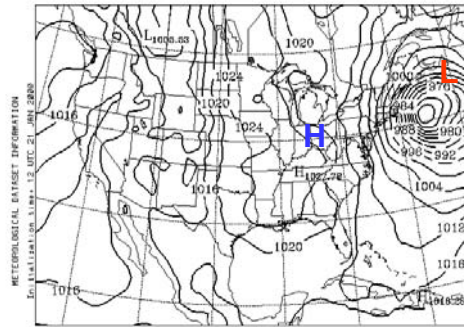
NATIONAL OCEANIC AND ATMOSPHERIC ADMINISTRATION - AIR RESOURCES LABORATORY

## Winter Case Study with Shift in Wind Direction January 21, 2000: 12Z – Sea-level Pressure

- Surface area of high pressure moved eastward and became centered in Tennessee
- Northerly winds on January 20 rotated to northeasterly, and easterly on January 21, as the high pressure center moved across the northern edge of the modeling domain

NORR Air Resources Laboratory  
This product was produced by an Internet user on the NORR Air Resources Laboratory's web site. See the disclaimer for further information (<http://www.arl.noaa.gov/read/Disclaimer.html>).

EDAS Archive



MEAN SEA-LEVEL PRESSURE

MSLP (HPA). LVL= SFC. 12 UTC 21 JAN 2000 (+ 00 H)

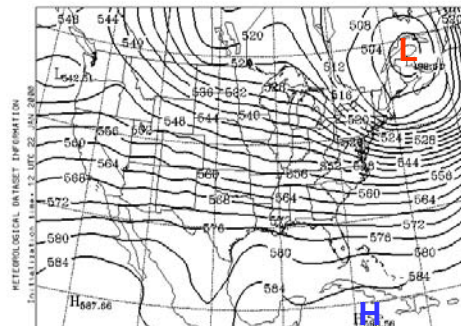


## Winter Case Study with Shift in Wind Direction January 22, 2000: 12Z – 500-mb Heights

- Upper-level ridge at 500 mb broke down across the western United States
- Upper-level area of low pressure at 500 mb was centered over New England
- Generally zonal flow occurred across the United States
- A shortwave ridge was analyzed in the western Gulf of Mexico and a shortwave trough was analyzed in the eastern Gulf of Mexico

NORR Air Resources Laboratory  
This product was produced by an Internet user on the NORR Air Resources Laboratory's web site. See the disclaimer for further information (<http://www.arl.noaa.gov/read/Disclaimer.html>).

EDAS Archive



HEIGHT

HGTS ( DM ). LVL= 600.. 12 UTC 22 JAN 2000 (+ 00 H)



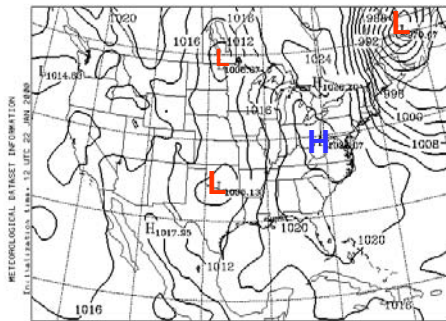
## Winter Case Study with Shift in Wind Direction January 22, 2000: 12Z – Sea-level Pressure



NOAA Air Resources Laboratory  
This product was produced by an Internet user on the NOAA Air Resources Laboratory's web site. See the disclaimer for further information. (<http://www.arl.noaa.gov/ready/disclaim.html>).

EDAS Archive

Strong onshore, southerly flow at the surface was associated with a departing surface high along the eastern seaboard and an approaching low pressure system centered over Nebraska



MEAN SEA-LEVEL PRESSURE

MSLP (HPA). LVL= SFC. 12 UTC 22 JAN 2000 (+ 00 H)



NATIONAL OCEANIC AND ATMOSPHERIC ADMINISTRATION - AIR RESOURCES LABORATORY

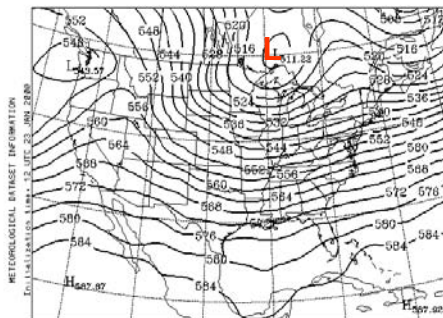
## Winter Case Study with Shift in Wind Direction January 23, 2000: 12Z – 500-mb Heights



NOAA Air Resources Laboratory  
This product was produced by an Internet user on the NOAA Air Resources Laboratory's web site. See the disclaimer for further information. (<http://www.arl.noaa.gov/ready/disclaim.html>).

EDAS Archive

- Strengthening upper-level area of low pressure at 500 mb again dominated the eastern two-thirds of the United States
- Upper-level ridge at 500 mb built across the West



HEIGHT

HQTS (DM). LVL= 500.. 12 UTC 23 JAN 2000 (+ 00 H)



NATIONAL OCEANIC AND ATMOSPHERIC ADMINISTRATION - AIR RESOURCES LABORATORY

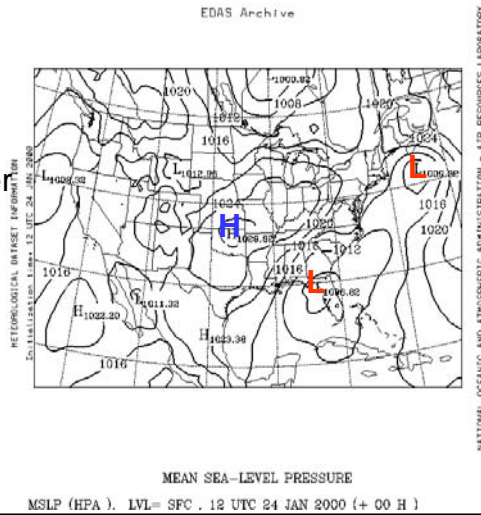


## Winter Case Study with Shift in Wind Direction January 24, 2000: 12Z – Sea-level Pressure



NOAA Air Resources Laboratory  
This product was produced by an Internet user on the NOAA Air Resources Laboratory's web site. See the disclaimer for further information (<http://www.arl.noaa.gov/ready/disclaimer.html>).

Offshore, northerly flow across the modeling domain was associated with an approaching surface high centered over the Great Plains and a departing area of low pressure centered over Florida

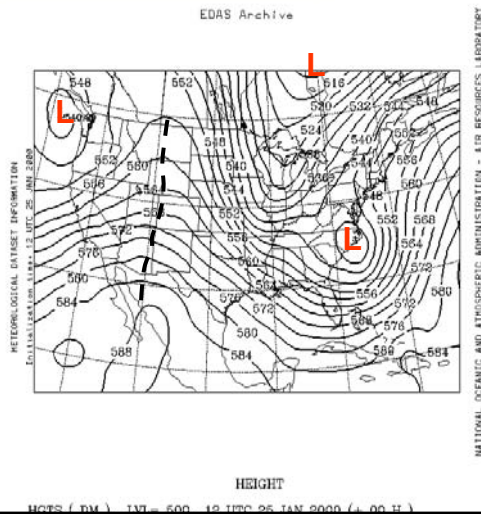


## Winter Case Study with Shift in Wind Direction January 25, 2000: 12Z – 500-mb Heights



NOAA Air Resources Laboratory  
This product was produced by an Internet user on the NOAA Air Resources Laboratory's web site. See the disclaimer for further information (<http://www.arl.noaa.gov/ready/disclaimer.html>).

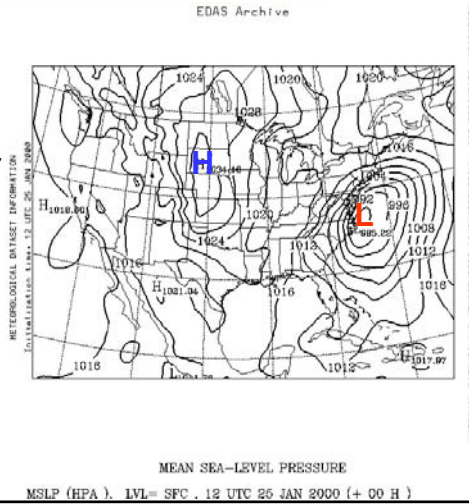
- Upper-level area of low pressure at 500 mb dominated the entire eastern half of the United States, including the modeling domain
- Upper-level ridge strengthened across the West



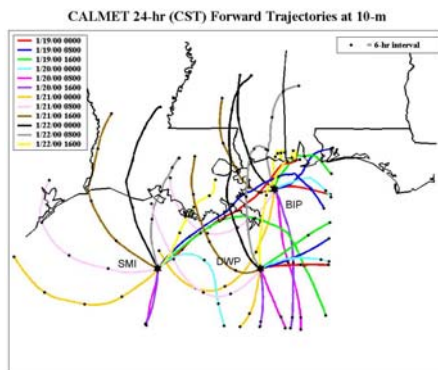
## Winter Case Study with Shift in Wind Direction January 25, 2000: 12Z – Sea-level Pressure


 NOAA Air Resources Laboratory  
This product was produced by an Internet user on the NOAA Air Resources Laboratory's web site. See the disclaimer for further information. (Date: 2/2/2000, URL: www.noaa.gov/ready/disclaim.html).

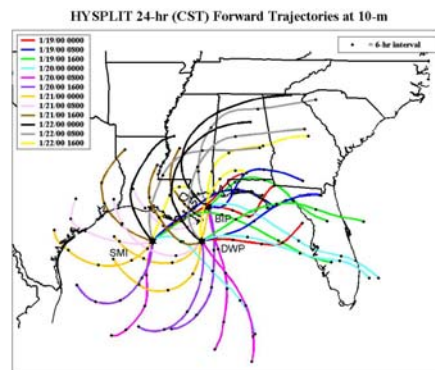
Offshore, northerly flow across the modeling domain was again associated with the surface high centered over the Great Plains and the surface area of low pressure centered off the Mid-Atlantic coast



## Forward Trajectories (10 m) from SMI, BIP, and DWP on January 19-22, 2000



CALMET 24-hr forward trajectories based on CALMET diagnostic wind fields (1/19/00 0000 – 1/22/00 1600 CST)



HYSPLIT 24-hr forward trajectories based on EDAS wind fields (1/19/00 0000 – 1/22/00 1600 CST)

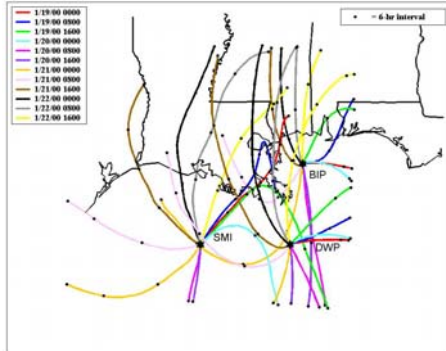
Trajectories at 10 m begin with SW flow on 1/19, changing to strong offshore transport on 1/20 and early on 1/21 before turning onshore late on 1/21/01 through 1/22/01. Note the clockwise progression of the trajectories on 1/20 through 1/22.

CALMET and EDAS winds agree for the most part.



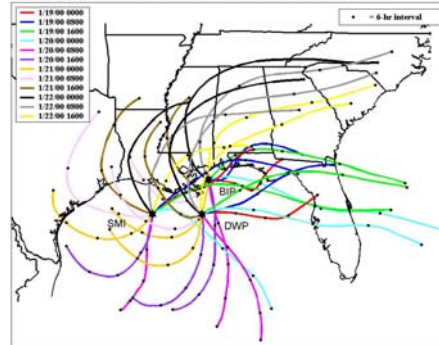
## Forward Trajectories (75 m) from SMI, BIP, and DWP on January 19-22, 2000

CALMET 24-hr (CST) Forward Trajectories at 75-m



CALMET 24-hr forward trajectories based on CALMET diagnostic wind fields (1/19/00 0000 – 1/22/00 1600 CST)

HYSPLIT 24-hr (CST) Forward Trajectories at 75-m



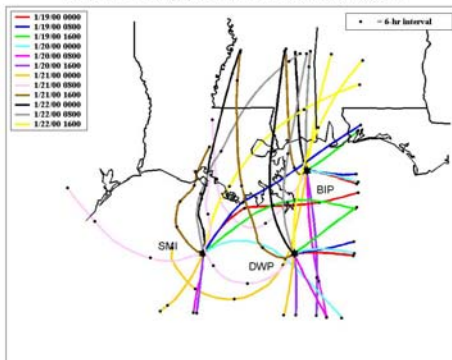
HYSPLIT 24-hr forward trajectories based on EDAS wind fields (1/19/00 0000 – 1/22/00 1600 CST)

The trajectories at 75 m are similar to those at 10 m (see previous slide)



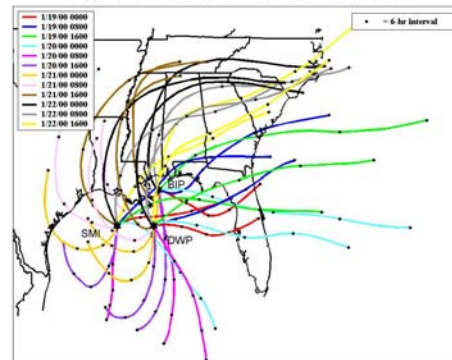
## Forward Trajectories (350 m) from SMI, BIP, and DWP on January 19-22, 2000

CALMET 24-hr (CST) Forward Trajectories at 350-m



CALMET 24-hr forward trajectories based on CALMET diagnostic wind fields (1/19/00 0000 – 1/22/00 1600 CST)

HYSPLIT 24-hr (CST) Forward Trajectories at 350-m



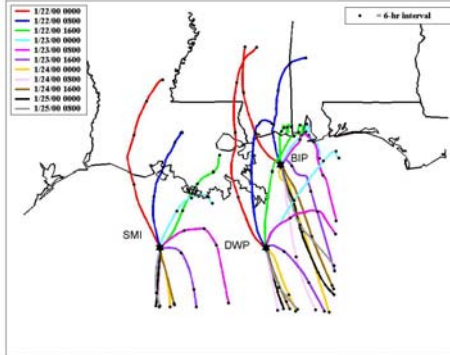
HYSPLIT 24-hr forward trajectories based on EDAS wind fields (1/19/00 0000 – 1/22/00 1600 CST)

As expected, trajectories at 350 m indicate stronger winds and longer transport distances. The general behavior with time is similar to that for 10 m and 75 m (see previous two slides)

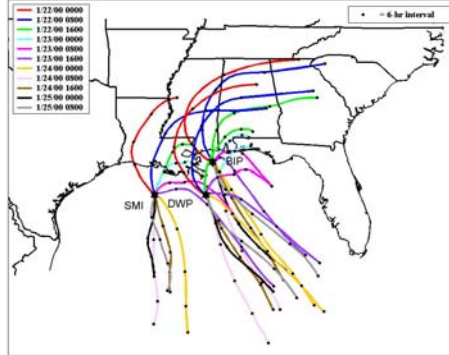


## Forward Trajectories (10 m) from SMI, BIP, and DWP on January 23-25, 2000

CALMET 24-hr (CST) Forward Trajectories at 10-m



HYSPLIT 24-hr (CST) Forward Trajectories at 10-m



CALMET 24-hr forward trajectories based on CALMET diagnostic wind fields (1/22/00 0000 – 1/25/00 0800 CST)

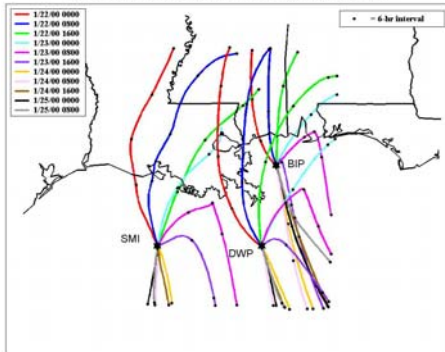
HYSPLIT 24-hr forward trajectories based on EDAS wind fields (1/22/00 0000 – 1/25/00 0800 CST)

Trajectories at 10 m begin with onshore flow on 1/22, changing to offshore flow from midday on 1/23 through 1/25. The trajectories agree fairly well for the CALMET and EDAS wind fields.

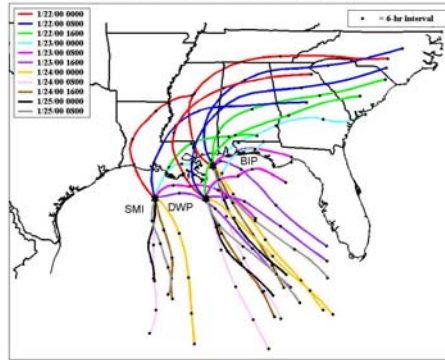


## Forward Trajectories (75 m) from SMI, BIP, and DWP on January 23-25, 2000

CALMET 24-hr (CST) Forward Trajectories at 75-m



HYSPLIT 24-hr (CST) Forward Trajectories at 75-m



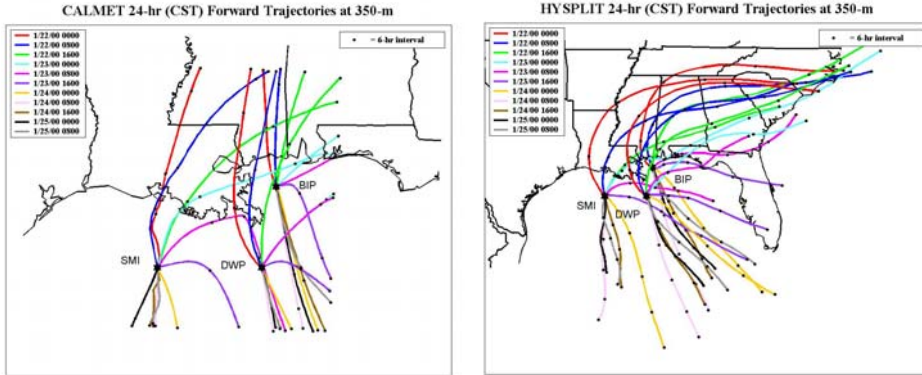
CALMET 24-hr forward trajectories based on CALMET diagnostic wind fields (1/22/00 0000 – 1/25/00 0800 CST)

HYSPLIT 24-hr forward trajectories based on EDAS wind fields (1/22/00 0000 – 1/25/00 0800 CST)

The trajectories at 75 m are similar to those at 10 m (see previous slide)



## Forward Trajectories (350-m) from SMI, BIP, and DWP on January 23-25, 2000



CALMET 24-hr forward trajectories based on CALMET diagnostic wind fields (1/22/00 0000 – 1/25/00 0800 CST)

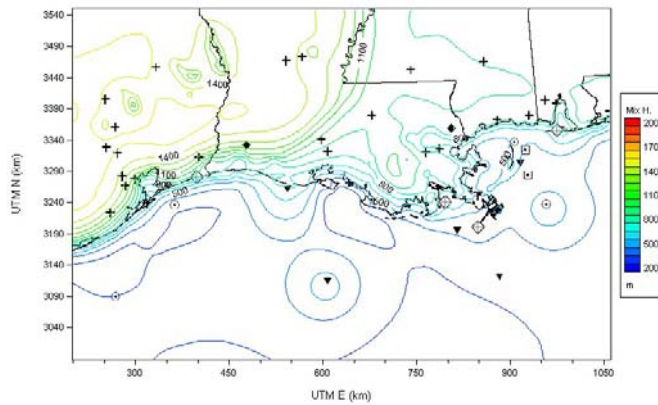
HYSPLIT 24-hr forward trajectories based on EDAS wind fields (1/22/00 0000 – 1/25/00 0800 CST)

The trajectories at 350 m are similar to those at 10 m and 75 m (see previous two slides). There are stronger winds and longer transport distances at 350 m as expected.



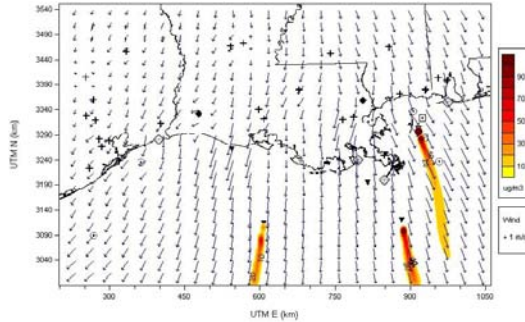
## CALMET Derived Mixing Heights January 20, 2000

1/20/00 1400 CST - Mixing Heights



## Dispersion Patterns from SMI, BIP, and DWP – January 20, 2000

- Same source emission rate assumed at each platform
  - Strong, offshore northerly winds transported the hypothetical tracers out into the Gulf of Mexico, causing no onshore impact
  - The strong winds contributed to decreasing the concentration

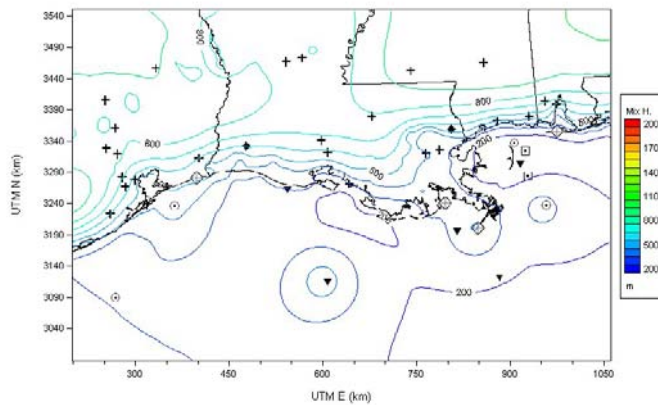


Start time 1600 CST



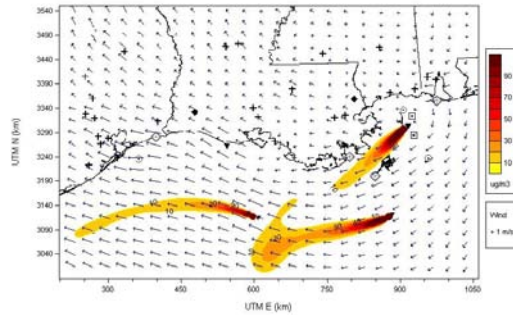
## CALMET Derived Mixing Heights January 21, 2000

1/21/00 1400 CST - Mixing Heights



## Dispersion Patterns from SMI, BIP, and DWP – January 21, 2000

- Same source emission rate assumed at each platform
  - East winds caused BIP plume to pass over Breton Island
  - Minimal onshore impact

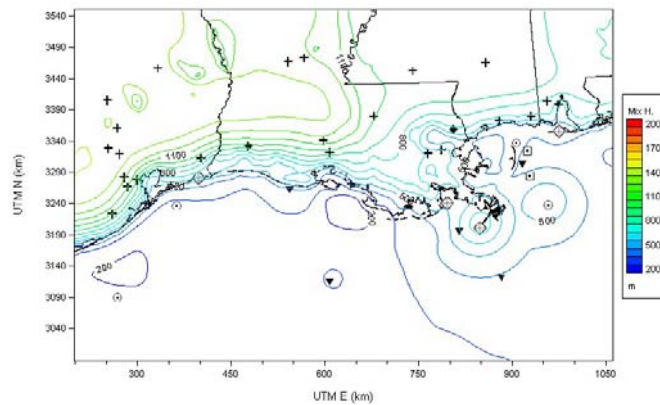


Start time 1600 CST



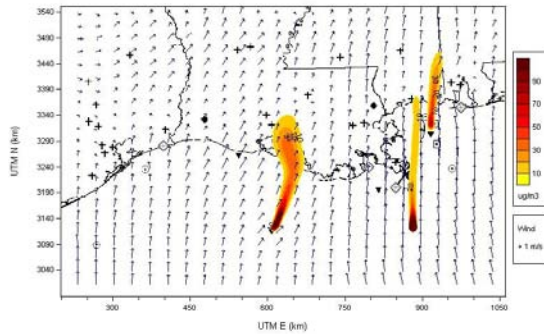
## CALMET Derived Mixing Heights January 22, 2000

1/22/00 1400 CST - Mixing Heights



## Dispersion Patterns from SMI, BIP, and DWP – January 22, 2000

- Same source emission rate assumed at each platform
  - Southerly flow was observed at all three sites, causing the plumes to impact onshore areas

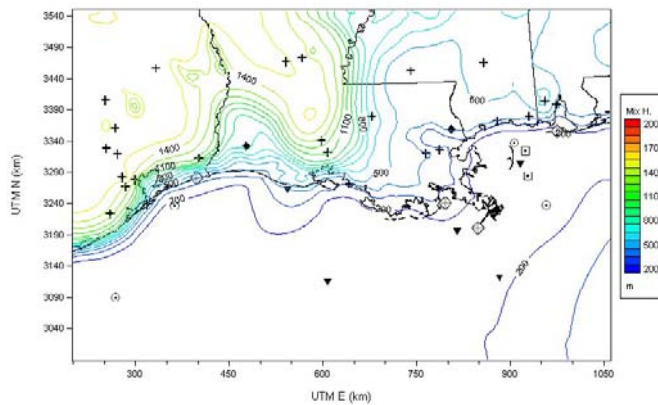


Start time 1900 CST



## CALMET Derived Mixing Heights January 23, 2000

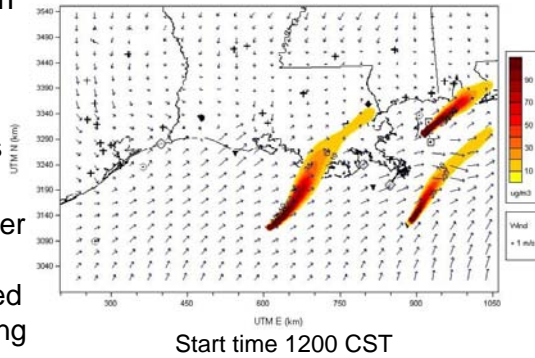
1/23/00 1400 CST - Mixing Heights



## Dispersion Patterns from SMI, BIP, and DWP – January 23, 2000

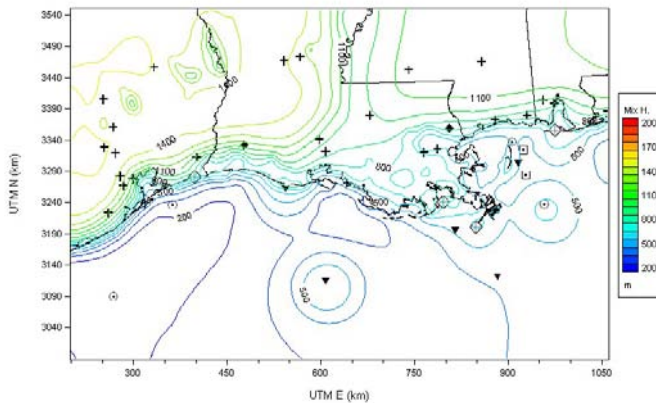
Same source emission rate assumed at each platform

- Southerly flow allows hypothetical tracers emitted at SMI and BIP to impact onshore areas along the Gulf Coast
- Concentrations are higher than on Jan 22 due to lighter winds and reduced CALMET assumed mixing heights on Jan 23



## CALMET Derived Mixing Heights January 24, 2000

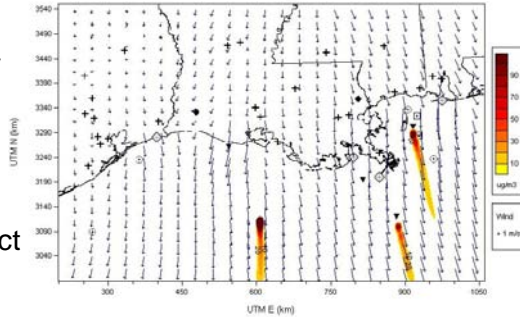
1/24/00 1400 CST - Mixing Heights



## Dispersion Patterns from SMI, BIP, and DWP – January 24, 2000

Same source emission rate assumed at each platform

- Strong, offshore northerly winds behind the front transported the hypothetical tracers out into the Gulf of Mexico, causing no onshore impact
- The strong winds caused increased dilution and increased mixing depth
- Similar situation as on January 20

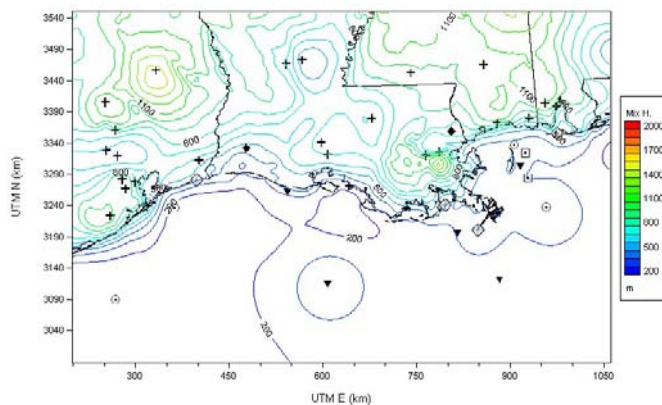


Start time 1200 CST



## CALMET Derived Mixing Heights January 25, 2000

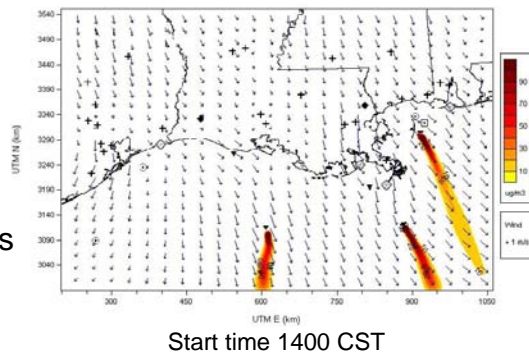
1/25/00 1400 CST - Mixing Heights



## Dispersion Patterns from SMI, BIP, and DWP – January 25, 2000

Same source emission rate assumed at each platform

- Similar to January 24
- Strong, offshore northerly winds transported the plumes out into the Gulf of Mexico, causing no onshore impact



**STI**

## Spring Case Study with Regional High Ozone May 14-15, 2001

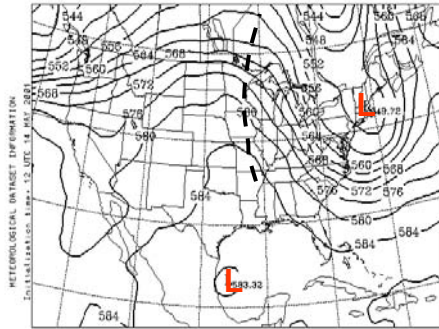
**STI**

## Spring Case Study with Regional High Ozone May 14, 2001: 12Z – 500-mb Heights


 NOAA Air Resources Laboratory  
This product was produced by an Internet user on the NOAA Air Resources Laboratory's web site. See the disclaimer for further information. (<http://www.arl.noaa.gov/ready/disclaimer.html>).

EDAS Archive

Ridge of high pressure extended from Texas, north through the Central Plains, and into Canada



NATIONAL OCEANIC AND ATMOSPHERIC ADMINISTRATION - AIR RESOURCES LABORATORY



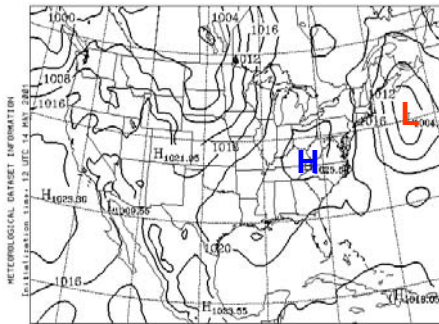
HEIGHT  
 HGTS ( DM ), LVL= 500, 12 UTC 14 MAY 2001 (+ 00 H )

## Spring Case Study with Regional High Ozone May 14, 2001 12Z – Sea-level Pressure


 NOAA Air Resources Laboratory  
This product was produced by an Internet user on the NOAA Air Resources Laboratory's web site. See the disclaimer for further information. (<http://www.arl.noaa.gov/ready/disclaimer.html>).

EDAS Archive

Light east-northeasterly surface winds across the Gulf of Mexico region are associated with the large area of high pressure that was centered over the central Appalachian Mts.



NATIONAL OCEANIC AND ATMOSPHERIC ADMINISTRATION - AIR RESOURCES LABORATORY



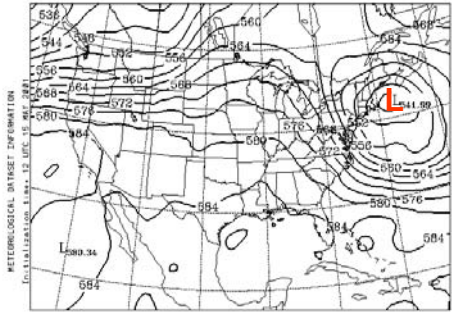
MEAN SEA-LEVEL PRESSURE  
 MSLP ( HPA ), LVL= SFC, 12 UTC 14 MAY 2001 (+ 00 H )

## Spring Case Study with Regional High Ozone May 15, 2001 12Z – 500-mb Heights


 NOAA Air Resources Laboratory  
 This product was produced by an Internet user on the NOAA Air Resources Laboratory's web site. See the disclaimer for further information (<http://www.arl.noaa.gov/read/disclaimer.html>).

EDAS Archive

Upper-level area of high pressure in the Midwest weakened



NATIONAL OCEANIC AND ATMOSPHERIC ADMINISTRATION - AIR RESOURCES LABORATORY



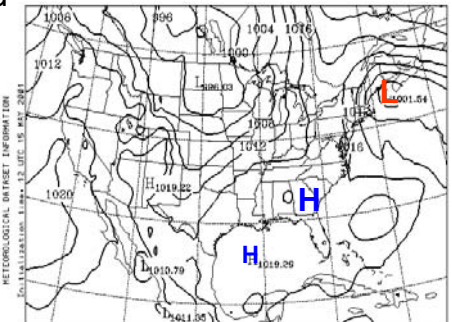
HEIGHT  
 HGTS ( DM ). LVL= 500.. 12 UTC 15 MAY 2001 (+ 00 H )

## Spring Case Study with Regional High Ozone May 15, 2001 12Z – Sea-level Pressure


 NOAA Air Resources Laboratory  
 This product was produced by an Internet user on the NOAA Air Resources Laboratory's web site. See the disclaimer for further information (<http://www.arl.noaa.gov/read/disclaimer.html>).

EDAS Archive

- Large, weakening area of high pressure centered over the southeastern United States
- High pressure area includes the Gulf of Mexico region



NATIONAL OCEANIC AND ATMOSPHERIC ADMINISTRATION - AIR RESOURCES LABORATORY

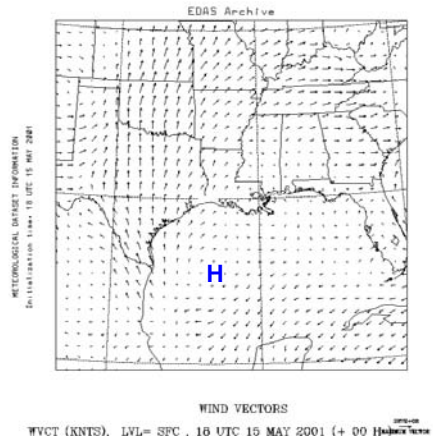


MEAN SEA-LEVEL PRESSURE  
 MSLP ( HPA ). LVL= SFC . 12 UTC 15 MAY 2001 (+ 00 H )

## Spring Case Study with Regional High Ozone May 15, 2001 18Z – EDAS Surface Winds

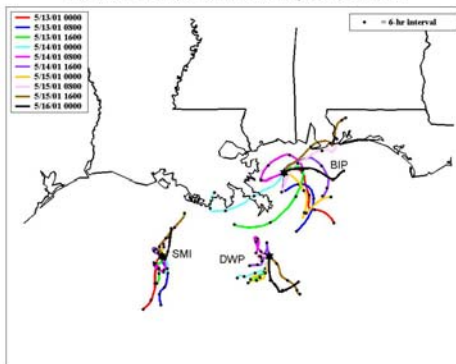
- Generally light winds in center of high pressure
- Weak, anticyclonic circulation centered south of the Louisiana/Texas border in the Gulf of Mexico driving
  - southwesterly flow across the western sections of the modeling domain
  - light and variable flow off the coasts of Louisiana through Florida

NOAA ERL Resources Laboratory  
This product was produced by an Internet user on the NOAA ERL Resources Laboratory's web site. See the disclaimer for further information. (http://www.erl.noaa.gov/ready/ModelData.html)



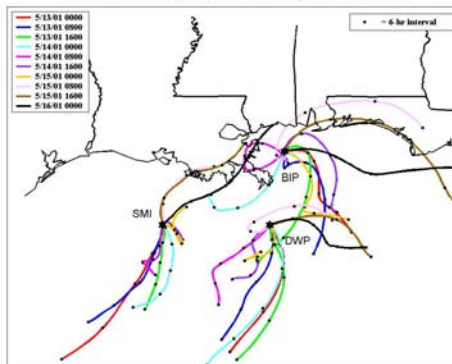
## Forward Trajectories (10 m) from SMI, BIP, and DWP on May 13-16, 2001

CALMET 24-hr (CST) Forward Trajectories at 10-m



CALMET 24-hr forward trajectories based on CALMET diagnostic wind fields (5/13/01 0000 – 5/16/01 0000 CST)

HYSPLIT 24-hr (CST) Forward Trajectories at 10-m



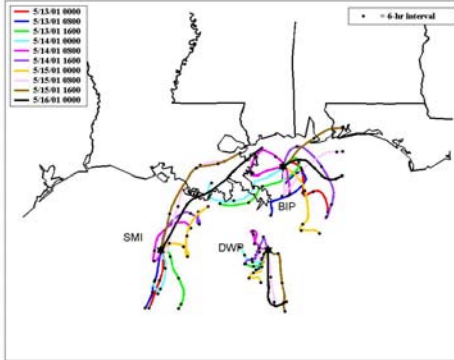
HYSPLIT 24-hr forward trajectories based on EDAS wind fields (5/13/01 0000 – 5/16/01 0000 CST)

- Lower wind speeds calculated by CALMET than by EDAS at 10 m
- Light and variable winds across the Gulf of Mexico associated with the area of high pressure
- Few trajectories at 10 m impact onshore locations



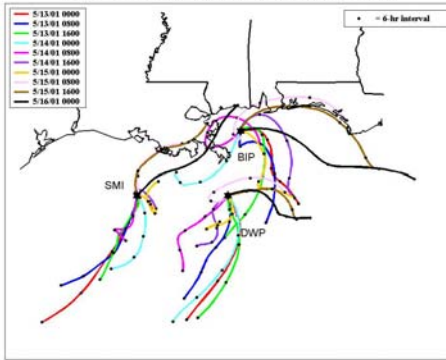
## Forward Trajectories (75 m) from SMI, BIP, and DWP on May 13-16, 2001

CALMET 24-hr (CST) Forward Trajectories at 75-m



CALMET 24-hr forward trajectories based on CALMET diagnostic wind fields (5/13/01 0000 – 5/16/01 0000 CST)

HYSPLIT 24-hr (CST) Forward Trajectories at 75-m



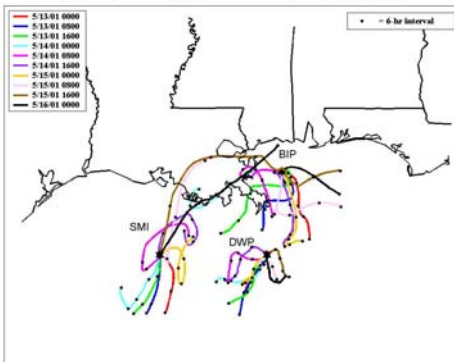
HYSPLIT 24-hr forward trajectories based on EDAS wind fields (5/13/01 0000 – 5/16/01 0000 CST)

- Conclusions similar to those for 75 m (see previous slide)
- Wind speed and transport distances are slightly larger at 75 m than at 10 m, as expected



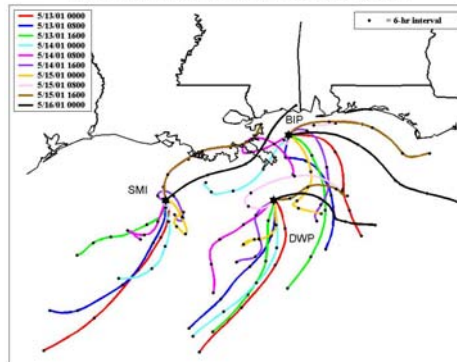
## Forward Trajectories (350 m) from SMI, BIP, and DWP on May 13-16, 2001

CALMET 24-hr (CST) Forward Trajectories at 350-m



CALMET 24-hr forward trajectories based on CALMET diagnostic wind fields (5/13/01 0000 – 5/16/01 0000 CST)

HYSPLIT 24-hr (CST) Forward Trajectories at 350-m



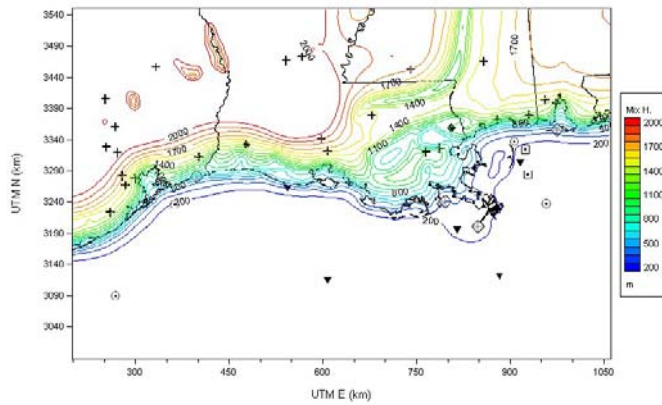
HYSPLIT 24-hr forward trajectories based on EDAS wind fields (5/13/01 0000 – 5/16/01 0000 CST)

- Conclusions at 350 m similar to those for 10 m and 75 m (see previous two slides)
- Little onshore impact of trajectories originating at 350 m
- Exception being transport late in the case study period originating from SMI at 350 m begins to impact onshore areas across the Mississippi River Delta in response to the southwest winds generated by the anticyclonic circulation developing in the western sections of the modeling domain



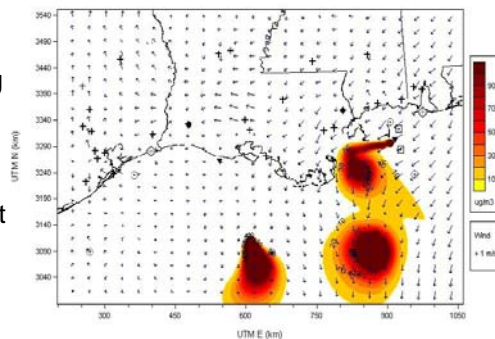
## CALMET Derived Mixing Heights May 14, 2001

5/14/01 1400 CST - Mixing Heights



## Dispersion Patterns from SMI, BIP, and DWP – May 14, 2001

- Same source emission rate assumed at each platform
  - Light and variable winds, combined with low mixing depths contributed to the accumulation of tracers near each source
  - A period of light winds out of the northeast caused hypothetical tracers from BIP to impact coastal regions of the Mississippi River Delta

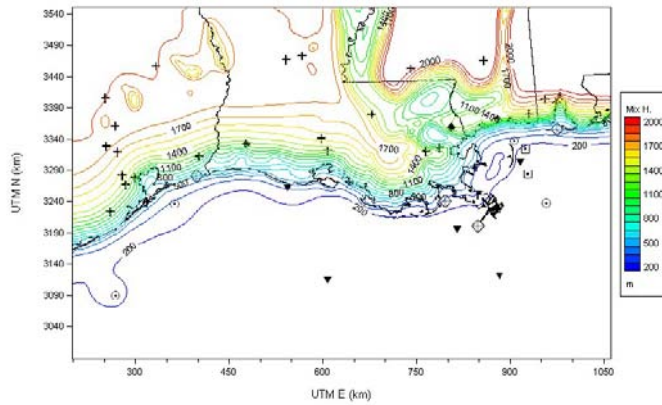


Start time 0600 CST



## CALMET Derived Mixing Heights May 15, 2001

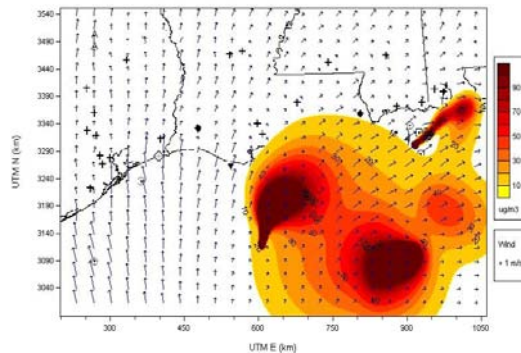
5/15/01 1400 CST - Mixing Heights



STI

## Dispersion Patterns from SMI, BIP, and DWP – May 15, 2001

- Same source emission rate assumed at each platform
  - Winds remained light with an onshore component at SMI and BIP
  - Mixing depth remained low (200 m or less)
  - Relatively high concentrations of tracer are seen, covering a much larger area than found for the January or April case studies



Start time 2200 CST

STI

## Meteorological Characterization of the ABL – COARE

- Background
- Data requirements and availability
- Estimation of fluxes and other ABL parameters
- Average monthly variables
- Diurnal variation by month
- Case studies



## COARE Background (1 of 4)

- Derived from the Tropical Ocean-Global Atmosphere Coupled-Ocean Atmosphere Response Experiment (TOGA COARE) project
- Allows surface fluxes and other scaling parameters over the ocean to be accurately parameterized using routine observations in the surface boundary layer (Fairall et al., 1996)
  - Heat fluxes
  - Surface roughness length
  - Friction velocity
  - Scaling temperature
  - Scaling water vapor mixing ratio
  - Monin-Obukhov length, etc.
- Originally designed for deep tropical ocean
- Outgrowth of the Liu-Katsaros-Businger method (Liu et al., 1979)



## COARE Background (2 of 4)

- COARE originated in 1993.
- Three newer versions were used in the current Gulf of Mexico ABL study.
- Version 2.5b, released in May 1997, included updated transfer coefficients and was used until January 2000 when Version 2.6b was released.
- The major difference between Versions 2.5b and 2.6b was a change in the Charnook “constant” to a parameter based on wind speed data.



## COARE Background (3 of 4)

- Version 2.6b was used for this Gulf of Mexico study until June 2000.
- Version 2.6bw was released in June 2000, and all COARE outputs presented are from this latest version.
- Version 2.6bw incorporates surface gravity wave information, based on wave height and period data.



## COARE Background (4 of 4)

- We modified COARE to
  - Use Eta model predictions to estimate short and long wave radiation for warm layer and cool skin temperature calculation
  - Read configuration for easy data processing
  - Interpolate missing data
  - Calculate wave height and period when not observed
  - Impose a minimum stress of  $.002 \text{ N/m}^2$  for warm layer calculation only
  - Better parameterize net absorption by the ocean
  - Incorporate data quality descriptors flags



## Data Requirements and Availability

- Data used by COARE
- Data availability
- Data issues and assumptions



## Data Used by COARE

- Surface layer wind speed
- Surface layer air temperature
- Skin temperature ( $T_s$ ) or near-surface underwater sea temperature
- Surface layer relative humidity or mixing ratio at two levels
- Mixing height
- Site time and position
- Long- and short-wave radiation (not required)
- Precipitation (not required)



## Data Availability – 1998 through 2001

Offshore buoys (7), C-MAN stations (5), platforms (7)

Site Name	Site	Latitude (degrees N)	Longitude (degrees W)	Elevation (m msl)	Air Temperature Height Above Site (m)	Anemometer Height Above Site (m)	Sea Temperature Height (m)
Mid Gulf 180 nm South of Southwest Pass LA	42001	25.93	89.65	0.0	10.0	10.0	-1.0
West Gulf 240 nm South-Southeast of Sabine TX	42002	25.89	93.57	0.0	10.0	10.0	-1.0
Biloxi 22 nm South-Southeast of Biloxi MS	42007	30.10	88.78	0.0	4.0	5.0	-0.6
Freeport TX, 60 nm South of Freeport TX	42019	27.92	95.35	0.0	4.0	5.0	-0.6
Corpus Christi TX 50 nm Southeast of Corpus Christi	42020	26.92	96.70	0.0	4.0	5.0	-0.6
Galveston 22 nm East of Galveston TX	42035	29.25	94.41	0.0	4.0	5.0	-0.6
Mobile South 64 nm South of Dauphin Island AL	42040	29.18	88.30	0.0	4.0	5.0	-0.6
Southwest Pass LA	BURL1	28.90	89.43	0.0	11.9	30.5	-0.5
Dauphin Island AL	DP1A1	30.25	88.07	0.0	9.1	17.4	-0.5
Grand Isle LA	GDIL1	29.27	89.96	1.8	15.2	15.8	-0.5
Port Arkansas TX	PTAT2	27.83	97.05	0.0	9.1	14.9	-0.5
Sabine TX	SRST2	29.67	94.05	0.9	11.9	12.5	-0.5
Breton Island Platform	BIP	29.77	88.71	20.0	2.0	3.0	0.0
Deep Water Platform	DWP	28.15	89.10	41.0	2.0	3.0	0.0
Shallow Water Platform	SWP	29.98	88.60	20.0	2.0	3.0	0.0
Mid Buoy Platform	MBP	29.62	88.57	20.0	2.0	3.0	0.0
West Delta Platform	WDP	28.83	89.78	20.0	2.0	3.0	0.0
Vermillion Gulf of Mexico	VRM	29.47	92.55	21.0	2.0	3.0	0.0
South Marsh Gulf of Mexico	SMI	28.15	91.91	25.0	2.0	3.0	0.0



## Data Issues and Assumptions (1 of 3)

- **Issue** – Platform wind and temperature monitors are placed about 25 m msl.  
**Assumption** – The measurements are within the surface layer.
- **Issue** – VRM, some buoys, and C-MAN stations are not deep-water sites.  
**Assumption** – The sea-state at VRM and buoy sites behaves like the sea-state at deep-water sites, and the wave data should give a better estimate of roughness.
- **Issue** – Mixing height data are not available for all days and sites.  
**Assumption** – Analysis shows that mixing heights are typically 600 m msl.



## Data Issues and Assumptions (2 of 3)

- **Issue** – Buoy sites do not provide  $T_s$  or radiation data from which to estimate  $T_s$  using the cool-skin or warm layer correction.  
**Solution** – Use Eta cloud predictions to estimate short- and long-wave radiation.
- **Issue** – Platform sites do not provide wave data.  
**Solution** – Estimate wave data from wind speed.
- **Issue** – Roughness is overestimated at very low wind speeds.  
**Solution** – Informed Christopher Fairall of problem; he is investigating cause.

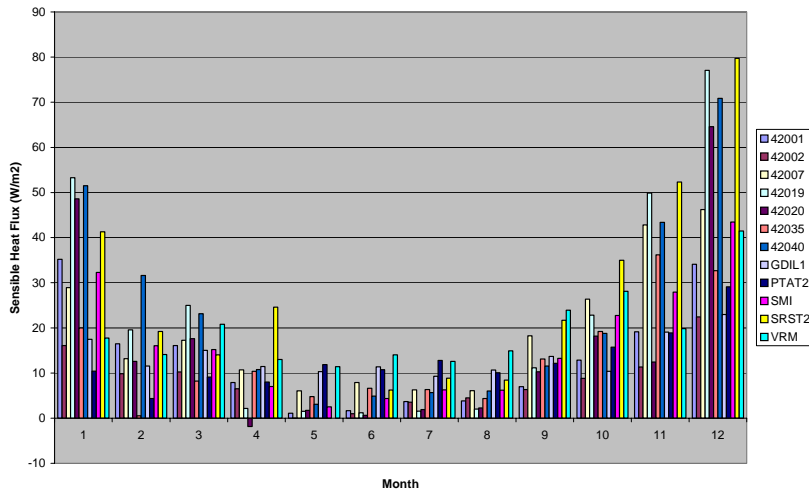


## Estimation of Fluxes and Other ABL Parameters

- BAMP sites now included
- Average monthly variables by total study period, synoptic class, and surface flow
- Diurnal variation by month
- $H_s$ ,  $H_e$ , Total,  $u^*$ ,  $T^*$ ,  $q^*$ ,  $u$ ,  $T$ ,  $T_s$ , RH,  $Z_o$ , wave height and period, Eta data, radiation
- Case studies
  - July 30 through August 1, 1999
  - January 20 through 25, 2000
  - January 4 through 6, 2001
  - September 18 through 20, 2001



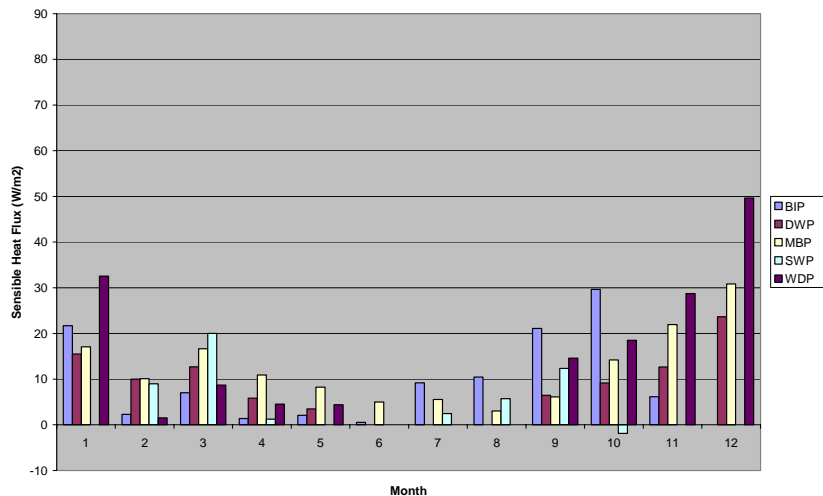
## COARE monthly average sensible heat fluxes (1 of 2)



COARE monthly average sensible heat fluxes by site for May 1998 through October 2001



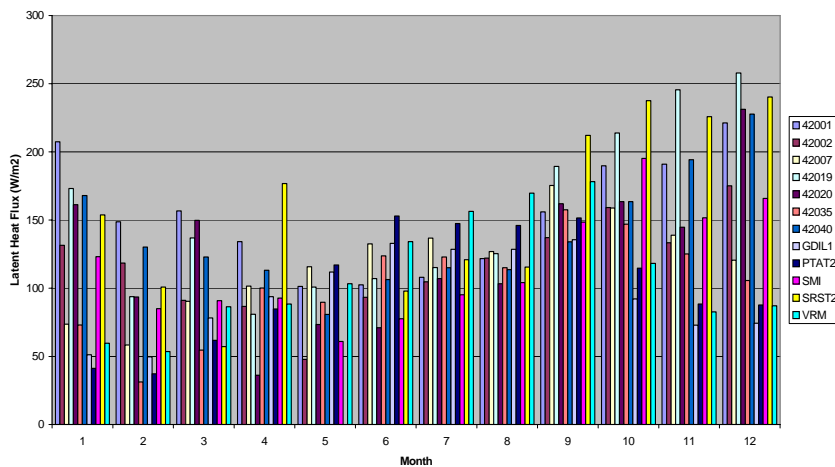
### COARE monthly average sensible heat fluxes (2 of 2)



COARE monthly average sensible heat fluxes by BAMP site for September 2000 through September 2001



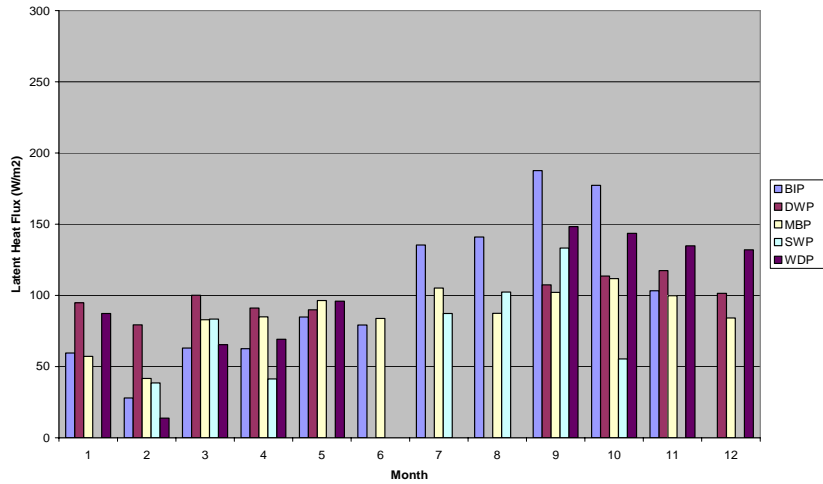
### COARE monthly average latent heat fluxes (1 of 2)



COARE monthly average latent heat fluxes by site for May 1998 through October 2001



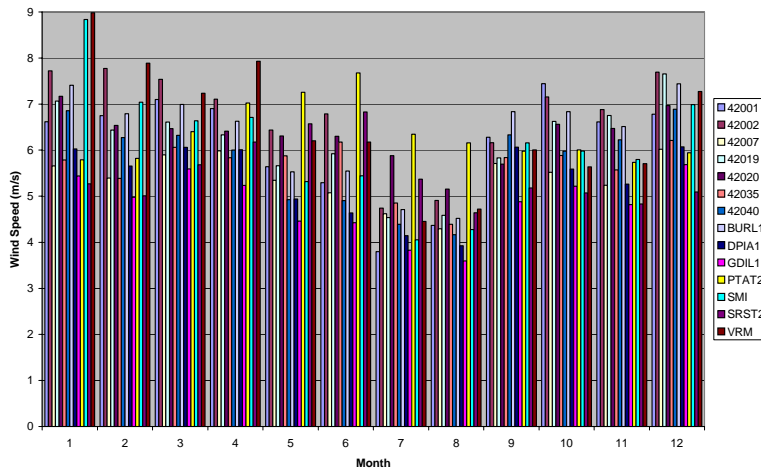
### COARE monthly average latent heat fluxes (2 of 2)



COARE monthly average latent heat fluxes by BAMP site for September 2000 through September 2001



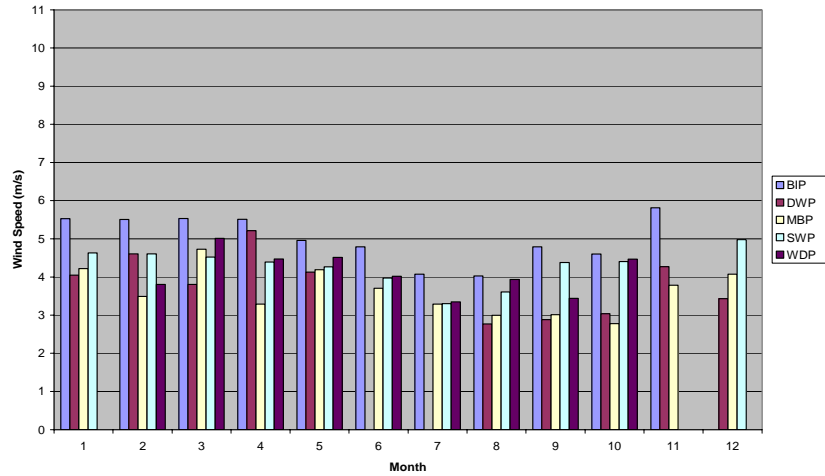
### Observed monthly average wind speed (1 of 2)



Observed monthly average wind speed by site for May 1998 through October 2001



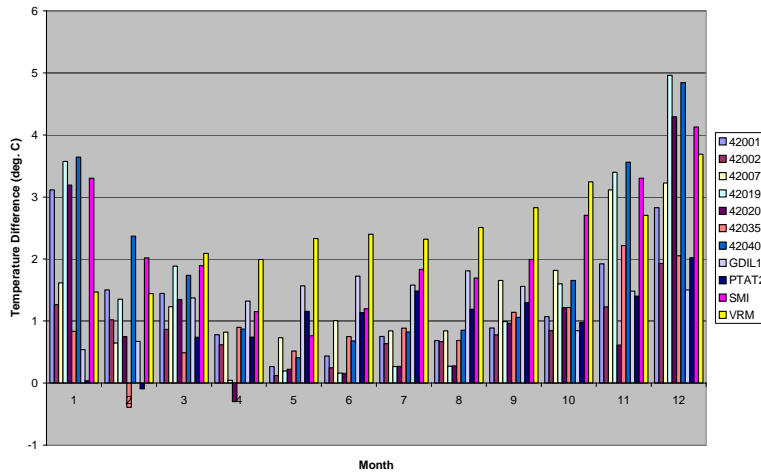
### Observed monthly average wind speed (2 of 2)



Observed monthly average wind speed by BAMP site for September 2000 through September 2001



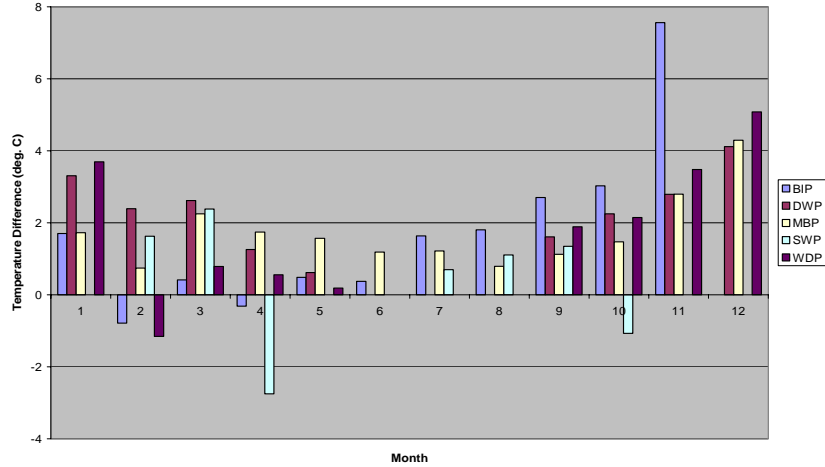
### Monthly average skin temperature minus air temperature (1 of 2)



Monthly average skin temperature minus air temperature by site for May 1998 through October 2001



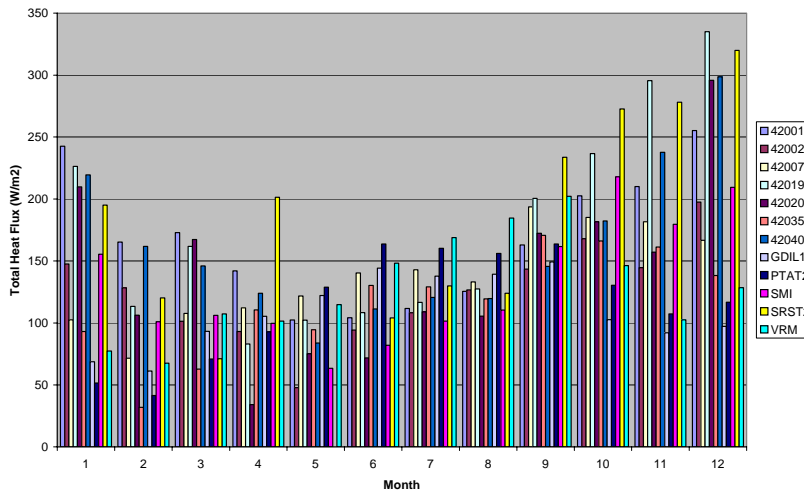
### Monthly average skin temperature minus air temperature (2 of 2)



COARE monthly average skin temperature minus air temperature by BAMP site for September 2000 through September 2001



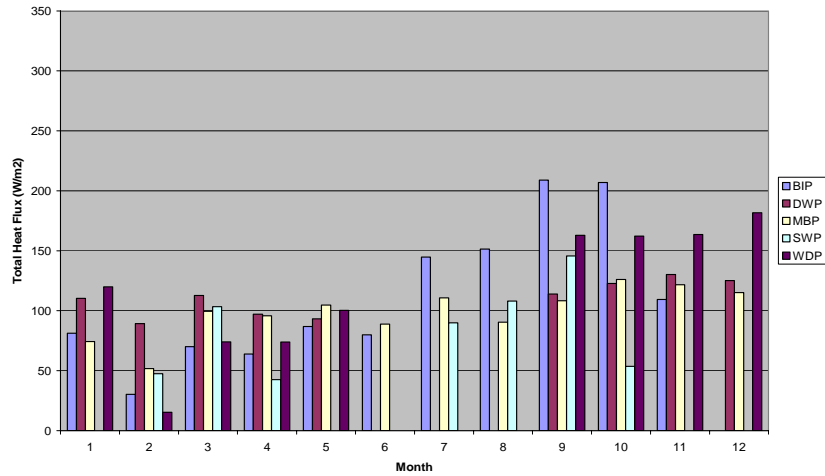
### COARE monthly average of total heat fluxes (1 of 2)



COARE monthly average of total heat fluxes (sensible plus latent) by site for May 1998 through October 2001



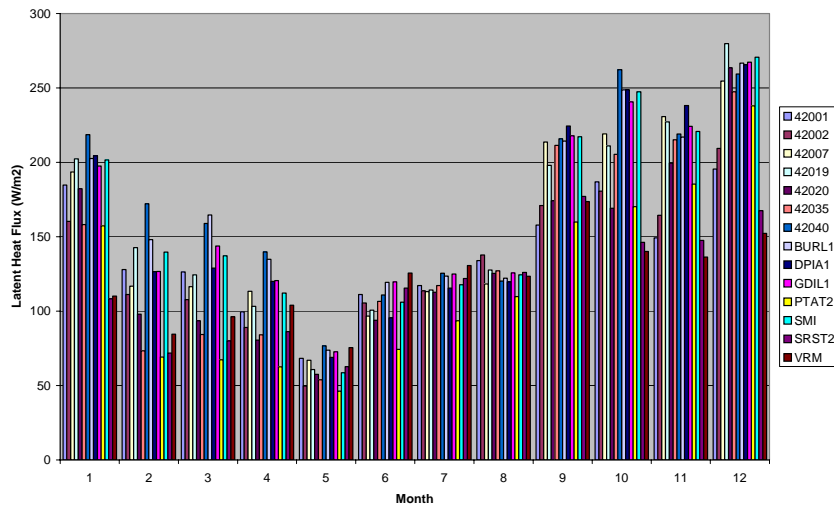
### COARE monthly average total heat fluxes (2 of 2)



COARE monthly average total heat fluxes (sensible plus latent) by BAMP site for September 2000 through September 2001



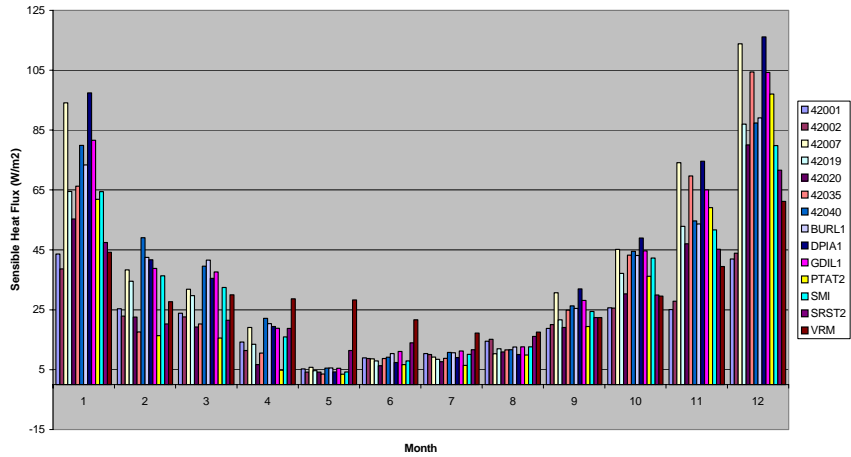
### Eta monthly average latent heat fluxes



Eta monthly average latent heat fluxes by site for May 1998 through October 2001 for the 6- to 12-hr forecast



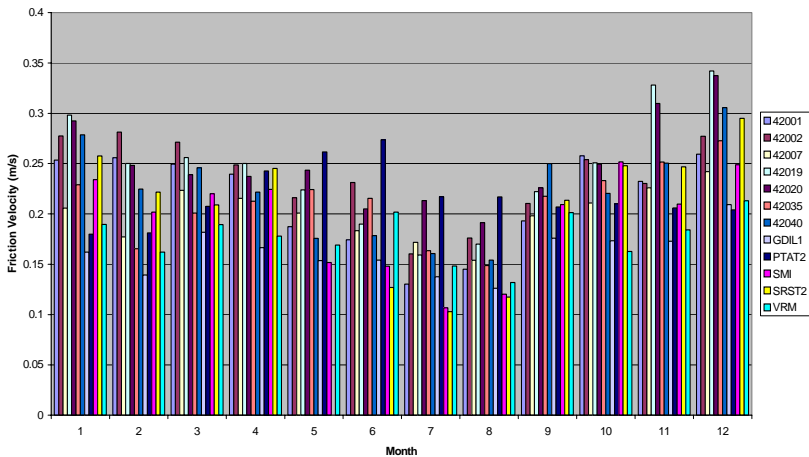
**Eta monthly average sensible heat fluxes**



Eta monthly average sensible heat fluxes by site for May 1998 through October 2001 for the 6- to 12-hr forecast



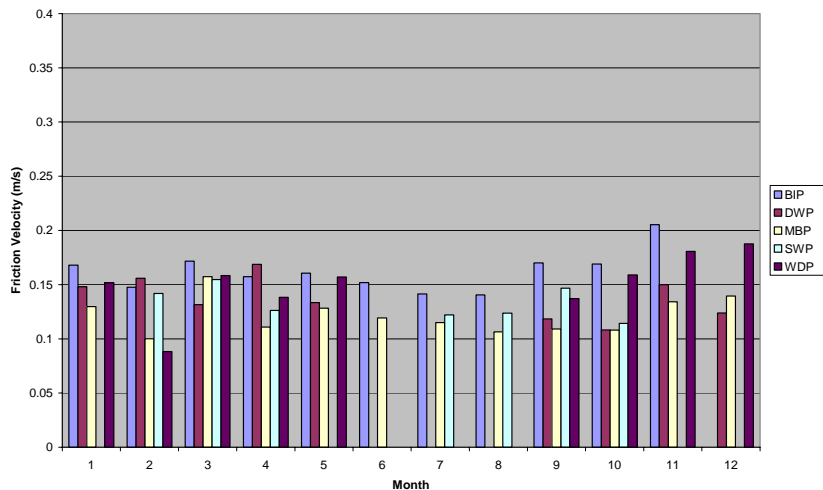
**COARE monthly average friction velocity (1 of 2)**



COARE monthly average friction velocity by site for May 1998 through October 2001



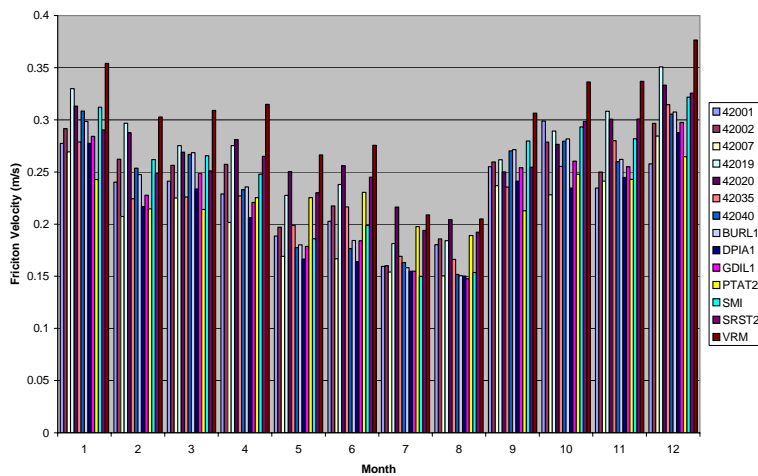
### COARE monthly average friction velocity (2 of 2)



COARE monthly average friction velocity by BAMP site for September 2000 through September 2001



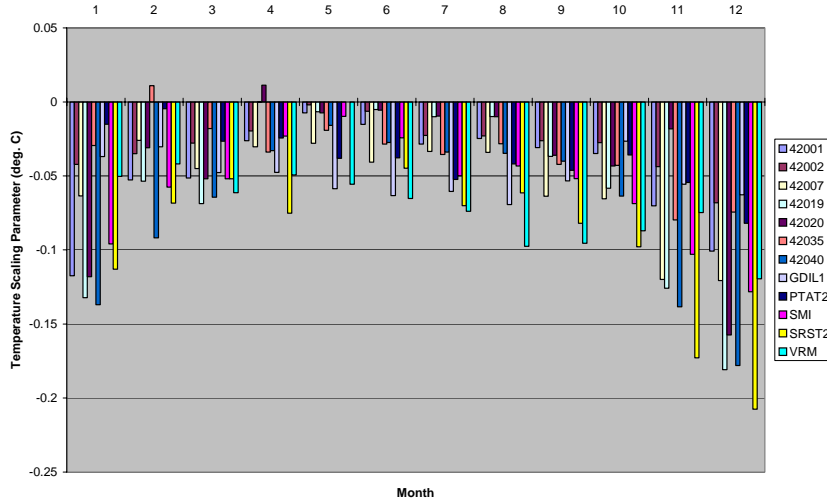
### Eta monthly average friction velocity by site



Eta monthly average friction velocity by site for May 1998 through October 2001 for the 6- to 12-hr forecast



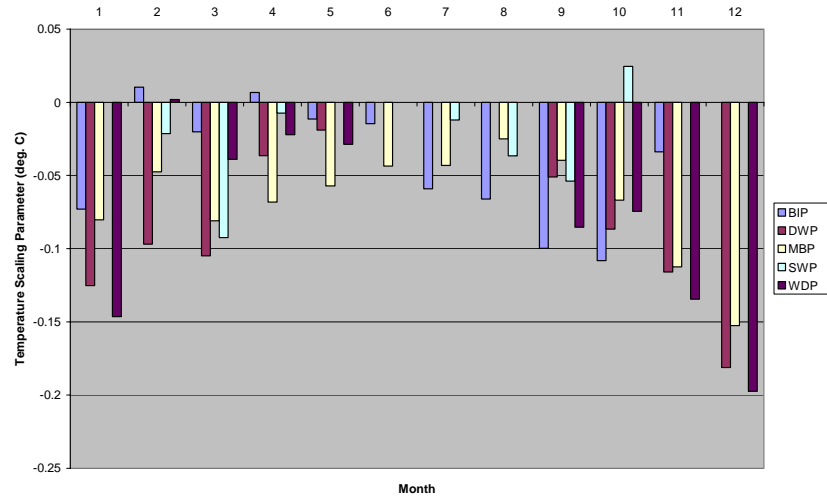
**COARE calculated monthly average temperature scaling parameter (1 of 2)**



COARE calculated monthly average temperature scaling parameter by site for May 1998 through October 2001



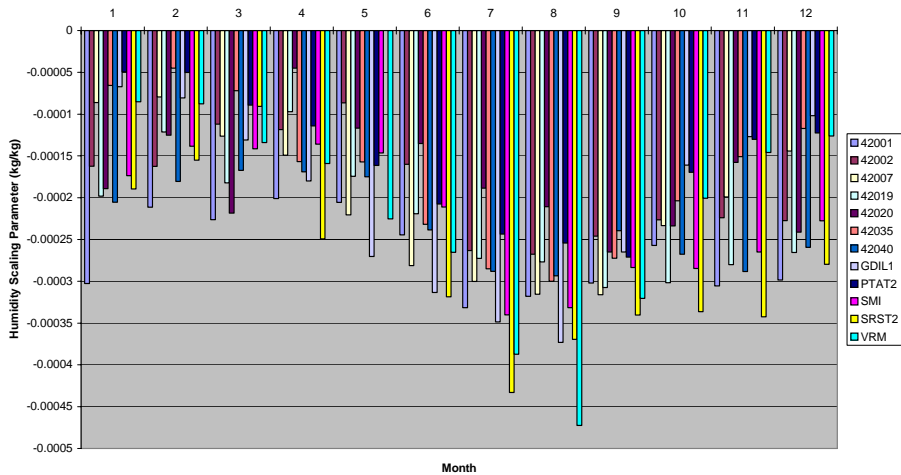
**COARE calculated monthly average temperature scaling parameter (2 of 2)**



COARE calculated monthly average temperature scaling parameter by BAMP site for September 2000 through September 2001



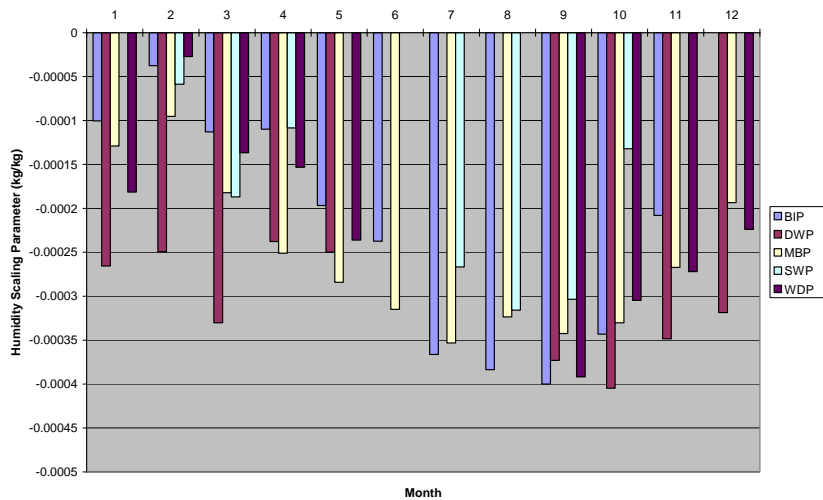
### COARE calculated monthly average humidity scaling parameter (1 of 2)



COARE calculated monthly average humidity scaling parameter by site for May 1998 through October 2001



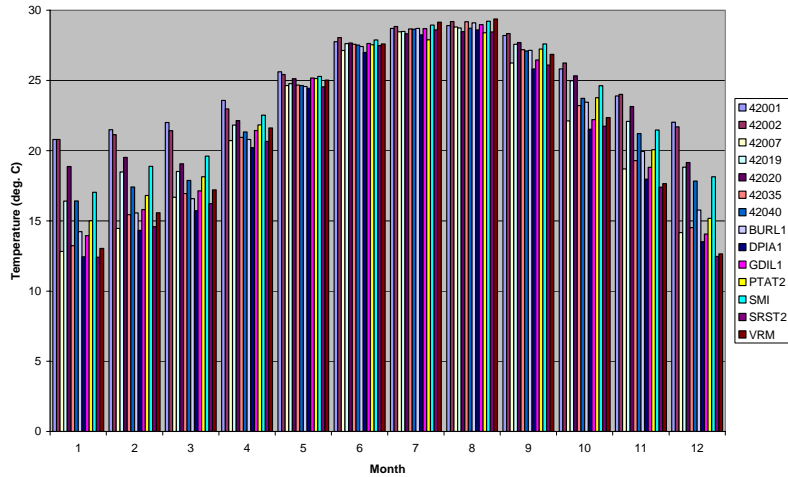
### COARE calculated monthly average humidity scaling parameter (2 of 2)



COARE calculated monthly average humidity scaling parameter by BAMP site for September 2000 through September 2001



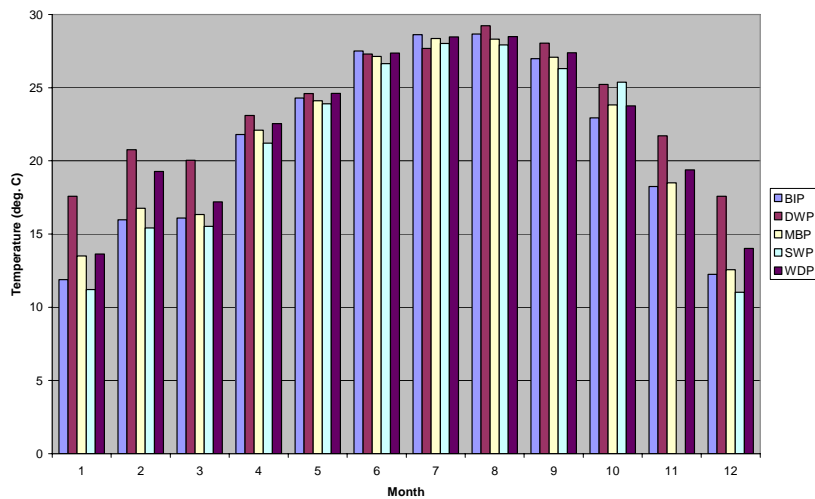
### Observed monthly average air temperature (1 of 2)



Observed monthly average air temperature by site for May 1998 through October 2001



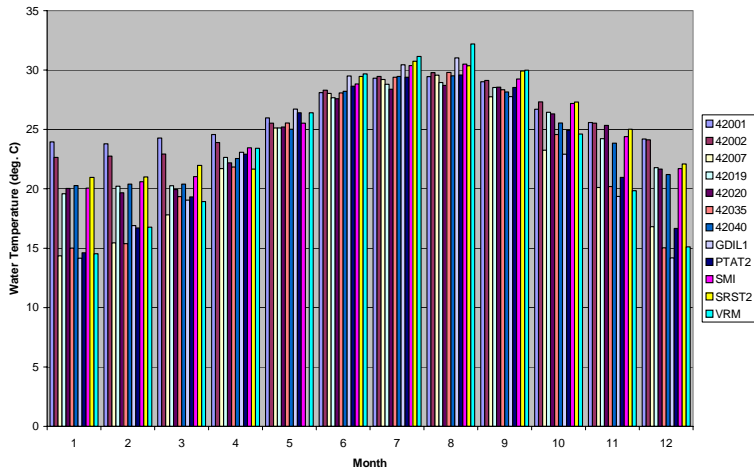
### Observed monthly average air temperature (2 of 2)



Observed monthly average air temperature by BAMP site for September 2000 through September 2001



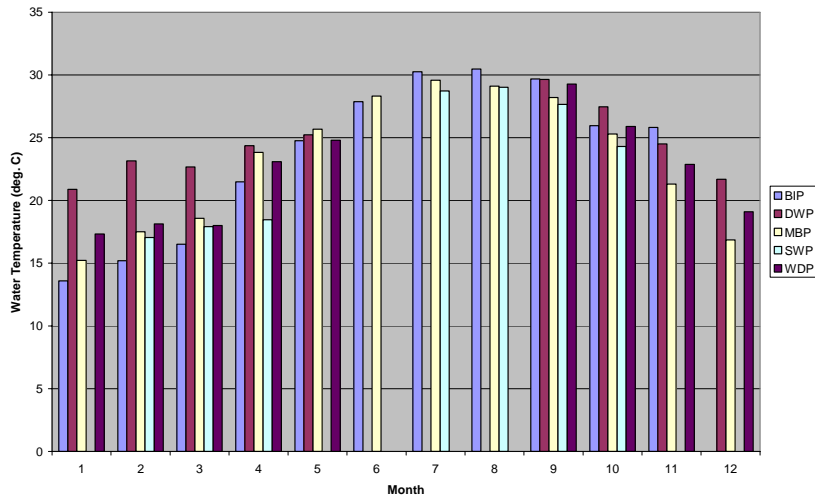
**Observed or estimated (at buoys) monthly average skin temperature (1 of 2)**



Observed monthly average skin temperature by site for May 1998 through October 2001



**Observed monthly estimated (at buoys) average skin temperature (2 of 2)**



Observed monthly average skin temperature by BAMP site for September 2000 through September 2001



## Summary of Monthly Averages (1 of 7)

- Sensible and latent heat fluxes are typical of other non-Gulf, over-water sites.
- Average sensible heat fluxes in the Gulf of Mexico are about 5 to 30  $\text{w/m}^2$ , typical of other over-water sites.
- Average latent heat fluxes are about 50 to 150  $\text{w/m}^2$ , also typical of other over-water sites.
- Latent and sensible heat fluxes are higher in the late fall and winter and are lowest in the summer, which is consistent with the light winds and smaller skin temperature-to-air temperature differences in the summer.



## Summary of Monthly Averages (2 of 7)

- The monthly average calculated total heat flux is in fair agreement (within a factor of 2 most of the time) among the sites in the Gulf of Mexico
- The largest relative variations (ranging from 20 to 170  $\text{w/m}^2$ ) occurred in February when the total heat flux was relatively small due to the cool water temperatures and the small difference between the skin and air temperatures.
- The smallest relative variations (ranging from 110 to 235  $\text{w/m}^2$ ) occurred in September when the total heat flux was relatively large due to the warm water temperatures and large difference between the skin and air temperature.



## Summary of Monthly Averages (3 of 7)

- Eta model latent and sensible heat fluxes are generally in good agreement with the calculated fluxes.
- However, the model fluxes do not show as great a variation among sites as do the calculated fluxes.
- The model fluxes are about 20% greater than the calculated fluxes in the fall and early winter but are very similar during the spring and summer.



## Summary of Monthly Averages (4 of 7)

- $u^*$  is within a factor of two and often within 20% among sites.
- However, the platform sites (except SMI) show mean friction velocities that are about 30% or 40% less than the other sites.
- Possible explanations are that the wave height and frequency are estimated from wind speed at the platforms, whereas, they are measured at the buoys. Also, the platform wind observations are corrected from 20+ meters to 10 meters and are, on average, less than the other non-BAMP sites.



## Summary of Monthly Averages (5 of 7)

- $u^*$  is slightly lower from May through August and peaks in late fall and early winter.
- Eta friction velocity shows the same yearly pattern as the calculated friction velocity.
- However, the Eta model friction velocity is about 10% to 20% higher than the calculated friction velocity in the fall and early winter. This is most likely why the Eta model fluxes are high during the same period.



## Summary of Monthly Averages (6 of 7)

- The difference between skin temperature minus the air temperature is about +1 to +3°C at most sites all year and reaches a maximum of about +8°C at BIP in November.
- The difference is less in late spring and is greater in late fall and early winter.
- This persistent positive temperature difference has been noted by Dr. Christopher Fairall at most other sites located on warm water oceans.

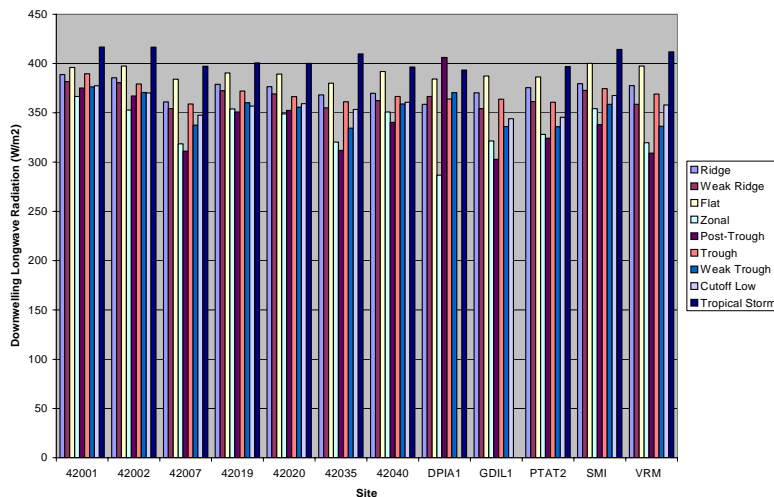


## Summary of Monthly Averages (7 of 7)

- Wind speed shows good agreement among sites.
- The lowest speeds occur in July and August and the highest in December and January.
- For some years, there is a transition between lower wind speeds in August to higher winds speeds in September.
- Weather maps indicate that high wind speeds in October are a result of strong continental winds and tropical storms.
- RH is in good agreement at all sites and is about 80% year-round.



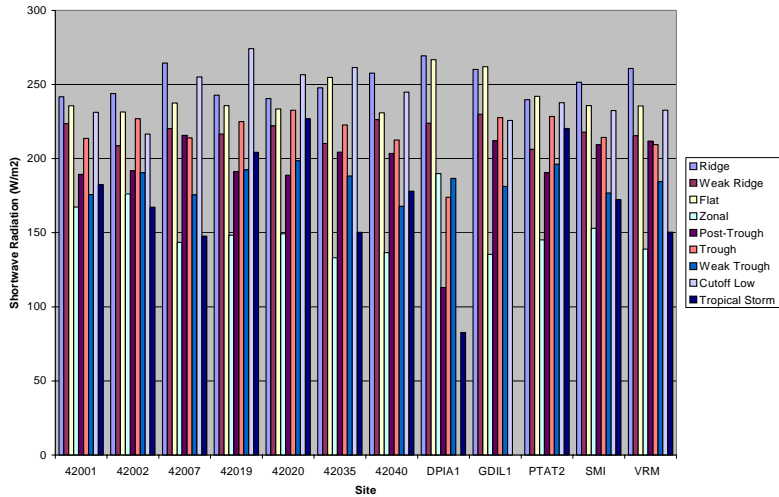
## Eta average downwelling longwave radiation by synoptic pattern



Eta average downwelling longwave radiation by synoptic class by site for May 1998 through October 2001 for the 6- to 12-hr forecast



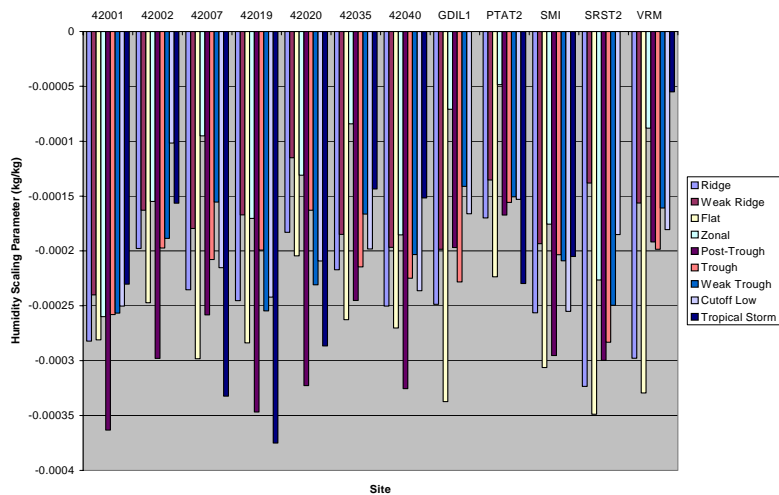
**Eta average shortwave radiation by synoptic pattern by synoptic pattern**



Eta average shortwave radiation by synoptic class by site for May 1998 through October 2001 for the 6- to 12-hr forecast



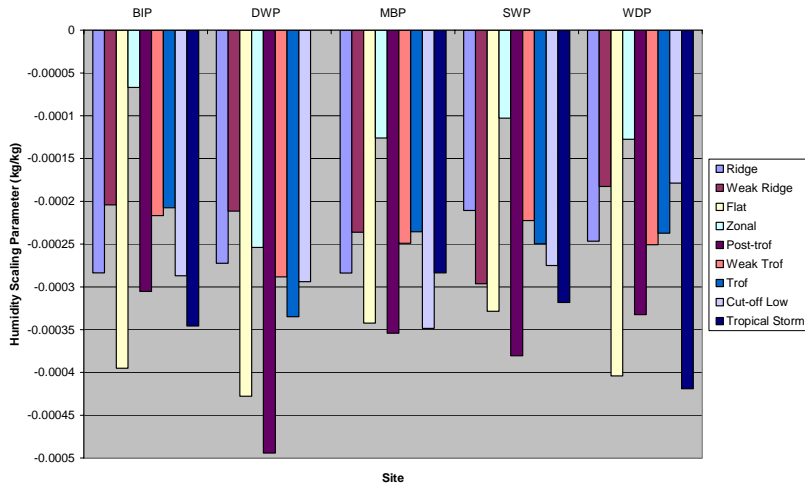
**COARE average humidity scaling parameter by synoptic pattern (1 of 2)**



COARE average humidity scaling parameter by synoptic class by site for May 1998 through October 2001



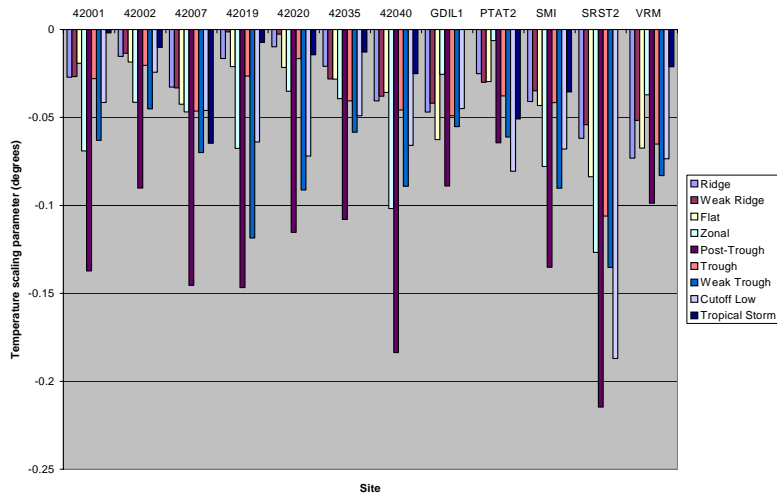
### COARE average humidity scaling parameter by synoptic pattern (2 of 2)



COARE average humidity scaling parameter by synoptic class by BAMP site for September 2000 through September 2001



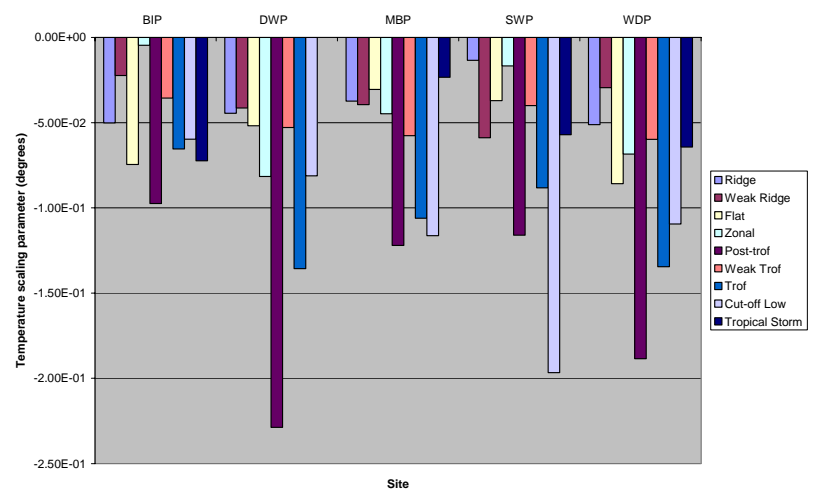
### COARE average temperature scaling parameter by synoptic pattern (1 of 2)



COARE average temperature scaling parameter by synoptic class by site for May 1998 through October 2001



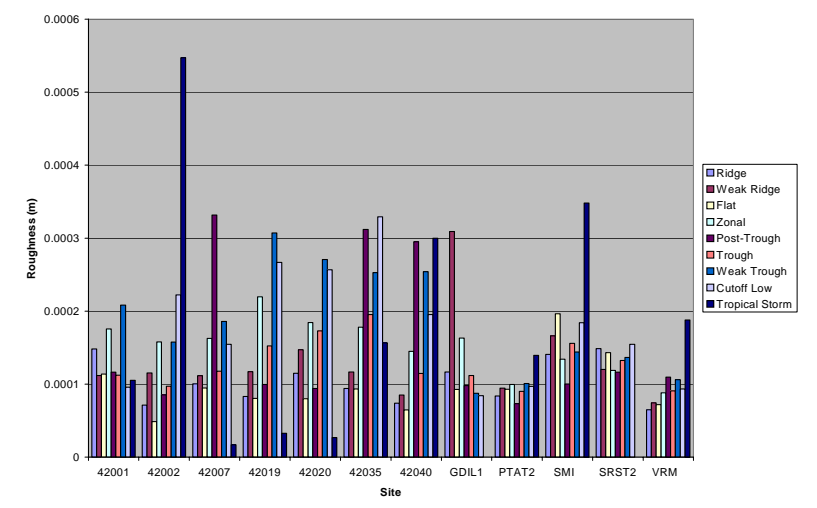
**COARE average temperature scaling parameter by synoptic pattern (2 of 2)**



COARE average temperature scaling parameter by synoptic class by BAMP site for September 2000 through September 2001



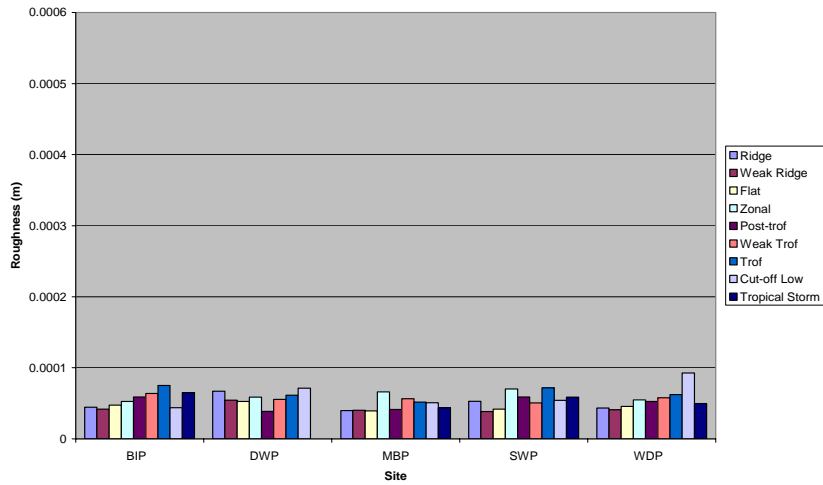
**COARE surface roughness by synoptic pattern by synoptic pattern (1 of 2)**



COARE surface roughness by synoptic class by site for May 1998 through October 2001



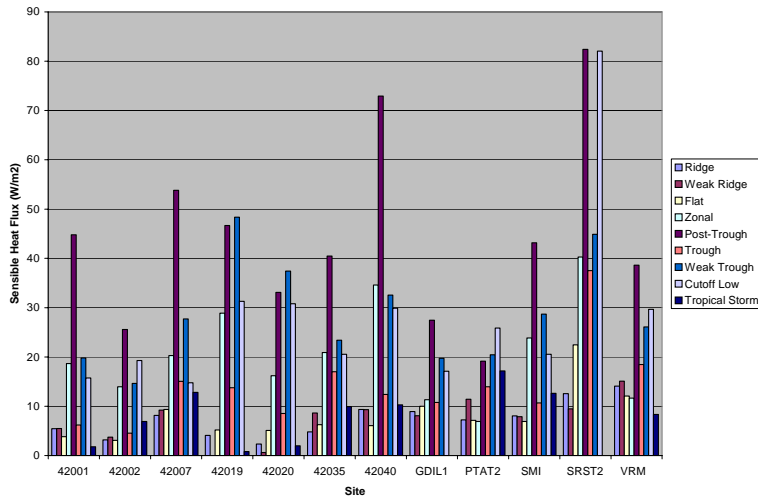
**COARE surface roughness by synoptic pattern by synoptic pattern (2 of 2)**



COARE surface roughness by synoptic class by BAMP site for September 2000 through September 2001



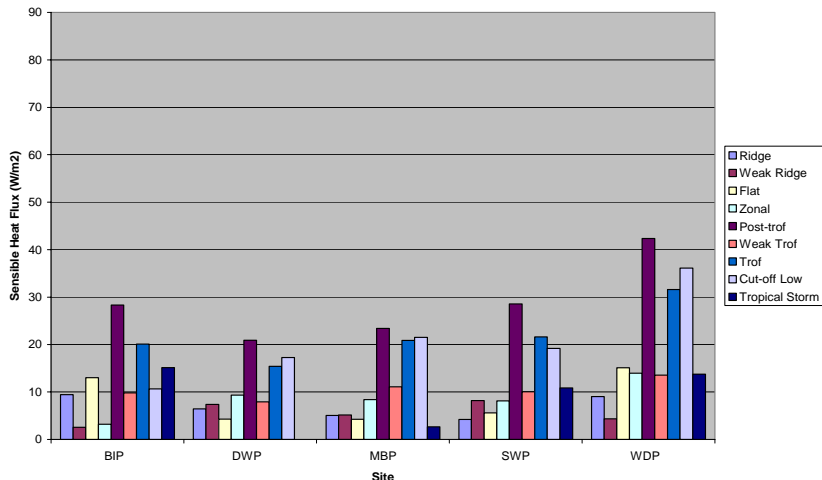
**COARE average sensible heat fluxes by synoptic pattern (1 of 2)**



COARE average sensible heat fluxes by synoptic class by site for May 1998 through October 2001



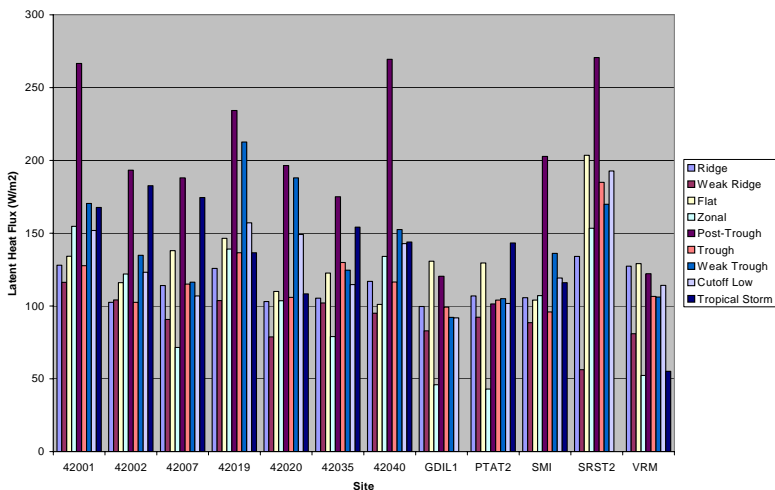
### COARE average sensible heat fluxes by synoptic pattern (2 of 2)



COARE average sensible heat fluxes by synoptic class by BAMP site for September 2000 through September 2001



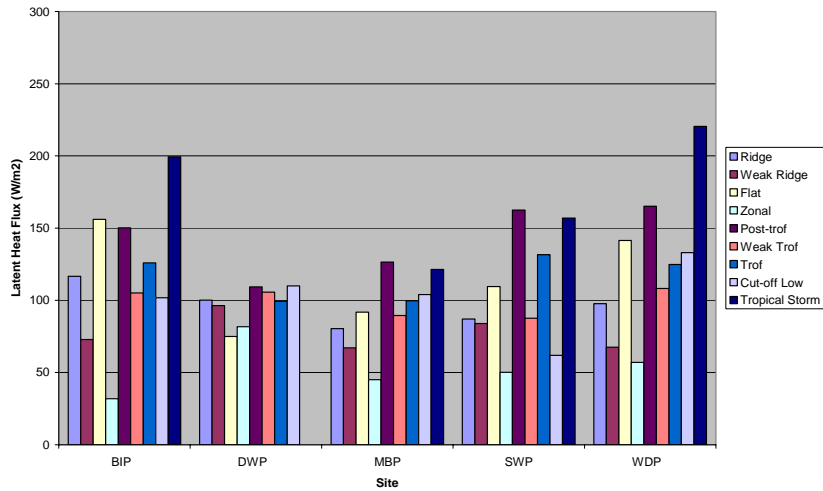
### COARE average latent heat fluxes by synoptic pattern (1 of 2)



COARE average latent heat fluxes by synoptic class by site for May 1998 through October 2001



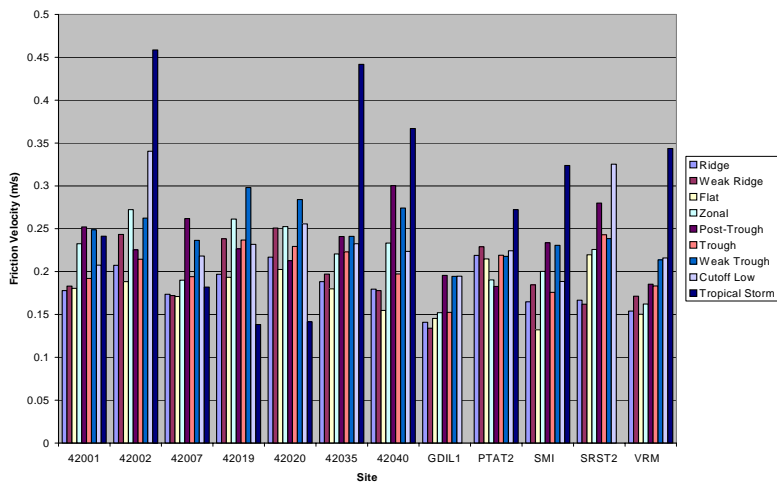
### COARE average latent heat fluxes by synoptic pattern (2 of 2)



COARE average latent heat fluxes by synoptic class by BAMP site for September 2000 through September 2001



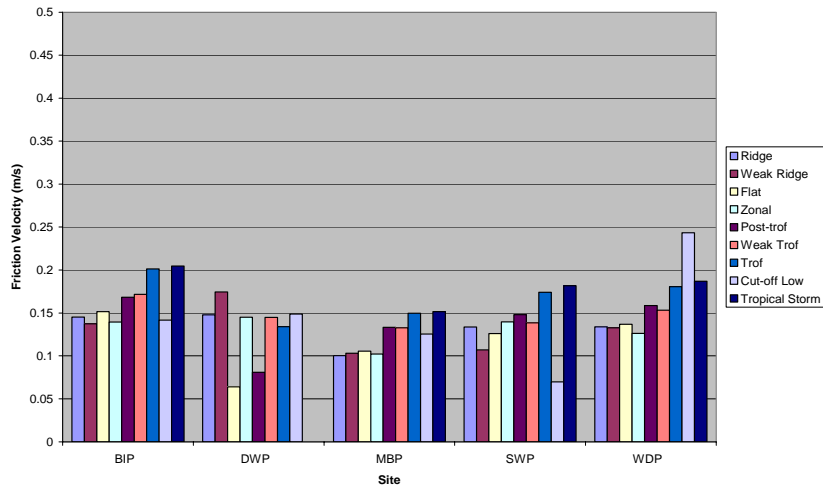
### COARE average friction velocity by synoptic pattern (1 of 2)



COARE average friction velocity by synoptic class by site for May 1998 through October 2001



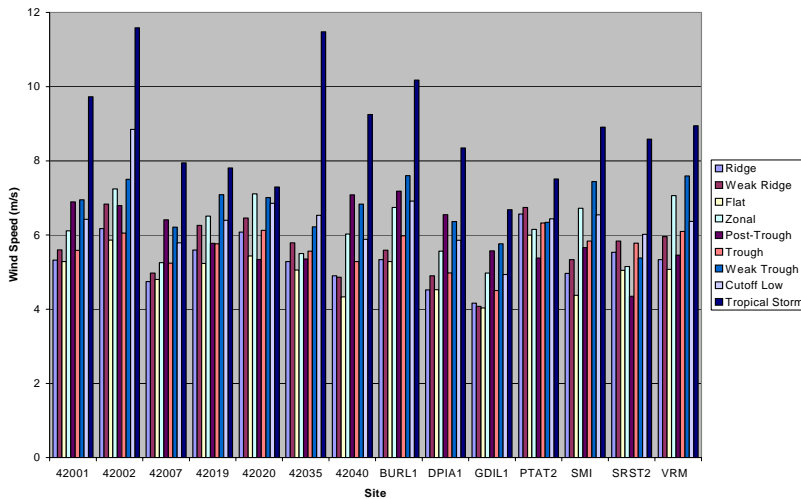
**COARE average friction velocity by synoptic pattern (2 of 2)**



COARE average friction velocity by synoptic class by BAMP site for September 2000 through September 2001



**Observed average wind speed by synoptic pattern**



Observed average wind speed by synoptic class by site for May 1998 through October 2001



### **Synoptic Average Summary – Sensible Heat**

- There is a large factor of 10 variability across the nine synoptic classes. There are some differences among the sites.
- Sensible heat flux is maximized for post-trough (i.e., post-frontal) synoptic conditions, which are likely to be marked by above-average wind speeds and by low air temperature.



### **Synoptic Average Summary – Latent Heat Flux**

- The latent heat flux is about one order of magnitude greater than the sensible heat flux.
- There is also less variability in the latent heat flux.
- Latent heat flux is largest during the “post-trough” synoptic condition due to higher wind speeds and relatively low dew points that follow a cold front.



### **Synoptic Average Summary – Wind Speed and Friction Velocity**

- Aside from the anomaly during tropical storms, there is relatively little variability in  $u^*$  in synoptic class.
- The BAMP sites and VRM friction velocity is about 20% less than the other sites.
- Wind speed averages about 6 m/s for non-BAMP sites and 4 m/sec for BAMP sites and varies in a similar manner to  $u^*$ .



### **Synoptic Average Summary – Temperature Scaling Parameter**

- The temperature scaling parameter varies widely, from near zero to about  $-0.22^\circ$ .
- The temperature scaling factor is much larger during “post-trough” periods.
- It is smallest during tropical storms when the air and water are likely to be at the same temperature.

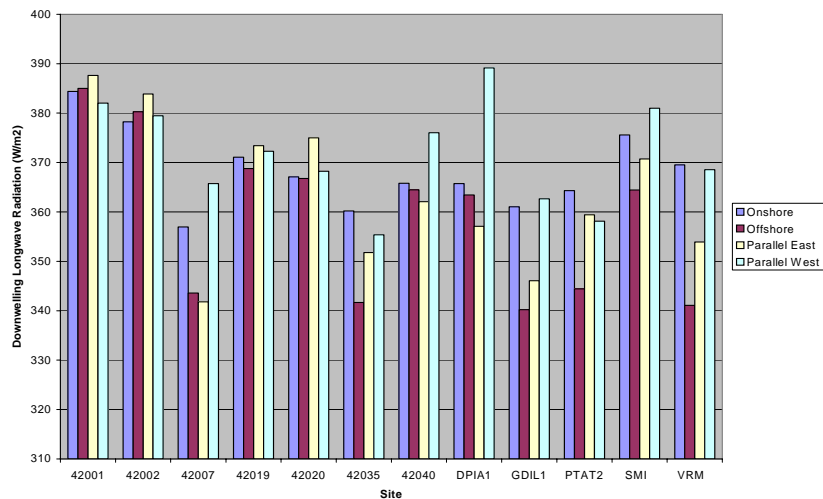


## Synoptic Average Summary – Roughness

- Roughness is typically about .0001 to .0015 m.
- Roughness is much less variable among the synoptic patterns for the platform sites compared to the buoy sites.
- Possible explanations are that the wave height and frequency are estimated from wind speed at the platforms, whereas, they are measured at the buoys. Also, the platform wind observations are corrected from 20+ meters to 10 meters and are, on average, less than the other non-BAMP sites.



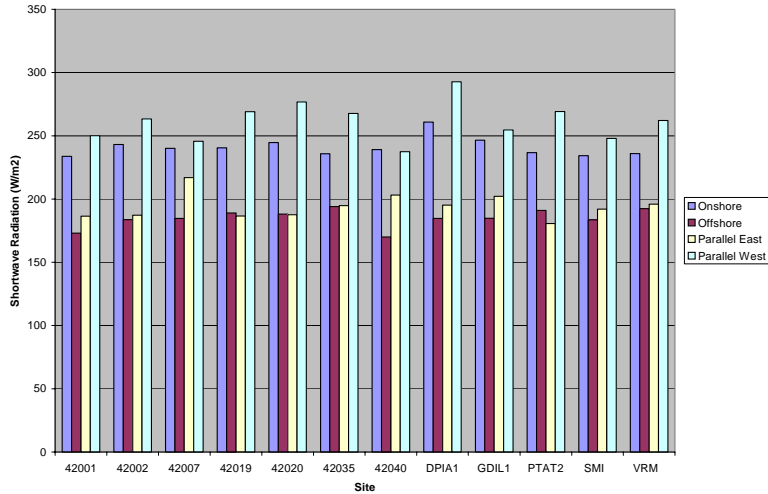
## Eta average downwelling longwave radiation by flow direction



Eta average downwelling longwave radiation by general flow direction by site  
for May 1998 through October 2001 for the 6-to 12-hr forecast



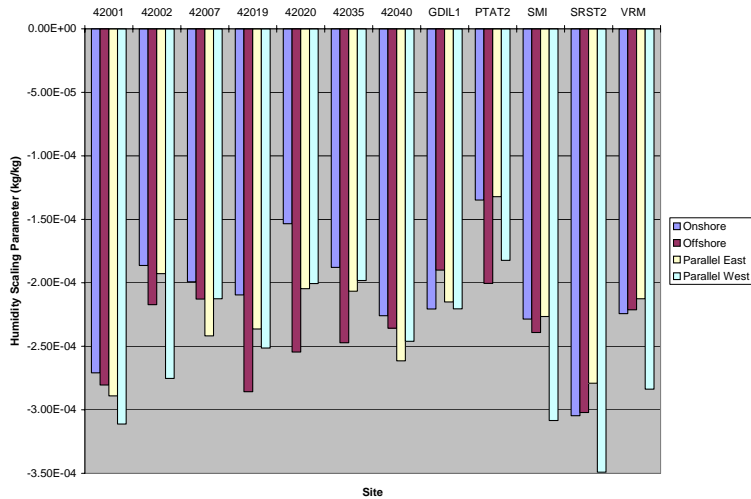
### Eta average shortwave radiation by flow direction



Eta average shortwave radiation by general flow direction by site for May 1998 through October 2001 for the 6-to 12-hr forecast



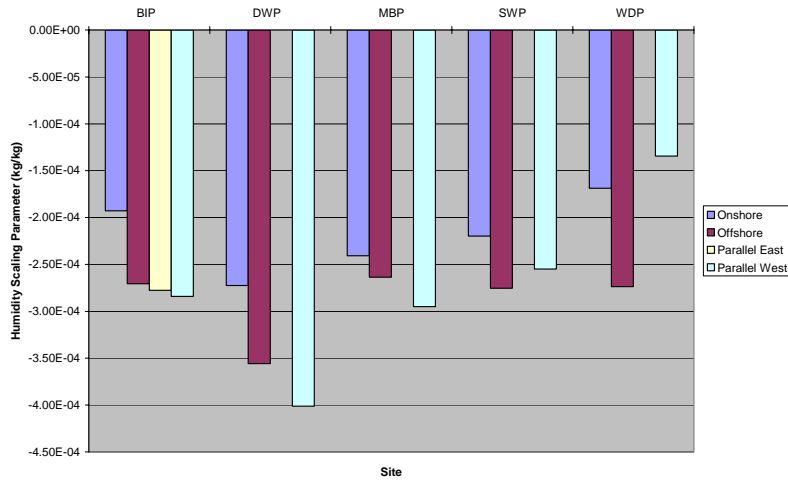
### COARE average humidity scaling parameter by flow direction (1 of 2)



COARE average humidity scaling parameter by general flow direction by site for May 1998 through October 2001



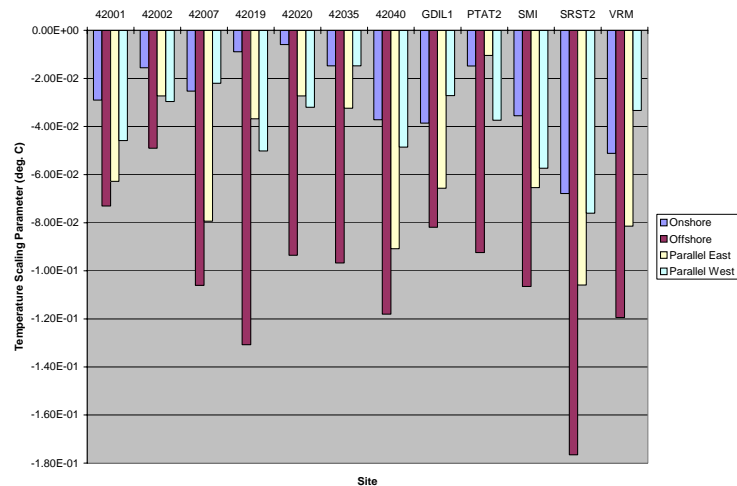
### COARE average humidity scaling parameter by flow direction (2 of 2)



COARE average humidity scaling parameter by general flow direction by BAMP site for September 2000 through September 2001



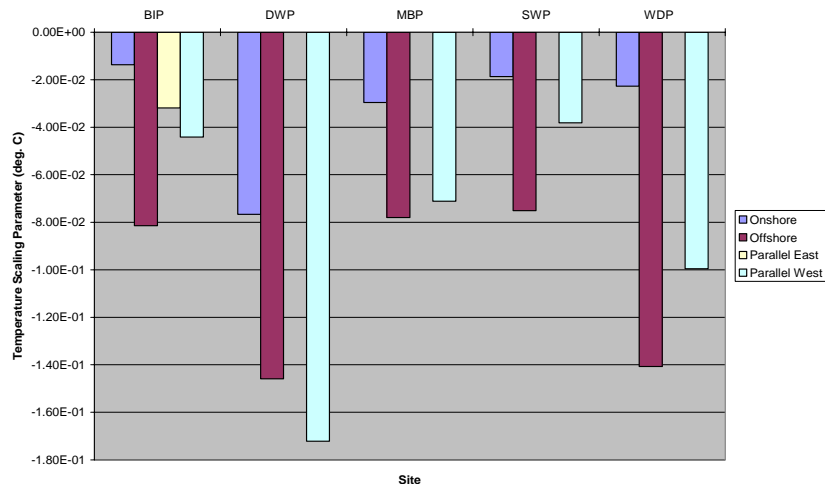
### COARE average temperature scaling parameter by flow direction (1 of 2)



COARE average temperature scaling parameter by general flow direction by site for May 1998 through October 2001



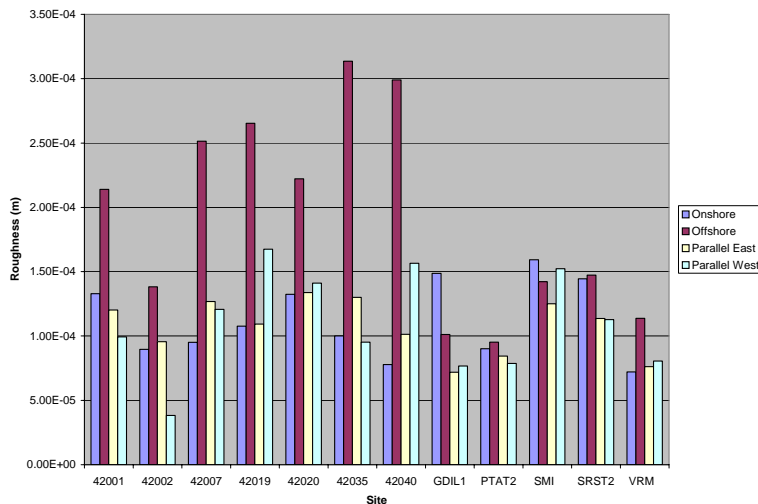
### COARE average temperature scaling parameter by flow direction (2 of 2)



COARE average temperature scaling parameter by general flow direction by BAMP site for September 2000 through September 2001



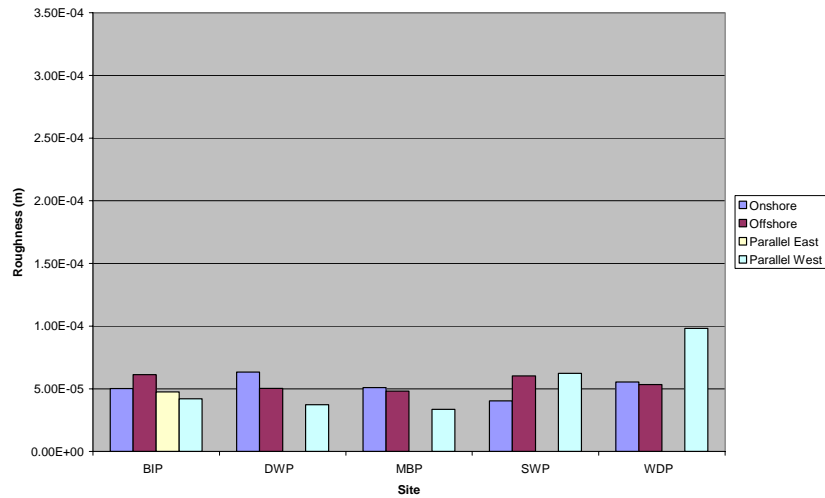
### COARE average surface roughness by flow direction (1 of 2)



COARE average surface roughness by general flow direction by site for May 1998 through October 2001



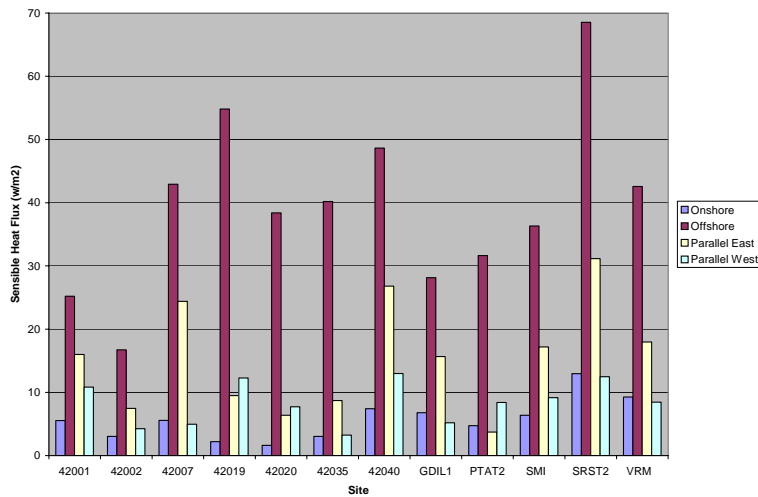
### COARE average surface roughness by flow direction (2 of 2)



COARE average surface roughness by general flow direction by BAMP site for September 2000 through September 2001



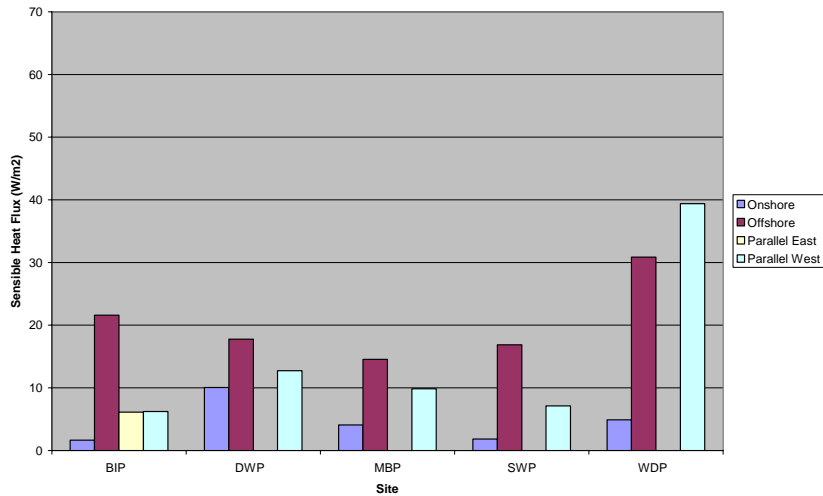
### COARE average sensible heat fluxes by flow direction (1 of 2)



COARE average sensible heat fluxes by general flow direction by site for May 1998 through October 2001



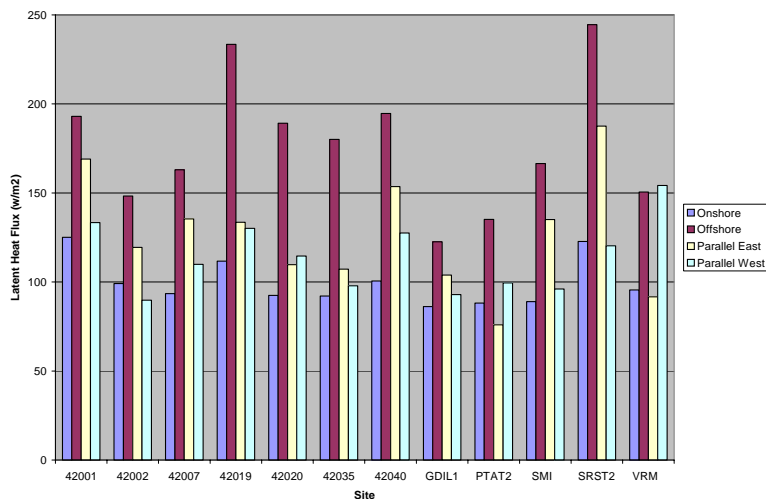
### COARE average sensible heat fluxes by flow direction (2 of 2)



COARE average sensible heat fluxes by general flow direction by BAMP site for September 2000 through September 2001



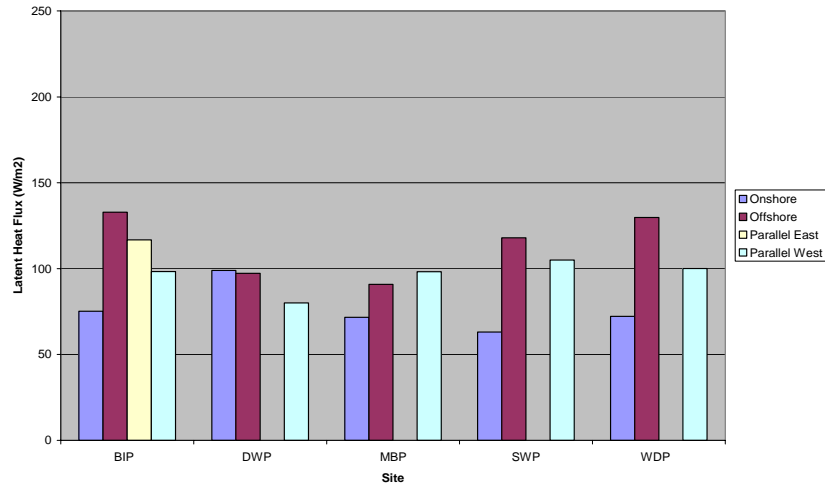
### COARE average latent heat fluxes by flow direction (1 of 2)



COARE average latent heat fluxes by general flow direction by site for May 1998 through October 2001



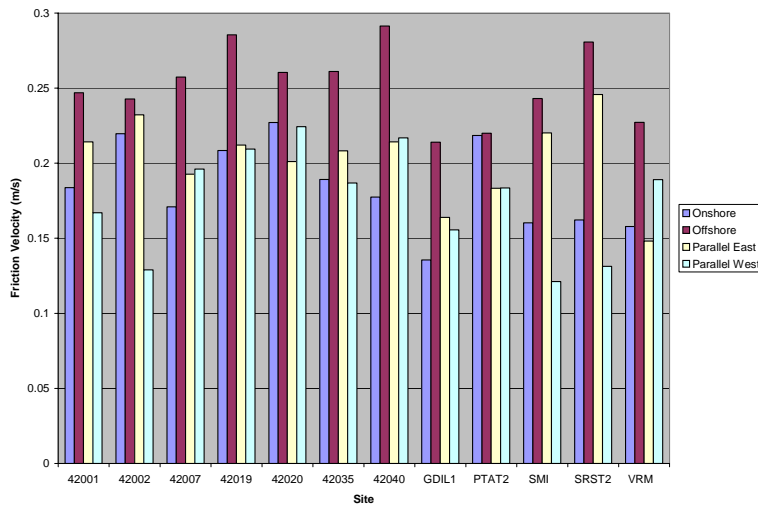
**COARE average latent heat fluxes by flow direction (2 of 2)**



COARE average latent heat fluxes by general flow direction by BAMP site for September 2000 through September 2001



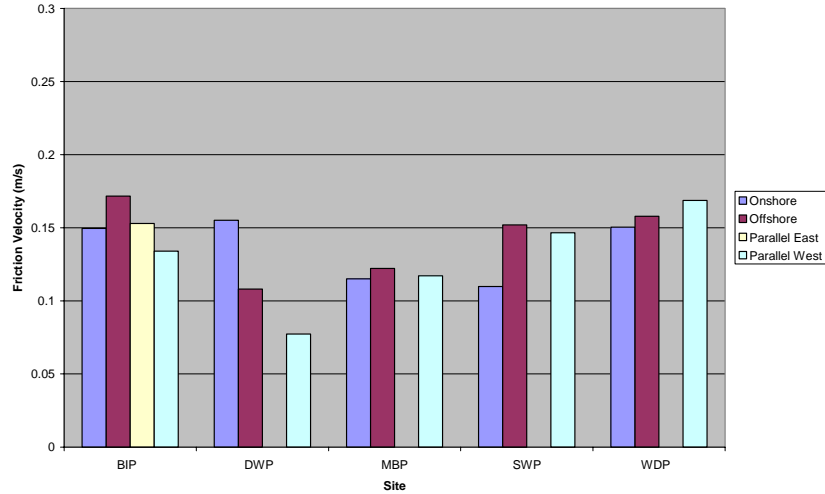
**COARE average friction velocity by flow direction (1 of 2)**



COARE average friction velocity by general flow direction by site for May 1998 through October 2001



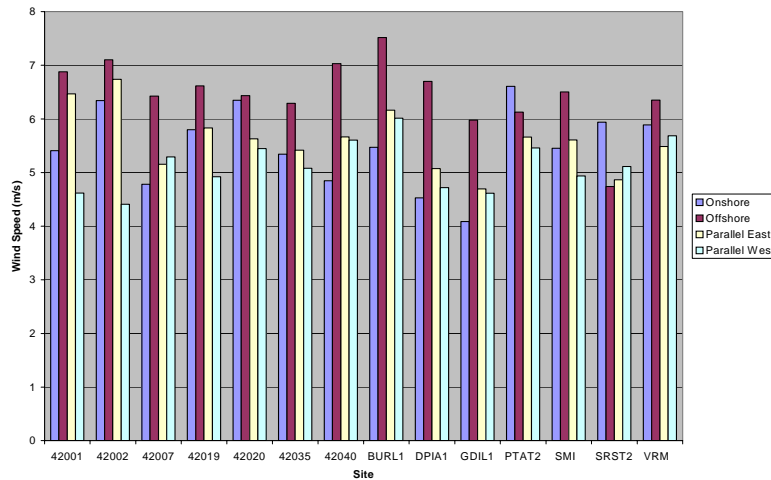
**COARE average friction velocity by flow direction (2 of 2)**



COARE average friction velocity by general flow direction by BAMP site for September 2000 through September 2001



**Observed average wind speed by flow direction**



Observed average wind speed by general flow direction by site for May 1998 through October 2001



### General Flow Summary – Sensible Heat Flux

- At the non-BAMP sites, sensible heat flux is maximized for northerly flow conditions, which are more likely to be marked by above-average wind speeds and relatively low air temperatures.
- At BAMP sites, sensible heat flux is maximized for northerly and westerly flow conditions.
- The difference in sensible heat flux between offshore and onshore flow directions across the nine synoptic classes is about a factor of 10.



### General Flow Summary – Latent Heat Flux

- The latent heat flux is largest during northerly flow conditions, which tend to be associated with “post-trough” synoptic conditions, higher wind speeds, and relatively low dew points.
- The latent heat is less variable for the BAMP sites compared to the non-BAMP sites.
- The minimum latent heat fluxes occur during onshore flow conditions, which tend to happen when boundary layer flows are in balance with the water surface and maximum dew points.



### **General Flow Summary – Friction Velocity and Wind Speed**

- High  $u^*$  values are associated with high-wind periods, which tend to occur during offshore flow.
- $U^*$  is less variable for the BAMP sites compared to the non-BAMP sites.



### **General Flow Summary – Temperature Scaling Parameter**

- The temperature scaling parameter tends to be maximized during periods when the air is cooler than the water, such as during northerly offshore wind flow patterns.
- It is smallest during onshore flow periods at the buoy sites when the air and water are likely to be at the same temperature.
- At the oil platform (VRM and SMI) and C-MAN sites, the temperature scaling parameter is smallest during either onshore or parallel west flow directions.
- At DWP and WDP the temperature scaling parameter is not smallest during parallel west flow direction.

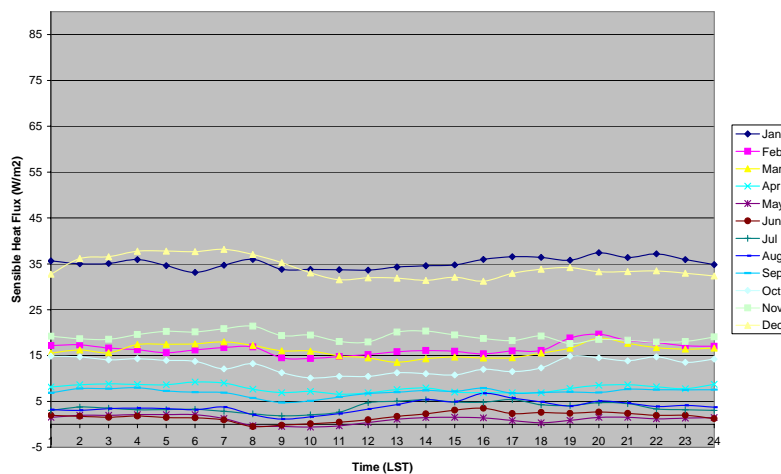


## Diurnal Statistics

- Buoy 42001 (a deep-water buoy), the VRM, SMI, BIP, and DWP platforms, buoy 42040 (a near-shore site), and C-MAN site GDIL were selected for analysis.
- Diurnal variations of latent and sensible heat flux, friction velocity, wind speed, and sea-to-air temperature difference were analyzed by month.
- Selected examples are shown in the following slides.



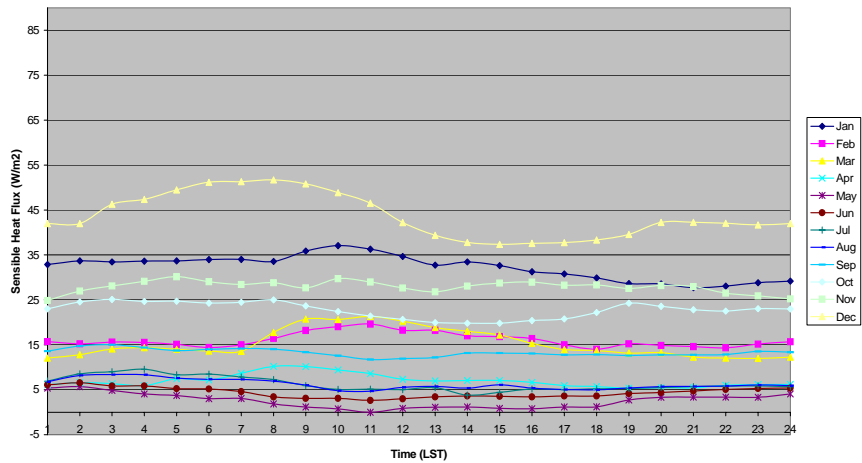
## Diurnal – COARE hourly average sensible heat fluxes



COARE hourly average sensible heat fluxes over 42001 for May 1998 through October 2001



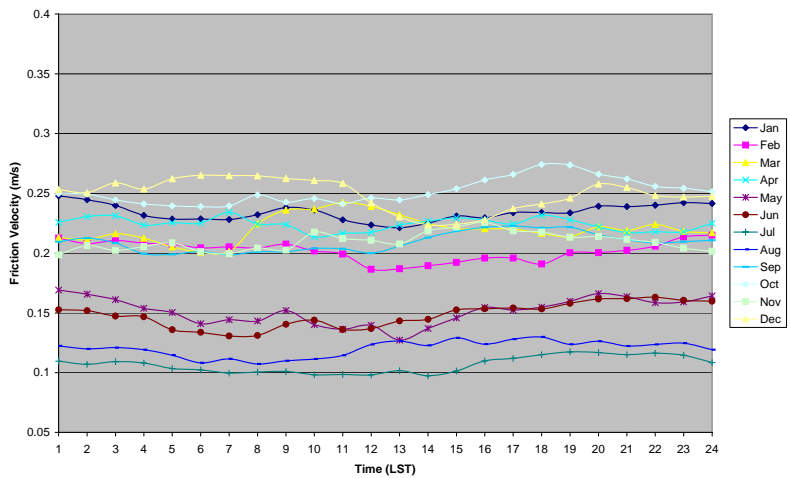
### Diurnal – COARE hourly average sensible heat fluxes



COARE hourly average sensible heat fluxes over SMI for May 1998 through October 2001



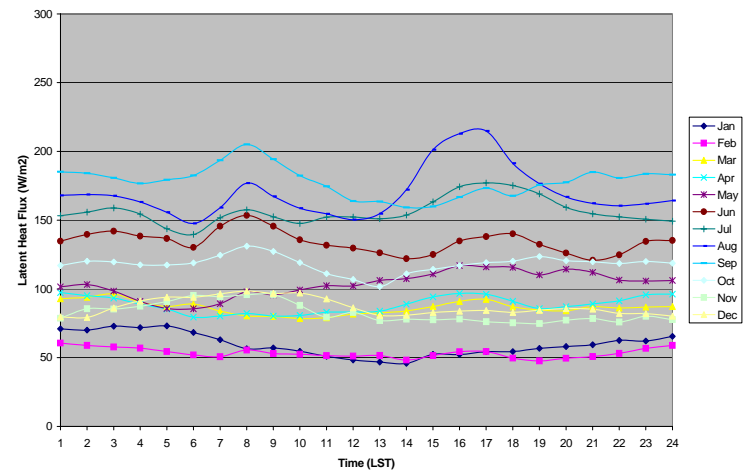
### Diurnal – COARE hourly average friction velocity



COARE hourly average friction velocity over SMI for May 1998 through October 2001



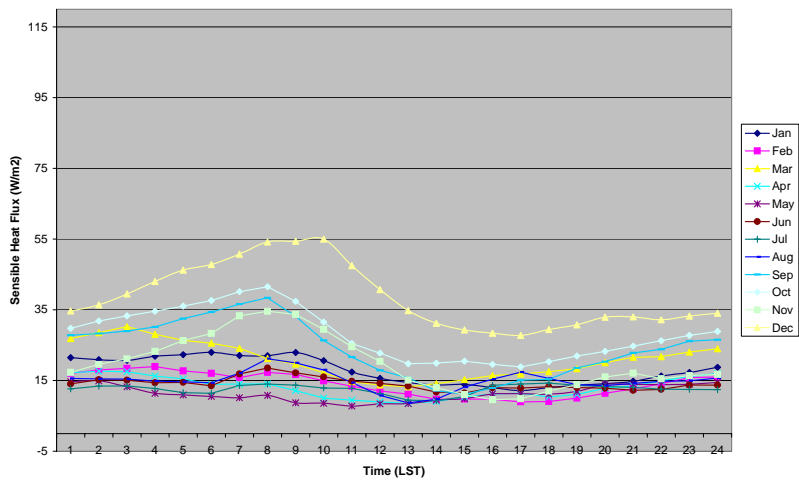
### Diurnal – COARE hourly average latent heat fluxes



COARE hourly average latent heat fluxes over VRM for May 1998 through October 2001



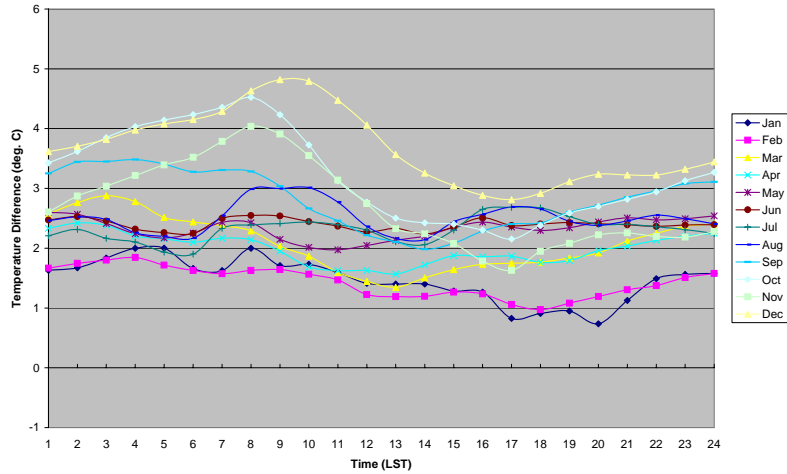
### Diurnal – COARE hourly average sensible heat fluxes



COARE hourly average sensible heat fluxes over VRM for May 1998 through October 2001



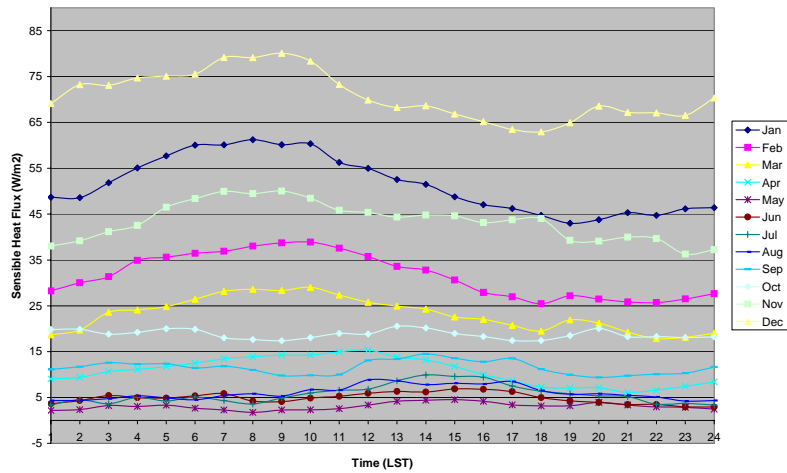
### Diurnal – Hourly average skin temperature minus air temperature



Hourly average skin temperature minus air temperature over VRM for May 1998 through October 2001



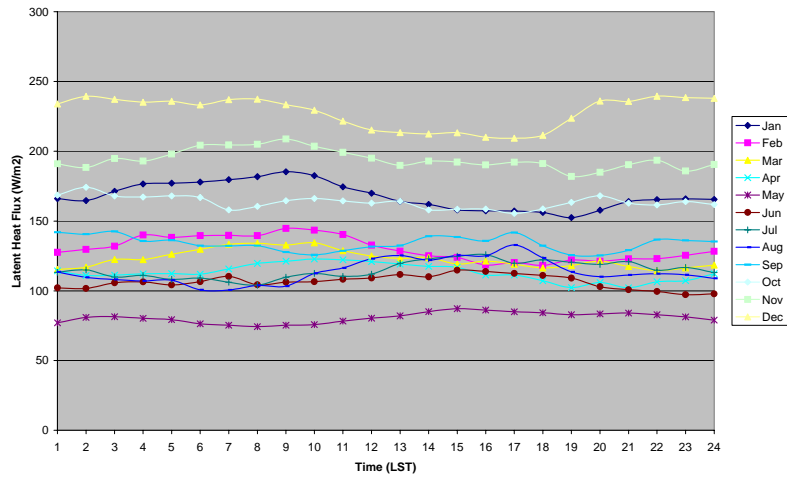
### Diurnal – COARE hourly average sensible heat fluxes



COARE hourly average sensible heat fluxes over buoy 42040 for May 1998 through October 2001



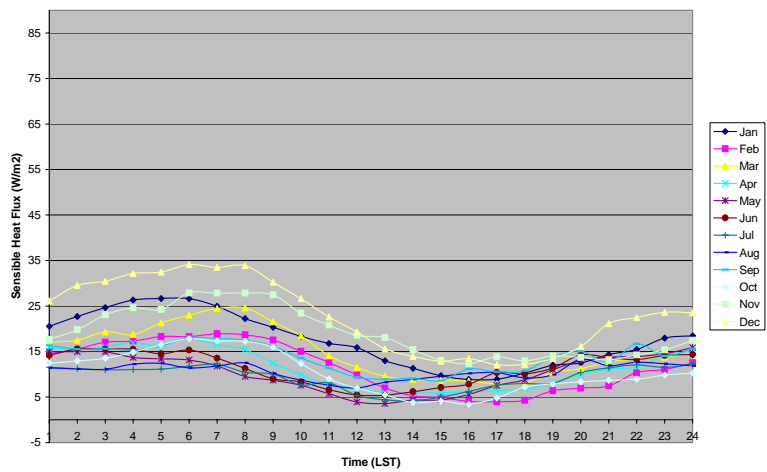
### Diurnal – COARE hourly average latent heat fluxes



COARE hourly average latent heat fluxes over buoy 42040 for May 1998 through October 2001



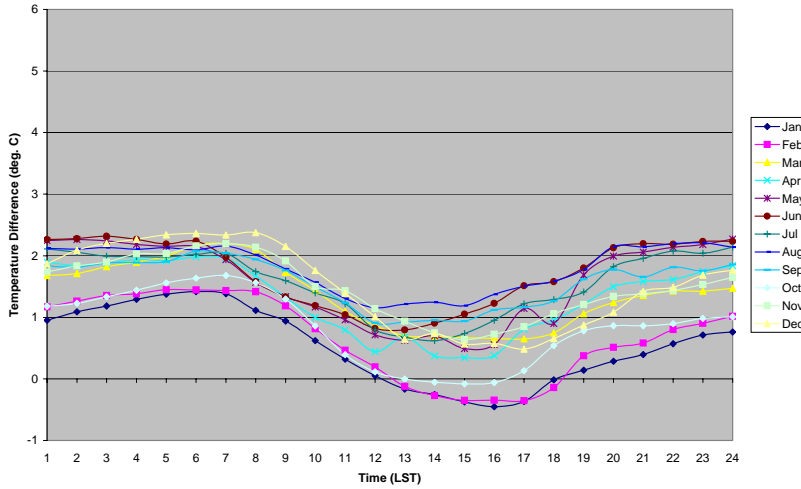
### Diurnal – COARE hourly average sensible heat fluxes



COARE hourly average sensible heat fluxes over GDIL1 for May 1998 through October 2001



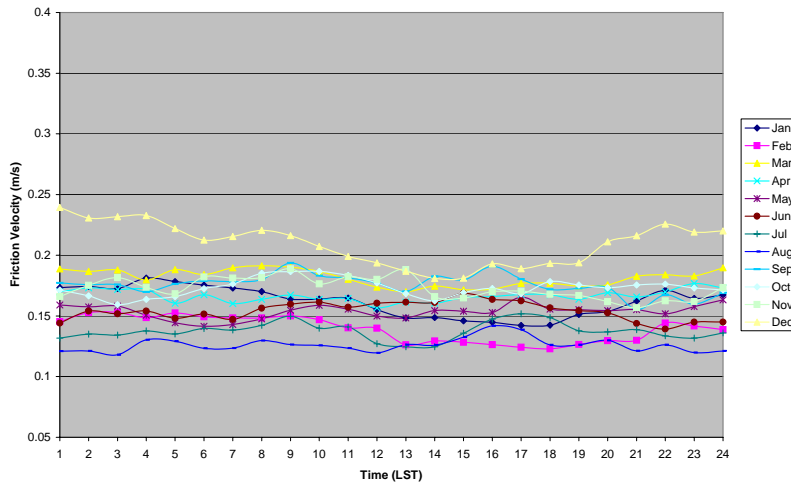
### Diurnal – Hourly skin temperature minus air temperature



Hourly skin temperature minus air temperature over GDIL1 for May 1998 through October 2001



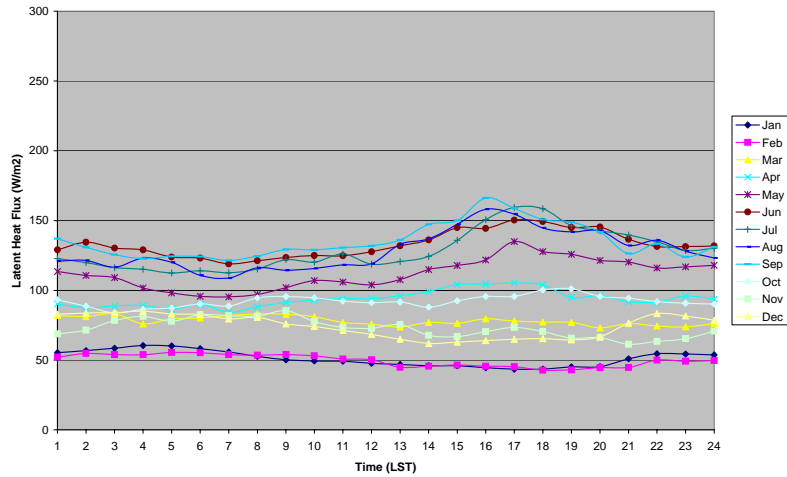
### Diurnal – COARE hourly friction velocity



COARE hourly friction velocity over GDIL1 for May 1998 through October 2001



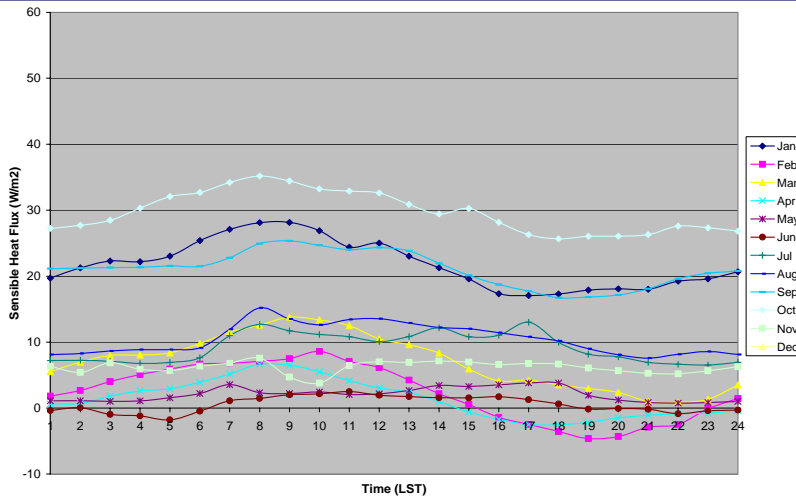
### Diurnal – COARE hourly average latent heat fluxes



COARE hourly average latent heat fluxes over GDIL1 for May 1998 through October 2001



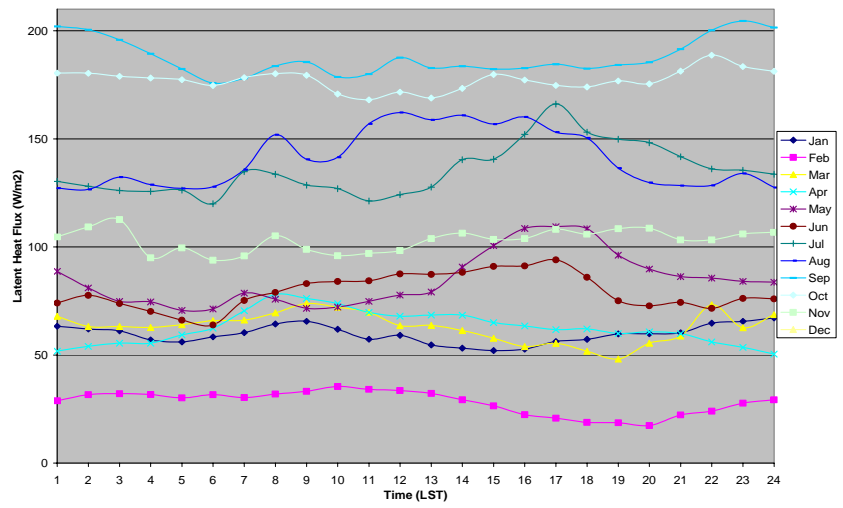
### Diurnal – COARE hourly average sensible heat fluxes



COARE hourly average sensible heat fluxes over BIP for September 2000 through September 2001



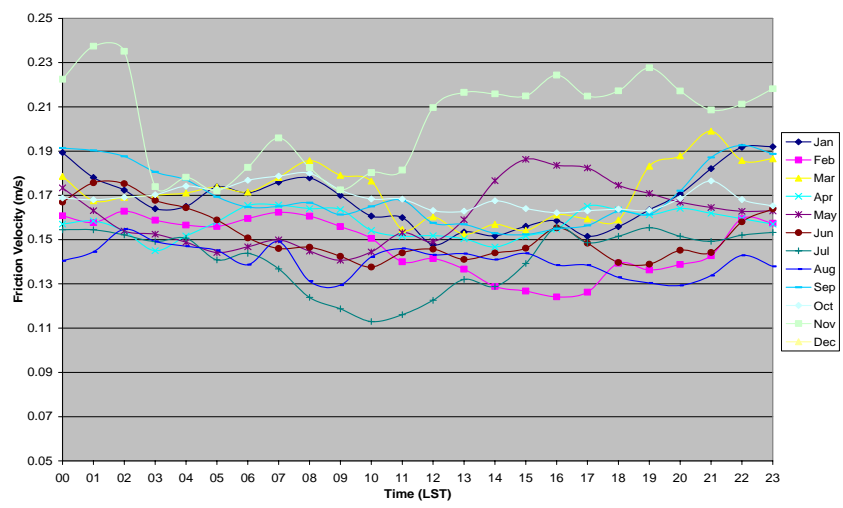
### Diurnal – COARE hourly average latent heat fluxes



COARE hourly average latent heat fluxes over BIP for September 2000 through September 2001



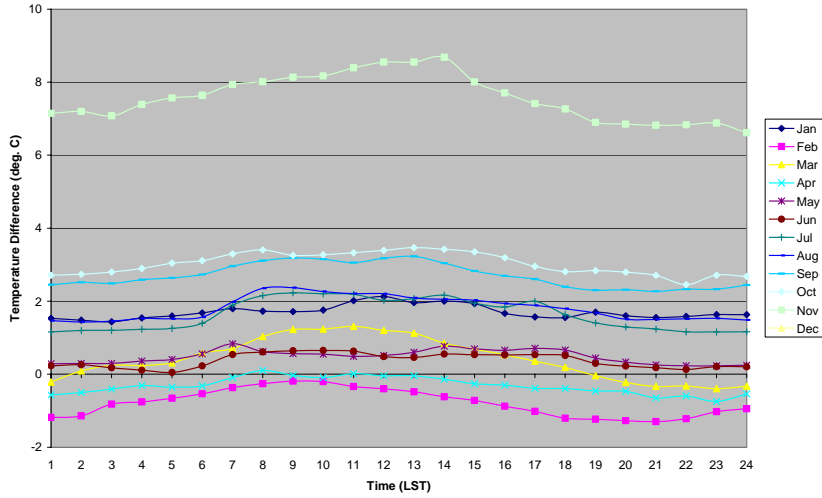
### Diurnal – COARE hourly average friction velocity



COARE hourly average friction velocity over BIP for September 2000 through September 2001



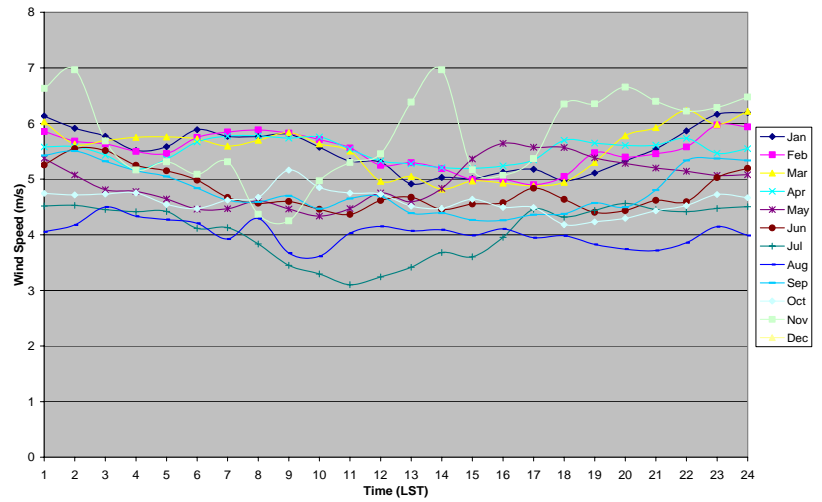
### Diurnal – Hourly skin temperature minus air temperature



Hourly skin temperature minus air temperature over BIP  
for September 2000 through September 2001



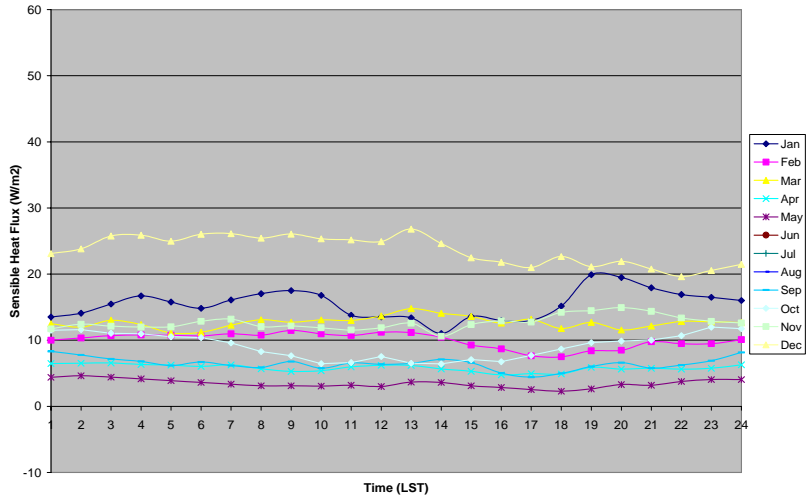
### Diurnal – Observed hourly average wind speed



Observed hourly average wind speed over BIP  
for September 2000 through September 2001



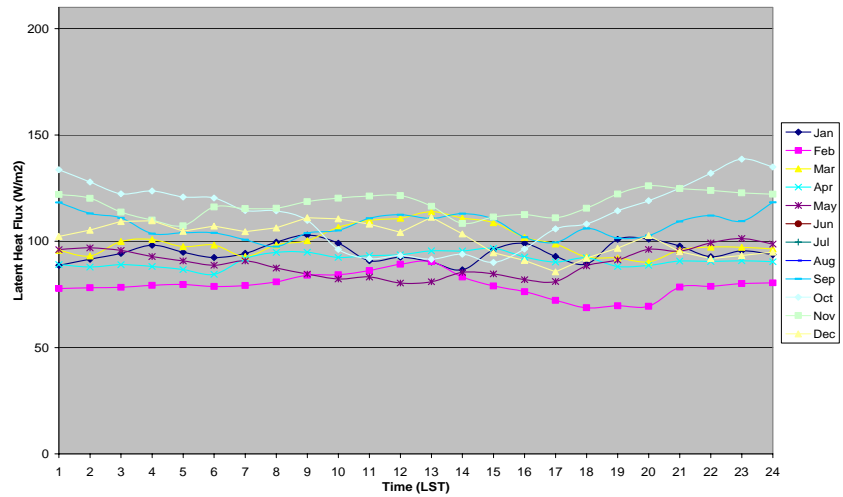
### Diurnal – COARE hourly average sensible heat fluxes



COARE hourly average sensible heat fluxes over DWP for September 2000 through September 2001



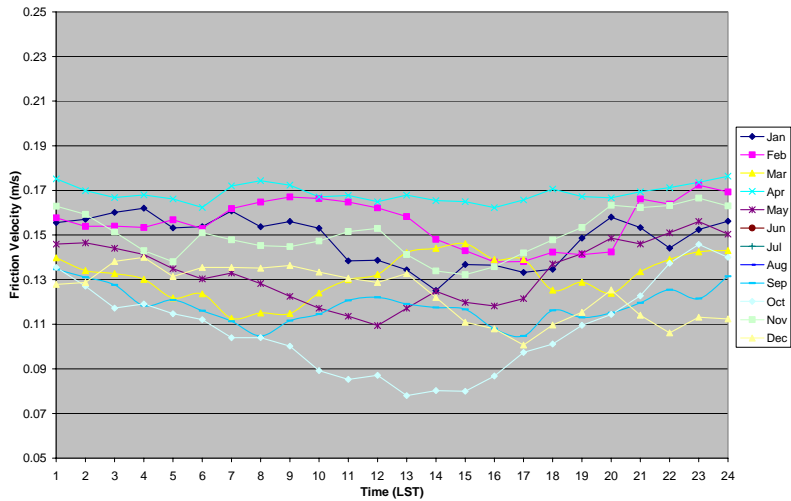
### Diurnal – COARE hourly average latent heat fluxes



COARE hourly average latent heat fluxes over DWP for September 2000 through September 2001



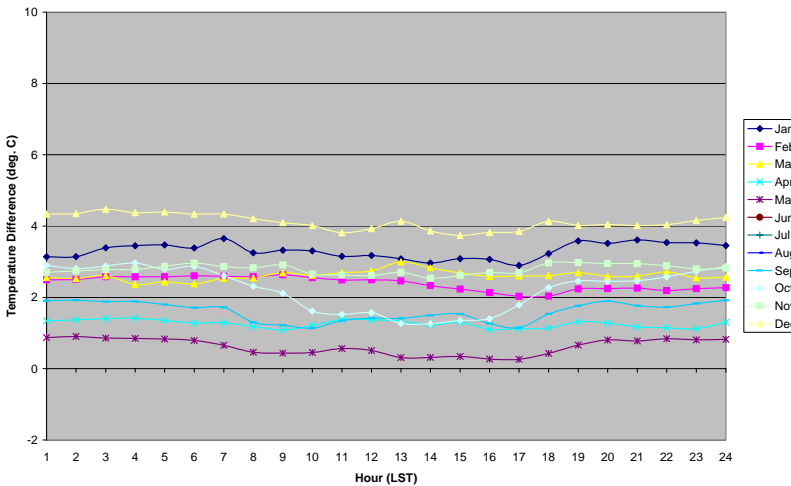
### Diurnal – COARE hourly average friction velocity



COARE hourly average friction velocity over DWP for September 2000 through September 2001



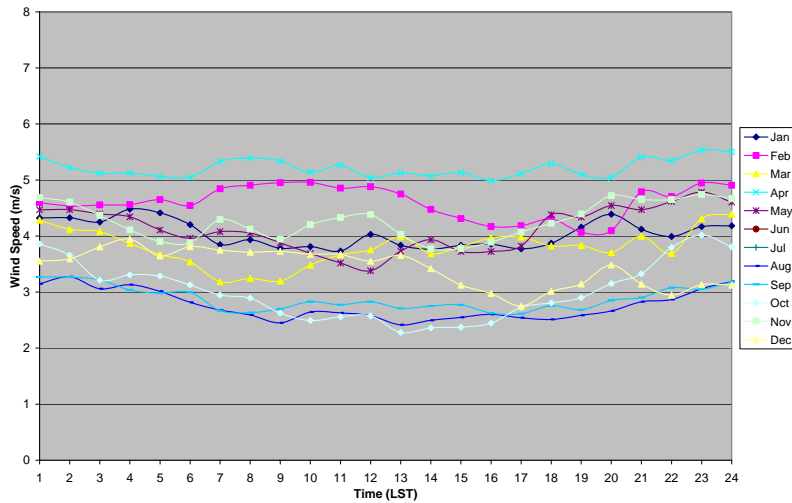
### Diurnal – Hourly skin temperature minus air temperature



Hourly skin temperature minus air temperature over DWP for September 2000 through September 2001



### Diurnal – Observed hourly average wind speed



Observed hourly average wind speed over DWP for September 2000 through September 2001



### Diurnal Summary – Buoy 42001

The latent and sensible heat fluxes, friction velocity, and skin temperature-minus-air temperature difference show almost no diurnal variation, which makes physical sense at an over-water site



## Diurnal Summary – SMI

- The latent and sensible heat fluxes show very little diurnal variation but slightly more than buoy 42001.
- In December, the greatest diurnal variation in sensible heat flux, about 20%, is observed. The variation is associated with a smaller friction velocity in the afternoon and not due to variations in the vertical temperature gradients.
- In May, sensible heat fluxes are near zero during most of the daylight hours and are associated with vertical temperature gradients near zero.



## Diurnal Summary – VRM

- From June through September, latent heat fluxes peak in both the morning and afternoon.
- During other months, latent heat fluxes show very little diurnal variation.
- In the winter months, sensible heat fluxes have strong diurnal cycles, peaking at sunrise. The morning peaks in the sensible heat flux are due to peaks in the skin temperature-minus-air temperature difference.
- Sensible heat flux in December is much higher than in other months. The high sensible heat flux in December is a result of a higher-than-average skin temperature-minus-air temperature difference and higher-than-average friction velocity.



## Diurnal Summary – Buoy 42040

- The sensible heat flux is similar to that at SMI.
- There is a maximum diurnal variation of about 20% in December and January.
- The maximum sensible heat flux occurs in December due to a combination of higher-than-average friction velocity and skin temperature-minus-air temperature difference.
- The latent heat flux shows little diurnal variation and is also greatest in December.



## Diurnal Summary – C-MAN GDIL1

- The sensible heat flux indicates that GDIL1 is not strongly influenced by land since sensible heat flux is lowest in mid-afternoon.
- Sensible heat flux is never negative at night.
- However, the sensible heat flux curve shows a diurnal cycle.
- The diurnal cycle closely follows the diurnal cycle in skin temperature-minus-air temperature difference and not frictional velocity.
- The latent heat flux is somewhat flat but peaks in the afternoon during the summer months



## Diurnal Summary – BIP

- Sensible heat flux has minimal diurnal variation and is largest (about 20 to 30  $\text{w/m}^2$ ) in late fall and early winter, when the water temperature is warm relative to the air temperature.
- During the other months, the sensible heat flux is small (less than 10  $\text{w/m}^2$ ).
- Latent heat flux also has minimal diurnal variation and is largest (about 150 to 200  $\text{w/m}^2$ ) in July – October, when the water temperature is the greatest.
- In February, when water temperatures are cool, the latent heat flux drops to about 30  $\text{w/m}^2$ .



## Diurnal Summary – BIP

- The COARE-calculated friction velocity shows minimal diurnal variation and varies by as much as a factor of 2 from month to month. However, the month-to-month variation appears random and no physical causes can be identified.
- The difference between skin (water surface) and air temperature shows about a 1° or 2°C diurnal variation.
- As mentioned for other sites, the temperature difference is larger (2°C or greater) in the fall and is smaller (between -1° and +1°C in the late winter).
- The wind speeds show little diurnal variation and are about 30% less in July–September when they are about 4 m/s versus 5 m/s for most of the other months.



## Diurnal Summary – DWP

- The DWP wind speeds show little diurnal variation and are about 30% less in July–October (behavior similar to BIP wind speeds) when they are about 3 m/s versus 4 to 5 m/s for most of the other months.
- Sensible heat flux has very little diurnal variation and is largest (about 15 to 25 w/m<sup>2</sup>) in late fall and early winter when the water temperature is warm relative to the air temperature (behavior similar to that found in BIP data).
- During the other months, the sensible heat flux is small (less than 10 w/m<sup>2</sup>, with the minimal average of about 4 w/m<sup>2</sup> in May).



## Diurnal Summary – DWP

- The latent heat flux has insignificant diurnal variation and is largest (about 120 w/m<sup>2</sup>) in the fall when the water temperature is the greatest.
- In February, when water temperatures are cool, the latent heat flux drops to about 70 w/m<sup>2</sup>.
- The COARE-calculated friction velocity shows some diurnal variations but the variations are not consistent from month to month. The average friction velocity varies by as much as a factor of 2 from month to month. However, the month-to-month variation appears random and no physical causes can be identified.



## Diurnal Summary – DWP

- The difference between skin (water surface) and air temperature shows about a 1° or 2°C diurnal variation.
- As mentioned for other sites, the temperature difference is larger (4°C or greater) in the late fall and is smaller (between –1° and 1°C in the spring (e.g., negative or stable temperature differences occur in May in the afternoon). A negative temperature difference will lead to a negative sensible heat flux.



## Case Studies

- Four periods
- Buoy 42040, VRM, and SMI
- Large-scale meteorology
- Surface meteorological observations
- Profiler and RASS data
- COARE output
- Comparisons to Eta
- Mixing height



## Abbreviations

- Sensible Heat -  $H_s$
- Latent Heat -  $H_e$
- Friction Velocity -  $u^*$
- Temperature Scaling Parameter -  $T^*$
- Humidity Scaling Parameter -  $q^*$
- Wind Speed -  $u$
- Air Temperature -  $T$
- Virtual Temperature -  $T_v$
- Skin Temperature -  $T_s$
- Relative Humidity - RH
- Monin-Obukhov Length –  $z/L$
- Surface Roughness -  $Z_o$

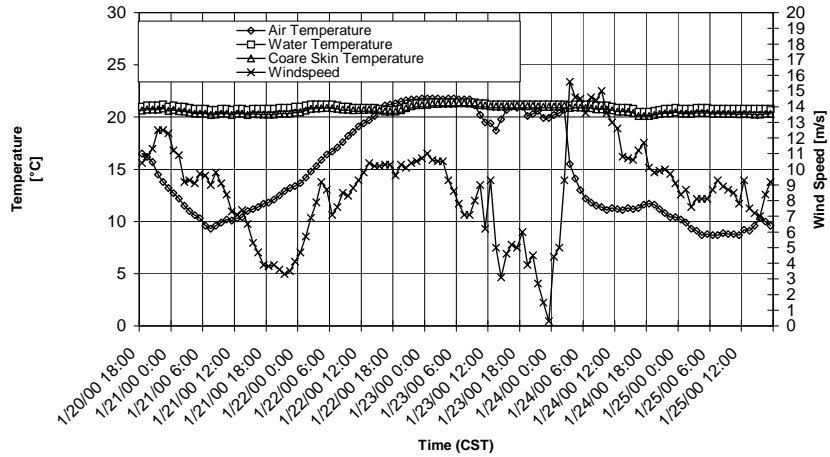


## Case Studies – General Meteorology

- July 30 through August 1, 1999
  - Strong upper-level ridge, surface high pressure, and light winds
- January 20 through 25, 2000
  - Post frontal offshore flow on January 20 and 21
  - Onshore flow on January 22 and 23
  - Strong offshore flow on January 24 and 25 behind another cold front
- January 4 through 6, 2001
  - Post upper-level trough (January 4 and 5) fading into weak ridge
  - Air temperature much warmer than skin temperature
- September 18 through 20, 2001
  - Weak onshore flow
  - A weak cold front orientated west to east along the Gulf Coast from Houston to Mobile on September 20



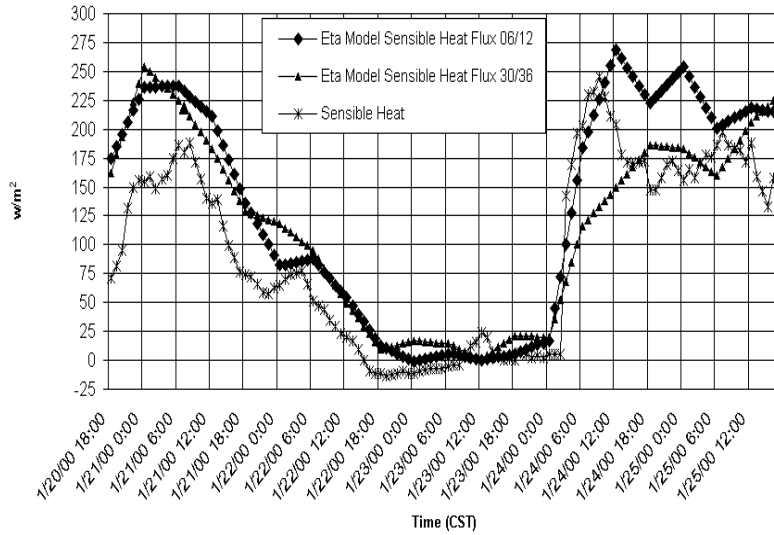
**Buoy 42040**  
**Air and Water Temperatures and Wind Speed**



Air and water temperatures and wind speed at buoy 42040, January 20 through 25, 2000

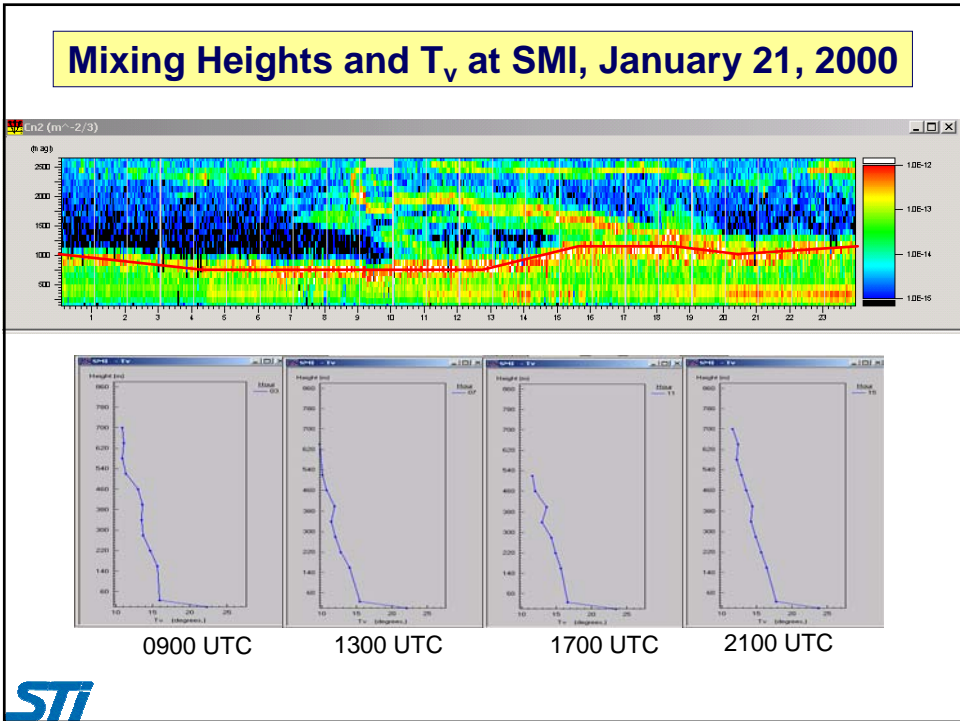
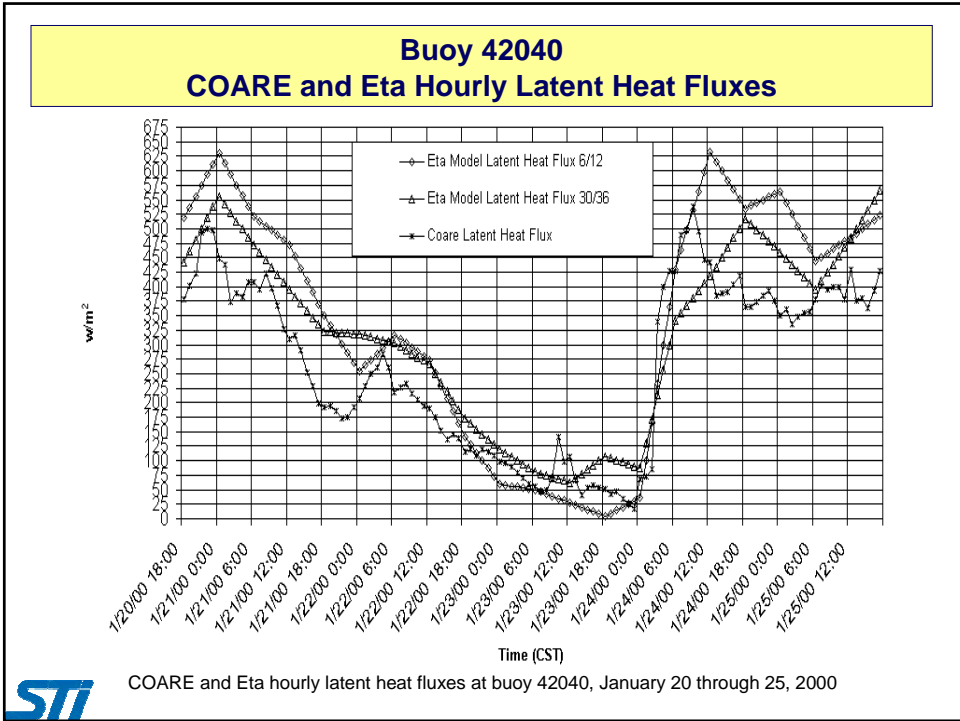


**Buoy 42040**  
**COARE and Eta Hourly Sensible Heat Fluxes**

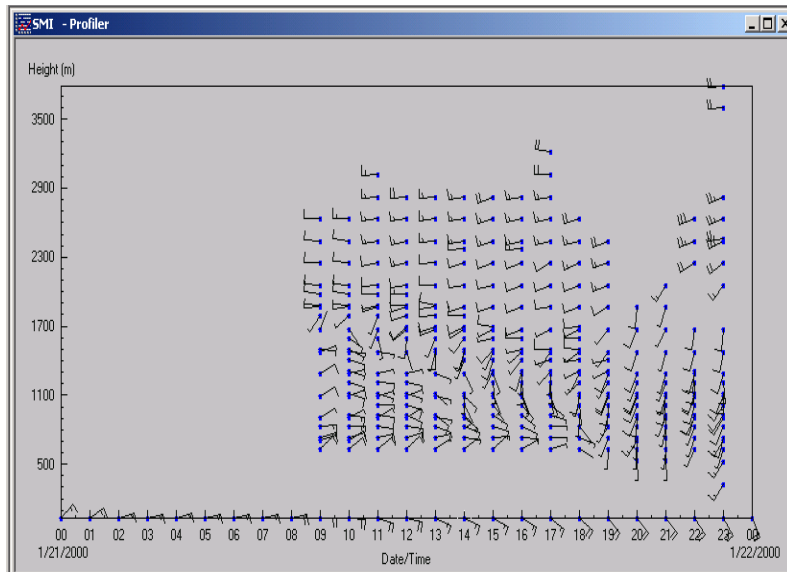


COARE and Eta hourly sensible heat fluxes at buoy 42040, January 20 through 25, 2000





## Winds at SMI, January 21, 2000



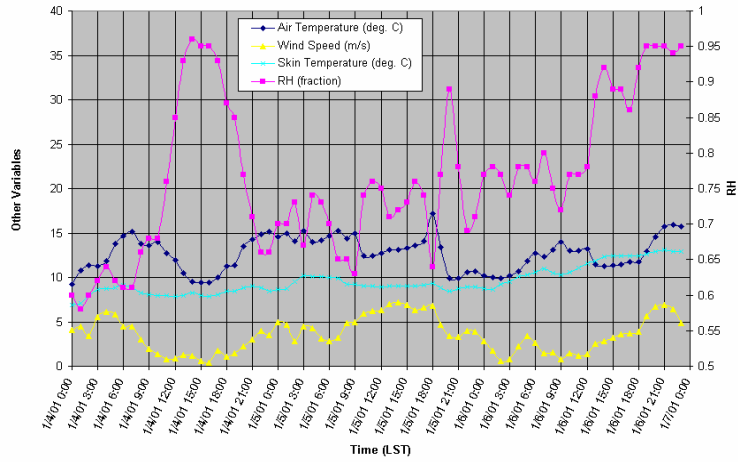
STI

## January 21, 2000, Summary

- The mixing heights were estimated to be about 750 m from midnight through 0400 to 1300 UTC. An increase was observed from 1300 to 1600 UTC, at which time the mixing heights peaked at about 1150 m. The mixing heights were estimated to have remained at about 1100 m through 2400 UTC.
- The virtual temperature ( $T_v$ ) data during this period of time showed a weak inversion at about 150 m. The lowest 30 m show a superadiabatic layer because the air temperature was much cooler than the skin temperature on this day.
- Winds within the lowest 1400 m switched from moderate easterly to light-to-moderate southwesterly at about 1800 CST.

STI

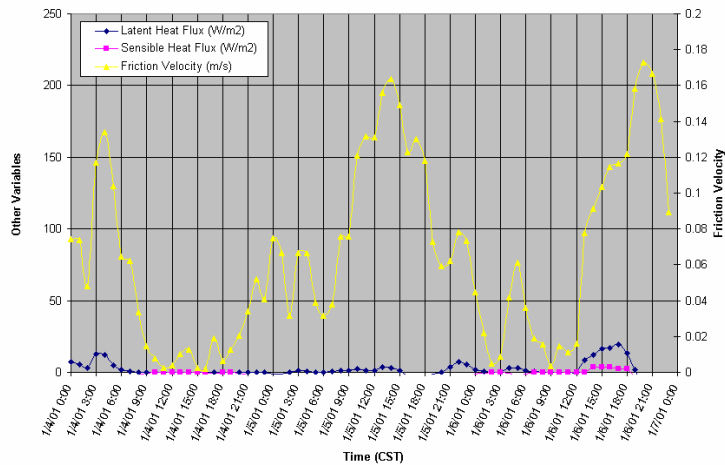
## VRM Hourly Air and Skin Temperatures, Wind Speed, and Relative Humidity



Hourly air and skin temperatures, wind speed and relative humidity at VRM, January 4 through 6, 2001



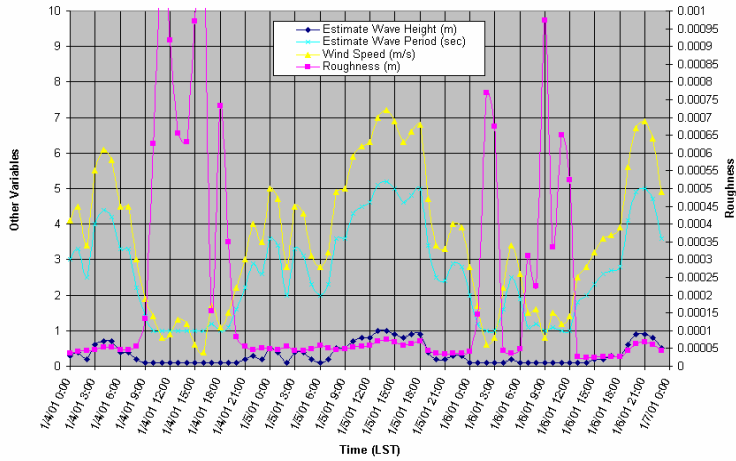
## VRM COARE Hourly Average Latent and Sensible Heat Fluxes and Friction Velocity



COARE hourly average latent and sensible heat fluxes and friction velocity at VRM, January 4 through 6, 2001



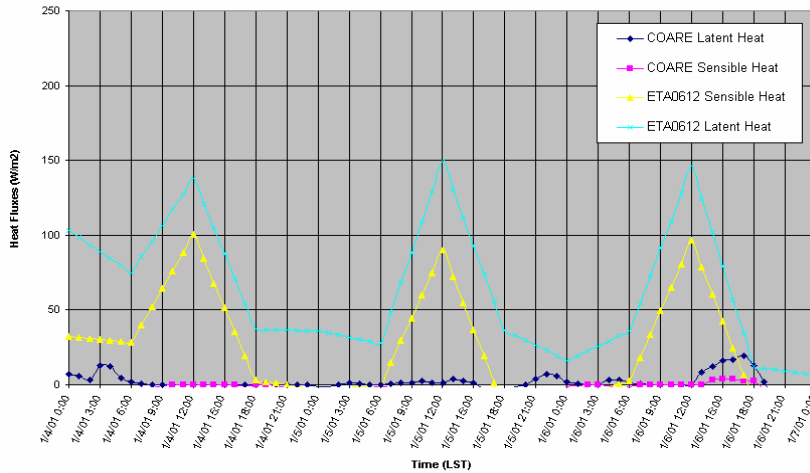
## VRM Estimated Wave Height and Period, Wind Speed, and Surface Roughness Length



Estimated wave height and period, wind speed, and surface roughness length at VRM, January 4 through 6, 2001



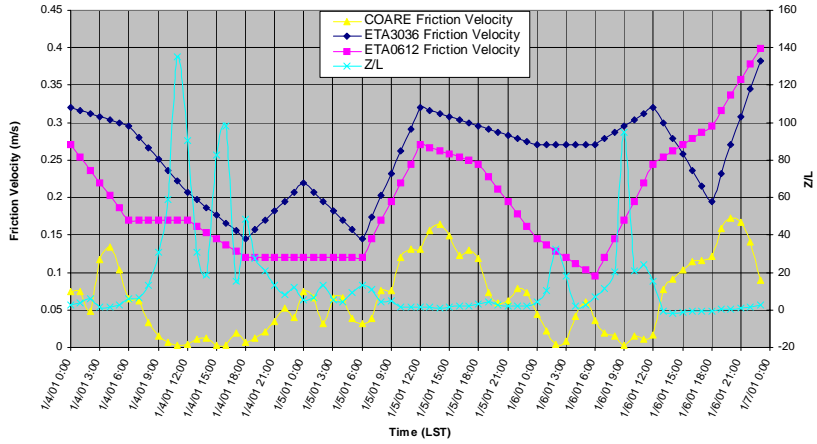
## VRM COARE and Eta Latent and Sensible Heat Fluxes



COARE and Eta latent and sensible heat fluxes at VRM, January 4 through 6, 2001  
Note: the four-digit number after Eta in the key indicates the forecast period (i.e., 0612 is the 6- to 12-hr forecast).



## VRM COARE and Eta Friction Velocity and z/L



COARE and Eta friction velocity and z/L at VRM, January 4 through January 6, 2001  
 Note: the four-digit number after Eta in the key indicates the forecast period (i.e., 0612 is the 6- to 12-hr forecast and 3036 is the 30- to 36-hr forecast).

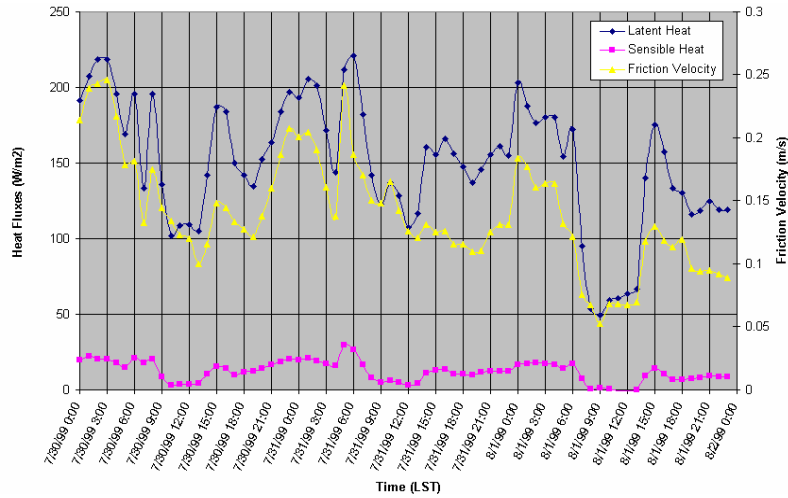


## January 4, 2001, Summary

No data available



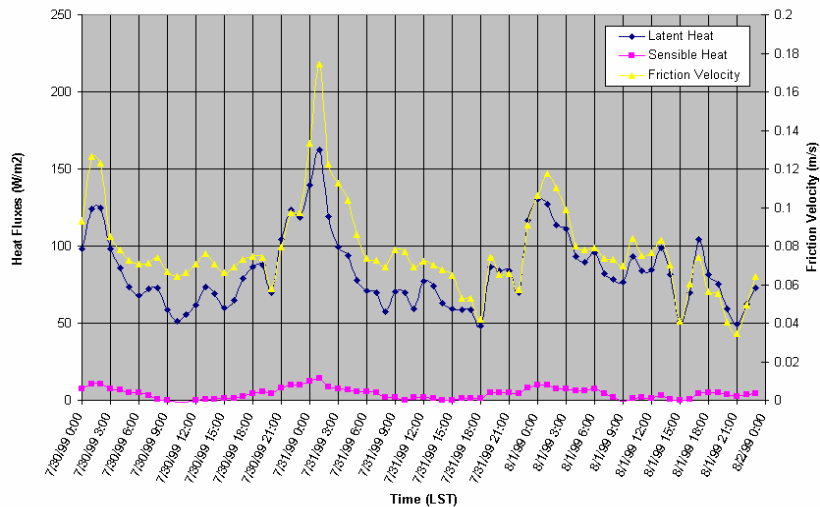
### VRM COARE Latent and Sensible Heat Fluxes and Friction Velocity



COARE latent and sensible heat fluxes and friction velocity at VRM, July 30 through August 1, 1999



### SMI COARE Latent and Sensible Heat and Friction Velocity

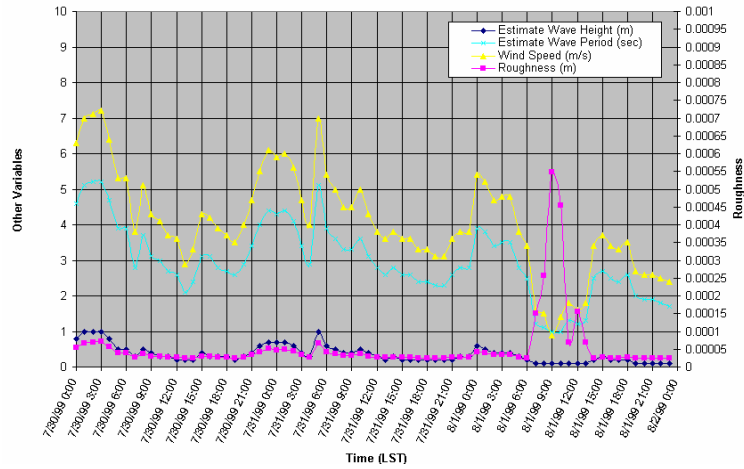


COARE latent and sensible heat fluxes and friction velocity at SMI, July 30 through August 1, 1999



## VRM

### Estimated Wave Height and Period, Wind Speed, and Surface Roughness Length

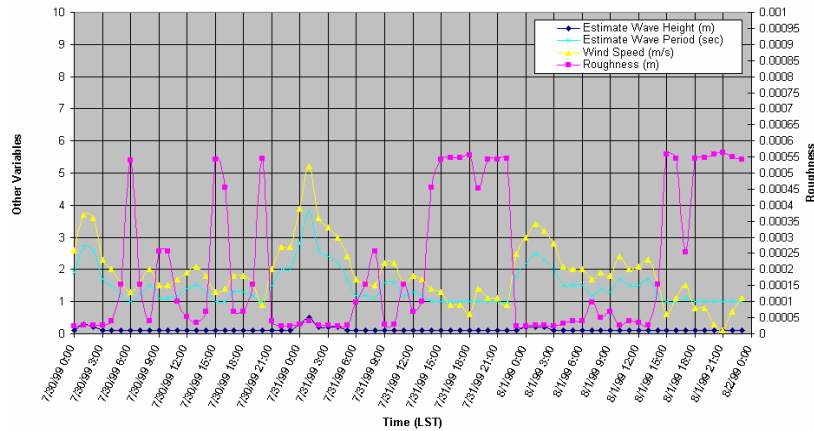


Estimated wave height and period, wind speed, and surface roughness length at VRM, July 30 through August 1, 1999



## SMI

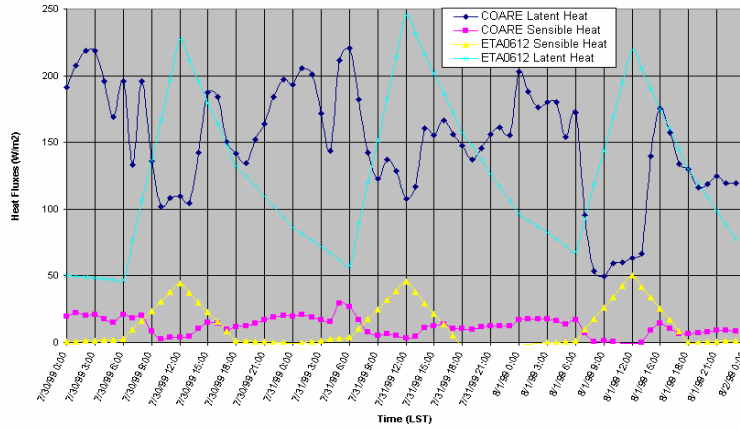
### Estimated Wave Height and Period, Wind Speed, and Surface Roughness Length



Estimated wave height and period, wind speed, and surface roughness length at SMI, July 30 through August 1, 1999



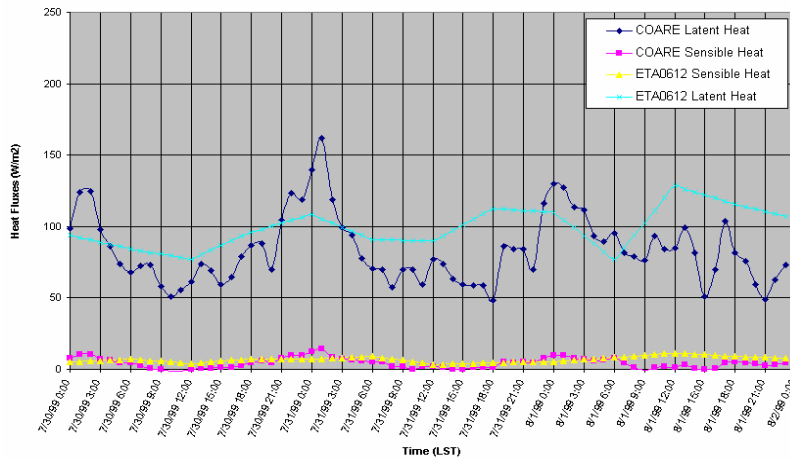
## VRM COARE and Eta Latent and Sensible Heat Fluxes



COARE and Eta latent and sensible heat fluxes at VRM, July 30 through August 1, 1999  
 Note: the four-digit number after Eta in the key indicates the forecast period (i.e., 0612 is the 6- to 12-hr forecast).



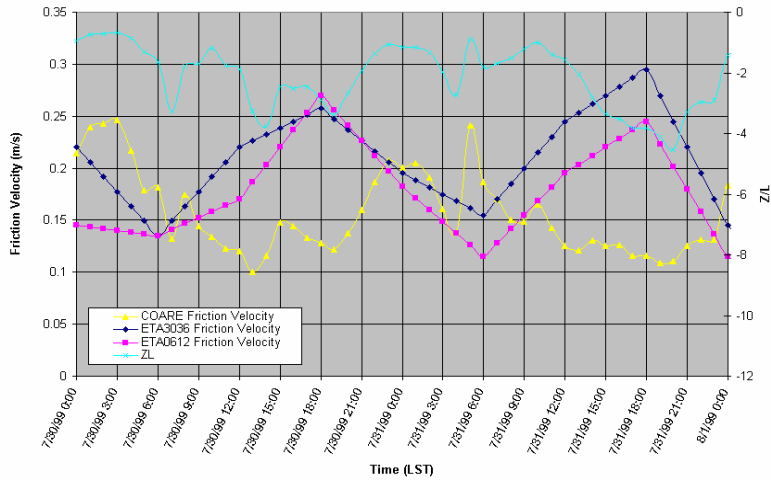
## SMI COARE and Eta Latent and Sensible Heat Fluxes



COARE and Eta latent and sensible heat fluxes at SMI, July 30 through August 1, 1999  
 Note: the four-digit number after Eta in the key indicates the forecast period (i.e., 0612 is the 6- to 12-hr forecast).



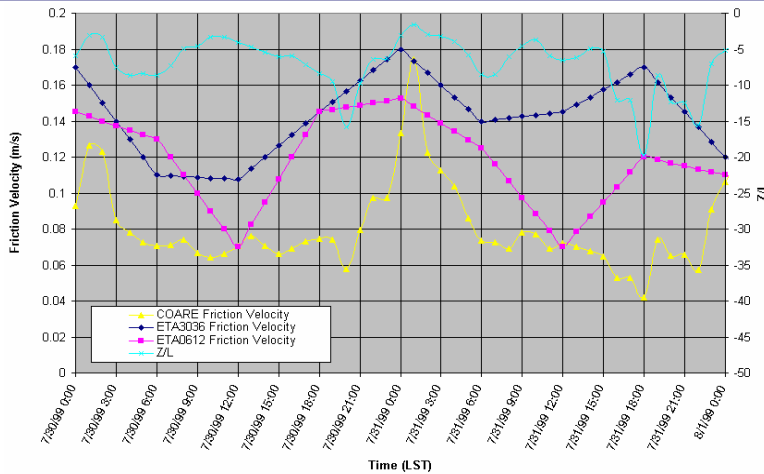
### VRM COARE and Eta Friction Velocity and z/L



COARE and Eta friction velocity and z/L at VRM, July 30 through August 1, 1999  
 Note: the four-digit number after Eta in the key indicates the forecast period (i.e., 0612 is the 6- to 12-hr forecast and 3036 is the 30- to 36-hr forecast).



### SMI COARE and Eta Friction Velocity and z/L

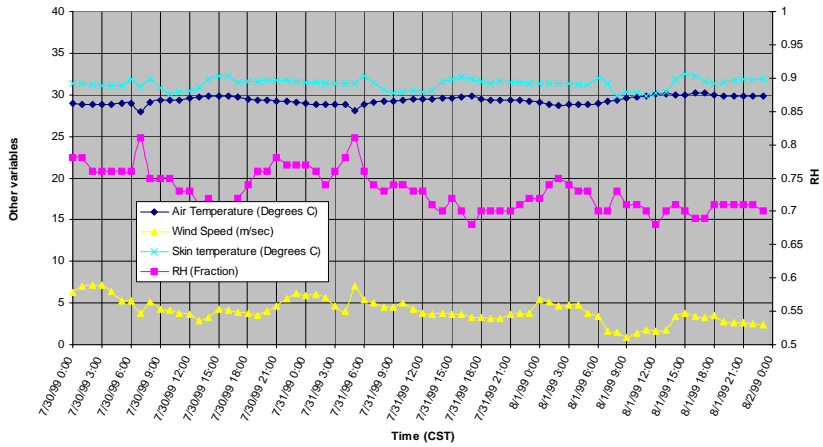


COARE and Eta friction velocity and z/L at SMI, July 30 through August 1, 1999  
 Note: the four-digit number after Eta in the key indicates the forecast period (i.e., 0612 is the 6- to 12-hr forecast and 3036 is the 30- to 36-hr forecast).



## VRM

### Hourly Air and Skin Temperatures, Wind Speed, and Relative Humidity

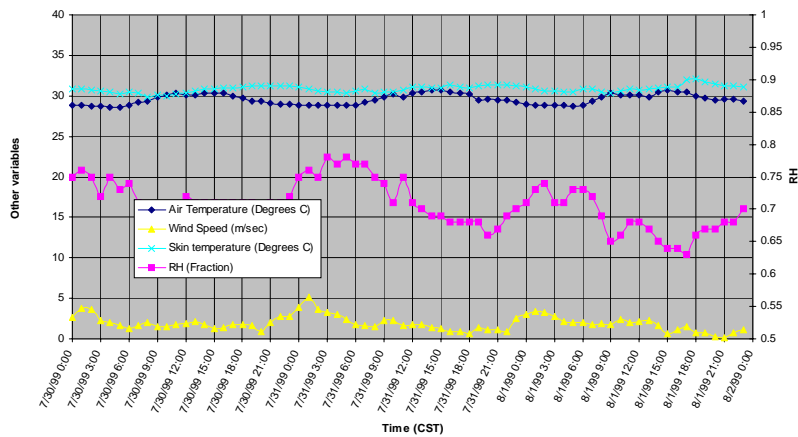


Hourly air and skin temperatures, wind speed, and relative humidity at VRM, July 30 through August 1, 1999



## SMI

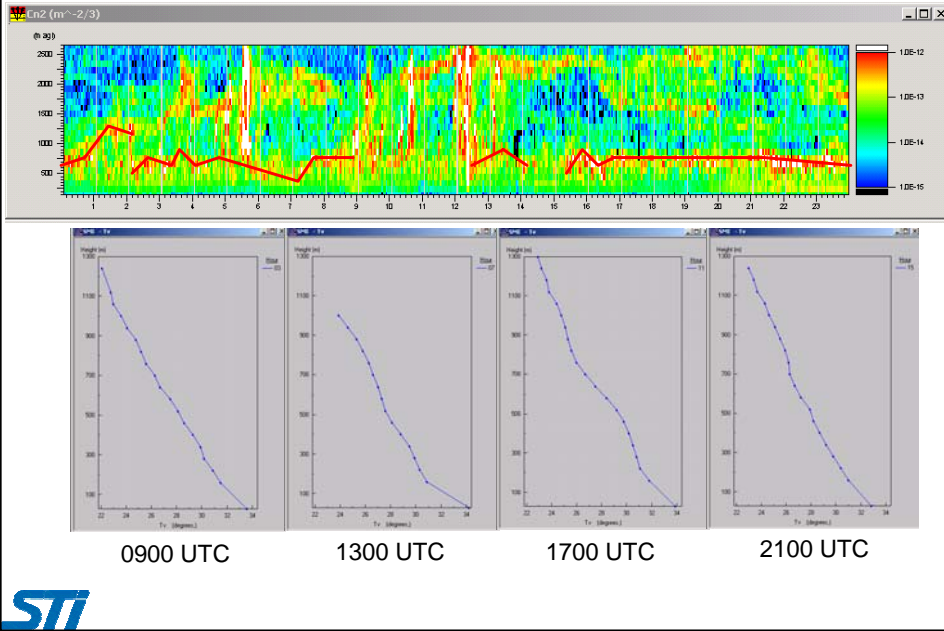
### Hourly Air and Skin Temperatures, Wind Speed, and Relative Humidity



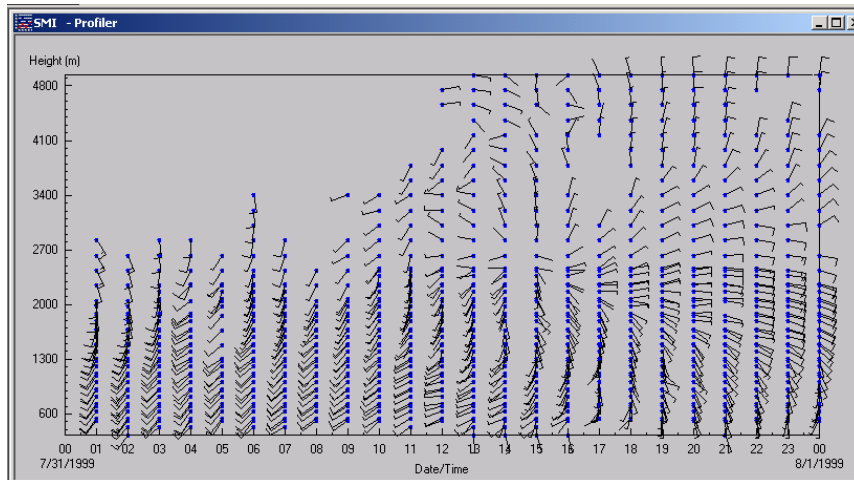
Hourly air and skin temperatures, wind speed, and relative humidity at SMI, July 30 through August 1, 1999



## SMI, July 31, 1999



## Winds at SMI, July 31, 1999

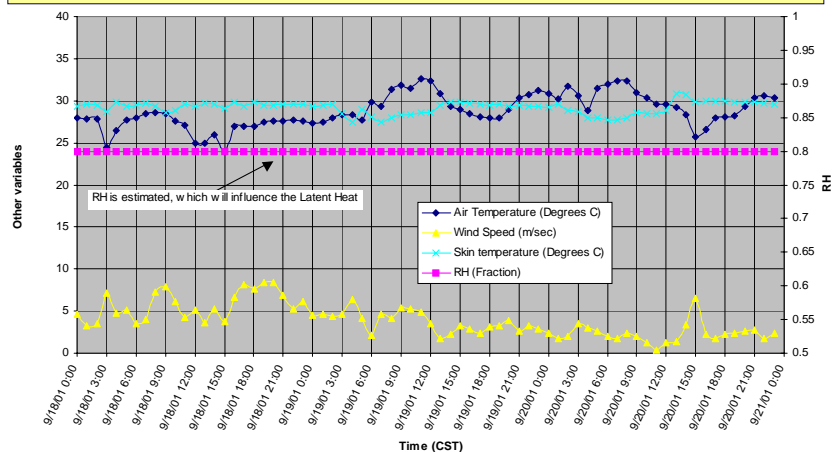


## July 31, 1999, Summary

- In general, mixing heights were about 750 to 850 m. Mixing heights remained fairly constant with relatively little variation.
- The  $T_v$  data revealed stable profiles throughout the day, with the exception of a shallow layer at 1300 UTC below about 150 m.
- Winds within the lowest 1000 m at SMI were primarily moderate southwesterly; however, a wind shift to light southerly began around 2200 UTC. The depth through which the southwesterly winds were observed was greater than the previous day, extending to above 2000 m.



### VRM Hourly Air and Skin Temperatures, Wind Speed, and Relative Humidity

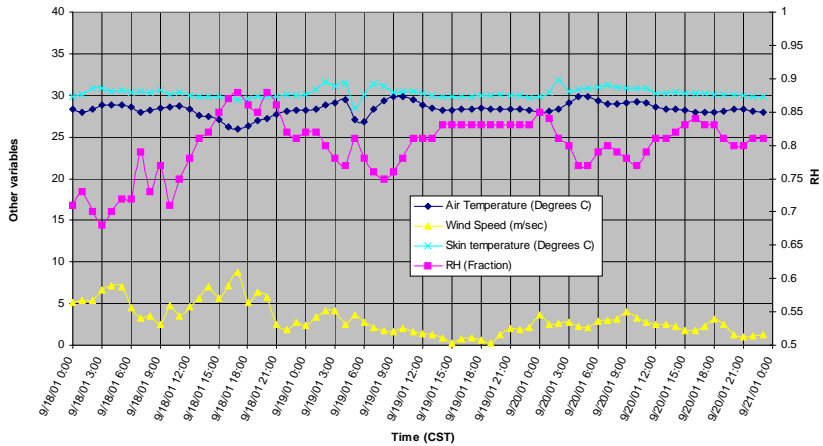


Hourly air and skin temperatures, wind speed, and relative humidity at VRM, September 18 through 20, 2001



### SMI

#### Hourly Air and Skin Temperatures, Wind Speed, and Relative Humidity

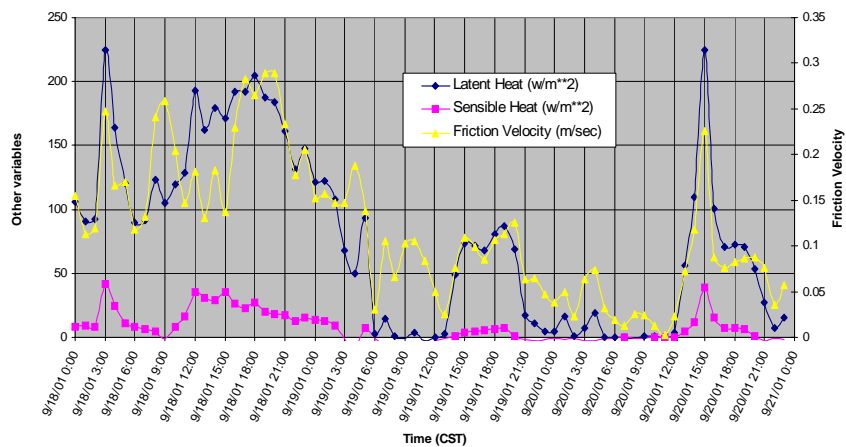


Hourly air and skin temperatures, wind speed, and relative humidity at SMI, September 18 through 20, 2001



### VRM

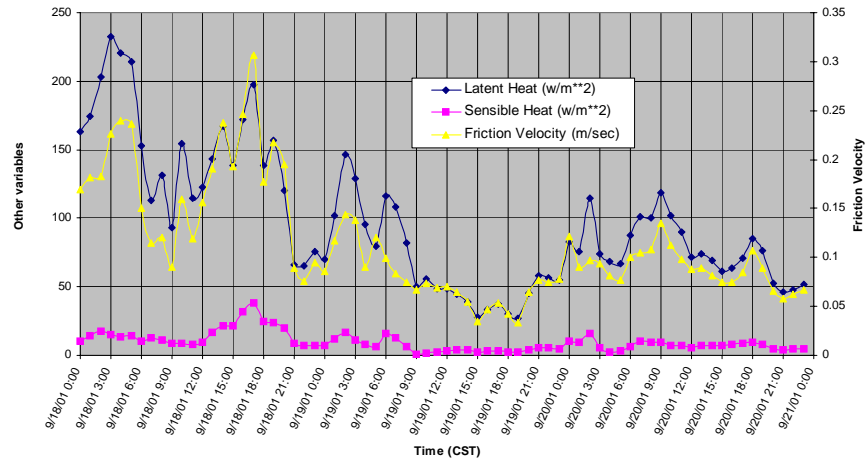
#### COARE Latent and Sensible Heat Fluxes and Friction Velocity



COARE latent and sensible heat fluxes and friction velocity at VRM, September 18 through 20, 2001



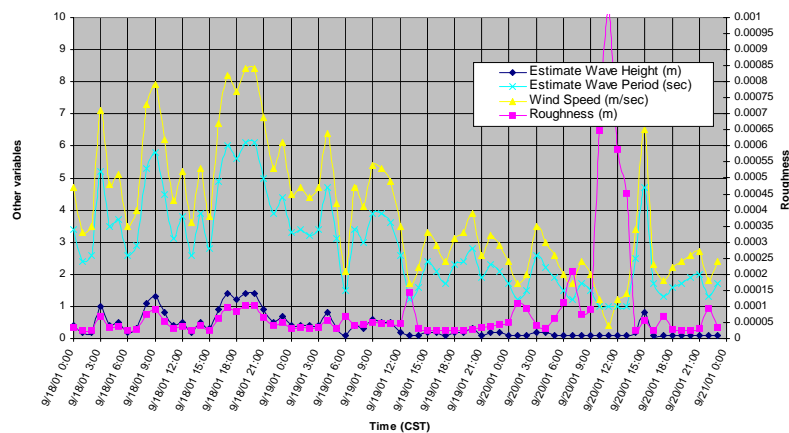
## SMI COARE Latent and Sensible Heat Fluxes and Friction Velocity



COARE latent and sensible heat fluxes and friction velocity at SMI, September 18 through 20, 2001



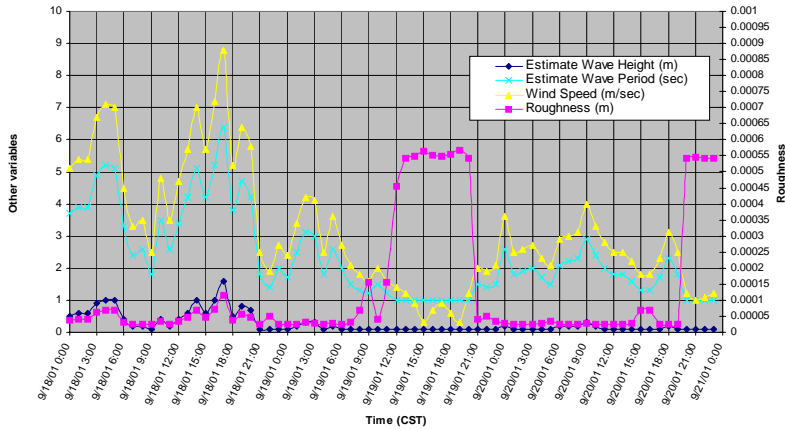
## VRM Estimated Wave Height and Period, Wind Speed, and Surface Roughness Length



Estimated wave height and period, wind speed, and surface roughness length at VRM, September 18 through 20, 2001



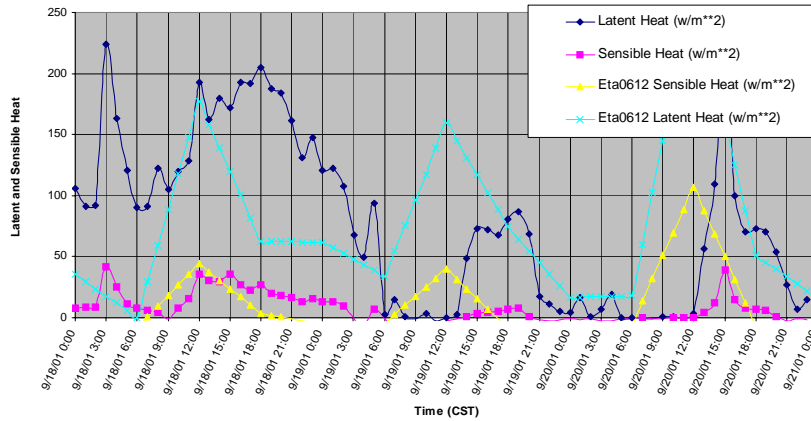
**SMI**  
**Estimated Wave Height and Period, Wind Speed, and Surface Roughness Length**



Estimated wave height and period, wind speed, and surface roughness length at SMI, September 18 through 20, 2001



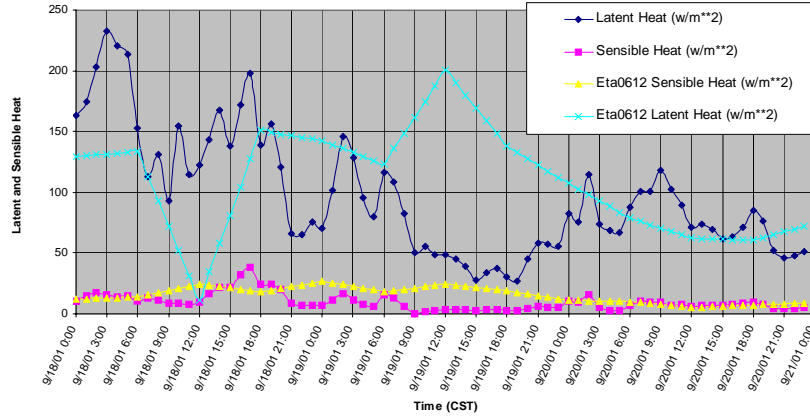
**VRM**  
**COARE and Eta Latent and Sensible Heat Fluxes**



COARE and Eta latent and sensible heat fluxes at VRM, September 18 through 20, 2001  
 Note: the four-digit number after Eta in the key indicates the forecast period (i.e., 0612 is the 6- to 12-hr forecast).



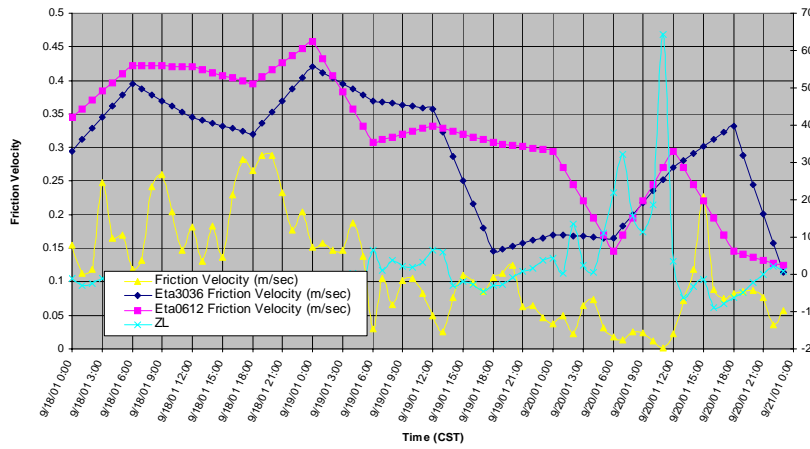
## SMI COARE and Eta Latent and Sensible Heat Fluxes



COARE and Eta latent and sensible heat fluxes at SMI, September 18 through 20, 2001  
 Note: the four-digit number after Eta in the key indicates the forecast period (i.e., 0612 is the 6- to 12-hr forecast).



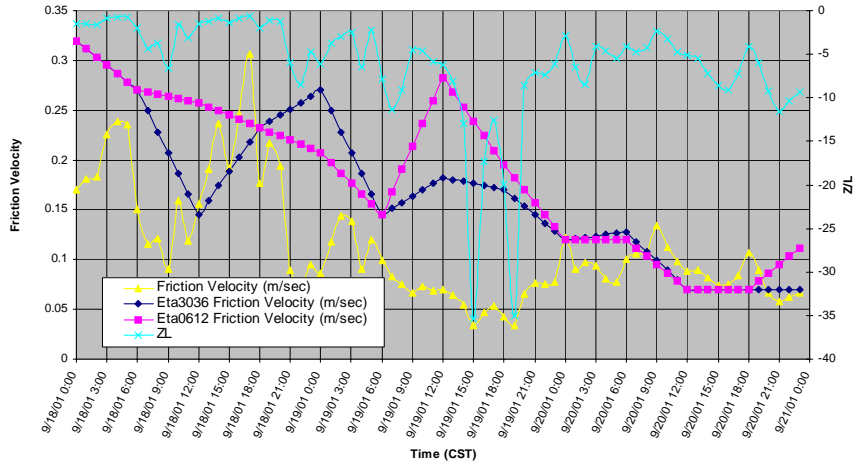
## VRM COARE and Eta Friction Velocity and z/L



COARE and Eta friction velocity and z/L at VRM, September 18 through 20, 2001  
 Note: the four-digit number after Eta in the key indicates the forecast period (i.e., 0612 is the 6- to 12-hr forecast and 3036 is the 30- to 36-hr forecast).



## SMI COARE and Eta Friction Velocity and z/L

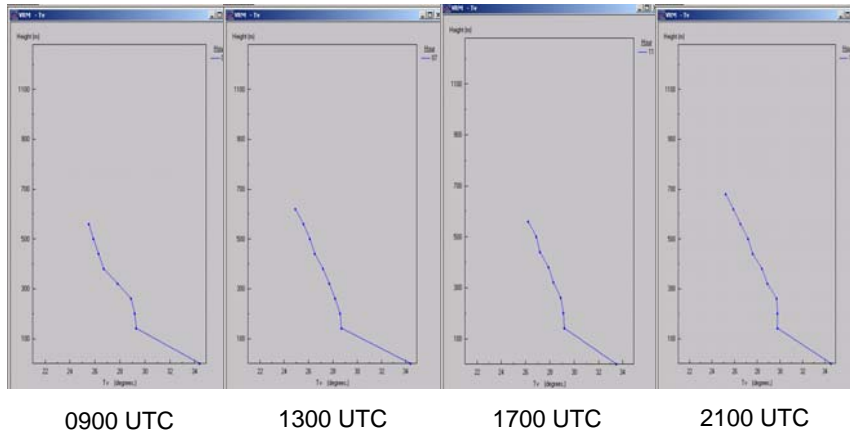


COARE and Eta friction velocity and z/L at SMI for September 18 through 20, 2001  
 Note: the four-digit number after Eta in the key indicates the forecast period  
 (i.e., 0612 is the 6- to 12-hr forecast and 3036 is the 30- to 36-hr forecast).

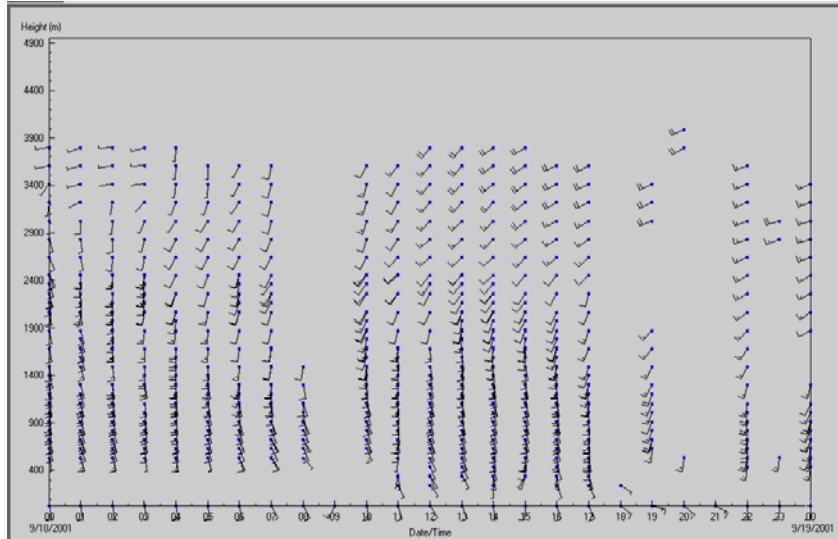


## T<sub>v</sub> at VRM, September 18, 2001

Reflectivity data did not reveal a specific mixing height during this period at either site.



## Winds at VRM, September 18, 2001



STI

## September 18, 2001, Summary

- No  $C_n^2$ , RASS, or wind data for SMI were available.
- Winds within the lowest 1500 m were light to moderate southerly.
- The  $T_v$  data showed an adiabatic profile with the exception of the lowest 100 m, which showed a superadiabatic layer because the air temperature was cooler than the skin temperature on this day.

STI

## Case Study Summary (1 of 5)

- January 20-24, 2000, was an active synoptic period, with frequent moderate winds, large fluctuations in air temperature, and large swings in latent and sensible heat.
- January 5-6, 2001, was a relatively cool period but with the air temperature warmer than the skin temperature most of the time, leading to frequent stable conditions.
- The July 1999 and September 2001 periods were typical summertime periods with air temperature usually cooler than skin temperature (i.e., unstable conditions) and with light to moderate winds.



## Case Study Summary (2 of 5)

- During most periods with an unstable temperature gradient, the COARE latent heat fluxes are about 5 to 10 times larger than the sensible heat fluxes. At these times, both latent and sensible heat fluxes are roughly proportional to  $u^*$ .
- Skin temperature is greater than air temperature most of the time in the four years of Gulf of Mexico data, as it is at most ocean sites at low to mid-latitudes.



### Case Study Summary (3 of 5)

- Latent heat is about 100 to 200 W/m<sup>2</sup> when air temperature is greater than skin temperature during typical summertime periods.
- During the January 20-25, 2000, case study, there was a period with a large skin temperature-minus-air temperature difference and large wind speed, which led to an exceptionally large latent heat flux of about 500 W/m<sup>2</sup>.
- Rarely does the latent heat flux become negative. During periods when skin temperature is less than air temperature and RH is high, its magnitude is less than 10 W/m<sup>2</sup>.



### Case Study Summary (4 of 5)

- Sensible heat flux is usually positive upward with magnitudes of 50 W/m<sup>2</sup> or less when skin temperature is greater than air temperature (i.e., most of the time).
- When skin temperature is less than air temperature, it becomes negative but has a magnitude less than 10 W/m<sup>2</sup>.
- Sensible heat flux is negative more often than latent heat flux because the sensible heat is negative whenever skin temperature is less than air temperature, but latent heat becomes negative only when skin temperature is less than air temperature and the RH of the air near the surface is very high.
- On average, the Eta-predicted u\*s are about 50% to a factor of 2 larger than the COARE u\*s.



## Case Study Summary (5 of 5)

- COARE latent and sensible heat fluxes agree fairly well with Eta forecasts of these fluxes.
- Agreement is best during warm summer periods for which COARE was derived and calibrated, and Eta also does well with these periods.
- Despite the fact that Eta appears to match the average and the maximum COARE latent and sensible heat fluxes well, the time variations are not well-simulated, especially at VRM.
- Part of the reason for the diurnal fluctuations forecasted by Eta may be that the grid cell in which VRM is located includes a large fraction of land surface.



## Recommendations: Collaboration (1 of 2)

Follow-on work involving collaboration with outside organizations:

- Work with NCEP to better understand over-water wind differences between the Eta model and observed profiler winds. Analysis has shown that Eta model winds are biased from the profiler winds.
- Compare Eta 12-km gridded predictions to observed data; compare the comparisons done with EDAS 40-km predictions/observations. The results will help guide how finer-resolution Eta model data should be used in high-resolution modeling efforts.



## Recommendations: Collaboration (2 of 2)

- Work with NOAA ETL to design a scheme to remove sea-clutter from profiler data so that mixing heights can be automatically estimated for this study and future studies using existing mixing height algorithms.
- Work with Christopher Fairall at NOAA to improve COARE predictions at high surface roughness. Roughness increases under very low wind speeds, which influences estimations of the boundary layer parameters.
- Make better use of BL measurements/analyses in other MMS-sponsored projects by reviewing plans and progress and recommending ways to incorporate BL data and analysis/modeling results.



## Recommendations: Publish

Plan a special issue (of JAM, JGR, or ?) on BL issues in the Gulf and prepare specific papers on the following:

- Eta/profiler wind comparisons.
- 3-year climatology of surface boundary layer parameters calculated using COARE in a shallow water ocean and modifications made to COARE (joint with NOAA?).
- Modeled and estimated mixing heights in the Gulf of Mexico.
- Results from other related MMS-sponsored projects.



## Recommendations: Analysis (1 of 2)

- Compare satellite-derived sea-surface temperatures to radiometer temperatures and buoy temperatures collected during this study. Accurate spatial sea-surface temperatures are important for accurate modeling.
- Compare estimates of sea-surface temperatures to the radiometer temperatures when clouds obscure the satellite's view of the Gulf (currently estimated using hole-filling techniques).
- Identify several additional periods of super-stable conditions in the existing data set (i.e. a period of southerly flow after a cold outbreak has cooled the water in the shallow portion of the Gulf) and perform a BL case study similar to other case studies.



## Recommendations: Analysis (2 of 2)

- Determine the best scheme for estimating wave height and frequency as a function of water depth from wind speed alone. When wave data is not available at the platforms, inaccurate estimations of wave characteristics can result in inaccurate estimations of surface roughness, which influence boundary layer parameterizations. Evaluate the roughness estimations estimated from wind speed alone; compare to observed wave data.
- Integrate onshore and offshore air quality data into the meteorological data set and analyses performed during this project. This will expand the applicability of the results and provide further evaluation of the methods used.
- Revise the NEGOM Met Statistical Expert System to use improved model output and now-available data; this will result in a more accurate tool for visualization of meteorological data and of estimates of transport and dispersion from specific locations offshore.



## Recommendations: Modeling

- Update the Calmet model to better estimate mixing heights and perform additional comparisons of observation-based estimations of mixing heights to model mixing heights. Currently, CALMET does a poor job estimating mixing heights in the Gulf of Mexico.
- Update the CALPUFF dispersion runs using new CALMET output created with an improved mixing height scheme. Compare the new runs to those created as part of this project.
- Compare CALMET diagnostic model runs to MM5 prognostic model runs and observational data and create best estimates of gridded mixing heights and winds.
- Modify the way diagnostic and prognostic models treat the diffuse shoreline of the Gulf; operate the models and compare results with observations.



## Recommendations: Measurements (1 of 2)

- Collocate a radiometer and underwater temperature sensor to determine the relationship and the accuracy of the COARE estimated warm layer and cool skin effect. This effect is used to estimate skin temperature at buoys, an important parameter for the estimation of boundary layer parameters and for model initial conditions. Work with NOAA to adjust COARE as needed.
- On a platform, operate temperature, relative humidity, and wind sensors at two heights within the surface layer, as well as a solar radiometer. Use this data to verify COARE estimations of boundary layer parameters that used surface boundary layer data at only one level.



## Recommendations: Measurements (2 of 2)

- Continue routine operations of surface and upper-air meteorological parameters at the IMPROVE site in the Mississippi River Delta.
- Routinely operate a mini-Sodar, a profiler/RASS system, and a surface meteorological monitoring system on a platform to obtain wind and temperature measurements through the depth of the surface layer and boundary layer. This data could be used for routine comparisons with Eta, for routine estimates of BL characteristics, for real-time modeling, and for special research studies involving BL gradients on- and off-shore, etc. The addition of the mini-Sodar would fill the measurement hole that exists from 30 m to about 200 m; this hole is often the location of plumes.





### The Department of the Interior Mission

As the Nation's principal conservation agency, the Department of the Interior has responsibility for most of our nationally owned public lands and natural resources. This includes fostering sound use of our land and water resources; protecting our fish, wildlife, and biological diversity; preserving the environmental and cultural values of our national parks and historical places; and providing for the enjoyment of life through outdoor recreation. The Department assesses our energy and mineral resources and works to ensure that their development is in the best interests of all our people by encouraging stewardship and citizen participation in their care. The Department also has a major responsibility for American Indian reservation communities and for people who live in island territories under U.S. administration.



### The Minerals Management Service Mission

As a bureau of the Department of the Interior, the Minerals Management Service's (MMS) primary responsibilities are to manage the mineral resources located on the Nation's Outer Continental Shelf (OCS), collect revenue from the Federal OCS and onshore Federal and Indian lands, and distribute those revenues.

Moreover, in working to meet its responsibilities, the **Offshore Minerals Management Program** administers the OCS competitive leasing program and oversees the safe and environmentally sound exploration and production of our Nation's offshore natural gas, oil and other mineral resources. The MMS **Minerals Revenue Management** meets its responsibilities by ensuring the efficient, timely and accurate collection and disbursement of revenue from mineral leasing and production due to Indian tribes and allottees, States and the U.S. Treasury.

The MMS strives to fulfill its responsibilities through the general guiding principles of: (1) being responsive to the public's concerns and interests by maintaining a dialogue with all potentially affected parties and (2) carrying out its programs with an emphasis on working to enhance the quality of life for all Americans by lending MMS assistance and expertise to economic development and environmental protection.